

Electronic Thesis and Dissertation Repository

7-26-2021 2:00 PM

Nanoorthogonal Surface Modifications of Gold Nanoparticles and Nanoclusters through Strain-Promoted Cycloaddition Chemistry

Praveen N. Gunawardene, *The University of Western Ontario*

Supervisor: Mark S. Workentin, *The University of Western Ontario*

A thesis submitted in partial fulfillment of the requirements for the Doctor of Philosophy degree in Chemistry

© Praveen N. Gunawardene 2021

Follow this and additional works at: <https://ir.lib.uwo.ca/etd>

 Part of the [Materials Chemistry Commons](#), and the [Organic Chemistry Commons](#)

Recommended Citation

Gunawardene, Praveen N., "Nanoorthogonal Surface Modifications of Gold Nanoparticles and Nanoclusters through Strain-Promoted Cycloaddition Chemistry" (2021). *Electronic Thesis and Dissertation Repository*. 8013.
<https://ir.lib.uwo.ca/etd/8013>

This Dissertation/Thesis is brought to you for free and open access by Scholarship@Western. It has been accepted for inclusion in Electronic Thesis and Dissertation Repository by an authorized administrator of Scholarship@Western. For more information, please contact wlsadmin@uwo.ca.

Abstract

This thesis explores the preparation of thiolated gold nanoparticles (AuNPs) and thiolated gold nanoclusters (AuNCs) capable of undergoing post-assembly surface modifications using two common “*bioorthogonal*” click reactions: the strain-promoted alkyne-azide cycloaddition (SPAAC) reaction (which occurs between a strained-alkyne and an azide) and the strain-promoted alkyne-nitrone cycloaddition (SPANC) reaction (which occurs between a strained-alkyne and a nitron). Due to their rapid and modifiable reaction kinetics, high chemoselectivity, and stability of the reactive partners, these reactions were originally designed to tether functional substrates to biologically sensitive biomolecules, without altering their structure or perturb the biologically sensitive environments in which they operate in. The research presented herein explores using the SPAAC and SPANC reactions as “*nanoorthogonal*” click reactions, translating their advantageous characteristics towards surface modifications of thiolated AuNPs and AuNCs in an efficient and straightforward manner without perturbing their chemically sensitive structures.

Chapter 2 describes the development of a reactive AuNP platform with an aliphatic strained-alkyne (specifically, bicyclo[6.1.0]nonyne (BCN)) tethered to its surface. This platform could undergo both *interfacial* SPAAC (*I*-SPAAC) and *interfacial* SPANC (*I*-SPANC), whose reaction kinetics could be tuned through structural alterations to the complementary azide/nitrone dipolar species, respectively. When highly electron-deficient dipolar species were used, rapid surface modifications could be accomplished. Such predictable alterations to the kinetic profiles of *I*-SPAAC and *I*-SPANC allows exclusive reactivity with one highly reactive dipolar species in the presence of a less reactive dipolar species, which altogether provides an efficient and versatile route towards derivatizing AuNP surfaces. To further expand the scope of such rapid modifications of AuNP surfaces, **Chapter 3** explores the development of a nitron-terminated AuNP platform, in which the surface nitron dipolar species are delocalized into highly electron deficient pyridinium groups. In a prototype kinetic study, nitrones with pyridinium groups on the N α of the nitrones exhibited rapid reaction kinetics with BCN, whose reaction kinetics could be altered through modifications of the C α substituents of the nitron. Unfortunately, due to the high reactivity of the pyridinium-functionalized nitron group, attempts to incorporate this rapidly reactive moiety to the AuNP surface was not successful due to the synthetic incompatibilities

between pyridinium-functionalized nitrones and thiols. However, the development of such rapid SPANC chemistry serves as a promising tool for modifications of other nanomaterial systems in which thiols are not present.

Chapter 4 describes the first example of an azide-modified AuNC system (specifically, the $[\text{Au}_{25}(\text{SR})_{18}]^{-1}$ system) that could undergo post-assembly *cluster-surface* SPAAC (*CS-SPAAC*) chemistry with complementary strained-alkynes. The molecular structure of this azide-modified platform (specifically $[\text{Au}_{25}(\text{SCH}_2\text{CH}_2\text{-}p\text{-C}_6\text{H}_4\text{-N}_3)_{18}]^{-1}$ with *p*-azidophenylethanethiolate as the surface ligand) is reported. Whereas larger AuNP systems tend to be more rigid, the structures and integrity of smaller AuNC systems are more chemically sensitive, and the ability to conduct *CS-SPAAC* in a nanoorthogonal manner without altering the internal structure represents an exciting new paradigm towards AuNC surface modifications. **Chapter 5** explores how the reactivity, structure and physical properties of azide-modified $[\text{Au}_{25}(\text{SR})_{18}]^{-1}$ platforms are affected by changing the regioisomeric form of the azide-modified surface ligands. Two isomeric forms of $[\text{Au}_{25}(\text{SCH}_2\text{CH}_2\text{-}p\text{-C}_6\text{H}_4\text{-N}_3)_{18}]^{-1}$ were developed: $[\text{Au}_{25}(\text{SCH}_2\text{CH}_2\text{-}m\text{-C}_6\text{H}_4\text{-N}_3)_{18}]^{-1}$ and $[\text{Au}_{25}(\text{SCH}_2\text{CH}_2\text{-}o\text{-C}_6\text{H}_4\text{-N}_3)_{18}]^{-1}$. The molecular structures of the neutrally charged forms of these three isomers are reported. It was found that although the physical properties appeared to be largely unaffected, the structure and reactivity of these azide-modified platforms appear to be dependent on the regioisomeric form of the azide-modified surface ligand. **Chapter 6** describes the first example of a ferrocene-modified $[\text{Au}_{25}(\text{SR})_{18}]^{-1}$ system, which could be accomplished through a *CS-SPAAC* reaction between the azide-modified $[\text{Au}_{25}(\text{SCH}_2\text{CH}_2\text{-}p\text{-C}_6\text{H}_4\text{-N}_3)_{18}]^{-1}$ platform and BCN-terminated ferrocene, which highlights the true power of conducting *CS-SPAAC* chemistry on the surface of $[\text{Au}_{25}(\text{SR})_{18}]^{-1}$ frameworks to incorporate large, functional substrates.

In total, this work describes and explores innovative methodologies that can be used to conduct chemical modifications of AuNP and AuNC surfaces using SPAAC and SPANC, in an efficient and nanoorthogonal manner without altering the parent structures. Using such versatile and effective strategies, it will be possible to develop functional variants of these popular nanomaterial systems more easily for application-based research.

Keywords

Gold Nanoparticles, Gold Nanoclusters, Nanomaterials, Bioorthogonal Chemistry, Nanoorthogonal Chemistry, Click Chemistry, Interfacial Reactions, Surface-Functionalization, Strained-Alkyne, Azide, Nitron, Strain-Promoted Alkyne-Azide Cycloaddition, Strain-Promoted Alkyne-Nitron Cycloaddition, Cluster-Surface Strain-Promoted Alkyne-Azide Cycloaddition

Lay Summary

Gold nanoparticles (AuNPs) and gold nanoclusters (AuNCs) are popular nanomaterial frameworks that are promising candidates for application-based research in nanomedicine, bioimaging and catalysis. Both material frameworks have internal gold-containing cores in the nanometer size regime, which are stabilized by an external monolayer of surface ligands. The key distinction between them is that AuNPs are larger (> 2 nm) and typically polydisperse (i.e. broad size range), while AuNCs are smaller (< 2 nm) and typically monodisperse (i.e. narrow size range). To optimize the practicality of these nanomaterial systems, it is important to modify the chemical composition of their external surfaces with functional substrates that can tailor them for desired applications. Common methodologies that are currently employed to achieve such surface modifications share many mutual drawbacks that limit the ability to effectively modify their surfaces. This is caused by the chemical sensitivity of these nanomaterials and the synthetic challenges in developing functional substrates that can be incorporated onto the AuNP and AuNC surfaces. For these reasons, there is a need to explore alternate strategies to incorporate functionality to the surfaces of AuNPs and AuNCs.

This thesis explores the preparation of AuNPs and AuNCs with surface ligands that can undergo post-assembly surface modifications using the strain-promoted alkyne-azide cycloaddition reaction (SPAAC) and strain-promoted alkyne-nitrone cycloaddition reaction (SPANC). These “*bioorthogonal*” reactions are largely reserved for tethering functional substrates to biologically sensitive biomolecules in an efficient and selective manner without perturbing the biologically sensitive environments in which they reside and operate in. The goal of this thesis is to demonstrate that the SPAAC and SPANC reactions can also be used as “*nanoorthogonal*” reactions, which can be used to efficiently modify the surfaces of chemically sensitive AuNPs and AuNCs in a straightforward and robust manner without the limitations of other common surface modification strategies.

Co-Authorship Statement

The work described in this thesis contains contributions from the author, as well as co-authors: Max Weisman, Dr. Wilson Luo, Alex M. Polgar, Julia Martin, Jonathan M. Wong, Prof. Pierangelo Gobbo, Prof. Zhifeng Ding, Prof. John F. Corrigan and Prof. Mark S. Workentin. The contributions of each are described below.

Chapter 1 was written by the author and edited by Prof. Mark S. Workentin.

Chapter 2 describes a series of compounds and AuNPs that were synthesized and characterized, for the most part, by the author. Conceptual designs and experimental strategies were developed by author, Prof. Pierangelo Gobbo and Prof. Mark S. Workentin. Prof. Pierangelo Gobbo (at the time a graduate student), supervised by Prof. Mark S. Workentin, helped to develop synthetic strategies for AuNPs, and conducted TEM measurements of AuNP samples. Max Weisman, supervised by Prof. Mark S. Workentin, helped to synthesize AuNPs. All other experiments were conducted by the author. The chapter was written by author in manuscript format for submission, with input and final edits from Prof. Mark S. Workentin.

Gunawardene, P.N.; Gobbo, P.; Weismann, M.; Workentin, M.S. Towards the Development of Self-Sorting Nanomaterials Through Kinetically Directed Orthogonal Control over Interfacial Surface Chemistry. *Manuscript prepared for submission.*

Chapter 3 describes a series of nitrene compounds that were synthesized and characterized, for the most part, by the author. Conceptual designs and experimental strategies were developed by author and Prof. Mark S. Workentin. Dr. Wilson Luo (at the time a graduate student), supervised by Prof. Mark S. Workentin, helped to synthesize and characterize some of the nitrene and cycloadduct compounds. Alex M. Polgar, supervised by Prof. John F. Corrigan, carried out DFT analysis. All other experiments were performed by the author. The manuscript was written by the author, with input and final edits from Prof. John F. Corrigan and Prof. Mark S. Workentin.

Gunawardene, P.N.; Luo, W.; Polgar, A.M.; Corrigan, J.F.; Workentin, M.S. Highly Electron-Deficient Pyridinium-Nitrenes for Rapid and Tunable Inverse-Electron-Demand Strain-Promoted Alkyne-Nitrene Cycloaddition. *Org. Lett.* **2019**, *21* (14), 5547-5551.

Chapter 4 describes an AuNC project in which all synthesis and characterization were completed by the author. Conceptual designs and experimental strategies were developed by author. The manuscript was written by the author, with input and final edits from Prof. John F. Corrigan and Prof. Mark S. Workentin.

Gunawardene, P.N.; Corrigan, J.F.; Workentin, M.S. Golden Opportunity: A Clickable Azide-Functionalized $[\text{Au}_{25}(\text{SR})_{18}]$ Nanocluster Platform for Interfacial Surface Modifications. *J. Am. Chem. Soc.* **2019**, *141* (30), 11781-11785.

Chapter 5 describes a series of AuNCs and compounds that were synthesized and characterized, for the most part, by the author. Conceptual designs and experimental strategies were developed by author. Julia Martin, supervised by Prof. Mark S. Workentin, was a thesis student who helped to synthesize AuNCs and compounds under author's supervision. Jonathan M. Wong, supervised by Prof. Zhifeng Ding, conducted electrochemical measurements. All other experiments were performed by the author. The chapter was written by the author in manuscript format for submission, with input and final edits from Prof. John F. Corrigan and Prof. Mark S. Workentin.

Gunawardene, P.N.; Martin, J.; Wong, J.M.; Ding, Z.; Corrigan, J.F.; Workentin, M.S. Controlling the Structure, Properties and Surface Reactivity of Clickable Azide-Functionalized $\text{Au}_{25}(\text{SR})_{18}$ Nanocluster Platforms Through Regioisomeric Ligand Modifications. *Manuscript prepared for submission.*

Chapter 6 describes an AuNC project in which the synthesis and characterization were completed, for the most part, by the author. Conceptual designs and experimental strategies were developed by author. Jonathan M. Wong, supervised by Prof. Zhifeng Ding, conducted electrochemical measurements. All other experiments were performed by the author. The chapter was written by the author in manuscript format for submission, with input and final edits from Prof. John F. Corrigan and Prof. Mark S. Workentin.

Gunawardene, P.N.; Wong, J.M.; Ding, Z.; Corrigan, J.F.; Workentin, M.S. Expanding the Frontiers of Ultrasmall Gold Nanocluster Surface Composition through Cluster-Surface Click Chemistry: A Ferrocenyl-Modified $\text{Au}_{25}(\text{SR})_{18}$ Nanocluster. *Manuscript prepared for submission.*

Chapter 7 was written by the author and edited by Prof. Mark S. Workentin.

Acknowledgements

First and foremost, I would like to thank my supervisor, Mark Workentin. Thank you for your guidance and patience, especially when experiments were not working well (which was quite often) and giving me the freedom to explore my creativity as a chemist and graduate student. It is the supervisor that you were to me that I attribute my success to, and I am truly thankful to have had you as a supervisor!

Next, in no particular order, I'd like to acknowledge all past and present Workentin Research Group members: Dr. Wilson Luo, Prof. Pierangelo Gobbo, Dr. Mahdi Hesari, Dr. Sara Ghiassian, Dr. Sung Ju Cho, Alexander Van Belois, Julia Martin, Alec Ray Sherman, Andy Lim, Jun Hyeong Park, Kyle Classen, Johanna De Jong, Tomasso Romagnoli, Komal Patel, Max Weisman, Rajeshwar Vasdev, Kathleen Winger, Becky Wright, Mariachiara Zuin, Leila Zhu, Jennifer Keir, Alexis Prestwich, Sydney Legge and Christian Petrozza. I would also like to thank Alexander M. Polgar from the Corrigan Research Group and Jonathan M. Wong for the Ding Research Group. Thank you all for your support and friendship, which created such a fun environment to work in over the years.

I wish to express my supreme thanks to Prof. John F. Corrigan. In the middle of my graduate studies when I transitioned into working with nanoclusters, your patient guidance and advice helped me greatly in accomplishing many of my successes with these difficult systems.

I would also like to thank the members of the Department of Chemistry faculty and support staff that I had the pleasure to either work with or allowed me to use their equipment over these past years: Mathew Wilans, Yves Rambour, John Vanstone, John Aukema, Barakat Misk, Monica Chirigel, Marylou Hart, Yuhua Chen, Darlene McDonald, Anna Vandendries-Barr, Clara Fernandes, Prof. Zhifeng Ding, Prof. Michael Kerr, Prof. Joe Gilroy, Prof. Kim Baines, Prof. Paul Ragona. I would like to give a special thank you to Dr. Paul Boyle in the X-ray Facility for teaching me how to refine and solve very complex X-ray structures, and Doug Hairsine in the Mass Spectrometry facility for his patience and persistence in obtaining spectra that were very difficult to acquire.

A special thanks to my examiners for taking time out of their busy schedules to read and evaluate my doctoral thesis: Prof. Robert Hudson, Prof. Johanna Blacquiere, Prof. Amin Rizkalla and Prof. Kevin Stamplecoskie.

Furthermore, thank to you my mom and dad (“ammi” and “thathi”) and my brother (“mali”) for all your support and patience during this process. I would not have made it this far if it were not for you being by my side over these many years and your continued and indomitable faith in me. I will always be greatly appreciative that you always stood by me no matter what, and I love you dearly! I would also like to thank my in-laws: the Somasundaram family. I could not have asked for a better second family, and I love the time we spend together (especially our hikes) and I love you all.

Finally, I would like to thank my wife, Vaishnavi Somasundaram, a former Workentin Research Group member. We started off as friends, working next to each other on our own projects in the same lab and spending time getting to know each other, which blossomed into a love that I could not imagine my life without. I look forward to the upcoming roads ahead!

Table of Contents

Abstract.....	i
Lay Summary	iv
Co-Authorship Statement	v
Acknowledgements	viii
Table of Contents	x
List of Figures.....	xxiv
Chapter 1	xxiv
Chapter 2.....	xxvii
Chapter 3.....	xxxii
Chapter 4.....	xxxvii
Chapter 5.....	xli
Chapter 6.....	xlvi
Chapter 7.....	xlvii
List of Schemes.....	xlviii
Chapter 1	xlviii
Chapter 2.....	xlix
Chapter 3.....	xlix
Chapter 4.....	1
Chapter 5.....	1

Chapter 6.....	1
Chapter 7.....	1
List of Tables	lii
Chapter 3.....	lii
List of Appendices.....	liv
List of Abbreviations	lv
Chapter 1	1
1 Introduction – Strain-Promoted Click Chemistry for Nanoorthogonal Surface Modifications of Gold Nanoparticles and Gold Nanoclusters	1
1.1 “Golden Nanochemistry”.....	1
1.2 Gold Nanoparticles	2
1.2.1 Structure of Gold Nanoparticles	2
1.2.2 Synthesis of Gold Nanoparticles.....	3
1.2.3 Properties of Gold Nanoparticles.....	6
1.2.4 Applications of Gold Nanoparticles.....	8
1.3 Gold Nanoclusters.....	12
1.3.1 Structure of Gold Nanoclusters.....	12
1.3.2 Synthesis of Gold Nanoclusters	12
1.3.3 The Au ₂₅ (SR) ₁₈ Nanocluster Framework.....	16
1.3.4 Properties of the Au ₂₅ (SR) ₁₈ Framework.....	18

1.3.5 Applications of the Au ₂₅ (SR) ₁₈ Framework.....	21
1.4 Surface Modifications of AuNPs and AuNCs	24
1.5 Bioorthogonal Click Chemistry	27
1.5.1 General Characteristics of Bioorthogonal Click Reactions	27
1.5.2 Common Bioorthogonal Click Reactions	30
1.5.3 Strain-Promoted Alkyne-Azide Cycloaddition (SPAAC) Reaction	32
1.5.4 Strain-Promoted Alkyne-Nitrone Cycloaddition (SPANC) Reaction	34
1.5.5 Kinetically-Variable SPAAC/SPANC.....	35
1.6 Scope of Thesis	36
1.7 References.....	42
Chapter 2	61
2 Towards the Design of Self-Sorting Nanomaterials Through Kinetically Directed Orthogonal Control over Interfacial Surface Chemistry.....	61
2.1 Introduction.....	61
2.2 Results and Discussion	63
2.3 Conclusions.....	68
2.4 Acknowledgments.....	68
2.5 References.....	68
2.6 Supporting Information.....	71
2.6.1 General Methods and Methods	71

2.6.2 Experimental Procedures	72
2.6.2.1 Synthesis of HS-EG ₃ -Me	72
2.6.2.2 Synthesis of AuNP-OMe	73
2.6.2.3 Synthesis of STrityl-EG ₄ -NH ₂	73
2.6.2.4 Synthesis of HS-EG ₄ -NH ₂	73
2.6.2.5 Synthesis of AuNP-NH ₂	74
2.6.2.6 Synthesis of BCN _{exo} -OH	74
2.6.2.7 Synthesis of BCN _{exo} -O-pNP.....	75
2.6.2.8 Synthesis of AuNP-BCN	75
2.6.2.9 Synthesis of 1-azido-3-propanol (azide 1)	75
2.6.2.10 Synthesis of 1-azido-4-nitrobenzene (azide 4).....	76
2.6.2.11 Synthesis of 4-azidopyridine (azide 5).....	76
2.6.2.12 Synthesis of 1-azido-2,3,4,5,6-pentafluorobenzene (azide 6).....	77
2.6.2.13 Synthesis of <i>N</i> -methyl- <i>C</i> -nitrophenyl-nitrone (nitrone 1).....	77
2.6.2.14 Synthesis of <i>N</i> -phenylhydroxylamine	78
2.6.2.15 Synthesis of <i>N</i> -phenyl- <i>C</i> -methoxyphenyl-nitrone (nitrone 2)	78
2.6.2.16 Synthesis of <i>N</i> -phenyl- <i>C</i> -phenyl-nitrone (nitrone 3)	79
2.6.2.17 Synthesis of <i>N</i> -phenyl- <i>C</i> -nitrophenyl-nitrone (nitrone 4).....	79
2.6.2.18 Synthesis of <i>N</i> -phenyl- <i>C</i> -pyridine-nitrone (nitrone 5).....	79
2.6.2.19 Synthesis of <i>N</i> -cyanophenyl- <i>C</i> -pyridine-nitrone (nitrone 6)	80
2.6.3 Experimental Spectra and Diagrams.....	81
2.6.3.1 Experimental Spectra for HS-EG ₃ -Me.....	81
2.6.3.2 Experimental Spectra for AuNP-OMe.....	82
2.6.3.3 Experimental Spectra for HS-EG ₄ -NH ₂	83
2.6.3.4 Experimental Spectra for AuNP-NH ₂	84
2.6.3.5 Experimental Spectra for BCN _{exo} -OH.....	86
2.6.3.6 Experimental Spectra for BCN _{exo} -O-pNP	86
2.6.3.7 Experimental Spectra for AuNP-BCN	87
2.6.3.8 Experimental Spectra for 1-azido-3-propanol (azide 1).....	89
2.6.3.9 Experimental Spectra for 1-azido-4-nitrobenzene (azide 4)	90
2.6.3.10 Experimental Spectra for 4-azidopyridine (azide 5)	91
2.6.3.11 Experimental Spectra for 1-azido-2,3,4,5,6-pentafluorobenzene (azide 6)	92
2.6.3.12 Experimental Spectra for <i>N</i> -methyl- <i>C</i> -nitrophenyl-nitrone (nitrone 1)	93

2.6.3.13 Experimental Spectra for <i>N</i> -phenyl- <i>C</i> -methoxyphenyl-nitrone (nitrone 2).....	94
2.6.3.14 Experimental Spectra for <i>N</i> -phenyl- <i>C</i> -phenyl-nitrone (nitrone 3).....	95
2.6.3.15 Experimental Spectra for <i>N</i> -phenyl- <i>C</i> -nitrophenyl-nitrone (nitrone 4)	96
2.6.3.16 Experimental Spectra for <i>N</i> -phenyl- <i>C</i> -pyridine-nitrone (nitrone 5)	97
2.6.3.17 Experimental Spectra for <i>N</i> -cyanophenyl- <i>C</i> -pyridine-nitrone (nitrone 6).....	98
2.6.4 Thermogravimetric Analysis of AuNP-BCN.....	99
2.6.4.1 General Experimental Details	99
2.6.4.2 Experimental Spectra for TGA Analysis	99
2.6.5 Kinetic Measurements	101
2.6.5.1 General Experimental Details	101
2.6.5.2 Kinetic Measurements for 1-azido-3-propanol (azide 1).....	102
2.6.5.3 Kinetic Measurements for 4-azidoanisole (azide 2).....	103
2.6.5.4 Kinetic Measurements for azidobenzene (azide 3)	104
2.6.5.5 Kinetic Measurements for 1-azido-4-nitrobenzene (azide 4).....	105
2.6.5.6 Kinetic Measurements for 4-azidopyridine (azide 5).....	106
2.6.5.7 Kinetic Measurements for 1-azido-2,3,4,5,6-pentafluorobenzene (azide 6).....	107
2.6.5.8 Kinetic Measurements for <i>N</i> -methyl- <i>C</i> -nitrophenyl-nitrone (nitrone 1).....	108
2.6.5.9 Kinetic Measurements for <i>N</i> -phenyl- <i>C</i> -methoxyphenyl-nitrone (nitrone 2)	109
2.6.5.10 Kinetic Measurements for <i>N</i> -phenyl- <i>C</i> -phenyl-nitrone (nitrone 3)	110
2.6.5.11 Kinetic Measurements for <i>N</i> -phenyl- <i>C</i> -nitrophenyl-nitrone (nitrone 4).....	111
2.6.5.12 Kinetic Measurements for <i>N</i> -phenyl- <i>C</i> -pyridine-nitrone (nitrone 5).....	112
2.6.5.13 Kinetic Measurements for <i>N</i> -cyanophenyl- <i>C</i> -pyridine-nitrone (nitrone 6)	113
2.6.6 Competition Experiments for AuNP-BCN	114
2.6.6.1 General Experimental Details	114
2.6.6.2 ¹ H NMR Spectra for Competition Experiment between azide 1 and nitrone 6.....	115
2.6.6.3 ¹ H NMR Spectra for Competition Experiment between azide 3 and nitrone 4.....	116
2.6.6.4 ¹ H NMR Spectra for Competition Experiment between azide 4 and nitrone 4.....	117
2.6.6.5 ¹ H NMR Spectra for Competition Experiment between azide 5 and nitrone 2.....	118
2.6.6.6 ¹ H NMR Spectra for Competition Experiment between azide 6 and nitrone 1.....	119
2.6.7. References for Supporting Information	120
Chapter 3	121

3 Highly Electron-Deficient Pyridinium-Nitrones for Rapid and Tunable Inverse-Electron-Demand Strain-Promoted Alkyne-Nitrone Cycloaddition to Bicyclo[6.1.0]nonyne..... 121

3.1 Introduction.....	121
3.2 Results and Discussion	123
3.2.1 Towards the Development of Pyridinium-Functionalized Gold Nanoparticles	128
3.3 Conclusion	131
3.4 Acknowledgements.....	131
3.5 References.....	132
3.6 Supporting Information.....	134
3.6.1 General Materials and Methods.....	134
3.6.2 Synthesis of Nitrones	136
3.6.2.1 Synthesis of <i>N</i> -(4-methoxyphenyl)- <i>C</i> -(3-pyridine) Nitrone (2a)	136
3.6.2.2 Synthesis of <i>N</i> -(4-methoxyphenyl)- <i>C</i> -(3-methylpyridinium) Nitrone (3a).....	136
3.6.2.3 Synthesis of <i>N</i> -phenyl- <i>C</i> -(3-pyridine) Nitrone (2b).....	137
3.6.2.4 Synthesis of <i>N</i> -phenyl- <i>C</i> -(3-methylpyridinium) Nitrone (3b)	138
3.6.2.5 Synthesis of <i>N</i> -(4-cyanophenyl)- <i>C</i> -(3-pyridine) Nitrone (2c)	138
3.6.2.6 Synthesis of <i>N</i> -(4-cyanophenyl)- <i>C</i> -(3-methylpyridinium) Nitrone (3c).....	139
3.6.2.7 Synthesis of <i>N</i> -phenyl- <i>C</i> -phenyl Nitrone (4)	139
3.6.3 Synthesis of Cyclooctynes	140
3.6.3.1 Synthesis of BCN-OH _{exo} (5)	140
3.6.3.2 Synthesis of (<i>Z</i>)-5,6-dibromocyclooct-1-ene (6a).....	140
3.6.3.3 Synthesis of (<i>Z</i>)-cyclooct-1-ene-5-yne (6b).....	141
3.6.4 Synthesis of TEG Ligands	141
3.6.4.1 Synthesis of Nitrobenzyl-TEG-OH (A)	141
3.6.4.2 Synthesis of Nitrobenzyl-TEG-OTs (B)	142
3.6.4.3 Synthesis of Nitrobenzyl-TEG-Thioacetate (C).....	142

3.6.4.4 Synthesis of Synthesis of (C-Pyridinium, N-Phenyl-TEG-Thioacetate)-Nitron (E).....	143
3.6.5 Molecular Structures Of Nitrones	144
3.6.6 General Synthesis of Cycloadducts	147
3.6.6.1 Synthesis of Cycloadduct between BCN _{exo} -OH (5) with Nitrones 3a, 3b, 3c.....	147
3.6.6.2 Synthesis of Cycloadduct between BCN _{exo} -OH with Nitrone 4 and 2b.....	148
3.6.6.3 Synthesis of Cycloadduct between DBCO-amine with Nitrone 3c	148
3.6.6.4 Synthesis of Cycloadduct between (Z)-cyclooct-1-ene-5-yne (6b) with Nitrone 3c.....	148
3.6.7 NMR Spectra of Nitrones	149
3.6.7.1 Experimental Spectra for N-(4-methoxyphenyl)-C-(3-pyridine) nitron (Nitron 2a)	149
3.6.7.2 Experimental Spectra for N-(4-methoxyphenyl)-C-(3-methylpyridinium) nitron (Nitron 3a)	150
3.6.7.3 Experimental Spectra for N-phenyl-C-(3-pyridine) nitron (Nitron 2b).....	151
3.6.7.4 Experimental Spectra for N-phenyl-C-(3-methylpyridinium) nitron (Nitron 3b)	151
3.6.7.5 Experimental Spectra for N-(4-cyanophenyl)-C-(3-pyridine) nitron (Nitron 2c).....	152
3.6.7.6 Experimental Spectra for N-(4-cyanophenyl)-C-(3-methylpyridinium) nitron (Nitron 3c)	152
3.6.7.7 Experimental Spectra for N-phenyl-C-phenyl nitron (Nitron 4)	153
3.6.8 NMR Spectra of TEG Ligands	154
3.6.8.1 Experimental Spectra for Nitrobenzyl-TEG-OH (A).....	154
3.6.8.2 Experimental Spectra for Nitrobenzyl-TEG-OTs (B).....	155
3.6.8.3 Experimental Spectra for Nitrobenzyl-TEG-Thioacetate (C).....	156
3.6.8.4 Experimental Spectra for (C-Pyridinium, N-Phenyl-TEG-Thioacetate)-Nitron (E)	157
3.6.9 NMR Spectra of Cyclooctynes	158
3.6.9.1 Experimental Spectra for BCN _{exo} -OH (5)	158
3.6.9.2 Experimental Spectra for (Z)-5,6-dibromocyclooct-1-ene (6a)	159
3.6.9.3 Experimental Spectra for (Z)-cyclooct-1-ene-5-yne (6b).....	160
3.6.10 NMR Spectra of Cycloadducts between BCN _{exo} -OH (5) and Nitrones 4, 2b, 3a, 3b and 3c.....	161
3.6.11 ¹ H NMR Spectra of Cycloadducts between BCN _{exo} -OH (5) and Nitron 3c in Other Solvents.....	166

3.6.12 NMR Spectra of Cycloadduct between DBCO-amine and Nitron 3c.....	168
3.6.13 NMR Spectra of Cycloadduct between (Z)-cyclooct-1-ene-5-yne (6b) and Nitron 3c	169
3.6.14 Stability of Pyridinium-Nitrones 3a, 3b and 3c	170
3.6.15 Kinetic Measurements	175
3.6.15.1 Kinetic Measurements of Cycloaddition Reaction between (4) and BCN _{exo} -OH (5)	176
3.6.15.2 Kinetic Measurements of Cycloaddition Reaction between (2b) and BCN _{exo} -OH (5) ...	177
3.6.15.3 Kinetic Measurements of Cycloaddition Reaction between (3a) and BCN _{exo} -OH (5)....	178
3.6.15.4 Kinetic Measurements of Cycloaddition Reaction between (3b) and BCN _{exo} -OH (5) ...	179
3.6.15.5 Kinetic Measurements of Cycloaddition Reaction between (3c) and BCN _{exo} -OH (5)....	180
3.6.16 Crystallographic Information.....	181
3.6.16.1 Data Collection and Processing	181
3.6.16.2 Structure Solution and Refinement	182
3.6.16.3 Summary of Crystallographic Data.....	184
3.6.17 Computational Information.....	187
3.6.17.1 Computational Methods	187
3.6.17.2 Optimized Structural Coordinates.....	187
3.6.17.3 Comparison of DFT versus XRD.....	192
3.6.18 References – Supporting Information.....	193
Chapter 4	194
4 A Clickable Azide-Functionalized [Au₂₅(SR)₁₈]⁻ Nanocluster platform for Interfacial Surface Modifications.....	194
4.1 Introduction.....	194
4.2 Results and Discussion	196
4.3 Conclusions.....	201

4.4 Acknowledgements.....	202
4.5 References.....	202
4.6 Supporting Information.....	205
4.6.1 General Materials and Methods.....	205
4.6.2 Experimental Procedures.....	207
4.6.2.1 Synthesis of <i>p</i> -nitro-phenylethanethioacetate.....	207
4.6.2.2 Synthesis of <i>p</i> -ammonium-phenylethanethioacetate chloride.....	207
4.6.2.3 Synthesis of <i>p</i> -azido-phenylethanethioacetate.....	208
4.6.2.4 Synthesis of <i>p</i> -azido-phenylethanethiol.....	209
4.6.2.5 Synthesis of (<i>Z</i>)-5,6-dibromocyclooct-1-ene.....	209
4.6.2.6 Synthesis of (<i>Z</i>)-cyclooct-1-ene-5-yne.....	209
4.6.2.7 Synthesis of bicyclo[6.1.0]nonyne (BCN _{exo} -OH).....	210
4.6.2.8 Synthesis of [(CH ₃ -(CH ₂) ₇) ₄ N][Au ₂₅ (SCH ₂ CH ₂ - <i>p</i> -C ₆ H ₄ -N ₃) ₁₈] (4.1-azido).....	210
4.6.2.9 Synthesis of [(CH ₃ -(CH ₂) ₇) ₄ N][Au ₂₅ (SCH ₂ CH ₂ - <i>p</i> -C ₆ H ₄ -C ₈ H ₁₀ N ₃) ₁₈] (4.1-triazole).....	211
4.6.3 Experimental Spectra and Diagrams.....	213
4.6.3.1 Experimental Spectra and Diagrams for [Au ₂₅ (SCH ₂ CH ₂ - <i>p</i> -C ₆ H ₄ -N ₃) ₁₈][(CH ₃ -(CH ₂) ₇) ₄ N] (4.1-azido).....	213
4.6.3.2 Experimental Spectra for [(CH ₃ -(CH ₂) ₇) ₄ N][Au ₂₅ (SCH ₂ CH ₂ - <i>p</i> -C ₆ H ₄ -C ₈ H ₁₀ N ₃) ₁₈] (4.1-triazole).....	217
4.6.3.3 Experimental Spectra for [(CH ₃ -(CH ₂) ₇) ₄ N][Au ₂₅ (SCH ₂ CH ₂ - <i>p</i> -C ₆ H ₄ -C ₁₀ H ₁₄ N ₃ O) ₁₈] ⁻ . Reaction of 4.1-azido with BCN _{exo} -OH.....	220
4.6.3.4 Experimental Spectra for <i>p</i> -nitro-phenylethanethioacetate.....	223
4.6.3.5 Experimental Spectra for <i>p</i> -ammonium-phenylethanethioacetate chloride.....	225
4.6.3.6 Experimental Spectra for <i>p</i> -azido-phenylethanethioacetate.....	227
4.6.3.7 Experimental Spectra for <i>p</i> -azido-phenylethanethiol.....	229
4.6.3.8 Experimental Spectra for (<i>Z</i>)-5,6-dibromocyclooct-1-ene.....	231
4.6.3.9 Experimental Spectra for (<i>Z</i>)-cyclooct-1-ene-5-yne.....	232
4.6.4 Crystallographic Information.....	233
4.6.4.1 Data Collection and Processing.....	233
4.6.4.2 Structure Solution and Refinement.....	233

4.6.4.3 Summary of Crystal Data.....	234
4.6.5 References – Supporting Information.....	236
Chapter 5	237
5 Expanding the Library of Clickable Azide-Functionalized Au₂₅SR₁₈ Nanocluster Platforms: A study of Ligand Modifications on Structure, Properties and Surface Reactivity	237
5.1 Introduction.....	237
5.2 Results and Discussion	241
5.3 Conclusions.....	250
5.4 Acknowledgements.....	251
5.5 References.....	251
5.6 Supporting Information.....	256
5.6.1 General Materials and Methods.....	256
5.6.2 Experimental Procedures	258
5.6.2.1 Synthesis of <i>p</i> -nitro-phenylethanethioacetate	258
5.6.2.2 Synthesis of <i>p</i> -azido-phenylethanethioacetate	259
5.6.2.3 Synthesis of <i>p</i> -azido-phenylethanethiol	259
5.6.2.4 Synthesis of <i>m</i> -nitro-phenylethanethioacetate	260
5.6.2.5 Synthesis of <i>m</i> -azido-phenylethanethioacetate	260
5.6.2.6 Synthesis of <i>m</i> -azido-phenylethanethiol	261
5.6.2.7 Synthesis of <i>o</i> -nitro-phenylethanethioacetate	261
5.6.2.8 Synthesis of <i>o</i> -azido-phenylethanethioacetate	262
5.6.2.9 Synthesis of <i>o</i> -azido-phenylethanethiol	262
5.6.2.10 Synthesis of (<i>Z</i>)-cyclooct-1-ene-5-yne.....	263
5.6.2.11 Synthesis of BCN _{exo} -OH	263
5.6.2.12 Synthesis of [(CH ₃ -(CH ₂) ₇) ₄ N][Au ₂₅ (SCH ₂ CH ₂ - <i>p</i> -C ₆ H ₄ -N ₃) ₁₈] (<i>p</i> -azido ¹⁻).....	264

5.6.2.13 Synthesis of $[(\text{CH}_3-(\text{CH}_2)_7)_4\text{N}][\text{Au}_{25}(\text{SCH}_2\text{CH}_2-m\text{-C}_6\text{H}_4\text{-N}_3)_{18}]$ (<i>m</i> -azido ¹⁻).....	264
5.6.2.14 Synthesis of $[(\text{CH}_3-(\text{CH}_2)_7)_4\text{N}][\text{Au}_{25}(\text{SCH}_2\text{CH}_2-o\text{-C}_6\text{H}_4\text{-N}_3)_{18}]$ (<i>o</i> -azido ¹⁻).....	266
5.6.2.15 Synthesis of $[(\text{CH}_3-(\text{CH}_2)_7)_4\text{N}][\text{Au}_{25}(\text{SCH}_2\text{CH}_2-p\text{-C}_6\text{H}_4\text{-C}_8\text{H}_{10}\text{N}_3)_{18}]$ (<i>p</i> -triazole ¹⁻).....	267
5.6.2.16 Synthesis of $[(\text{CH}_3-(\text{CH}_2)_7)_4\text{N}][\text{Au}_{25}(\text{SCH}_2\text{CH}_2-m\text{-C}_6\text{H}_4\text{-C}_8\text{H}_{10}\text{N}_3)_{18}]$ (<i>m</i> -triazole ¹⁻).....	267
5.6.2.17 Synthesis of $[(\text{CH}_3-(\text{CH}_2)_7)_4\text{N}][\text{Au}_{25}(\text{SCH}_2\text{CH}_2-o\text{-C}_6\text{H}_4\text{-C}_8\text{H}_{10}\text{N}_3)_{18}]$ (<i>o</i> -triazole ¹⁻).....	268
5.6.3 Experimental Spectra and Diagrams.....	269
5.6.3.1 Experimental Spectra and Diagrams for $[(\text{CH}_3-(\text{CH}_2)_7)_4\text{N}][\text{Au}_{25}(\text{SCH}_2\text{CH}_2-p\text{-C}_6\text{H}_4\text{-N}_3)_{18}]$ (<i>p</i> -azido ¹⁻).....	269
5.6.3.2 Experimental Spectra and Diagrams for $[(\text{CH}_3-(\text{CH}_2)_7)_4\text{N}][\text{Au}_{25}(\text{SCH}_2\text{CH}_2-m\text{-C}_6\text{H}_4\text{-N}_3)_{18}]$ (<i>m</i> -azido ¹⁻).....	269
5.6.3.3 Experimental Spectra and Diagrams for $[(\text{CH}_3-(\text{CH}_2)_7)_4\text{N}][\text{Au}_{25}(\text{SCH}_2\text{CH}_2-o\text{-C}_6\text{H}_4\text{-N}_3)_{18}]$ (<i>o</i> -azido ¹⁻).....	271
5.6.3.4 Experimental Diagrams for $[\text{Au}_{25}(\text{SCH}_2\text{CH}_2-p\text{-C}_6\text{H}_4\text{-N}_3)_{18}]$ (<i>p</i> -azido ⁰).....	273
5.6.3.5 Experimental Diagrams for $[\text{Au}_{25}(\text{SCH}_2\text{CH}_2-m\text{-C}_6\text{H}_4\text{-N}_3)_{18}]$ (<i>m</i> -azido ⁰).....	273
5.6.3.6 Experimental Diagrams for $[\text{Au}_{25}(\text{SCH}_2\text{CH}_2-o\text{-C}_6\text{H}_4\text{-N}_3)_{18}]$ (<i>o</i> -azido ⁰).....	274
5.6.3.7 Experimental Spectra and Diagrams for $[(\text{CH}_3-(\text{CH}_2)_7)_4\text{N}][\text{Au}_{25}(\text{SCH}_2\text{CH}_2-p\text{-C}_6\text{H}_4\text{-C}_8\text{H}_{10}\text{N}_3)_{18}]$ (<i>p</i> -triazole ¹⁻).....	275
5.6.3.8 Experimental Spectra and Diagrams for $[(\text{CH}_3-(\text{CH}_2)_7)_4\text{N}][\text{Au}_{25}(\text{SCH}_2\text{CH}_2-m\text{-C}_6\text{H}_4\text{-C}_8\text{H}_{10}\text{N}_3)_{18}]$ (<i>m</i> -triazole ¹⁻).....	275
5.6.3.9 Experimental Spectra and Diagrams for $[(\text{CH}_3-(\text{CH}_2)_7)_4\text{N}][\text{Au}_{25}(\text{SCH}_2\text{CH}_2-o\text{-C}_6\text{H}_4\text{-C}_8\text{H}_{10}\text{N}_3)_{18}]$ (<i>o</i> -triazole ¹⁻).....	277
5.6.3.10 Experimental Spectra for <i>p</i> -nitro-phenylethanethioacetate.....	279
5.6.3.11 Experimental Spectra for <i>p</i> -azido-phenylethanethioacetate.....	279
5.6.3.12 Experimental Spectra for <i>p</i> -azido-phenylethanethiol.....	279
5.6.3.13 Experimental Spectra for <i>m</i> -nitro-phenylethanethioacetate.....	280
5.6.3.14 Experimental Spectra for <i>m</i> -azido-phenylethanethioacetate.....	282
5.6.3.15 Experimental Spectra for <i>m</i> -azido-phenylethanethiol.....	284
5.6.3.16 Experimental Spectra for <i>o</i> -nitro-phenylethanethioacetate.....	286
5.6.3.17 Experimental Spectra for <i>o</i> -azido-phenylethanethioacetate.....	288
5.6.3.18 Experimental Spectra for <i>o</i> -azido-phenylethanethiol.....	290
5.6.4 Electrochemical Graphs.....	292
5.6.4.1 Cyclic Voltammetry (CV) Graph of $[(\text{CH}_3-(\text{CH}_2)_7)_4\text{N}][\text{Au}_{25}(\text{SCH}_2\text{CH}_2-p\text{-C}_6\text{H}_4\text{-N}_3)_{18}]$ (<i>p</i> -azido ¹⁻).....	292
5.6.4.2 Cyclic Voltammetry (CV) Graph of $[(\text{CH}_3-(\text{CH}_2)_7)_4\text{N}][\text{Au}_{25}(\text{SCH}_2\text{CH}_2-m\text{-C}_6\text{H}_4\text{-N}_3)_{18}]$ (<i>m</i> -azido ¹⁻).....	293

5.6.4.3 Cyclic Voltammetry (CV) Graph of $[(\text{CH}_3-(\text{CH}_2)_7)_4\text{N}][\text{Au}_{25}(\text{SCH}_2\text{CH}_2-o\text{-C}_6\text{H}_4\text{-N}_3)_{18}] (o\text{-azido}^{1-})$	294
5.6.5 Kinetic Measurements	295
5.6.5.1 General Experimental Details	295
5.6.5.2 Kinetic Measurements for <i>p</i> -azidophenylethanethiol	296
5.6.5.3 Kinetic Measurements for <i>m</i> -azidophenylethanethiol.....	297
5.6.5.4 Kinetic Measurements for <i>o</i> -azidophenylethanethiol	298
5.6.5.5 Kinetic Measurements for $[(\text{CH}_3-(\text{CH}_2)_7)_4\text{N}][\text{Au}_{25}(\text{SCH}_2\text{CH}_2-p\text{-C}_6\text{H}_4\text{-N}_3)_{18}] (p\text{-azido}^{1-})$	299
5.6.5.6 Kinetic Measurements for $[(\text{CH}_3-(\text{CH}_2)_7)_4\text{N}][\text{Au}_{25}(\text{SCH}_2\text{CH}_2-m\text{-C}_6\text{H}_4\text{-N}_3)_{18}] (m\text{-azido}^{1-})$	300
5.6.6 Crystallographic Information.....	301
5.6.6.1 Data Collection and Processing	301
5.6.5.2 Structure Solution and Refinement	301
5.6.6.3 Summary of Crystal Data for $[(\text{CH}_3-(\text{CH}_2)_7)_4\text{N}][\text{Au}_{25}(\text{SCH}_2\text{CH}_2-p\text{-C}_6\text{H}_4\text{-N}_3)_{18}] (p\text{-azido}^{1-})$	302
5.6.6.4 Summary of Crystal Data for $[\text{Au}_{25}(\text{SCH}_2\text{CH}_2-p\text{-C}_6\text{H}_4\text{-N}_3)_{18}] (p\text{-azido}^0)$	302
5.6.6.5 Summary of Crystal Data for $[\text{Au}_{25}(\text{SCH}_2\text{CH}_2-m\text{-C}_6\text{H}_4\text{-N}_3)_{18}] (m\text{-azido}^0)$	304
5.6.6.6 Summary of Crystal Data for $[\text{Au}_{25}(\text{SCH}_2\text{CH}_2-o\text{-C}_6\text{H}_4\text{-N}_3)_{18}] (o\text{-azido}^0)$	307
5.6.7 References – Supporting Information.....	309
Chapter 6	311
6 Expanding the Frontiers of Ultrasmall Gold Nanocluster Surface Composition through Cluster-Surface Click Chemistry: A Ferrocenyl-Modified $\text{Au}_{25}(\text{SR})_{18}$ Nanocluster.....	311
6.1 Introduction.....	311
6.2 Results and Discussion	313
6.3 Conclusions.....	318
6.4 Acknowledgements.....	319
6.5 References.....	319

6.6 Supporting Information.....	322
6.6.1 General Methods and Reagents	322
6.6.2 Experimental Procedures	325
6.6.2.1 Synthesis of <i>p</i> -nitro-phenylethanethioacetate	325
6.6.2.2 Synthesis of <i>p</i> -azido-phenylethanethioacetate	325
6.6.2.3 Synthesis of <i>p</i> -azido-phenylethanethiol	325
6.6.2.4 Synthesis of [(CH ₃ -(CH ₂) ₇) ₄ N][Au ₂₅ (SCH ₂ CH ₂ - <i>p</i> -C ₆ H ₄ -C ₈ H ₁₀ N ₃) ₁₈] (6.1-azido)	326
6.6.2.5 Synthesis of BCN _{exo} -OH	326
6.6.2.6 Synthesis of Ferrocene-BCN _{exo}	326
6.6.2.7 Synthesis of Ferrocene-Triazole-Thioacetate	327
6.6.2.8 Synthesis of [(CH ₃ -(CH ₂) ₇) ₄ N][Au ₂₅ (SCH ₂ CH ₂ - <i>p</i> -C ₆ H ₄ -C ₂₁ H ₂₂ FeN ₃ O ₂) ₁₈] (6.1-ferrocenyl)	327
6.6.3 Experimental Spectra and Diagrams.....	329
6.6.3.1 Experimental Spectra for [(CH ₃ -(CH ₂) ₇) ₄ N][Au ₂₅ (SCH ₂ CH ₂ - <i>p</i> -C ₆ H ₄ -C ₈ H ₁₀ N ₃) ₁₈] (6.1-azido).....	329
6.6.3.2 Experimental Spectra for [(CH ₃ -(CH ₂) ₇) ₄ N][Au ₂₅ (SCH ₂ CH ₂ - <i>p</i> -C ₆ H ₄ -C ₂₁ H ₂₂ FeN ₃ O ₂) ₁₈] (6.1-ferrocenyl)	329
6.6.3.3 Experimental Spectra for Ferrocene-BCN _{exo}	331
6.6.3.4 Experimental Spectra of Ferrocene-Triazole-Thioacetate	333
6.6.4 Electrochemical Graphs	334
6.6.4.1 Cyclic Voltammogram (CV) of [(CH ₃ -(CH ₂) ₇) ₄ N][Au ₂₅ (SCH ₂ CH ₂ - <i>p</i> -C ₆ H ₄ -C ₈ H ₁₀ N ₃) ₁₈] (1-azido).....	334
6.6.4.2 Cyclic Voltammogram (CV) of [(CH ₃ -(CH ₂) ₇) ₄ N][Au ₂₅ (SCH ₂ CH ₂ - <i>p</i> -C ₆ H ₄ -C ₂₁ H ₂₂ FeN ₃ O ₂) ₁₈] (6.1-ferrocenyl)	334
6.6.4.3 Cyclic Voltammogram (CV) of <i>p</i> -azido-phenylethanethioacetate.....	335
6.6.4.4 Differential Pulse Voltammogram (DPV) of <i>p</i> -azido-phenylethanethioacetate	335
6.6.4.5 Cyclic Voltammogram (CV) of Ferrocene-Triazole-Thioacetate	336
6.6.4.6 Differential Pulse Voltammogram (DPV) of Ferrocene-Triazole-Thioacetate.....	336
6.6.5 References – Supporting Information	337
Chapter 7	338
7 Contributions and Future Perspectives	338

7.1 Contributions.....	338
7.2 Future Perspectives	345
7.2.1 General Comments.....	345
7.2.2 Future Perspectives for AuNPs	347
7.2.3 Future Perspectives for AuNCs	348
7.3 References.....	350
Appendices.....	352
A.1 Permission to Reproduce Copyrighted Material.....	352
A.2 Curriculum Vitae.....	370

List of Figures

Chapter 1

Figure 1.1. (a) TEM/SEM images of gold nanoparticles (AuNPs) with different morphologies. *Top left.* Spherical AuNPs (figure reproduced with permission from Ref [12].) *Top Right.* Rod-shaped AuNPs (Figure reproduced with permission from Ref [13]). *Bottom Left.* Prism-shaped AuNPs (Figure reproduced with permission from Ref [14]). *Bottom Right.* Octahedral AuNPs (Figure reproduced with permission from Ref [15]). **(b)** Solutions of rod-shaped AuNPs having different sizes. Figure reproduced with permission of Ref [16].....3

Figure 1.2. (a) Optical absorption spectra of 9, 22, 48 and 99 nm spherical AuNPs. The broad peaks correspond to the SPR of each system. Figure reproduced with permission from Ref. [33]. **(b)** Aggregation-induced shift in SPR wavelength as a function of particle center-center spacing for 72 and 84 nm spherical AuNPs. Figure reproduced with permission from Ref. [37].....6

Figure 1.3. (a) Uptake of AuNPs into mammalian cells (A) Number of AuNPs per vesicle diameter versus nanoparticle size (B-F) TEM images of AuNPs with sizes 14, 30, 50, 74 and 100 nm trapped inside vesicles of a HeLa cell, respectively. Figure reproduced with permission from Ref. [43] **(b)** Confocal cell images showing fluorescein-labelled transferrin AuNPs (AuNP-TF) internalized by NPC cells (A) NPC cells without AuNP-TF (B) NPC cells treated with AuNPs without surface transferrin (C) NPC cells treated with AuNP-TF (D) NPC cells treated with albumin-coated AuNPs (E and F) NPC cells co-treated with different proportions of AuNP-TF and albumin-coated AuNPs (1:2 and 1:5, respectively). Figure reproduced with permission from Ref. [45].....8

Figure 1.4. (a) *Left.* Colorimetric sensing of lead ions, whereby lead adsorption causes dismantling of ([15]-crown-5)-functionalized AuNP aggregates (A) into an AuNP dispersion (B). *Right.* UV/Vis spectra of A and B (spectra figure reproduced with permission from Ref. [48]). **(b)** *Left.* Colorimetric sensing of mercury ions, whereby mercury adsorption caused dispersion of carboxyl-terminated AuNPs (A) to from AuNP aggregates (B). *Right.* UV/Vis spectra of A and B (spectra figure reproduced with permission from Ref. [49]).....9

Figure 1.5. (a) Schematic representation of doxorubicin (DOX) adsorption onto AuNP surface and intracellular delivery. (b,c) Fluorescence microscopy images of MCF-7 tumor tissues after injection of DOX alone (b) and AuNP-DOX (c). Red = DOX; green = stained vasculature (lectin-FITC). Scale bar, 50 μm . (d) Normalized tumor growth curves after injection with AuNP-DOX (red), DOX alone (black) and phosphate buffered-saline (PBS) (blue). Figures in (b), (c) and (d) reproduced with permission from Ref. [53].....10

Figure 1.6. (a) Schematic representation of development of ‘nano-flare AuNP’ and *in vivo* release of fluorophore-conjugated reporter sequence after survivin mRNA binding. (b) Differential contrast and fluorescence imaging of survivin-expressing SKBR3 cells treated with survivin nano-flares (*left*) and non-complementary nano-flares (*right*). (c) Analogously treated non-survivin expressing C166 cells. Scale bar is 20 μm . Figure in (b) and (c) reproduced with permission from Ref. [56].....11

Figure 1.7. Some thiolated AuNC frameworks.

Top (left to right). The $\text{Au}_{20}(\text{SR})_{16}$ framework (where $\text{R} = \text{C}_6\text{H}_4\text{-C}(\text{CH}_3)_3$) (figure produced from data with permission from Ref. [59]). The $\text{Au}_{23}(\text{SR})_{16}$ framework (where $\text{R} = \text{C}_6\text{C}_{11}$) (figure produced from data with permission from Ref. [60]). The $\text{Au}_{24}(\text{SR})_{20}$ framework (where $\text{R} = \text{CH}_2\text{-C}_6\text{H}_4\text{-C}(\text{CH}_3)_3$) (figure produced from data with permission from Ref. [61]).

Middle (left to right). The $\text{Au}_{25}(\text{SR})_{18}$ framework (where $\text{R} = \text{CH}_2\text{CH}_2\text{-C}_6\text{H}_5$) (figure produced from data with permission from Ref. [62]). The $\text{Au}_{28}(\text{SR})_{20}$ framework (where $\text{R} = \text{C}_6\text{H}_4\text{-C}(\text{CH}_3)_3$) (figure produced from data with permission from Ref. [63]).

Bottom (left to right). The $\text{Au}_{38}(\text{SR})_{24}$ framework (where $\text{R} = \text{CH}_2\text{CH}_2\text{-C}_6\text{H}_5$) (figure produced from data with permission from Ref. [64]). The $\text{Au}_{44}(\text{SR})_{28}$ framework (where $\text{R} = \text{CH}_2\text{CH}_2\text{-C}_6\text{H}_5$) (figure produced from data with permission from Ref. [65]).....13

Figure 1.8. (a) Molecular structure of $[\text{TOA}][\text{Au}_{25}(\text{CH}_2\text{CH}_2\text{Ph})_{18}]$, where TOA = tetraoctylammonium (not shown). (b) Staple motifs, Au_{13} kernel, and inner/outer ligands in molecular structure of $[\text{Au}_{25}(\text{CH}_2\text{CH}_2\text{Ph})_{18}]^{-1}$. Figure produced from data with permission from Ref. [62].....18

Figure 1.9. (a) Optical absorption spectra of [TOA][Au₂₅(CH₂CH₂Ph)₁₈], where TOA = Tetraoctylammonium (black), Au₂₅(CH₂CH₂Ph)₁₈ (red) and [Au₂₅(CH₂CH₂Ph)₁₈][C₆F₅CO₂] (blue). Figure reproduced with permission from Ref. [88]. (b) Optical absorption spectrum of [TOA][Au₂₅(CH₂CH₂Ph)₁₈] showing principal transitions. Figure reproduced with permission from Ref. [62].....19

Figure 1.10. (a) Photoluminescence (PL) spectra of [Au₂₅(SR)₁₈]⁻¹ functionalized with phenylethanethiolate (black), dodecanethiolate (red) and hexanethiolate (blue). (b) PL spectra of [Au₂₅(SR)₁₈]⁻¹ (black), [Au₂₅(SR)₁₈]⁰ (red), [Au₂₅(SR)₁₈]⁺¹ (blue) and [Au₂₅(SR)₁₈]⁺² (blue-green). Figures reproduced with permission from Ref. [81].....20

Figure 1.11. Differential pulse voltammogram (DPV) of [Au₂₅(SCH₂CH₂Ph)₁₈]⁻¹ at 0.02 V/s in 0.1 M Bu₄NPF₆ in degassed CH₂Cl₂ at 0.4 mm diameter Pt working electrode, with Ag wire quasi-reference (AgQRE) and Pt wire counter electrode. * indicates wave for incompletely removed O₂. DPV reproduced with permission from Ref. [94].....21

Figure 1.12. *Left.* Schematic representation of Hg²⁺ sensing based on fluorescence quenching upon Hg²⁺ binding to Au₂₅-BSA. *Right.* Photoemission spectra (λ_{ex} = 470 nm) of Au₂₅-BSA before Hg²⁺ binding (1) and after Hg²⁺ binding (2). Spectra reproduced with permission from Ref. [97].....22

Figure 1.13. (a) Catalytic activity of [Au₂₅(SR)₁₈]⁻¹ thermally deposited onto CeO₂ support, using different capping ligands, for Ullman heterocoupling between 4-methyl-iodobenzene and 4-nitro-iodobenzene. Synthetic data taken from Ref. [102]. (b) Catalytic activity of [Au₂₅(SCH₂CH₂Ph)₁₈]⁻¹ thermally deposited onto TiO₂ support, for semi-hydrogenation of terminal alkynes. Synthetic data taken from Ref. [103].....23

Figure 1.14. *Left.* Schematic representation of DOX delivery by Au₂₅(SR)₁₈]⁻¹-DOX nanoconjugate. *Right.* Confocal images of A549 cells after incubation with Au₂₅(SR)₁₈]⁻¹-DOX nanoconjugate after 1 hour (top right) and 3 hours (bottom right). Red = doxorubicin. Confocal images reproduced with permission of Ref. [104].....24

Figure 1.15. Some commonly used cyclooctynes, with associated second-order rate constants for reaction with benzyl azide. Second-order rate constants taken from references [149] and [150]...35

Figure 1.16. *Top.* Kinetically variable SPAAC and SPANC through structural modifications to the azide and nitrono moieties, respectively. *Bottom.* Structures of azides and nitrones and their associated second-order rate constants.....37

Chapter 2

Figure 2.1. (a) Schematic representation of host/guest directed- and kinetically-directed self-assembly strategies. (b) The strain-promoted alkyne-azide cycloaddition reaction (SPAAC) to form a triazole cycloadduct (right), and the strain-promoted alkyne-nitrono cycloaddition reaction (SPANC) to form an isooxazoline cycloadduct (left). (c) Schematic representation of kinetically-directed self-assembly strategy using SPAAC and SPANC.....63

Figure 2.2. Estimated SPAAC/SPANC and I-SPAAC/I-SPANC reaction rates of azides and nitrones with free BCN and AuNP-BCN, respectively. All rate constants were determined under second order conditions in CD₂Cl₂ at 25°C in duplicate trials using ¹H NMR spectroscopy, and monitored over pre-determined time intervals to determine a second order rate constant. The k₂(rel) value indicates the rate of each k₂ relative to the slowest azide (azide 1).....66

Figure 2.3. Kinetically-directed competitive reactivity of AuNP-BCN, where one equivalent of AuNP-BCN was reacted with one equivalent of nitrono and one equivalent of azide, and the amount of cycloadduct that was formed was determined using ¹H NMR spectroscopy.....67

Figure S2.1. ¹H NMR spectrum of **HS-EG₃-Me** in CDCl₃ at 25°C. * denotes residual protio solvent.....81

Figure S2.2. ¹³C{¹H} NMR spectrum of **HS-EG₃-Me** in CDCl₃ at 25°C. * indicates CDCl₃ solvent.....81

Figure S2.3. ¹H NMR spectrum of **AuNP-OMe** in CDCl₃ at 25°C. * denotes residual protio solvent.....82

Figure S2.4. ¹H NMR spectrum of **HS-EG₄-NH₂** in CDCl₃ at 25°C. * denotes residual protio solvent.....83

Figure S2.5. $^{13}\text{C}\{^1\text{H}\}$ NMR spectrum of HS-EG₄-NH₂ in CDCl_3 at 25°C . * indicates CDCl_3 solvent.....	83
Figure S2.6. ^1H NMR spectrum of AuNP-NH₂ in D_2O at 25°C . * denotes residual protio solvent.....	84
Figure S2.7. TEM image for AuNP-NH₂	84
Figure S2.8. (a) High-resolution carbon 1s XPS spectrum of AuNP-NH₂ (b) High-resolution oxygen 1s XPS spectrum of AuNP-NH₂	85
Figure S2.9. (a) XPS survey scan of AuNP-NH₂	85
Figure S2.10. ^1H NMR spectrum of BCN_{exo}-OH in CDCl_3 at 25°C . * denotes residual protio solvent.....	86
Figure S2.11. ^1H NMR spectrum of BCN_{exo}-O-pNP in CDCl_3 at 25°C . * denotes residual protio solvent.....	86
Figure S2.12. ^1H NMR spectrum of AuNP-BCN in CDCl_3 at 25°C . * denotes residual protio solvent.....	87
Figure S2.13. TEM image for AuNP-BCN	87
Figure S2.14. (a) High-resolution carbon 1s XPS spectrum of AuNP-BCN (b) High-resolution oxygen 1s XPS spectrum of AuNP-BCN	88
Figure S2.15. (a) XPS survey scan of AuNP-BCN	88
Figure S2.16. ^1H NMR spectrum of azide 1 in CDCl_3 at 25°C . * denotes residual protio solvent.....	89
Figure S2.17. $^{13}\text{C}\{^1\text{H}\}$ NMR spectrum of azide 1 in CDCl_3 at 25°C . * indicates CDCl_3 solvent.....	89
Figure S2.18. ^1H NMR spectrum of azide 4 in CDCl_3 at 25°C . * denotes residual protio solvent.....	90

Figure S2.19. $^{13}\text{C}\{^1\text{H}\}$ NMR spectrum of azide 4 in CDCl_3 at 25°C . * indicates CDCl_3 solvent.....	90
Figure S2.20. ^1H NMR spectrum of azide 5 in CDCl_3 at 25°C . * denotes residual protio solvent.....	91
Figure S2.21. $^{13}\text{C}\{^1\text{H}\}$ NMR spectrum of azide 5 in CDCl_3 at 25°C . * indicates CDCl_3 solvent.....	91
Figure S2.22. ^{19}F NMR spectrum of azide 6 in CDCl_3 at 25°C	92
Figure S2.23. $^{13}\text{C}\{^1\text{H}\}$ NMR spectrum of azide 6 in CDCl_3 at 25°C . * indicates CDCl_3 solvent.....	92
Figure S2.24. ^1H NMR spectrum of nitrone 1 in CD_2Cl_2 at 25°C . * denotes residual protio solvent.....	93
Figure S2.25. $^{13}\text{C}\{^1\text{H}\}$ NMR spectrum of nitrone 1 in CD_2Cl_2 at 25°C . * indicates CD_2Cl_2 solvent.....	93
Figure S2.26. ^1H NMR spectrum of nitrone 2 in CD_2Cl_2 at 25°C . * denotes residual protio solvent.....	94
Figure S2.27. $^{13}\text{C}\{^1\text{H}\}$ NMR spectrum of nitrone 2 in CD_2Cl_2 at 25°C . * indicates CD_2Cl_2 solvent.....	94
Figure S2.28. ^1H NMR spectrum of nitrone 3 in CD_2Cl_2 at 25°C . * denotes residual protio solvent.....	95
Figure S2.29. $^{13}\text{C}\{^1\text{H}\}$ NMR spectrum of nitrone 3 in CD_2Cl_2 at 25°C . * indicates CD_2Cl_2 solvent.....	95
Figure S2.30. ^1H NMR spectrum of nitrone 4 in CD_2Cl_2 at 25°C . * denotes residual protio solvent.....	96

Figure S2.31. $^{13}\text{C}\{^1\text{H}\}$ NMR spectrum of nitron 4 in CD_2Cl_2 at 25°C . * indicates CD_2Cl_2 solvent.....	96
Figure S2.32. ^1H NMR spectrum of nitron 5 in CD_2Cl_2 at 25°C . * denotes residual protio solvent.....	97
Figure S2.33. $^{13}\text{C}\{^1\text{H}\}$ NMR spectrum of nitron 5 in CD_2Cl_2 at 25°C . * indicates CD_2Cl_2 solvent.....	97
Figure S2.34. ^1H NMR spectrum of nitron 6 in CD_2Cl_2 at 25°C . * denotes residual protio solvent.....	98
Figure S2.35. $^{13}\text{C}\{^1\text{H}\}$ NMR spectrum of nitron 6 in CD_2Cl_2 at 25°C . * indicates CD_2Cl_2 solvent.....	98
Figure S2.36. TGA spectrum for AuNP-BCN	99
Figure S2.37. First-derivative of TGA spectrum for AuNP-BCN	100
Figure S2.38. Second order kinetics graph for azide 1 with BCN_{exo}-OH	102
Figure S2.39. Second order kinetics graph for azide 1 with AuNP-BCN	102
Figure S2.40. Second order kinetics graph for azide 2 with BCN_{exo}-OH	103
Figure S2.41. Second order kinetics graph for azide 2 with AuNP-BCN	103
Figure S2.42. Second order kinetics graph for azide 3 with BCN_{exo}-OH	104
Figure S2.43. Second order kinetics graph for azide 3 with AuNP-BCN	104
Figure S2.44. Second order kinetics graph for azide 4 with BCN_{exo}-OH	105
Figure S2.45. Second order kinetics graph for azide 4 with AuNP-BCN	105
Figure S2.46. Second order kinetics graph for azide 5 with BCN_{exo}-OH	106
Figure S2.47. Second order kinetics graph for azide 5 with AuNP-BCN	106

Figure S2.48. Second order kinetics graph for azide 6 with BCN_{exo}-OH	107
Figure S2.49. Second order kinetics graph for azide 6 with AuNP-BCN	107
Figure S2.50. Second order kinetics graph for nitron 1 with BCN_{exo}-OH	108
Figure S2.51. Second order kinetics graph for nitron 1 with AuNP-BCN	108
Figure S2.52. Second order kinetics graph for nitron 2 with BCN_{exo}-OH	109
Figure S2.53. Second order kinetics graph for nitron 2 with AuNP-BCN	109
Figure S2.54. Second order kinetics graph for nitron 3 with BCN_{exo}-OH	110
Figure S2.55. Second order kinetics graph for nitron 3 with AuNP-BCN	110
Figure S2.56. Second order kinetics graph for nitron 4 with BCN_{exo}-OH	111
Figure S2.57. Second order kinetics graph for nitron 4 with AuNP-BCN	111
Figure S2.58. Second order kinetics graph for nitron 5 with BCN_{exo}-OH	112
Figure S2.59. Second order kinetics graph for nitron 5 with AuNP-BCN	112
Figure S2.60. Second order kinetics graph for nitron 6 with BCN_{exo}-OH	113
Figure S2.61. Second order kinetics graph for nitron 6 with AuNP-BCN	113
Figure S2.62. ¹ H NMR spectrum of equimolar mixture of azide 1 and nitron 6 in CD ₂ Cl ₂ at 25°C. * denotes residual protio solvent.....	115
Figure S2.63. ¹ H NMR spectrum of equimolar mixture of azide 1 and nitron 6 and interfacial BCN (in AuNP-BCN) in CD ₂ Cl ₂ at 25°C. * denotes residual protio solvent.....	115
Figure S2.64. ¹ H NMR spectrum of equimolar mixture of azide 3 and nitron 4 in CD ₂ Cl ₂ at 25°C. * denotes residual protio solvent.....	116

Figure S2.65. ^1H NMR spectrum of equimolar mixture of azide 3 and nitron 4 and interfacial BCN (in AuNP-BCN) in CD_2Cl_2 at 25°C . * denotes residual protio solvent.....	116
Figure S2.66. ^1H NMR spectrum of equimolar mixture of azide 4 and nitron 4 in CD_2Cl_2 at 25°C . * denotes residual protio solvent.....	117
Figure S2.67. ^1H NMR spectrum of equimolar mixture of azide 4 and nitron 4 and interfacial BCN (in AuNP-BCN) in CD_2Cl_2 at 25°C . * denotes residual protio solvent.....	117
Figure S2.68. ^1H NMR spectrum of equimolar mixture of azide 5 and nitron 2 in CD_2Cl_2 at 25°C . * denotes residual protio solvent.....	118
Figure S2.69. ^1H NMR spectrum of equimolar mixture of azide 5 and nitron 2 and interfacial BCN (in AuNP-BCN) in CD_2Cl_2 at 25°C . * denotes residual protio solvent.....	118
Figure S2.70. ^1H NMR spectrum of equimolar mixture of azide 6 and nitron 1 in CD_2Cl_2 at 25°C . * denotes residual protio solvent.....	119
Figure S2.71. ^1H NMR spectrum of equimolar mixture of azide 6 and nitron 1 and interfacial BCN (in AuNP-BCN) in CD_2Cl_2 at 25°C . * denotes residual protio solvent.....	119

Chapter 3

Figure 3.1. Isosurface plots (isoval = 0.03 e au^{-3}) for the HOMO of BCN- OH_{exo} (5) and the LUMO of 3a-c , 4 , 2b , and energy diagram of the frontier orbitals involved in SPANC between 3a-c , 4 , 2b and BCN- OH_{exo} (5).....	127
Figure S3.1. Thermal ellipsoid plot of molecular structure of nitron 4 at 50% probability level. Hydrogens are drawn in with arbitrary radii (black = carbon, red = oxygen, green = nitrogen, grey = hydrogen).....	144
Figure S3.2. Space-filling diagrams of X-ray structure of nitron 4 (black = carbon, red = oxygen, green = nitrogen, grey = hydrogen, purple = iodine).....	144

Figure S3.3. Thermal ellipsoid plot of molecular structure of nitrone 2b at 50% probability level. Hydrogens are drawn in with arbitrary radii (black = carbon, red = oxygen, green = nitrogen, grey = hydrogen).....	145
Figure S3.4. Space-filling diagrams of X-ray structure of nitrone 2b (black = carbon, red = oxygen, green = nitrogen, grey = hydrogen, purple = iodine).....	145
Figure S3.5. Thermal ellipsoid plot of molecular structure of nitrone 3a at 50% probability level. Hydrogens are drawn in with arbitrary radii (black = carbon, red = oxygen, green = nitrogen, grey = hydrogen, purple = iodine).....	145
Figure S3.6. Space-filling diagrams of X-ray structure of nitrone 3a (black = carbon, red = oxygen, green = nitrogen, grey = hydrogen, purple = iodine).....	146
Figure S3.7. Thermal ellipsoid plot of molecular structure of nitrone 3b at 50% probability level. Hydrogens are drawn in with arbitrary radii (black = carbon, red = oxygen, green = nitrogen, grey = hydrogen, purple = iodine).....	146
Figure S3.8. Space-filling diagrams of X-ray structure of nitrone 3b (black = carbon, red = oxygen, green = nitrogen, grey = hydrogen, purple = iodine).....	146
Figure S3.9. Thermal ellipsoid plot of molecular structure of nitrone 3c at 50% probability level. Hydrogens are drawn in with arbitrary radii (black = carbon, red = oxygen, green = nitrogen, grey = hydrogen, purple = iodine).....	147
Figure S3.10. Space-filling diagrams of X-ray structure of nitrone 3c (black = carbon, red = oxygen, green = nitrogen, grey = hydrogen, purple = iodine).....	147
Figure S3.11. ¹ H NMR spectrum of nitrone 2a in (CD ₃) ₂ SO at 25°C. * denotes residual protio solvent.....	149
Figure S3.12. ¹³ C{ ¹ H} NMR spectrum of nitrone 2a in (CD ₃) ₂ SO at 25°C. * indicates (CD ₃) ₂ SO solvent.....	149

Figure S3.13. ^1H NMR spectrum of nitrone 3a in $(\text{CD}_3)_2\text{SO}$ at 25°C . * denotes residual protio solvent.....	150
Figure S3.14. $^{13}\text{C}\{^1\text{H}\}$ NMR spectrum of nitrone 3a in $(\text{CD}_3)_2\text{SO}$ at 25°C . * indicates $(\text{CD}_3)_2\text{SO}$ solvent.....	150
Figure S3.15. ^1H NMR spectrum of nitrone 3b in $(\text{CD}_3)_2\text{SO}$ at 25°C . * denotes residual protio solvent.....	151
Figure S3.16. $^{13}\text{C}\{^1\text{H}\}$ NMR spectrum of nitrone 3b in $(\text{CD}_3)_2\text{SO}$ at 25°C . * indicates $(\text{CD}_3)_2\text{SO}$ solvent.....	151
Figure S3.17. ^1H NMR spectrum of nitrone 3c in $(\text{CD}_3)_2\text{SO}$ at 25°C . * denotes residual protio solvent.....	152
Figure S3.18. $^{13}\text{C}\{^1\text{H}\}$ NMR spectrum of nitrone 3c in $(\text{CD}_3)_2\text{SO}$ at 25°C . * indicates $(\text{CD}_3)_2\text{SO}$ solvent.....	153
Figure S3.19. ^1H NMR spectrum of nitrobenzyl-TEG-OH (A) in CDCl_3 at 25°C . * denotes residual protio solvent.....	154
Figure S3.20. $^{13}\text{C}\{^1\text{H}\}$ NMR spectrum of nitrobenzyl-TEG-OH (A) in CDCl_3 at 25°C . * indicates CDCl_3 solvent.....	154
Figure S3.21. ^1H NMR spectrum of nitrobenzyl-TEG-OTs (B) in CDCl_3 at 25°C . * denotes residual protio solvent.....	155
Figure S3.22. $^{13}\text{C}\{^1\text{H}\}$ NMR spectrum of nitrobenzyl-TEG-OTs (B) in CDCl_3 at 25°C . * indicates CDCl_3 solvent.....	155
Figure S3.23. ^1H NMR spectrum of nitrobenzyl-TEG-Thioacetate (C) in CDCl_3 at 25°C . * denotes residual protio solvent.....	156
Figure S3.24. $^{13}\text{C}\{^1\text{H}\}$ NMR spectrum of nitrobenzyl-TEG-Thioacetate (C) in CDCl_3 at 25°C . * indicates CDCl_3 solvent.....	156

Figure S3.25. ^1H NMR spectrum of (<i>C</i> -pyridinium, <i>N</i> -phenyl-TEG-thioacetate)-nitron (E) in CDCl_3 at 25°C . * denotes residual protio solvent.....	157
Figure S3.26. $^{13}\text{C}\{^1\text{H}\}$ NMR spectrum of (<i>C</i> -pyridinium- <i>N</i> -phenyl-TEG-thioacetate)-nitron (E) in CDCl_3 at 25°C . * indicates CDCl_3 solvent.....	157
Figure S3.27. ^1H NMR spectrum of $\text{BCN}_{\text{exo}}\text{-OH}$ (5) in in $(\text{CD}_3)_2\text{SO}$ at 25°C . Made according to reference 2. * denotes residual protio solvent.....	158
Figure S3.28. ^1H NMR spectrum of 6a in in CD_2Cl_2 at 25°C . * denotes residual protio solvent.....	159
Figure S3.29. $^{13}\text{C}\{^1\text{H}\}$ NMR spectrum of 6a in CD_2Cl_2 at 25°C . * indicates CD_2Cl_2 solvent.....	159
Figure S3.30. ^1H NMR spectrum of 6b in in CD_2Cl_2 at 25°C . * denotes residual protio solvent.....	160
Figure S3.31. $^{13}\text{C}\{^1\text{H}\}$ NMR spectrum of 6b in CD_2Cl_2 at 25°C . * indicates CD_2Cl_2 solvent.....	160
Figure S3.32. ^1H NMR spectrum of 4-BCN_{exo}-OH cycloadduct (2 isomers) in $(\text{CD}_3)_2\text{SO}$ at 25°C . * denotes residual protio solvent.....	161
Figure S3.33. $^{13}\text{C}\{^1\text{H}\}$ NMR spectrum of 4-BCN_{exo}-OH cycloadduct (2 isomers) in $(\text{CD}_3)_2\text{SO}$ at 25°C . * indicates $(\text{CD}_3)_2\text{SO}$ solvent.....	161
Figure S3.34. ^1H NMR spectrum of 2b-BCN_{exo}-OH cycloadduct (2 isomers) in $(\text{CD}_3)_2\text{SO}$ at 25°C . * denotes residual protio solvent.....	162
Figure S3.35. $^{13}\text{C}\{^1\text{H}\}$ NMR spectrum of 2b-BCN_{exo}-OH cycloadduct (2 isomers) in $(\text{CD}_3)_2\text{SO}$ at 25°C . * indicates $(\text{CD}_3)_2\text{SO}$ solvent.....	162
Figure S3.36. ^1H NMR spectrum of 3a-BCN_{exo}-OH cycloadduct (2 isomers) in $(\text{CD}_3)_2\text{SO}$ at 25°C . * denotes residual protio solvent.....	163

Figure S3.37. $^{13}\text{C}\{^1\text{H}\}$ NMR spectrum of 3a-BCN_{exo}-OH cycloadduct (2 isomers) in $(\text{CD}_3)_2\text{SO}$ at 25°C. * indicates $(\text{CD}_3)_2\text{SO}$ solvent.....	163
Figure S3.38. ^1H NMR spectrum of 3b-BCN_{exo}-OH cycloadduct (2 isomers) in $(\text{CD}_3)_2\text{SO}$ at 25°C. * denotes residual protio solvent.....	164
Figure S3.39. $^{13}\text{C}\{^1\text{H}\}$ NMR spectrum of 3b-BCN_{exo}-OH cycloadduct (2 isomers) in $(\text{CD}_3)_2\text{SO}$ at 25°C. * indicates $(\text{CD}_3)_2\text{SO}$ solvent.....	164
Figure S3.40. ^1H NMR spectrum of 3c-BCN_{exo}-OH cycloadduct (2 isomers) in $(\text{CD}_3)_2\text{SO}$ at 25°C. * denotes residual protio solvent.....	165
Figure S3.41. $^{13}\text{C}\{^1\text{H}\}$ NMR spectrum of 3c-BCN_{exo}-OH cycloadduct (2 isomers) in $(\text{CD}_3)_2\text{SO}$ at 25°C. * indicates $(\text{CD}_3)_2\text{SO}$ solvent.....	165
Figure S3.42. ^1H NMR spectrum of 3c-BCN_{exo}-OH cycloadduct (2 isomers) in 6:1 $\text{D}_2\text{O}:(\text{CD}_3)_2\text{SO}$ at 25°C. The solvents were suppressed by software. * denotes residual protio solvent.....	166
Figure S3.43. ^1H NMR spectrum of 3c-BCN_{exo}-OH cycloadduct (2 isomers) in 1:1 $\text{D}_2\text{O}:(\text{CD}_3)_2\text{SO}$ at 25°C. * denotes residual protio solvent.....	166
Figure S3.44. ^1H NMR spectrum of 3c-BCN_{exo}-OH cycloadduct (2 isomers) in CD_3OD at 25°C. * denotes residual protio solvent.....	167
Figure S3.45. ^1H NMR spectrum of 3c-DBCO-amine cycloadduct (2 isomers) in $(\text{CD}_3)_2\text{SO}$ at 25°C. * denotes residual protio solvent.....	168
Figure S3.46. $^{13}\text{C}\{^1\text{H}\}$ NMR spectrum of 3c-DBCO-amine cycloadduct (2 isomers) in $(\text{CD}_3)_2\text{SO}$ at 25°C. * indicates $(\text{CD}_3)_2\text{SO}$ solvent.....	168
Figure S3.47. ^1H NMR spectrum of 3c-6b cycloadduct (2 isomers) in $(\text{CD}_3)_2\text{SO}$ at 25°C. * denotes residual protio solvent.....	169
Figure S3.48. $^{13}\text{C}\{^1\text{H}\}$ NMR spectrum of 3c-6b cycloadduct (2 isomers) in $(\text{CD}_3)_2\text{SO}$ at 25°C. * indicates $(\text{CD}_3)_2\text{SO}$ solvent.....	169

Figure S3.49. ^1H NMR spectrum of nitrone 3a in 6:1 $\text{D}_2\text{O}:(\text{CD}_3)_2\text{SO}$ at 25°C after 5 minutes. * denotes residual protio solvent.....	172
Figure S3.50. ^1H NMR spectrum of nitrone 3a in 6:1 $\text{D}_2\text{O}:(\text{CD}_3)_2\text{SO}$ at 25°C after 12 hours. * denotes residual protio solvent.....	172
Figure S3.51. ^1H NMR spectrum of nitrone 3b in 6:1 $\text{D}_2\text{O}:(\text{CD}_3)_2\text{SO}$ at 25°C after 5 minutes. * denotes residual protio solvent.....	173
Figure S3.52. ^1H NMR spectrum of nitrone 3b in 6:1 $\text{D}_2\text{O}:(\text{CD}_3)_2\text{SO}$ at 25°C after 12 hours. * denotes residual protio solvent.....	173
Figure S3.53. ^1H NMR spectrum of nitrone 3c in 6:1 $\text{D}_2\text{O}:(\text{CD}_3)_2\text{SO}$ at 25°C after 5 minutes. * denotes residual protio solvent.....	174
Figure S3.54. ^1H NMR spectrum of nitrone 3c in 6:1 $\text{D}_2\text{O}:(\text{CD}_3)_2\text{SO}$ at 25°C after 12 hours. * denotes residual protio solvent.....	174
Figure S3.55. Pseudo-first order kinetics graph for nitrone 4 with $\text{BCN}_{exo}\text{-OH}$ (5).....	176
Figure S3.56. Pseudo-first order kinetics graph for nitrone 2b with $\text{BCN}_{exo}\text{-OH}$ (5).....	177
Figure S3.57. Pseudo-first order kinetics graph for nitrone 3a with $\text{BCN}_{exo}\text{-OH}$ (5).....	178
Figure S3.58. Pseudo-first order kinetics graph for nitrone 3b with $\text{BCN}_{exo}\text{-OH}$ (5).....	179
Figure S3.59. Pseudo-first order kinetics graph for nitrone 3c with $\text{BCN}_{exo}\text{-OH}$ (5).....	180

Chapter 4

Figure 4.1. Synthesis of $[(\text{CH}_3\text{-(CH}_2)_7)_4\text{N}][\text{Au}_{25}(\text{SCH}_2\text{CH}_2\text{-}p\text{-C}_6\text{H}_4\text{-N}_3)_{18}]$ (1-azido).....	196
Figure 4.2 (a) Molecular structure of the anion $[\text{Au}_{25}(\text{SCH}_2\text{CH}_2\text{-}p\text{-C}_6\text{H}_4\text{-N}_3)_{18}]^-$ of 4.1-azido (crystallized in R-3 space group). Tetraoctylammonium counterion is not shown. Au = yellow, S	

= red, C = grey, N = green (b) Au₂₅ core configuration (c) Staple motif with three μ₂-thiolate ligands (d) p-azido-phenylethanethiolate.....197

Figure 4.3 (a) UV-Vis absorption spectrum of 0.2 mM solution of [(CH₃-(CH₂)₇)₄N][Au₂₅(SCH₂CH₂-*p*-C₆H₄-N₃)₁₈] (**4.1-azido**) (black) and surface modified [(CH₃-(CH₂)₇)₄N][Au₂₅(SCH₂CH₂-*p*-C₆H₄-C₈H₁₀N₃)₁₈] (**4.1-triazole**) (red) in dichloromethane at 23°C (b) ATR-IR spectrum of **4.1-azido** (black) and **4.1-triazole** (red) (c) ¹H NMR spectrum of **4.1-azido** (black) and **4.1-triazole** (red), taken in CD₂Cl₂ at 25°C. Chemical shifts of relevant protons are shown for inner ligands (blue) and outer ligands (green). * denotes residual H₂O.....200

Figure S4.1. 600 MHz ¹H NMR spectrum of [(CH₃-(CH₂)₇)₄N][Au₂₅(SCH₂CH₂-*p*-C₆H₄-N₃)₁₈] (**4.1-azido**) in CD₂Cl₂ at 25°C. Red insets are zoom-in regions of relevant sections of spectrum. * indicates residual protio solvents.....213

Figure S4.2. COSY NMR spectrum of [(CH₃-(CH₂)₇)₄N][Au₂₅(SCH₂CH₂-*p*-C₆H₄-N₃)₁₈] (**4.1-azido**) in CD₂Cl₂ at 25°C.....214

Figure S4.3. Negative ion mode ESI mass spectrum of anionic [Au₂₅(SCH₂CH₂-*p*-C₆H₄-N₃)₁₈]¹⁻.....214

Figure S4.4. Space-filling X-ray structure diagram of [(CH₃-(CH₂)₇)₄N][Au₂₅(SCH₂CH₂-*p*-C₆H₄-N₃)₁₈] (**4.1-azido**). Yellow = gold, red = sulfur, black = carbon, green = nitrogen. Tetraoctylammonium counterion is not shown.....215

Figure S4.5. Molecular structure of [(CH₃-(CH₂)₇)₄N][Au₂₅(SCH₂CH₂-*p*-C₆H₄-N₃)₁₈] (**4.1-azido**) showing disordered tetraoctylammonium counterion. Yellow = gold, red = sulfur, black = carbon_{cluster}, light blue = carbon_{counterion}, green = nitrogen.....215

Figure S4.6. Photoluminescence spectrum of a 3 μmol/L solution of [(CH₃-(CH₂)₇)₄N][Au₂₅(SCH₂CH₂-*p*-C₆H₄-N₃)₁₈] (**4.1-azido**) in dichloromethane at 22°C, recorded with a 532 nm laser and 0.1 second exposure time.....216

Figure S4.7. 600 MHz ^1H NMR spectrum of $[(\text{CH}_3-(\text{CH}_2)_7)_4\text{N}][\text{Au}_{25}(\text{SCH}_2\text{CH}_2-p\text{-C}_6\text{H}_4\text{-C}_8\text{H}_{10}\text{N}_3)_{18}]$ (4.1-triazole) in CD_2Cl_2 at 25°C . Red insets are zoom-in regions of relevant sections of spectrum. * indicates residual protio solvents.....	217
Figure S4.8. COSY spectrum of $[(\text{CH}_3-(\text{CH}_2)_7)_4\text{N}][\text{Au}_{25}(\text{SCH}_2\text{CH}_2-p\text{-C}_6\text{H}_4\text{-C}_8\text{H}_{10}\text{N}_3)_{18}]$ (4.1-triazole) in CD_2Cl_2 at 25°C	218
Figure S4.9. Linear negative mode MALDI-TOF mass spectrum of anionic $[\text{Au}_{25}(\text{SCH}_2\text{CH}_2-p\text{-C}_6\text{H}_4\text{-C}_8\text{H}_{10}\text{N}_3)_{18}]^{1-}$	218
Figure S4.10. Photoluminescence spectrum of a $3\ \mu\text{mol/L}$ solution of $[(\text{CH}_3-(\text{CH}_2)_7)_4\text{N}][\text{Au}_{25}(\text{SCH}_2\text{CH}_2-p\text{-C}_6\text{H}_4\text{-C}_8\text{H}_{10}\text{N}_3)_{18}]$ (4.1-triazole) in dichloromethane at 22°C , recorded with a 532 nm laser and 0.1 second exposure time.....	219
Figure S4.11. 600 MHz ^1H NMR spectrum of $[(\text{CH}_3-(\text{CH}_2)_7)_4\text{N}][\text{Au}_{25}(\text{SCH}_2\text{CH}_2-p\text{-C}_6\text{H}_4\text{-C}_{10}\text{H}_{14}\text{N}_3\text{O})_{18}]$ in CD_2Cl_2 at 25°C . Red insets are zoom-in region of relevant section of spectrum. * indicates residual protio solvents.....	220
Figure S4.12. Linear negative mode MALDI-TOF mass spectrum of anionic $[(\text{CH}_3-(\text{CH}_2)_7)_4\text{N}][\text{Au}_{25}(\text{SCH}_2\text{CH}_2-p\text{-C}_6\text{H}_4\text{-C}_{10}\text{H}_{14}\text{N}_3\text{O})_{18}]^{1-}$	221
Figure S4.13. UV-Vis absorption spectrum of 1×10^{-4} M solution of $[(\text{CH}_3-(\text{CH}_2)_7)_4\text{N}][\text{Au}_{25}(\text{SCH}_2\text{CH}_2-p\text{-C}_6\text{H}_4\text{-C}_{10}\text{H}_{14}\text{N}_3\text{O})_{18}]$ in dichloromethane at 23°C	221
Figure S4.14. Infrared spectrum of $[(\text{CH}_3-(\text{CH}_2)_7)_4\text{N}][\text{Au}_{25}(\text{SCH}_2\text{CH}_2-p\text{-C}_6\text{H}_4\text{-C}_{10}\text{H}_{14}\text{N}_3\text{O})_{18}]$	222
Figure S4.15. ^1H NMR spectrum of <i>p</i> -nitro-phenylethanethioacetate in CDCl_3 at 25°C . * indicates residual protio solvent.....	223
Figure S4.16. $^{13}\text{C}\{^1\text{H}\}$ NMR spectrum of <i>p</i> -nitro-phenylethanethioacetate in CDCl_3 at 25°C . * indicates CDCl_3 solvent.....	223
Figure S4.17. Infrared spectrum of <i>p</i> -nitro-phenylethanethioacetate.....	224

Figure S4.18. UV-Vis absorption spectrum of 1×10^{-4} M solution of <i>p</i>-nitro-phenylethanethioacetate in dichloromethane at 23°C.....	224
Figure S4.19. ^1H NMR spectrum of <i>p</i>-ammonium-phenylethanethioacetate chloride in $(\text{CD}_3)_2\text{SO}$ at 25°C. * indicates residual protio solvent.....	225
Figure S4.20. $^{13}\text{C}\{^1\text{H}\}$ NMR spectrum of <i>p</i>-ammonium-phenylethanethioacetate chloride in $(\text{CD}_3)_2\text{SO}$ at 25°C. * indicates $(\text{CD}_3)_2\text{SO}$ solvent.....	225
Figure S4.21. Infrared spectrum of <i>p</i>-ammonium-phenylethanethioacetate chloride	226
Figure S4.22. UV-Vis absorption spectrum of 1×10^{-4} M solution of <i>p</i>-ammonium-phenylethanethioacetate chloride in dichloromethane at 23°C.....	226
Figure S4.23. ^1H NMR spectrum of <i>p</i>-azido-phenylethanethioacetate in CDCl_3 at 25°C. * indicates residual protio solvent.....	227
Figure S4.24. $^{13}\text{C}\{^1\text{H}\}$ NMR spectrum of <i>p</i>-azido-phenylethanethioacetate in CDCl_3 at 25°C. * indicates CDCl_3 solvent.....	227
Figure S4.25. Infrared spectrum of <i>p</i>-azido-phenylethanethioacetate	228
Figure S4.26. UV-Vis absorption spectrum of 1×10^{-4} M solution of <i>p</i>-azido-phenylethanethioacetate in dichloromethane at 23°C.....	228
Figure S4.27. ^1H NMR spectrum of <i>p</i>-azido-phenylethanethiol in CD_2Cl_2 at 25°C. * indicates residual protio solvent.....	229
Figure S4.28. $^{13}\text{C}\{^1\text{H}\}$ NMR spectrum of <i>p</i>-azido-phenylethanethiol in CD_2Cl_2 at 25°C. * indicates CD_2Cl_2 solvent.....	229
Figure S4.29. Infrared spectrum of <i>p</i>-azido-phenylethanethiol	230
Figure S4.30. UV-Vis absorption spectrum of 1×10^{-4} M solution of <i>p</i>-azido-phenylethanethiol in dichloromethane at 23°C.....	230

Figure S4.31. Infrared spectrum of (Z)-5,6-dibromocyclooct-1-ene	231
Figure S4.32. UV-Vis absorption spectrum of 1×10^{-4} M solution of (Z)-5,6-dibromocyclooct-1-ene in dichloromethane at 23°C.....	231
Figure S4.33. Infrared spectrum of (Z)-cyclooct-1-ene-5-yne	232
Figure S4.34. UV-Vis absorption spectrum of 1×10^{-4} M solution of (Z)-cyclooct-1-ene-5-yne in dichloromethane at 23°C.....	232

Chapter 5

Figure 5.1. (a) <i>Left to right.</i> Molecular structure of the neutral form $[\text{Au}_{25}(\text{SCH}_2\text{CH}_2\text{-}p\text{-C}_6\text{H}_4\text{-N}_3)_{18}]^0$ of <i>p</i>-azido (<i>p</i>-azido⁰) , the neutral form $[\text{Au}_{25}(\text{SCH}_2\text{CH}_2\text{-}m\text{-C}_6\text{H}_4\text{-N}_3)_{18}]^0$ of <i>m</i>-azido (<i>m</i>-azido⁰) and the neutral form $[\text{Au}_{25}(\text{SCH}_2\text{CH}_2\text{-}o\text{-C}_6\text{H}_4\text{-N}_3)_{18}]^0$ of <i>o</i>-azido (<i>o</i>-azido⁰) . Au = yellow, S = red, C = black, N = green. (b) <i>Left to right.</i> Comparison of core structures of <i>p</i>-azido⁰ , <i>p</i>-azido⁰ , <i>m</i>-azido⁰ and <i>o</i>-azido⁰	243
Figure 5.2. <i>Left to right.</i> Differential pulse voltammogram (DPV) spectrum of 0.1 mM solution of <i>p</i>-azido¹⁻ , <i>m</i>-azido¹⁻ and <i>o</i>-azido¹⁻ , in 1:1 acetonitrile:benzene. Supporting electrolyte for DPV measurements was 0.1 M tetra- <i>n</i> -butylammonium perchlorate (TBAP). Arrows indicate scanning potential direction, and asterisk indicates starting position of measurements. Formal potentials of first oxidation reactions are indicated.....	245
Figure 5.3. (a) ATR-IR spectra of <i>p</i>-azido¹⁻ (black), <i>m</i>-azido¹⁻ (blue) and <i>o</i>-azido¹⁻ (red). (b) ATR-IR spectra of <i>p</i>-triazole¹⁻ (dotted black), <i>m</i>-triazole¹⁻ (dotted blue) and <i>o</i>-triazole¹⁻ (dotted red). (c) UV-Vis absorption spectra of 0.2 mM solutions of <i>p</i>-azido¹⁻ (black), <i>m</i>-azido¹⁻ (blue) and <i>o</i>-azido¹⁻ (red) in dichloromethane at 23°C. (d) UV-Vis absorption spectra of 0.2 mM solutions of <i>p</i>-triazole¹⁻ (dotted black), <i>m</i>-triazole¹⁻ (dotted blue) and <i>o</i>-triazole¹⁻ (dotted red) in dichloromethane at 23°C.....	248

Figure S5.1. 600 MHz ¹ H NMR spectrum of [(CH ₃ -(CH ₂) ₇) ₄ N][Au ₂₅ (SCH ₂ CH ₂ - <i>m</i> -C ₆ H ₄ -N ₃) ₁₈] (<i>m</i> -azido ¹⁻) in CD ₂ Cl ₂ at 25°C. Red insets are zoom-in regions of relevant sections of spectrum. * indicates residual protio solvents.....	269
Figure S5.2. Negative ion mode ESI mass spectrum of anionic [Au ₂₅ (SCH ₂ CH ₂ - <i>m</i> -C ₆ H ₄ -N ₃) ₁₈] ¹⁻	270
Figure S5.3. 600 MHz ¹ H NMR spectrum of [(CH ₃ -(CH ₂) ₇) ₄ N][Au ₂₅ (SCH ₂ CH ₂ - <i>o</i> -C ₆ H ₄ -N ₃) ₁₈] (<i>o</i> -azido ¹⁻) in CD ₂ Cl ₂ at 25°C. Red insets are zoom-in regions of relevant sections of spectrum. * indicates residual protio solvents.....	271
Figure S5.4. Negative ion mode ESI mass spectrum of anionic [Au ₂₅ (SCH ₂ CH ₂ - <i>o</i> -C ₆ H ₄ -N ₃) ₁₈] ¹⁻	272
Figure S5.5. Space-filling X-ray structure diagram of [Au ₂₅ (SCH ₂ CH ₂ - <i>p</i> -C ₆ H ₄ -N ₃) ₁₈] (<i>p</i> -azido ⁰). Au = yellow, S = red, C = black, N = green.....	273
Figure S5.6. Space-filling X-ray structure diagram of [Au ₂₅ (SCH ₂ CH ₂ - <i>m</i> -C ₆ H ₄ -N ₃) ₁₈] (<i>m</i> -azido ⁰). Au = yellow, S = red, C = black, N = green.....	273
Figure S5.7. Space-filling X-ray structure diagram of [Au ₂₅ (SCH ₂ CH ₂ - <i>o</i> -C ₆ H ₄ -N ₃) ₁₈] (<i>o</i> -azido ⁰). Au = yellow, S = red, C = black, N = green.....	274
Figure S5.8. 600 MHz ¹ H NMR spectrum of [(CH ₃ -(CH ₂) ₇) ₄ N][Au ₂₅ (SCH ₂ CH ₂ - <i>m</i> -C ₆ H ₄ -C ₈ H ₁₀ N ₃) ₁₈] in CD ₂ Cl ₂ at 25°C. Red insets are zoom-in regions of relevant sections of spectrum. * indicates residual protio solvents.....	275
Figure S5.9. Linear negative mode MALDI-TOF mass spectrum of anionic [Au ₂₅ (SCH ₂ CH ₂ - <i>m</i> -C ₆ H ₄ -C ₈ H ₁₀ N ₃) ₁₈] ¹⁻	276
Figure S5.10. 600 MHz ¹ H NMR spectrum of [(CH ₃ -(CH ₂) ₇) ₄ N][Au ₂₅ (SCH ₂ CH ₂ - <i>o</i> -C ₆ H ₄ -C ₈ H ₁₀ N ₃) ₁₈] in CD ₂ Cl ₂ at 25°C. * indicates residual protio solvents.....	277
Figure S5.11. Linear negative mode MALDI-TOF mass spectrum of anionic [Au ₂₅ (SCH ₂ CH ₂ - <i>o</i> -C ₆ H ₄ -C ₈ H ₁₀ N ₃) ₁₈] ¹⁻	278

Figure S5.12. ^1H NMR spectrum of <i>m</i> -nitro-phenylethanethioacetate in CDCl_3 at 25°C . * indicates residual protio solvent.....	280
Figure S5.13. $^{13}\text{C}\{^1\text{H}\}$ NMR spectrum of <i>m</i> -nitro-phenylethanethioacetate in CDCl_3 at 25°C . * indicates CDCl_3 solvent.....	280
Figure S5.14. Infrared spectrum of <i>m</i> -nitro-phenylethanethioacetate.....	281
Figure S5.15. ^1H NMR spectrum of <i>m</i> -azido-phenylethanethioacetate in CDCl_3 at 25°C . * indicates residual protio solvent.....	282
Figure S5.16. $^{13}\text{C}\{^1\text{H}\}$ NMR spectrum of <i>m</i> -azido-phenylethanethioacetate in CDCl_3 at 25°C . * indicates CDCl_3 solvent.....	282
Figure S5.17. Infrared spectrum of <i>m</i> -azido-phenylethanethioacetate.....	283
Figure S5.18. ^1H NMR spectrum of <i>m</i> -azido-phenylethanethiol in CD_2Cl_2 at 25°C . * indicates residual protio solvent.....	284
Figure S5.19. $^{13}\text{C}\{^1\text{H}\}$ NMR spectrum of <i>m</i> -azido-phenylethanethiol in CD_2Cl_2 at 25°C . * indicates CD_2Cl_2 solvent.....	284
Figure S5.20. Infrared spectrum of <i>m</i> -azido-phenylethanethiol.....	285
Figure S5.21. ^1H NMR spectrum of <i>o</i> -nitro-phenylethanethioacetate in CDCl_3 at 25°C . * indicates residual protio solvent.....	286
Figure S5.22. $^{13}\text{C}\{^1\text{H}\}$ NMR spectrum of <i>o</i> -nitro-phenylethanethioacetate in CDCl_3 at 25°C . * indicates CDCl_3 solvent.....	286
Figure S5.23. Infrared spectrum of <i>o</i> -nitro-phenylethanethioacetate.....	287
Figure S5.24. ^1H NMR spectrum of <i>o</i> -azido-phenylethanethioacetate in CDCl_3 at 25°C . * indicates residual protio solvent.....	288

Figure S5.25. $^{13}\text{C}\{^1\text{H}\}$ NMR spectrum of <i>o</i> -azido-phenylethanethioacetate in CDCl_3 at 25°C . * indicates CDCl_3 solvent.....	288
Figure S5.26. Infrared spectrum of <i>o</i> -azido-phenylethanethioacetate.....	289
Figure S5.27. ^1H NMR spectrum of <i>o</i> -azido-phenylethanethiol in CD_2Cl_2 at 25°C . * indicates residual protio solvent.....	290
Figure S5.28. $^{13}\text{C}\{^1\text{H}\}$ NMR spectrum of <i>o</i> -azido-phenylethanethiol in CD_2Cl_2 at 25°C . * indicates CD_2Cl_2 solvent.....	290
Figure S5.29. Infrared spectrum of <i>o</i> -azido-phenylethanethiol.....	291
Figure S5.30. Cyclic voltammetry (CV) graph of 0.1 mM solution of $[(\text{CH}_3\text{-(CH}_2)_7)_4\text{N}][\text{Au}_{25}(\text{SCH}_2\text{CH}_2\text{-}i{p}\text{-C}_6\text{H}_4\text{-N}_3)_{18}]$ (<i>p</i> -azido $^{1-}$) in 1:1 acetonitrile:benzene. Supporting electrolyte for CV measurements was 0.1 M tetra- <i>n</i> -butylammonium perchlorate (TBAP).....	292
Figure S5.31. Cyclic voltammetry (CV) graph of 0.1 mM solution of $[(\text{CH}_3\text{-(CH}_2)_7)_4\text{N}][\text{Au}_{25}(\text{SCH}_2\text{CH}_2\text{-}i{m}\text{-C}_6\text{H}_4\text{-N}_3)_{18}]$ (<i>m</i> -azido $^{1-}$) in 1:1 acetonitrile:benzene. Supporting electrolyte for CV measurements was 0.1 M tetra- <i>n</i> -butylammonium perchlorate (TBAP).....	293
Figure S5.32. Cyclic voltammetry (CV) graph of 0.1 mM solution of $[(\text{CH}_3\text{-(CH}_2)_7)_4\text{N}][\text{Au}_{25}(\text{SCH}_2\text{CH}_2\text{-}i{o}\text{-C}_6\text{H}_4\text{-N}_3)_{18}]$ (<i>o</i> -azido $^{1-}$) in 1:1 acetonitrile:benzene. Supporting electrolyte for CV measurements was 0.1 M tetra- <i>n</i> -butylammonium perchlorate (TBAP).....	294
Figure S5.33. Second order kinetics graph for <i>p</i> -azidophenylethanethiol with $\text{BCN}_{\text{exo-OH}}$ (Trial 1).....	296
Figure S5.34. Second order kinetics graph for <i>p</i> -azidophenylethanethiol with $\text{BCN}_{\text{exo-OH}}$ (Trial 2).....	296
Figure S5.35. Second order kinetics graph for <i>m</i> -azidophenylethanethiol with $\text{BCN}_{\text{exo-OH}}$ (Trial 1).....	297
Figure S5.36. Second order kinetics graph for <i>m</i> -azidophenylethanethiol with $\text{BCN}_{\text{exo-OH}}$ (Trial 2).....	297

Figure S5.37. Second order kinetics graph for <i>o</i> -azidophenylethanethiol with BCN_{exo}-OH (Trial 1).....	298
Figure S5.38. Second order kinetics graph for <i>o</i> -azidophenylethanethiol with BCN_{exo}-OH (Trial 2).....	298
Figure S5.39. Second order kinetics graph for <i>p</i> -azido ¹⁻ with BCN_{exo}-OH (Trial 1).....	299
Figure S5.40. Second order kinetics graph for <i>p</i> -azido ¹⁻ with BCN_{exo}-OH (Trial 2).....	299
Figure S5.41. Second order kinetics graph for <i>m</i> -azido ¹⁻ with BCN_{exo}-OH (Trial 1).....	300
Figure S5.42. Second order kinetics graph for <i>m</i> -azido ¹⁻ with BCN_{exo}-OH (Trial 2).....	300

Chapter 6

Figure 6.1. (a) ATR-IR spectrum of [(CH ₃ -(CH ₂) ₇) ₄ N][Au ₂₅ (SCH ₂ CH ₂ - <i>p</i> -C ₆ H ₄ -N ₃) ₁₈] (6.1-azido) (black), [(CH ₃ -(CH ₂) ₇) ₄ N][Au ₂₅ (SCH ₂ CH ₂ - <i>p</i> -C ₆ H ₄ -C ₂₁ H ₂₂ FeN ₃ O ₂) ₁₈] (6.1-ferrocenyl) (red) and ferrocene-BCN_{exo} (blue). (b) UV-Vis absorption spectrum of (6.1-azido) (black, 0.2 mM), 6.1-ferrocenyl (red, 0.2 mM) and ferrocene-BCN_{exo} (blue, 5 μM) in dichloromethane at 23°C. (c) ¹ H NMR spectrum of 6.1-ferrocenyl taken in CD ₂ Cl ₂ at 25°C. Red insets shows expanded sections of spectrum of 6.1-ferrocenyl , and black inset shows relevant expanded section of ¹ H spectrum of 6.1-azido , which was also taken in CD ₂ Cl ₂ at 25°C.....	316
Figure 6.2. (a) Differential pulse voltammogram (DPV) of 0.1 mM solution of 6.1-azido in 1:1 acetonitrile with 0.1M tetra-n-butylammonium perchlorate (TBAP) as a supporting electrolyte. (b) Differential pulse voltammogram (DPV) of 0.1 mM solution of 6.1-ferrocenyl in 1:1 acetonitrile with 0.1M tetra-n-butylammonium perchlorate (TBAP) as a supporting electrolyte. Arrows indicate scanning potential direction. Note the different vertical scales for the two nanoclusters.....	318

Figure S6.1. 600 MHz ^1H NMR spectrum of $[(\text{CH}_3-(\text{CH}_2)_7)_4\text{N}][\text{Au}_{25}(\text{SCH}_2\text{CH}_2-p\text{-C}_6\text{H}_4\text{-C}_{21}\text{H}_{22}\text{FeN}_3\text{O}_2)_{18}]$ (6.1-ferrocenyl) in CD_2Cl_2 at 25°C . Red insets are zoom-in regions of relevant sections of spectrum. * indicates residual protio solvents.....	329
Figure S6.2. Linear negative mode MALDI-TOF mass spectrum of anionic $[\text{Au}_{25}(\text{SCH}_2\text{CH}_2-p\text{-C}_6\text{H}_4\text{-C}_{21}\text{H}_{22}\text{FeN}_3\text{O}_2)_{18}]^{1-}$	330
Figure S6.3. ^1H NMR spectrum of ferrocene-BCN_{exo} in CD_2Cl_2 at 25°C . * indicates residual protio solvent.....	331
Figure S6.4. $^{13}\text{C}\{^1\text{H}\}$ NMR spectrum of ferrocene-BCN_{exo} in CD_2Cl_2 at 25°C . * indicates residual protio solvent.....	331
Figure S6.5. Infrared spectrum of ferrocene-BCN_{exo}	332
Figure S6.6. ^1H NMR spectrum of ferrocene-triazole-thioacetate in CD_2Cl_2 at 25°C . * indicates residual protio solvent.....	333
Figure S6.7. Cyclic voltammogram of a 0.1 mM solution of $[(\text{CH}_3-(\text{CH}_2)_7)_4\text{N}][\text{Au}_{25}(\text{SCH}_2\text{CH}_2-p\text{-C}_6\text{H}_4\text{-C}_{21}\text{H}_{22}\text{FeN}_3\text{O}_2)_{18}]$ (6.1 ferrocenyl) in 1:1 acetonitrile:benzene, containing 0.1 M TBAP as the supporting electrolyte, with a scan rate of 100 mV/s. The arrows show the potential scanning direction.....	334
Figure S6.8. Cyclic voltammogram of a 1 mM solution of <i>p</i>-azido-phenylethanethioacetate in 1:1 acetonitrile:benzene, containing 0.1 M TBAP as the supporting electrolyte, with a scan rate of 100 mV/s. The arrows show the potential scanning direction.....	335
Figure S6.9. Differential pulse voltammogram of a 1 mM solution of <i>p</i>-azido-phenylethanethioacetate in 1:1 acetonitrile:benzene, containing 0.1 M TBAP as the supporting electrolyte, with a scan rate of 100 mV/s. The arrows show the potential scanning direction...	335
Figure S6.10. Cyclic voltammogram of a 3 mM solution of ferrocene-triazole-thioacetate in 1:1 acetonitrile:benzene, containing 0.1 M TBAP as the supporting electrolyte, with a scan rate of 100 mV/s. The arrows show the potential scanning direction.....	336

Figure S6.11. Differential pulse voltammogram of a 3 mM solution of **ferrocene-triazole-thioacetate** in 1:1 acetonitrile:benzene, containing 0.1 M TBAP as the supporting electrolyte, with a scan rate of 100 mV/s. The arrows show the potential scanning direction.....336

Chapter 7

Figure 7.1. *Chapter 5.* Investigation of isomeric effects of the azide position on the surface ligands in azide-functionalized $[\text{Au}_{25}(\text{SR})_{18}]^{-1}$ platforms, and related properties and surface reactivity.....344

Figure 7.2. Development of functional $[\text{Au}_{25}(\text{SR})_{18}]^{-1}$ systems using nanoorthogonal CS-SPAAC chemistry for applications in drug delivery, bioimaging and catalysis.....349

List of Schemes

Chapter 1

Scheme 1.1. *Modern methods for synthesizing AuNPs.* (**Method 1**) The Brust-Schiffrin method to generate 1.5 to 5 nm AuNPs. (**Method 2**) The Turkevich method to generate 10 to 100 nm AuNPs. (**Method 3**) The seed growth method to generate 50 to 200 nm AuNPs.....5

Scheme 1.2. *Modern methods for synthesizing AuNCs.* (**Method 1**) The kinetic size-focusing method. (**Method 2**) The ligand exchange method. (**Method 3**) The high temperature thiol etching method.....15

Scheme 1.3. *Synthesis of functional AuNP or AuNC systems* for application-based research, using the direct synthetic method (**Method 1**) or the ligand exchange method (**Method 2**).....27

Scheme 1.4. A “*bioorthogonal click reaction*”. The first reactive group is exogenously added and intracellularly incorporated into the target biomolecule using the cellular machinery. A chemical reporter possessing the second (complementary) reactive group is then exogenously added. The reaction between the first and second reactive groups need to proceed selectively in the presence of all the functionalities found within cellular systems, some of which are shown, and the biomolecule is then labelled with the chemical reporter.....29

Scheme 1.5. *Three common “bioorthogonal click reactions”.* (**a**) The Staudinger-Bertozzi ligation between a terminal azide and phenyl ester-functionalized phosphine. (**b**) The *trans*-cyclooctene-tetrazine ligation. (**c**) The azide-oxanorbornadiene cycloaddition.....31

Scheme 1.6. *Common reactions between terminal azides and alkyne moieties.* (**a**) The alkyne-azide Huisgen cycloaddition reaction between a terminal alkyne and terminal azide under high temperature (and/or pressure). (**b**) The copper(I)-catalyzed alkyne-azide cycloaddition (CuAAC) reaction between a terminal alkyne and terminal azide in the presence of a copper (I) catalyst. (**c**) The strain-promoted alkyne-azide cycloaddition (SPAAC) reaction between a cyclooctyne and terminal azide.....33

Scheme 1.7. The strain-promoted alkyne-nitrone cycloaddition (SPANC) reaction between a nitrone and cyclooctyne.....34

Scheme 1.8. (a) *Synthesis of functional AuNP/AuNC through ligand exchange reaction.* Addition of chemical reporter possessing thiol group undergoes exchange with native thiols at the metallic core. Reaction at core can result in altered core framework. Quantitative exchange is difficult to accomplish, leading to mixed monolayer. **(b)** *Synthesis of functional AuNP/AuNC through “nanoorthogonal click reaction”.* Addition of chemical reporter possessing second reactive group (azide or cyclooctyne) undergoes chemoselective reaction with nanomaterial platform possessing first (complementary) reactive group on the exterior interface. Reaction at interface less likely to result in altered core framework. Quantitative interfacial reaction can be achieved reliably.....39

Chapter 2

Scheme 2.1. Synthesis of AuNP-BCN platform. *Right inset.* TEM image of AuNP-BCN.....65

Chapter 3

Scheme 3.1. Synthesis of pyridinium–nitrones possessing anisole (**3a**), phenyl (**3b**) and benzonitrile (**3c**) substituents. Top inset shows general scheme for strain–promoted alkyne–nitrone cycloaddition (SPANC) reaction between nitrone (blue) and cyclooctyne (red). Bottom: molecular structures of **3a**, **3b**, **3c** in the crystal. Thermal ellipsoids are drawn at the 50% probability level with hydrogen atoms drawn with arbitrary radii (black = carbon, red = oxygen, green = nitrogen, purple = iodine).....124

Scheme 3.2. (a) Proposed synthetic strategy for incorporating the pyridinium-nitrone moiety to the surface of AuNPs, using a pyridinium-functionalized thiol ligand. **(b)** Synthetic strategy for pyridinium-functionalized thiol ligand.....130

Chapter 4

Scheme 4.1. CS-SPAAC reaction between $[(\text{CH}_3-(\text{CH}_2)_7)_4\text{N}][\text{Au}_{25}(\text{SCH}_2\text{CH}_2-p\text{-C}_6\text{H}_4\text{-N}_3)_{18}]$ (**1-azido**) and (**Z**)-cyclooct-1-ene-5-yne, giving surface modified $[(\text{CH}_3-(\text{CH}_2)_7)_4\text{N}][\text{Au}_{25}(\text{SCH}_2\text{CH}_2-p\text{-C}_6\text{H}_4\text{-C}_8\text{H}_{10}\text{N}_3)_{18}]$ (**1-triazole**).....198

Chapter 5

Scheme 5.1. Synthesis of $[(\text{CH}_3-(\text{CH}_2)_7)_4\text{N}][\text{Au}_{25}(\text{SCH}_2\text{CH}_2-p\text{-C}_6\text{H}_4\text{-N}_3)_{18}]$ (**p-azido¹⁻**, black), $[(\text{CH}_3-(\text{CH}_2)_7)_4\text{N}][\text{Au}_{25}(\text{SCH}_2\text{CH}_2-m\text{-C}_6\text{H}_4\text{-N}_3)_{18}]$ (**m-azido¹⁻**, blue) and $[(\text{CH}_3-(\text{CH}_2)_7)_4\text{N}][\text{Au}_{25}(\text{SCH}_2\text{CH}_2-o\text{-C}_6\text{H}_4\text{-N}_3)_{18}]$ (**o-azido¹⁻**, red). Rate of reaction (k_2) between AuNCs and $\text{BCN}_{exo}\text{-OH}$ were determined under second order conditions using ^1H NMR spectroscopy, and are indicated for *p*-azidophenylethanethiol, *m*-azidophenylethanethiol, *o*-azidophenylethanethiol, **p-azido¹⁻** and **m-azido¹⁻**.....241

Chapter 6

Scheme 6.1. Synthetic approach to the preparation of fully-ferrocenated $[(\text{CH}_3-(\text{CH}_2)_7)_4\text{N}][\text{Au}_{25}(\text{SCH}_2\text{CH}_2-p\text{-C}_6\text{H}_4\text{-C}_{21}\text{H}_{22}\text{FeN}_3\text{O}_2)_{18}]$ (**6.1-ferrocenyl**) through CS-SPAAC between $[(\text{CH}_3-(\text{CH}_2)_7)_4\text{N}][\text{Au}_{25}(\text{SCH}_2\text{CH}_2-p\text{-C}_6\text{H}_4\text{-N}_3)_{18}]$ (**6.1-azido**) and **ferrocene-BCN_{exo}**.....314

Chapter 7

Scheme 7.1. Scheme illustrating ligand exchange chemistry and nanoorthogonal surface chemistry for surface modifications of polydisperse AuNPs and atomically precise AuNCs. Green = first reactive partner. Blue = second, complementary reactive partner. Brown = functional substrate.....339

Scheme 7.2. *Chapter 2.* Development of BCN-functionalized AuNP platform (AuNP) for kinetically variable SPAAC and SPANC, and kinetically directed competitive reactions.....341

Scheme 7.3. *Chapter 3.* (a) Development of highly reactive pyridinium-nitrones for rapid and tunable SPANC chemistry. (b) Proposed synthesis for the development of pyridinium-nitrone-functionalized AuNP platform. However, the necessary thiolated-ligand possessing the terminal pyridinium-nitrone moiety could not be isolated.....342

Scheme 7.4. *Chapter 4.* Development of azide-functionalized $[\text{Au}_{25}(\text{SR})_{18}]^{-1}$ platform for nanoorthogonal CS-SPAAC chemistry for efficient and reliable surface modifications.....343

Scheme 7.5. *Chapter 6.* Development of ferrocene-modified $[\text{Au}_{25}(\text{SR})_{18}]^{1-}$ framework through nanoorthogonal CS-SPAAC chemistry.....345

List of Tables

Chapter 3

Table 3.1. Key parameters of pyridinium–nitrones that vary as electron deficiency (and corresponding reactivity) is increased. ¹ H NMR spectra were taken in deuterated dimethylsulfoxide at 25°C. Bond lengths were determined from crystallographic data. Mulliken charges (Q) and the energy gap between the HOMO of BCN and LUMO of the nitrone ($\Delta E_{\text{HOMO-LUMO}}$) were determined from DFT calculations. Bimolecular rate constants (k_2) were determined under pseudo–first order conditions in 2:1 acetonitrile:tetrahydrofuran at 22°C by UV-Vis spectroscopy.....	126
Table S3.1. Percentage of nitrone 3a remaining in 6:1 D ₂ O:(CD ₃) ₂ SO over time, measured as a change in the H _{α} NMR signal intensity relative to the peak from residual H ₂ O solvent.....	170
Table S3.2. Percentage of nitrone 3b remaining in 6:1 D ₂ O:(CD ₃) ₂ SO over time, measured as a change in the H _{α} NMR signal intensity relative to the peak from residual H ₂ O solvent.....	170
Table S3.3. Percentage of nitrone 3c remaining in 6:1 D ₂ O:(CD ₃) ₂ SO over time, measured as a change in the H _{α} NMR signal intensity relative to the peak from residual H ₂ O solvent.....	171
Table S3.4. Kinetic data for nitrone 4 and BCN_{exo}-OH (5)	176
Table S3.5. Kinetic data for nitrone 2b and BCN_{exo}-OH (5)	177
Table S3.6. Kinetic data for nitrone 3a and BCN_{exo}-OH (5)	178
Table S3.7. Kinetic data for nitrone 3b and BCN_{exo}-OH (5)	179
Table S3.8. Kinetic data for nitrone 3c and BCN_{exo}-OH (5)	180
Table S3.9. Crystallographic information of for molecular structures of nitrones.....	184
Table S3.10. Structural coordinates for BCN_{exo}-OH (5)	187
Table S3.11. Structural coordinates for nitrone 3a	188

Table S3.12. Structural coordinates for nitron 3b	188
Table S3.13. Structural coordinates for nitron 3c	189
Table S3.14. Structural coordinates for nitron 2b	190
Table S3.15. Structural coordinates for nitron 4	191
Table S3.16. Comparison of actual bond lengths and bond angles in molecular structures of nitrones to theoretical bond lengths and bond angles from DFT analysis.....	192

List of Appendices

A1.1 Permission to Reproduce Copyrighted Material.....	352
A1.2 Curriculum Vitae.....	370

List of Abbreviations

°C	degree Celsius
^{13}C	carbon-13
$^{13}\text{C} \{^1\text{H}\}$	carbon-13 (proton-decoupled)
^1H	proton
^{19}F	fluorine-19
μL	microliter
μm	micrometer
μmol	micromole
λ	wavelength
λ_{ex}	excitation wavelength
λ_{max}	wavelength of maximum absorption
δ	chemical shift
\AA	angstrom
ATR	attenuated total reflectance
AuNP	gold nanoparticle
AuNC	gold nanoclusters
BARAC	biarylcyclooctynone
BCN	bicyclo[6.1.0]nonyne
$\text{BCN}_{\text{exo}}\text{-OH}$	<i>exo</i> isomer of bicyclo[6.1.0]nonyne
br (in NMR data)	broad signal
BSA	bovine serum albumin
bp	boiling point
CD_3CN	acetonitrile- D_3
CD_3OD	methanol- D_4
CDCl_3	chloroform- D_1
CD_2Cl_2	dichloromethane- D_2
CD_3OD	methanol- D_4
$(\text{CD}_3)_2\text{SO}$	dimethylsulfoxide- D_6

CeO ₂	cerium (IV) oxide
CH ₂ Cl ₂	dichloromethane
CH ₃ I	iodomethane
cm ⁻¹	wavenumber
CuAAC	copper(I)-catalyzed alkyne-azide cycloaddition
CV	cyclic voltammetry
d (in NMR data)	doublet
Da	Dalton
D ₂ O	water-d ₂
DBCO	dibenzocyclooctyne
DCM	dichloromethane
dd (in NMR data)	doublet of doublets
DIBAC	dibenzoazacyclooctyne
DIFO	difluorinated cyclooctyne
DFT	density functional theory
DNA	deoxyribonucleic acid
DMF	dimethylformamide
DMSO	dimethylsulfoxide
DOX	doxorubicin
DPV	differential pulse voltammetry
dt (in NMR data)	doublet of triplets
EG	ethylene glycol
EG ₃	triethylene glycol
EG ₄	tetraethylene glycol
eq.	equivalent
ESI-MS	electrospray ionization-mass spectrometry
EtOH	ethanol
eV	electron volts
F(000)	structure factor
FRET	fluorescence resonance energy transfer

FT	Fourier transform
g	gram
GFP	green fluorescent protein
GSH	glutathione
HAuCl ₄	tetrachloroauric acid
<i>hν</i>	light
HOMO	highest occupied molecular orbital
HRMS	high-resolution mass spectrometry
Hz	hertz
<i>I</i> -SPAAC	interfacial strain-promoted alkyne-azide cycloaddition
<i>I</i> -SPANC	interfacial strain-promoted alkyne-nitrone cycloaddition
IED	inverse electron demand
IR	infrared
<i>J</i>	coupling constant
LDI-MS	laser desorption ionization mass spectrometry
LUMO	lowest unoccupied molecular orbital
K	degrees Kelvin
<i>k</i> ₂	bimolecular rate constant
<i>k</i> _{obs}	observed rate constant
KBr	potassium bromide
kcal	kilocalorie
kcps	kilocounts per second
kDa	kilodalton
kJ	kilojoule
KSCoCH ₃	potassium thioacetate
kV	kilovolt
m (in NMR data)	multiplet
M	molar (mol/L)
mA	milliamp
MBA	4-mercaptobenzoic acid

MeCN	acetonitrile
MeO	methoxy
MgSO ₄	magnesium sulphate
MHz	megahertz
min	minute
mL	milliliter
mg	milligram
mM	millimolar (mmol/L)
mol	mole
MPA	3-mercaptopropionic acid
<i>m/z</i>	mass to charge ratio
NaBH ₄	sodium borohydride
NaH	sodium hydride
NaHCO ₃	sodium bicarbonate
NaOH	sodium hydroxide
NH ₄ Cl	ammonium chloride
NIR	near infrared
NH ₂	amino
nm	nanometer
N ₃	azide
NEt ₃	triethylamine
NMR	nuclear resonance spectroscopy
NPC	nasopharyngeal carcinoma
OH	hydroxyl
PBS	phosphate buffer solution
Ph	phenyl
PL	photoluminescence
ppm	parts per million
q (in NMR data)	quartet
Q	Mulliken charge

quin (in NMR data)	quintet
QRE	quasi-reference electrode
r.t.	room temperature
Ref	reference
RSH	thiol molecule
rpm	revolutions per minute
s (in NMR data)	singlet
s	second
SPAAC	strain-promoted alkyne-azide cycloaddition
SPANC	strain-promoted alkyne-nitrone cycloaddition
SPR	surface plasmon resonance
SR	thiolate molecule
t (in NMR data)	triplet
t ₀	time zero
t ₂₄	time twenty-four hours
TCO	<i>trans</i> -cyclooctene
TEG	tetraethylene glycol
TEM	transmission electron microscope
THF	tetrahydrofuran
TsCl	tosyl chloride
TLC	thin layer chromatography
TGA	thermogravimetric analysis
TiO ₂	titanium (IV) oxide
UV-Vis	ultraviolet-visible
V	volts
XPS	x-ray photoelectron spectroscopy
XRD	x-ray diffraction
Z	number of molecules in asymmetric unit cell

Chapter 1

1 Introduction – Strain-Promoted Click Chemistry for Nanoorthogonal Surface Modifications of Gold Nanoparticles and Gold Nanoclusters

1.1 “Golden Nanochemistry”

Colloidal solutions of gold, in which bulk metallic gold is dismantled into distinct metallic particles on the nanoscale, has been a great source of scientific interest that dates back to Michael Faraday’s time, when he reported his synthesis of “fine particles of gold”, by reducing tetrachloroauric acid (HAuCl_4) with phosphorus and stabilizing the particles through addition of carbon disulfide, producing a “beautiful ruby fluid”.¹ This pioneering study triggered intensive systematic research towards developing colloidal solutions of inorganic metals (such as silver and copper)² but developing different gold colloids received particular interest due to their stunning and vibrant array of colors.

Initial efforts in the early 20th century were directed towards developing different methods for reducing HAuCl_4 ,³ and as the documentation of different gold colloids started to expand, important concepts of colloidal gold formation started to mature, such as nucleation and growth mechanisms,⁴ surface adsorption of ions⁵ and chemical protection of colloidal dispersions.³ In 1918, Scherrer recognized that the size of colloidal gold could be estimated using X-ray diffraction,⁶ a size-determination strategy that is often still used today. With the commercialization of the transmission electron microscope (TEM) in the mid 20th century, Turkevich later reported that the size and shape of colloidal gold species could be more easily determined using TEM microscopy by directly visualizing them,⁷ which is the primary method for size- and shape-determination used today. This progressively evolving understanding of colloidal gold systems seeded a renaissance of nanoscale gold research in the late 1900s, when the term “nanotechnology” started to emerge. Since then, the age of “golden nanochemistry” has blossomed, dedicated to research on gold colloids that has become one of the dominant fields in nanomaterial research.

The field of “golden nanochemistry” can be dissected into two primary research pursuits. The first and initial pursuit is towards developing synthetic control over the size and shape of the colloidal gold particles, and researchers have developed excellent control over these parameters to construct different three-dimensional structures and frameworks (**Section 1.2.1 and Section 1.3.1**).⁸⁻¹⁰ With the maturation of synthetic strategies for developing colloidal gold particles with different structures and sizes has come a binary distinction that is based on the size (diameter) of the particles. When colloidal gold particles are greater than approximately 2 nm and *polydisperse*, they are classified as “*gold nanoparticles (AuNPs)*” (**Section 1.2**), and when they are less than approximately 2 nm and *monodisperse*, they are classified as “*gold nanoclusters (AuNCs)*” (**Section 1.3**). Although collectively they have properties that are distinct to bulk metallic gold, individually their properties have sub-distinctions that distinguishes them from each other, with the “nanoparticle size regime” having its own properties (**Section 1.2.3**), and the “nanocluster size regime” having separate properties that are more molecule-like (as the molecular size threshold is approached) (**Section 1.3.4**).

The second pursuit within “golden nanochemistry” is dedicated to surface functionalization of colloidal gold particles. Early synthetic efforts afforded colloidal gold particles with largely inert surfaces, and their properties were largely dependent on the properties of the metallic arrangements of the core. However, as our understanding of their overall structure began to improve, structure-property relationships started to arise. The realization that the metallic core cannot exist on its own and requires a protecting surface monolayer was an imperative discovery. It is through manipulations of the surface monolayer, and functionalization with different substrates, that has led to extensive application-based research utilizing gold nanoparticles (**Section 1.2.4**) and gold nanoclusters (**Section 1.3.5**) for several scientific disciplines.

1.2 Gold Nanoparticles

1.2.1 Structure of Gold Nanoparticles

When colloidal gold particles are greater than approximately 2 nm, they are classified as “gold nanoparticles (AuNPs)”. Most syntheses for obtaining AuNPs follow a similar mechanism as that first reported by Faraday in 1857 whereby a gold (III) precursor is reduced in the presence of a

surface capping ligand to prevent metallic aggregation and stabilize the internal core. As described in **Section 1.2.2**, using different synthetic strategies, particle size can be adjusted by varying the relative gold ion : reducing agent or gold ion : stabilizer ratios, with larger (and more polydisperse) systems being obtained when using larger ratios.¹¹ Several different strategies have also been developed to furnish AuNPs with different shapes, where AuNPs having spherical,¹² rod-shaped,¹³ prism-shaped,¹⁴ and octahedral¹⁵ morphologies have been reported (**Figure 1.1a**), among many others. As shown in **Figure 1.1b**, as the size of the particles are increased, the size-dependent properties (such as optical properties) changes correspondingly.¹⁶ Although there have been different three-dimensional structures reported, spherical AuNPs are arguably the most common as it is easier to functionalize their surfaces and require simple reaction conditions.

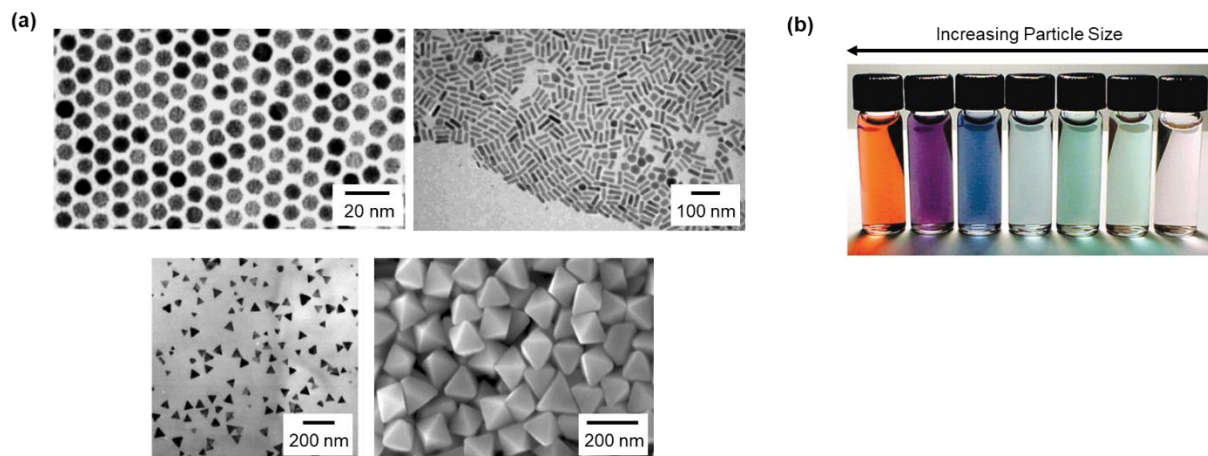


Figure 1.1. (a) TEM/SEM images of gold nanoparticles (AuNPs) with different morphologies. Top left. Spherical AuNPs (Figure reproduced with permission from Ref [12].) Top Right. Rod-shaped AuNPs (Figure reproduced with permission from Ref [13]). Bottom Left. Prism-shaped AuNPs (Figure reproduced with permission from Ref [14]). Bottom Right. Octahedral AuNPs (Figure reproduced with permission from Ref [15]). (b) Solutions of rod-shaped AuNPs having different sizes. (Figure reproduced with permission of Ref [16]).

1.2.2 Synthesis of Gold Nanoparticles

One of the major advantages of operating in the nanoparticle size regime for colloidal gold is the versatility and adaptability of the synthetic strategies available to furnish AuNP systems of different size, shape and surface functionalization/complexity. Given that their larger size imparts greater chemical and physical stability, compared to the nanocluster size regime, and that monodispersity is not an expected feature, the desired AuNP structures are less delicate to the chosen synthetic conditions and are typically made in a particle size distribution, which provides

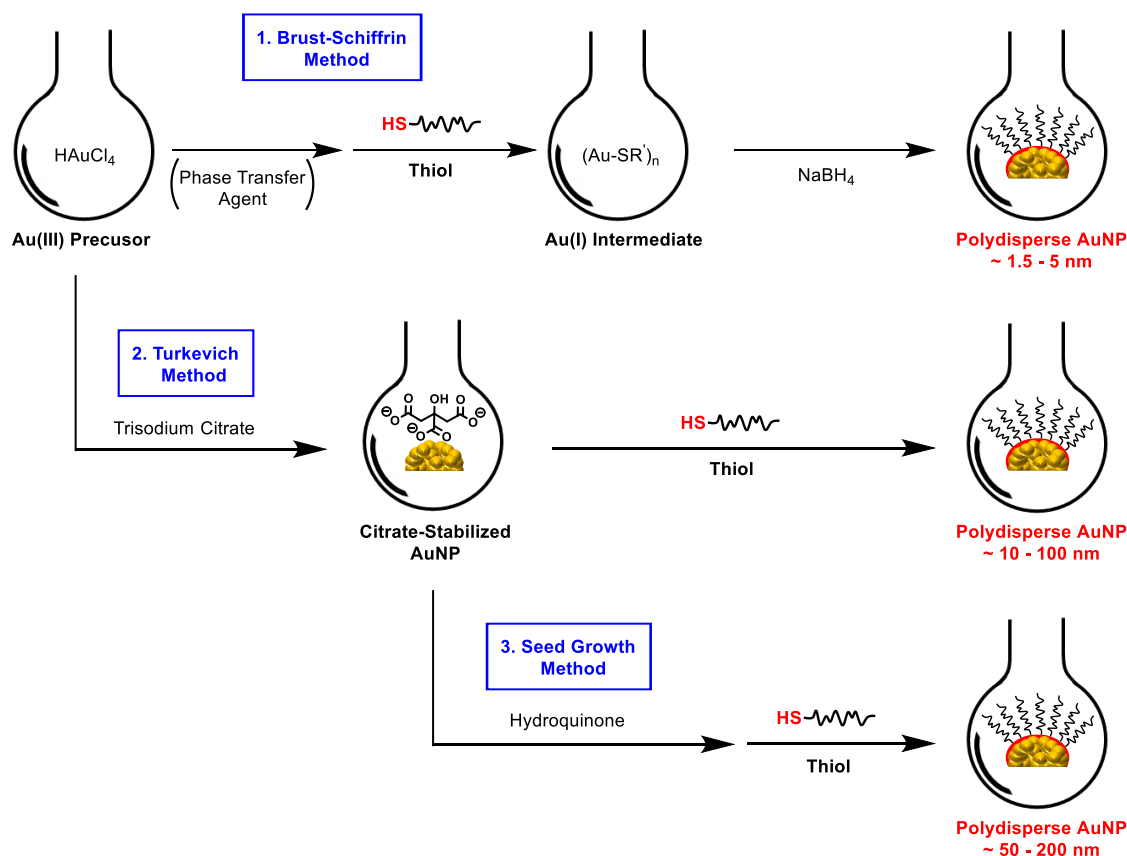
greater freedom over the methodologies that are employed to acquire these rigid structures. The universal paradigm for all AuNP synthetic strategies is a bottom-up reduction of a gold(III) precursor salt (most commonly tetrachloroauric acid, HAuCl_4) by a reducing agent to form an Au(I)/Au(0) core that is stabilized by an external stabilizing ligand on the core surface. Modern procedures can be classified into three major methods: the Brust-Schiffrin method, the Turkevich Method and the seed growth method (**Scheme 1.1**).

The classical Brust-Schiffrin method is a modification of Faraday's two-phase pioneering synthesis,¹ in which HAuCl_4 is phase-transferred from water into toluene in the presence of a phase-transfer agent (most commonly tetraoctylammonium bromide). The Au(III) precursor is then reduced by an external thiol (RSH, where R is an alkyl or aryl group) ligand that strongly binds to gold due to the soft character of both gold and sulfur, which leads to the formation of an Au(I) polymeric intermediate $[(\text{Au(I)-SR})_n]$.¹⁷ This intermediate is subsequently reduced by excess sodium borohydride (NaBH_4), which results in a Au(I)/Au(0) core that is stabilized by $[-\text{SR-Au(I)-SR-}]$ core surface motifs,^{18,19} and furnishes organic-soluble AuNPs with a particle size distribution of approximately 1.5 to 5 nm (**Scheme 1.1, Method 1**).²⁰ It should be noted that contemporary Brust-Schiffrin syntheses may or may not include an external phase-transfer agent depending on the thiol chosen, and this method is amendable to different one-phase solvent systems that eliminates the necessity of the phase-transfer agent.²¹ The Brust-Schiffrin method is arguably the most versatile of the three methods for synthesizing AuNP structures, because the size and shape of the structures can be controlled through careful choice of: (1) ratio of thiol to gold (III) precursor (2) structure of the thiol ligand and (3) temperature and rate at which the sodium borohydride is added.²² Furthermore, the method is amenable to a wide variety of different alkyl and aromatic thiol ligands,²³ including thiol ligands possessing nucleophilic groups such as OH and NH_2 groups, providing exceptional control over the surface derivatization of the AuNP structures.

In the Turkevich method, an aqueous solution of HAuCl_4 is reduced by trisodium citrate, which also serves as the required stabilizing ligand for the resultant Au(0) core.²⁴ This method furnishes citrate-stabilized water-soluble AuNPs with a particle size distribution between approximately 10 to 100 nm (**Scheme 1.1, Method 2**), whose size distribution can primarily be controlled through changing the ratio of citrate to gold (III) precursor.²⁵ As surface citrate anions are bound through a weak electrostatic interaction to the core gold atoms, the template citrate-

stabilized AuNPs can be augmented through addition of a supplementary thiol ligand, in the presence of a surfactant to prevent nanoparticle aggregation during the exchange process.^{26, 27}

The largest AuNP systems can be fabricated using the seed growth method, in which smaller AuNP systems serve as seed particles, or nucleation centers, allowing for the hierarchal assembly of AuNP systems that are larger than can be made by the Brust-Schiffrin and Turkevich methods. Seed particles are most commonly citrate-stabilized AuNPs, and upon addition of a growth solution containing HAuCl_4 and a weak reducing agent, such as hydroquinone, the Au(III) salt is reduced and nascent metal ions are affixed to the surface of the pre-existing seed particles.²⁸ As with the Turkevich method, surface anions can be exchanged with thiol ligands to establish the desired surface functionalization. This method furnishes AuNP systems with a particle size distribution between approximately 50 to 200 nm (**Scheme 1.1, Method 3**),²⁹ where the size distribution can be controlled through changing the ratio of Au(III) precursor to seed particle.³⁰



Scheme 1.1. Modern methods for synthesizing AuNPs. (**Method 1**) The Brust-Schiffrin method to generate 1.5 to 5 nm AuNPs. (**Method 2**) The Turkevich method to generate 10 to 100 nm AuNPs. (**Method 3**) The seed growth method to generate 50 to 200 nm AuNPs.

1.2.3 Properties of Gold Nanoparticles

Colloidal gold particles in the nanoparticle size regime exhibit physical properties that are distinct to both smaller particles in the nanocluster size regime, and bulk metallic gold. One of the most highly exploited intrinsic properties that is unique to AuNPs is the physical nature in which they interact and respond to incident electromagnetic radiation in the ultraviolet-visible (UV-Vis) range, which is a consequence of their electronic surface structure. Spherical AuNPs above 8 nm exhibit a sharp absorption peak between 500 to 600 nm,³¹ which is a result from the collective oscillation of free conduction electrons across the AuNP surface due to the resonant excitation by the incident UV-Vis radiation,³² and is known as “surface plasmon resonance (SPR)”. It is the SPR that produces the intense colors observed with AuNPs in solution and is primarily influenced by the size of the AuNP system, with smaller AuNPs giving blue-shifted (hypochromic) SPR peaks and larger AuNPs giving red-shifted (bathochromic) SPR peaks (**Figure 1.2a**).³³ The position of the SPR peak is also influenced by the shape, solvent, surface ligand, core charge and temperature.³⁴⁻³⁶ Although the SPR peak on its own serves as an absorption fingerprint for a given AuNP system, one feature of it that is exploitable for application-based research is that AuNP aggregation causes the SPR peak to become broader, and also undergoes a significant red-shift that increases as the interparticle distance decreases (**Figure 1.2b**).³⁷

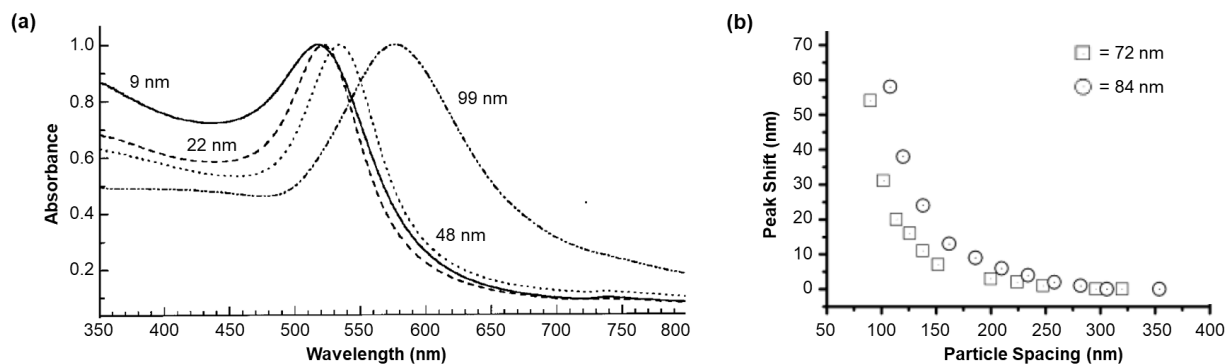


Figure 1.2. (a) Optical absorption spectra of 9, 22, 48 and 99 nm spherical AuNPs. The broad peaks correspond to the SPR of each system. Figure reproduced with permission from Ref. [33]. (b) Aggregation-induced shift in SPR wavelength as a function of particle center-center spacing for 72 and 84 nm spherical AuNPs. Figure reproduced with permission from Ref. [37].

Another intrinsic property unique to AuNPs is their superior ability to quench fluorescence of adsorbed or covalently linked fluorophore molecules to their surfaces. This quenching phenomenon is a result of nonradiative fluorescence resonance energy transfer (FRET) that is caused by good overlap between the emission profile of excited donor fluorophores in the UV-Vis region, and the SPR profile of the AuNP core, which serves as a ground state electron acceptor, leading to emission deactivation of the proximal fluorophore.³⁸ The degree of quenching is dependent on two main factors. The first is the extent of spectral overlap, which is determined by both the identity and emission profile of the surface fluorophore, and size and shape of the AuNP, which determines the spectral position of the SPR.³⁹ The second factor is the distance between the donor fluorophore and AuNP acceptor, with FRET-based quenching decreasing as the distance between the fluorophore and AuNP core increases.⁴⁰

An extrinsic property of AuNPs is their excellent biocompatibility, which has resulted in substantial AuNP-based applications in biological settings (**Section 1.2.4**). The ability for AuNP systems to be internalized by cells appear to be largely independent of the cell type and surface functionalization of the AuNP,⁴¹ which is a surprising phenomenon given the high density of surface ligands and foreign nature of the metallic core in intracellular settings, and only requires simple incubation of the desired AuNP system with the cell line that is to internalize the functionalized AuNP.⁴² However, polymeric coatings are often tethered to the AuNP surface to enhance cellular permeability and prevent premature extracellular degradation.¹⁶ Cellular entry can also be affected by the size and shape of the AuNP system, with spherical ~50 nm AuNPs having the highest internalization rates (**Figure 1.3a**).⁴³ The method of internalization is not well understood, but it is thought to occur through a receptor-mediated endocytotic pathway, in which membrane-bound transport proteins recognize and internalize the functionalized AuNP system through vesicle formation.⁴⁴ Evidence of this endocytotic pathway was demonstrated in a study in which transferrin-coated AuNPs were highly internalized by human nasopharyngeal carcinoma (NPC) cells under physiologically relevant conditions, whereas AuNPs not coated with the transferrin protein were not (**Figure 1.3b**), implicating the transferrin receptor-mediated endocytotic pathway for AuNP internalization.⁴⁵

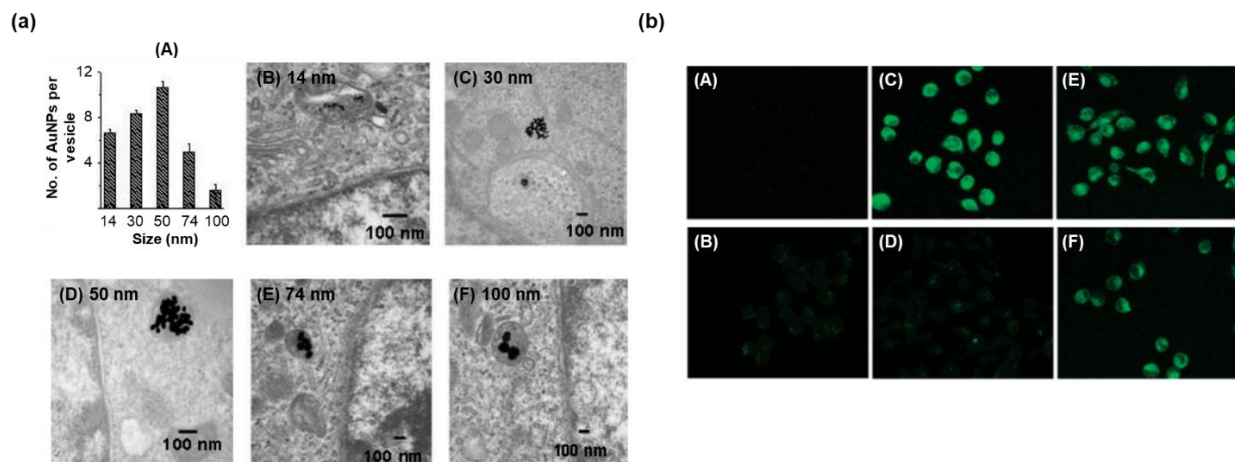


Figure 1.3. (a) Uptake of AuNPs into mammalian cells (A) Number of AuNPs per vesicle diameter versus nanoparticle size (B-F) TEM images of AuNPs with sizes 14, 30, 50, 74 and 100 nm trapped inside vesicles of a HeLa cell, respectively. Figure reproduced with permission from Ref. [43] (b) Confocal cell images showing fluorescein-labelled transferrin AuNPs (AuNP-TF) internalized by NPC cells (A) NPC cells without AuNP-TF (B) NPC cells treated with AuNPs without surface transferrin (C) NPC cells treated with AuNP-TF (D) NPC cells treated with albumin-coated AuNPs (E and F) NPC cells co-treated with different proportions of AuNP-TF and albumin-coated AuNPs (1:2 and 1:5, respectively). Figure reproduced with permission from Ref. [45].

1.2.4 Applications of Gold Nanoparticles

Compared to many other nanomaterial systems, AuNP systems can be synthesized using straightforward yet modifiable strategies that can be manipulated to construct AuNP systems of different size and three-dimensional complexity simply through careful choice of reaction stoichiometries and reactive partners. Furthermore, due to the affinity of thiol moieties towards gold surfaces, the composition and arrangement of their surfaces can be modulated with high precision using a variety of different thiol ligands, most often through simple mix-and-stir reactions. This ability to amend their core and surface structures allow for their size- and composition-dependent properties to be reliably modified in a very predictable manner. This has led to the maturation of a rich and dynamic application-based research field over the past several decades, focusing on the use of functional AuNP systems in a variety of different scientific disciplines.

One of the most exploitable properties of AuNPs for application-based research is their plasmonic optical properties. AuNP aggregation induces interparticle surface plasmon coupling,

resulting in a color change from red to blue that can be measured both visually and spectrophotometrically⁴⁶. This makes AuNPs useful platforms for spectral-based colorimetric sensing of target analytes, whereby the target analyte induces either AuNP aggregation or dispersion.⁴⁷ Lin *et al.* reported the development of an AuNP system functionalized with [15]-crown-5 moieties, which have a high binding affinity for lead ions. In the absence of lead ions, the surface [15]-crown-5 moieties undergo interparticle hydrogen bonding in aqueous solutions, causing AuNP aggregation. Addition of lead ions causes competitive adsorption, preventing interparticle hydrogen bonding and dismantling of the AuNP aggregates, affording a measurable color change (**Figure 1.4a**).⁴⁸ Conversely, Huang *et al.* reported an AuNP system where the surface ligands were 3-mercaptopropionic acid (MPA), which was a highly sensitive colorimetric sensor for mercury ions. Their MPA-functionalized AuNPs were dispersed in aqueous solution, and addition of mercury ions led to an interaction between surface carboxyl groups and the lead ions that caused AuNP aggregation, causing a change in the spectral pattern of the AuNP system that could be measured (**Figure 1.4b**).⁴⁹

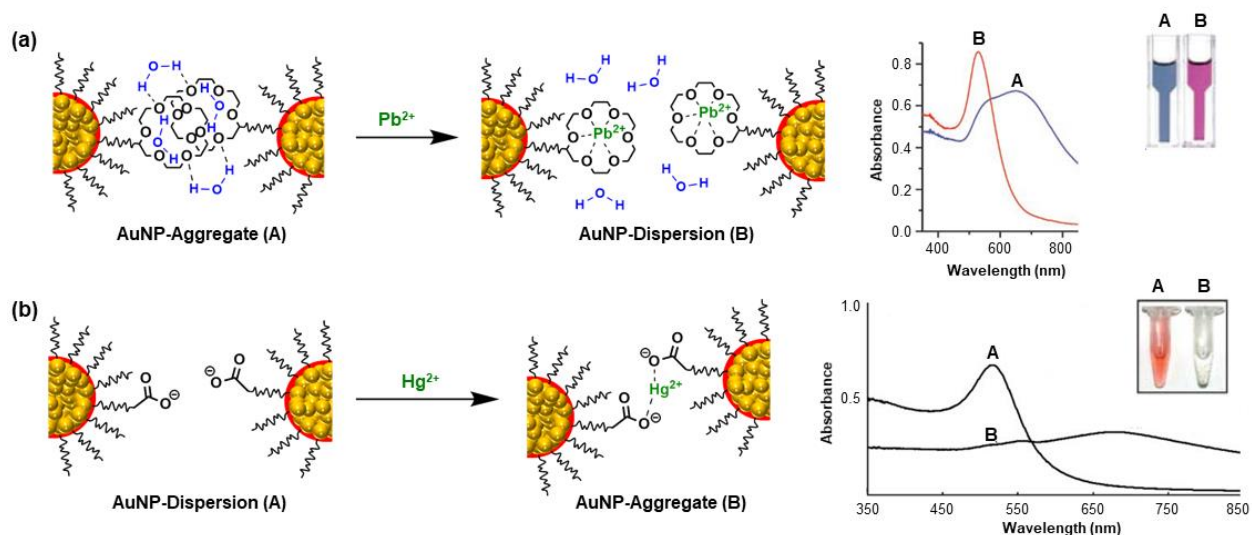


Figure 1.4. (a) *Left.* Colorimetric sensing of lead ions, whereby lead adsorption causes dismantling of ([15]-crown-5)-functionalized AuNP aggregates (A) into an AuNP dispersion (B). *Right.* UV/Vis spectra of A and B (Spectra figure reproduced with permission from Ref. [48]). (b) *Left.* Colorimetric sensing of mercury ions, whereby mercury adsorption caused dispersion of carboxyl-terminated AuNPs (A) to from AuNP aggregates (B). *Right.* UV/Vis spectra of A and B (Spectra figure reproduced with permission from Ref. [49]).

AuNP systems are also promising candidates for macromolecular delivery platforms, especially in the delivery of drug molecules.⁴¹ Drug inoculation is often accompanied by premature

deterioration by extracellular matrix proteases due to the foreign nature of the drug molecules, preventing effective intracellular entry and lowering the overall efficacy of the drug.⁵⁰ Given the excellent biocompatibility of AuNPs, drug molecules tethered onto AuNP surfaces has proven to be an effective strategy for their delivery. Due to the high surface area-to-volume ratio, drug molecules are packed densely on the AuNP surface.⁵¹ This both allows for a high loading of drug molecules per AuNP, and also sterically prevents access to extracellular enzymes, improving therapeutic delivery.⁵² Peng *et al.* reported an AuNP system in which doxorubicin (DOX) was adsorbed onto the surface of 4-mercaptopbenzoic acid (MBA)-functionalized AuNPs, in which DOX was able to adsorb onto the surface through π - π interactions (**Figure 1.5a**).⁵³ DOX is one of the most effective anti-cancer chemotherapeutics available today and is used for the treatment of a variety of cancer types.⁵⁴ They found that when these DOX-loaded AuNPs were introduced into breast cancer cell line MCF-7, there was higher delivery of DOX (**Figure 1.5c**) than when DOX was inoculated on its own (**Figure 1.5b**).⁵³ They also found a greater reduction in tumor volume in mice when the DOX was delivered on the AuNP surface (**Figure 1.5d**).⁵³

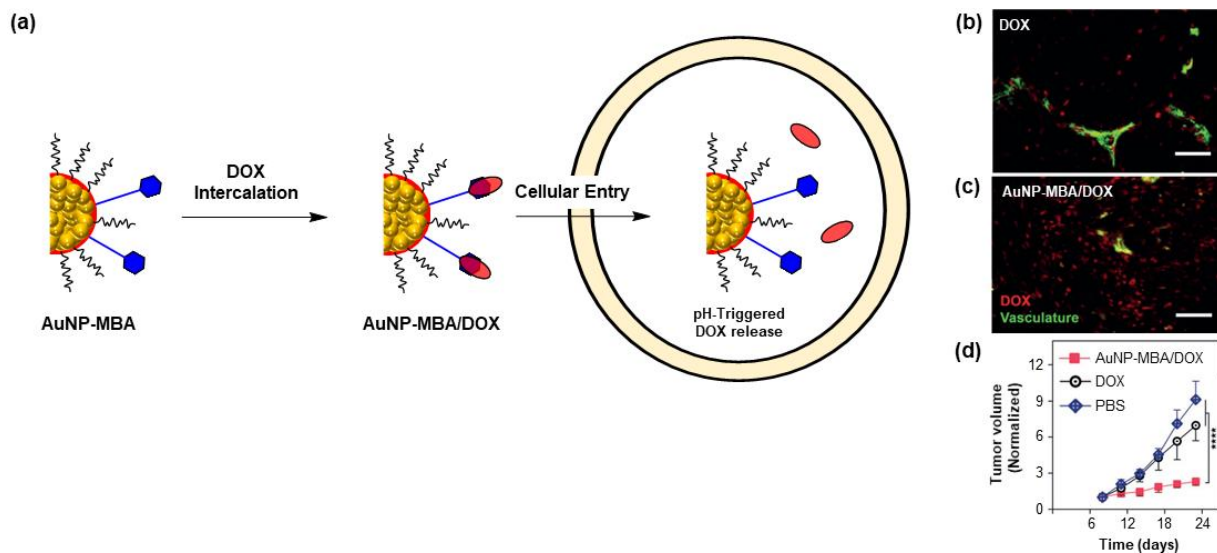


Figure 1.5. (a) Schematic representation of doxorubicin (DOX) adsorption onto AuNP surface and intracellular delivery. (b,c) Fluorescence microscopy images of MCF-7 tumor tissues after injection of DOX alone (b) and AuNP-DOX (c). Red = DOX; green = stained vasculature (lectin-FITC). Scale bar, 50 μ m. (d) Normalized tumor growth curves after injection with AuNP-DOX (red), DOX alone (black) and phosphate buffered-saline (PBS) (blue). Figures in (b), (c) and (d) reproduced with permission from Ref. [53].

Functionalized AuNPs have also found extensive use in bioimaging applications, which typically involves using AuNPs as molecular beacons whereby ‘reporter’ macromolecules are tethered to the AuNP surface that also have an attached fluorophore, where the fluorescence of the fluorophore is quenched due to non-radiative FRET.^{41, 55} Upon introduction of the AuNP system to the intracellular environment, competitive binding of target analytes causes a release of the fluorophore-conjugated reporter agents, which reestablishes fluorescence.⁴¹ Seferos *et al.* developed an AuNP “nano-flare” system (**Figure 1.6a**),⁵⁶ in which oligonucleotide-functionalized AuNPs were synthesized through a ligand exchange between citrate-functionalized AuNPs and a thiol-terminated oligonucleotide sequence. The attached sequence (‘reporter sequence’ with attached fluorophore) was complementary to an oligonucleotide sequence that is present in the mRNA sequence of survivin, a protein that is commonly over-expressed in cancer cell lines. When introduced to the intracellular environment of cancer cells, ‘survivin mRNA’ displaced the fluorophore-conjugated reporter sequence, which released the reported sequence from the AuNP surface and reestablished fluorescence of the attached fluorophore. They observed high fluorescence in cancer cell type SKBR3 when the survivin recognition sequence was on the AuNP surface, as opposed to when a different sequence was tethered to the AuNP surface (**Figure 1.6b**).⁵⁶

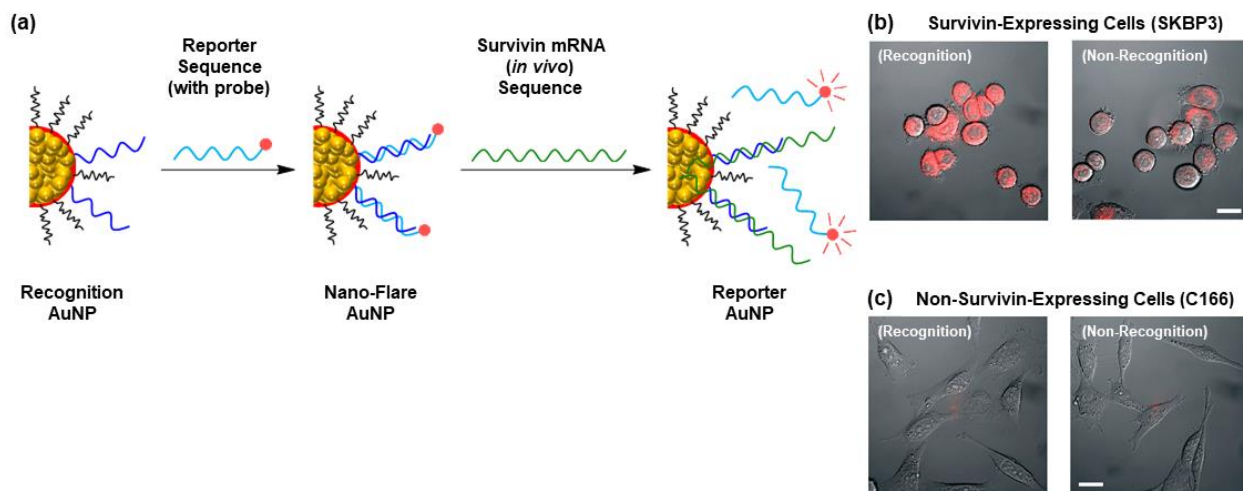


Figure 1.6. (a) Schematic representation of development of ‘nano-flare AuNP’ and *in vivo* release of fluorophore-conjugated reporter sequence after survivin mRNA binding. (b) Differential contrast and fluorescence imaging of survivin-expressing SKBR3 cells treated with survivin nano-flares (*left*) and non-complementary nano-flares (*right*). (c) Analogously treated non-survivin expressing C166 cells. Scale bar is 20 μm . Figure in (b) and (c) reproduced with permission from Ref. [56].

Furthermore, they found the highest fluorescence in survivin-expressing SKBR3 cells as opposed to cell lines that did not express survivin, such as mouse endothelial cell type C166 (**Figure 1.6c**).⁵⁶

1.3 Gold Nanoclusters

1.3.1 Structure of Gold Nanoclusters

Atomically precise gold particles are known as gold nanoclusters (AuNCs) and have received tremendous research interest in recent years due to their unique and extraordinary properties that are not seen from their larger AuNP counterparts. Unlike AuNPs, whose optical properties are largely plasmonic, when the nanocluster size regime is accessed, non-plasmonic molecular-type properties begin to manifest that is one of the primary distinctions.⁵⁷ Furthermore, whereas AuNP systems exist as polydisperse systems, AuNC systems can be furnished in an atomically precise fashion, generating true molecules with well-defined molecular weights and formulas, which permits analysis techniques largely reserved for small molecules, such as single crystal X-ray diffraction. Although there has been other capping ligands reported to stabilize the central metallic core, such as carbenes,⁵⁸ as with AuNPs the predominant capping ligand used in AuNC systems has been thiols. This is due to the structural versatility of thiolated ligands, allowing for different AuNC frameworks to be generated through careful choice of reaction conditions and strategies (**Figure 1.7**).⁵⁹⁻⁶⁵

1.3.2 Synthesis of Gold Nanoclusters

Synthetic strategies for AuNPs are aimed towards developing colloidal gold systems with a general size and shape, and although these strategies are highly versatile in developing different three-dimensional nanostructures, AuNPs are synthesized as polydisperse systems, with a particle size distribution that is dependent on the conditions of the reaction. Unlike with AuNPs, when entering the nanocluster size regime, synthetic strategies are often aimed towards developing atomically precise, and thus monodisperse AuNC systems. Most AuNC synthetic strategies involve an initial reaction using the Brust-Schiffrin method, whereby a gold (III) precursor (most commonly HAuCl_4) is reduced by a thiol ligand to form an Au(I) polymeric intermediate $[(\text{Au(I)-SR})_n]$, which is subsequently reduced by sodium borohydride (NaBH_4) to form an Au(I)/Au(0) nanostructure.⁶⁶ While the Brust-Schiffrin method can also be used to fashion AuNP systems (**Section 1.2.2**),

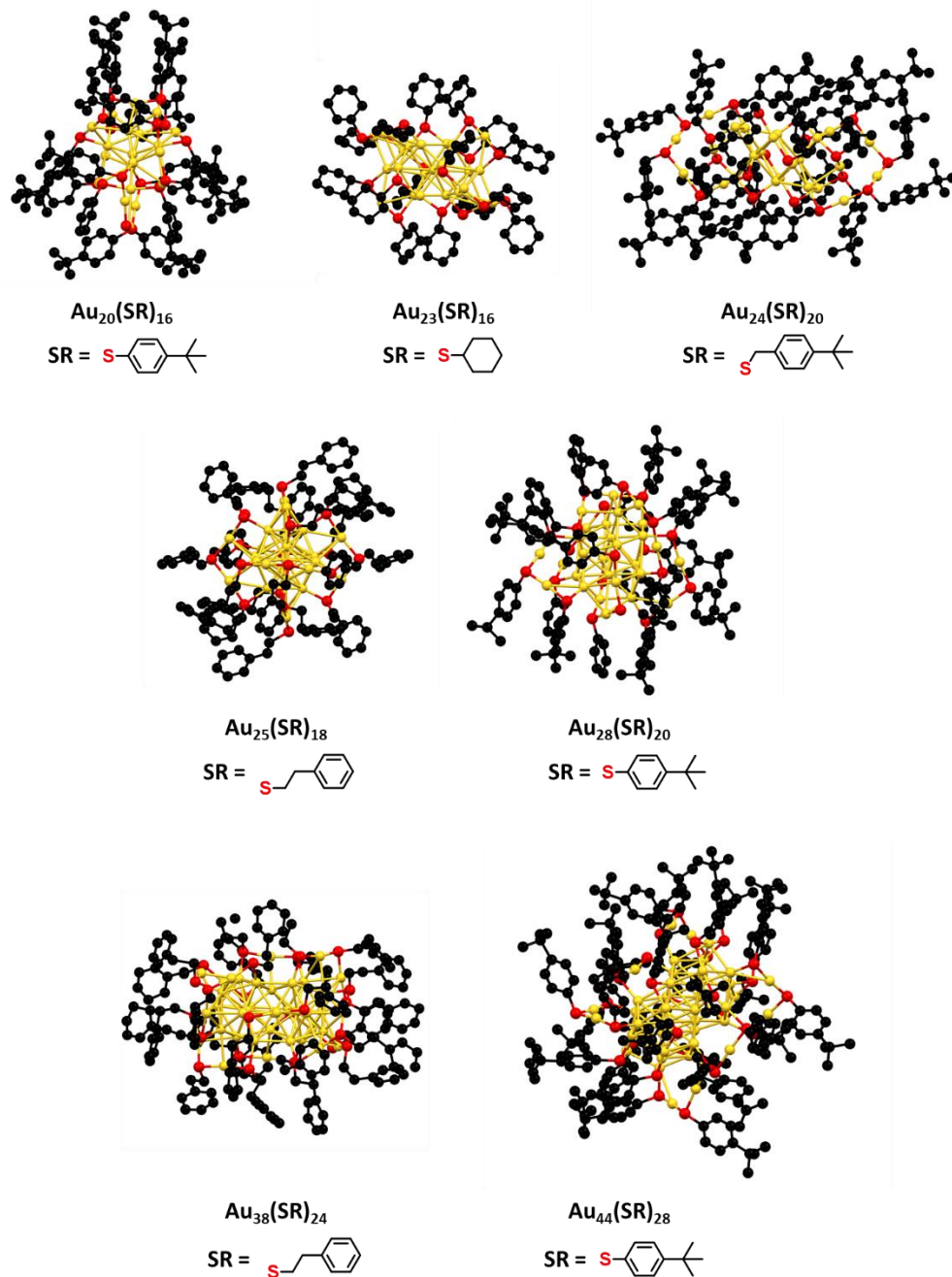


Figure 1.7. Some thiolated AuNC frameworks.

Top (left to right). The $\text{Au}_{20}(\text{SR})_{16}$ framework (where $\text{R} = \text{C}_6\text{H}_4-\text{C}(\text{CH}_3)_3$) (Figure produced from data with permission from Ref. [59]). The $\text{Au}_{23}(\text{SR})_{16}$ framework (where $\text{R} = \text{C}_6\text{C}_{11}$) (Figure produced from data with permission from Ref. [60]). The $\text{Au}_{24}(\text{SR})_{20}$ framework (where $\text{R} = \text{CH}_2-\text{C}_6\text{H}_4-\text{C}(\text{CH}_3)_3$) (Figure produced from data with permission from Ref. [61]).

Middle (left to right). The $\text{Au}_{25}(\text{SR})_{18}$ framework (where $\text{R} = \text{CH}_2\text{CH}_2-\text{C}_6\text{H}_5$) (Figure produced from data with permission from Ref. [62]). The $\text{Au}_{28}(\text{SR})_{20}$ framework (where $\text{R} = \text{C}_6\text{H}_4-\text{C}(\text{CH}_3)_3$) (Figure produced from data with permission from Ref. [63]).

Bottom (left to right). The $\text{Au}_{38}(\text{SR})_{24}$ framework (where $\text{R} = \text{CH}_2\text{CH}_2-\text{C}_6\text{H}_5$) (Figure produced from data with permission from Ref. [64]). The $\text{Au}_{44}(\text{SR})_{28}$ framework (where $\text{R} = \text{CH}_2\text{CH}_2-\text{C}_6\text{H}_5$) (Figure produced from data with permission from Ref. [65]).

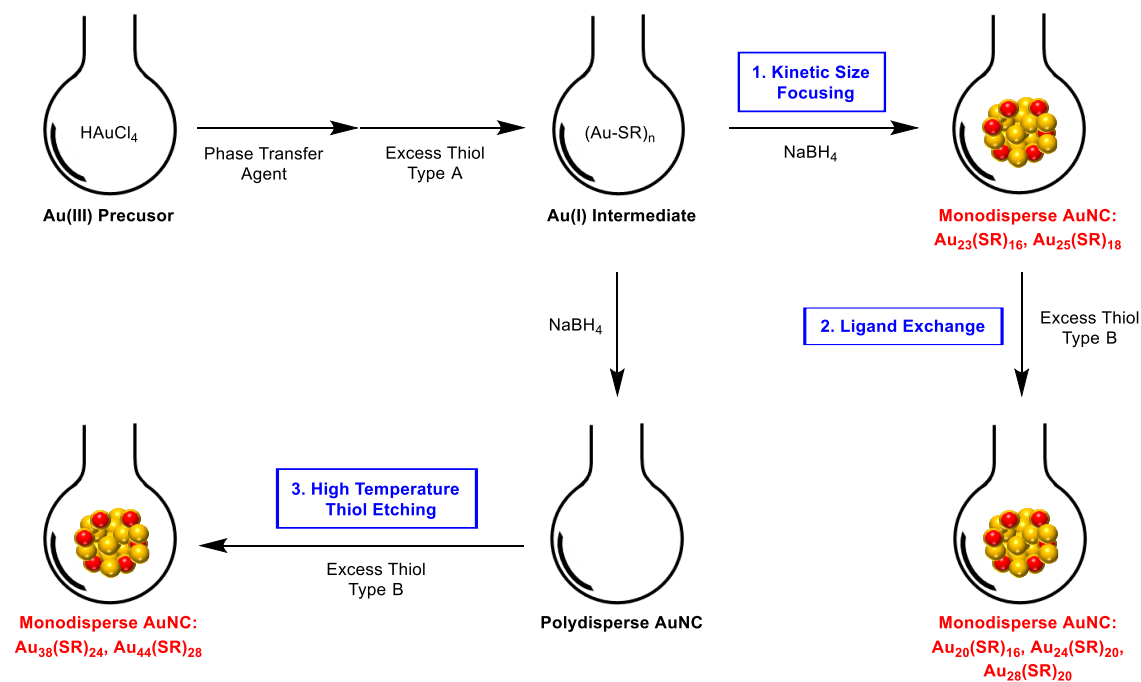
careful choice of reaction conditions, stoichiometries and reactive partners also allows access to the AuNC size regime using the same method. Modern AuNC syntheses can generally be classified depending on whether this Au(I)/Au(0) nanostructure is the desired AuNC, or whether it is subsequently treated in some way to generate the desired AuNC.

During AuNP synthesis, the structure of the $[(\text{Au(I)-SR})_n]$ intermediate not well-defined, which leads to the formation of a polydisperse system after reduction by sodium borohydride. However, since monodispersity is a desired trait for AuNC systems, more careful attention needs to be given to the structure of the $[(\text{Au(I)-SR})_n]$ intermediate, which needs to have a more unambivalent arrangement.⁶⁷ The structure of the $[(\text{Au(I)-SR})_n]$ intermediate is very sensitive to the ratio of gold (III) precursor to thiol, the rate of thiol addition, the temperature at which the gold (III) precursor and thiol are combined/stirred together and the time over which they are stirred,⁶⁸ all of which need to be more carefully considered when synthesizing the $[(\text{Au(I)-SR})_n]$ intermediate. Upon addition of NaBH_4 , it is generally accepted that larger particles initially form, but then begin to ‘size-focus’ into smaller atomically precise core configurations over time, which is dependent on the amount and rate of sodium borohydride addition, the temperature of the reaction, and structure of the $[(\text{Au(I)-SR})_n]$ intermediate.⁶⁹ If the acquired Au(I)/Au(0) structure is the desired AuNC system, it is said to have been furnished using this ‘kinetic size-focusing’ method (**Scheme 1.2, Method 1**),⁷⁰ because typically the structure of the $[(\text{Au(I)-SR})_n]$ is ‘kinetically controlled’ through careful choice of the reaction conditions, followed by size focusing into the desired configuration after NaBH_4 addition. Monodisperse samples of the $\text{Au}_{23}(\text{SR})_{16}$ and $\text{Au}_{25}(\text{SR})_{18}$ frameworks have been synthesized using this kinetic size-focusing strategy,^{60, 62} which have been successfully characterized by single-crystal X-ray diffraction (**Figure 1.7, Section 1.3.1**).

Another common strategy involves using pre-made AuNC templates furnished using the kinetic size-focusing method and altering their core configurations through exchange chemistry with a second (structurally different) thiol ligand, which leads to a transformation of the core configuration and overall structure of the AuNC framework.⁷¹ Various AuNC systems have been furnished using this ‘ligand exchange’ structure-transformation method (**Scheme 1.2, Method 2**). Using the $\text{Au}_{25}(\text{SR})_{18}$ framework as the template, monodisperse samples of the $\text{Au}_{20}(\text{SR})_{16}$ and $\text{Au}_{28}(\text{SR})_{20}$ frameworks have been synthesized,⁵⁹ and using the $\text{Au}_{23}(\text{SR})_{16}$ framework as the

template, monodisperse samples of the $\text{Au}_{24}(\text{SR})_{20}$ framework has been synthesized,⁶¹ which have been successfully characterized by single-crystal X-ray diffraction (**Figure 1.7, Section 1.3.1**).

Many monodisperse AuNC systems have been synthesized using a third common strategy, in which the $[(\text{Au(I)-SR})_n]$ intermediate is less meticulously synthesized, and then rapidly reduced using NaBH_4 to form a polydisperse AuNC system. This polydisperse AuNC sample is then heated to high temperature (typically ≥ 80 °C) in the presence of a second (structurally different) thiol ligand, which leads to ligand exchange/thiol etching on the AuNC surface and size-transformation to fabricate a monodisperse AuNC system (**Scheme 1.2, Method 3**).⁷² Monodisperse samples of the $\text{Au}_{38}(\text{SR})_{24}$ and $\text{Au}_{44}(\text{SR})_{28}$ frameworks have been synthesized using this ‘high temperature thiol etching’ strategy,^{64, 65} which have been successfully characterized by single-crystal X-ray diffraction (**Figure 1.7, Section 1.3.1**).



Scheme 1.2. Modern methods for synthesizing AuNCs. (**Method 1**) The kinetic size-focusing method. (**Method 2**) The ligand exchange method. (**Method 3**) The high temperature thiol etching method.

1.3.3 The Au₂₅(SR)₁₈ Nanocluster Framework

Early AuNC research by the Whetten group reported the synthesis of large polydisperse glutathione (SG)-protected particles (>30,000 Da).⁷³ In a later study in which they modified the reaction conditions, they analyzed a sample of SG-protected particles by laser desorption ionization mass spectrometry (LDI-MS), in which they identified a species with an approximate mass of ~8000 Da,⁷⁴ among the many other larger species that formed, but couldn't conclusively determine a molecular formula due to excessive fragmentation of this species. This ~8000 Da species triggered interest because it started to display non-plasmonic optical properties not seen in the larger SG-protected gold particles that formed. The Tsukuda group were then able to suppress the fragmentation during their mass spectrometric analysis, using electrospray ionization (ESI) mass spectrometry, allowing them to unambiguously determine the molecular formula of the ~8000 Da species as [Au₂₅(SG)₁₈]¹⁻.⁷⁵ This assignment was later confirmed in subsequent studies.^{76,77} In 2007, the Jin group synthesized an [Au₂₅(SR)₁₈]¹⁻ system which used the more rigid phenylethanethiol (HSCH₂CH₂Ph) as the capping ligand instead of glutathione and tetraoctylammonium bromide as a phase-transfer agent, using the kinetic size-focusing method that they first described (**Section 1.3.2**).⁶⁸ It should be noted that it is the anionic form of the Au₂₅(SR)₁₈ framework that is directly accessible using the kinetic size-focusing method, having a tetraoctylammonium counterion. They were able to synthesize a highly monodisperse sample of [Au₂₅(SCH₂CH₂Ph)₁₈]¹⁻ in high yield that was of sufficient purity and monodispersity to confirm its structure by single-crystal X-ray diffraction.⁶²

Since 2007, when the synthetic strategy for [Au₂₅(SCH₂CH₂Ph)₁₈]¹⁻ was optimized, and its molecular structure was confirmed, the [Au₂₅(SR)₁₈]¹⁻ framework has become the dominant thiolate-protected AuNC, especially for structure-property and application-based research. This can largely be attributed to its superior core stability at ambient conditions in a variety of environments and settings, due to its closed-shell superatom electron configuration (an 8 electron system (i.e. 25 – 18 + 1 = 8) that corresponds to a noble-gas like 1S²1P⁶ configuration).⁷⁸ It is because of its superior stability that, unlike many thiolate-protected AuNC systems, the [Au₂₅(SR)₁₈]¹⁻ system is very amenable to different capping thiol ligands other than SG or HSCH₂CH₂Ph,⁷⁹⁻⁸¹ which is one of the most attractive features of the [Au₂₅(SR)₁₈]¹⁻ system. Furthermore, the stability of the [Au₂₅(SR)₁₈]¹⁻ framework makes it comparatively easily to

synthesize, and under kinetic control, can be synthesized in high yield reproducibly at ambient conditions.

Another important feature of the $[\text{Au}_{25}(\text{SR})_{18}]^{1-}$ framework is the ability to alter the oxidation state of the framework through redox chemistry, with several examples of $[\text{Au}_{25}(\text{SR})_{18}]^z$ (where $z = -1, 0$ and $+1$) with different capping ligands having been reported. With respects to the $[\text{Au}_{25}(\text{SCH}_2\text{CH}_2\text{Ph})_{18}]^z$ framework, the Jin group first reported the synthesis of the $[\text{Au}_{25}(\text{SCH}_2\text{CH}_2\text{Ph})_{18}]^0$ framework through air oxidation of the $[\text{Au}_{25}(\text{SCH}_2\text{CH}_2\text{Ph})_{18}]^{1-}$ framework.⁸² In a later study, they were able to oxidize the $[\text{Au}_{25}(\text{SCH}_2\text{CH}_2\text{Ph})_{18}]^{1-}$ framework using hydrogen peroxide to form the same neutral framework.⁸³ Whereas the anionic form is a closed-shell 8 electron system, $[\text{Au}_{25}(\text{SCH}_2\text{CH}_2\text{Ph})_{18}]^0$ is a 7 electron paramagnetic system (i.e. $25 - 18 = 7$) that corresponds to a $1\text{S}^21\text{P}^5$ electron configuration,⁷⁸, attributing its lower stability than the anionic form. The Maran group subsequently reported the synthesis of the cationic $[\text{Au}_{25}(\text{SCH}_2\text{CH}_2\text{Ph})_{18}]^{1+}$ framework by treating the anionic $[\text{Au}_{25}(\text{SCH}_2\text{CH}_2\text{Ph})_{18}]^{1-}$ framework with bis(pentafluorobenzoyl) peroxide.⁸⁴ The cationic $[\text{Au}_{25}(\text{SCH}_2\text{CH}_2\text{Ph})_{18}]^{1+}$ framework is now a 6 electron diamagnetic system (i.e. $25 - 18 - 1 = 6$) that corresponds to a $1\text{S}^21\text{P}^4$ electron configuration.⁷⁸

The discovery of the molecular structure of the $[\text{Au}_{25}(\text{SCH}_2\text{CH}_2\text{Ph})_{18}]^{1-}$ framework in 2007 by the Jin group (**Figure 1.8a**)⁶² has also provided valuable insight into the general molecular and bonding features that are common to most thiolate-protected AuNCs. One molecular feature of $[\text{Au}_{25}(\text{SCH}_2\text{CH}_2\text{Ph})_{18}]^{1-}$ that is common to most thiolate-protected AuNCs are the $[-\text{SR}-\text{Au}(\text{I})-\text{SR}-\text{Au}(\text{I})-\text{SR}-]$ core surface motifs (also known as staple motifs) shown in **Figure 1.8b**, which comprise μ_2 -thiolate ligands that are bonded to two gold atoms, with each gold atom concurrently bonded to two thiolate ligands. In the core structure, there is an internal Au_{13} icosahedral kernel at the center, with twelve $[-\text{SR}-\text{Au}(\text{I})-\text{SR}-\text{Au}(\text{I})-\text{SR}-]$ staple motifs at the 12 vertices (**Figure 1.8b**).^{62, 80, 82} A feature that is unique to $[\text{Au}_{25}(\text{SR})_{18}]^{1-}$ frameworks is the existence of two distinguishable surface ligands sites in each of the twelve $[-\text{SR}-\text{Au}(\text{I})-\text{SR}-\text{Au}(\text{I})-\text{SR}-]$ staple motifs.⁶² Ligands on the two edges of each staple motif occupies one distinguishable surface site, and they are known as “inner ligands”, while ligands attached at the center of each staple motif occupies a separate distinguishable surface site, and they are known as “outer ligands” (**Figure 1.8b**).⁸⁴ Pengo *et al.* demonstrated that the inner surface sites are more reactive towards exchange chemistry than the

outer ligands,⁸⁵ which creates important consequences in the ligand exchange chemistry of $[\text{Au}_{25}(\text{SR})_{18}]^{1-}$ frameworks.

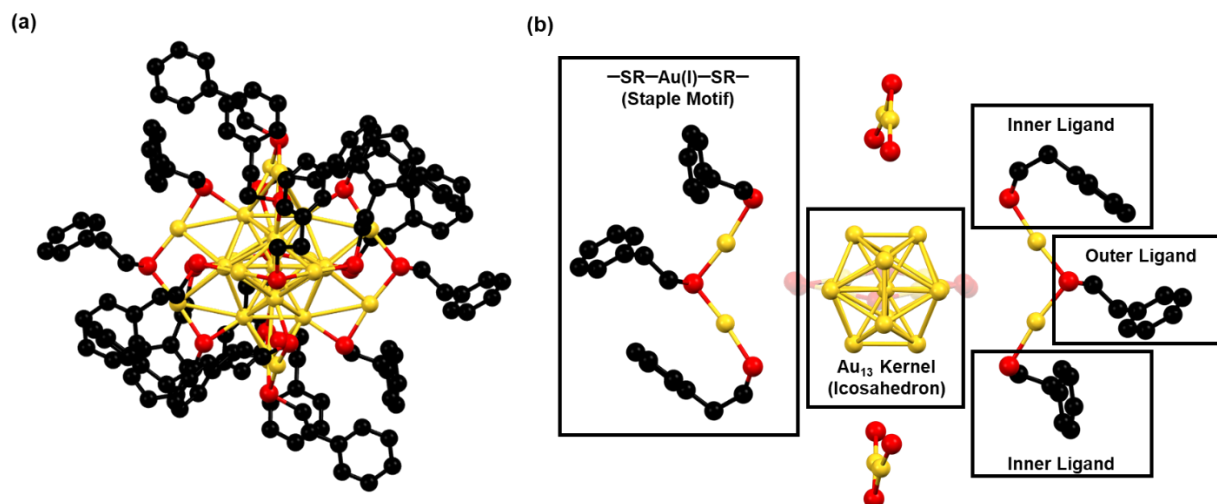


Figure 1.8. (a) Molecular structure of $[\text{TOA}][\text{Au}_{25}(\text{CH}_2\text{CH}_2\text{Ph})_{18}]$, where TOA = tetraoctylammonium (not shown). (b) Staple motifs, Au_{13} kernel, and inner/outer ligands in molecular structure of $[\text{Au}_{25}(\text{CH}_2\text{CH}_2\text{Ph})_{18}]^{1-}$. Figure produced from data with permission from Ref. [62].

1.3.4 Properties of the $\text{Au}_{25}(\text{SR})_{18}$ Framework

Colloidal gold particles in the nanocluster size regime exhibit molecular-type physical properties that are distinct from the physical properties of larger AuNPs, as the molecular size regime is approached.⁸⁶ Furthermore, unlike with AuNPs, the properties of AuNCs are highly sensitive to small changes in the structure of the internal core configuration and ligand structure. One of the most distinctive features of AuNC systems, that distinguishes them from larger AuNPs, is the way in which they interact with incident light in the UV-Vis range. Whereas the absorption patterns of AuNPs with particle size distributions above 8 nm exhibit an SPR peak, AuNCs response to incident light that resembles that of molecular species due to the molecular-type electronic structure, with the SPR disappearing entirely below ~ 2 nm.⁸⁷ When the AuNC size regime (< 2 nm) is accessed, the absorption pattern exhibits discrete quantized electronic transitions due to the presence of discrete molecular-type energy levels, which is distinct to the continuous energy band in the metallic state of larger AuNPs.⁸⁷

With respects to the $[\text{Au}_{25}(\text{SCH}_2\text{CH}_2\text{Ph})_{18}]^{1-}$ framework, there are characteristic absorption peaks at ~ 670 , ~ 450 and ~ 400 nm,⁶² which are common to most $[\text{Au}_{25}(\text{SR})_{18}]^{1-}$ frameworks (**Figure 1.9a,b**). The Aitken group determined that the transition at ~ 670 nm is a HOMO-to-LUMO transition (intraband $\text{sp} \leftarrow \text{sp}$ transition) (**Figure 1.9b**), where the HOMO and LUMO are composed of atomic orbital contributions from the Au atoms in the internal Au_{13} icosahedral atoms,⁶² which is characteristic of the $[\text{Au}_{25}(\text{SCH}_2\text{CH}_2\text{Ph})_{18}]^{1-}$ framework. In the absorption pattern for $[\text{Au}_{23}(\text{SR})_{16}]^{1-}$, which has the same charge state and free electron configuration as $[\text{Au}_{25}(\text{SR})_{18}]^{1-}$, but has an internal Au_{13} cuboctahedron instead of an internal Au_{13} icosahedron, there is a peak at ~ 570 nm (with no peak at ~ 670 nm),⁶⁰ indicating the correlation of this transition to the structure of the internal core configuration. In this way, the peak at 670 nm is a characteristic feature in the absorption pattern of $[\text{Au}_{25}(\text{SR})_{18}]^{1-}$. The peaks at ~ 450 nm and ~ 400 nm occur from electronic metal-ligand interband transitions (**Figure 1.9b**), which are also characteristic for $[\text{Au}_{25}(\text{SR})_{18}]^{1-}$ frameworks.⁶² In the absorption pattern of $[\text{Au}_{25}(\text{SCH}_2\text{CH}_2\text{Ph})_{18}]^0$ and $[\text{Au}_{25}(\text{SCH}_2\text{CH}_2\text{Ph})_{18}]^{1+}$, the qualitative appearance of the peaks does not change, and there is a retention of the peak at ~ 670 nm, albeit that the intensity of these peaks changes as the atomic orbital contributions changes as the free electron configuration of the system is changed (**Figure 1.9a**).⁸⁸

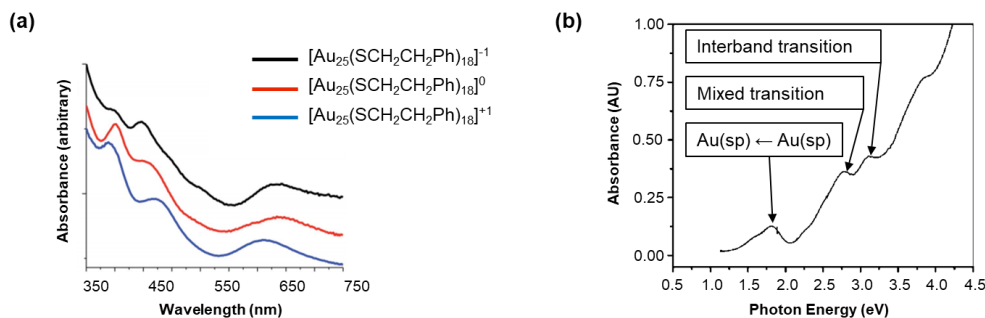


Figure 1.9. (a) Optical absorption spectra of $[\text{TOA}][\text{Au}_{25}(\text{CH}_2\text{CH}_2\text{Ph})_{18}]$, where TOA = Tetraoctylammonium (black), $\text{Au}_{25}(\text{CH}_2\text{CH}_2\text{Ph})_{18}$ (red) and $[\text{Au}_{25}(\text{CH}_2\text{CH}_2\text{Ph})_{18}][\text{C}_6\text{F}_5\text{CO}_2]$ (blue). Figure reproduced with permission from Ref. [88]. (b) Optical absorption spectrum of $[\text{TOA}][\text{Au}_{25}(\text{CH}_2\text{CH}_2\text{Ph})_{18}]$ showing principal transitions. Figure reproduced with permission from Ref. [62].

Another important optical property of thiolate-protected AuNCs, that is not exhibited by AuNP systems, is their photoluminescence (PL). Thiolate-protected AuNCs typically have PL in the near infrared (NIR) region, that originates from the structure of the ligands in the $[-\text{SR}-\text{Au}(\text{I})-\text{SR}-\text{Au}(\text{I})-\text{SR}-]$ staple motifs,⁸⁹ and in the visible region, which originates from the electronic

composition and structure of the metallic core, with stronger PL being observed in the NIR region than in the visible region.⁹⁰ Regardless of its weak contribution, the PL in the visible region can be enhanced through structural changes to the internal metallic framework,⁹¹ or especially through doping the core with metals such as silver.⁹² As the NIR PL is stronger, the role of the capping ligand structure on the PL of thiolate-protected AuNCs, especially from Au₂₅(SR)₁₈ frameworks, has received significant attention. Water soluble Au₂₅(SR)₁₈ frameworks (having water soluble surface ligands such as glutathione (SG)) generally have higher NIR PL than their organic soluble counterparts (having organic soluble surface ligands such as phenylethanethiol (SCH₂CH₂Ph)).⁸¹ Wu and Jin reported the strong correlation between the PL of organic-soluble [Au₂₅(SR)₁₈]¹⁻ frameworks and the electronic composition of the capping thiol ligands, with stronger PL being observed when more electron-donating capping ligands were used (**Figure 1.10a**).⁸¹ They also found that the charge of the Au₂₅(SR)₁₈ framework has important consequences on the PL, with the PL of [Au₂₅(SCH₂CH₂Ph)₁₈]¹⁺ being more than 5 times higher than the PL of [Au₂₅(SCH₂CH₂Ph)₁₈]¹⁻ (**Figure 1.10b**).⁸¹

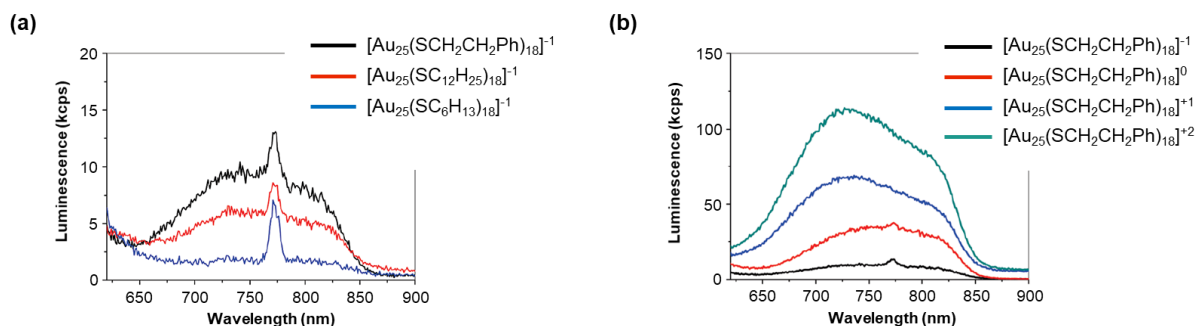


Figure 1.10. (a) Photoluminescence (PL) spectra of [Au₂₅(SR)₁₈]¹⁻ functionalized with phenylethanethiolate (black), dodecanethiolate (red) and hexanethiolate (blue). (b) PL spectra of [Au₂₅(SR)₁₈]¹⁻ (black), [Au₂₅(SR)₁₈]⁰ (red), [Au₂₅(SR)₁₈]¹⁺ (blue) and [Au₂₅(SR)₁₈]²⁺ (blue-green). Figures reproduced with permission from Ref. [81].

Another important feature of thiolate-protected AuNC is their electrochemical behaviour. Cyclic voltammetry (CV) and differential pulse voltammetry (DPV) are the most frequently used methods for evaluating their electrochemical behaviour. Electrochemistry reveals the energies of the HOMO and LUMO of the thiolate-protected AuNC, and the corresponding HOMO-LUMO energy gap, which is defined as the difference between the first oxidation (O1) and first reduction (R1) potentials.⁹³ Furthermore, the electrochemical pattern exhibited by a given AuNC system provides an electrochemical fingerprint for the AuNC system. In this way, electrochemistry is a

useful characterization technique to evaluate the core configuration of the AuNC system. Lee *et al.* reported the CV and DPV for the $[\text{Au}_{25}(\text{SCH}_2\text{CH}_2\text{Ph})_{18}]^{1-}$ framework at 25 °C,⁹⁴ which contains peaks at potentials of -1.5 (R1), 0.1 (O1), 0.4 (O2) and 1.1 (O3) V versus an Ag wire quasi-reference electrode (AgQRE) that correspond to the Au_{25}^{2+} , Au_{25}^{1+} , Au_{25}^0 and Au_{25}^{1-} charge states, respectively (**Figure 1.11**). Using this data, the HOMO-LUMO gap for $[\text{Au}_{25}(\text{SCH}_2\text{CH}_2\text{Ph})_{18}]^{1-}$ (i.e. the R1-O1 difference) was 1.5 V, which is typical for other $[\text{Au}_{25}(\text{SR})_{18}]^{1-}$ frameworks.^{80, 95}

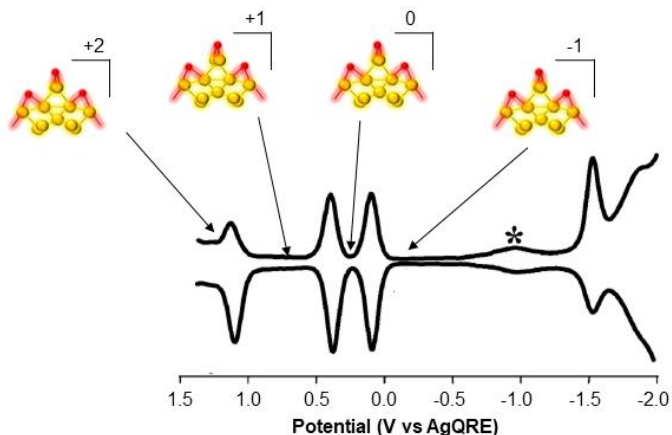


Figure 1.11. Differential pulse voltammogram (DPV) of $[\text{Au}_{25}(\text{SCH}_2\text{CH}_2\text{Ph})_{18}]^{1-}$ at 0.02 V/s in 0.1 M Bu_4NPF_6 in degassed CH_2Cl_2 at 0.4 mm diameter Pt working electrode, with Ag wire quasi-reference (AgQRE) and Pt wire counter electrode. * indicates wave for incompletely removed O_2 . DPV reproduced with permission from Ref. [94].

1.3.5 Applications of the $\text{Au}_{25}(\text{SR})_{18}$ Framework

Due to the comparatively newer discovery of AuNCs and the more recent optimization of their syntheses, application-based research for AuNCs is less developed, and is receiving significant attention in contemporary literature as the relationship between the physical properties and framework structure is becoming more well-defined. The maturation of the synthetic strategies available to acquire different AuNC core configuration and surface structures, and the concurrent ability to fine-tune the associated structure-dependent properties, has made thiolate-protected AuNCs a promising candidate for a variety of applications. Given the synthetic accessibility and chemical robustness of the Au_{25} framework and its amenability to the capping thiol ligand, the Au_{25} framework has received the most attention in terms of application-based research.

One exploitable property of Au₂₅ systems is the way in which they interact with light, which has been used towards colorimetric sensing applications. Whereas colorimetric sensing applications using AuNP systems relies on aggregation-induced variations in the SPR absorption patterns, colorimetric sensing using Au₂₅ systems relies on changes in the PL before and after adsorption of the target analyte. Xie *et al.* developed a “green synthesis” of an Au₂₅ system in which treatment with HAuCl₄ with bovine serum albumin (BSA) in alkaline solution resulted in the formation of a BSA-encapsulated Au₂₅ core (Au₂₅-BSA),⁹⁶ with the internal core being stabilized through [-SR-Au(I)-SR] motifs where the surface thiolates are thiol-containing amino acids in BSA. This Au₂₅-BSA nanoconjugate exhibited high PL, which was even stronger than the PL from Au₂₅(SG)₁₈.⁹⁶ In a later study, they found that their Au₂₅-BSA nanoconjugate was an excellent colorimetric sensor for mercury ions. Treatment of Au₂₅-BSA with lead ions led to the adsorption of the lead ions to the internal Au₂₅ core (due to the strong interaction between mercury and gold ions), which led to a subsequent quenching of the PL, which could be monitored visually and using fluorescence spectroscopy (**Figure 1.12**).⁹⁷

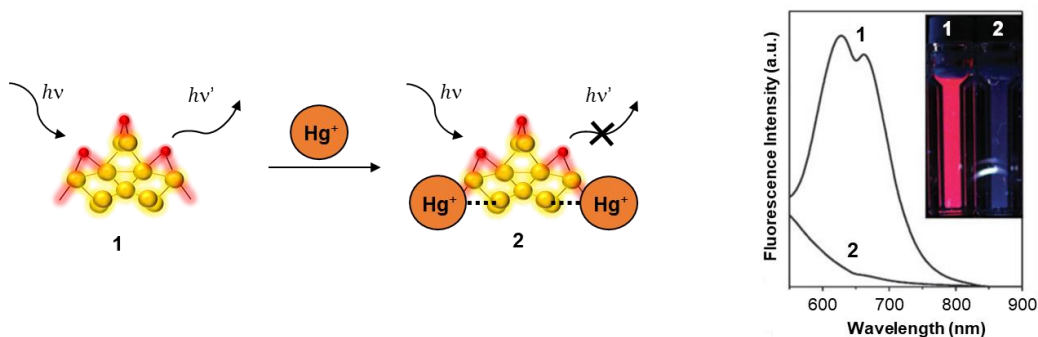


Figure 1.12. *Left.* Schematic representation of Hg²⁺ sensing based on fluorescence quenching upon Hg²⁺ binding to Au₂₅-BSA. *Right.* Photoemission spectra ($\lambda_{\text{ex}} = 470 \text{ nm}$) of Au₂₅-BSA before Hg²⁺ binding (1) and after Hg²⁺ binding (2). Spectra figure reproduced with permission from Ref. [97].

Catalysis is one of the most significant applications of [Au₂₅(SR)₁₈]¹⁻ nanoclusters that is currently being investigated. Catalytic applications of [Au₂₅(SR)₁₈]¹⁻ typically involve thermal deposition of the [Au₂₅(SR)₁₈]¹⁻ system onto a metallic oxide support, which is a necessary component to achieve optimal catalytic activity, with free [Au₂₅(SR)₁₈]¹⁻ systems typically undergoing deterioration under catalytic conditions.⁹⁸ Density functional theory (DFT) has provided valuable insight in the molecular and structural features of [Au₂₅(SR)₁₈]¹⁻ contributes to its catalytic activity.⁹⁹ The Zeng group used DFT to propose that the post-deposition catalytic sites

are the Au(I) atoms in the staple motifs, instead of the internal Au(0) atoms in the Au₁₃ core.¹⁰⁰ There is also a strong dependence on the structure and electronic composition of the capping thiol ligand on the surface, which essentially provides an ‘active site’ (similar to the active sites in enzymes) to orient the substrate on the [Au₂₅(SR)₁₈]¹⁻ surface and catalyze the desired transformation. Smaller capping ligands gives reactants better access to the internal catalytic sites,¹⁰¹ and ligands containing phenyl moieties are especially effective in increasing catalytic performance that is likely through facilitation of π - π stacking between substrates and ligand (**Figure 1.13a**).¹⁰² To highlight a notable catalytic application of oxide-supported [Au₂₅(SR)₁₈]¹⁻, the Jin group thermally deposited [Au₂₅(SCH₂CH₂Ph)₁₈]¹⁻ onto a titanium dioxide support, which was an excellent catalytic system for semi-hydrogenation of terminal alkynes to alkenes (**Figure 1.13b**),¹⁰³ that was more effective than most analogous catalytic systems.

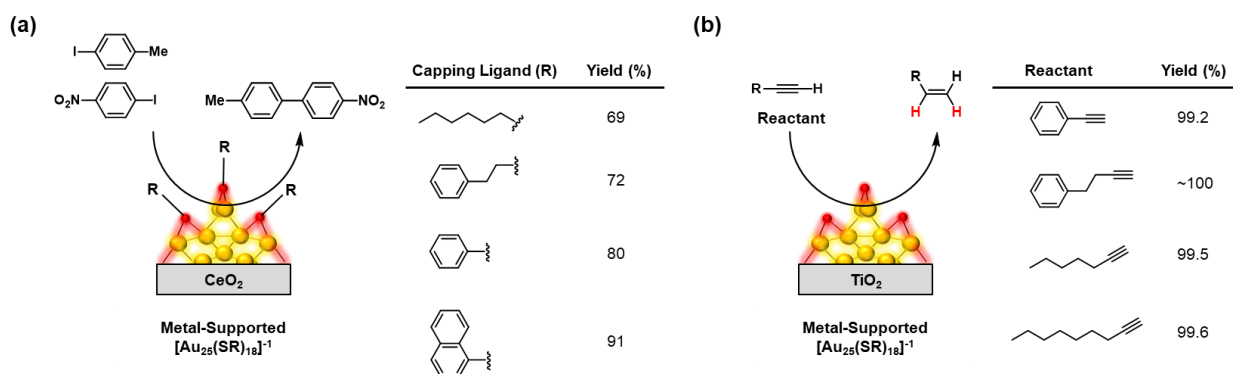


Figure 1.13. (a) Catalytic activity of [Au₂₅(SR)₁₈]¹⁻ thermally deposited onto CeO₂ support, using different capping ligands, for Ullmann heterocoupling between 4-methyl-iodobenzene and 4-nitro-iodobenzene, in presence of K₂CO₃ in DMF at 130°C for 24 hours. Synthetic data taken from Ref. [101]. (b) Catalytic activity of [Au₂₅(SCH₂CH₂Ph)₁₈]¹⁻ thermally deposited onto TiO₂ support, for semi-hydrogenation of terminal alkynes, in presence of pyridine and H₂ at 100°C for 20 hours. Synthetic data taken from Ref. [103].

The [Au₂₅(SR)₁₈]¹⁻ framework has also been used towards drug delivery applications. As described in **Section 1.2.4**, when therapeutic drugs such as doxorubicin (DOX) is inoculated as a free molecule, there oftentimes is excessive extracellular degradation by enzymes, preventing optimal therapeutic effects.⁵⁰ However, when these same agents are conjugated onto the surface of nanomaterial carriers, the dense packing of the agent on the nanomaterial surface prevents premature degradation, enhancing their therapeutic effects. Although the mechanism of internalization is not yet known, as with AuNP systems, [Au₂₅(SR)₁₈]¹⁻ frameworks are internalized by a variety of cellular lines. Zhang *et al.* synthesized a carboxyl-terminated

$[\text{Au}_{25}(\text{SR})_{18}]^{1-}$ framework, and then conjugated DOX to the terminal carboxyl groups via electrostatic interactions to create a $[\text{Au}_{25}(\text{SR})_{18}]^{1-}$ -DOX nanoconjugate (**Figure 1.14**).¹⁰⁴ This conjugate was readily internalized by A549 lung cancer cells, and due to the fluorescence of the DOX molecules, the efficacy of internalization could be evaluated by fluorescence microscopy. As with AuNP delivery of DOX, they also found that the $[\text{Au}_{25}(\text{SR})_{18}]^{1-}$ -DOX nanoconjugate was more effective and decreasing A549 cell viability, compared to DOX on its own.¹⁰⁴

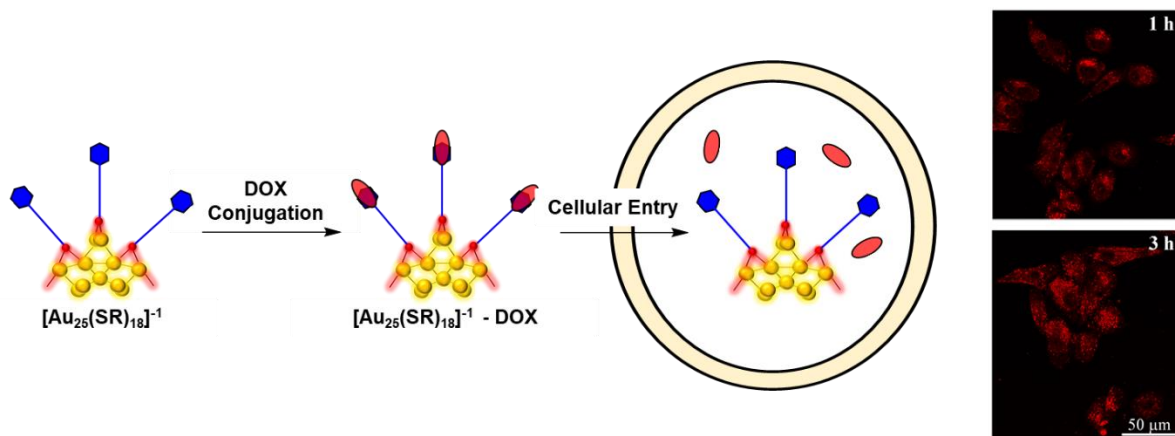


Figure 1.14. *Left.* Schematic representation of DOX delivery by $[\text{Au}_{25}(\text{SR})_{18}]^{1-}$ -DOX nanoconjugate. *Right.* Confocal images of A549 cells after incubation with $[\text{Au}_{25}(\text{SR})_{18}]^{1-}$ -DOX nanoconjugate after 1 hour (top right) and 3 hours (bottom right). Red = doxorubicin. Figures of confocal images reproduced with permission of Ref. [104].

1.4 Surface Modifications of AuNPs and AuNCs

As outlined in **Section 1.2.4** and **Section 1.3.5**, the ability to modulate the surface compositions of AuNPs and AuNCs (particularly the $[\text{Au}_{25}(\text{SR})_{18}]^{1-}$ framework) is of paramount importance for application-based research, in order to either fine-tune their structure-dependent properties (which is in large part dependent on the surface configurations) or passivate relevant substrates on their surface to induce the desired chemical or biological effect. To this end, in addition to application-based research itself, there has been an extensive pursuit towards developing methodologies capable of modifying the surface structure of AuNPs and AuNCs (particularly the $[\text{Au}_{25}(\text{SR})_{18}]^{1-}$ framework).

The most obvious strategy would be a direct synthetic approach using the Brust-Schiffrin method, in which the thiolated metallic frameworks are fabricated using a gold (III) precursor and a thiolated ligand possessing the desired structure and/or surface functionality (**Scheme 1.3, Method 1**). Although simple frameworks such as the $[\text{Au}_{25}(\text{SCH}_2\text{CH}_2\text{Ph})_{18}]^{1-}$ framework can be synthesized using direct methods, more complex systems such as oligonucleotide-functionalized AuNPs or $[\text{Au}_{25}(\text{SR})_{18}]^{1-}$ frameworks with therapeutic agents passivated on their surfaces, typically cannot be fabricated using direct synthetic methods because of:

1. The chemical sensitivity of the substrates (such as carbonyl groups) with sodium borohydride.
2. The inability to acquire the desired framework with large, complex thiolated ligands, with this mismatched relationship between ligand structure and framework structure being especially present in $[\text{Au}_{25}(\text{SR})_{18}]^{1-}$ syntheses.

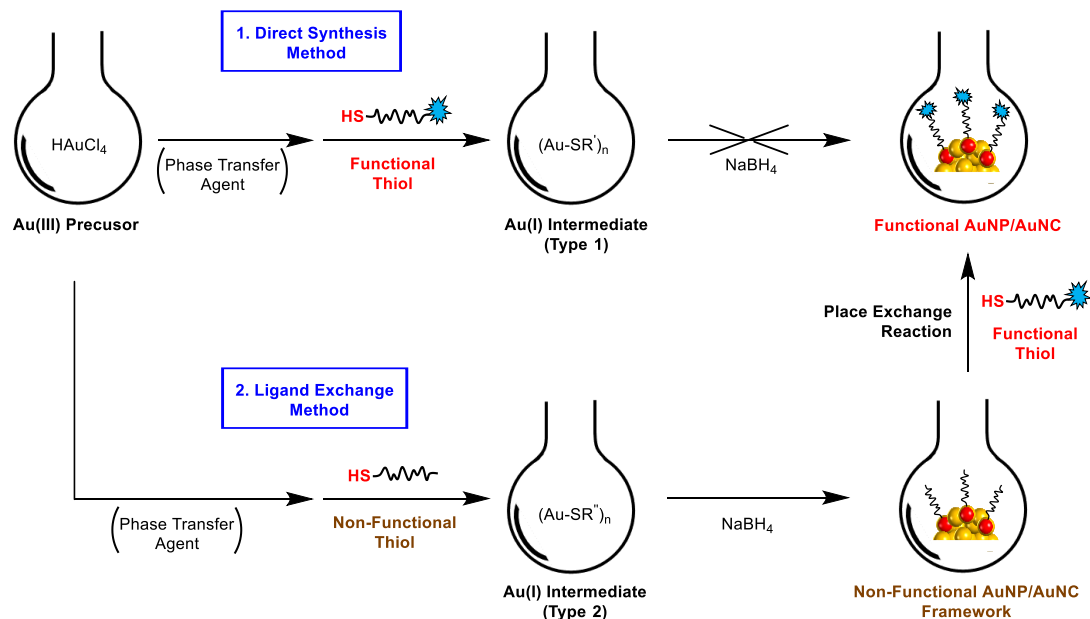
As direct synthetic approaches are generally inaccessible to generate functionally complex systems, approaches using post-assembly modifications are generally employed. One strategy is to incorporate reactive nucleophilic handles (such as -OH or -NH₂) to the exterior of the surface monolayers using direct synthetic methods, and conduct coupling reactions to electrophilically-activated substrates.^{105, 106} Another strategy is to manufacture carboxyl-terminated systems using direct synthetic methods and perform post-assembly acyl coupling reactions in the presence of coupling agents.^{107, 108} Although such strategies have found some utility, the main problems associated with them are:

1. The nucleophilicity and reactivity of the reactive handles makes such systems difficult to synthesize and purify.
2. Such post-assembly coupling strategies are often limited by their less than quantitative yields, preventing efficient surface derivatization and can lead to AuNP degradation.
3. The presence of competing reactive groups (such as -NH₂ moieties in oligonucleotides) can initiate undesired reactivity.

Due to these synthetic complexities, the most common method for engineering functional AuNP and $[\text{Au}_{25}(\text{SR})_{18}]^{1-}$ systems is through ligand exchange chemistry, which was employed in all the studies described in **Section 1.2.4** and **Section 1.3.5** in which functional systems were fabricated. In this method, simple and chemically inert thiolated ligands are used to construct AuNP or $[\text{Au}_{25}(\text{SR})_{18}]^{1-}$ templates using direct synthetic methods, after which native ligands are exchanged with thiolated-ligands possessing the desired structure or functional substrate, typically through simple mix-and-stir reactions (**Scheme 1.3, Method 2**). The degree of ligand exchange is dependent on several factors, such as the structure of the native and incoming ligands,¹⁰⁹ the electronic charge of the framework¹¹⁰ and the molar ratio of the metallic system and incoming thiol,¹¹¹ with typically large concentrations of thiol being necessary for efficient ligand exchange. Although the ligand exchange strategy has found great utility in developing functional AuNP and $[\text{Au}_{25}(\text{SR})_{18}]^{1-}$ systems, there are three common problems associated with it:

1. The functional substrate and thiol moiety are oftentimes not chemically compatible. Furthermore, due to the reactivity of thiols, protection/deprotection strategies are often required to successfully tether the thiol moiety. These conditions may not be compatible with the desired functional substrate and leads to low yields for the desired thiolated-substrate (such as the in the synthesis of thiolated-oligonucleotides).
2. Exchange of native thiols with functional thiolated-substrates that are too largely different in structure can lead to an alteration of the parent system. This especially presents a problem in ligand exchange strategies using $[\text{Au}_{25}(\text{SR})_{18}]^{1-}$ systems, in which ligand exchange can alter the internal framework.
3. Finally, the excessive concentrations of the incoming thiol can be limiting if they are synthesized in low yield and/or expensive to make.

It is because of the complications inherent to direct synthetic methods, post-assembly coupling strategies and ligand exchange strategies that it is of paramount importance to develop alternative strategies to engineer functional AuNP and $[\text{Au}_{25}(\text{SR})_{18}]^{1-}$ systems to minimize or entirely eliminate such limitations and enhance their usage for application-based research.



Scheme 1.3. Synthesis of functional AuNP or AuNC systems for application-based research, using the direct synthetic method (**Method 1**) or the ligand exchange method (**Method 2**).

1.5 Bioorthogonal Click Chemistry

1.5.1 General Characteristics of Bioorthogonal Click Reactions

The inception of “bioorthogonal chemistry” is rooted in the early investigations from the late 20th century when scientists began to develop an intense interest in how biomolecules behave, organize and interact with one another in their natural settings. Although the general shape of cellular systems could be observed with the development of the TEM, the visualization and understanding of internal biochemical processes required scientists to develop *in vivo* strategies to manipulate biomolecules on the atomic level to produce measurable and visualizable responses. Such manipulations need to be done (1) without altering the structure and spatiotemporal responses of the biomolecule and (2) not perturb the native settings in which they operate in; these criteria encompass the term “bioorthogonal”.

One of the earliest and foremost discoveries towards understanding cellular processes through bioorthogonal strategies was “the discovery and development of green fluorescent protein

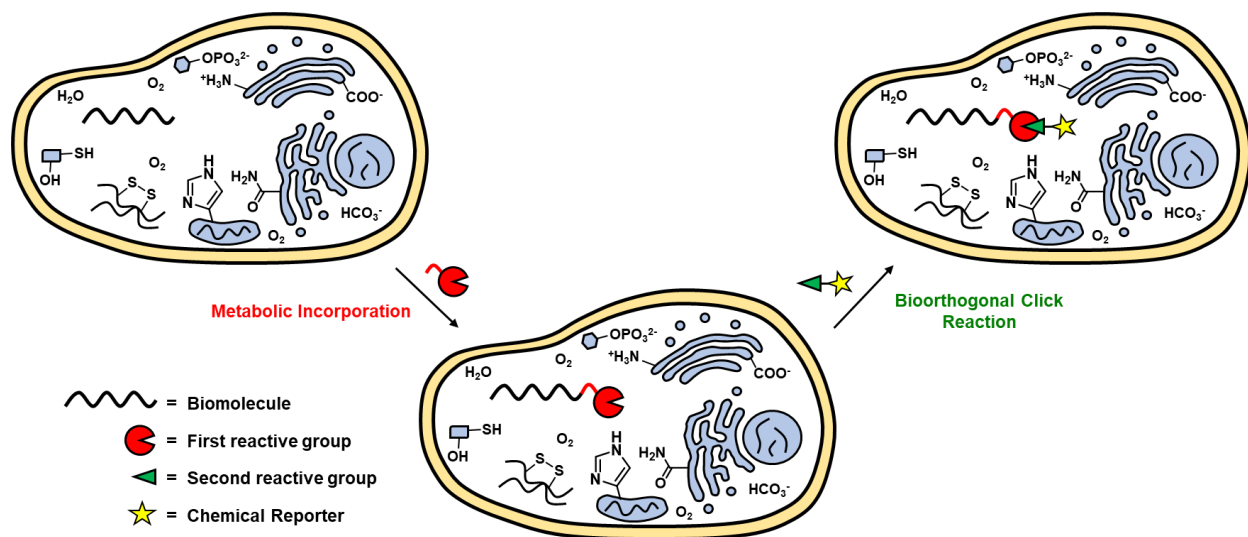
(GFP)”, which earned the shared 2008 Nobel Prize in Chemistry to Osamu Shimomura (for first isolating GFP from the jellyfish *Aequorea victoria*)¹¹² Martin Chalfie (for demonstrating the usefulness of GFP as a luminescent genetic tag)¹¹³ and Roger Tsien (for understanding the structural features that makes it florescent).¹¹⁴ Once the nucleic acid sequence of GFP was determined,¹¹⁵ its sequence could be fused to the ends of recombinant pre-translational sequences as a genetic “reporter”, and cellular translation of the entire sequence furnished fluorescent analogues of the native protein that could be visualized and monitored.¹¹⁶⁻¹¹⁸ Although the discovery of GFP marked a landmark breakthrough in understanding native cellular activities, the post-translational size of the GFP protein (238 amino acids) renders it incompatible with some protein structures.¹¹⁸ Furthermore, GFP can only serve as a genetically encoded tag for proteins, and other important biomolecules such as nucleic acids, lipids and glycans cannot be monitored using genetically encoded reporters.

A major breakthrough in circumventing this limitation came from Roger Tsien’s group in 1998, when he reported the first example of *in vivo* protein labelling, in which recombinant proteins possessing a tetracysteine domain were labelled with small, reactively complementary biarsenical dyes inside the cell.¹¹⁹ The small size of the organic dye, compared to post-translational size of GFP, presented an important advantage over GFP labelling strategies. However, the most important difference is that the exogenous agent in GFP labelling strategies is recombinant sequences containing the GFP gene, which relies on intracellular translation. This new strategy proposed a revolutionary new labelling paradigm, in which the exogenous agent was a small chemical dye, which was integrated into the cell, bound to the target recombinant protein, and then imaged using florescence microscopy. This early research triggered an intense interest in developing strategies to modify and observe biomolecules in their natural environments with “bioorthogonal chemical reporters” (instead of genetically encoded reporters).

Since the report by the Tsien group, there have been extensive studies describing different strategies for bioorthogonal labeling. Of these, no class of strategies has embodied the concept of “bioorthogonal chemical reporters” better than that first proposed by Carolyn Bertozzi in 2009, who not only first coined the term “bioorthogonal”, but also proposed that biomolecules and reporters be linked together intracellularly using “click chemistry”, and iconized the term “bioorthogonal click chemistry”.¹²⁰ The concept of “click chemistry” pre-dates Bertozzi’s

exemplar study, and was a term first coined in 2001 by chemists Barry Sharpless, Hartmuth Kolb and M.G. Finn to describe a series of highly efficient reactions in synthetic chemistry that simply ‘clicked’ together, such as the Diel-Alder reaction and additions to carbon-carbon multiple bonds.¹²¹ They constrained the term “click reactions” to those that:

1. Have high thermodynamic driving forces.
2. Proceeds rapidly to completion (i.e. rapid reaction kinetics).
3. Be highly selective for one another in the presence of other reactive functional groups (i.e. *chemoselective*).
4. Proceed in the absence of catalysts.
5. Ideally produce no by-products, that if present, can easily be removed and is non-perturbing.



Scheme 1.4. A “bioorthogonal click reaction”. The first reactive group is exogenously added and intracellularly incorporated into the target biomolecule using the cellular machinery. A chemical reporter possessing the second (complementary) reactive group is then exogenously added. The reaction between the first and second reactive groups need to proceed selectively in the presence of all the functionalities found within cellular systems, some of which are shown, and the biomolecule is then labelled with the chemical reporter.

The term “click chemistry” was initially confined to highly efficient organic transformations in synthetic settings, and in 2009, Bertozzi recognized the potential for using such highly efficient click reactions for *in vivo* labelling studies. Unlike in synthetic settings, these need

to be done in more delicate settings, and thus she coined the term “bioorthogonal click chemistry” to describe sets of reactions that can be used to ‘click’ reporters and chemically sensitive biomolecules within biologically sensitive environments (**Scheme 1.4**).

1.5.2 Common Bioorthogonal Click Reactions

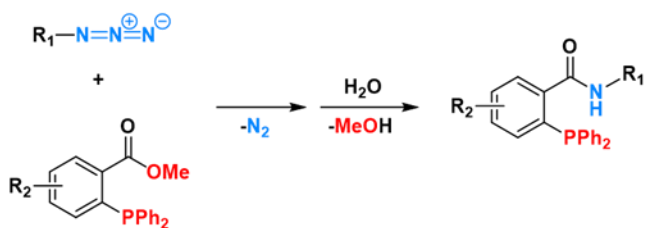
To date, there have been many chemical reactions that meet many of the criteria of both “click reactions” and “bioorthogonality”, albeit to different extents. One of the most widely utilized bioorthogonal click reactions is the Staudinger-Bertozzi ligation, which is a modification of the classical Staudinger reaction first reported by Hermann Staudinger in 1919.¹²² The classical Staudinger reaction is between a terminal azide (N_3) dipole and triarylphosphine to form an aza-ylide (and nitrogen gas), which is subsequently hydrolyzed to form a phosphine oxide and primary amine.¹²³ In 2000, Bertozzi reported a modification of the classical Staudinger reaction whereby an ester group was tethered ortho to the phosphorus atom in one of the three phenyl rings in the triarylphosphine. Upon reaction of the terminal azide and the phosphine, the aza-ylide reacts with the ester group to form an amide linkage (instead of a primary amine), ligating the group attached to the azide to the triarylphosphine (**Scheme 1.5a**).¹²⁴ Although it is one of the predominant bioorthogonal click reactions utilized to conjugate two chemically sensitive substrates,¹²⁵⁻¹²⁷ the major limitation of the Staudinger-Bertozzi ligation is the slow reaction kinetics ($\sim 10^{-3}$ to $10^{-1} \text{ M}^{-1}\text{s}^{-1}$),¹²⁸ which necessitates larger concentrations of the reactive partners in order to drive successful amide formation, limiting their usage *in vivo*. Furthermore, although the azide moiety is exceptionally stable, the sensitivity of the phosphine moiety to air oxidation, and the lability of the phosphine to enzymatic cellular degradation is another common problem associated with using phosphines, limiting the “bioorthogonal” aspect of the reaction.¹²⁹

Addressing the slow reaction kinetics of the Staudinger-Bertozzi ligation, in 2008 the Fox group developed another bioorthogonal click reaction between a *trans*-cyclooctene (TCO) and *s*-tetrazines, which is known as the “TCO-tetrazine ligation” (**Scheme 1.5b**), which forms nitrogen gas as the only by-product and proceeds with reaction kinetics reaching as high as $2000 \text{ M}^{-1}\text{s}^{-1}$ (in 9:1 methanol:water).¹³⁰ The reaction has shown to be tolerable to a variety of solvent systems, although the reaction kinetics are affected by the solvent system used. Although the TCO-tetrazine ligation has found usage for *in vivo* applications,¹³¹⁻¹³³ the major limitation of the TCO-tetrazine

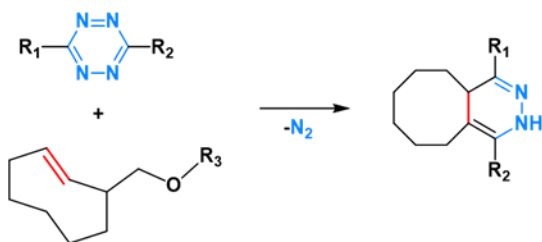
ligation is the conformationally strained TCO moiety, which in many conditions can spontaneously cycloisomerize into the more stable, less strained *cis*-isomer.¹³⁴ The TCO moiety is also very reactive towards thiols, which can be problematic when used *in vivo* due to thiol moieties present in protein backbones.¹³⁵

Another noteworthy bioorthogonal click reaction that was developed to mitigate the slow reaction kinetics of the Staudinger-Bertozzi ligation is the reaction between a terminal azide and an oxanorbornadiene, which forms a triazole moiety in a 1,3-dipolar cycloaddition reaction, generating a molecule of furan as the only by-product (**Scheme 1.5c**).¹³⁶ This bioorthogonal click reaction has found usage in biomedical applications.^{137, 138} However, as with the Staudinger-Bertozzi ligation, whereas the azide moiety is chemically stable, the major limitation of the azide-

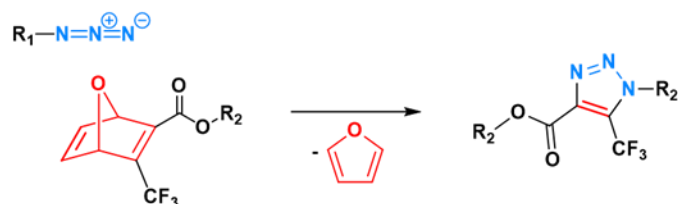
(a) Staudinger-Bertozzi Ligation



(b) *Trans*-Cyclooctene-Tetrazine Ligation



(c) Azide-Oxanorbornadiene Cycloaddition



Scheme 1.5. Three common “bioorthogonal click reactions”. (a) The Staudinger-Bertozzi ligation between a terminal azide and phenyl ester-functionalized phosphine. (b) The *trans*-cyclooctene-tetrazine ligation. (c) The azide-oxanorbornadiene cycloaddition.

oxanorbornadiene cycloaddition reaction is the oxanorbornadiene, which requires electron-deficient moieties to be tethered on to the oxanorbornadiene in order to activate it for the reaction to proceed successfully, a structural restriction that dually presents a risk in biological settings.¹³⁸

1.5.3 Strain-Promoted Alkyne-Azide Cycloaddition (SPAAC) Reaction

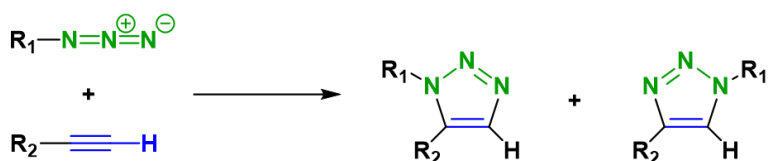
Most of the limitations commonly associated with other bioorthogonal click reactions, primarily the chemical instability of the reactive groups, can be largely mitigated by the reaction between an azide and terminal alkyne moieties. The prototype reaction was presented in 1963 by Rolf Huisgen, who reported a [3+2] cycloaddition between an azide dipole and terminal alkyne dipolarophile to afford an equimolar mixture of 1,4- and 1,5-disubstituted 1,2,3-triazole cycloadducts (**Scheme 1.6a**), without the formation of any by-products.¹³⁹ As these two π -systems rarely exist in nature, are largely inert within biological and natural settings, and also feature excellent functional group compatibility, this made the “Huisgen cycloaddition reaction” a promising candidate as a bioorthogonal click reaction. However, in the absence of activation of the alkyne by delocalizing it into electron withdrawing substituents (such as ester groups), the reaction does not proceed efficiently without elevated temperatures and pressure,¹³⁹ which diminishes its bioorthogonality.

In 2002, the Sharpless and Meldal groups independently discovered that the reaction can be made to proceed in the presence of a catalytic amounts of copper (I) salts, which activates the alkyne towards the [3+2] cycloaddition reaction in the absence of functional group activation (**Scheme 1.6b**), again in the absence of by-product formation.^{140, 141} This “copper (I)-catalyzed alkyne-azide cycloaddition (CuAAC)” reaction can be performed at physiological temperatures with reaction kinetics $\sim 10^6$ fold faster than the Huisgen cycloaddition reaction.¹⁴¹ It also generates a single 1,4-disubstituted triazole regioisomer, though the regioisomeric nature of the cycloaddition reaction is not generally problematic in biological labelling studies. The ability to conduct the CuAAC reaction under milder reaction conditions made it a more bioorthogonal variant of the Huisgen cycloaddition reaction, but the necessity of the copper(I) catalyst, which is typically cytotoxic,¹⁴² still limited the bioorthogonality of this alkyne-azide reaction.

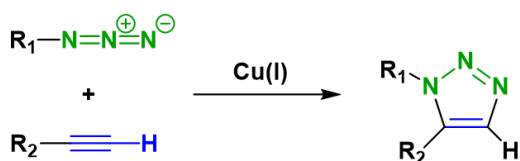
The first reported [3+2] cycloaddition reaction between cyclooctyne, the smallest stable non-linear cycloalkyne, and phenylazide was reported by Krebs and Wittig in 1961, who reported that two reacted “like an explosion”.¹⁴³ The utility of this reaction as a potential bioorthogonal

click reaction wasn't realized until 2004, when the Bertozzi group reported that the reaction can be used to label biomolecules bioorthogonally.¹⁴⁴ By constraining the sp-hybridized alkyne moiety within an eight-membered ring, this creates a large amount of strain energy (~18 kcal/mol),¹⁴⁵ which 'activates' the alkyne, and permits the reaction to proceed in the absence of high temperatures, functional group activation or catalysts. Remarkably, although the ring strain associated with the non-linear alkyne activates it towards [3+2] cycloaddition chemistry, it remains largely inert in biological and other chemically sensitive settings. This reaction between a strained-cyclooctyne and azide moiety is termed the "strain-promoted alkyne-azide cycloaddition (SPAAC)" reaction (**Scheme 1.6c**).¹⁴⁴ As with the Huisgen cycloaddition reaction, it produces two

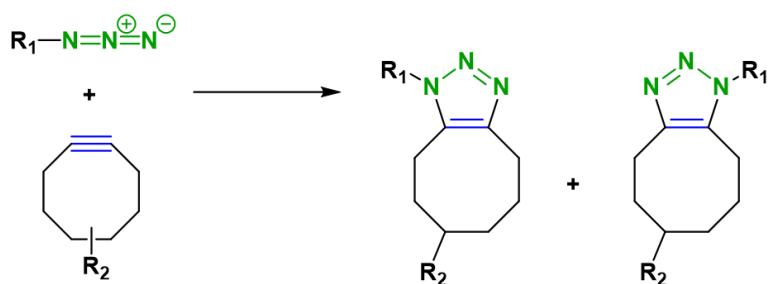
(a) Alkyne-Azide Huisgen Cycloaddition Reaction



(b) Copper(I)-Catalyzed Alkyne-Azide Cycloaddition (CuAAC) Reaction



(c) Strain-Promoted Alkyne-Azide Cycloaddition (SPAAC) Reaction



Scheme 1.6. Common reactions between terminal azides and alkyne moieties. (a) The alkyne-azide Huisgen cycloaddition reaction between a terminal alkyne and terminal azide under high temperature (and/or pressure). (b) The copper(I)-catalyzed alkyne-azide cycloaddition (CuAAC) reaction between a terminal alkyne and terminal azide in the presence of a copper (I) catalyst. (c) The strain-promoted alkyne-azide cycloaddition (SPAAC) reaction between a cyclooctyne and terminal azide.

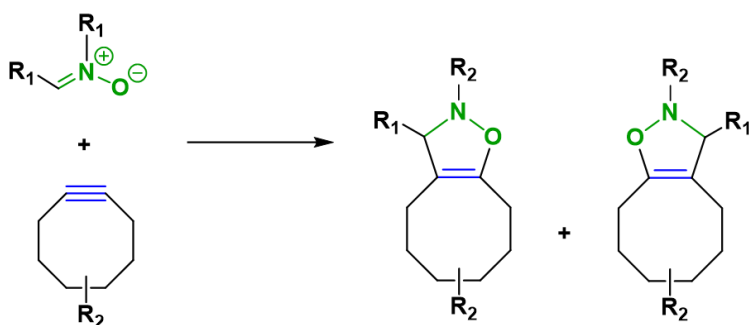
regioisomers that are not typically problematic in biological labelling studies.

The discovery of SPAAC as a bioorthogonal click reaction represented a landmark breakthrough in chemical biology that can be used to combine two chemically sensitive substrates in biological settings, that would otherwise be difficult or impossible to achieve. It features the same functional group tolerance and biocompatibility of the two reactive partners used in the Huisgen cycloaddition and CuAAC reactions, but also comes without the limitations of not just these two alkyne-azide cycloaddition variants, but also without the limitations associated with other bioorthogonal click reactions, making it a truly bioorthogonal reaction.

1.5.4 Strain-Promoted Alkyne-Nitrone Cycloaddition (SPANC) Reaction

An analogous variant of the SPAAC reaction was developed by the Pezacki group, where the azide dipole was replaced with a nitron dipole, and is termed the “strain-promoted alkyne-nitrone cycloaddition (SPANC)” reaction (**Scheme 1.7**).¹⁴⁶ Although the nitron dipole is prone to hydrolysis in the presence of strong acids, whereas the azide is not, the SPANC reaction has found great utility in biological labelling studies.^{147, 148} One of the key advantages of the SPANC reaction, compared to the SPAAC reaction, is that while the terminal azide moiety has one modifiable site, the nitron moiety has two modifiable sites, namely the nitrogen (N α) and carbon (C α) atoms of the nitron moiety. As shall be discussed in **Section 1.5.5**, the ability to more fine-tune the composition of the nitron dipolar moiety through substituent modifications has important implications on their reactive profile, that cannot be achieved to the same extent using azides.

Strain-Promoted Alkyne-Nitrone Cycloaddition (SPANC) Reaction

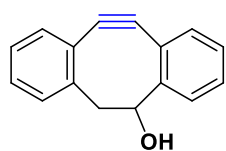


Scheme 1.7. The strain-promoted alkyne-nitrone cycloaddition (SPANC) reaction between a nitron and cyclooctyne.

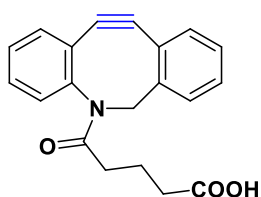
1.5.5 Kinetically-Variable SPAAC/SPANC

In addition to the chemical stability, biocompatibility, functional group tolerance and ability to perform the reactions under ambient physiological conditions, one of the key features of the SPAAC and SPANC reactions that renders it an important tool is the ability to tune their reaction kinetics. Compared to the Staudinger ligation, which is the other predominant bioorthogonal click reaction used in contemporary literature, the SPAAC and SPANC reactions feature more rapid reaction kinetics. Although the TCO-tetrazine ligation is more rapid than the SPAAC and SPANC reactions, trans-cyclooctenes are susceptible to isomerization that inactivates them towards the reaction, which limits its utility. Rapid reaction kinetics is a key feature towards developing efficient bioorthogonal click reactions, because it reduces the effective concentrations of the two reactive partners necessary to obtain optimal coupling yields. If the reaction were too slow, then larger excess of the two reactive partners would be required to acquire the same yield than if the reaction were faster.

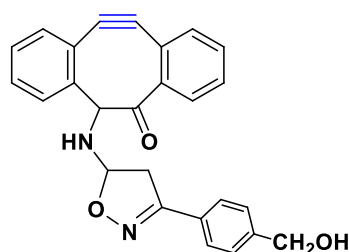
Benzoannulated Strained-Alkynes:



DIBO
 $k_2 = 0.057 \text{ M}^{-1}\text{s}^{-1}$

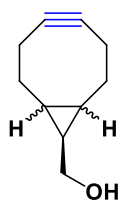


DIBAC
 $k_2 = 0.31 \text{ M}^{-1}\text{s}^{-1}$

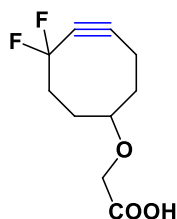


BARAC
 $k_2 = 0.96 \text{ M}^{-1}\text{s}^{-1}$

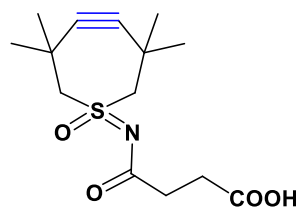
Aliphatic Strained-Alkynes:



BCN
 $k_2 = 0.070 \text{ M}^{-1}\text{s}^{-1}$



DIFO
 $k_2 = 0.076 \text{ M}^{-1}\text{s}^{-1}$



TMTH
 $k_2 = 0.80 \text{ M}^{-1}\text{s}^{-1}$

Figure 1.15. Some commonly used cyclooctynes, with associated second-order rate constants for reaction with benzyl azide. Second-order rate constants taken from references [149] and [150].

Much of the rapid kinetic profiles of the SPAAC and SPANC reactions can be attributed to the ring strain in the cyclooctyne moieties. In recent years, there has been an interest in further improving the kinetic profiles of the SPAAC and SPANC reactions through structural changes to the cyclooctyne (**Figure 1.15**).^{149, 150} Although addition of electron-withdrawing substituents provides a minor change to their kinetic profile, the greatest increase in reaction kinetics can be achieved by fusing the cyclooctyne ring to aryl rings, rigidifying the cyclooctyne ring and vastly increasing the ring strain of the alkyne moiety.¹⁴⁹ Although such ‘benzoannulated’ cyclooctynes have shown to react much more rapidly than their ‘aliphatic’ counterparts, increasing the ring strain of the cyclooctyne moiety is associated with a problematic tradeoff, in that it concurrently makes them less stable. Benzoannulated strained-alkynes also tend to have shorter shelf lives, and are synthetically more inaccessible than aliphatic cyclooctynes.¹⁵¹ This presents a restrictive constraint on improving the reactive profiles of the cyclooctyne reactive partner in the SPAAC and SPANC reactions.

It is for this reason that contemporary efforts have converged on improving the reaction profiles of the SPAAC and SPANC reactions through structural modifications to the azide or nitron dipoles. The Pezacki group first reported that delocalizing the nitron moieties into electron withdrawing substituents (such as cyano groups) greatly increases the reaction kinetics of the SPANC reactions, and conversely when the nitron moieties are delocalized in electron donating substituents (such as methoxy groups), the SPANC reaction is decelerated (**Figure 1.16**).^{146, 152} In a later study, the Dommerholt group reported the same effect in the SPAAC reaction with aromatic azides. Delocalizing the azide moiety into electron withdrawing substituents such as pyridinium and pentafluorophenyl groups greatly improved the reaction kinetics of the SPAAC reaction. Conversely, delocalization into electron donating substituents such as anisole groups greatly decelerated the reaction rates (**Figure 1.16**).¹⁵³

1.6 Scope of Thesis

As outlined in **Section 1.2.4** and **Section 1.3.5**, the ability to adjust and modulate the surface structure of AuNPs and AuNCs (specifically $[\text{Au}_{25}(\text{SR})_{18}]^{1-}$) and develop functional varieties of these nanomaterial frameworks is of paramount importance for application-based research. As direct synthetic methods are typically inaccessible, ligand exchange strategies are often employed.

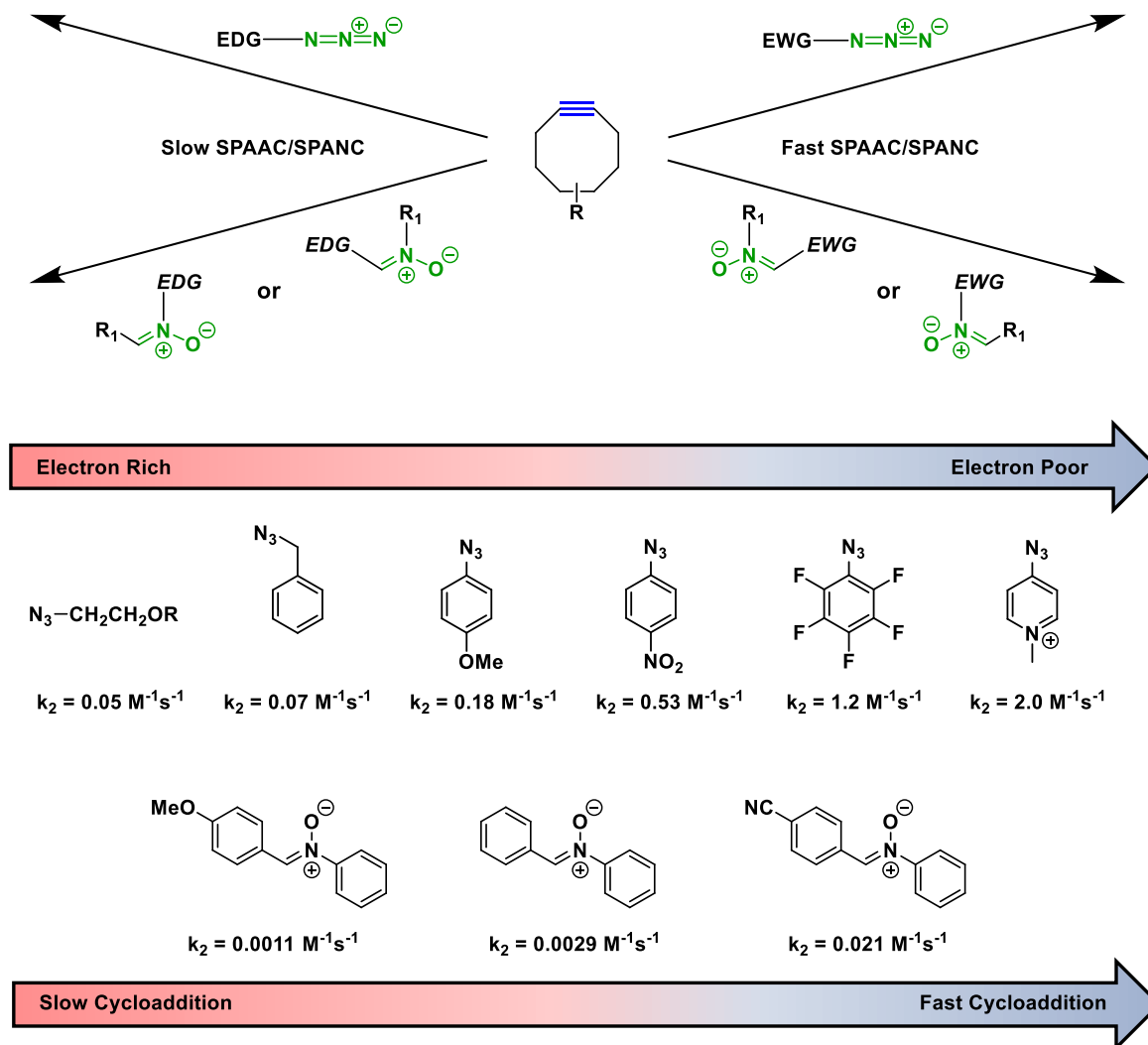


Figure 1.16. *Top.* Kinetically variable SPAAC and SPANC through structural modifications to the azide and nitronium moieties, respectively. *Bottom.* Structures of azides and nitrones and their associated second-order rate constants.

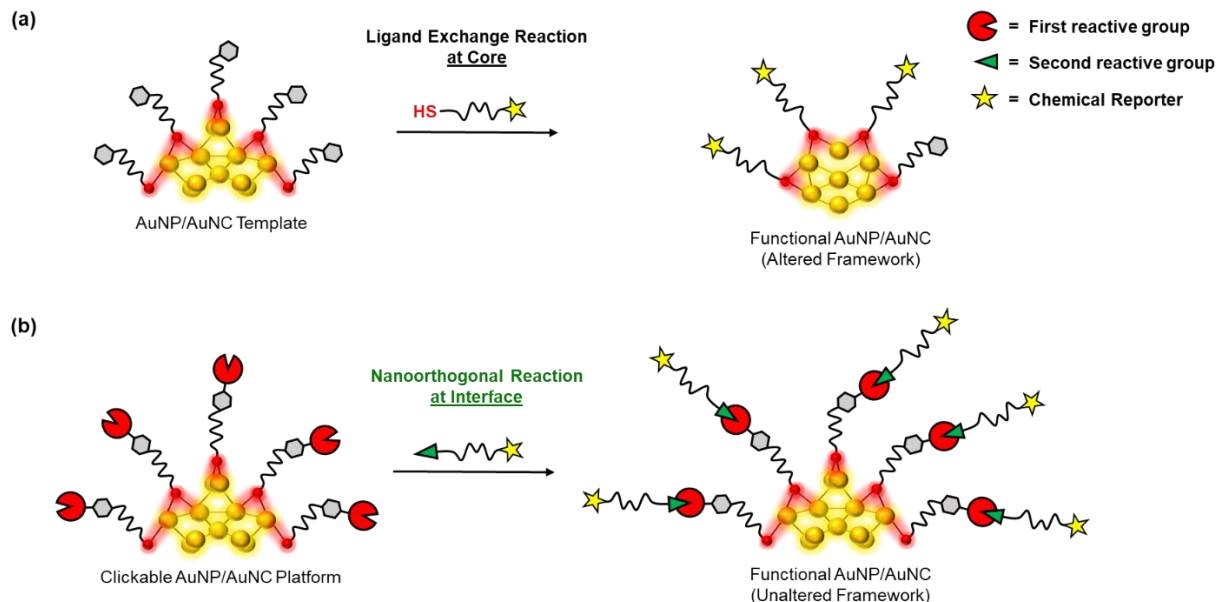
This can have limited utility that can be attributed to the reactivity of the thiol moiety, difficulty in fabricating thiolated functional substrates and an inability to establish efficient surface ligand exchanges (**Scheme 1.8a**). In particular, whereas polydisperse AuNP structures tend to be quite chemically rigid and less affected by ligand exchange processes, the sensitive relationship between surface ligand structure and core configuration of monodisperse $[Au_{25}(SR)_{18}]^{-1}$ frameworks presents a risk when attempting similar exchange processes, which can lead to undesired alterations to the parent metallic core and loss of monodispersity (**Scheme 1.8a**). Such drawbacks of ligand exchange strategies necessitate investigations into alternative strategies to modify the surface structure of these nanomaterial frameworks more reliably, without altering their chemically sensitive core structures.

The conceptual development of “bioorthogonal click chemistry” was a major breakthrough in chemical biology, defining a set of reactions that can be conducted to tether ‘chemical reporters’ to chemically-sensitive biomacromolecule frameworks (e.g. proteins etc.) within biologically sensitive environments. The ideal bioorthogonal click reaction binds the reporter to the biological framework without altering the parent structure (and related properties and functions), and at the same time produce measurable changes to the framework that is inherent to the choice of reporter (e.g. fluorophore-tagged proteins). Of the repertoire of bioorthogonal click reactions currently available, the strain-promoted dipolar cycloaddition reactions, SPAAC and SPANC, have proved to be the most versatile because of they have following the following advantages not shared among other common bioorthogonal click reactions:

1. The terminal azide and cyclooctyne moieties are very stable under most conditions, but at the same time have a high thermodynamic driving force to react chemoselectively with each other.
2. They are functional group and solvent tolerant.
3. Can be performed under mild reactions conditions at room temperature, typically through simple mix-and-stir reactions.
4. Have fast reaction kinetics, which can be modulated through structural considerations to the reactive partners, and so lowers the effective concentrations required to achieve efficient coupling compared to slower reactions.

The aim of this thesis is to translate these advantageous features of the SPAAC and SPANC reactions towards more efficient surface modifications of AuNPs and the $[\text{Au}_{25}(\text{SR})_{18}]^{1-}$ framework, as a more reliable and efficient alternative to ligand exchange strategies that can lead to undesired structural alterations. The conception of these versatile “bioorthogonal” reactions as a tool in chemical biology is rooted in the ability to conduct them without perturbing sensitive biological structures and the sensitive environments in which they operate. Not only does the SPAAC and SPANC reactions meet these criteria, but unlike many other bioorthogonal reactions, the two reactive partners are very stable in biological settings, making the SPAAC and SPANC reactions truly “*bioorthogonal click reactions*”. Given the ability to conduct them in *biologically*

sensitive environments, the research herein presented demonstrates that SPAAC and SPANC reactions can likewise be conducted in the *chemically sensitive* AuNP and (in particular) $[\text{Au}_{25}(\text{SR})_{18}]^{-1}$ surface environments. In this way, the aim of this thesis is to present the SPAAC and SPANC reactions as “*nanoorthogonal click reactions*” (**Scheme 1.8b**), capable of linking function-altering ‘reporters’ nanoorthogonally to the surfaces of chemically sensitive nanomaterial platforms in an efficient manner without altering their parent structure (**Scheme 1.8**).



Scheme 1.8. (a) *Synthesis of functional AuNP/AuNC through ligand exchange reaction.* Addition of chemical reporter possessing thiol group undergoes exchange with native thiols at the metallic core. Reaction at core can result in altered core framework. Quantitative exchange is difficult to accomplish, leading to mixed monolayer. (b) *Synthesis of functional AuNP/AuNC through “nanoorthogonal click reaction”.* Addition of chemical reporter possessing second reactive group (azide or cyclooctyne) undergoes chemoselective reaction with nanomaterial platform possessing first (complementary) reactive group on the exterior interface. Reaction at interface less likely to result in altered core framework. Quantitative interfacial reaction can be achieved reliably.

Our group has recently explored the use of SPAAC for nanoorthogonal surface modifications of AuNPs. Due to the superior stability and chemical inertness of the azide moiety (compared to the cyclooctyne moiety), our seminal study reported the development of an azide-functionalized AuNP platform (giving “AuNP-azide”) that could undergo post-assembly interfacial SPAAC (I-SPAAC) chemistry with complementary strained-alkynes.¹⁵⁴ Realizing that the azide and strained-alkyne groups were compatible with the AuNP surface environments, and

that the I-SPAAC reaction was nanoorthogonal to AuNPs, laid the foundation for many studies to follow.

We subsequently reported a complementary variant of the AuNP-azide platform by incorporating the strained-alkyne moiety, dibenzocyclooctyne (DBCO), to the AuNP surface (giving “AuNP-DBCO”).¹⁵⁵ The advantage of this approach is that the superior stability of the azide moiety makes it easier to tether to complementary functional substrate reporters. However, as described in **Section 1.5.5**, benzoannulated cyclooctynes are inherently less stable than their aliphatic counterparts, and have shorter self-lives, which can create compatibility issues when trying to conduct surface chemistry in sensitive environments. To make a more stable variant of AuNP-DBCO, **Chapter 2** focuses on the incorporation the more stable, aliphatic strained-alkyne bicyclo[6.1.0]nonyne (BCN), to give “AuNP-BCN”. The characterization of AuNP-BCN and quantification of interfacial BCN is described. The kinetically variable reactivity of AuNP-BCN towards a suite of different azides (through I-SPAAC) and nitrones (through I-SPANC) was also explored. Using this kinetic study, competition experiments between equimolar amounts of AuNP-BCN, an azide and a nitronone was investigated.

After the development of AuNP-azide, we also reported a synonymous variant by incorporating the nitronone moiety to the AuNP surface (giving “AuNP-nitronone”), which could undergo interfacial SPANC (I-SPANC) with cyclooctynes.¹⁵⁶ The main drawback of this platform was the slow reactivity of the nitronone chosen for this study, which had kinetically-decelerating electron-donating groups on both the N α and C α positions (see **Section 1.5.5**). To make a more reactive variant of AuNP-nitronone, **Chapter 3** reports the development of highly electron-deficient nitronones possessing pyridinium functionalities on the C α position. Alterations to the kinetic profiles of these “pyridinium-nitronones” could be accomplished through modifications to the N α position, with either electron-donating or electron-withdrawing substituents. Attempts were made to synthesize a thiolated ligand with a terminal pyridinium-nitronone group to incorporate it to the AuNP surface through either a direct or ligand exchange strategy. However, the pyridinium-nitronone group appears to undergo hydrolysis in the presence of the thiol group, preventing the development of such a ligand.

Having thoroughly explored nanoorthogonal click chemistry for surface modifications of AuNPs, our group became interested in conducting such strategies with AuNCs. This presents a particularly advantageous paradigm for AuNC surface modifications, which relies on coronal surface modifications, instead of risky ligand exchanges at the metallic core that would likely alter the internal configuration and diminish the monodispersity of the parent AuNC system (see **Section 1.4**). As with our seminal studies exploring SPAAC chemistry on AuNPs, the incorporation of the surface azide moieties was explored due to its superior chemical stability. **Chapter 4** describes the first example of an azide-functionalized $[\text{Au}_{25}(\text{SR})_{18}]^{1-}$ platform (giving “*p*-azido”), which was confirmed by single-crystal X-ray diffraction. This *p*-azido platform is capable of undergoing cluster-surface SPAAC (CS-SPAAC) quantitatively, without altering the chemically sensitive core structure. This study demonstrates that the SPAAC reaction can be conducted as a nanoorthogonal reaction for surface modifications of the most popular AuNC framework that is currently being used towards application-based research.

Having developed the *p*-azido platform, **Chapter 5** describes the development of two isomeric forms of *p*-azido (namely, “*m*-azido” and “*o*-azido”) to explore how the optical properties, electrochemical properties, and reactivity of these azide-functionalized $[\text{Au}_{25}(\text{SR})_{18}]^{1-}$ platforms correlated with the isomeric forms of the azide-functionalized surface ligands. The molecular structures of the neutral forms of the isomers, $[\text{Au}_{25}(\text{SR})_{18}]^0$, are reported. Although the optical properties of the three isomeric forms are nearly identical, the electrochemical responses appear to correlate with the position of the azide groups. Kinetic studies indicate that the reactivity of *p*-azido is higher than that of *m*-azido, while the *o*-azido platform undergoes deterioration when reacted with a strained-alkyne and so is not nanoorthogonal to CS-SPAAC chemistry.

Having established that the *p*-azido platform is the most reactive and the most reliable of the three isomeric variants, **Chapter 6** highlights the development of the first example of a ferrocene-functionalized $[\text{Au}_{25}(\text{SR})_{18}]^{1-}$ framework, through CS-SPAAC between *p*-azido and a strained-alkyne-modified ferrocene derivative (to give “*p*-ferrocenyl”). The optical properties of this modified $[\text{Au}_{25}(\text{SR})_{18}]^{1-}$ framework is reported. The electrochemical pattern of *p*-azido and *p*-ferrocenyl is presented, with the spectra of *p*-ferrocenyl containing a large peak that indicates that all surface ferrocene groups are electrochemically accessible.

Chapter 7 summarizes the overall contributions of this work and provides a commentary on how the work presented can be used towards surface modifications of AuNPs and the $[\text{Au}_{25}(\text{SR})_{18}]^{-1}$ framework for application-based research.

1.7 References

1. Faraday, M., The Bakerian Lecture: Experimental Relations of Gold (and Other Metals) to Light. *Philos. Trans. R. Soc.* **1857**, *147*, 145-181.
2. Weiser, H. B., *Inorganic Colloid Chemistry*. John Wiley & Sons, Inc.: London, 1993.
3. Zsigmondy, R., *Colloids and the Ultramicroscope, a Manual of Colloid Chemistry and Ultramicroscopy*. John Wiley & Sons: New York, 1909.
4. von Weimarn, P. P., The Precipitation Laws. *Chem. Rev.* **1925**, *2* (2), 217-242.
5. Beans, H. T.; Eastlack, H. E., The Electrical Synthesis Of Colloids. *J. Am. Chem. Soc.* **1915**, *37* (12), 2667-2683.
6. Scherrer, P., Bestimmung der Grosse und der Inneren Struktur von Kolloidteilchen Mittels Rontgenstrahlen. *Mathematisch-Physikalische Klasse* **1918**, 98–100.
7. Turkevich, J.; Hillier, J., Electron Microscopy of Colloidal Systems. *Anal. Chem.* **1949**, *21* (4), 475-485.
8. Gole, A.; Murphy, C. J., Seed-Mediated Synthesis of Gold Nanorods: Role of the Size and Nature of the Seed. *Chem. Mat.* **2004**, *16* (19), 3633-3640.
9. Liebig, F.; Sarhan, R. M.; Bargheer, M.; Schmitt, C. N. Z.; Poghosyan, A. H.; Shahinyan, A. A.; Koetz, J., Spiked gold nanotriangles: formation, characterization and applications in surface-enhanced Raman spectroscopy and plasmon-enhanced catalysis. *RSC Adv.* **2020**, *10* (14), 8152-8160.

10. Grzelczak, M.; Pérez-Juste, J.; Mulvaney, P.; Liz-Marzán, L. M., Shape control in gold nanoparticle synthesis. *Chem. Soc. Rev.* **2008**, *37* (9), 1783-1791.
11. Li, N.; Zhao, P.; Astruc, D., Anisotropic Gold Nanoparticles: Synthesis, Properties, Applications, and Toxicity. *Angew. Chem. Int. Ed.* **2014**, *53* (7), 1756-1789.
12. Shimizu, T.; Teranishi, T.; Hasegawa, S.; Miyake, M., Size Evolution of Alkanethiol-Protected Gold Nanoparticles by Heat Treatment in the Solid State. *J. Phys. Chem. B* **2003**, *107* (12), 2719-2724.
13. Sau, T. K.; Murphy, C. J., Seeded High Yield Synthesis of Short Au Nanorods in Aqueous Solution. *Langmuir* **2004**, *20* (15), 6414-6420.
14. Millstone, J. E.; Park, S.; Shuford, K. L.; Qin, L.; Schatz, G. C.; Mirkin, C. A., Observation of a Quadrupole Plasmon Mode for a Colloidal Solution of Gold Nanoprisms. *J. Am. Chem. Soc.* **2005**, *127* (15), 5312-5313.
15. Niu, W.; Zheng, S.; Wang, D.; Liu, X.; Li, H.; Han, S.; Chen, J.; Tang, Z.; Xu, G., Selective Synthesis of Single-Crystalline Rhombic Dodecahedral, Octahedral, and Cubic Gold Nanocrystals. *J. Am. Chem. Soc.* **2009**, *131* (2), 697-703.
16. Dreaden, E. C.; Alkilany, A. M.; Huang, X.; Murphy, C. J.; El-Sayed, M. A., The golden age: gold nanoparticles for biomedicine. *Chem. Soc. Rev.* **2012**, *41* (7), 2740-2779.
17. Brust, M.; Walker, M.; Bethell, D.; Schiffrin, D. J.; Whyman, R., Synthesis of thiol-derivatised gold nanoparticles in a two-phase Liquid-Liquid system. *J. Chem. Soc., Chem. Commun.* **1994**, (7), 801-802.
18. Häkkinen, H., The gold-sulfur interface at the nanoscale. *Nat. Chem.* **2012**, *4* (6), 443-455.
19. Bürgi, T., Properties of the gold-sulphur interface: from self-assembled monolayers to clusters. *Nanoscale* **2015**, *7* (38), 15553-15567.
20. Yeh, Y.-C.; Creran, B.; Rotello, V. M., Gold nanoparticles: preparation, properties, and applications in bionanotechnology. *Nanoscale* **2012**, *4* (6), 1871-1880.

21. Brust, M.; Fink, J.; Bethell, D.; Schiffrin, D. J.; Kiely, C., Synthesis and reactions of functionalised gold nanoparticles. *J. Chem. Soc., Chem. Commun.* **1995**, (16), 1655-1656.
22. Hostetler, M. J.; Wingate, J. E.; Zhong, C.-J.; Harris, J. E.; Vachet, R. W.; Clark, M. R.; Londono, J. D.; Green, S. J.; Stokes, J. J.; Wignall, G. D.; Glish, G. L.; Porter, M. D.; Evans, N. D.; Murray, R. W., Alkanethiolate Gold Cluster Molecules with Core Diameters from 1.5 to 5.2 nm: Core and Monolayer Properties as a Function of Core Size. *Langmuir* **1998**, *14* (1), 17-30.
23. Chen, S.; Murray, R. W., Alkanethiolate Monolayer-Protected Gold Clusters. *Langmuir* **1999**, *15* (3), 682-689.
24. Turkevich, J.; Stevenson, P. C.; Hillier, J., A study of the nucleation and growth processes in the synthesis of colloidal gold. *Discuss. Faraday Soc.* **1951**, *11* (0), 55-75.
25. Frens, G., Controlled Nucleation for the Regulation of the Particle Size in Monodisperse Gold Suspensions. *Nat. Phys. Sci.* **1973**, *241* (105), 20-22.
26. Aslan, K.; Pérez-Luna, V. H., Surface Modification of Colloidal Gold by Chemisorption of Alkanethiols in the Presence of a Nonionic Surfactant. *Langmuir* **2002**, *18* (16), 6059-6065.
27. Lin, S.-Y.; Tsai, Y.-T.; Chen, C.-C.; Lin, C.-M.; Chen, C.-h., Two-Step Functionalization of Neutral and Positively Charged Thiols onto Citrate-Stabilized Au Nanoparticles. *J. Phys. Chem. B* **2004**, *108* (7), 2134-2139.
28. Jana, N. R.; Gearheart, L.; Murphy, C. J., Seeding Growth for Size Control of 5–40 nm Diameter Gold Nanoparticles. *Langmuir* **2001**, *17* (22), 6782-6786.
29. Perrault, S. D.; Chan, W. C. W., Synthesis and Surface Modification of Highly Monodispersed, Spherical Gold Nanoparticles of 50–200 nm. *J. Am. Chem. Soc.* **2009**, *131* (47), 17042-17043.
30. Brown, K. R.; Walter, D. G.; Natan, M. J., Seeding of Colloidal Au Nanoparticle Solutions. 2. Improved Control of Particle Size and Shape. *Chem. Mater.* **2000**, *12* (2), 306-313.

31. Huang, X.; El-Sayed, M. A., Gold nanoparticles: Optical properties and implementations in cancer diagnosis and photothermal therapy. *J. Adv. Res.* **2010**, *1* (1), 13-28.
32. Templeton, A. C.; Pietron, J. J.; Murray, R. W.; Mulvaney, P., Solvent Refractive Index and Core Charge Influences on the Surface Plasmon Absorbance of Alkanethiolate Monolayer-Protected Gold Clusters. *J. Phys. Chem. B* **2000**, *104* (3), 564-570.
33. Eustis, S.; El-Sayed, M. A., Why gold nanoparticles are more precious than pretty gold: Noble metal surface plasmon resonance and its enhancement of the radiative and nonradiative properties of nanocrystals of different shapes. *Chem. Soc. Rev.* **2006**, *35* (3), 209-217.
34. Härtling, T.; Alaverdyan, Y.; Wenzel, M. T.; Kulloch, R.; Käll, M.; Eng, L. M., Photochemical Tuning of Plasmon Resonances in Single Gold Nanoparticles. *The J. Phys. Chem. C* **2008**, *112* (13), 4920-4924.
35. Srivastava, S.; Frankamp, B. L.; Rotello, V. M., Controlled Plasmon Resonance of Gold Nanoparticles Self-Assembled with PAMAM Dendrimers. *Chem.Mater.* **2005**, *17* (3), 487-490.
36. Link, S.; El-Sayed, M. A., Shape and size dependence of radiative, non-radiative and photothermal properties of gold nanocrystals. *Int. Rev. Phys. Chem.* **2000**, *19* (3), 409-453.
37. Su, K. H.; Wei, Q. H.; Zhang, X.; Mock, J. J.; Smith, D. R.; Schultz, S., Interparticle Coupling Effects on Plasmon Resonances of Nanogold Particles. *Nano Lett.* **2003**, *3* (8), 1087-1090.
38. Oh, E.; Hong, M.-Y.; Lee, D.; Nam, S.-H.; Yoon, H. C.; Kim, H.-S., Inhibition Assay of Biomolecules based on Fluorescence Resonance Energy Transfer (FRET) between Quantum Dots and Gold Nanoparticles. *J. Am. Chem. Soc.* **2005**, *127* (10), 3270-3271.
39. Sapsford, K. E.; Berti, L.; Medintz, I. L., Materials for Fluorescence Resonance Energy Transfer Analysis: Beyond Traditional Donor–Acceptor Combinations. *Angew. Chem. Int. Ed.* **2006**, *45* (28), 4562-4589.
40. Dubertret, B.; Calame, M.; Libchaber, A. J., Single-mismatch detection using gold-quenched fluorescent oligonucleotides. *Nature Biotechnol.* **2001**, *19* (4), 365-370.

41. Giljohann, D. A.; Seferos, D. S.; Daniel, W. L.; Massich, M. D.; Patel, P. C.; Mirkin, C. A., Gold Nanoparticles for Biology and Medicine. *Angew. Chem. Int. Ed.* **2010**, *49* (19), 3280-3294.
42. Dykman, L.; Khlebtsov, N., Gold nanoparticles in biomedical applications: recent advances and perspectives. *Chem. Soc. Rev.* **2012**, *41* (6), 2256-2282.
43. Chithrani, B. D.; Ghazani, A. A.; Chan, W. C. W., Determining the Size and Shape Dependence of Gold Nanoparticle Uptake into Mammalian Cells. *Nano Lett.* **2006**, *6* (4), 662-668.
44. Chithrani, B. D.; Chan, W. C. W., Elucidating the Mechanism of Cellular Uptake and Removal of Protein-Coated Gold Nanoparticles of Different Sizes and Shapes. *Nano Lett.* **2007**, *7* (6), 1542-1550.
45. Yang, P.-H.; Sun, X.; Chiu, J.-F.; Sun, H.; He, Q.-Y., Transferrin-Mediated Gold Nanoparticle Cellular Uptake. *Bioconjug. Chem.* **2005**, *16* (3), 494-496.
46. Verma, A.; Srivastava, S.; Rotello, V. M., Modulation of the Interparticle Spacing and Optical Behavior of Nanoparticle Ensembles Using a Single Protein Spacer. *Chem. Mater.* **2005**, *17* (25), 6317-6322.
47. Liu, R.; Liew, R.; Zhou, J.; Xing, B., A Simple and Specific Assay for Real-Time Colorimetric Visualization of β -Lactamase Activity by Using Gold Nanoparticles. *Angew. Chem. Int. Ed.* **2007**, *46* (46), 8799-8803.
48. Lin, S.-Y.; Wu, S.-H.; Chen, C.-h., A Simple Strategy for Prompt Visual Sensing by Gold Nanoparticles: General Applications of Interparticle Hydrogen Bonds. *Angew. Chem. Int. Ed.* **2006**, *45* (30), 4948-4951.
49. Huang, C.-C.; Chang, H.-T., Parameters for selective colorimetric sensing of mercury(ii) in aqueous solutions using mercaptopropionic acid-modified gold nanoparticles. *Chem. Commun.* **2007**, (12), 1215-1217.

50. Ajnai, G.; Chiu, A.; Kan, T.; Cheng, C.-C.; Tsai, T.-H.; Chang, J., Trends of Gold Nanoparticle-based Drug Delivery System in Cancer Therapy. *J. Exper. Clin. Med.* **2014**, *6* (6), 172-178.
51. Azzazy, H.; Mansour, M.; Samir, T.; Franco, R., Gold nanoparticles in the clinical laboratory: Principles of preparation and applications. *Clin. Chem. Lab. Med.* **2011**, *50*, 193-209.
52. Ghosh, P.; Han, G.; De, M.; Kim, C. K.; Rotello, V. M., Gold nanoparticles in delivery applications. *Adv. Drug Deliv. Rev.* **2008**, *60* (11), 1307-1315.
53. Peng, C.; Xu, J.; Yu, M.; Ning, X.; Huang, Y.; Du, B.; Hernandez, E.; Kapur, P.; Hsieh, J.-T.; Zheng, J., Tuning the In Vivo Transport of Anticancer Drugs Using Renal-Clearable Gold Nanoparticles. *Angew. Chem. Int. Ed.* **2019**, *58* (25), 8479-8483.
54. Tacar, O.; Sriamornsak, P.; Dass, C. R., Doxorubicin: an update on anticancer molecular action, toxicity and novel drug delivery systems. *J. Pharm. Pharmacol.* **2013**, *65* (2), 157-170.
55. Peng, X.-H.; Cao, Z.-H.; Xia, J.-T.; Carlson, G.; Lewis, M.; Wood, W.; Yang, L., Real-time Detection of Gene Expression in Cancer Cells Using Molecular Beacon Imaging: New Strategies for Cancer Research. *Cancer Res.* **2005**, *65*, 1909-17.
56. Seferos, D. S.; Giljohann, D. A.; Hill, H. D.; Prigodich, A. E.; Mirkin, C. A., Nano-Flares: Probes for Transfection and mRNA Detection in Living Cells. *J. Am. Chem. Soc.* **2007**, *129* (50), 15477-15479.
57. Philip, R.; Chantharasupawong, P.; Qian, H.; Jin, R.; Thomas, J., Evolution of Nonlinear Optical Properties: From Gold Atomic Clusters to Plasmonic Nanocrystals. *Nano Lett.* **2012**, *12* (9), 4661-4667.
58. Narouz, M. R.; Osten, K. M.; Unsworth, P. J.; Man, R. W. Y.; Salorinne, K.; Takano, S.; Tomihara, R.; Kaappa, S.; Malola, S.; Dinh, C.-T.; Padmos, J. D.; Ayoo, K.; Garrett, P. J.; Nambo, M.; Horton, J. H.; Sargent, E. H.; Häkkinen, H.; Tsukuda, T.; Crudden, C. M., N-heterocyclic carbene-functionalized magic-number gold nanoclusters. *Nat. Chem.* **2019**, *11* (5), 419-425.

59. Zeng, C.; Liu, C.; Chen, Y.; Rosi, N. L.; Jin, R., Gold–Thiolate Ring as a Protecting Motif in the Au₂₀(SR)₁₆ Nanocluster and Implications. *J. Am. Chem. Soc.* **2014**, *136* (34), 11922-11925.
60. Das, A.; Li, T.; Nobusada, K.; Zeng, C.; Rosi, N. L.; Jin, R., Nonsuperatomic [Au₂₃(SC₆H₁₁)₁₆][−] Nanocluster Featuring Bipyramidal Au₁₅ Kernel and Trimeric Au₃(SR)₄ Motif. *J. Am. Chem. Soc.* **2013**, *135* (49), 18264-18267.
61. Das, A.; Li, T.; Li, G.; Nobusada, K.; Zeng, C.; Rosi, N. L.; Jin, R., Crystal structure and electronic properties of a thiolate-protected Au₂₄ nanocluster. *Nanoscale* **2014**, *6* (12), 6458-6462.
62. Zhu, M.; Aikens, C. M.; Hollander, F. J.; Schatz, G. C.; Jin, R., Correlating the Crystal Structure of A Thiol-Protected Au₂₅ Cluster and Optical Properties. *J. Am. Chem. Soc.* **2008**, *130* (18), 5883-5885.
63. Zeng, C.; Li, T.; Das, A.; Rosi, N. L.; Jin, R., Chiral Structure of Thiolate-Protected 28-Gold-Atom Nanocluster Determined by X-ray Crystallography. *J. Am. Chem. Soc.* **2013**, *135* (27), 10011-10013.
64. Qian, H.; Eckenhoff, W. T.; Zhu, Y.; Pintauer, T.; Jin, R., Total Structure Determination of Thiolate-Protected Au₃₈ Nanoparticles. *J. Am. Chem. Soc.* **2010**, *132* (24), 8280-8281.
65. Zeng, C.; Chen, Y.; Iida, K.; Nobusada, K.; Kirschbaum, K.; Lambright, K. J.; Jin, R., Gold Quantum Boxes: On the Periodicities and the Quantum Confinement in the Au₂₈, Au₃₆, Au₄₄, and Au₅₂ Magic Series. *J. Am. Chem. Soc.* **2016**, *138* (12), 3950-3953.
66. Hostetler, M. J.; Green, S. J.; Stokes, J. J.; Murray, R. W., Monolayers in Three Dimensions: Synthesis and Electrochemistry of ω-Functionalized Alkanethiolate-Stabilized Gold Cluster Compounds. *J. Am. Chem. Soc.* **1996**, *118* (17), 4212-4213.
67. Plascencia-Villa, G.; Mendoza-Cruz, R.; Bazán-Díaz, L.; José-Yacamán, M., Gold Nanoclusters, Gold Nanoparticles, and Analytical Techniques for Their Characterization. In *Nanoparticles in Biology and Medicine: Methods and Protocols*, Ferrari, E.; Soloviev, M., Eds. Springer US: New York, NY, 2020; pp 351-382.

68. Zhu, M.; Lanni, E.; Garg, N.; Bier, M. E.; Jin, R., Kinetically Controlled, High-Yield Synthesis of Au₂₅ Clusters. *J. Am. Chem. Soc.* **2008**, *130* (4), 1138-1139.
69. Qian, H.; Zhu, M.; Andersen, U. N.; Jin, R., Facile, Large-Scale Synthesis of Dodecanethiol-Stabilized Au₃₈ Clusters. *J. Phys. Chem. A* **2009**, *113* (16), 4281-4284.
70. Jin, R.; Qian, H.; Wu, Z.; Zhu, Y.; Zhu, M.; Mohanty, A.; Garg, N., Size Focusing: A Methodology for Synthesizing Atomically Precise Gold Nanoclusters. *J. Phys. Chem. Lett.* **2010**, *1* (19), 2903-2910.
71. Zeng, C.; Chen, Y.; Das, A.; Jin, R., Transformation Chemistry of Gold Nanoclusters: From One Stable Size to Another. *J. Phys. Chem. Lett.* **2015**, *6* (15), 2976-2986.
72. Qian, H.; Zhu, Y.; Jin, R., Size-Focusing Synthesis, Optical and Electrochemical Properties of Monodisperse Au₃₈(SC₂H₄Ph)₂₄ Nanoclusters. *ACS Nano* **2009**, *3* (11), 3795-3803.
73. Whetten, R. L.; Khoury, J. T.; Alvarez, M. M.; Murthy, S.; Vezmar, I.; Wang, Z. L.; Stephens, P. W.; Cleveland, C. L.; Luedtke, W. D.; Landman, U., Nanocrystal gold molecules. *Adv. Mater.* **1996**, *8* (5), 428-433.
74. Schaaff, T. G.; Shafigullin, M. N.; Khoury, J. T.; Vezmar, I.; Whetten, R. L.; Cullen, W. G.; First, P. N.; Gutiérrez-Wing, C.; Ascensio, J.; Jose-Yacamán, M. J., Isolation of Smaller Nanocrystal Au Molecules: Robust Quantum Effects in Optical Spectra. *J. Phys. Chem. B* **1997**, *101* (40), 7885-7891.
75. Negishi, Y.; Nobusada, K.; Tsukuda, T., Glutathione-Protected Gold Clusters Revisited: Bridging the Gap between Gold(I)-Thiolate Complexes and Thiolate-Protected Gold Nanocrystals. *J. Am. Chem. Soc.* **2005**, *127* (14), 5261-5270.
76. Schaaff, T. G.; Knight, G.; Shafigullin, M. N.; Borkman, R. F.; Whetten, R. L., Isolation and Selected Properties of a 10.4 kDa Gold:Glutathione Cluster Compound. *J. Phys. Chem. B* **1998**, *102* (52), 10643-10646.
77. Tracy, J. B.; Crowe, M. C.; Parker, J. F.; Hampe, O.; Fields-Zinna, C. A.; Dass, A.; Murray, R. W., Electrospray Ionization Mass Spectrometry of Uniform and Mixed Monolayer

Nanoparticles: $\text{Au}_{25}[\text{S}(\text{CH}_2)_2\text{Ph}]_{18}$ and $\text{Au}_{25}[\text{S}(\text{CH}_2)_2\text{Ph}]_{18-x}(\text{SR})_x$. *J. Am. Chem. Soc.* **2007**, *129* (51), 16209-16215.

78. Akola, J.; Walter, M.; Whetten, R. L.; Häkkinen, H.; Grönbeck, H., On the Structure of Thiolate-Protected Au_{25} . *J. Am. Chem. Soc.* **2008**, *130* (12), 3756-3757.

79. Parker, J. F.; Weaver, J. E. F.; McCallum, F.; Fields-Zinna, C. A.; Murray, R. W., Synthesis of Monodisperse $[\text{Oct}_4\text{N}][\text{Au}_{25}(\text{SR})_{18}]$ Nanoparticles, with Some Mechanistic Observations. *Langmuir* **2010**, *26* (16), 13650-13654.

80. Dainese, T.; Antonello, S.; Gascón, J. A.; Pan, F.; Perera, N. V.; Ruzzi, M.; Venzo, A.; Zoleo, A.; Rissanen, K.; Maran, F., $\text{Au}_{25}(\text{SET})_{18}$, a Nearly Naked Thiolate-Protected Au_{25} Cluster: Structural Analysis by Single Crystal X-ray Crystallography and Electron Nuclear Double Resonance. *ACS Nano* **2014**, *8* (4), 3904-3912.

81. Wu, Z.; Jin, R., On the Ligand's Role in the Fluorescence of Gold Nanoclusters. *Nano Lett.* **2010**, *10* (7), 2568-2573.

82. Zhu, M.; Eckenhoff, W. T.; Pintauer, T.; Jin, R., Conversion of Anionic $[\text{Au}_{25}(\text{SCH}_2\text{CH}_2\text{Ph})_{18}]^-$ Cluster to Charge Neutral Cluster via Air Oxidation. *J. Phys. Chem. C* **2008**, *112* (37), 14221-14224.

83. Zhu, M.; Aikens, C. M.; Hendrich, M. P.; Gupta, R.; Qian, H.; Schatz, G. C.; Jin, R., Reversible Switching of Magnetism in Thiolate-Protected Au_{25} Superatoms. *J. Am. Chem. Soc.* **2009**, *131* (7), 2490-2492.

84. Venzo, A.; Antonello, S.; Gascón, J. A.; Guryanov, I.; Leapman, R. D.; Perera, N. V.; Sousa, A.; Zamuner, M.; Zanella, A.; Maran, F., Effect of the Charge State ($z = -1, 0, +1$) on the Nuclear Magnetic Resonance of Monodisperse $\text{Au}_{25}[\text{S}(\text{CH}_2)_2\text{Ph}]_{18}^z$ Clusters. *Anal. Chem.* **2011**, *83* (16), 6355-6362.

85. Pengo, P.; Bazzo, C.; Boccalon, M.; Pasquato, L., Differential reactivity of the inner and outer positions of $\text{Au}_{25}(\text{SCH}_2\text{CH}_2\text{Ph})_{18}$ dimeric staples under place exchange conditions. *Chem. Commun.* **2015**, *51* (15), 3204-3207.

86. Yau, S. H.; Varnavski, O.; Goodson, T., An Ultrafast Look at Au Nanoclusters. *Acc. Chem. Res.* **2013**, *46* (7), 1506-1516.
87. Alvarez, M. M.; Khoury, J. T.; Schaaff, T. G.; Shafigullin, M. N.; Vezmar, I.; Whetten, R. L., Optical Absorption Spectra of Nanocrystal Gold Molecules. *J. Phys. Chem. B* **1997**, *101* (19), 3706-3712.
88. Qian, H.; Zhu, M.; Wu, Z.; Jin, R., Quantum Sized Gold Nanoclusters with Atomic Precision. *Acc. Chem. Res.* **2012**, *45* (9), 1470-1479.
89. Devadas, M. S.; Kim, J.; Sinn, E.; Lee, D.; Goodson, T.; Ramakrishna, G., Unique Ultrafast Visible Luminescence in Monolayer-Protected Au₂₅ Clusters. *J. Phys. Chem. C* **2010**, *114* (51), 22417-22423.
90. Wang, G.; Guo, R.; Kalyuzhny, G.; Choi, J.-P.; Murray, R. W., NIR Luminescence Intensities Increase Linearly with Proportion of Polar Thiolate Ligands in Protecting Monolayers of Au₃₈ and Au₁₄₀ Quantum Dots. *J. Phys. Chem. B* **2006**, *110* (41), 20282-20289.
91. Ghosh, A.; Udayabhaskararao, T.; Pradeep, T., One-Step Route to Luminescent Au₁₈SG₁₄ in the Condensed Phase and Its Closed Shell Molecular Ions in the Gas Phase. *J. Phys. Chem. Lett.* **2012**, *3* (15), 1997-2002.
92. Wang, S.; Meng, X.; Das, A.; Li, T.; Song, Y.; Cao, T.; Zhu, X.; Zhu, M.; Jin, R., A 200-fold Quantum Yield Boost in the Photoluminescence of Silver-Doped Ag_xAu_{25-x} Nanoclusters: The 13 th Silver Atom Matters. *Angew. Chem. Int. Ed.* **2014**, *53* (9), 2376-2380.
93. Kang, X.; Chen, S.; Jin, S.; Song, Y.; Xu, Y.; Yu, H.; Sheng, H.; Zhu, M., Heteroatom Effects on the Optical and Electrochemical Properties of Ag₂₅(SR)₁₈ and Its Dopants. *ChemElectroChem* **2016**, *3* (8), 1261-1265.
94. Lee, D.; Donkers, R. L.; Wang, G.; Harper, A. S.; Murray, R. W., Electrochemistry and Optical Absorbance and Luminescence of Molecule-like Au₃₈ Nanoparticles. *J. Am. Chem. Soc.* **2004**, *126* (19), 6193-6199.

95. García-Raya, D.; Madueño, R.; Blázquez, M.; Pineda, T., Formation of 1,8-Octanedithiol Mono- and Bilayers under Electrochemical Control. *J. Phys. Chem. C* **2010**, *114* (8), 3568-3574.
96. Xie, J.; Zheng, Y.; Ying, J. Y., Protein-Directed Synthesis of Highly Fluorescent Gold Nanoclusters. *J. Am. Chem. Soc.* **2009**, *131* (3), 888-889.
97. Xie, J.; Zheng, Y.; Ying, J. Y., Highly selective and ultrasensitive detection of Hg^{2+} based on fluorescence quenching of Au nanoclusters by Hg^{2+} - Au^+ interactions. *Chem. Commun.* **2010**, *46* (6), 961-963.
98. Dreier, T. A.; Andrea Wong, O.; Ackerson, C. J., Oxidative decomposition of $\text{Au}_{25}(\text{SR})_{18}$ clusters in a catalytic context. *Chem. Commun.* **2015**, *51* (7), 1240-1243.
99. Haruta, M., When Gold Is Not Noble: Catalysis by Nanoparticles. *Chem. Record* **2003**, *3* (2), 75-87.
100. Liu, C.; Lin, S.; Pei, Y.; Zeng, X. C., Semiring Chemistry of $\text{Au}_{25}(\text{SR})_{18}$: Fragmentation Pathway and Catalytic Active site. *J. Am. Chem. Soc.* **2013**, *135* (48), 18067-18079.
101. Li, G.; Abroshan, H.; Liu, C.; Zhuo, S.; Li, Z.; Xie, Y.; Kim, H. J.; Rosi, N. L.; Jin, R., Tailoring the Electronic and Catalytic Properties of Au_{25} Nanoclusters via Ligand Engineering. *ACS Nano* **2016**, *10* (8), 7998-8005.
102. Li, J.; Nasaruddin, R. R.; Feng, Y.; Yang, J.; Yan, N.; Xie, J., Tuning the Accessibility and Activity of $\text{Au}_{25}(\text{SR})_{18}$ Nanocluster Catalysts through Ligand Engineering. *Chem. Eur. J.* **2016**, *22* (42), 14816-14820.
103. Li, G.; Jin, R., Gold Nanocluster-Catalyzed Semihydrogenation: A Unique Activation Pathway for Terminal Alkynes. *J. Am. Chem. Soc.* **2014**, *136* (32), 11347-11354.
104. Zhang, X.; Wu, F.-G.; Liu, P.; Wang, H.-Y.; Gu, N.; Chen, Z., Synthesis of ultrastable and multifunctional gold nanoclusters with enhanced fluorescence and potential anticancer drug delivery application. *J. Colloid Interface Sci.* **2015**, *455*, 6-15.

105. Li, L.; Chen, S.; Jiang, S., Molecular-Scale Mixed Alkanethiol Monolayers of Different Terminal Groups on Au(111) by Low-Current Scanning Tunneling Microscopy. *Langmuir* **2003**, *19* (8), 3266-3271.
106. Chen, S.; Kimura, K., Synthesis and Characterization of Carboxylate-Modified Gold Nanoparticle Powders Dispersible in Water. *Langmuir* **1999**, *15* (4), 1075-1082.
107. Bartczak, D.; Kanaras, A. G., Preparation of Peptide-Functionalized Gold Nanoparticles Using One Pot EDC/Sulfo-NHS Coupling. *Langmuir* **2011**, *27* (16), 10119-10123.
108. Keleştemur, S.; Altunbek, M.; Culha, M., Influence of EDC/NHS coupling chemistry on stability and cytotoxicity of ZnO nanoparticles modified with proteins. *Appl. Surf. Sci.* **2017**, *403*, 455-463.
109. Hong, R.; Fernández, J. M.; Nakade, H.; Arvizo, R.; Emrick, T.; Rotello, V. M., In situ observation of place exchange reactions of gold nanoparticles. Correlation of monolayer structure and stability. *Chem. Commun.* **2006**, (22), 2347-2349.
110. Song, Y.; Murray, R. W., Dynamics and Extent of Ligand Exchange Depend on Electronic Charge of Metal Nanoparticles. *J. Am. Chem. Soc.* **2002**, *124* (24), 7096-7102.
111. Kassam, A.; Bremner, G.; Clark, B.; Ulibarri, G.; Lennox, R. B., Place Exchange Reactions of Alkyl Thiols on Gold Nanoparticles. *J. Am. Chem. Soc.* **2006**, *128* (11), 3476-3477.
112. Shimomura, O.; Johnson, F. H.; Saiga, Y., Extraction, Purification and Properties of Aequorin, a Bioluminescent Protein from the Luminous Hydromedusan, Aequorea. *J. Cell. Comp. Physiol.* **1962**, *59* (3), 223-239.
113. Chalfie, M.; Tu, Y.; Euskirchen, G.; Ward, W. W.; Prasher, D. C., Green Fluorescent Protein as a Marker for Gene Expression. *Science* **1994**, *263* (5148), 802.
114. Tsien, R. Y., Th Green Fluorescent Protein. *Annu. Rev. Biochem.* **1998**, *67* (1), 509-544.

115. Prasher, D. C.; Eckenrode, V. K.; Ward, W. W.; Prendergast, F. G.; Cormier, M. J., Primary Structure of the Aequorea Victoria Green-Fluorescent Protein. *Gene* **1992**, *111* (2), 229-233.
116. Kakimoto, Y.; Tashiro, S.; Kojima, R.; Morozumi, Y.; Endo, T.; Tamura, Y., Visualizing Multiple Inter-Organelle Contact Sites using the Organelle-Targeted Split-GFP system. *Sci. Rep.* **2018**, *8* (1), 6175.
117. Yuste, R., Fluorescence Microscopy Today. *Nature Methods* **2005**, *2* (12), 902-904.
118. Chalfie, M., GFP: Lighting up life. *Proc. Nat. Acad. Sci.* **2009**, *106* (25), 10073.
119. Griffin, B. A.; Adams, S. R.; Tsien, R. Y., Specific Covalent Labeling of Recombinant Protein Molecules Inside Live Cells. *Science* **1998**, *281* (5374), 269.
120. Sletten, E. M.; Bertozzi, C. R., Bioorthogonal Chemistry: Fishing for Selectivity in a Sea of Functionality. *Angew. Chem. Int. Ed.* **2009**, *48* (38), 6974-6998.
121. Kolb, H. C.; Finn, M. G.; Sharpless, K. B., Click Chemistry: Diverse Chemical Function from a Few Good Reactions. *Angew. Chem. Int. Ed.* **2001**, *40* (11), 2004-2021.
122. Staudinger, H.; Meyer, J., Über neue organische Phosphorverbindungen III. Phosphinmethylenderivate und Phosphinimine. *Helvetica Chimica Acta* **1919**, *2* (1), 635-646.
123. Gololobov, Y. G.; Kasukhin, L. F., Recent advances in the staudinger reaction. *Tetrahedron* **1992**, *48* (8), 1353-1406.
124. Saxon, E.; Bertozzi, C. R., Cell Surface Engineering by a Modified Staudinger Reaction. *Science* **2000**, *287* (5460), 2007.
125. Wang, C. C. Y.; Seo, T. S.; Li, Z.; Ruparel, H.; Ju, J., Site-Specific Fluorescent Labeling of DNA Using Staudinger Ligation. *Bioconjug. Chem.* **2003**, *14* (3), 697-701.
126. Grandjean, C.; Boutonnier, A.; Guerreiro, C.; Fournier, J.-M.; Mulard, L. A., On the Preparation of Carbohydrate-Protein Conjugates Using the Traceless Staudinger Ligation. *J. Org. Chem.* **2005**, *70* (18), 7123-7132.

127. Parkhouse, S. M.; Garnett, M. C.; Chan, W. C., Targeting of polyamidoamine–DNA nanoparticles using the Staudinger ligation: Attachment of an RGD motif either before or after complexation. *Bioorg. Med. Chem.* **2008**, *16* (13), 6641-6650.
128. Soellner, M. B.; Nilsson, B. L.; Raines, R. T., Reaction Mechanism and Kinetics of the Traceless Staudinger Ligation. *J. Am. Chem. Soc.* **2006**, *128* (27), 8820-8828.
129. Bednarek, C.; Wehl, I.; Jung, N.; Schepers, U.; Bräse, S., The Staudinger Ligation. *Chem. Rev.* **2020**, *120* (10), 4301-4354.
130. Blackman, M. L.; Royzen, M.; Fox, J. M., Tetrazine Ligation: Fast Bioconjugation Based on Inverse-Electron-Demand Diels–Alder Reactivity. *J. Am. Chem. Soc.* **2008**, *130* (41), 13518-13519.
131. Devaraj, N. K.; Thurber, G. M.; Keliher, E. J.; Marinelli, B.; Weissleder, R., Reactive polymer enables efficient in vivo bioorthogonal chemistry. *Proc. Nat. Acad. Sci.* **2012**, *109* (13), 4762.
132. Rashidian, M.; Keliher, E. J.; Bilate, A. M.; Duarte, J. N.; Wojtkiewicz, G. R.; Jacobsen, J. T.; Cragolini, J.; Swee, L. K.; Victora, G. D.; Weissleder, R.; Ploegh, H. L., Noninvasive imaging of immune responses. *Proc. Nat. Acad. Sci.* **2015**, *112* (19), 6146.
133. Rossin, R.; van Duijnhoven, S. M. J.; ten Hoeve, W.; Janssen, H. M.; Kleijn, L. H. J.; Hoeben, F. J. M.; Versteegen, R. M.; Robillard, M. S., Triggered Drug Release from an Antibody–Drug Conjugate Using Fast “Click-to-Release” Chemistry in Mice. *Bioconjug. Chem.* **2016**, *27* (7), 1697-1706.
134. Hoffmann, J.-E.; Plass, T.; Nikić, I.; Aramburu, I. V.; Koehler, C.; Gillandt, H.; Lemke, E. A.; Schultz, C., Highly Stable trans-Cyclooctene Amino Acids for Live-Cell Labeling. *Chem. Eur. J.* **2015**, *21* (35), 12266-12270.
135. Devaraj, N. K., The Future of Bioorthogonal Chemistry. *ACS Cent. Sci.* **2018**, *4* (8), 952-959.

136. van Berkel, S. S.; Dirks, A. J.; Debets, M. F.; van Delft, F. L.; Cornelissen, J. J. L. M.; Nolte, R. J. M.; Rutjes, F. P. J. T., Metal-Free Triazole Formation as a Tool for Bioconjugation. *ChemBioChem* **2007**, *8* (13), 1504-1508.
137. van Berkel, S. S.; Dirks, A. J.; Meeuwissen, S. A.; Pinggen, D. L. L.; Boerman, O. C.; Laverman, P.; van Delft, F. L.; Cornelissen, J. J. L. M.; Rutjes, F. P. J. T., Application of Metal-Free Triazole Formation in the Synthesis of Cyclic RGD–DTPA Conjugates. *ChemBioChem* **2008**, *9* (11), 1805-1815.
138. Henry, L.; Schneider, C.; Mützel, B.; Simpson, P. V.; Nagel, C.; Fucke, K.; Schatzschneider, U., Amino acid bioconjugation via iClick reaction of an oxanorbornadiene-masked alkyne with a MnI(bpy)(CO)₃-coordinated azide. *Chem. Commun.* **2014**, *50* (99), 15692-15695.
139. Huisgen, R., 1,3-Dipolar Cycloadditions. Past and Future. *Angew. Chem. Int. Ed.* **1963**, *2* (10), 565-598.
140. Tornøe, C. W.; Christensen, C.; Meldal, M., Peptidotriazoles on Solid Phase: [1,2,3]-Triazoles by Regiospecific Copper(I)-Catalyzed 1,3-Dipolar Cycloadditions of Terminal Alkynes to Azides. *J. Org. Chem.* **2002**, *67* (9), 3057-3064.
141. Rostovtsev, V. V.; Green, L. G.; Fokin, V. V.; Sharpless, K. B., A Stepwise Huisgen Cycloaddition Process: Copper(I)-Catalyzed Regioselective “Ligation” of Azides and Terminal Alkynes. *Angew. Chem. Int. Ed.* **2002**, *41* (14), 2596-2599.
142. Lallana, E.; Riguera, R.; Fernandez-Megia, E., Reliable and Efficient Procedures for the Conjugation of Biomolecules through Huisgen Azide–Alkyne Cycloadditions. *Angew. Chem. Int. Ed.* **2011**, *50* (38), 8794-8804.
143. Wittig, G.; Krebs, A., Zur Existenz niedergliedriger Cycloalkine, I. *Chemische Berichte* **1961**, *94* (12), 3260-3275.
144. Agard, N. J.; Prescher, J. A.; Bertozzi, C. R., A Strain-Promoted [3 + 2] Azide–Alkyne Cycloaddition for Covalent Modification of Biomolecules in Living Systems. *J. Am. Chem. Soc.* **2005**, *127* (31), 11196-11196.

145. Turner, R. B.; Jarrett, A. D.; Goebel, P.; Mallon, B. J., Heats of hydrogenation. IX. Cyclic acetylenes and some miscellaneous olefins. *J. Am. Chem. Soc.* **1973**, *95* (3), 790-792.
146. McKay, C. S.; Moran, J.; Pezacki, J. P., Nitrones as dipoles for rapid strain-promoted 1,3-dipolar cycloadditions with cyclooctynes. *Chem. Commun.* **2010**, *46* (6), 931-933.
147. MacKenzie, D. A.; Sherratt, A. R.; Chigrinova, M.; Kell, A. J.; Pezacki, J. P., Bioorthogonal labelling of living bacteria using unnatural amino acids containing nitrones and a nitrone derivative of vancomycin. *Chem. Commun.* **2015**, *51* (62), 12501-12504.
148. Sherratt, A. R.; Chigrinova, M.; MacKenzie, D. A.; Rastogi, N. K.; Ouattara, M. T. M.; Pezacki, A. T.; Pezacki, J. P., Dual Strain-Promoted Alkyne–Nitrone Cycloadditions for Simultaneous Labeling of Bacterial Peptidoglycans. *Bioconjug. Chem.* **2016**, *27* (5), 1222-1226.
149. Sletten, E. M.; Bertozzi, C. R., From Mechanism to Mouse: A Tale of Two Bioorthogonal Reactions. *Acc. Chem. Res.* **2011**, *44* (9), 666-676.
150. Weterings, J.; Rijcken, C. J. F.; Veldhuis, H.; Meulemans, T.; Hadavi, D.; Timmers, M.; Honing, M.; Ippel, H.; Liskamp, R. M. J., TMTHSI, a superior 7-membered ring alkyne containing reagent for strain-promoted azide–alkyne cycloaddition reactions. *Chem. Sci.* **2020**, *11* (33), 9011-9016.
151. Dommerholt, J.; Schmidt, S.; Temming, R.; Hendriks, L. J. A.; Rutjes, F. P. J. T.; van Hest, J. C. M.; Lefeber, D. J.; Friedl, P.; van Delft, F. L., Readily Accessible Bicyclononynes for Bioorthogonal Labeling and Three-Dimensional Imaging of Living Cells. *Angew. Chem. Int. Ed.* **2010**, *49* (49), 9422-9425.
152. Bilodeau, D. A.; Margison, K. D.; Serhan, M.; Pezacki, J. P., Bioorthogonal Reactions Utilizing Nitrones as Versatile Dipoles in Cycloaddition Reactions. *Chem. Rev.* **2021**.
153. Dommerholt, J.; van Rooijen, O.; Borrmann, A.; Guerra, C. F.; Bickelhaupt, F. M.; van Delft, F. L., Highly accelerated inverse electron-demand cycloaddition of electron-deficient azides with aliphatic cyclooctynes. *Nat. Commun.* **2014**, *5* (1), 5378.

154. Gobbo, P.; Novoa, S.; Biesinger, M. C.; Workentin, M. S., Interfacial strain-promoted alkyne–azide cycloaddition (I-SPAAC) for the synthesis of nanomaterial hybrids. *Chem. Commun.* **2013**, *49* (38), 3982-3984.
155. Gobbo, P.; Mossman, Z.; Nazemi, A.; Niaux, A.; Biesinger, M. C.; Gillies, E. R.; Workentin, M. S., Versatile strained alkyne modified water-soluble AuNPs for interfacial strain promoted azide–alkyne cycloaddition (I-SPAAC). *J. Mat. Chem. B* **2014**, *2* (13), 1764-1769.
156. Ghiassian, S.; Yu, L.; Gobbo, P.; Nazemi, A.; Romagnoli, T.; Luo, W.; Luyt, L. G.; Workentin, M. S., Nitrene-Modified Gold Nanoparticles: Synthesis, Characterization, and Their Potential as ¹⁸F-Labeled Positron Emission Tomography Probes via I-SPANC. *ACS Omega* **2019**, *4* (21), 19106-19115.
157. Safont-Sempere, M. M.; Fernández, G.; Würthner, F., Self-Sorting Phenomena in Complex Supramolecular Systems. *Chem. Rev.* **2011**, *111* (9), 5784-5814.
158. Morris, K. L.; Chen, L.; Raeburn, J.; Sellick, O. R.; Cotanda, P.; Paul, A.; Griffiths, P. C.; King, S. M.; O'Reilly, R. K.; Serpell, L. C.; Adams, D. J., Chemically programmed self-sorting of gelator networks. *Nat. Commun.* **2013**, *4* (1), 1480.
159. Xiao, Q.; Rubien, J. D.; Wang, Z.; Reed, E. H.; Hammer, D. A.; Sahoo, D.; Heiney, P. A.; Yadavalli, S. S.; Goulian, M.; Wilner, S. E.; Baumgart, T.; Vinogradov, S. A.; Klein, M. L.; Percec, V., Self-Sorting and Coassembly of Fluorinated, Hydrogenated, and Hybrid Janus Dendrimers into Dendrimersomes. *J. Am. Chem. Soc.* **2016**, *138* (38), 12655-12663.
160. Jędrzejewska, H.; Szumna, A., Making a Right or Left Choice: Chiral Self-Sorting as a Tool for the Formation of Discrete Complex Structures. *Chem. Rev.* **2017**, *117* (6), 4863-4899.
161. He, Z.; Jiang, W.; Schalley, C. A., Integrative self-sorting: a versatile strategy for the construction of complex supramolecular architecture. *Chem. Soc. Rev.* **2015**, *44* (3), 779-789.
162. Li, L.; Sun, R.; Zheng, R., Tunable morphology and functionality of multicomponent self-assembly: A review. *Mater. Design* **2021**, *197*, 109209.

163. Griffin, D. R.; Weaver, W. M.; Scumpia, P. O.; Di Carlo, D.; Segura, T., Accelerated wound healing by injectable microporous gel scaffolds assembled from annealed building blocks. *Nat. Mater.* **2015**, *14* (7), 737-744.
164. South, A. B.; Lyon, L. A., Autonomic Self-Healing of Hydrogel Thin Films. *Angew. Chem. Int. Ed.* **2010**, *49* (4), 767-771.
165. de Feijter, I.; Albertazzi, L.; Palmans, A. R. A.; Voets, I. K., Stimuli-Responsive Colloidal Assembly Driven by Surface-Grafted Supramolecular Moieties. *Langmuir* **2015**, *31* (1), 57-64.
166. Xu, H.; Hong, R.; Lu, T.; Uzun, O.; Rotello, V. M., Recognition-Directed Orthogonal Self-Assembly of Polymers and Nanoparticles on Patterned Surfaces. *J. Am. Chem. Soc.* **2006**, *128* (10), 3162-3163.
167. Zhu, B.; Jasinski, N.; Benitez, A.; Noack, M.; Park, D.; Goldmann, A. S.; Barner-Kowollik, C.; Walther, A., Hierarchical Nacre Mimetics with Synergistic Mechanical Properties by Control of Molecular Interactions in Self-Healing Polymers. *Angew. Chem. Int. Ed.* **2015**, *54* (30), 8653-8657.
168. Granado, L.; Burel, C.; Giordanengo, R.; Alsayed, A.; Bendejacq, D.; Ganachaud, F., Hydrophilic and Double Hydrophilic/Hydrophobic Microcapsules using a Single, Thermally Responsive, Self-Sorting Dispersant. *ACS App. Poly. Mater.* **2021**, *3* (4), 1707-1711.
169. Chen, G.; Jiang, M., Cyclodextrin-based inclusion complexation bridging supramolecular chemistry and macromolecular self-assembly. *Chem. Soc. Rev.* **2011**, *40* (5), 2254-2266.
170. Han, K.; Go, D.; Tigges, T.; Rahimi, K.; Kuehne, A. J. C.; Walther, A., Social Self-Sorting of Colloidal Families in Co-Assembling Microgel Systems. *Angew. Chem. Int. Ed.* **2017**, *56* (8), 2176-2182.
171. Jin, L.-M.; Xu, X.; Lu, H.; Cui, X.; Wojtas, L.; Zhang, X. P., Effective Synthesis of Chiral N-Fluoroaryl Aziridines through Enantioselective Aziridination of Alkenes with Fluoroaryl Azides. *Angew. Chem. Int. Ed.* **2013**, *52* (20), 5309-5313.

172. Draper, E. R.; Adams, D. J., Self-sorting shows its true colours. *Nat. Chem.* **2016**, *8* (8), 737-738.
173. Nguyen, S. S.; Prescher, J. A., Developing bioorthogonal probes to span a spectrum of reactivities. *Nat. Rev. Chem.* **2020**, *4* (9), 476-489.
174. Gunawardene, P. N.; Luo, W.; Polgar, A. M.; Corrigan, J. F.; Workentin, M. S., Highly Electron-Deficient Pyridinium-Nitrones for Rapid and Tunable Inverse-Electron-Demand Strain-Promoted Alkyne-Nitrone Cycloaddition. *Org. Lett.* **2019**, *21* (14), 5547-5551.
175. Dommerholt, J.; Rutjes, F. P. J. T.; van Delft, F. L., Strain-Promoted 1,3-Dipolar Cycloaddition of Cycloalkynes and Organic Azides. *Top. Curr. Chem.* **2016**, *374* (2), 16.
176. Gobbo, P.; Workentin, M. S., Improved Methodology for the Preparation of Water-Soluble Maleimide-Functionalized Small Gold Nanoparticles. *Langmuir* **2012**, *28* (33), 12357-12363.

Chapter 2

2 Towards the Design of Self-Sorting Nanomaterials Through Kinetically Directed Orthogonal Control over Interfacial Surface Chemistry

This chapter is being submitted as a short paper and is in manuscript format. Max Weismann and Prof. Pierangelo Gobbo are co-authors, along with Prof. Mark S. Workentin.

Max Weismann was an undergraduate student under co-supervision of myself and Prof. Pierangelo Gobbo (who was a graduate student at the time), along with our supervisor Prof. Mark S. Workentin, who assisted in the synthesis and characterization of the AuNP-BCN platform. The draft of the chapter was written by the author and edited by Prof. Mark S. Workentin.

2.1 Introduction

Recent progresses in self-assembly research have explored the development of self-sorting materials, which are materials capable of exclusively reacting orthogonally with complementary analytes in a complex media containing non-competing analytes to form “asocial” or “social” hierarchical structures.¹⁻⁴ Asocial self-sorting encompasses orthogonal assembly of materials systems that are compositionally identical, whereas socially self-sorting materials are capable of orthogonally hetero-assembling in multicomponent structures possessing compositionally different material systems.⁵ Such pre-defined organization is achieved by designing material building blocks that store defined chemical information, which determines their role in the self-assembly process and their final location in the self-assembled material. Unlike indiscriminate self-assembly, which involves structural organization that is independent of material type and chemical composition, directed control over assembly of simpler material building blocks to construct complex structures makes it possible to develop material systems whose structure and function can be programmed depending on the chemically pre-determined assembly instructions. Such an approach has led to the generation of hierarchical structures that would not be possible to generate otherwise, paving the way towards the design of new classes of materials that presents new collective properties and extends their potential applications.⁶⁻⁹

Self-assembly is primarily governed by selective orthogonal interactions between material building blocks to trigger co-assembly.^{10, 11} Such orthogonality can be pre-programmed in the chemical information on the surface of the constituent building blocks, which allows for a great deal of control over which higher-order structures can be attained in a complex media containing multiple building blocks.¹² The most common method to accomplish asocial/social self-sorting is to install molecular units on the surface of individual building blocks, each of which is capable of orthogonally interacting with other complementary units on the surface of other building blocks. Such programmable control is typically achieved through lock/key (specifically host/guest) molecular interactions between hetero-complementary groups, in which a multi-component mixture can be made to assemble into supramolecular structures based on the “lock” and “key” group that is installed on individual components (**Figure 2.1a**).¹³ Han *et al.* demonstrated the social self-sorting of different co-assembled families of colloid structures using a mixture of four building blocks, which was programmed using high-interaction host/guest recognition chemistry between cyclodextrins (host/lock) and ferrocene/azobenzene (guest/key)¹⁴. Although such strategies are notable due to the highly predictable manner in which building blocks can assemble, it is limited by the requirement of designing different host material frameworks that is capable of interacting with complementary guest groups on different material building blocks.

The development of self-sorting nanomaterials has not received much attention, because of the difficulty in programming the nanomaterials to display well-defined orthogonal interactions so that self-assembly can be triggered.^{15, 16} Furthermore, host/guest chemistry is difficult to implement on nanomaterial surfaces because of the sensitive relationship between nanomaterial integrity and surface composition. In this work, we not only address the challenge of designing nanomaterial systems in which orthogonal control over surface modifications can be achieved, but also provide an alternative approach to accomplish orthogonal control. As opposed to implementing a *host/guest-directed approach* to accomplish self-sorting (**Figure 2.1a**), we herein present a kinetics study where we propose that self-sorting can be accomplished using a *kinetically-directed* approach (**Figure 2.1b**). The major drawback to the most common lock/key self-sorting methodologies is the necessity of developing a library of host material frameworks capable of orthogonally interacting with their individual complementary guest partners. Instead of relying on the development of a library of nanomaterial frameworks possessing unique lock groups, we report a singular nanomaterial *platform* possessing one reactive lock group, which can

orthogonally react with a wide variety of complementary key groups in a kinetically predictable manner, depending on the chemical composition of the key groups.

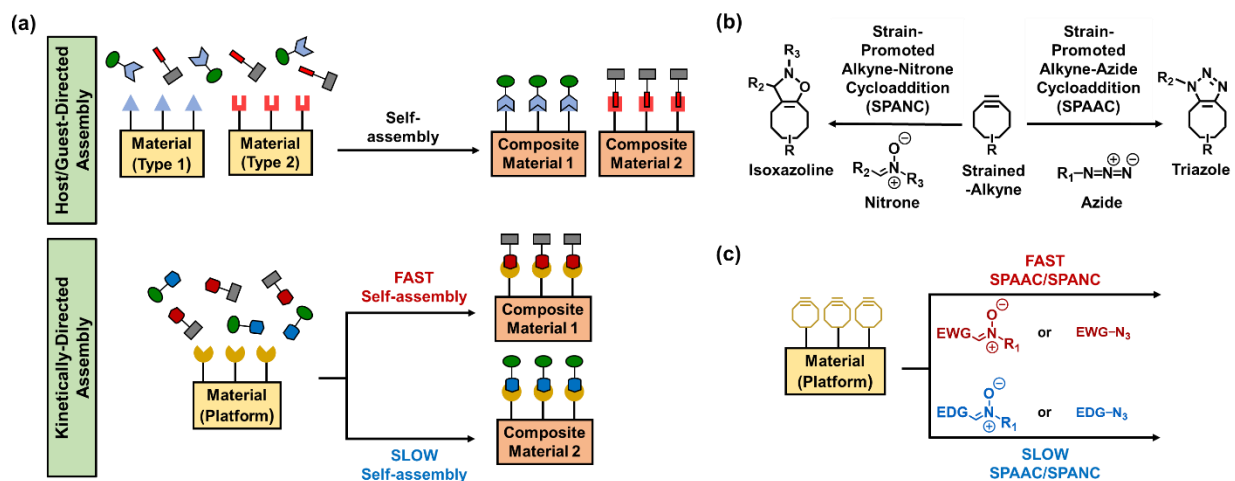


Figure 2.1. (a) Schematic representation of host/guest directed- and kinetically-directed self-assembly strategies. (b) The strain-promoted alkyne-azide cycloaddition reaction (SPAAC) to form a triazole cycloadduct (right), and the strain-promoted alkyne-nitrone cycloaddition reaction (SPANC) to form an isoxazoline cycloadduct (left). (c) Schematic representation of kinetically-directed self-assembly strategy using SPAAC and SPANC.

2.2 Results and Discussion

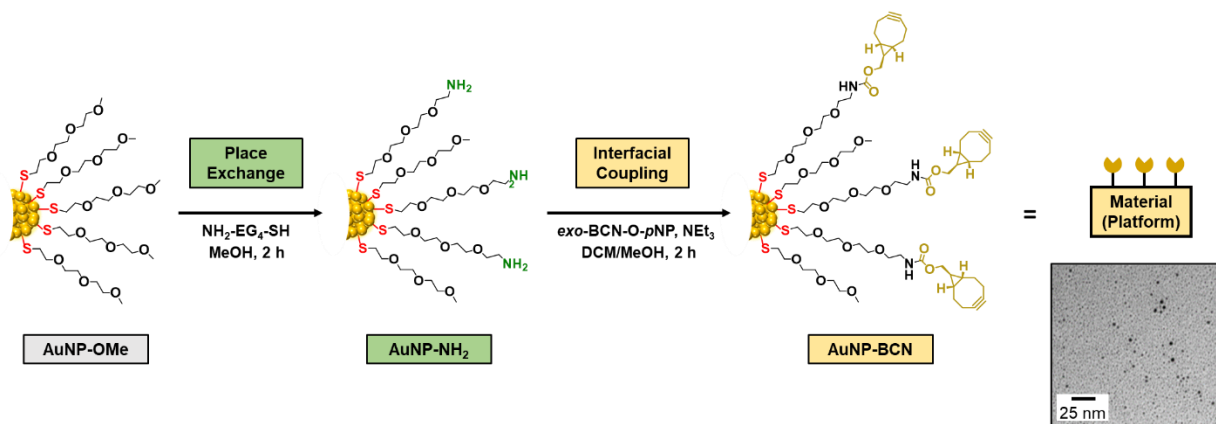
For our proof-of-concept study to demonstrate our kinetically-directed approach for modifying nanomaterial surfaces, we used small (~3 nm) gold nanoparticles as a model nanomaterial, which was chosen because they are comparatively stable, easy to characterize, but most importantly, because changes in surface composition can be easily monitored by ¹H NMR spectroscopy. To develop a prototype gold nanoparticle platform capable of kinetically-directed surface modifications, a reactive strained-alkyne moiety (the lock group) was tethered to the nanomaterial surface. The surface strained-alkynes are capable of orthogonally reacting with both azide and nitrone moieties (the key groups) through the strain-promoted alkyne-azide cycloaddition (SPAAC) or the strain-promoted alkyne-nitrone cycloaddition (SPANC), respectively.¹⁷ In addition to the high chemoselectivity and atom efficiency,¹⁸ these cycloaddition reactions were chosen because the reaction kinetics of both SPAAC and SPANC can be regulated through structural modifications to the dipolar species. Directly delocalizing the azide/nitrone moieties into

electron-donating groups decelerates reaction kinetics, while delocalization into electron-withdrawing groups accelerates reaction kinetics (**Figure 2.1c**).¹⁹⁻²¹ The ability to tailor the reaction kinetics of the SPAAC and SPANC reactions presents an opportunity to develop nanomaterial systems that is capable of kinetically-directed orthogonal surface modifications that can be used to trigger reactivity with individual complementary partners in a kinetically pre-determined way. The ability to isolate the reactivity between one lock group and one key group in a mixture of key groups based on pre-defined kinetic information, as opposed to the requirement of changing the chemical information inherent to common host/guest strategies, provides an exciting kinetically-directed alternative to self-sorting methodologies.

The strained-alkyne that was chosen for this study was an aliphatic strained-alkyne known as bicyclononyne (BCN). It was chosen because, compared to other popular benzoannulated strained-alkynes (such as dibenzocyclooctyne (DBCO)), it can be synthesized on large scale using a relatively straightforward protocol and demonstrates exceptional stability. In order to append the BCN moiety to the gold nanoparticle surface, a direct synthesis using a BCN terminated thiol via the typical Brust-Shiffrin method that is most commonly employed to synthesize gold nanoparticles could not be used due to the incompatibility of the strained-alkyne moiety towards the reducing conditions of the reaction. Furthermore, a place exchange reaction with a BCN-terminated thiol onto a template AuNP system could not be performed due to the ability of thiols to undergo a Michael addition onto strained-alkynes.

To mitigate these synthetic complications, an AuNP system with a nucleophilic moiety appended to the surface was first developed, which could then undergo an interfacial substitution reaction with a BCN derivative that had been electrophilically activated (**Scheme 2.1**, see Supporting Information **Sections 2.6.2.2, 2.6.2.5 and 2.6.2.8** for experimental details). First, an inert AuNP system was synthesized by reaction of HAuCl₄ and MeO-EG₃-SH (EG = ethylene glycol) as the protecting ligand in a Brust-Shiffrin synthesis, to give **AuNP-OMe**. Next, a place exchange reaction was performed between **AuNP-OMe** and NH₂-EG₄-SH, where the native methoxy-terminated ligands were exchanged with the incoming amine-terminated ligands to incorporate the nucleophilic amine moiety. The surface amino groups in **AuNP-NH₂** were then reacted with bicyclo[6.1.0]non-4-yn-9-ylmethyl-(4-nitrophenyl)-carbonate (*exo*-BCN-O-*p*NP) to create a new carbamate linkage through an interfacial acyl substitution reaction, which

successfully incorporated the BCN moiety to make **AuNP-BCN**. X-ray photoelectron (XPS) spectroscopy confirmed the new carbamate linkage after the interfacial acyl substitution reaction (**Figure S2.8** and **Figure S2.14**), and transmission electron microscopy (TEM) indicated that the **AuNP-BCN** particles are approximately 3 nm in diameter (**Figure S2.13**), which was similar to the diameter of the **AuNP-NH₂** particles (**Figure S2.7**). The successful incorporation of the strained-alkyne moiety was also confirmed by ¹H NMR spectroscopy. The ¹H NMR spectrum of **AuNP-NH₂** has two signals at 3.34 ppm and 3.15 ppm (**Figure S2.6**), which are produced by surface methoxy moieties in the MeO-EG₃-S⁻ ligands and surface methylene protons alpha to the amino moiety in the NH₂-EG₄-S⁻ ligands, respectively. After the interfacial reaction, the signal at 3.15 ppm disappears due to the surface methylene protons now being alpha to a carbamate linkage, and new signals occur at 3.98, 2.41, 2.32, 2.22, 1.38 and 0.80 ppm that correspond to the newly incorporated *exo*-bicyclononyne moiety (**Figure S2.12**). The thermogravimetric analysis (TGA) spectrum of AuNP-BCN showed two primary organic components (**Figure S2.36**), namely the surface MeO-EG₃-S⁻ and BCN-O-(CO-NH)-EG₄-S⁻ ligands, which constituted 28% and 72% of the organic mass, respectively (**Figure S2.37**). It should be noted that the quantity of surface BCN can be tuned by changing the reaction time and concentration of the place exchange reaction to adjust the amount of surface amine groups, which will amend the number of strained-alkyne groups being introduced to the AuNP surface.



Scheme 2.1. Synthesis of AuNP-BCN platform. *Right inset.* TEM image of AuNP-BCN.

Subsequently, we designed and synthesized a library of azides and nitrones that were delocalized into either electron donating or electron-withdrawing substituents, giving each their own kinetic profile. Each azide and nitron were reacted with both *exo*-bicyclo[6.1.0]non-4-yn-9-ol (BCN_{exo}-OH) and **AuNP-BCN**, and the second order kinetic rate constants were determined by

^1H NMR spectroscopy by following the decrease in signals from free azide or nitron. **Figure 2.2** summarizes the bimolecular rate constants for the SPAAC and SPANC reactions with free $\text{BCN}_{\text{exo-OH}}$ and the *interfacial* SPAAC (*I*-SPAAC) and *interfacial* SPANC (*I*-SPANC) reactions with **AuNP-BCN**. In most cases, the *I*-SPAAC kinetics of **AuNP-BCN** were similar to the SPAAC kinetics of free BCN. However, nitro-functionalized **azide 4** exhibited a two-fold faster *I*-SPAAC reaction with **AuNP-BCN** versus free $\text{BCN}_{\text{exo-OH}}$. A similar two-fold enhancement in *I*-SPANC kinetics was observed between nitro-functionalized **nitrone 1** and **nitrone 4** with **AuNP-BCN**, providing further evidence that nitro-functionalized dipoles interestingly display faster interfacial cycloaddition kinetics compared to their non-interfacial counterparts.

Increasing SPAAC Kinetics							
	Azide 1	Azide 2	Azide 3	Azide 4	Azide 5	Azide 6	
k_2 ($\text{M}^{-1}\text{s}^{-1}$) ($k_2(\text{rel})$)	0.034 (1.0)	0.13 (3.8)	0.17 (5.0)	0.92 (27)	0.59 (17)	1.6 (47)	<i>I</i> -SPAAC
k_2 ($\text{M}^{-1}\text{s}^{-1}$) ($k_2(\text{rel})$)	0.034 (1.0)	0.14 (4.1)	0.18 (5.3)	0.45 (13)	0.58 (17)	1.5 (44)	SPAAC
k_2 ($\text{M}^{-1}\text{s}^{-1}$) ($k_2(\text{rel})$)	2.0 (59)	0.63 (19)	0.61 (18)	0.087 (2.6)	0.033 (0.97)	0.015 (0.44)	<i>I</i> -SPANC
k_2 ($\text{M}^{-1}\text{s}^{-1}$) ($k_2(\text{rel})$)	2.0 (59)	0.68 (20)	0.31 (9.1)	0.080 (2.4)	0.036 (1.1)	0.0077 (0.23)	SPANC
	Nitrone 6	Nitrone 5	Nitrone 4	Nitrone 3	Nitrone 2	Nitrone 1	
Increasing SPANC Kinetics							

Figure 2.2. Estimated SPAAC/SPANC and *I*-SPAAC/*I*-SPANC reaction rates of azides and nitrones with free BCN and AuNP-BCN, respectively. All rate constants were determined under second order conditions in CD_2Cl_2 at 25°C in duplicate trials using ^1H NMR spectroscopy, and monitored over pre-determined time intervals to determine a second order rate constant. The $k_2(\text{rel})$ value indicates the rate of each k_2 relative to the slowest azide (azide 1).

Having established that surface reactivity of **AuNP-BCN** is kinetically modifiable depending on the chemical composition of the complementary azide/nitron species, we sought to demonstrate that the nanomaterial platform can react exclusively with one reactive partner over another in a mixture of two reactive partners (**Figure 2.3**). **AuNP-BCN** was challenged to equimolar quantities of an azide and nitron and the reaction was monitored by ^1H NMR

spectroscopy. The percentage of each resulting cycloadduct was determined by measuring the change in non-coinciding signals from the constituent azide and nitrones before and after the introduction of **AuNP-BCN**. As shown in **Figure 2.3**, when **AuNP-BCN** was challenged to an azide and nitronone with similar rate constants, similar amounts of each cycloadduct system was observed. However, as the difference between rate constants were increased, exclusive reactivity to one dipolar species over the other was observed. When a equimolar mixture of **nitronone 4** ($k_2 (I\text{-SPANC}) = 0.61 \text{ M}^{-1}\text{s}^{-1}$) and **azide 4** ($k_2 (I\text{-SPAAC}) = 0.92 \text{ M}^{-1}\text{s}^{-1}$) was added to **AuNP-BCN**, similar amounts of each of the two triazole and isooxazoline cycloadduct systems was observed. However, when a mixture of **nitronone 4** ($k_2 (I\text{-SPANC}) = 0.61 \text{ M}^{-1}\text{s}^{-1}$) and **azide 3** ($k_2 (I\text{-SPAAC}) = 0.17 \text{ M}^{-1}\text{s}^{-1}$), a significantly greater amount of the isooxazoline cycloadduct was observed. When the difference between the rate constants was increased even further, as exists between **azide 1** ($k_2 (I\text{-SPAAC}) = 0.034 \text{ M}^{-1}\text{s}^{-1}$) and **nitronone 6** ($k_2 (I\text{-SPANC}) = 2.0 \text{ M}^{-1}\text{s}^{-1}$), there was no observable change in the intensity of the ^1H NMR signal from the azide protons, indicating exclusive formation of the isooxazoline cycloadduct. Similarly, when **AuNP-BCN** was challenged to a mixture of **azide 6** ($k_2 (I\text{-SPAAC}) = 1.6 \text{ M}^{-1}\text{s}^{-1}$) and **nitronone 1** ($k_2 (I\text{-SPANC}) = 0.015 \text{ M}^{-1}\text{s}^{-1}$), there was no observable change in the ^1H NMR signal from the nitronone protons, indicating exclusive formation of the triazole cycloadduct. This data is exciting because it demonstrates that **AuNP-BCN** can not only undergo orthogonal surface chemistry, but it can be done to isolate reactivity to one complementary partner over another in a kinetically predictable way, that is dependent on the electronic composition of the complementary dipolar species.

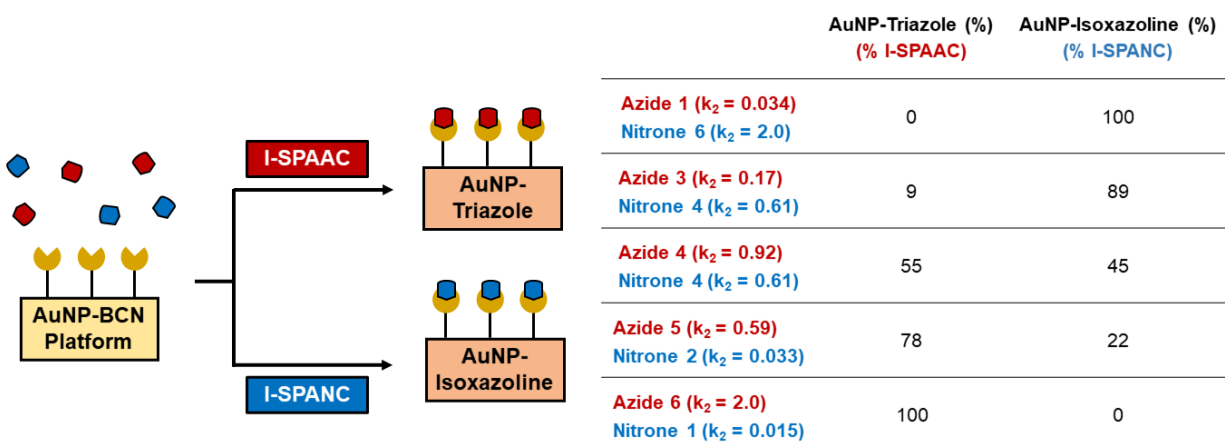


Figure 2.3. Kinetically-directed competitive reactivity of AuNP-BCN, where one equivalent of AuNP-BCN was reacted with one equivalent of nitronone and one equivalent of azide, and the amount of cycloadduct that was formed was determined using ^1H NMR spectroscopy.

2.3 Conclusions

We herein report a versatile nanomaterial platform in which kinetically variable surface modifications can be performed in a multi-component mixture, depending on the electronic and chemical composition of the complementary reactive species in the mixture. By delocalizing the azide and nitrene species into different electronic groups, unique kinetic profiles can be bestowed onto these reactive partners, permitting exclusive reactivity with one species over another in a kinetically predictable way. In this way, complex systems can be constructed from simpler ones simultaneously in a self-sorting manner in a way that depends on the kinetic profile of the desired complementary building block, rather than the chemical identity of large moieties that are tethered to the building blocks that are more difficult to install than azides and nitrenes. This presents an exciting new fabrication process for predictable hierarchical construction of chemically distinct materials from a complex mixture of building blocks through a kinetically-directed approach, that doesn't rely on the common lock-and-key approaches that is most commonly employed to date in self-sorting technology.

2.4 Acknowledgments

This work was funded by NSERC-DG and the University of Western Ontario. We would like to thank D. Hairsine (ESI-MS Facility) and M. Biesinger (Surface Science Western).

2.5 References

1. Safont-Sempere, M. M.; Fernández, G.; Würthner, F., Self-Sorting Phenomena in Complex Supramolecular Systems. *Chem. Rev.* **2011**, *111* (9), 5784-5814.
2. Morris, K. L.; Chen, L.; Raeburn, J.; Sellick, O. R.; Cotanda, P.; Paul, A.; Griffiths, P. C.; King, S. M.; O'Reilly, R. K.; Serpell, L. C.; Adams, D. J., Chemically programmed self-sorting of gelator networks. *Nat. Commun.* **2013**, *4* (1), 1480.
3. Xiao, Q.; Rubien, J. D.; Wang, Z.; Reed, E. H.; Hammer, D. A.; Sahoo, D.; Heiney, P. A.; Yadavalli, S. S.; Goulian, M.; Wilner, S. E.; Baumgart, T.; Vinogradov, S. A.; Klein, M.

L.; Percec, V., Self-Sorting and Coassembly of Fluorinated, Hydrogenated, and Hybrid Janus Dendrimers into Dendrimersomes. *J. Am. Chem. Soc.* **2016**, *138* (38), 12655-12663.

4. Jędrzejewska, H.; Szumna, A., Making a Right or Left Choice: Chiral Self-Sorting as a Tool for the Formation of Discrete Complex Structures. *Chem. Rev.* **2017**, *117* (6), 4863-4899.

5. He, Z.; Jiang, W.; Schalley, C. A., Integrative self-sorting: a versatile strategy for the construction of complex supramolecular architecture. *Chem. Soc. Rev.* **2015**, *44* (3), 779-789.

6. Li, L.; Sun, R.; Zheng, R., Tunable morphology and functionality of multicomponent self-assembly: A review. *Mater. Des.* **2021**, *197*, 109209.

7. Griffin, D. R.; Weaver, W. M.; Scumpia, P. O.; Di Carlo, D.; Segura, T., Accelerated wound healing by injectable microporous gel scaffolds assembled from annealed building blocks. *Nat. Mater.* **2015**, *14* (7), 737-744.

8. South, A. B.; Lyon, L. A., Autonomic Self-Healing of Hydrogel Thin Films. *Angew. Chem. Int. Ed.* **2010**, *49* (4), 767-771.

9. de Feijter, I.; Albertazzi, L.; Palmans, A. R. A.; Voets, I. K., Stimuli-Responsive Colloidal Assembly Driven by Surface-Grafted Supramolecular Moieties. *Langmuir* **2015**, *31* (1), 57-64.

10. Xu, H.; Hong, R.; Lu, T.; Uzun, O.; Rotello, V. M., Recognition-Directed Orthogonal Self-Assembly of Polymers and Nanoparticles on Patterned Surfaces. *J. Am. Chem. Soc.* **2006**, *128* (10), 3162-3163.

11. Zhu, B.; Jasinski, N.; Benitez, A.; Noack, M.; Park, D.; Goldmann, A. S.; Barner-Kowollik, C.; Walther, A., Hierarchical Nacre Mimetics with Synergistic Mechanical Properties by Control of Molecular Interactions in Self-Healing Polymers. *Angew. Chem. Int. Ed.* **2015**, *54* (30), 8653-8657.

12. Granado, L.; Burel, C.; Giordanengo, R.; Alsayed, A.; Bendejacq, D.; Ganachaud, F., Hydrophilic and Double Hydrophilic/Hydrophobic Microcapsules using a Single, Thermally Responsive, Self-Sorting Dispersant. *ACS Appl. Polym. Mater.* **2021**, *3* (4), 1707-1711.

13. Chen, G.; Jiang, M., Cyclodextrin-based inclusion complexation bridging supramolecular chemistry and macromolecular self-assembly. *Chem. Soc. Rev.* **2011**, *40* (5), 2254-2266.
14. Han, K.; Go, D.; Tigges, T.; Rahimi, K.; Kuehne, A. J. C.; Walther, A., Social Self-Sorting of Colloidal Families in Co-Assembling Microgel Systems. *Angew. Chem. Int. Ed.* **2017**, *56* (8), 2176-2182.
15. Jin, L.-M.; Xu, X.; Lu, H.; Cui, X.; Wojtas, L.; Zhang, X. P., Effective Synthesis of Chiral N-Fluoroaryl Aziridines through Enantioselective Aziridination of Alkenes with Fluoroaryl Azides. *Angew. Chem. Inter. Ed.* **2013**, *52* (20), 5309-5313.
16. Draper, E. R.; Adams, D. J., Self-sorting shows its true colours. *Nat. Chem.* **2016**, *8* (8), 737-738.
17. Nguyen, S. S.; Prescher, J. A., Developing bioorthogonal probes to span a spectrum of reactivities. *Nat. Rev. Chem.* **2020**, *4* (9), 476-489.
18. Sletten, E. M.; Bertozzi, C. R., From Mechanism to Mouse: A Tale of Two Bioorthogonal Reactions. *Acc. Chem. Res.* **2011**, *44* (9), 666-676.
19. Gunawardene, P. N.; Luo, W.; Polgar, A. M.; Corrigan, J. F.; Workentin, M. S., Highly Electron-Deficient Pyridinium-Nitrones for Rapid and Tunable Inverse-Electron-Demand Strain-Promoted Alkyne-Nitrone Cycloaddition. *Org. Lett.* **2019**, *21* (14), 5547-5551.
20. Dommerholt, J.; van Rooijen, O.; Borrmann, A.; Guerra, C. F.; Bickelhaupt, F. M.; van Delft, F. L., Highly accelerated inverse electron-demand cycloaddition of electron-deficient azides with aliphatic cyclooctynes. *Nat. Commun.* **2014**, *5* (1), 5378.
21. Dommerholt, J.; Rutjes, F. P. J. T.; van Delft, F. L., Strain-Promoted 1,3-Dipolar Cycloaddition of Cycloalkynes and Organic Azides. *Top. Curr. Chem.* **2016**, *374* (2), 16.
22. Gobbo, P.; Workentin, M. S., Improved Methodology for the Preparation of Water-Soluble Maleimide-Functionalized Small Gold Nanoparticles. *Langmuir* **2012**, *28* (33), 12357-12363.

2.6 Supporting Information

2.6.1 General Methods and Methods

Reagents and Solvents. The following materials were used as received. Tetraethylene glycol (99%), p-toluenesulfonyl chloride ($\geq 99\%$), sodium azide ($\geq 99.5\%$), triethylamine ($\geq 99\%$), triphenylmethanethiol (97%), triphenylphosphine (99%), trifluoroacetic acid (99%), triisopropylsilane (98%), gold (III) chloride trihydrate ($\geq 99.9\%$ trace metal basis), sodium borohydride ($\geq 98\%$), rhodium (II) acetate dimer (99.99% trace metals basis), ethyl diazoacetate (contains ≥ 13 wt% dichloromethane), bromine (reagent grade), lithium aluminum hydride (95%), potassium *tert*-butoxide (1.0 M in THF), 4-nitrophenyl chloroformate (96%), 3-bromo-1-propanol (97%), 4-azidoanisole solution (0.5 M in *tert*-butyl methyl ether, $\geq 90\%$), azidobenzene solution (0.5 M in *tert*-butyl methyl ether), 4-nitroaniline ($\geq 99\%$), 4-bromopyridine hydrochloride (99%), 2,3,4,5,6-pentafluoroaniline, N-methylhydroxylamine hydrochloride (98%), nitrobenzene ($\geq 99\%$), zinc dust ($< 10\mu\text{m}$, $\geq 98\%$), p-anisaldehyde (98%), benzaldehyde ($\geq 99\%$), 4-nitrobenzaldehyde (98%), 3-pyridinecarboxaldehyde (98%), 4-nitrobenzotrile (97%) and dichloromethane-D₂ (CD₂Cl₂, 99.5 atom %D) were purchased from Sigma-Aldrich (Millipore Sigma). Chloroform-D₁ (CDCl₃, 99.8 atom %D) was purchased from Cambridge Isotope Laboratories. Sodium chloride, sodium hydroxide pellets, tetrahydrofuran and toluene were purchased from Fischer Scientific. Technical grade ammonium chloride, magnesium sulphate, sodium nitrite, hexanes, dichloromethane, di-ethyl ether, methanol, acetic acid, acetonitrile, pentane and 12 M hydrochloric acid were purchased from Caledon. Ethanol (anhydrous) was purchased from Commercial Alcohols.

Unless otherwise stated, all reactions were performed at ambient conditions.

NMR Spectroscopy. ¹H and ¹³C{¹H} spectra were recorded on either a Bruker AvIII HD 400 spectrometer or Varian INOVA 600 spectrometer, as indicated. ¹H NMR spectra are reported as δ in units of parts per million (ppm), and referenced against residual protio chloroform (7.27 ppm, s) or dichloromethane (5.32 ppm, t), as indicated. Multiplicities are reported as follows: s (singlet), d (doublet), t (triplet), q (quartet), quin (quintuplet), m (multiplet) and br (broad signal). Coupling constants are reported as a *J* value in Hertz (Hz) according to the spectrometer frequency. The

number of protons (n) for a given resonance is indicated as $n\text{H}$, and is based on spectral integration values. $^{13}\text{C}\{^1\text{H}\}$ NMR spectra are reported as δ in units of parts per million (ppm) and referenced against the indicated deuterated solvent: chloroform- D_1 (77.0 ppm, t) or dichloromethane- D_2 (54.0 ppm, quin).

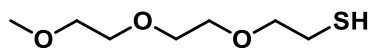
Thermogravimetric Analysis (TGA). TGA was performed using a Mettler Toledo TGA/SDTA 851 instrument from 25°C to 750°C at a heating rate of 10°C/min under a nitrogen flow of 70 mL/min. The sample was prepared by adding a small sample of AuNP-BCN dissolved in dichloromethane onto a pre-weighed alumina crucible, removing the solvent under argon gas flow and drying the sample overnight under high vacuum, which resulted in the formation of a thin AuNP film on the crucible surface.

X-Ray Photoelectron Spectroscopy (XPS). The XPS analyses were carried out with a Kratos Axis Ultra spectrometer using a monochromatic Al K(alpha) source (15mA, 14kV). Specimens were mounted on a double side adhesive and the Kratos charge neutralizer system was used on all specimens. Survey scan analyses were carried out with an analysis area of 300 x 700 microns and a pass energy of 160 eV. High resolution analyses were carried out with an analysis area of 300 x 700 microns and a pass energy of 20 eV. Spectra have been charge corrected to the main line of the carbon 1s spectrum set to 284.5 eV for graphitic/nanotube type species. Spectra were analyzed using CasaXPS software (version 2.3.14)

2.6.2 Experimental Procedures

4-Azidoanisole (**azide 2**) and azidobenzene (**azide 3**) were purchased from Sigma Aldrich as a 0.5 M solution in *tert*-butyl methyl ether, which was partitioned between water and ether. The resulting ether phase was dried over magnesium sulphate and the solvent was evaporated under reduced pressure.

2.6.2.1 Synthesis of HS-EG₃-Me

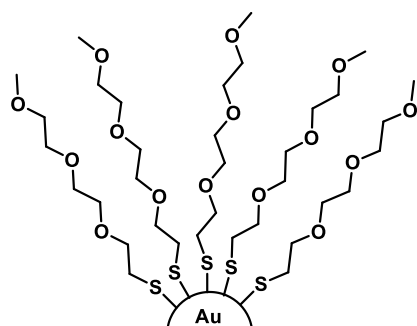


* Synthesized to our previously reported procedure¹⁷⁶.

^1H NMR (CDCl_3 , 400 MHz) δ (ppm): 3.66 (m, 8H), 3.57 (m, 2H), 3.39 (s, 3H), 2.71 (q, $J = 8$ Hz, 2H), 1.60 (t, $J = 8$ Hz, 1H). ^{13}C NMR (CDCl_3 , 400 MHz) δ (ppm):

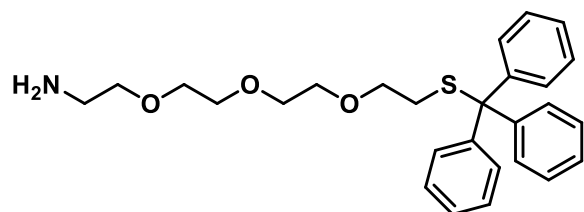
72.8, 17.8, 70.5, 70.3, 70.1, 58.9, 24.2. HRMS (ESI) m/z calc. for $C_7H_{16}O_3S(M)^+$: 180.0820, found: 180.0825.

2.6.2.2 Synthesis of AuNP-OMe



*Synthesized to our previously reported procedure¹.

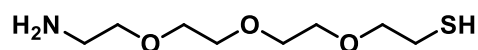
2.6.2.3 Synthesis of STrityl-EG₄-NH₂



*synthesized according to our previously reported procedure.²

¹H NMR (400 MHz, CDCl₃): δ 7.39 – 7.43 (m, 6H), 7.18 – 7.30 (m, 9H), 3.55 – 3.63 (m, 6H), 3.49 (t, J = 5.2 Hz, 2H), 3.45 (dd, J_1 = 5.7 Hz, J_2 = 3.9 Hz, 2H), 3.30 (t, J = 6.9 Hz, 2H), 2.85 (t, J = 5.1 Hz, 2H), 2.43 (t, J = 6.9 Hz, 2H), 1.97 (s, 2H). ¹³C NMR (400 MHz, CDCl₃): δ 144.8, 129.6, 127.8, 126.6, 73.0, 70.5, 70.4, 70.2, 70.1, 69.6, 41.6, 31.6. ESI-MS calc. for $C_{27}H_{34}NO_3S^+$ [M+H⁺] 452.2259, found 452.2240. ¹³C NMR (400 MHz, CDCl₃): δ 72.7, 70.2, 70.1, 69.9, 69.7, 66.8, 39.6, 24.0.

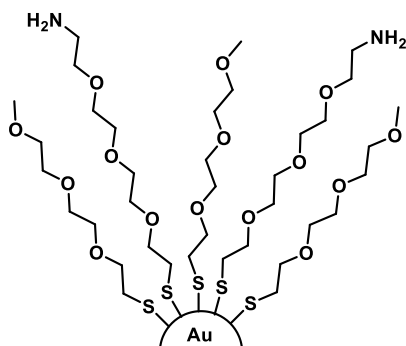
2.6.2.4 Synthesis of HS-EG₄-NH₂



To 4.0 g (8.9 mmol) **STrityl-EG₄-NH₂** in 100 mL dry dichloromethane was added 2.2 mL (10.6 mmol) triisopropylsilane and then 34 mL (45 mmol) trifluoroacetic acid. The reaction mixture was stirred for 1 hour while monitoring carefully by TLC, after which the solvent was removed via rotary evaporation. The crude residue was purified by flash column chromatography (3:1

dichloromethane:methanol) to give **HS-TEG-NH₂** as a thick white oil in 83% yield (1.55 g). ¹H NMR (400 MHz, CDCl₃): δ 3.73 (m, 2H), 3.62 (m, 6H), 3.46 (m, 6H), 3.15 (t, *J* = 8 Hz, 2H), 2.68 (t, *J* = 8 Hz, 2H), 1.58 (t, *J* = 4 Hz, 1H). ¹³C NMR (400 MHz, CDCl₃): 72.7, 70.2, 70.1, 69.9, 69.7, 66.8, 39.6, 24.0. HRMS (ESI) *m/z* calc. for C₈H₁₉NO₃S (M)⁺: 209.1086, found: 209.1083.

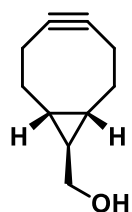
2.6.2.5 Synthesis of AuNP-NH₂



To 0.3 g **AuNP-OMe** in 25 mL methanol was added 0.3 g **HS-EG₄-NH₂** in 5 mL methanol in a round bottom flask. The resulting solution was stirred for 2 hours at room temperature, after which the solvent was removed thoroughly via rotary evaporation to form a black AuNP film in the round bottom flask. The film was washed vigorously by added 100 mL portions of dichloromethane and swirling the sample for 15 minutes. The dichloromethane was then poured out, and the film

was re-dissolved in methanol and removed under reduced pressure to re-form the AuNP film, which was subsequently washed with two more 100 mL portions of dichloromethane in the same way. After the final wash, the sample was dried thoroughly under high vacuum to give AuNP-NH₂ in quantitative yield (0.3 g).

2.6.2.6 Synthesis of BCN_{exo}-OH

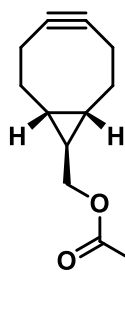


*Synthesized according to Dommerholt *et al.*³

¹H NMR (400 MHz, CDCl₃): δ 3.56 (d, *J* = 8 Hz, 2H), 2.42 (d, *J* = 16 Hz, 2H), 2.30 (t, *J* = 16 Hz, 2H), 2.17 (d, *J* = 16 Hz, 2H), 1.42 (m, 3H), 0.69 (m, 3H). ¹³C NMR (400 MHz, CDCl₃): 98.8, 67.1, 33.4, 27.3, 22.6, 21.5. HRMS (ESI) *m/z* calc. for C₁₀H₁₄O

(M)⁺: 150.1045, found: 150.1052.

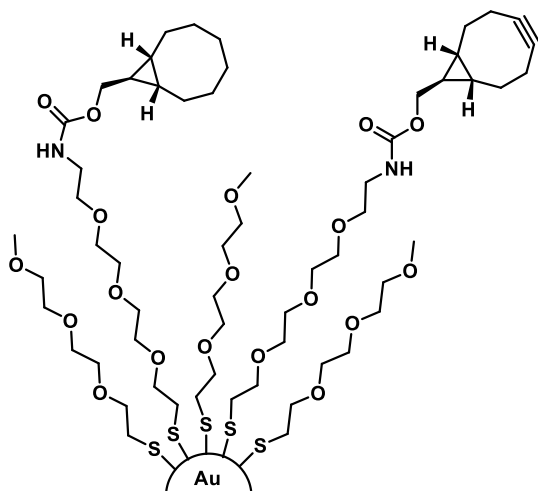
2.6.2.7 Synthesis of BCN_{exo}-O-pNP



*Synthesized according to Dommerholt *et al.*³

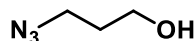
¹H NMR (CDCl₃, 400MHz): 8.29 (d, *J* = 8 Hz, 2H), 7.40 (d, *J* = 8 Hz, 2H), 4.23 (d, *J* = 8 Hz, 2H), 2.46 (m, 2H), 2.32 (m, 2H), 2.20 (m, 2H), 1.44 (m, 2H), 0.86 (m, 3H). ¹³C NMR (CDCl₃, 150MHz): 155.6, 152.4, 145.2, 125.3, 121.7, 98.7, 68.0, 29.1, 21.3, 20.5, 17.2. HRMS (ESI) *m/z* calc. for C₁₇H₁₇NO₅ (M)⁺: 315.1107, found: 315.1223.

2.6.2.8 Synthesis of AuNP-BCN



To 350 mg **AuNP-NH₂** in 2 mL methanol, 14 mL dichloromethane and 3.5 mL trimethylamine was added **BCN_{exo}-O-pNP** in 2 mL dichloromethane. The solution was stirred overnight, after which the solvent was removed under reduced pressure and the resulting black film was dried thoroughly under high vacuum. The dried film was washed thoroughly with several 100 mL portions of di ethyl ether to give **AuNP-BCN** as a shiny black solid (370 mg).

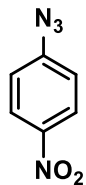
2.6.2.9 Synthesis of 1-azido-3-propanol (azide 1)



To 0.65 mL (1.0 g, 7.2 mmol) 3-bromo-1-propanol in 5 mL 1:1 water:ethanol was added 1.4 g (21 mmol) sodium azide. After refluxing the resulting solution at 55°C for 4 hours, the solution was cooled to room temperature and 50 mL water was added. The aqueous phase was extracted with dichloromethane (3 x 10 mL) and the collected organic phases were dried over magnesium sulphate, and concentrated under streaming Ar(g) to give **azido-propanol (azide 1)** as a light yellow oil in 67% yield (0.49 g). *Note:* Due to volatility of azido-propanol, solvent should not be evaporated under reduced pressure. ¹H NMR (CDCl₃, 400 MHz): δ 3.74 (t, *J* = 8 Hz, 2H), 3.44 (t, *J* = 8 Hz, 2H), 2.03 (s, 1H), 1.82 (quin, *J* = 4 Hz, 2H). ¹³C NMR

(CDCl₃, 400 MHz): δ 59.8, 48.4, 31.4. HRMS (CI) m/z calc. for C₃H₈N₃O (M+1)⁺: 102.0667, found: 102.0672. IR (KBr, cm⁻¹): 3336, 2930, 2882, 2091, 1455, 1344, 1259, 1047.

2.6.2.10 Synthesis of 1-azido-4-nitrobenzene (azide 4)

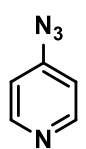


Synthesized according to Kwok *et al.*, with minor modifications.⁴

To 40 mL 12 M HCl and 40 mL water was slowly added 2.1 g (15 mmol) 4-nitroaniline, after which 15 mL ethanol was slowly added until the solution became transparent yellow.

After cooling the solution to 0°C, 1.6 g (23 mmol) sodium nitrite was added slowly and the solution was stirred for 45 minutes at 0°C. Next, sodium azide (1.5 g, 23 mmol) was added very slowly at room temperature and the resulting solution was stirred for 2 hours, after which 50 mL water and 100 mL ether was added. The organic phase was removed and the aqueous phase was extracted with ether (2 x 50 mL). The collected organic phases were extracted with saturated NaHCO₃ (3 x 50 mL) and brine (3 x 50 mL), dried over magnesium sulphate and concentrated via rotary evaporation to give **1-azido-4-nitrobenzene (azide 4)** as a yellow solid in 98% yield (2.4 g). ¹H NMR (CDCl₃, 400 MHz): δ 8.25 (d, J = 8 Hz, 2H), 7.15 (d, J = 8 Hz, 2H). ¹³C NMR (CDCl₃, 400 MHz): δ 147.2, 145.0, 125.9, 119.7. HRMS (ESI) m/z calc. for C₆H₄N₄O₂ (M)⁺: 164.0334, found: 164.0335. IR (KBr, cm⁻¹): 3113, 3069, 2922, 2403, 2122, 1605, 1590, 1512, 1489, 1444, 1369, 1328, 1287, 1177, 1130, 1118, 1105.

2.6.2.11 Synthesis of 4-azidopyridine (azide 5)

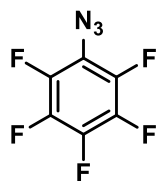


Synthesized according to Zhao and Qing, with minor modifications.⁵

To 0.60 g (3.1 mmol) 4-bromopyridine hydrochloride in 6 mL 1:1 water:ethanol (95%) was added 0.060 g (1.5 mmol) sodium hydroxide and 0.50 g (7.7 mmol) sodium azide. After refluxing the resulting solution at 110°C for 4 hours, the solution was cooled to room temperature and 50 mL water and 10 mL dichloromethane was added. The organic phase was removed, and the aqueous phase was extracted with dichloromethane (2 x 10 mL). The collected organic phases were extracted with brine (3 x 30 mL), dried over magnesium sulphate and concentrated under streaming Ar(g) to give **4-azidopyridine (azide 5)** as a light yellow oil in 86% yield (0.42 g). *Note:* Due to volatility of 4-azidopyridine, solvent should not be removed under

reduced pressure. ^1H NMR (CDCl_3 , 400 MHz): 8.54 (d, $J = 4$ Hz, 2H), 6.96 (d, $J = 4$ Hz, 2H). ^{13}C NMR (CDCl_3 , 400 MHz): δ 151.3, 148.9, 114.3. HRMS (ESI) m/z calc. for $\text{C}_5\text{H}_4\text{N}_4$ (M) $^+$: 120.0436, found: 120.0439. IR (KBr, cm^{-1}): 3037, 2919, 2850, 2430, 2136, 1614, 1580, 1565, 1493, 1416, 1343, 1298, 1281, 1215, 1137.

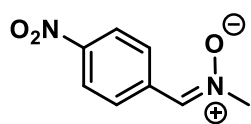
2.6.2.12 Synthesis of 1-azido-2,3,4,5,6-pentafluorobenzene (azide 6)



Synthesized according to Li-Mei *et. al.*, with minor modifications.⁶

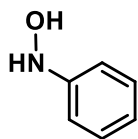
To 2.1 g (10 mmol) 2,3,4,5,6-pentafluoroaniline in 25 mL trifluoroacetic acid was slowly added 0.83 g (12 mmol) sodium nitrite at 0°C . The resulting solution was stirred for 1 hour at 0°C , after which 0.98 g (15 mmol) sodium azide was added portion-wise at 0°C . After stirring the solution for 1 hour at 0°C , 50 mL diethyl-ether was added and the aqueous phase was removed. The organic phase was extracted with water (3 x 50 mL) and NaHCO_3 (3 x 50 mL), dried over magnesium sulphate and concentrated via rotary evaporation. The resulting crude residue was purified via flash column chromatography (hexanes) to give **1-azido-2,3,4,5,6-pentafluorobenzene (azide 6)** as a light yellow oil in 89% yield (2.1 g). ^{19}F NMR (CDCl_3 , 400 MHz): -151.6 (d, 2F), -159.8 (t, 1F), -161.6 (t, 2F). ^{13}C NMR (CDCl_3 , 400 MHz): δ 142.2, 139.5, 136.9, 110.0. HRMS (ESI) m/z calc. for $\text{C}_6\text{F}_5\text{N}_3$ (M) $^+$: 209.0012, found: 209.0014. IR (KBr, cm^{-1}): 2407, 2120, 1638, 1507, 1462, 1326, 1243, 1103, 1013.

2.6.2.13 Synthesis of *N*-methyl-*C*-nitrophenyl-nitrone (nitrone 1)



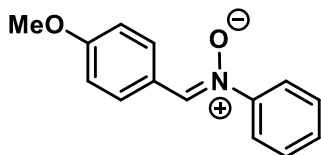
To 0.25 g (3.0 mmol) *N*-methylhydroxylamine and 0.36 g (9.0 mmol) sodium hydroxide in 10 mL methanol was added 0.70 g (4.5 mmol) nitrobenzaldehyde. After stirring the mixture overnight at room temperature, the solvent was removed via rotary evaporation, the crude solid was suspended in ether, and the resulting insoluble yellow solid was collected by filtration to give ***N*-methyl-*C*-nitrophenyl-nitrone (nitrone 1)** in 72% yield (0.39 g). ^1H NMR (CD_2Cl_2 , 400 MHz): 8.38 (d, $J = 8$ Hz, 2H), 8.23 (d, $J = 8$ Hz, 2H), 7.53 (s, 1H), 3.90 (s, 3H). ^{13}C NMR (CD_2Cl_2 , 400 MHz): δ 148.2, 137.0, 133.2, 128.9, 124.2, 55.7. HRMS (ESI) m/z calc. for $\text{C}_8\text{H}_8\text{N}_2\text{O}_3$ (M) $^+$: 180.0535, found: 180.0531. IR (KBr, cm^{-1}): 3108, 3082, 3024, 2958.3, 1597, 1956, 1506, 1333, 1184, 1164, 1110.

2.6.2.14 Synthesis of *N*-phenylhydroxylamine



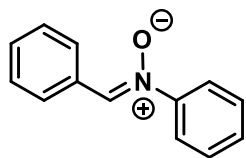
To 2.0 g (16 mmol, 1.7 mL) nitrobenzene and 0.95 g (18 mmol) ammonium chloride in 25 mL 1:1 water:ethanol was added 2.1g (32 mmol) zinc dust portion-wise over 5 minutes. Note: rate of zinc dust addition was adjusted so as to maintain the elevated temperature at ~60°C. After stirring the resulting suspension for 20 minutes, the grey solid was removed by vacuum filtration, and washed with 50 mL water and 10 mL ether. The organic phase in the filtrate was removed, the aqueous phase was extracted with ether (2 x 10 mL) until the aqueous phase was nearly colorless, and the collected organic phases were dried over magnesium sulphate and concentrated via rotary evaporation to give ***N*-phenylhydroxylamine** in 81% crude yield (1.4 g), which was used without further purification towards the syntheses of Nitrone 2, Nitrone 3, Nitrone 4 and Nitrone 5. Note: Due to the instability of the hydroxylamine, it should be used immediately.

2.6.2.15 Synthesis of *N*-phenyl-*C*-methoxyphenyl-nitrone (nitrone 2)



To 0.23 g (2.1 mmol) crude ***N*-phenylhydroxylamine** in 5 mL dichloromethane was added 0.34 g (2.5 mmol, 0.30 mL) 4-anisaldehyde and a small amount of magnesium sulphate. The resulting solution was stirred overnight at room temperature, after which the solvent was removed via rotary evaporation. The crude residue was suspended in ether, and the resulting off-white insoluble solid was collected by vacuum filtration to give ***N*-phenyl-*C*-methoxyphenyl-nitrone (nitrone 2)** in 70% overall yield (0.33g). ¹H NMR (CD₂Cl₂, 400 MHz): 8.41 (d, *J* = 8 Hz, 2H), 7.88 (s, 1H), 7.76 (d, *J* = 8 Hz, 2H), 7.48 (m, 3H), 7.00 (d, *J* = 8 Hz, 2H), 3.87 (s, 3H). ¹³C NMR (CD₂Cl₂, 400 MHz): δ 162.0, 149.6, 134.0, 131.4, 130.0, 129.6, 124.5, 122.1, 114.4, 55.9. HRMS (ESI) *m/z* calc. for C₁₄H₁₃NO₂ (M)⁺: 227.0946, found: 227.0940. IR (KBr, cm⁻¹): 3050, 3013, 2962, 2931, 2839, 1603, 1554, 1506, 1484, 1461, 1399, 1305, 1259, 1193, 1176, 1108, 1064, 1023.

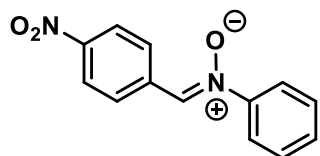
2.6.2.16 Synthesis of *N*-phenyl-*C*-phenyl-nitrone (nitrone 3)



See **Section 3.6.2.7** for detailed synthesis of *N*-phenyl-*C*-phenyl-nitrone (**nitrone 3**)

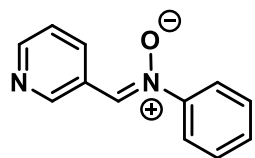
^1H NMR (CD_2Cl_2 , 400 MHz): 8.41 (m, 2H), 7.95 (s, 1H), 7.78 (m, 2H), 7.49 (m, 6H). ^{13}C NMR (CD_2Cl_2 , 400 MHz): δ 149.8, 134.5, 131.6, 131.2, 130.4, 129.6, 129.3, 129.1, 122.2. HRMS (ESI) m/z calc. for $\text{C}_{13}\text{H}_{11}\text{NO}$ (M^+): 197.0841, found: 197.0837. IR (KBr, cm^{-1}): 3060, 1593, 1547, 1510, 1484, 1461, 1445, 1396, 1340, 1324, 1298, 1191, 1163, 1067, 1025.

2.6.2.17 Synthesis of *N*-phenyl-*C*-nitrophenyl-nitrone (nitrone 4)



To 0.21 g (1.9 mmol) crude *N*-phenylhydroxylamine in 5 mL dichloromethane was added 0.26 g (2.5 mmol, 0.25 mL) benzaldehyde and a small amount of magnesium sulphate. The resulting solution was stirred overnight at room temperature, after which the solvent was removed via rotary evaporation. The crude residue was suspended in ether, and the resulting white insoluble solid was collected by vacuum filtration to give *N*-phenyl-*C*-nitrophenyl-nitrone (**nitrone 4**) in 64% overall yield (0.29 g). ^1H NMR (CD_2Cl_2 , 400 MHz): 8.56 (d, $J = 8$ Hz, 2H), 8.30 (d, $J = 8$ Hz, 2H), 8.10 (s, 1H), 7.80 (m, 2H), 7.54 (m, 3H). ^{13}C NMR (CD_2Cl_2 , 400 MHz): δ 149.6, 148.4, 137.0, 132.6, 131.1, 129.9, 129.6, 124.4, 122.2. HRMS (ESI) m/z calc. for $\text{C}_{13}\text{H}_{10}\text{N}_2\text{O}_3$ (M^+): 242.0691, found: 242.0693. IR (KBr, cm^{-1}): 3104, 3065, 1596, 1544, 1509, 1483, 1459, 1403, 1340, 1319, 1193, 1176, 1157, 1101, 1072.

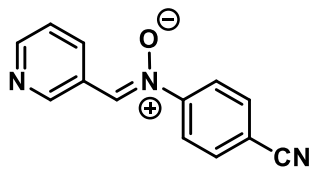
2.6.2.18 Synthesis of *N*-phenyl-*C*-pyridine-nitrone (nitrone 5)



* See **Section 3.6.2.3** for detailed synthesis of *N*-phenyl-*C*-pyridine-nitrone (**nitrone 5**)

^1H NMR (CD_2Cl_2 , 400 MHz): δ 9.19 (s, 1H), 9.07 (d, $J = 8$ Hz, 1H), 8.65 (d, $J = 4$ Hz, 1H), 8.05 (s, 1H), 7.95 (d, $J = 8$ Hz, 2H), 7.83 (d, $J = 8$ Hz, 2H), 7.43 (m, 1H). ^{13}C NMR (CD_2Cl_2 , 400 MHz): δ 151.9, 150.9, 135.4, 133.9, 132.8, 127.5, 124.1, 123.1, 118.1, 114.6. HRMS (ESI) m/z calc. for $\text{C}_{12}\text{H}_{10}\text{N}_2\text{O}$ (M^+): 198.0793, found: 198.0796. IR (ATR, cm^{-1}): 3130, 3065, 3062, 1582, 1555, 1484, 1466, 1403, 1335, 1272, 1203, 1175, 1164, 1072, 1022.

2.6.2.19 Synthesis of *N*-cyanophenyl-*C*-pyridine-nitrone (nitrone 6)



See **Section 3.6.2.5** for detailed synthesis of *N*-phenyl-*C*-phenyl-nitrone (**nitrone 6**)

$^1\text{H NMR}$ (CD_2Cl_2 , 400 MHz): δ 9.17 (s, 1H), 9.09 (d, $J = 8.0$ Hz, 1H), 8.62 (d, $J = 8.0$ Hz, 1H), 8.00 (s, 1H), 7.79 (m, 2H), 7.50 (m, 3H), 7.41 (m, 1H). $^{13}\text{C NMR}$ (CD_2Cl_2 , 400 MHz): δ 151.3, 150.7, 149.4, 135.1, 131.6, 130.8, 129.7, 128.0, 124.0, 122.11, 114.4. HRMS (ESI) m/z calc. for $\text{C}_{13}\text{H}_9\text{N}_3\text{O}$ (M) $^+$: 223.0746, found: 223.0735. IR (ATR, cm^{-1}): 3104, 3082, 3065, 3054, 2242, 1584, 1498, 1425, 1413, 1338, 1297, 1270, 1209, 1172, 1070, 1026.

2.6.3 Experimental Spectra and Diagrams

2.6.3.1 Experimental Spectra for HS-EG₃-Me

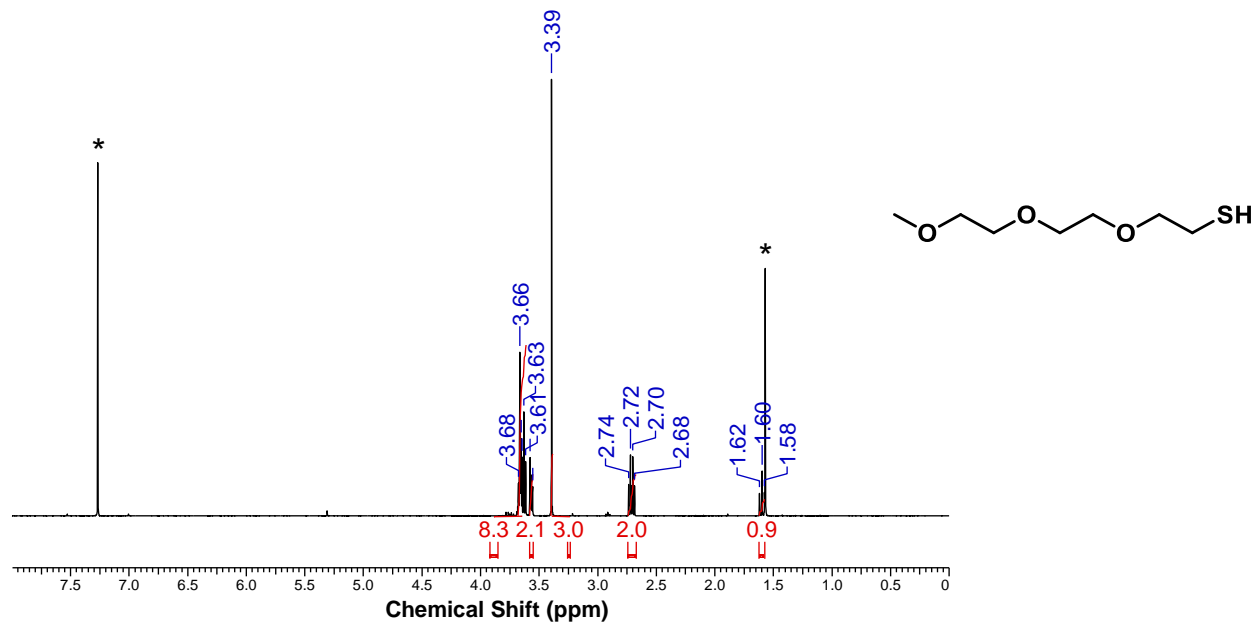


Figure S2.1. ¹H NMR spectrum of HS-EG₃-Me in CDCl₃ at 25°C. * denotes residual protio solvent and impurities.

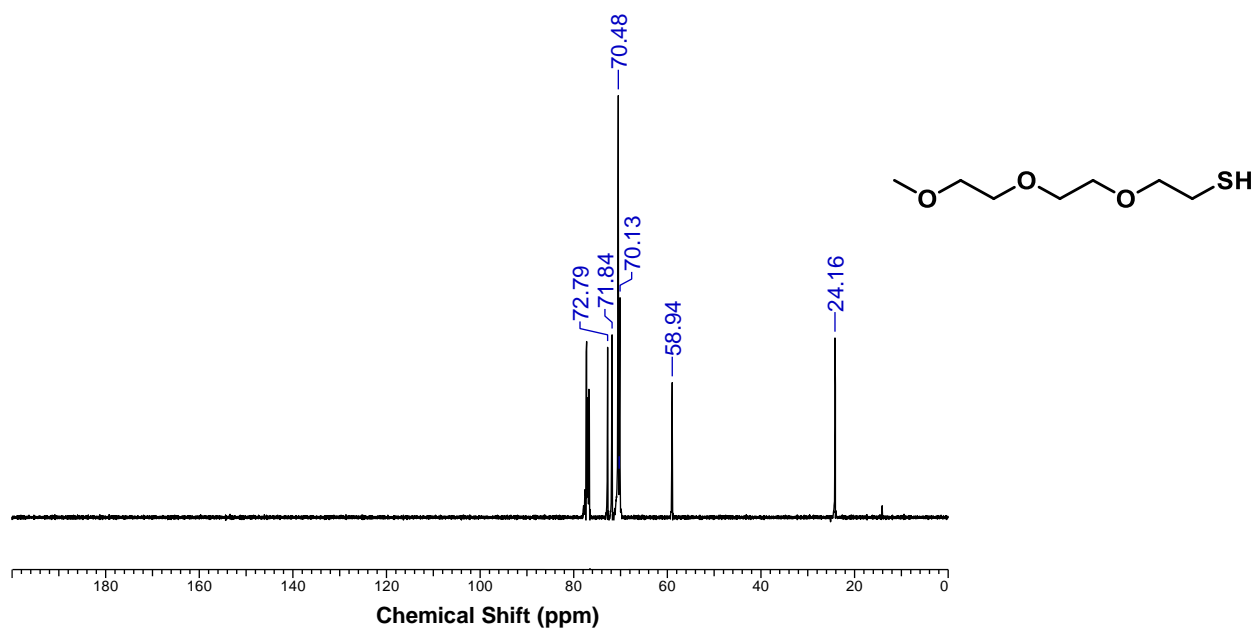


Figure S2.2. ¹³C{¹H} NMR spectrum of HS-EG₃-Me in CDCl₃ at 25°C.

2.6.3.2 Experimental Spectra for AuNP-OMe

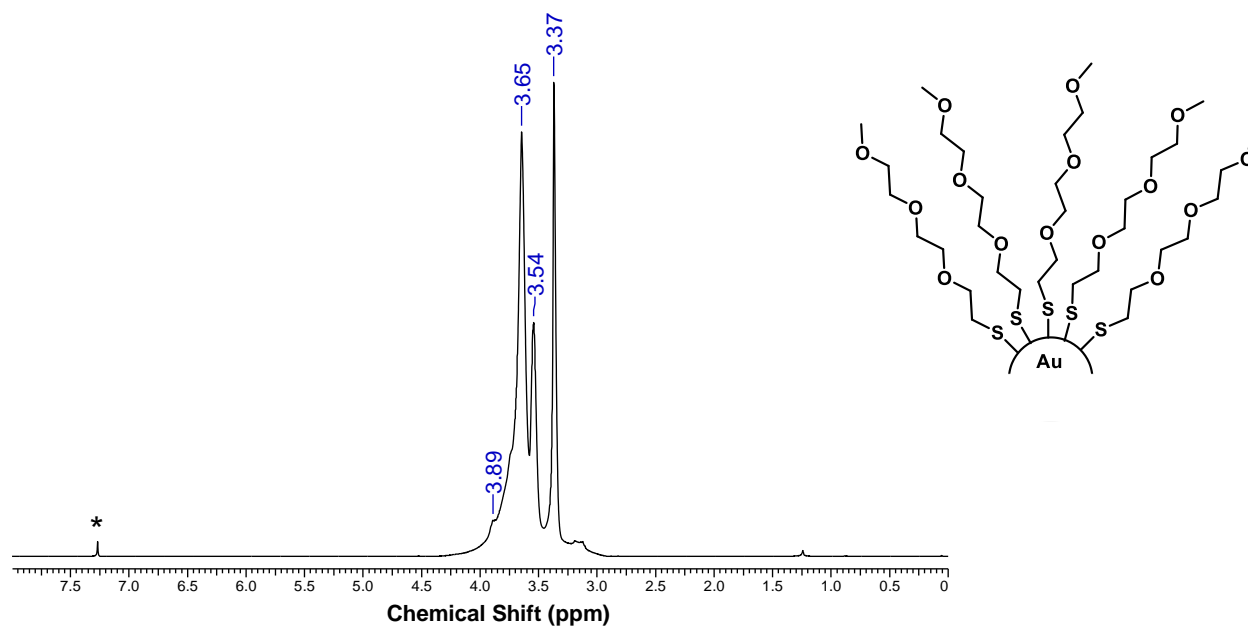


Figure S2.3. ^1H NMR spectrum of AuNP-OMe in CDCl_3 at 25°C . * denotes residual protio solvent.

2.6.3.3 Experimental Spectra for HS-EG₄-NH₂

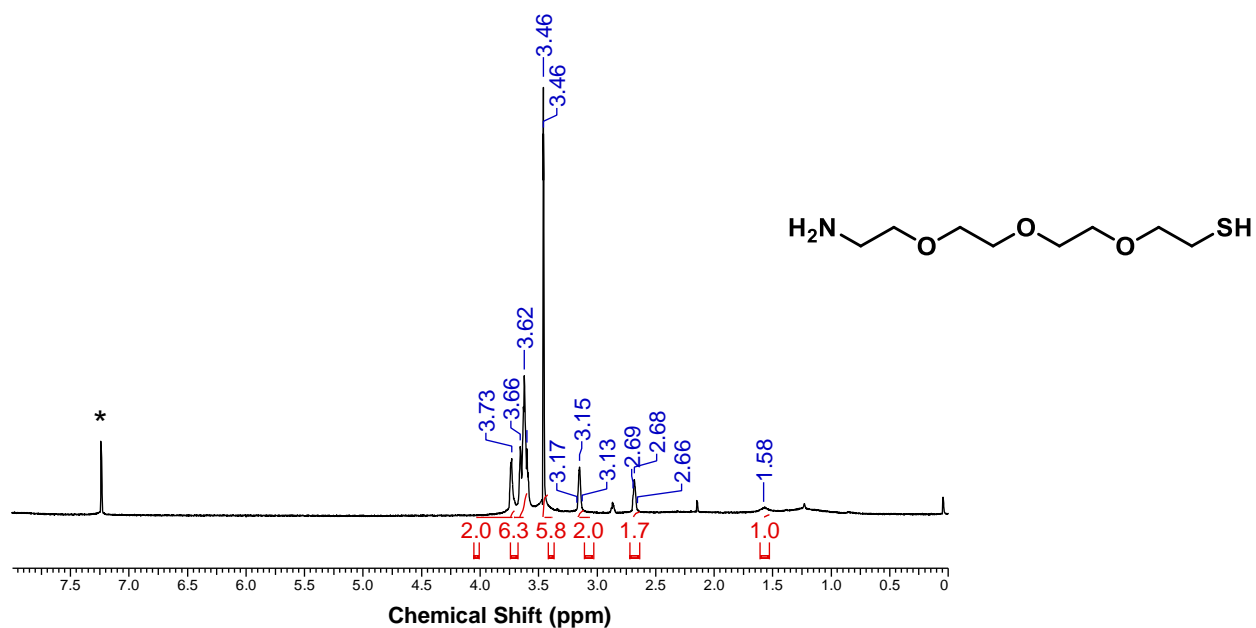


Figure S2.4. ¹H NMR spectrum of HS-EG₄-NH₂ in CDCl₃ at 25°C. * denotes residual protio solvent.

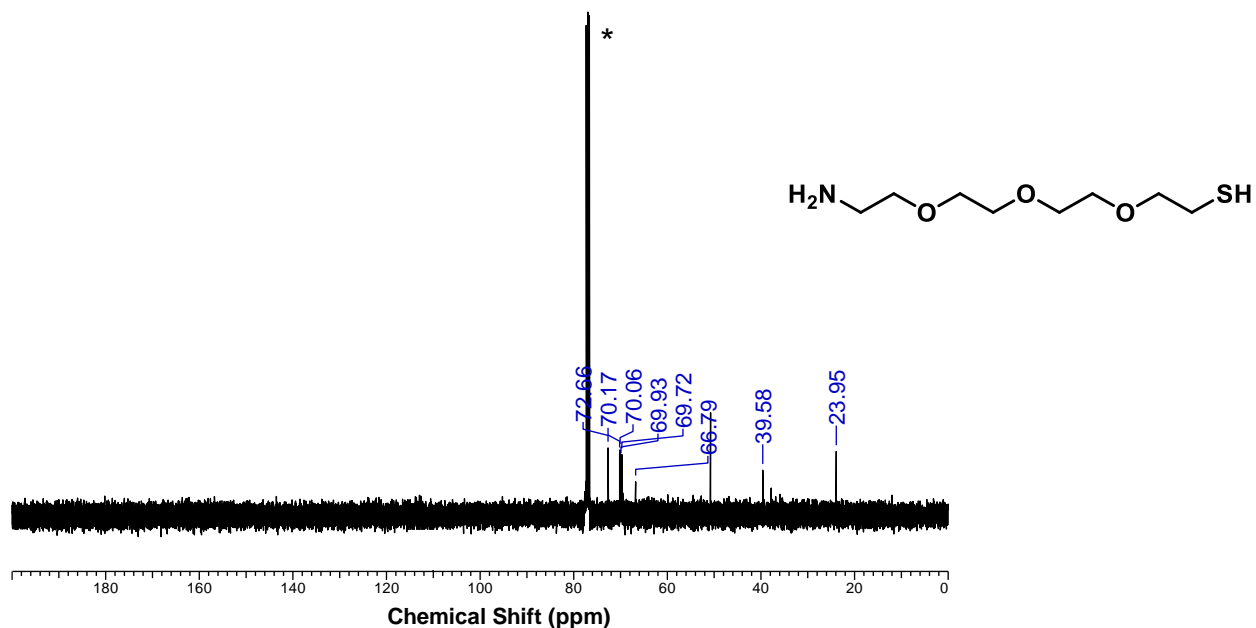


Figure S2.5. ¹³C{¹H} NMR spectrum of HS-EG₄-NH₂ in CDCl₃ at 25°C. * indicates CDCl₃ solvent.

2.6.3.4 Experimental Spectra for AuNP-NH₂

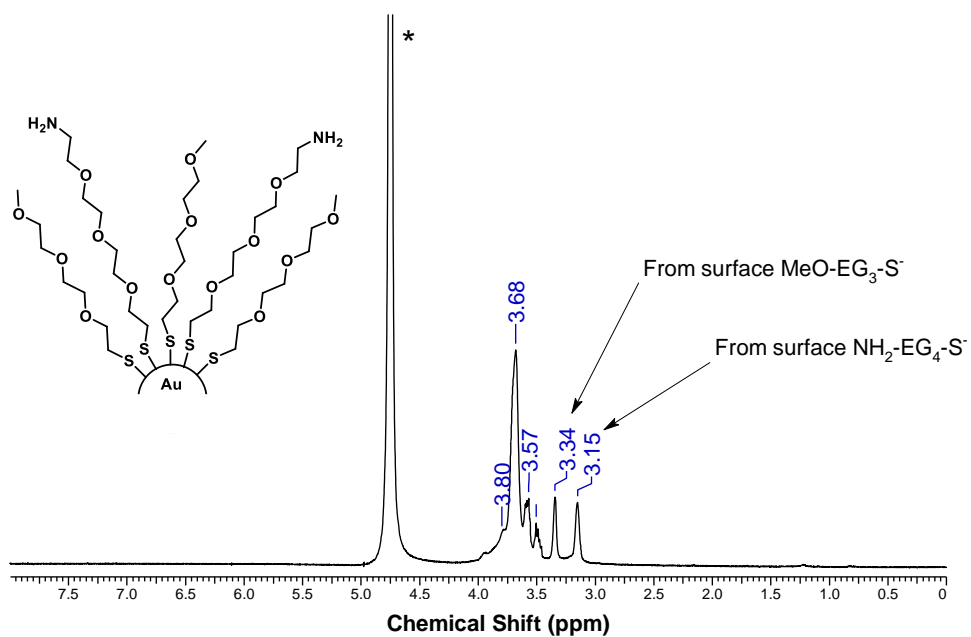


Figure S2.6. ¹H NMR spectrum of AuNP-NH₂ in D₂O at 25°C. * denotes residual protio solvent.

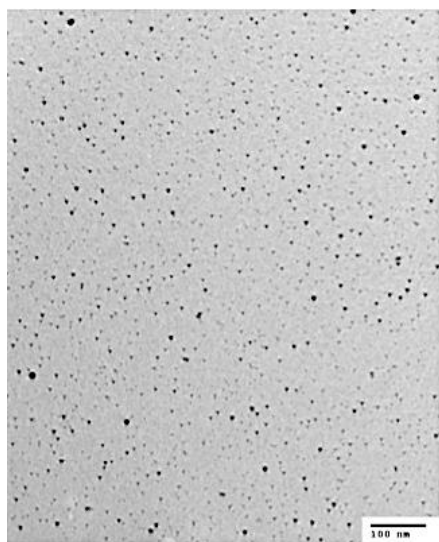


Figure S2.7. TEM image for AuNP-NH₂.

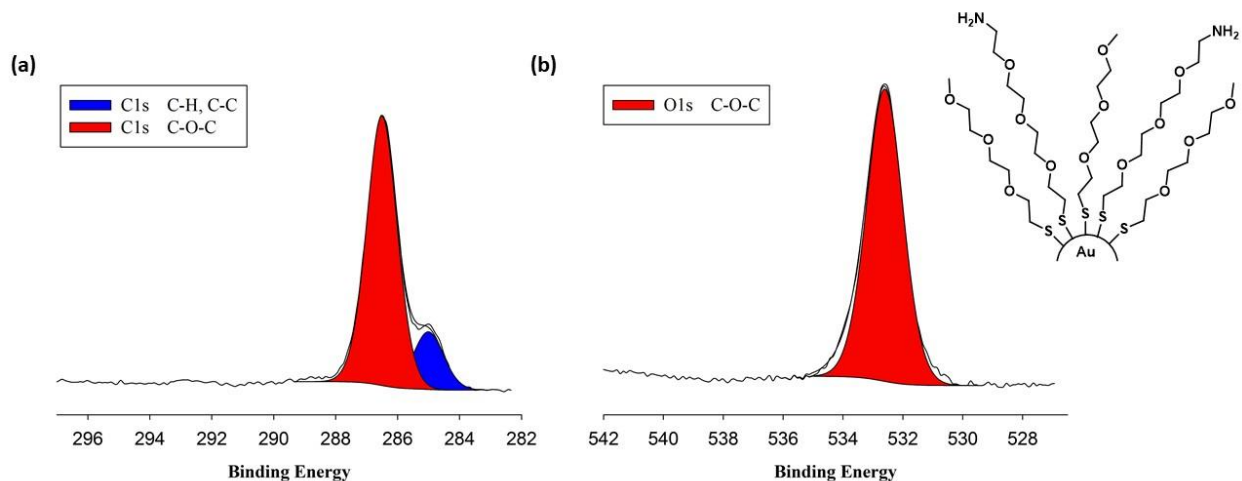


Figure S2.8. (a) High-resolution carbon 1s XPS spectrum of AuNP-NH₂ (b) High-resolution oxygen 1s XPS spectrum of AuNP-NH₂.

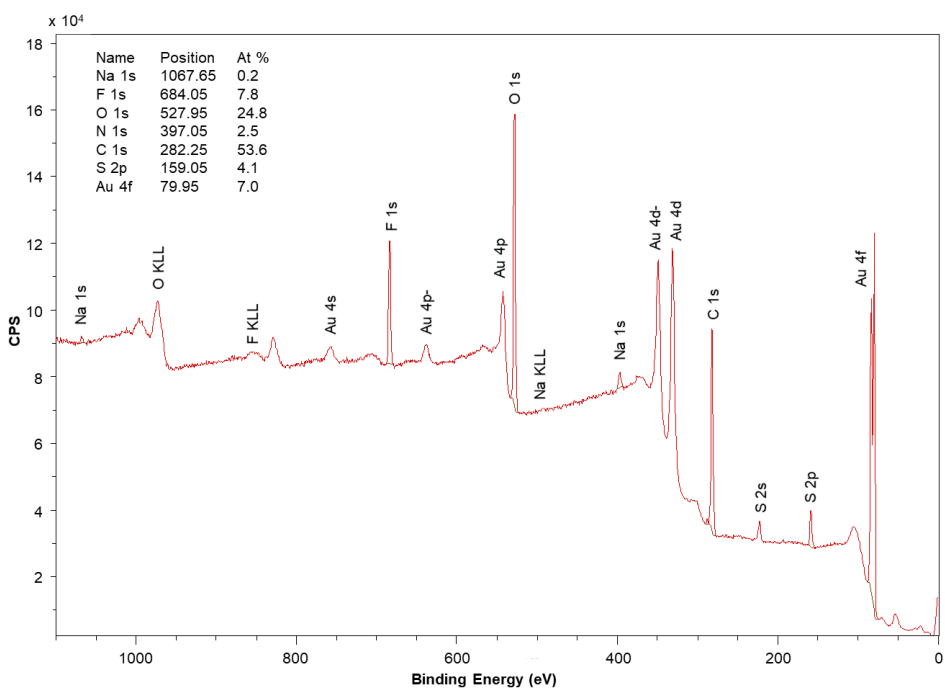


Figure S2.9. (a) XPS survey scan of AuNP-NH₂.

2.6.3.5 Experimental Spectra for BCN_{exo}-OH

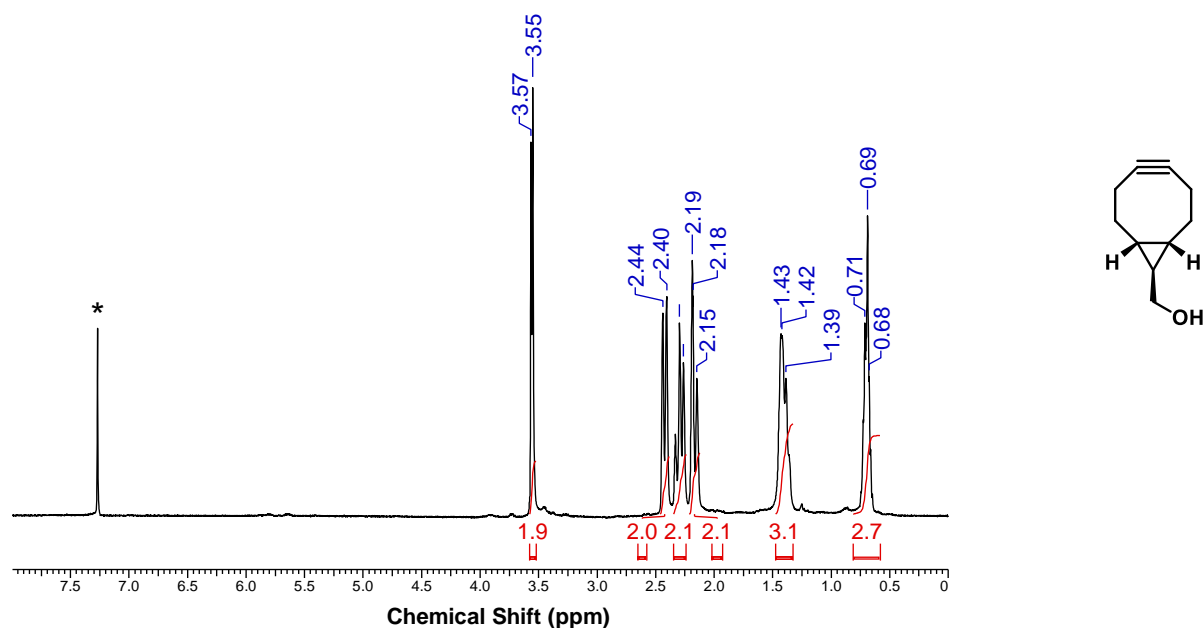


Figure S2.10. ¹H NMR spectrum of BCN_{exo}-OH in CDCl₃ at 25°C. * denotes residual protio solvent.

2.6.3.6 Experimental Spectra for BCN_{exo}-O-pNP

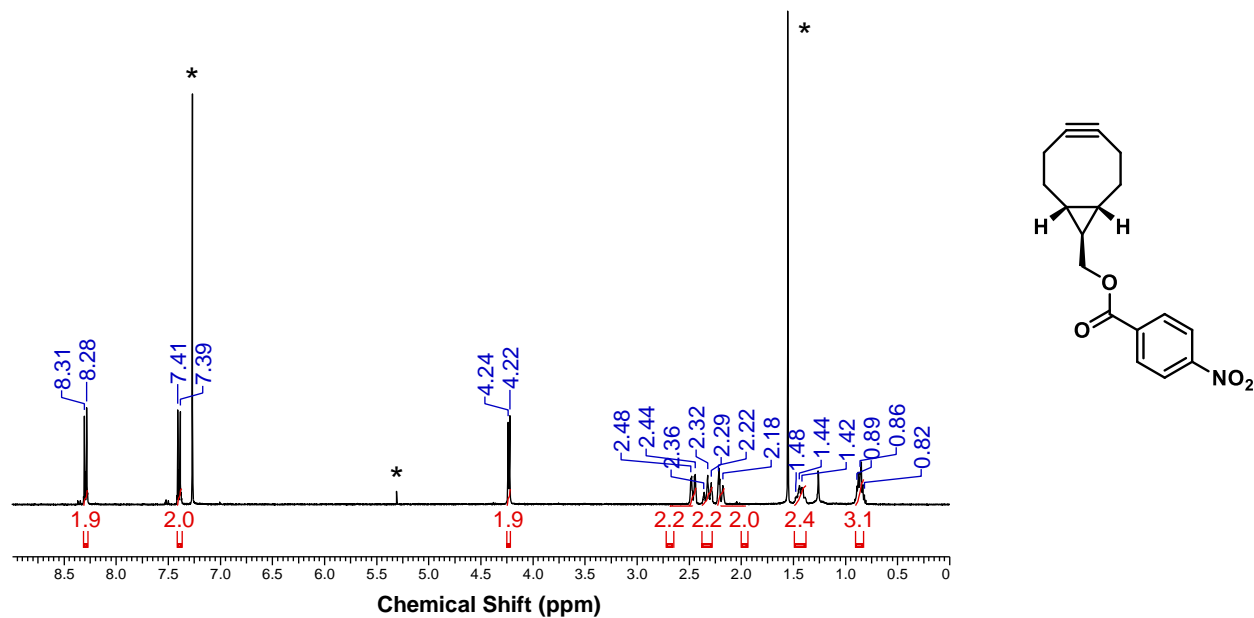


Figure S2.11. ¹H NMR spectrum of BCN_{exo}-O-pNP in CDCl₃ at 25°C. * denotes residual protio solvent and impurities.

2.6.3.7 Experimental Spectra for AuNP-BCN

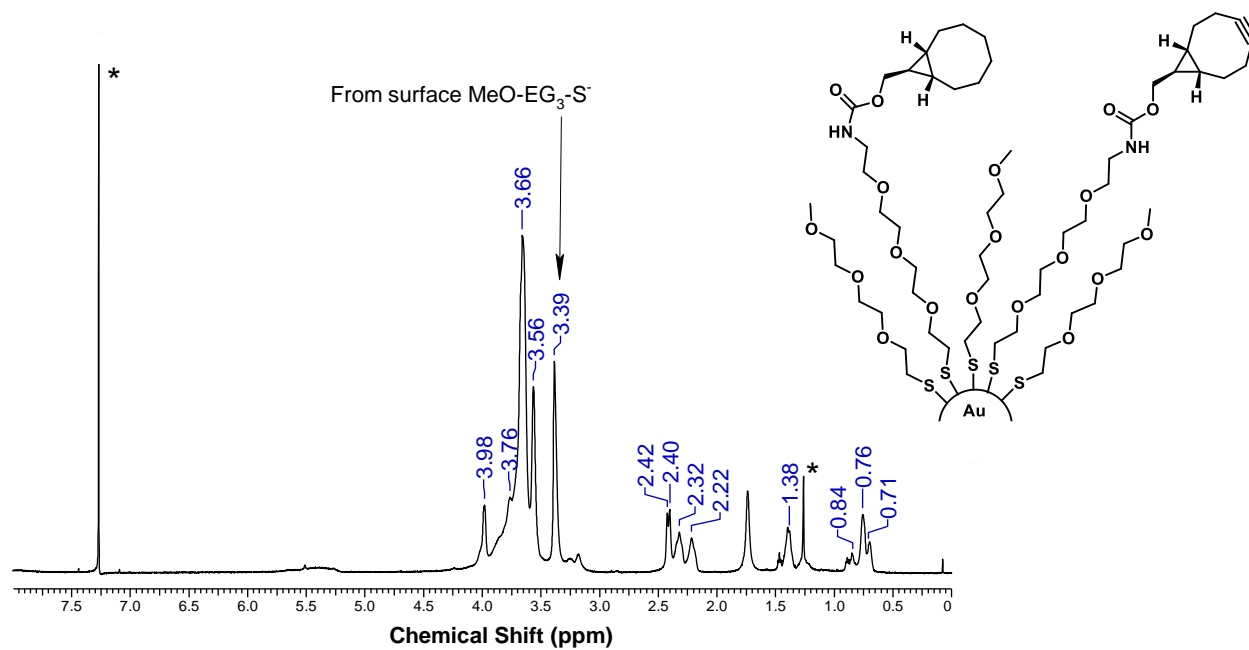


Figure S2.12. ^1H NMR spectrum of AuNP-BCN in CDCl_3 at 25°C . * denotes residual protio solvent and impurities.

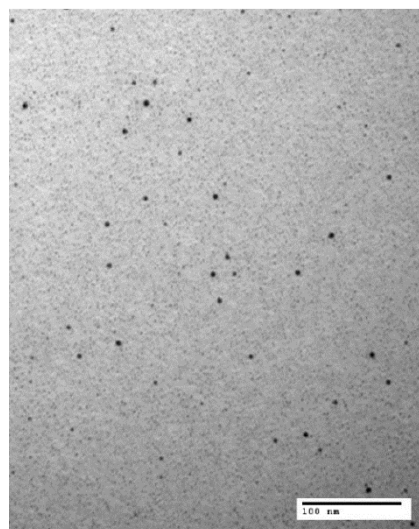


Figure S2.13. TEM image for AuNP-BCN.

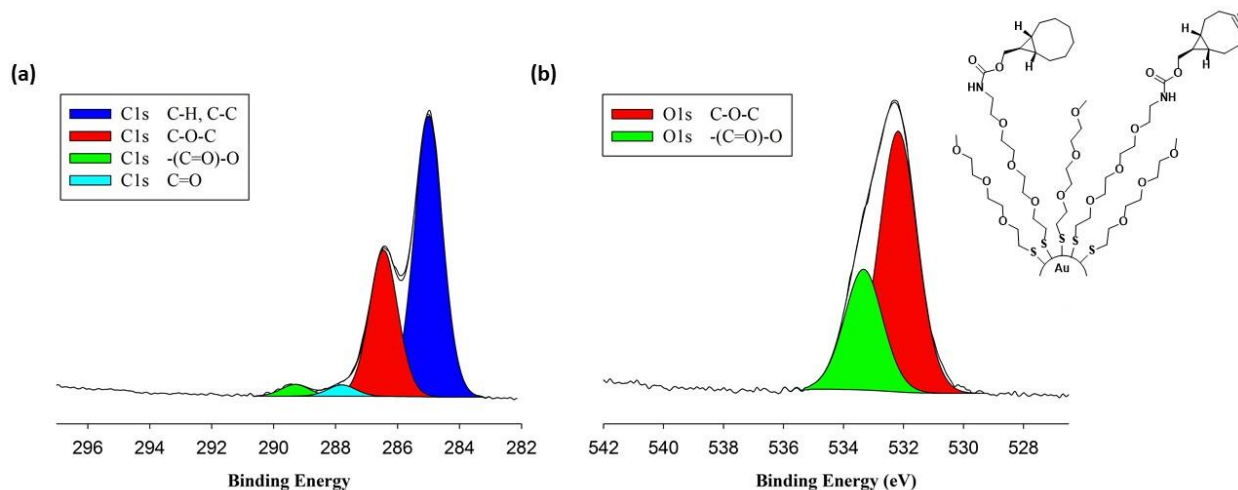


Figure S2.14. (a) High-resolution carbon 1s XPS spectrum of AuNP-BCN (b) High-resolution oxygen 1s XPS spectrum of AuNP-BCN.

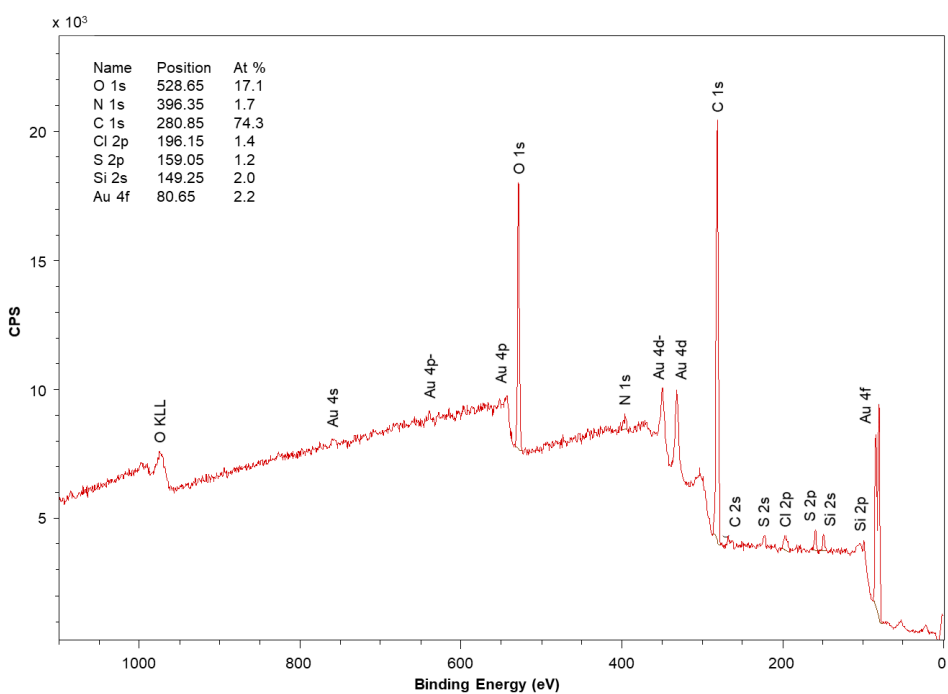


Figure S2.15. (a) XPS survey scan of AuNP-BCN.

2.6.3.8 Experimental Spectra for 1-azido-3-propanol (azide 1)

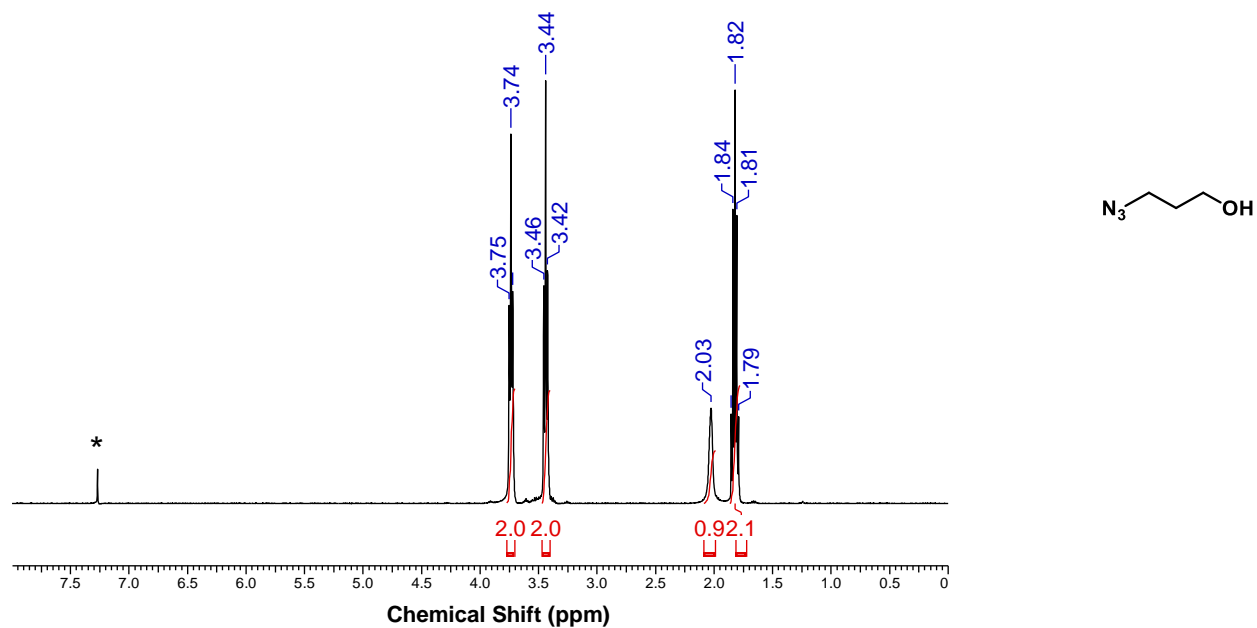


Figure S2.16. ^1H NMR spectrum of **azide 1** in CDCl_3 at 25°C . * denotes residual protio solvent.

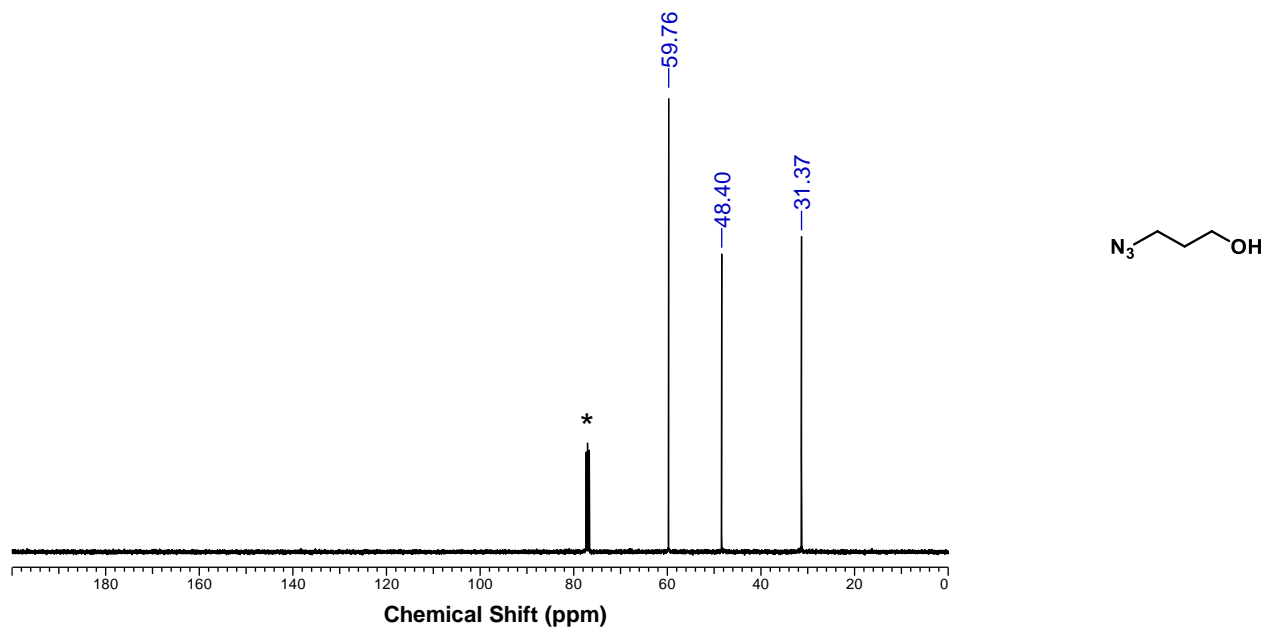


Figure S2.17. $^{13}\text{C}\{^1\text{H}\}$ NMR spectrum of **azide 1** in CDCl_3 at 25°C . * indicates CDCl_3 solvent.

2.6.3.9 Experimental Spectra for 1-azido-4-nitrobenzene (azide 4)

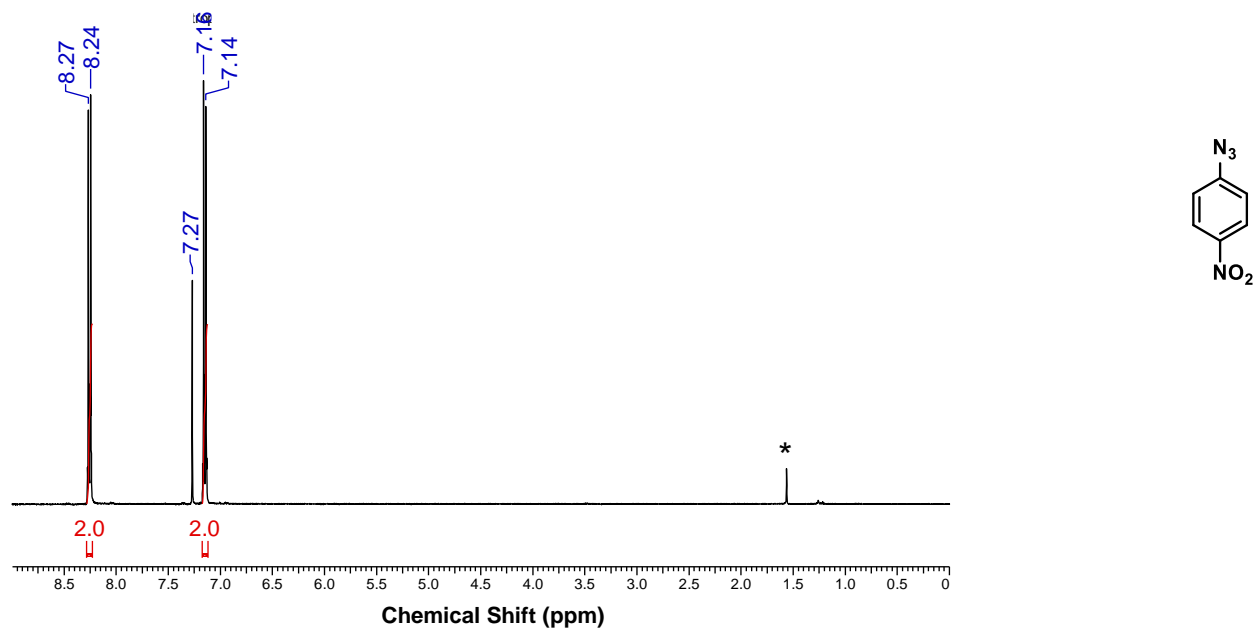


Figure S2.18. ^1H NMR spectrum of **azide 4** in CDCl_3 at 25°C . * denotes residual protio solvent and impurities.

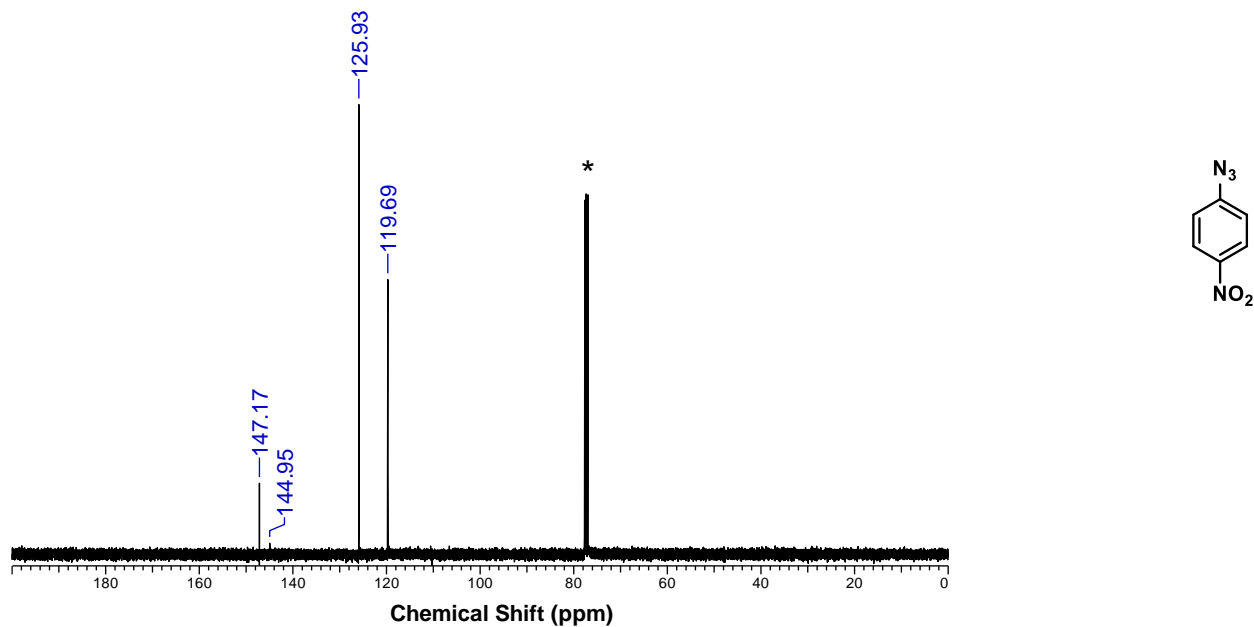


Figure S2.19. $^{13}\text{C}\{^1\text{H}\}$ NMR spectrum of **azide 4** in CDCl_3 at 25°C . * indicates CDCl_3 solvent.

2.6.3.10 Experimental Spectra for 4-azidopyridine (azide 5)

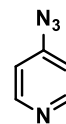
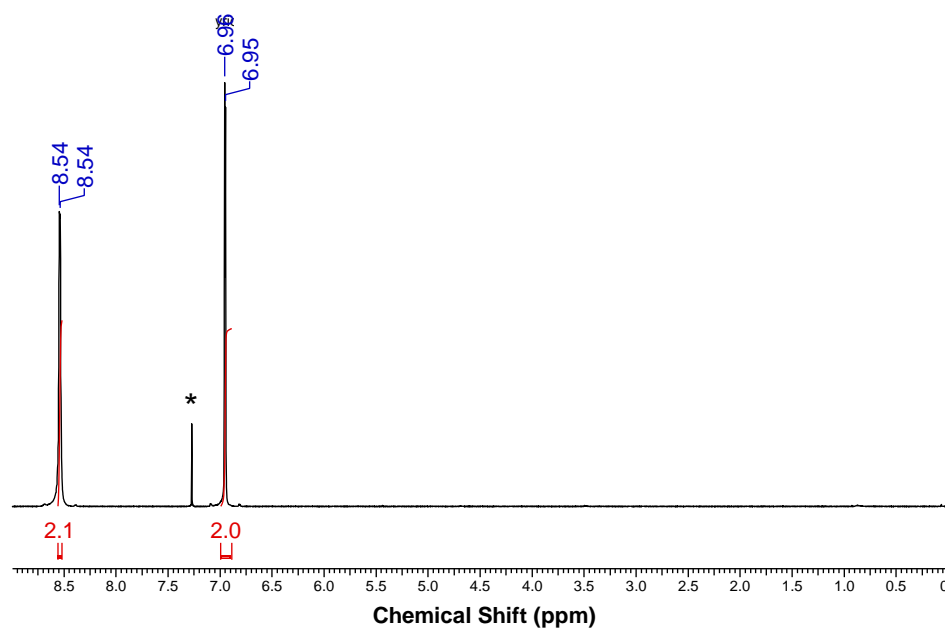


Figure S2.20. ^1H NMR spectrum of **azide 5** in CDCl_3 at 25°C . * denotes residual protio solvent.

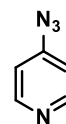
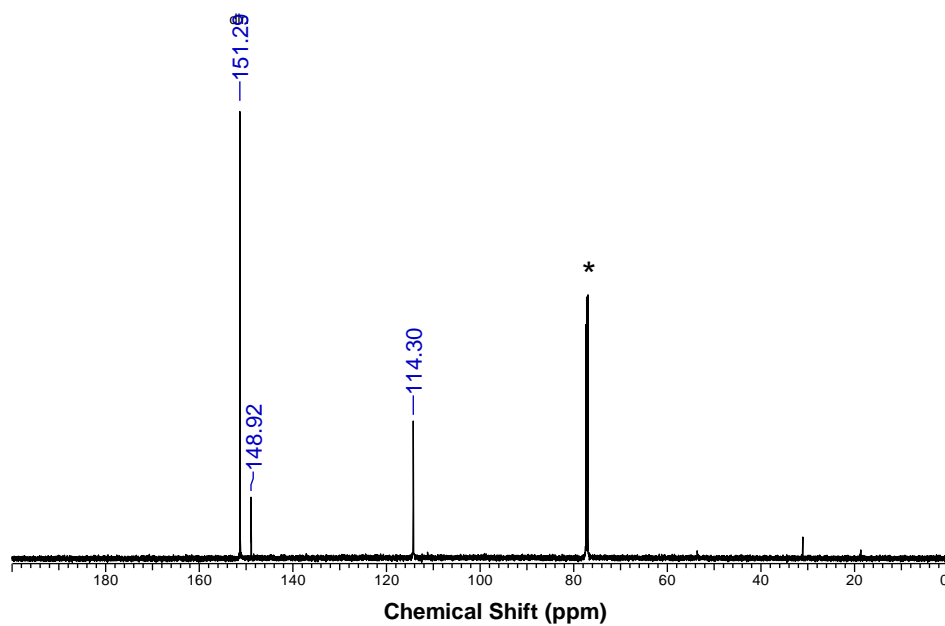


Figure S2.21. $^{13}\text{C}\{^1\text{H}\}$ NMR spectrum of **azide 5** in CDCl_3 at 25°C . * indicates CDCl_3 solvent.

2.6.3.11 Experimental Spectra for 1-azido-2,3,4,5,6-pentafluorobenzene (azide 6)

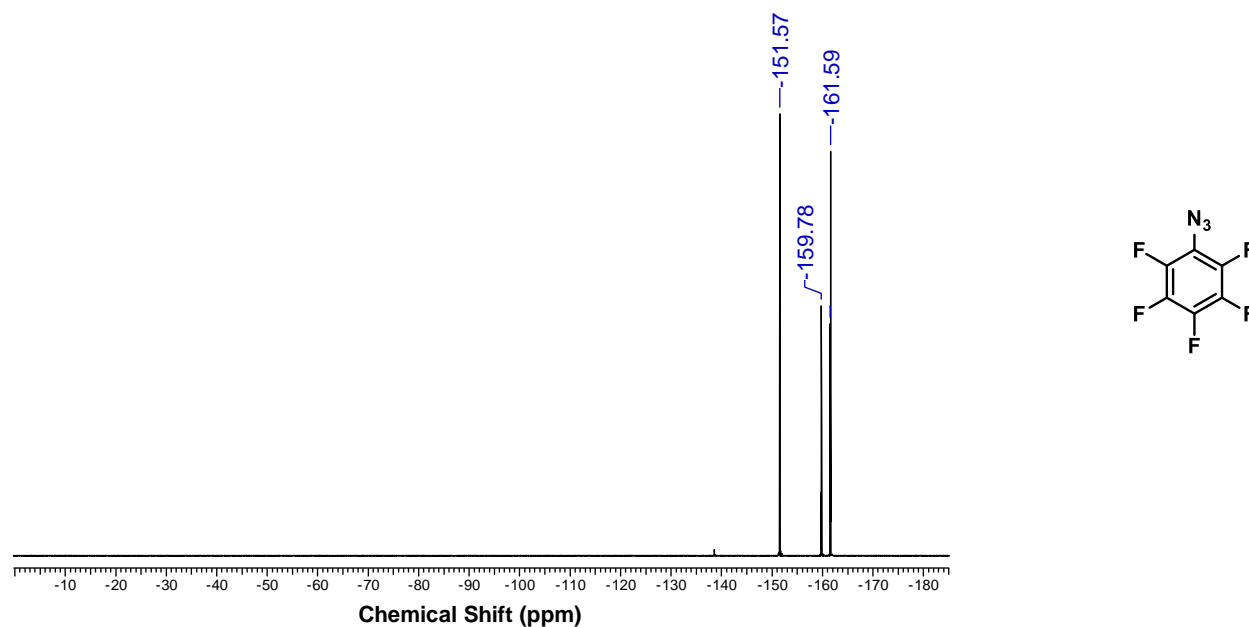


Figure S2.22. ^{19}F NMR spectrum of **azide 6** in CDCl_3 at 25°C .

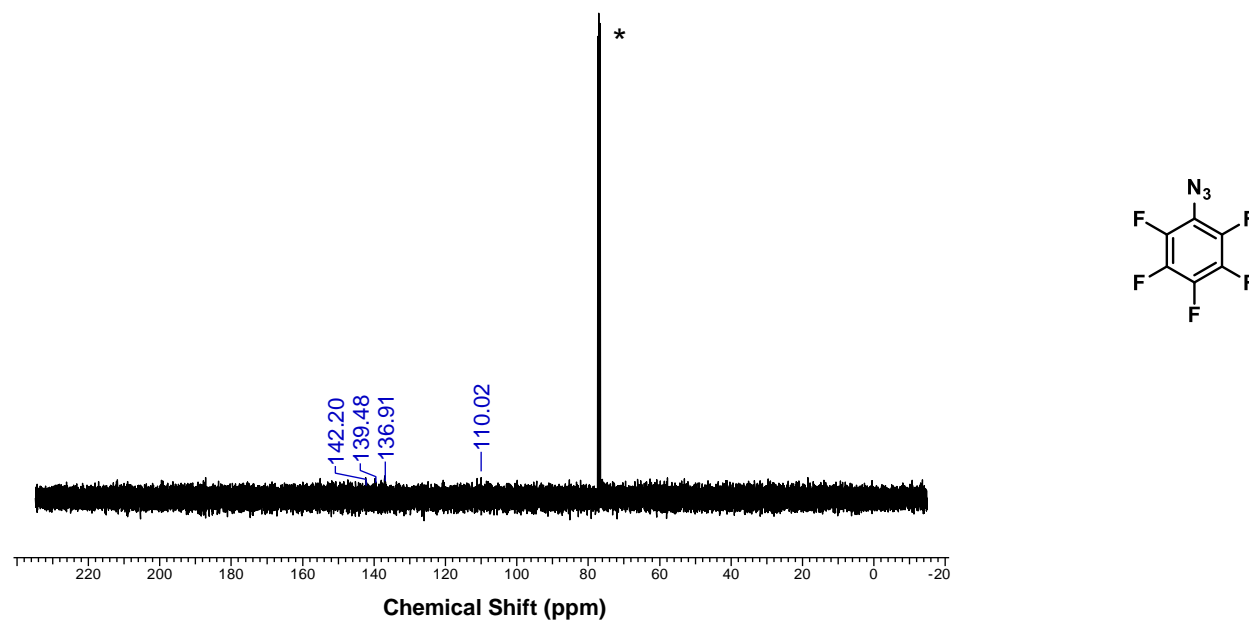


Figure S2.23. $^{13}\text{C}\{^1\text{H}\}$ NMR spectrum of **azide 6** in CDCl_3 at 25°C . * indicates CDCl_3 solvent.

2.6.3.12 Experimental Spectra for *N*-methyl-*C*-nitrophenyl-nitrone (nitrone 1)

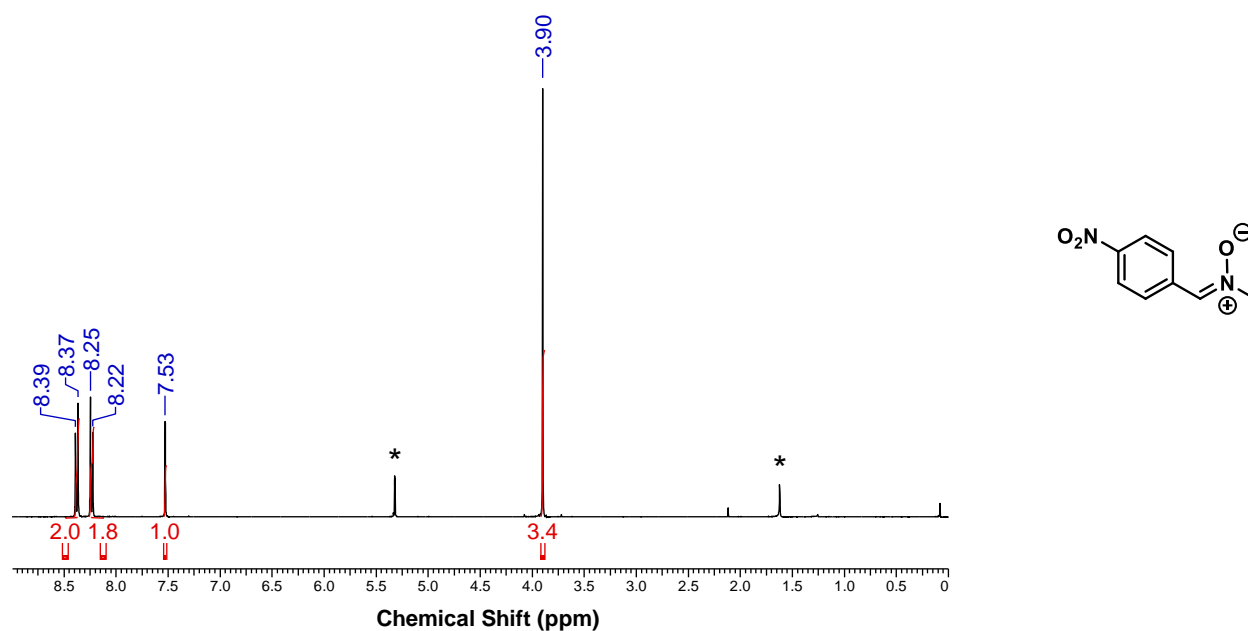


Figure S2.24. ^1H NMR spectrum of **nitrone 1** in CD_2Cl_2 at 25°C . * denotes residual protio solvent and impurities.

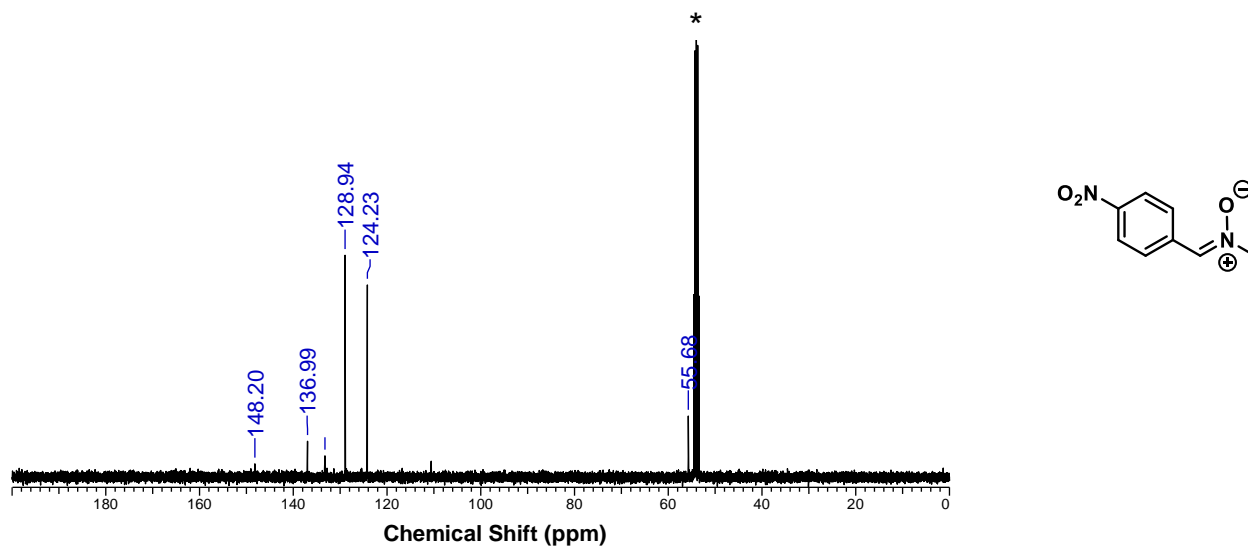


Figure S2.25. $^{13}\text{C}\{^1\text{H}\}$ NMR spectrum of **nitrone 1** in CD_2Cl_2 at 25°C . * indicates CD_2Cl_2 solvent.

2.6.3.13 Experimental Spectra for *N*-phenyl-*C*-methoxyphenyl-nitrone (nitrone 2)

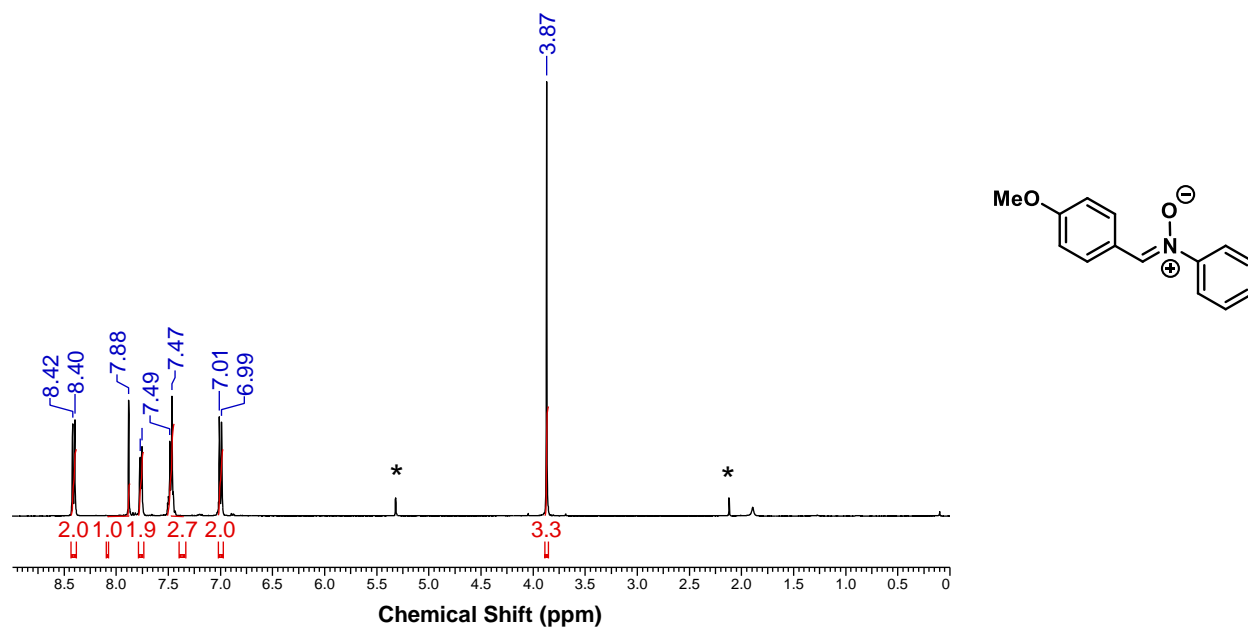


Figure S2.26. ^1H NMR spectrum of **nitrone 2** in CD_2Cl_2 at 25°C . * denotes residual protio solvent and impurities.

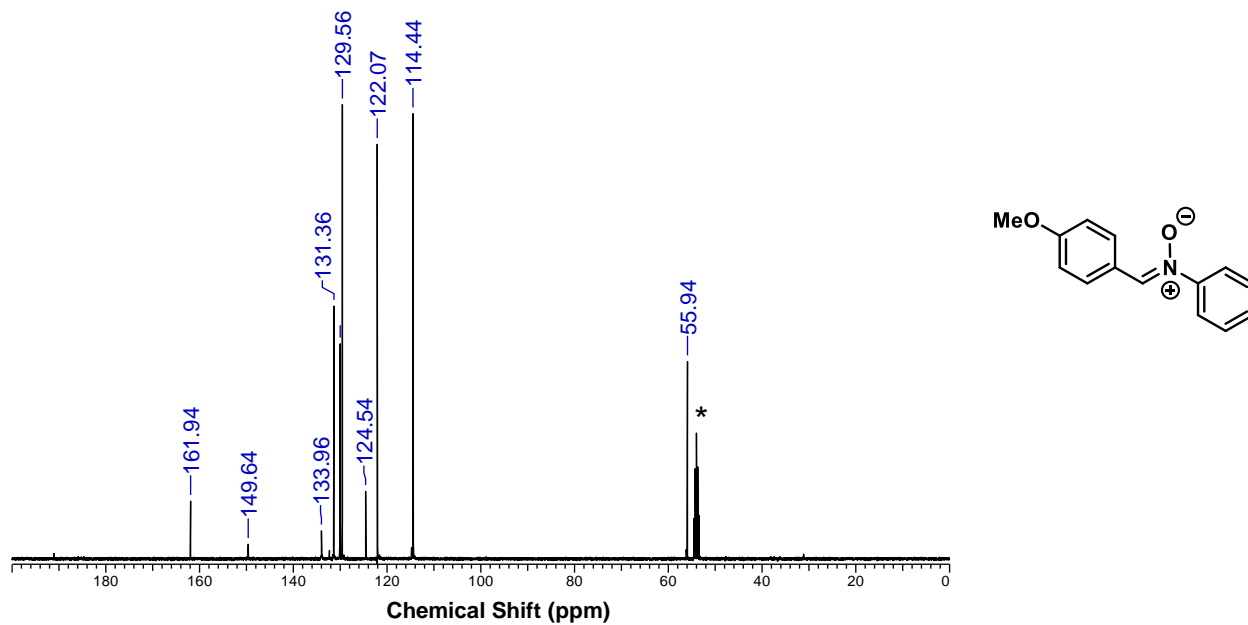


Figure S2.27. $^{13}\text{C}\{^1\text{H}\}$ NMR spectrum of **nitrone 2** in CD_2Cl_2 at 25°C . * indicates CD_2Cl_2 solvent.

2.6.3.14 Experimental Spectra for *N*-phenyl-*C*-phenyl-nitrone (nitron 3)

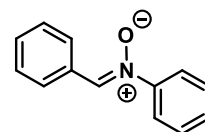
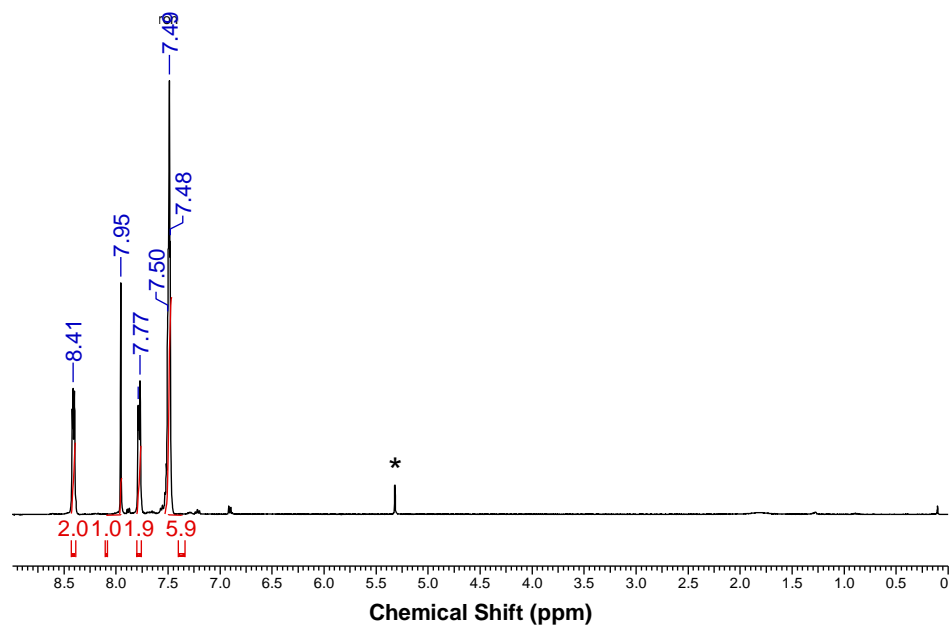


Figure S2.28. ^1H NMR spectrum of **nitron 3** in CD_2Cl_2 at 25°C . * denotes residual protio solvent.

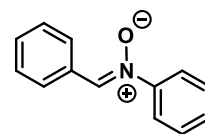
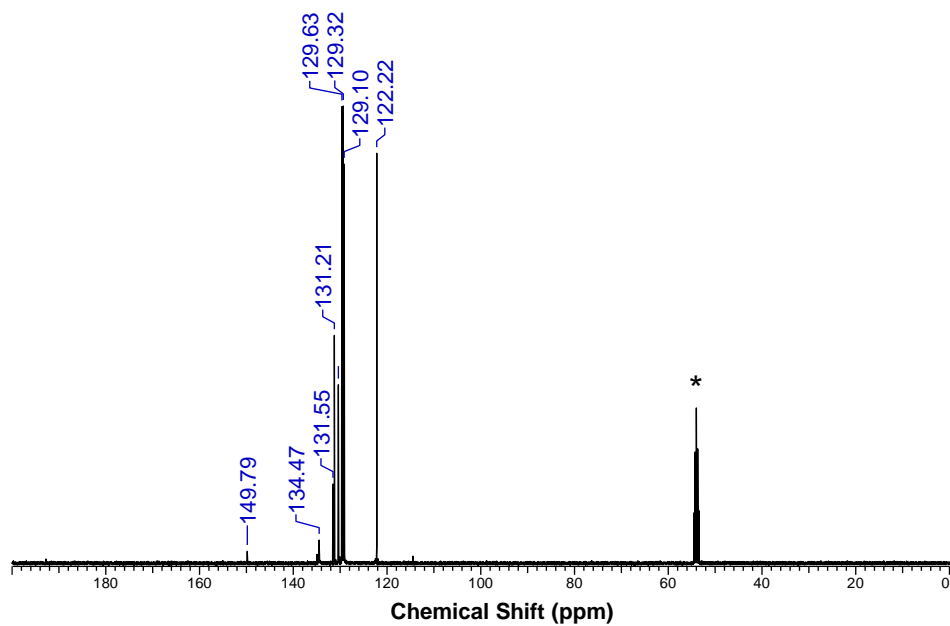


Figure S2.29. $^{13}\text{C}\{^1\text{H}\}$ NMR spectrum of **nitron 3** in CD_2Cl_2 at 25°C . * indicates CD_2Cl_2 solvent.

2.6.3.15 Experimental Spectra for *N*-phenyl-*C*-nitrophenyl-nitrone (nitrone 4)

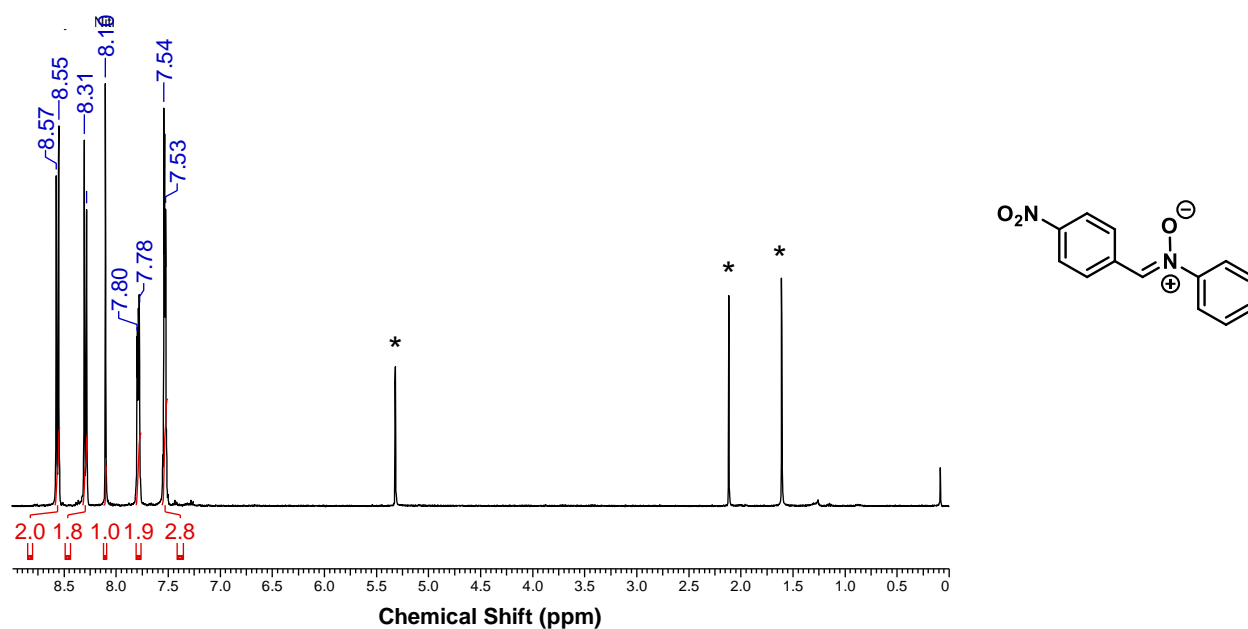


Figure S2.30. ^1H NMR spectrum of **nitrone 4** in CD_2Cl_2 at 25°C . * denotes residual protio solvent and impurities.

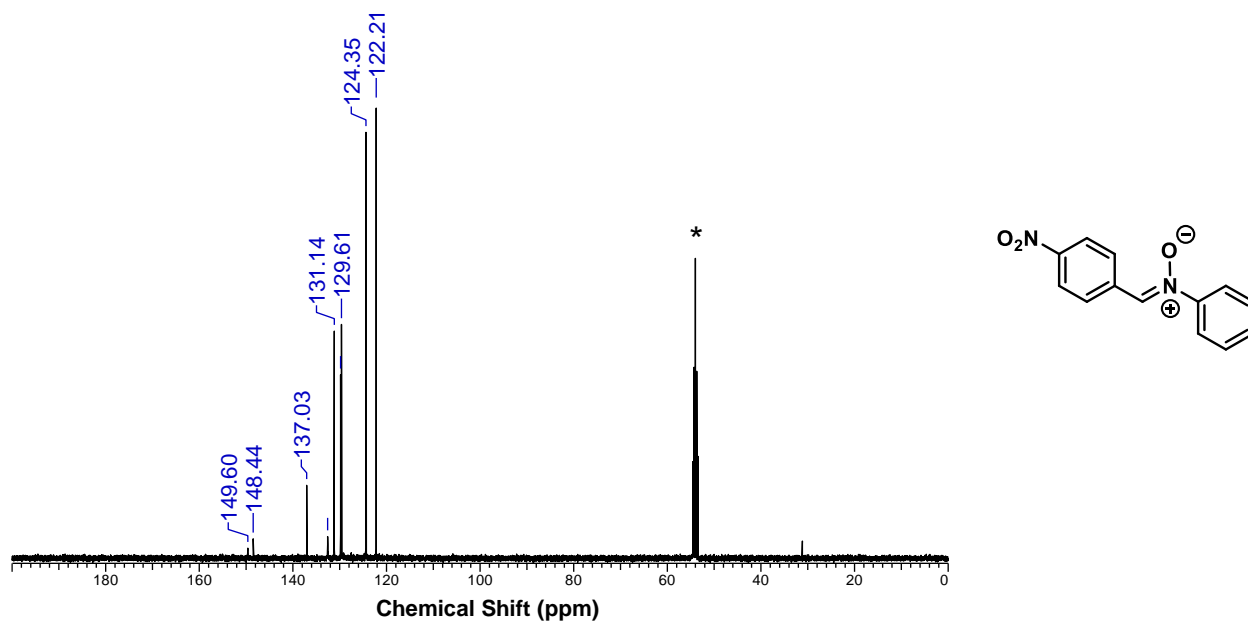


Figure S2.31. $^{13}\text{C}\{^1\text{H}\}$ NMR spectrum of **nitrone 4** in CD_2Cl_2 at 25°C . * indicates CD_2Cl_2 solvent.

2.6.3.16 Experimental Spectra for *N*-phenyl-*C*-pyridine-nitrone (nitrone 5)

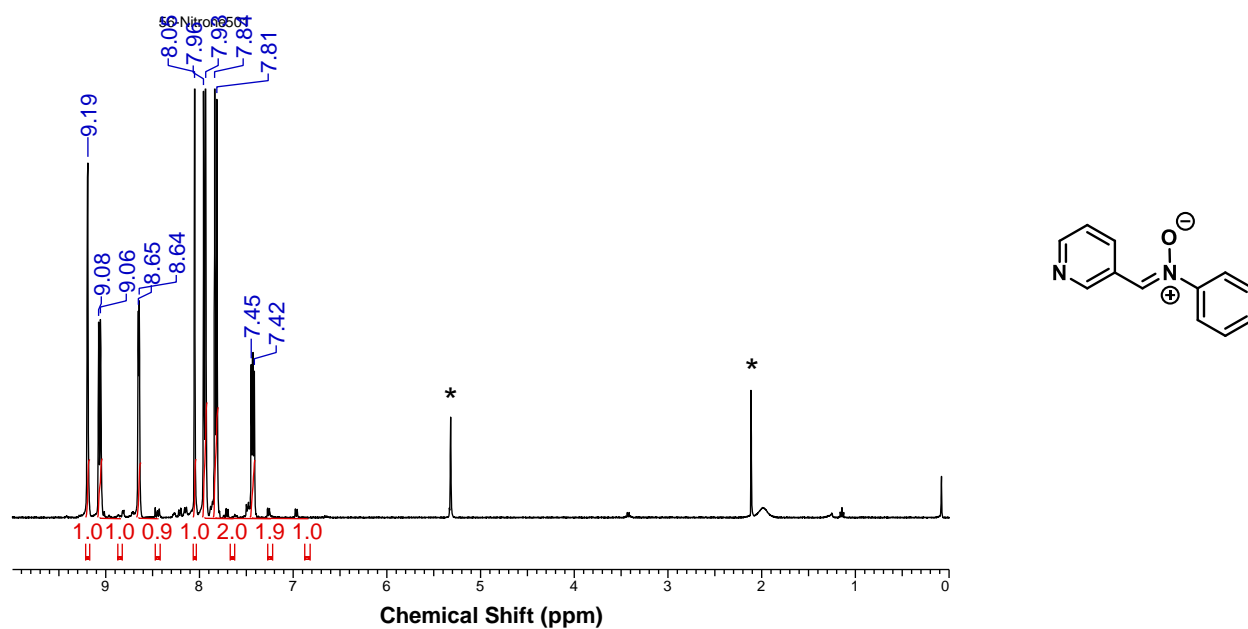


Figure S2.32. ^1H NMR spectrum of **nitrone 5** in CD_2Cl_2 at 25°C . * denotes residual protio solvent and impurities.

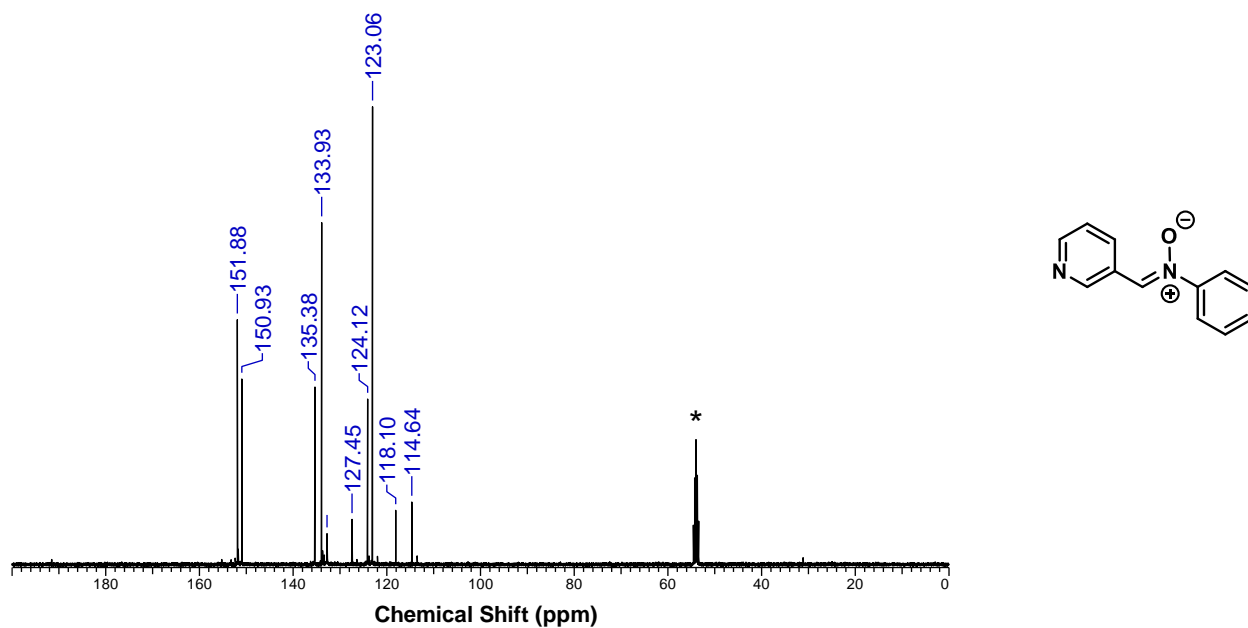


Figure S2.33. $^{13}\text{C}\{^1\text{H}\}$ NMR spectrum of **nitrone 5** in CD_2Cl_2 at 25°C . * indicates CD_2Cl_2 solvent.

2.6.3.17 Experimental Spectra for *N*-cyanophenyl-C-pyridine-nitrone (nitrone 6)

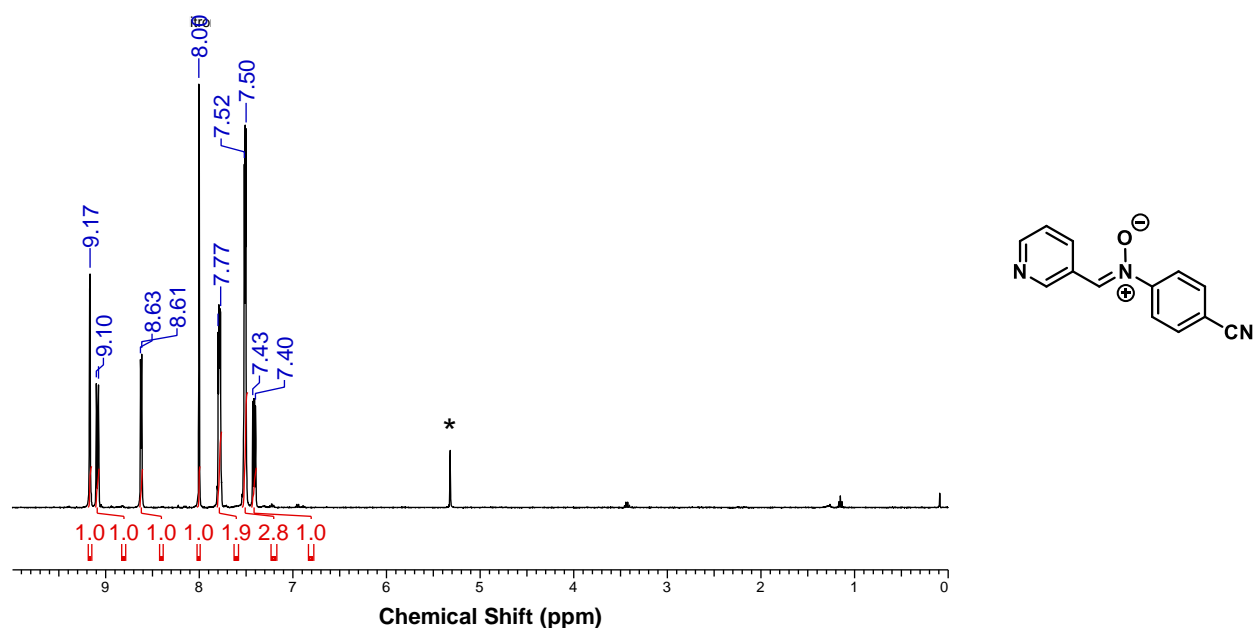


Figure S2.34. ^1H NMR spectrum of **nitrone 6** in CD_2Cl_2 at 25°C . * denotes residual protio solvent.

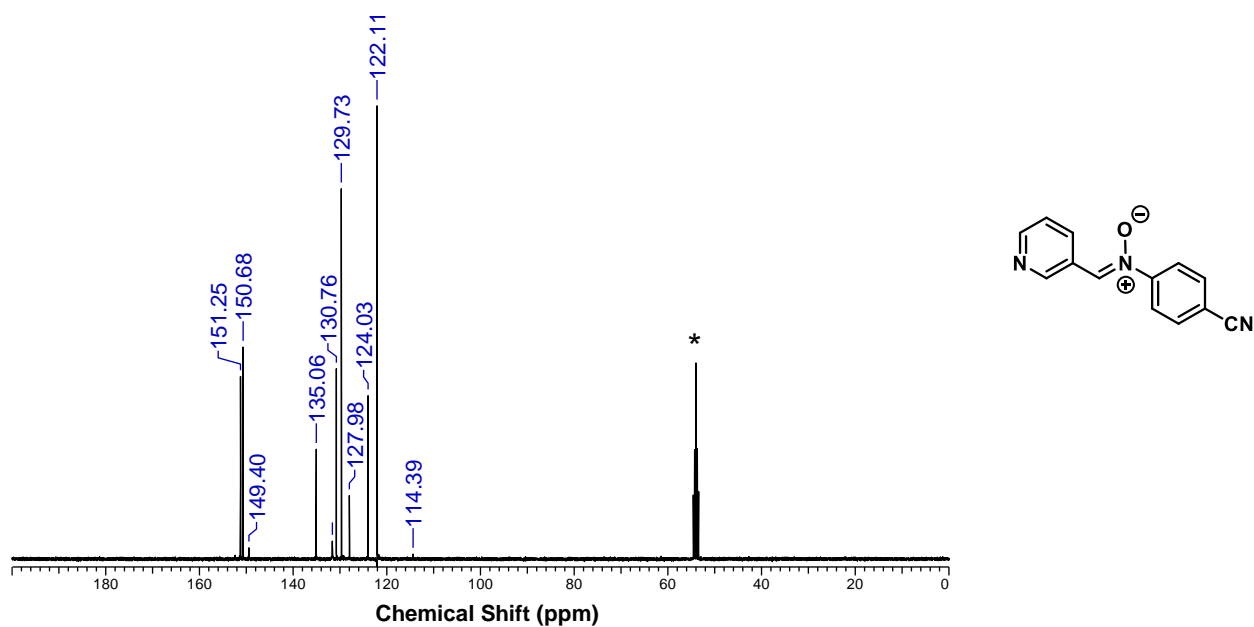


Figure S2.35. $^{13}\text{C}\{^1\text{H}\}$ NMR spectrum of **nitrone 6** in CD_2Cl_2 at 25°C . * indicates CD_2Cl_2 solvent.

2.6.4 Thermogravimetric Analysis of AuNP-BCN

2.6.4.1 General Experimental Details

A crucible containing 1.3 mg of **AuNP-BCN** was heated from 25°C to 750°C under nitrogen for TGA analysis, and the decrease in organic matter was determined with increasing temperature (**Figure S2.36**).

The derivative of the TGA curve shows two components centered at 233.2°C and 300.0°C resulting from the decomposition of the $\text{BCN}_{\text{exo}}\text{-EG}_4\text{-S}^-$ and $\text{OMe-EG}_3\text{-S}^-$ ligands, respectively, both of which constitutes 64% of the mass of the AuNP sample (**Figure S2.37**). The area under each normalized curve indicates that $\text{BCN}_{\text{exo}}\text{-EG}_4\text{-S}^-$ (MM = 384.492 g/mol) constitutes 28% of the total organic mass (0.23 mg per 1.3 mg AuNP) and $\text{OMe-EG}_3\text{-S}^-$ constitutes 72% of the total organic mass (0.60 mg per 1.3 mg AuNP). Correcting for the mass of the total mass of the AuNP sample, the TGA analysis indicates that there is 0.46 $\mu\text{mol}/\text{mg}$ of **AuNP-BCN**.

2.6.4.2 Experimental Spectra for TGA Analysis

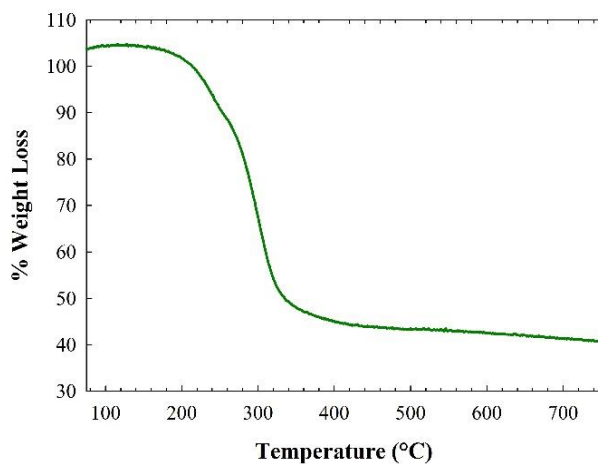


Figure S2.36. TGA spectrum for **AuNP-BCN**.

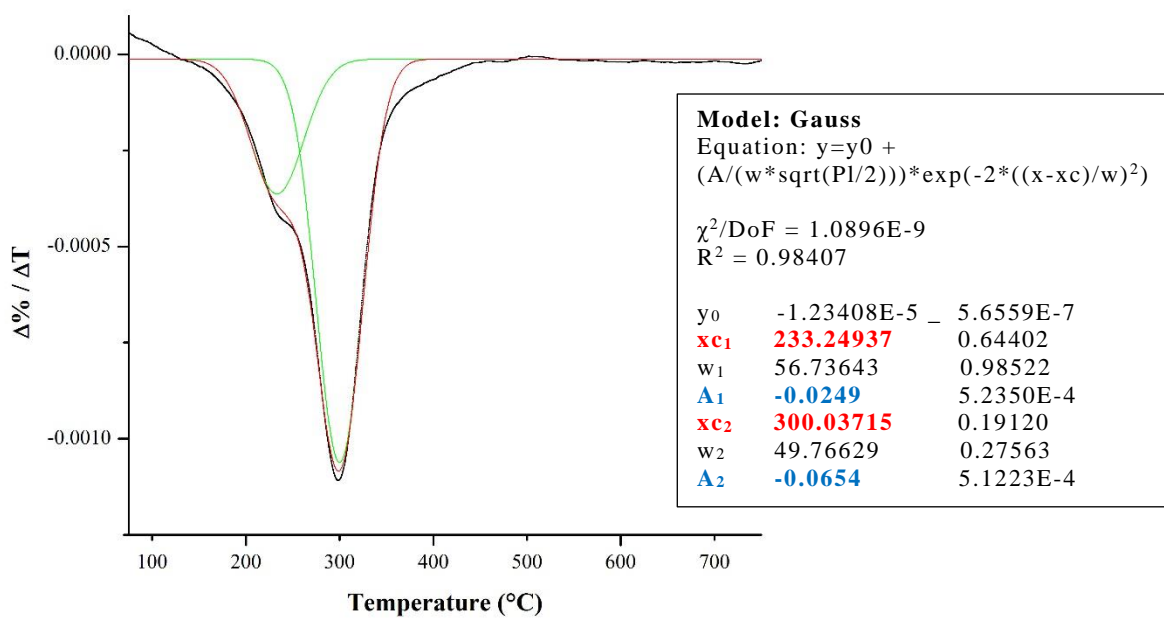


Figure S2.37. First-derivative of TGA spectrum for **AuNP-BCN**.

2.6.5 Kinetic Measurements

2.6.5.1 General Experimental Details

Estimate rate constants for all azides and nitrones were determined under second order conditions (k_2) in deuterated dichloromethane at 25°C using ^1H NMR spectroscopy, by reacting each with both **BCN_{exo}-OH** and **AuNP-BCN**.

In order to estimate k_2 values for each azide/nitron with **BCN_{exo}-OH**, stock solutions of the azides/nitrones and **BCN_{exo}-OH** were first prepared and then equimolar quantities of each were added to an NMR tube. Stock solutions of **BCN_{exo}-OH** and each azide/nitron were prepared by dissolving 100 μmol in 0.5 mL deuterated dichloromethane to give a 0.2 M stock solution of **BCN_{exo}-OH** and 0.2 M stock solution of each azide/nitron. Subsequently, 10 μL (2 μmol) of the azide/nitron stock solution was added to 0.3 mL deuterated dichloromethane in an NMR tube, and a t_0 (time zero) ^1H NMR spectrum was acquired. Next, 10 μL (2 μmol) of the **BCN_{exo}-OH** stock solution was added. This solution was shaken vigorously, and ^1H NMR spectra were acquired over pre-determined time intervals according to the speed of the reaction.

In order to estimate k_2 values for each azide/nitron with **BCN_{exo}-OH**, a solution was prepared by dissolving 4 mg (2 μmol) **AuNP-BCN** in 0.3 mL deuterated dichloromethane in an NMR tube. A t_0 (time zero) ^1H NMR spectra was taken of this sample. Subsequently, 10 μL (2 μmol) of the azide/nitron stock solution was added. This solution was shaken vigorously, and ^1H NMR spectra were acquired over pre-determined time intervals according to the speed of the reaction.

Upon cycloaddition to **BCN_{exo}-OH** and **AuNP-BCN**, the methylene protons alpha to the azide in **azide 1**, and the aromatic protons beta to the azide in **azide 2**, **azide 3**, **azide 4** and **azide 5** produce a ^1H NMR signal that decreases over time, and produces a new ^1H NMR signal at a higher chemical shift, and so the decrease in the ^1H NMR signal from the parent azide was used to obtain a rate of reaction. A rate of reaction for **azide 6** was determined by measuring the reduction in the signal at 4.0 ppm (that appears in the ^1H NMR spectrum of both **BCN_{exo}-OH** and **AuNP-BCN**), which is not present in the resulting cycloadduct. The hydrogen on the α -carbon on each of the nitrones produces a ^1H NMR signal that decreases over time, and produces a new ^1H NMR

signal at a higher chemical shift, and so the decrease in the ^1H NMR signal from the parent azide was used to obtain a rate of reaction.

2.6.5.2 Kinetic Measurements for 1-azido-3-propanol (azide 1)

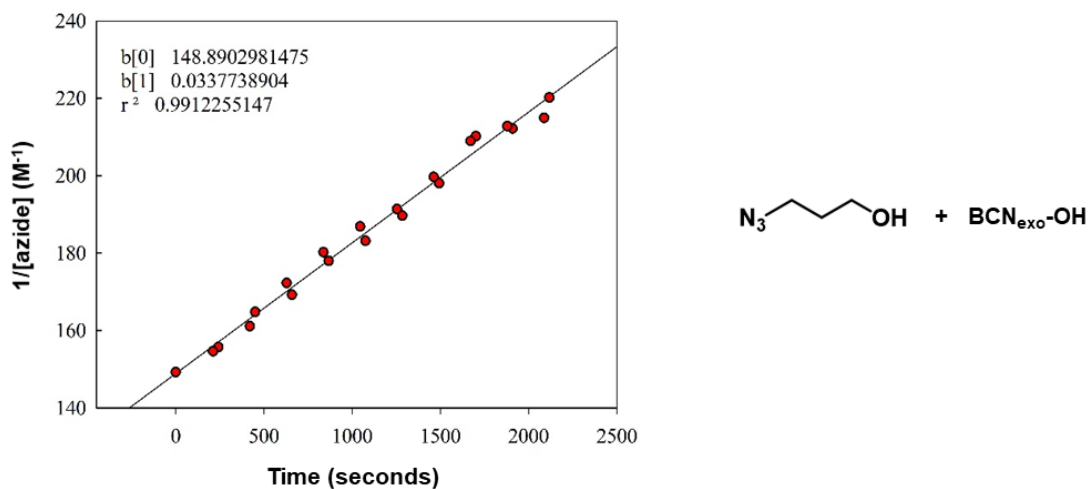


Figure S2.38. Second order kinetics graph for **azide 1** with **$\text{BCN}_{\text{exo}}\text{-OH}$** .

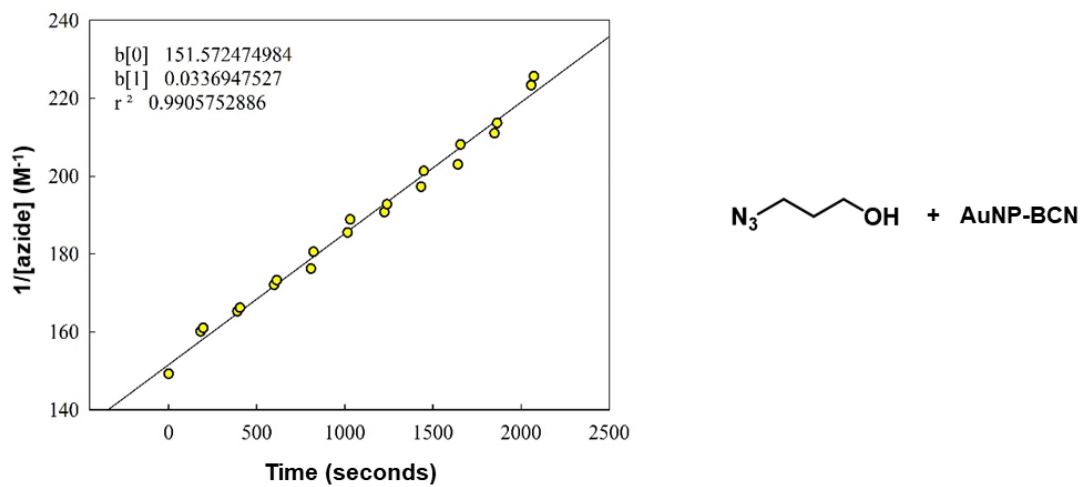


Figure S2.39. Second order kinetics graph for **azide 1** with **AuNP-BCN** .

2.6.5.3 Kinetic Measurements for 4-azidoanisole (azide 2)

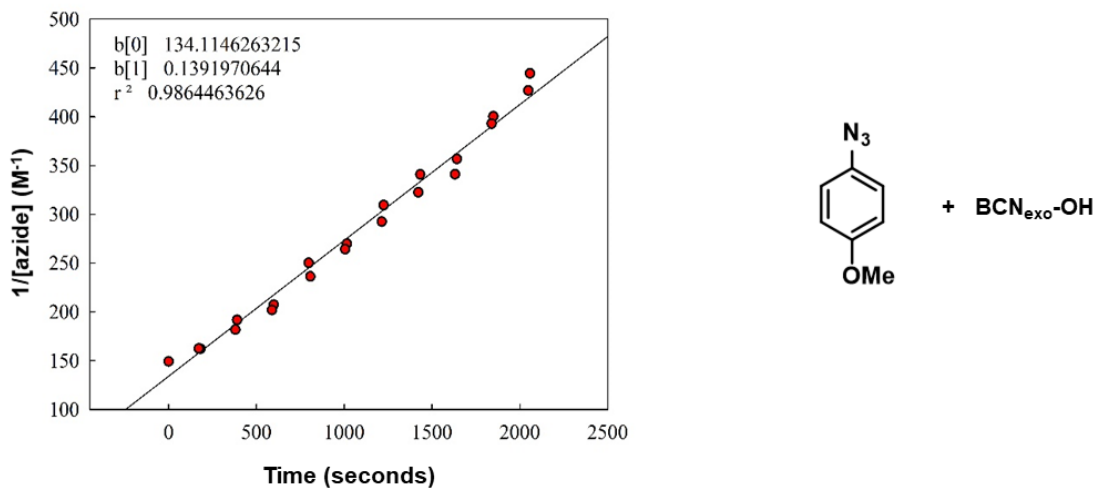


Figure S2.40. Second order kinetics graph for **azide 2** with BCN_{exo-OH} .

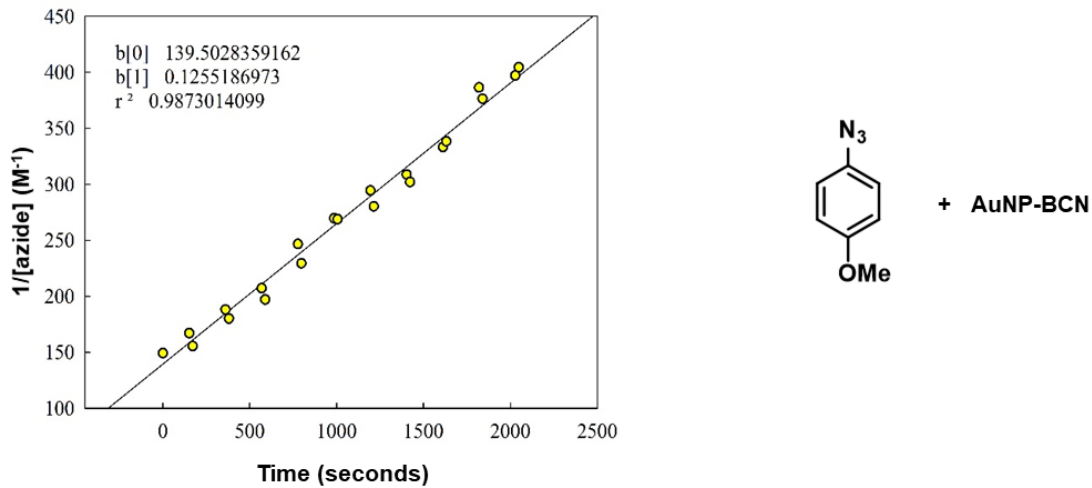


Figure S2.41. Second order kinetics graph for **azide 2** with AuNP-BCN.

2.6.5.4 Kinetic Measurements for azidobenzene (azide 3)

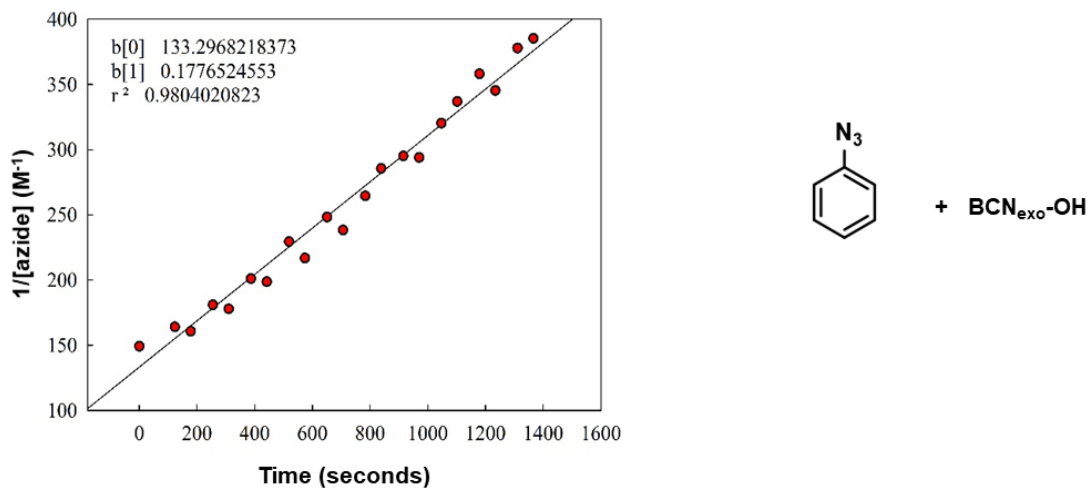


Figure S2.42. Second order kinetics graph for **azide 3** with BCN_{exo}-OH.

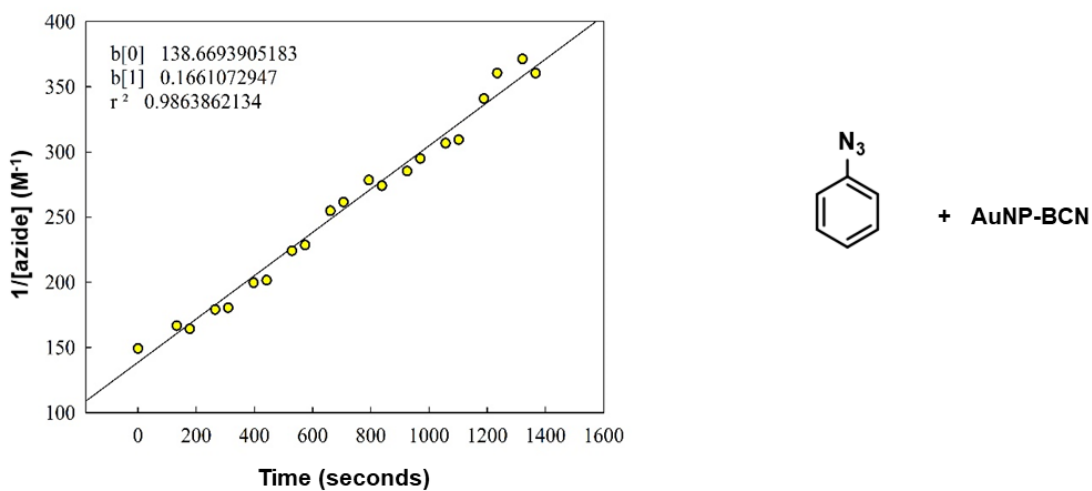


Figure S2.43. Second order kinetics graph for **azide 3** with AuNP-BCN.

2.6.5.5 Kinetic Measurements for 1-azido-4-nitrobenzene (azide 4)

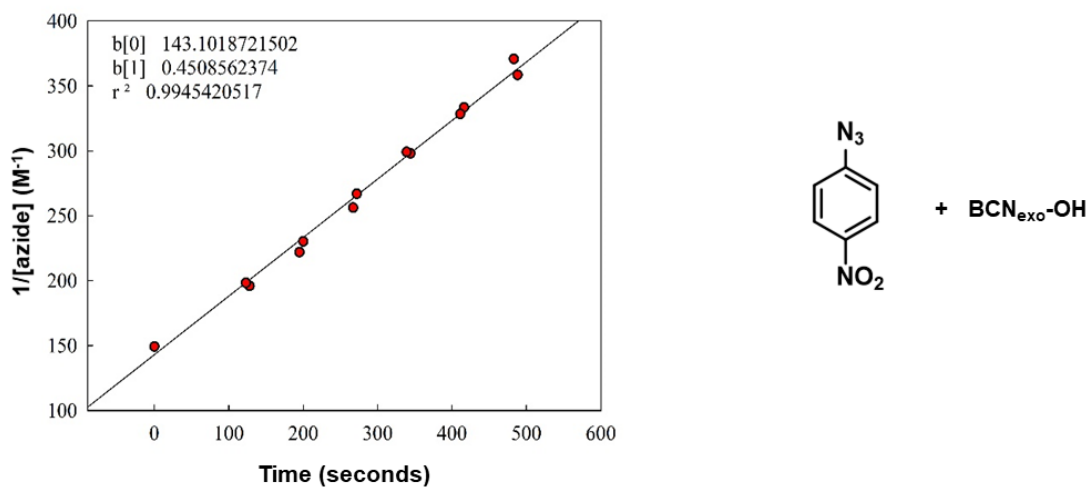


Figure S2.44. Second order kinetics graph for **azide 4** with BCN_{exo-OH} .

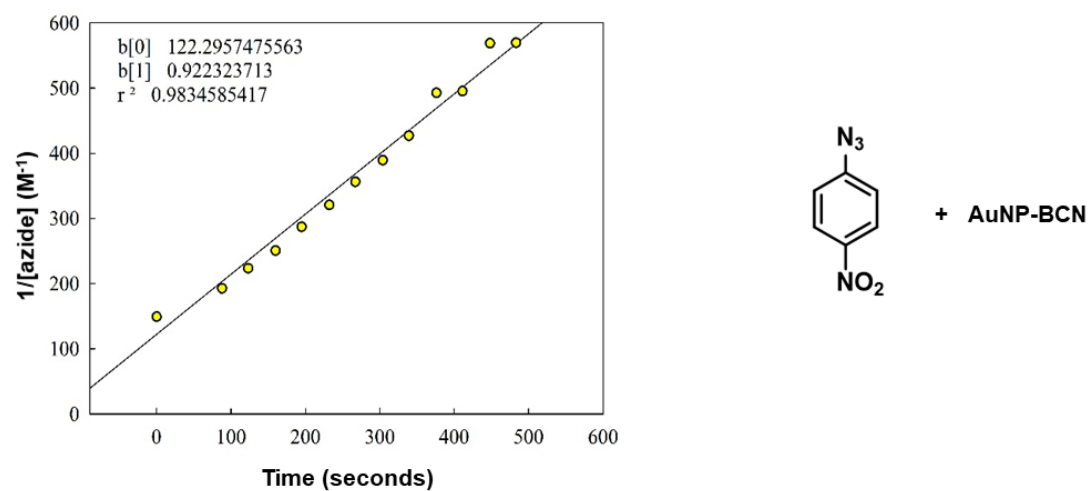


Figure S2.45. Second order kinetics graph for **azide 4** with $AuNP-BCN$.

2.6.5.6 Kinetic Measurements for 4-azidopyridine (azide 5)

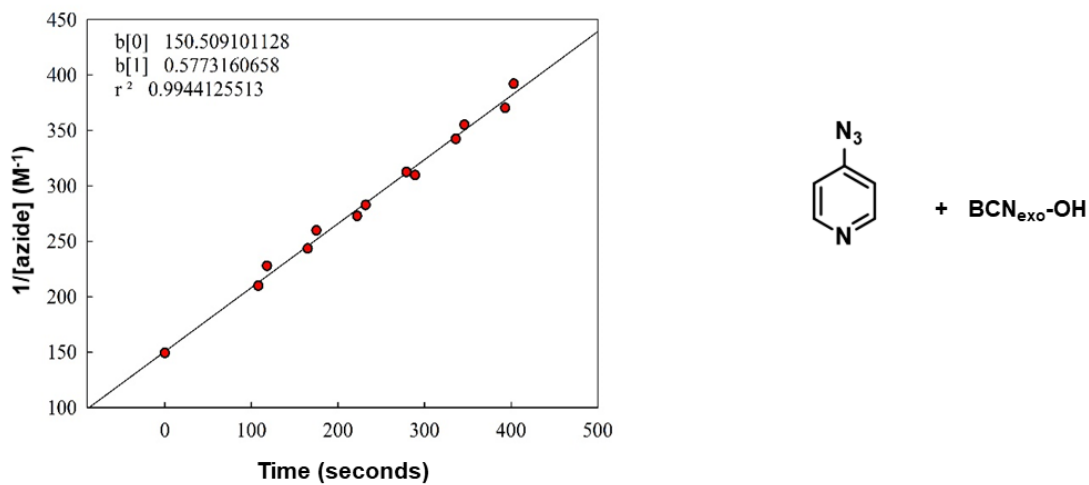


Figure S2.46. Second order kinetics graph for **azide 5** with BCN_{exo}-OH.

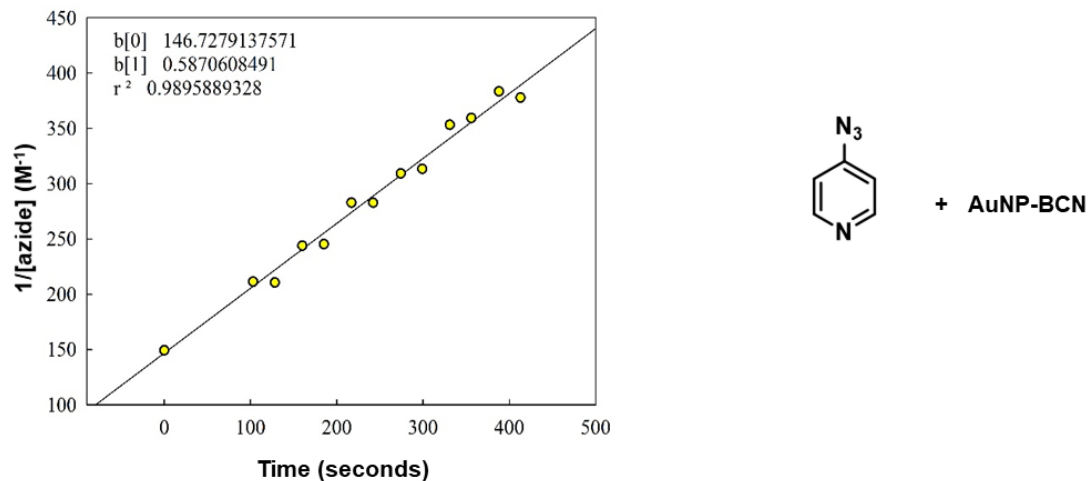


Figure S2.47. Second order kinetics graph for **azide 5** with AuNP-BCN.

2.6.5.7 Kinetic Measurements for 1-azido-2,3,4,5,6-pentafluorobenzene (azide 6)

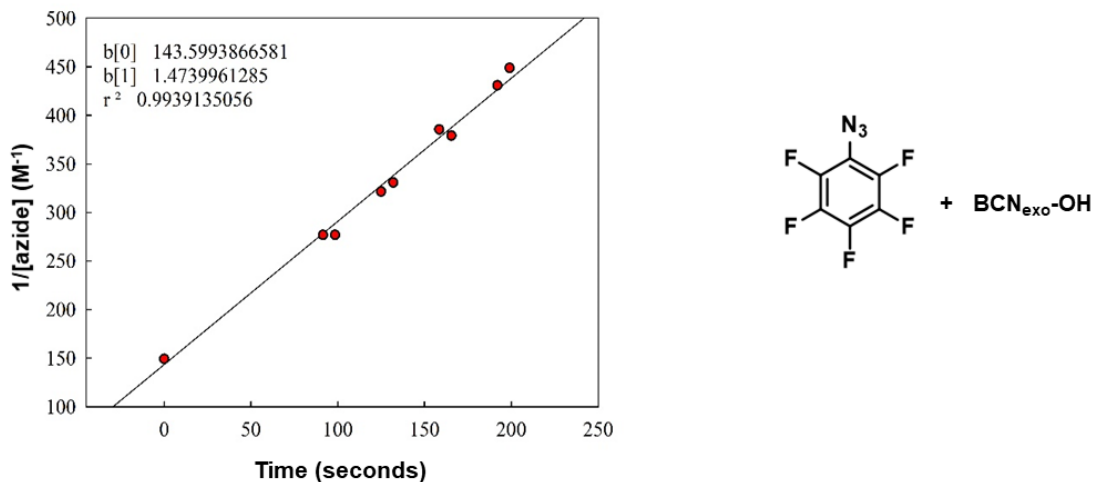


Figure S2.48. Second order kinetics graph for **azide 6** with BCN_{exo-OH} .

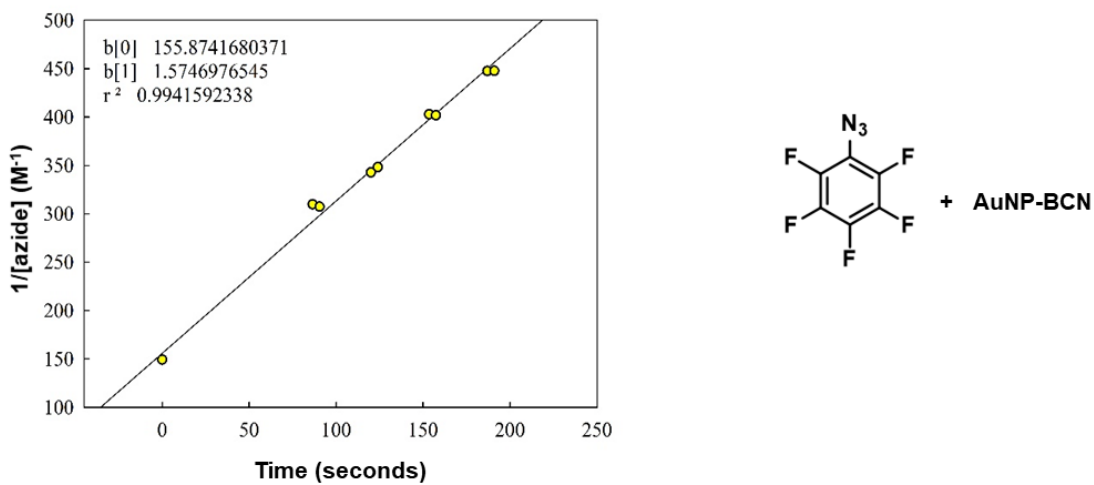


Figure S2.49. Second order kinetics graph for **azide 6** with $AuNP-BCN$.

2.6.5.8 Kinetic Measurements for *N*-methyl-*C*-nitrophenyl-nitrone (nitron 1)

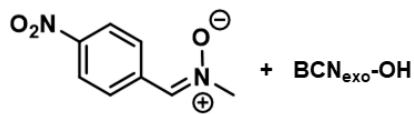
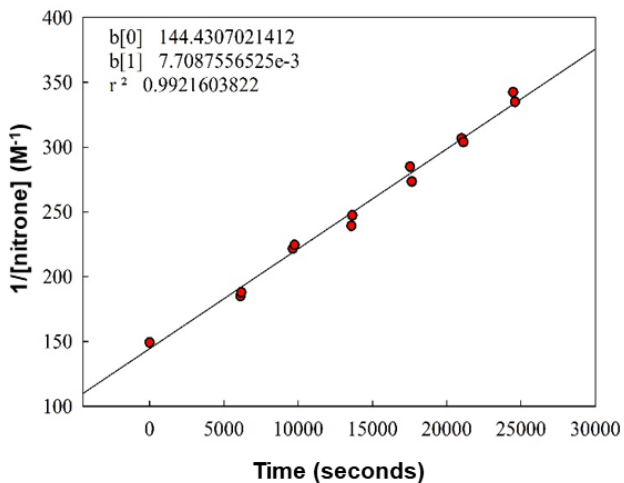


Figure S2.50. Second order kinetics graph for **nitron 1** with BCN_{exo}-OH.

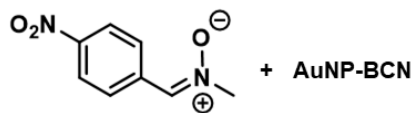
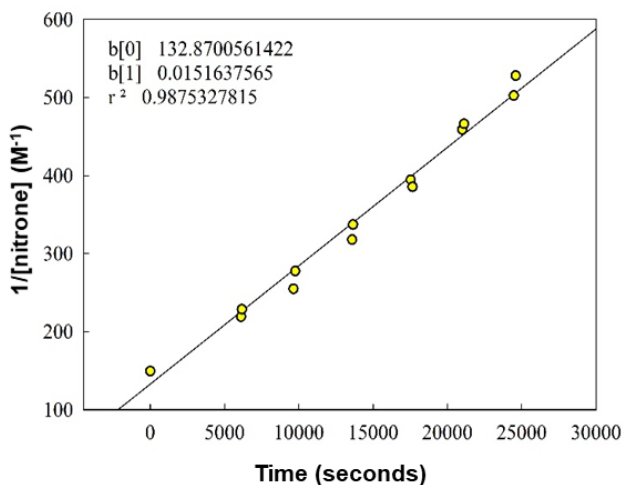


Figure S2.51. Second order kinetics graph for **nitron 1** with AuNP-BCN.

2.6.5.9 Kinetic Measurements for *N*-phenyl-*C*-methoxyphenyl-nitrone (nitron 2)

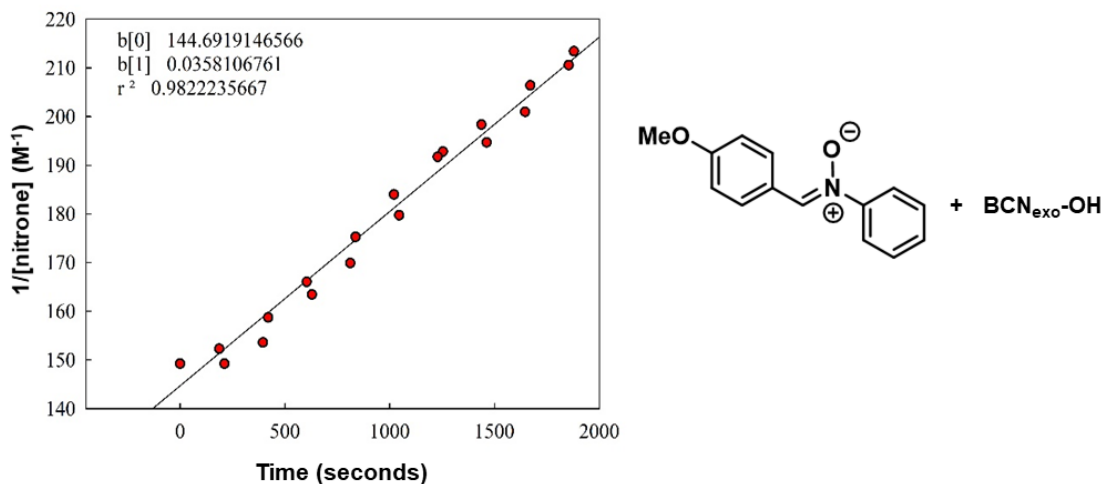


Figure S2.52. Second order kinetics graph for **nitron 2** with BCN_{exo-OH} .

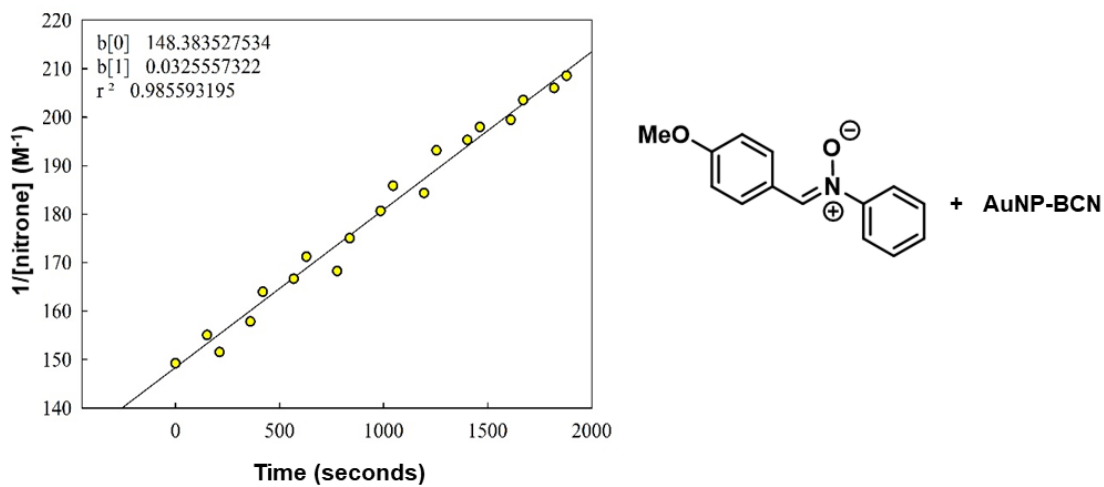


Figure S2.53. Second order kinetics graph for **nitron 2** with AuNP-BCN.

2.6.5.10 Kinetic Measurements for *N*-phenyl-*C*-phenyl-nitron (nitron 3)

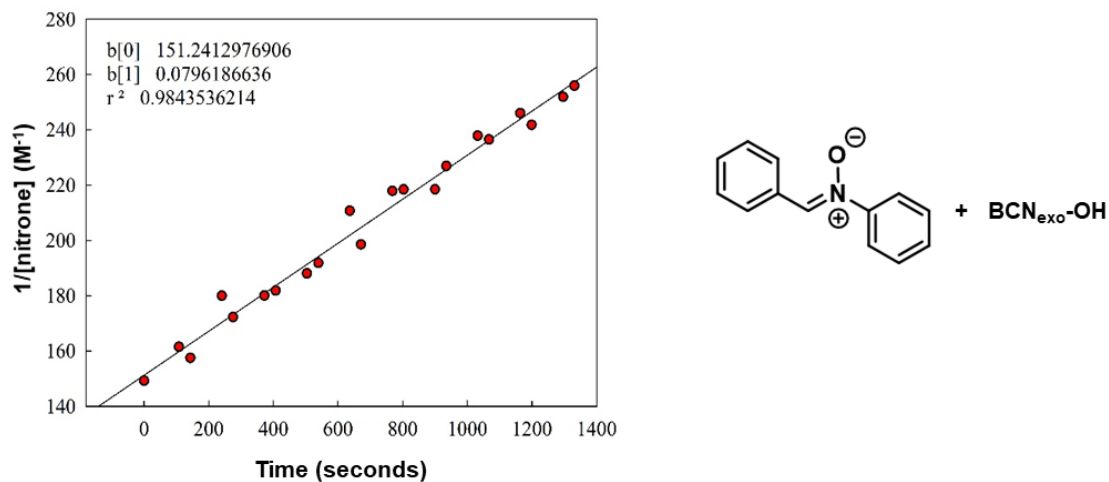


Figure S2.54. Second order kinetics graph for **nitron 3** with BCN_{exo-OH} .

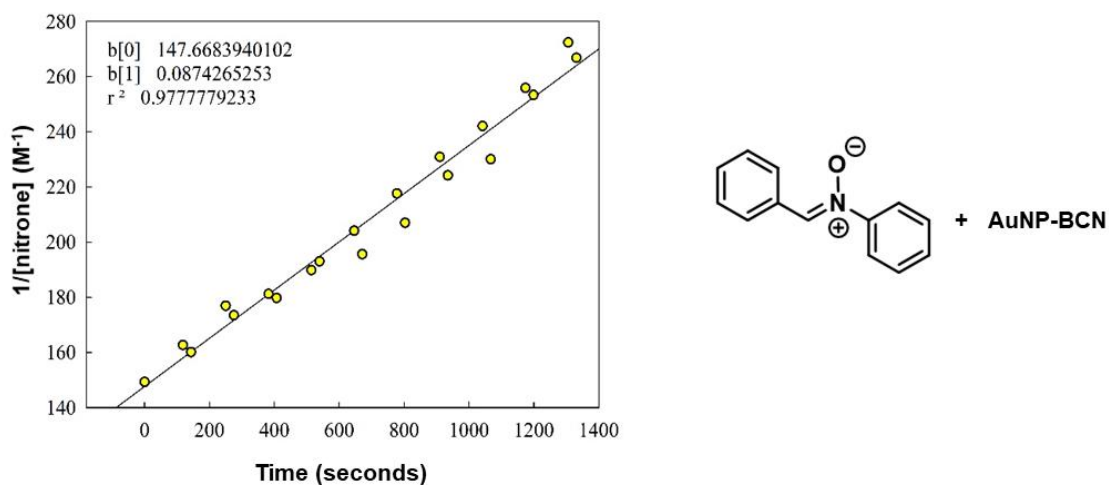


Figure S2.55. Second order kinetics graph for **nitron 3** with $AuNP-BCN$.

2.6.5.11 Kinetic Measurements for *N*-phenyl-*C*-nitrophenyl-nitrone (nitrone 4)

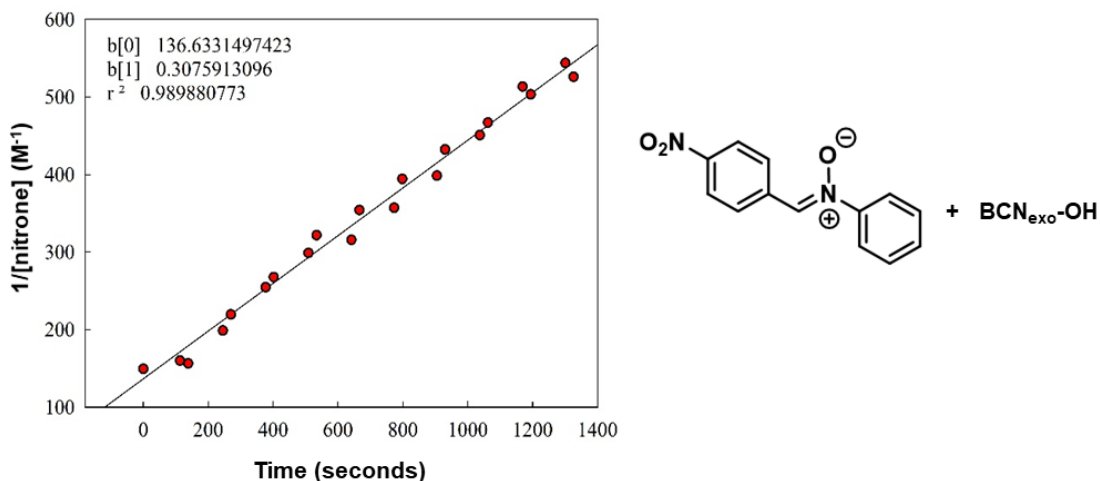


Figure S2.56. Second order kinetics graph for **nitrone 4** with BCN_{exo-OH} .

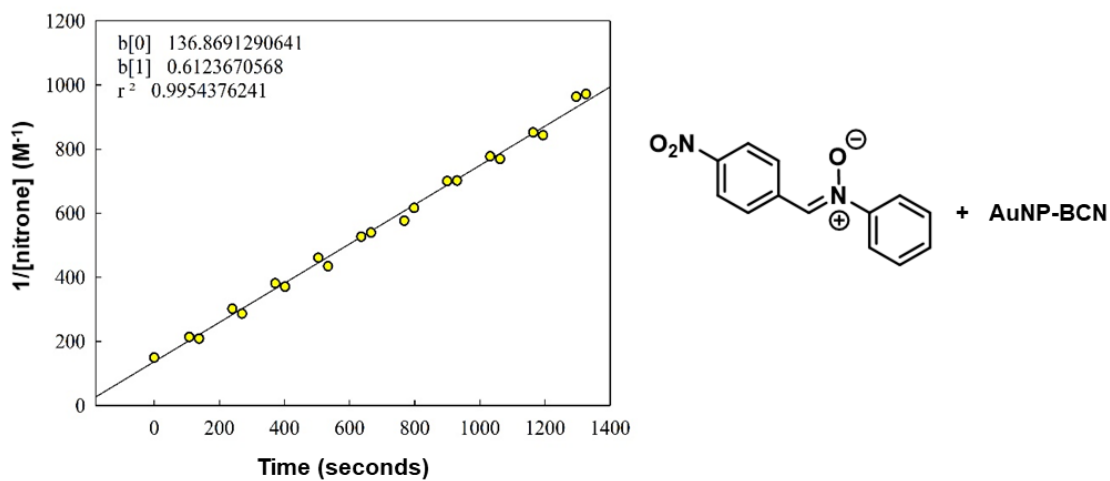


Figure S2.57. Second order kinetics graph for **nitrone 4** with $AuNP-BCN$.

2.6.5.12 Kinetic Measurements for *N*-phenyl-C-pyridine-nitrone (nitrone 5)

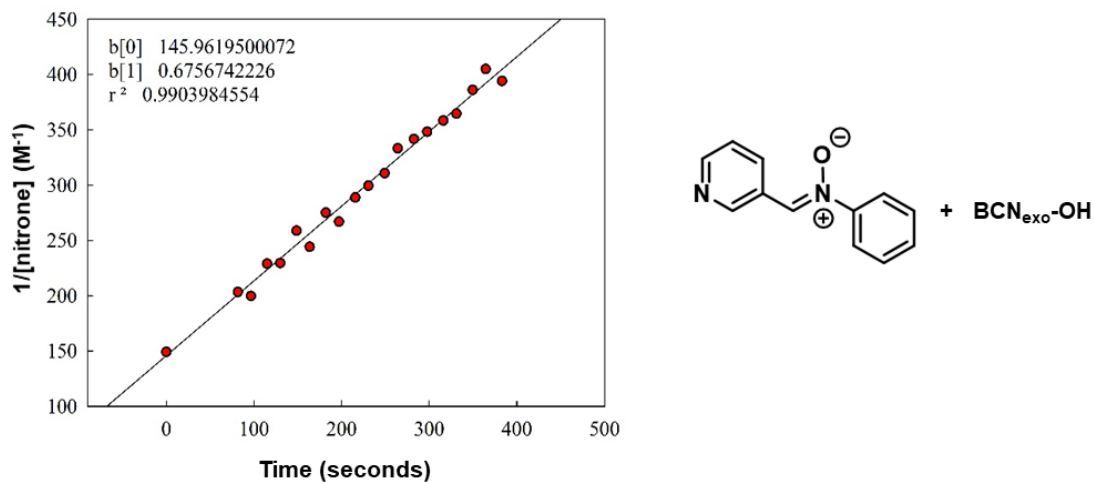


Figure S2.58. Second order kinetics graph for **nitrone 5** with BCN_{exo}-OH.

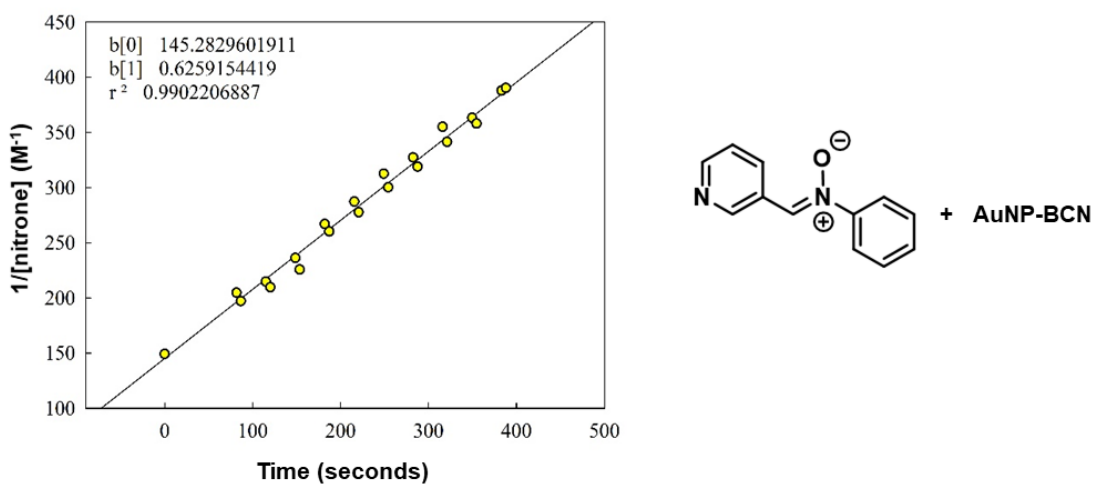


Figure S2.59. Second order kinetics graph for **nitrone 5** with AuNP-BCN.

2.6.5.13 Kinetic Measurements for *N*-cyanophenyl-*C*-pyridine-nitrone (nitrone 6)

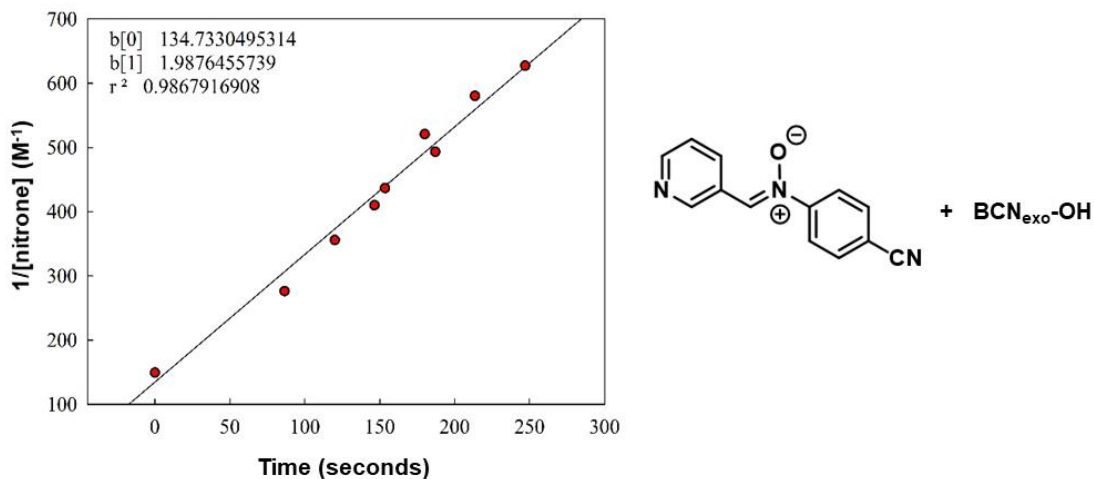


Figure S2.60. Second order kinetics graph for **nitrone 6** with BCN_{exo-OH} .

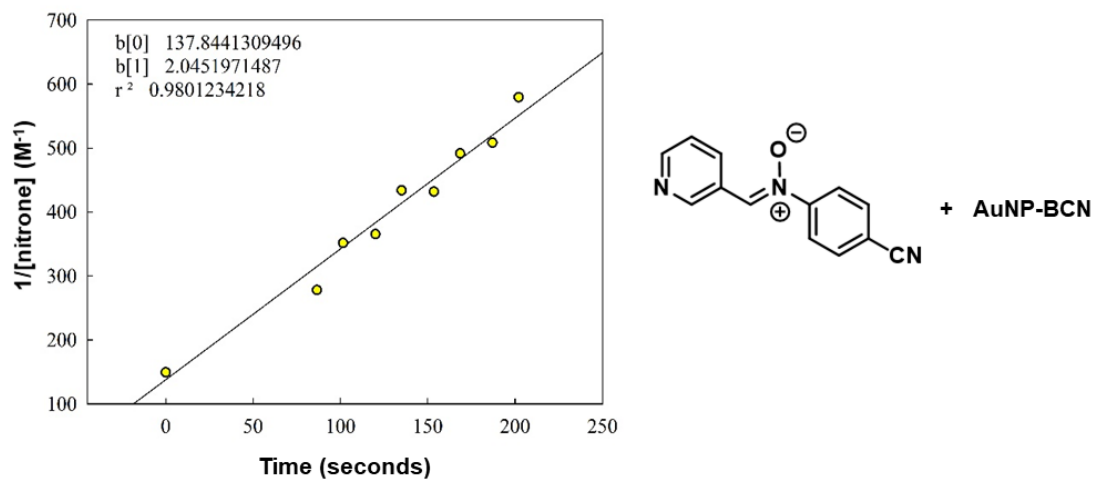


Figure S2.61. Second order kinetics graph for **nitrone 6** with AuNP-BCN.

2.6.6 Competition Experiments for AuNP-BCN

2.6.6.1 General Experimental Details

For the competition experiments between an azide and nitrene, equimolar quantities of one azide, one nitrene and AuNP-BCN were combined in deuterated dichloromethane and monitored by ^1H NMR spectroscopy.

First, stock solutions for the azide and nitrene used for each experiment were first prepared as described in **section 2.6.5.1** to generate 0.2 M solutions of each. Then 0.2 mL of azide stock solution was added to 0.2 mL of nitrene stock solution to obtain 1:1 azide:nitrene stock solutions. Subsequently, 20 μL (2 μmol azide and 2 μmol nitrene) of this 1:1 stock solution was added to 0.3 mL deuterated dichloromethane in an NMR tube, and a t_0 (time zero spectrum) ^1H NMR spectrum was acquired. Non-coinciding ^1H NMR signals were chosen, one produced from a proton environment in the azide, and one produced from a proton environment in the nitrene, and the integrals were determined for these signals to give the $t_{0(\text{azide})}$ and $t_{0(\text{nitrene})}$ integral values.

Next, a solution was prepared by dissolving 4 mg (2 μmol) **AuNP-BCN** in 0.3 deuterated dichloromethane in an NMR tube. Subsequently, 20 μL of the 1:1 azide:nitrene solution was added, the solution was shaken vigorously, and a ^1H NMR spectrum was taken after 24 hours to allow the interfacial reaction to go to completion (24 hour spectrum). The integral of non-coinciding signals from the same proton environments chosen before were determined (which decreased as the interfacial reaction had gone to completion), to give the $t_{24(\text{azide})}$ and $t_{24(\text{nitrene})}$ integral values. To determine the % I-SPAAC (i.e. degree of reaction between **AuNP-BCN** and the azide species), the $t_{24(\text{azide})}/t_{0(\text{azide})}$ ratio was determined. To determine the % I-SPAN (i.e. degree of reaction between **AuNP-BCN** and the nitrene species), the $t_{24(\text{nitrene})}/t_{0(\text{nitrene})}$ ratio was determined.

Since **azide 6** does not contain any protons, the reacted percentage of **nitrene 1** in the competition experiment against **azide 6** was determined, and the reacted percentage of **azide 6** was calculated by difference.

2.6.6.2 ¹H NMR Spectra for Competition Experiment between azide 1 and nitrone 6

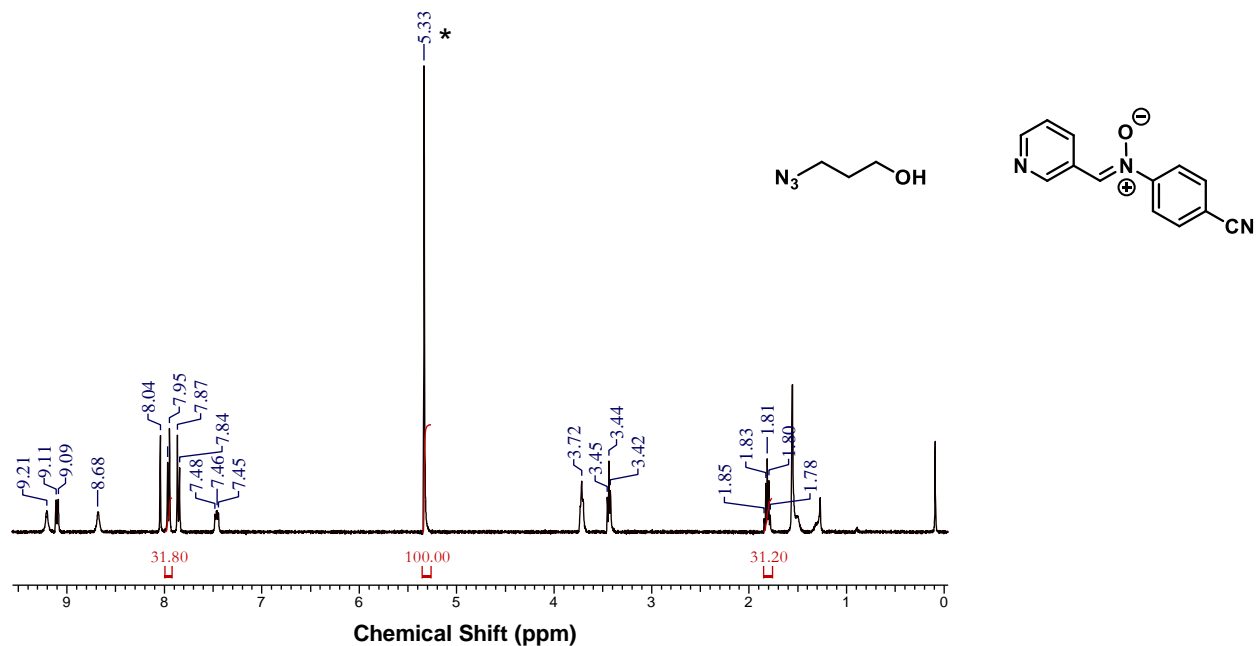


Figure S2.62. ¹H NMR spectrum of equimolar mixture of **azide 1** and **nitron 6** in CD₂Cl₂ at 25°C. * denotes residual protio solvent.

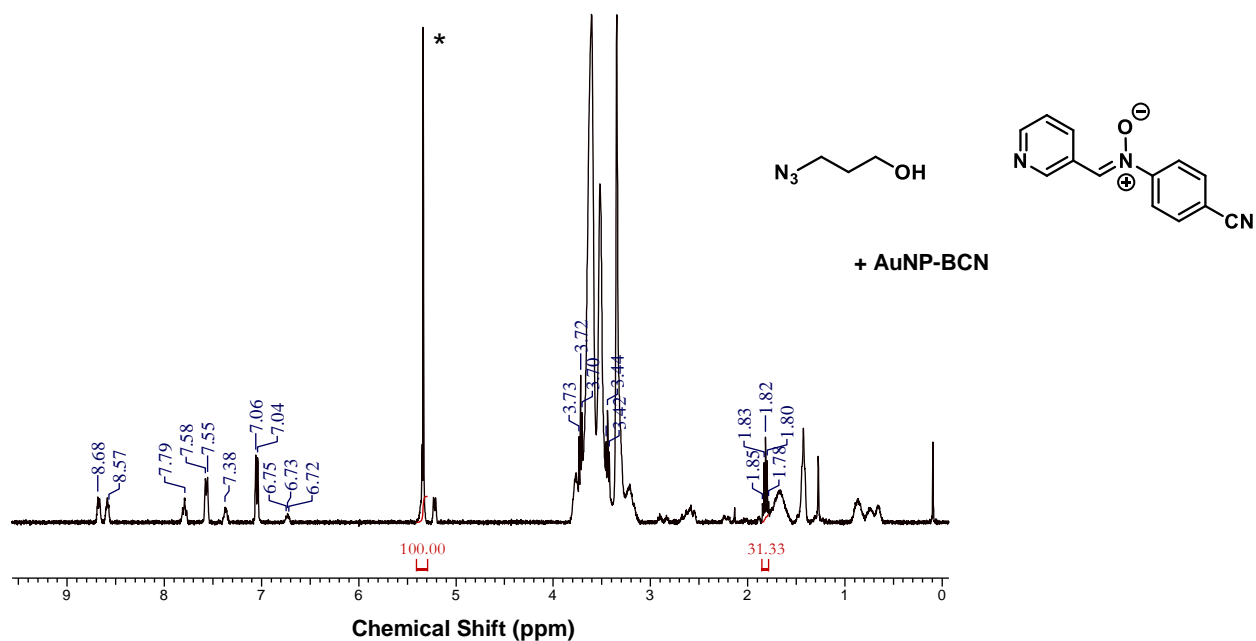


Figure S2.63. ¹H NMR spectrum of equimolar mixture of **azide 1** and **nitron 6** and interfacial BCN (in AuNP-BCN) in CD₂Cl₂ at 25°C. * denotes residual protio solvent.

2.6.6.3 ^1H NMR Spectra for Competition Experiment between azide **3** and nitron **4**

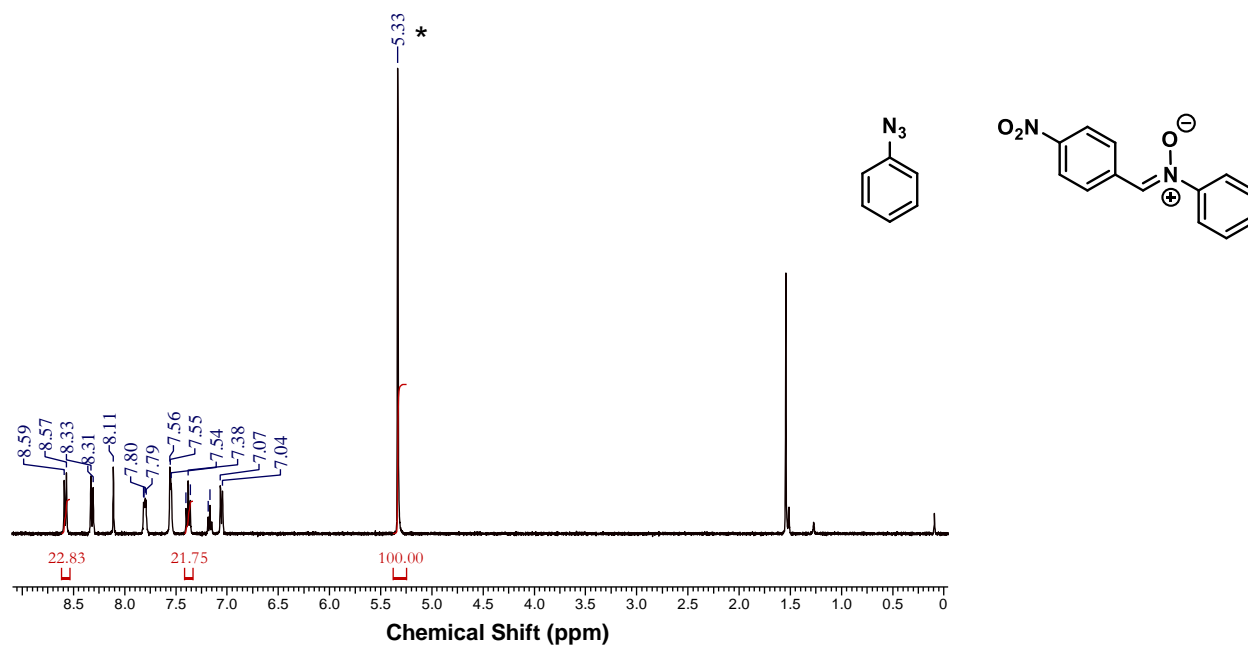


Figure S2.64. ^1H NMR spectrum of equimolar mixture of **azide 3** and **nitron 4** in CD_2Cl_2 at 25°C . * denotes residual protio solvent.

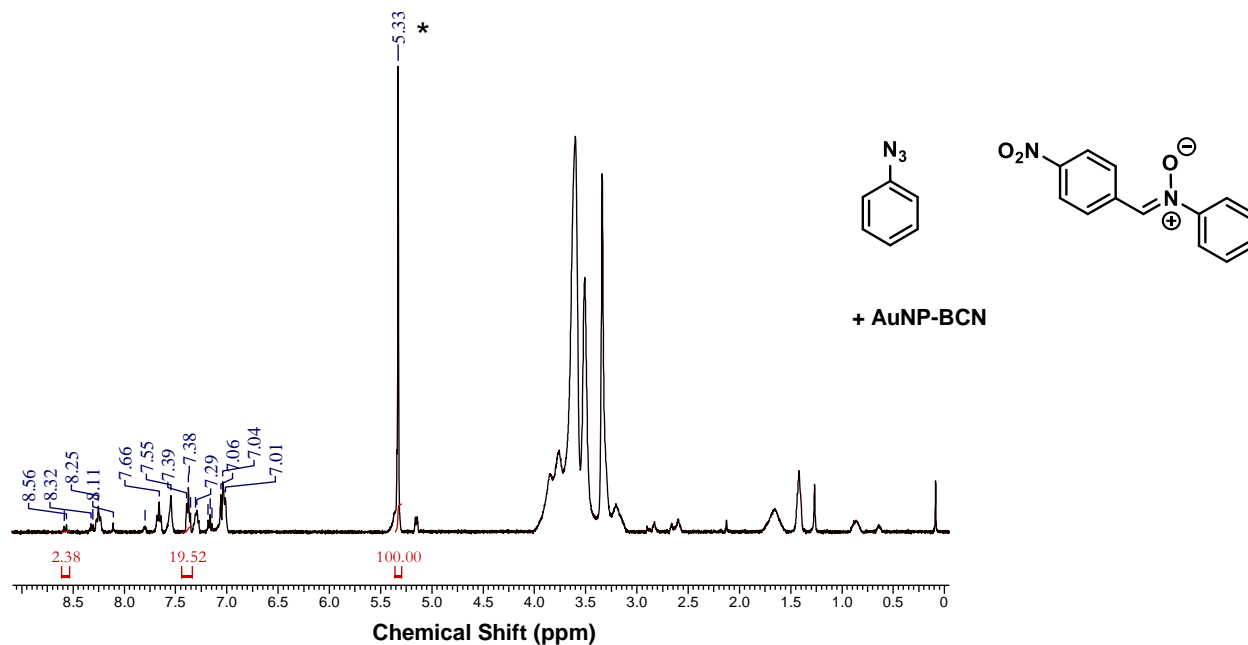


Figure S2.65. ^1H NMR spectrum of equimolar mixture of **azide 3** and **nitron 4** and interfacial BCN (in **AuNP-BCN**) in CD_2Cl_2 at 25°C . * denotes residual protio solvent.

2.6.6.4 ¹H NMR Spectra for Competition Experiment between azide 4 and nitrone 4

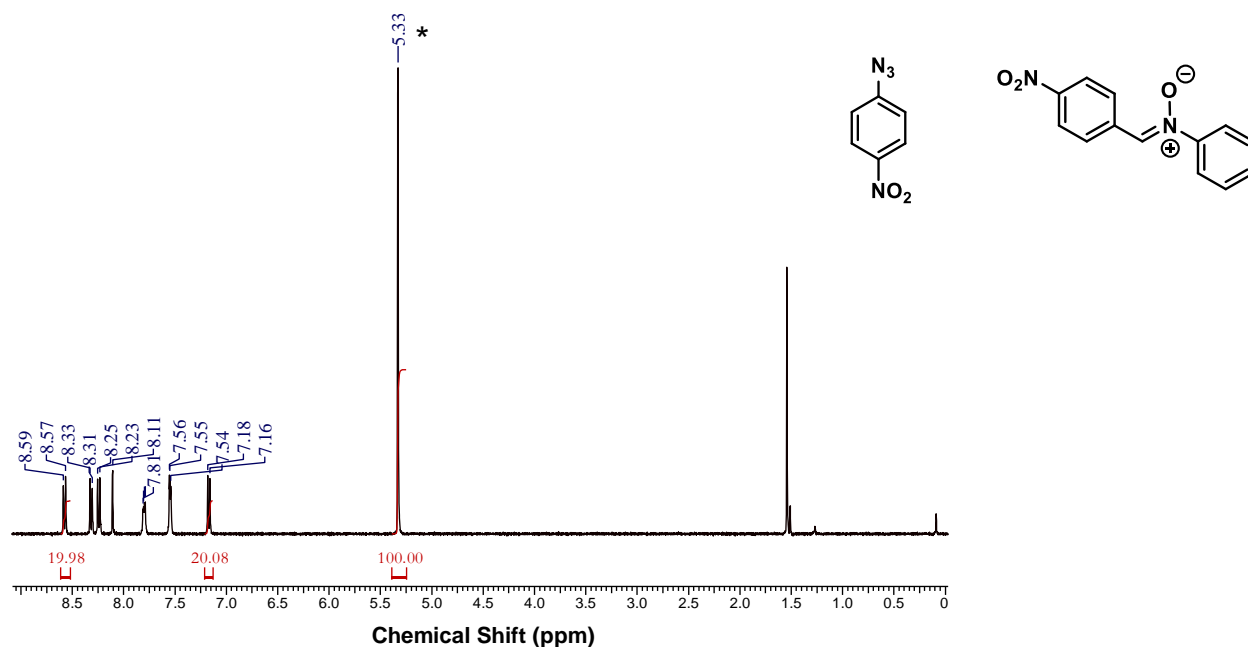


Figure S2.66. ¹H NMR spectrum of equimolar mixture of **azide 4** and **nitrone 4** in CD₂Cl₂ at 25°C. * denotes residual protio solvent.

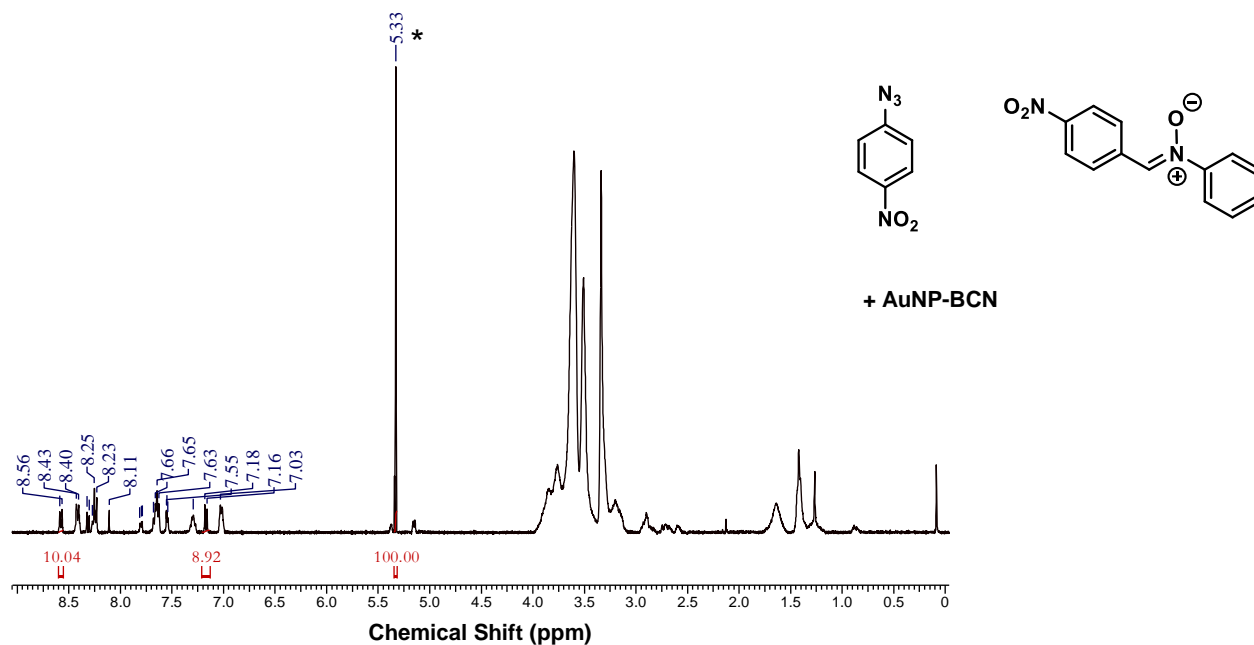


Figure S2.67. ¹H NMR spectrum of equimolar mixture of **azide 4** and **nitrone 4** and interfacial BCN (in **AuNP-BCN**) in CD₂Cl₂ at 25°C. * denotes residual protio solvent.

2.6.6.5 ^1H NMR Spectra for Competition Experiment between azide **5** and nitrone **2**

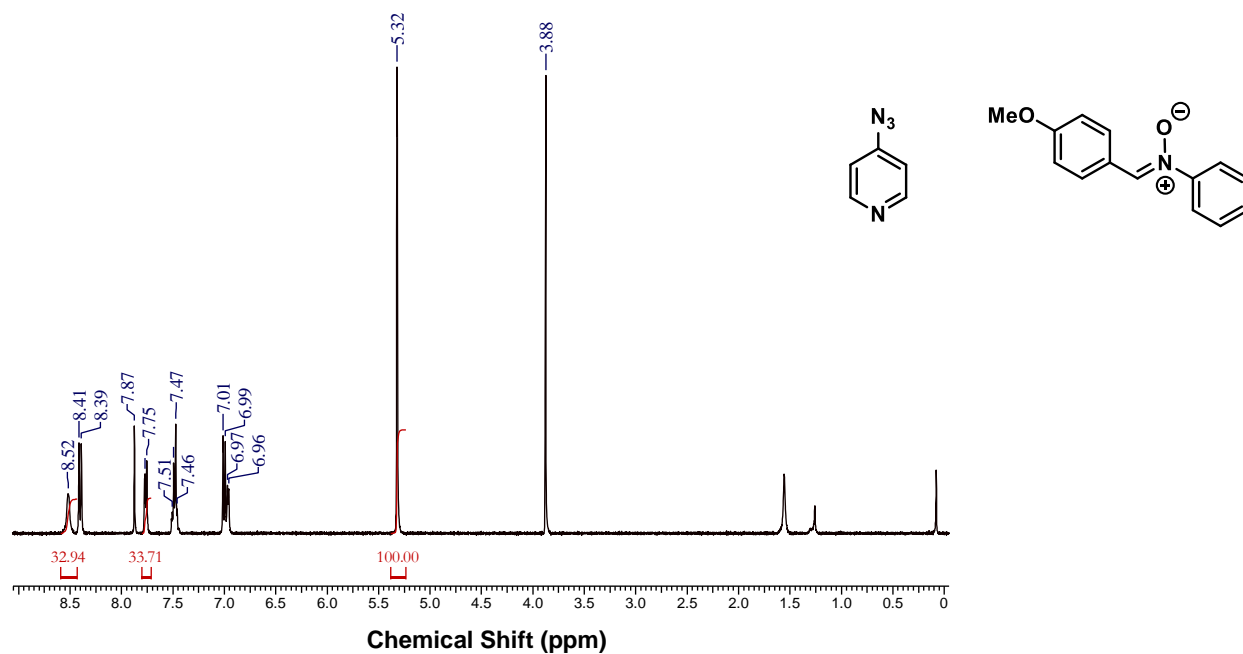


Figure S2.68. ^1H NMR spectrum of equimolar mixture of **azide 5** and **nitronium 2** in CD_2Cl_2 at 25°C . * denotes residual protio solvent.

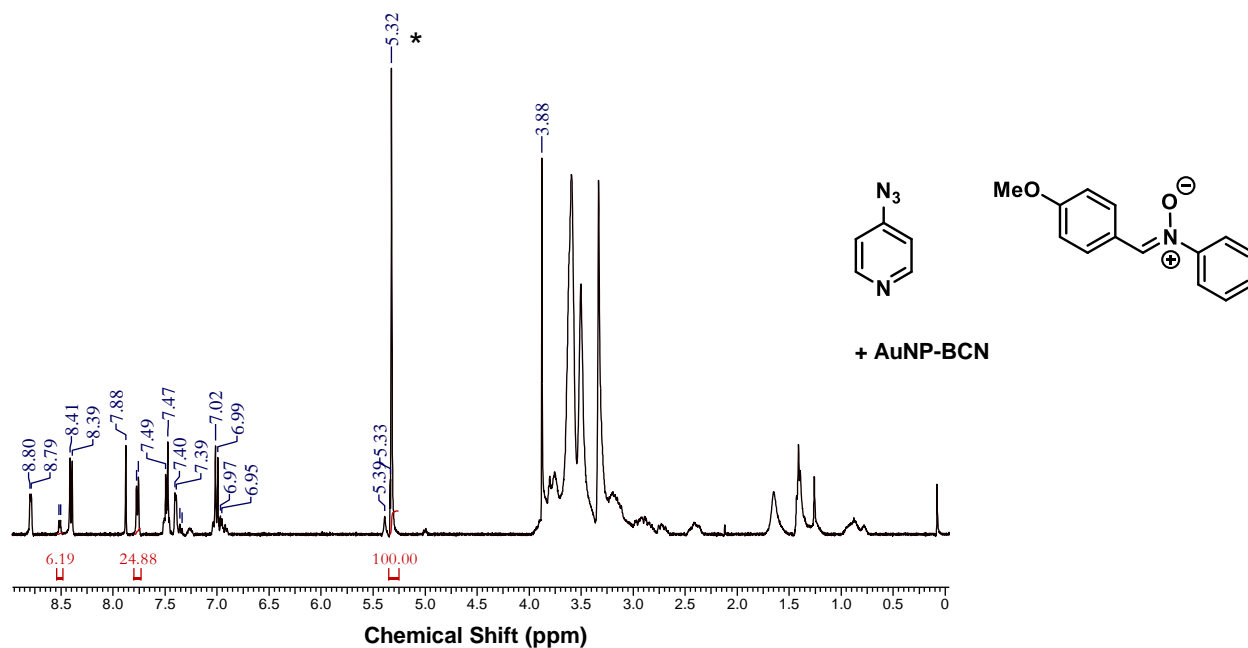


Figure S2.69. ^1H NMR spectrum of equimolar mixture of **azide 5** and **nitronium 2** and interfacial BCN (in AuNP-BCN) in CD_2Cl_2 at 25°C . * denotes residual protio solvent.

2.6.6.6 ^1H NMR Spectra for Competition Experiment between azide **6** and nitrone **1**

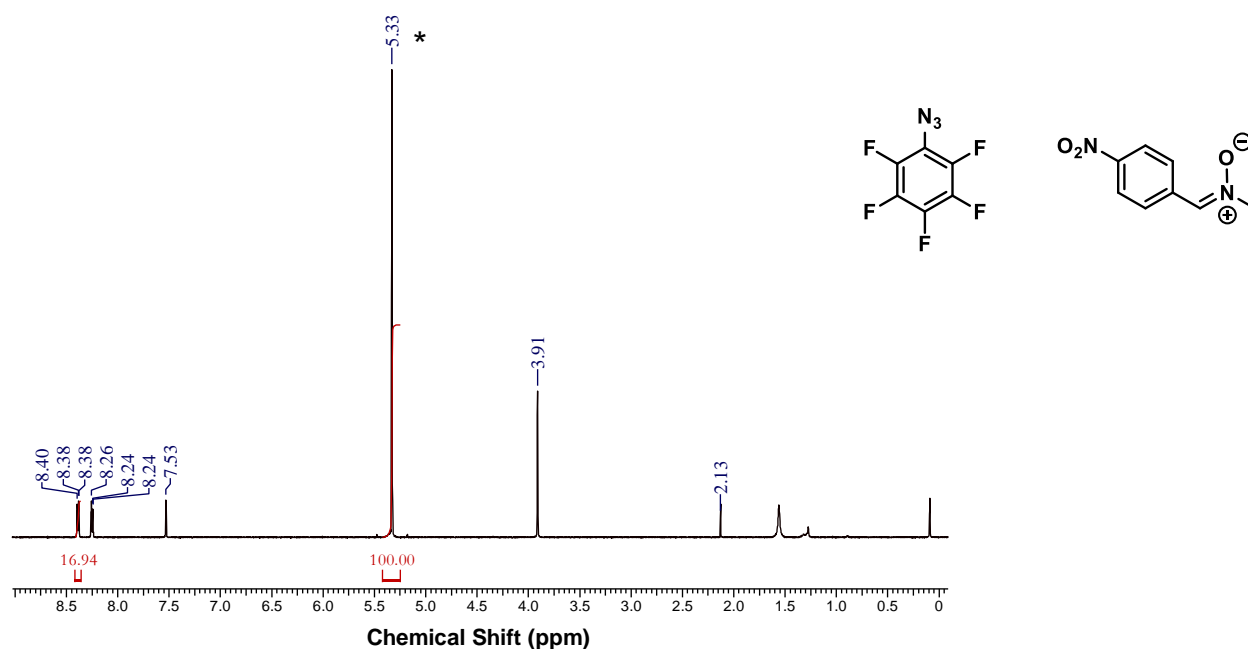


Figure S2.70. ^1H NMR spectrum of equimolar mixture of **azide 6** and **nitrone 1** in CD_2Cl_2 at 25°C . * denotes residual protio solvent.

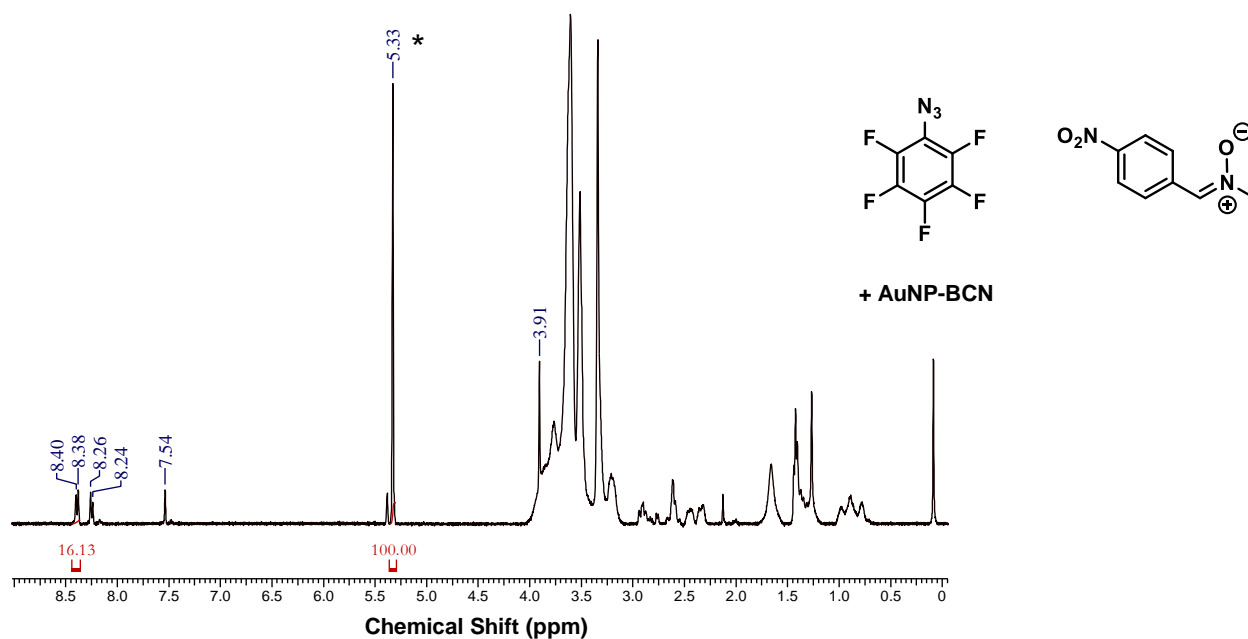


Figure S2.71. ^1H NMR spectrum of equimolar mixture of **azide 6** and **nitrone 1** and interfacial BCN (in AuNP-BCN) in CD_2Cl_2 at 25°C . * denotes residual protio solvent.

2.6.7. References for Supporting Information

1. Gobbo, P.; Workentin, M. S., Improved Methodology for the Preparation of Water-Soluble Maleimide-Functionalized Small Gold Nanoparticles. *Langmuir* **2012**, *28* (33), 12357-12363.
2. Gobbo, P.; Luo, W.; Cho, S. J.; Wang, X.; Biesinger, M. C.; Hudson, R. H. E.; Workentin, M. S., Small gold nanoparticles for interfacial Staudinger–Bertozzi ligation. *Org. Biomol. Chem.* **2015**, *13* (15), 4605-4612.
3. Dommerholt, J.; Schmidt, S.; Temming, R.; Hendriks, L. J. A.; Rutjes, F. P. J. T.; van Hest, J. C. M.; Lefeber, D. J.; Friedl, P.; van Delft, F. L., Readily Accessible Bicyclononynes for Bioorthogonal Labeling and Three-Dimensional Imaging of Living Cells. *Angew. Chem. Int. Ed.* **2010**, *49* (49), 9422-9425.
4. Kwok, S. W.; Fotsing, J. R.; Fraser, R. J.; Rodionov, V. O.; Fokin, V. V., Transition-Metal-Free Catalytic Synthesis of 1,5-Diaryl-1,2,3-triazoles. *Org. Lett.* **2010**, *12* (19), 4217-4219.
5. Jia, Z.; Zhu, Q., ‘Click’ assembly of selective inhibitors for MAO-A. *Bioorg. Med. Chem. Lett.* **2010**, *20* (21), 6222-6225.
6. Jin, L.-M.; Xu, X.; Lu, H.; Cui, X.; Wojtas, L.; Zhang, X. P., Effective Synthesis of Chiral N-Fluoroaryl Aziridines through Enantioselective Aziridination of Alkenes with Fluoroaryl Azides. *Angew. Chem. Int. Ed.* **2013**, *52* (20), 5309-5313.
7. Gunawardene, P. N.; Luo, W.; Polgar, A. M.; Corrigan, J. F.; Workentin, M. S., Highly Electron-Deficient Pyridinium-Nitrones for Rapid and Tunable Inverse-Electron-Demand Strain-Promoted Alkyne-Nitrone Cycloaddition. *Org. Lett.* **2019**, *21* (14), 5547-5551.

Chapter 3

3 Highly Electron-Deficient Pyridinium-Nitrones for Rapid and Tunable Inverse-Electron-Demand Strain-Promoted Alkyne-Nitrone Cycloaddition to Bicyclo[6.1.0]nonyne

This chapter has been published as a full paper, except for **Section 3.2.1** which describes unpublished results and discussion. The corresponding references is: P.N. Gunawardene, W. Luo, A.M. Polgar, John F. Corrigan, M.S. Workentin. *Org. Lett.* **2019**, *21*, *14*, 5547-5551.

Wilson Luo, under supervision by our supervisor Prof. Mark S. Workentin, assisted in the synthesis and characterization of some of the nitron and cycloadduct compounds. Alex M. Polgar, under supervision by Prof. John F. Corrigan, conducted DFT analysis on all nitron compounds and BCN_{exo}-OH. The draft of the manuscript was written by the author and edited by Prof. John F. Corrigan and Prof. Mark S. Workentin.

3.1 Introduction

Bimolecular strain-promoted cycloaddition reactions between cycloalkyne dipolarophiles and 1,3 dipoles are a subset of bioorthogonal ‘click’ reactions that have become a powerful tool in chemical biology¹⁻⁴ and nanomaterial science,⁵⁻⁸ for the fusion of two complex substrates that is otherwise inaccessible. Their practicality can be largely attributed to the high chemoselectivity and non-perturbing biocompatibility of the complementary reactive partners in the presence of other reactive moieties in both natural and synthetic settings.^{9, 10} At the same time, they maintain high reaction kinetics compared to other bioorthogonal reactions such as the Staudinger-Bertozzi ligation and thiol-maleimide reaction.¹¹ First developed by Bertozzi and co-workers, the prototype variant of such strain-promoted cycloaddition is the reaction between a cyclooctyne, which is the smallest stable cycloalkyne, and an azide dipole, and is more commonly known as the strain-promoted alkyne-azide cycloaddition (SPAAC).¹² A less well-known homologous variant of SPAAC is the reaction between a cyclooctyne and nitron dipole, and is termed the strain-promoted alkyne-nitron cycloaddition (SPANAC).¹³

In recent years, there has been a growing interest toward the acceleration of the reaction kinetics of both SPAAC and SPANC by tailoring the structure and electronic composition of the reactive partners to promote more favorable frontier orbital energy overlap. Such kinetic accelerations allow for tunable and rapid conjugation, reduces the effective concentration of expensively-modified labelling reagents,¹⁴ and provides a simple strategy for multi-component couplings. Initial efforts toward promoting faster cycloaddition kinetics focused on modifications to the cyclooctyne structure, but such strategies experience a problematic trade-off between cyclooctyne reactivity and stability. Benzoannulation of the cyclooctyne ring has furnished rapidly reactive strained-alkyne moieties, such as dibenzocyclooctyne (DBCO) and biarylazacyclooctynone (BARAC), but such rigidified aryl-fused strained-alkynes suffer from poor stability at ambient conditions. To mitigate these limitations, Dommerholt and co-workers developed an aliphatic cyclooctyne bicyclo[6.1.0]nonyne (BCN),¹⁵ that demonstrates exceptional stability and synthetic accessibility, but is kinetically less reactive than its benzoannulated counterparts. Regardless, the superior stability of BCN makes it a more convenient strained-alkyne to work with, compared to DBCO and BARAC.

Contemporary efforts toward enhancing the reaction kinetics of SPAAC/SPANC have converged on structural modifications to the complementary dipolar species. Delocalization of the dipolar species into electron-withdrawing substituents accelerates both SPAAC and SPANC reaction kinetics, while electron-donating substituents decelerate the reaction kinetics.^{14, 16, 17} It should be noted that, unlike SPAAC, an advantageous characteristic of SPANC is that there are three modifiable sites on the nitrene functionality, while terminal azides possess only one modifiable site. Much of the kinetic enhancement of SPANC has been pioneered by Pezacki and co-workers,^{14, 17} who demonstrated the kinetic consequences of substituent modifications on acyclic nitrenes, with their electron-deficient acyclic nitrenes having the most accelerated reaction rates. They proceeded to demonstrate that cyclic nitrenes possess even greater reaction kinetics through increasing the strain at the nitrene functionality. To the best of our knowledge, the fastest SPANC reaction between a cyclic nitrene and a stable cyclooctyne (BCN) has a bimolecular rate constant (k_2) of $1.5 \text{ M}^{-1}\text{s}^{-1}$ in methanol.¹⁷

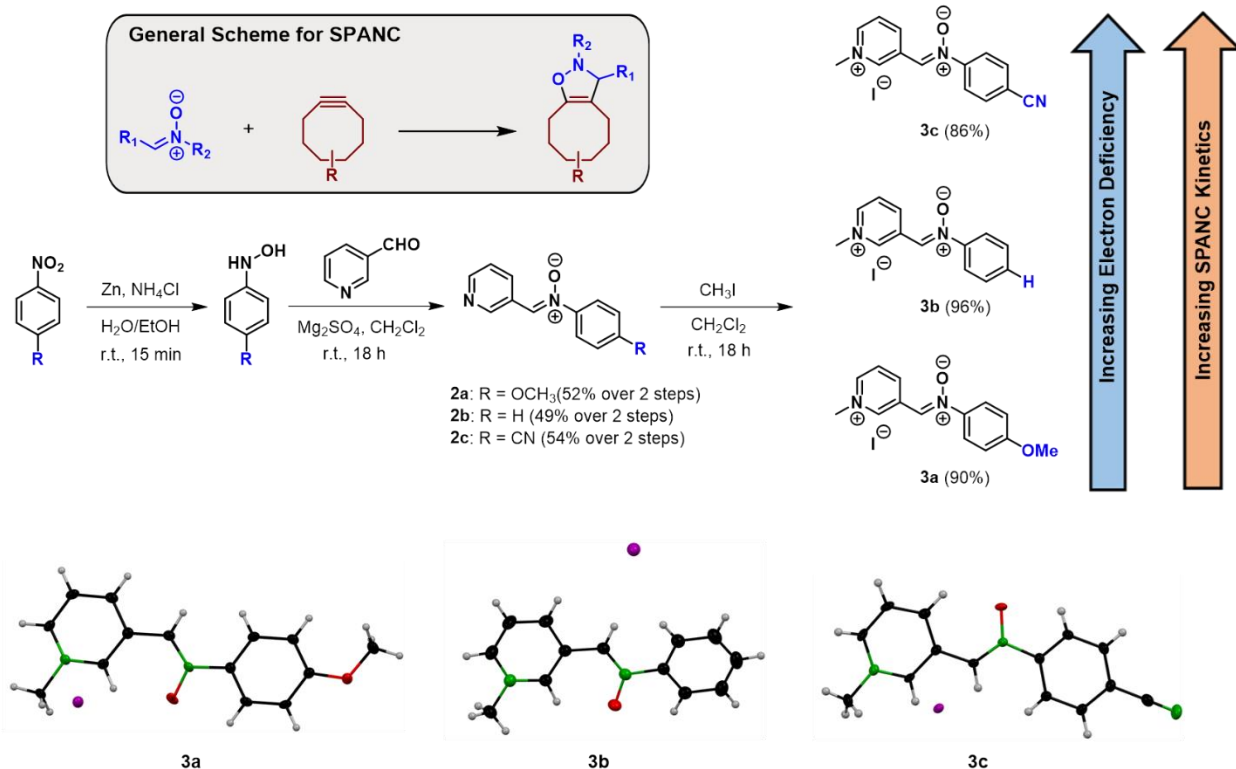
In order to investigate further acceleration of the SPANC reaction between a nitrene and BCN, we were intrigued by the fastest SPAAC reaction to BCN reported by Dommerholt and co-

workers,¹⁶ which occurs between a pyridinium-functionalized azide and BCN ($k_2 = 2.0 \text{ M}^{-1}\text{s}^{-1}$ in 9:1 THF:H₂O). We speculated that delocalizing the nitrono moiety into a pyridinium functionality would similarly hasten the SPANC reaction. To that end, we report rapid strain-promoted cycloaddition between a stable cyclooctyne (BCN_{exo}-OH) and highly electron-deficient nitrones possessing a pyridinium functionality on the nitrono α -carbon. The rapid reactivity of these “pyridinium-nitrones” can be rationalized in terms of favorable energetic overlap between the frontier orbitals of the two reactive partners, that is only observed through inclusion of the pyridinium functionality on the nitrono moiety. To further evaluate the tunability of the reaction kinetics and emphasize the advantageous opportunity for multi-site modifications to nitrones that cannot be achieved with azides, anisole (**3a**), phenyl (**3b**) and benzonitrile (**3c**) substituents were incorporated to the nitrono nitrogen, which results in substantial alterations to the kinetic profiles.

3.2 Results and Discussion

The three pyridinium-nitrones (**3a–c**) can be conveniently synthesized in gram-scale quantities using inexpensive, commercially available reagents and can be purified without the need of chromatography. They are made through condensation of the corresponding hydroxylamine onto 3-pyridinecarboxyaldehyde to generate the pyridine-nitrones (**2a–c**) in good yield, which can be subsequently *N*-alkylated using methyl iodide to generate the methylated pyridinium-nitrono species in high yield (**Scheme 3.1**). Due to the hydrophilicity of the pyridinium functionality, **3a–c** are most soluble in polar solvents such as dimethyl sulfoxide, acetonitrile, methanol and water. The characteristic ¹H NMR signals of **3a–c** are produced by the 2' aromatic proton in the pyridinium ring (**3a** and **3c**, 10.21 ppm and **3b**, 10.23 ppm) and the methyl protons of the pyridinium functionality (**3a**, 4.44 ppm, **3b** and **3c**, 4.46 ppm) (see **Section 3.5.7**). The infrared spectra of **3a–c** show a strong band between 1616–1629 cm⁻¹ that does not appear in the infrared spectra of **2a–c** (see **Section 3.6.2**) and can be assigned to C=N stretching vibrations characteristic of the quaternary nitrogen in the pyridinium ring.¹⁸

Single crystal X-ray crystallography has been used to verify the structures of **3a–c** (see **Section 3.6.16**), which confirms the planarity of the nitrono moiety and aromatic substituents, as

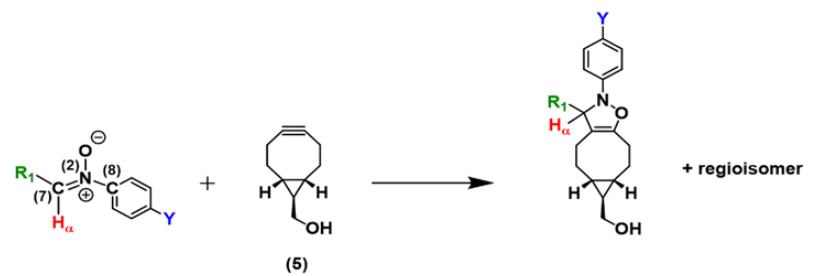


Scheme 3.1. Synthesis of pyridinium–nitrones possessing anisole (**3a**), phenyl (**3b**) and benzonitrile (**3c**) substituents. Top inset shows general scheme for strain–promoted alkyne–nitronium cycloaddition (SPANC) reaction between nitronium (blue) and cyclooctyne (red). Bottom: molecular structures of **3a**, **3b**, **3c** in the crystal. Thermal ellipsoids are drawn at the 50% probability level with hydrogen atoms drawn with arbitrary radii (black = carbon, red = oxygen, green = nitrogen, purple = iodine)

well as the trigonal planar geometry of the nitronium moiety. The bond length between the nitronium nitrogen (N₂) and α -carbon (C₇) in **3a–c** is consistent with previously reported C=N bond lengths in iminium ions ($\sim 1.305\text{\AA}$),¹⁹ which are longer than C=N bond lengths in imines ($\sim 1.279\text{\AA}$)²⁰ due to the larger single bond character in iminium ions. Interestingly, the crystallographic data indicates that there is a slight increase in this N₂–C₇ bond length in **3a–c** as increasingly electron–withdrawing substituents are fused to the nitronium moiety (**Table 3.1**), indicating a weakening of the N₂–C₇ double bond as more electron–withdrawing substituents are fused to the pyridinium–nitrones. Single crystal X-ray crystallography of model compounds **2b** and **4** are included for comparison. The molecular structure of **4** has been reported previously for data collected at room temperature,²¹ but the data included in **Table 3.1** is measured at 110 K for consistency with the data of **3a–3c**.

The reaction kinetics of **3a–c** with BCN_{exo}-OH (**5**) were evaluated under pseudo-first order conditions, according to a previously reported methodology using UV–Vis spectroscopy.¹⁷ A solvent mixture of 2:1 acetonitrile:tetrahydrofuran was used for this study, instead of methanol or water, to minimize any solvent–dependent acceleration in the more polar solvents that would make measuring the kinetics more difficult. This solvent choice was also chosen to minimize possible hydrolysis of the nitron, which was observed for **3b** in 6:1 D₂O:(CD₃)₂SO after 12 hours (although **3a** and **3c** were largely unaltered in this solvent after 12 hours) (see **Section 3.6.14**). Rate constants were measured in duplicate at 22°C (**Table 3.1**) by observing the decrease in absorption at 345 nm produced by the nitron moiety in **3a–c** that is not produced by the resulting isoxazoline product (see **Section 3.6.15**). It should be noted that the BCN_{exo}-OH isomer was used for this study as it produced in higher quantities during the strained–alkyne synthesis, but the *endo*–isomer can also be used as it would have similar kinetics. Mass spectrometry and NMR spectroscopy (in (CD₃)₂SO) was used to confirm that the pyridinium–nitrones undergoes the SPANC reaction with BCN_{exo}-OH (see **Section 3.6.10**). In addition to the three pyridinium–nitrones **3a–c**, the rate of reaction for two nitrones delocalized into a phenyl (**4**) and pyridine (**2b**) ring instead of a pyridinium ring was determined, by measuring the decrease in absorption at 316 nm and 320 nm, respectively. Nitron **4** displayed the slowest rate constant ($k_2 = 0.066 \text{ M}^{-1}\text{s}^{-1}$) in the series, due to the presence of the least electron-withdrawing α –carbon phenyl and *N*–phenyl substituents. Replacement of the α –carbon phenyl substituent with the more electron–withdrawing α –carbon pyridine substituent in nitron **2b** results in a two-fold acceleration ($k_2 = 0.15 \text{ M}^{-1}\text{s}^{-1}$). However, replacement of the α –carbon pyridine with an α –carbon pyridinium ring in **3b** results in an approximate twenty–fold acceleration in the reaction rate ($k_2 = 3.3 \text{ M}^{-1}\text{s}^{-1}$), which demonstrates the substantial acceleration of SPANC kinetics through pyridinium–conjugation. To illustrate the tunability of SPANC kinetics through the multi–site modification that only exists with SPANC, replacement of the *N*–phenyl substituent in **3b** with a more electron-donating *N*–anisole substituent in **3a** results in an approximate two-fold deceleration of the reaction rate ($k_2 = 1.6 \text{ M}^{-1}\text{s}^{-1}$). Conversely, exchange of the *N*–phenyl substituent in **3b** with the more electron-withdrawing *N*–benzonitrile substituent in **3c** triggered a significant three–fold acceleration in the reaction rate ($k_2 = 8.3 \text{ M}^{-1}\text{s}^{-1}$). This is the fastest click reaction between a dipolar species and BCN reported to date and represents a substantial improvement to the kinetic profile of strain–promoted cycloaddition chemistry.

Table 3.1. Key parameters of pyridinium–nitrones that vary as electron deficiency (and corresponding reactivity) is increased. ¹H NMR spectra were taken in deuterated dimethylsulfoxide at 25°C. Bond lengths were determined from crystallographic data. Mulliken charges (Q) and the energy gap between the HOMO of BCN and LUMO of the nitrone ($\Delta E_{\text{HOMO-LUMO}}$) were determined from DFT calculations. Bimolecular rate constants (k_2) were determined under pseudo-first order conditions in 2:1 acetonitrile:tetrahydrofuran at 22°C by UV-Vis spectroscopy.



		¹ H NMR δ of H_α (ppm)	N2–C7 Bond Length (Å)	N2–C8 Bond Length (Å)	Q at C7 (a.u.)	$\Delta E_{\text{BCN}_{\text{HOMO}}-\text{Nitron}_{\text{LUMO}}}$ (eV)	k_2 ($\text{M}^{-1}\text{s}^{-1}$)
4	R ₁ = phenyl Y = H	8.50	1.3126(17)	1.4612(16)	-0.0412	-4.81	0.066 ± 0.004
2b	R ₁ = pyridine Y = H	8.63	1.3126(12)	1.4555(12)	-0.0360	-4.58	0.15 ± 0.01
3a	R ₁ = pyridinium–CH ₃ Y = OCH ₃	8.91	1.305(4)	1.459(4)	-0.0371	-0.532	1.6 ± 0.1
3b	R ₁ = pyridinium–CH ₃ Y = H	8.98	1.3130(15)	1.4607(15)	-0.0302	-0.335	3.3 ± 0.2
3c	R ₁ = pyridinium–CH ₃ Y = CN	9.07	1.314(4)	1.485(4)	-0.0255	-0.0533	8.3 ± 0.3

To illustrate the flexibility of the reaction to solvent choice (that may be applicable for future biological applications), the SPANC reaction between **3c** and BCN_{exo}-OH was successfully carried out and products confirmed by ¹H NMR spectroscopy in 6:1 D₂O:(CD₃)₂SO, 1:1 D₂O:(CD₃)₂SO and CD₃OD (see **Section 3.6.11**). Furthermore, the generality of the reaction between **3c** and different strained alkynes other than BCN_{exo}-OH was probed by challenging **3c** to commercially available dibenzycyclooctyne-amine (DBCO-amine) (see **Section 3.6.12**) and a small symmetrical strained-alkyne, (Z)-cyclooct-1-ene-5-yne (**6b**) (see **Section 3.6.13**). Both SPANC reactions were confirmed by NMR spectroscopy and mass spectrometry.

¹H NMR spectroscopy allows for simple, preliminary estimations of nitronium reactivity by comparing the chemical shift of the H_α in the nitronium moiety. As shown in **Table 3.1**, the H_α in the electron-rich nitronium **3a**, which has the slowest reaction kinetics, has the lowest chemical shift (8.91 ppm). Incorporation of increasingly electron-deficient substituents results in ¹H NMR signal

of the H_α appearing at higher chemical shifts as the kinetic reactivity is increased, increasing to 8.98 ppm in **3b** and 9.07 ppm in **3c**. Determination of Mulliken atomic charges²² show that better electron withdrawing groups result in a smaller partial negative charge on the α -carbon (C_7) (**Table 3.1**), which is a consequence of a less electron-rich nitrone moiety and rationalizes the observed deshielding of the H_α as more electron-withdrawing substituents are fused to the pyridinium-nitrone.

The reactivity differences between **3a-c** were probed by density functional theory (DFT) computations using the GAUSSIAN09²³ suite of software at the level B3LYP/6-31G*.^{24,25} The geometries of the three pyridinium-nitrones were optimized and agree closely with the crystallographic data (see **Section 3.6.17**). The DFT data confirms that, as reported by Dommerholt and co-workers for the SPAAC reaction,¹⁷ the SPANC reaction proceeds via an inverse electron-demand mechanism (IED-SPANC). That is, the frontier orbitals involved in the SPANC reaction are the HOMO of **5**, which is localized mainly on the C-C triple bond, and the LUMO of the pyridinium-nitrones, which is delocalized primarily over the both the nitrone and pyridinium moieties, but also has contributions from the nitrone *N*-substituent (**Figure 3.1**). Because of these contributions, the energy of the LUMO in IED-SPANC varies according to the electronic nature of the *N*-substituent on the nitrone moiety, with the electron-donating anisole

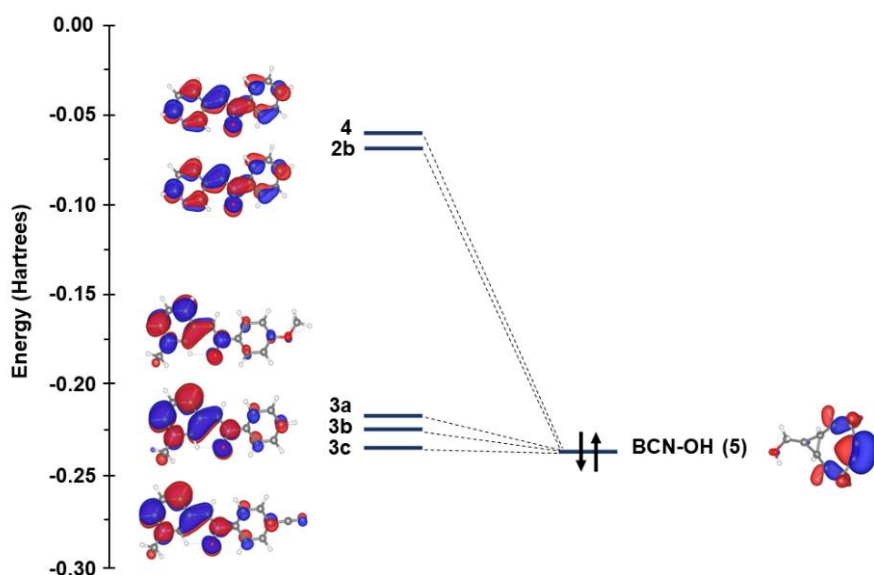


Figure 3.1. Isosurface plots (isoval = 0.03 e au^{-3}) for the HOMO of $\text{BCN}_{\text{exo}}\text{-OH}$ (**5**) and the LUMO of **3a-c**, **4**, **2b**, and energy diagram of the frontier orbitals involved in SPANC between **3a-c**, **4**, **2b** and $\text{BCN}_{\text{exo}}\text{-OH}$ (**5**).

substituent in **3a** destabilizing the LUMO relative to **3b**, and the electron-withdrawing benzonitrile substituent in **3c** lowering the LUMO energy relative to **3b**. This stabilizing effect results in the convergence of the pyridinium-nitrono LUMO energy level and the HOMO energy level of **5** in the IED-SPANC reaction (**Table 3.1**). The expected rate enhancement can hence be rationalized in terms of favorable energetic overlap between the two reactants when more electron-withdrawing nitrono *N*-substituents are present. In fact, our DFT calculations indicate that **3c** possesses a miniscule HOMO_{BCN}-LUMO_{nitrono} energy gap (-0.0533 eV). This suggests that **3c** is a highly idealized reactive partner for BCN (a stable cyclooctyne), and that any additional tuning to accelerate the reactivity further may provide only small enhancements to the cycloaddition reaction to BCN.

3.2.1 Towards the Development of Pyridinium-Functionalized Gold Nanoparticles

Having developed a general methodology for synthesizing pyridinium-functionalized nitrones, the ability to execute such rapid and tunable SPANC chemistry on the surface of gold nanoparticles (AuNPs) was investigated. AuNPs was chosen for this prototype study because they are easy to synthesize in high yield compared to other nanomaterial systems, and can be easily characterized by ¹H NMR spectroscopy, allowing for straightforward analyses of modifications to the organic surface structure. Given the potential use of functionally complex AuNPs in a variety of applications in biomedicine, imaging and nanoscience, the ability to implement rapid SPANC chemistry to tether functional substrates (such as biological macromolecules, targeting agents and other nanomaterial systems) to the surface of AuNPs would be a worthwhile investigation.

AuNPs are typically synthesized in the presence of moderate reducing agents, such as NaBH₄, in the presence of a thiol ligand (RSH) that serves to encircle and protect the interior metallic core. Given the chemical sensitivity of many functional substrates, direct synthetic strategies with a thiol ligand that has a functional substrate incorporated onto it is often unfeasible because of incompatibilities with reducing conditions of the synthesis. For this reason, the most common strategy to incorporate functional substrates to the surface of AuNPs is through place exchange chemistry, in which the inert AuNP system is mixed with a functional thiol ligand, and native inert thiol ligands are exchanged with the incoming functional thiol. The most common

problem with this strategy is that protection-deprotection strategies are often required to tether functional substrates to thiol ligands, which is often chemically incompatible with the functional substrate. Given this limitation, our group explores methodologies in which post-assembly modifications can be used, in which a AuNP platform is created that has a reactive group tethered to the surface, after which a functional substrate with the complementary reactive group can be added and reacts exclusively with the reactive group on the AuNP surface. To this end, if the reactive pyridinium-nitrone moiety could be incorporated to the gold nanoparticle surface, then functional substrates with the complementary strained-alkyne moiety could be tethered to the surface through rapid interfacial SPANC. Furthermore, if multiple nitrone moieties could be incorporated to the AuNP surface, each having a different kinetic profile, then this would provide temporal and kinetic control over surface modification chemistry, allowing for the development of multi-functional AuNP systems.

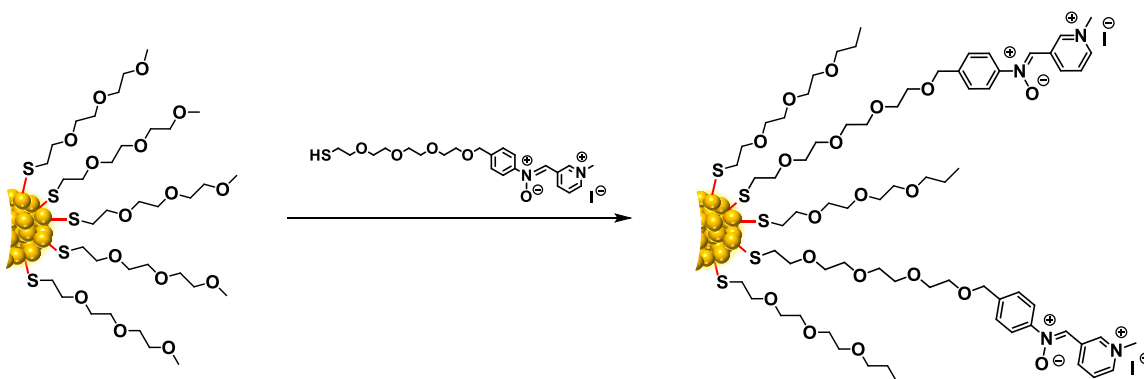
As with the bicyclononyne-functionalized gold nanoparticle system describe in **Chapter 2**, the inert AuNP system that was chosen was methoxy-functionalized AuNPs (**AuNP-OMe**), because they can be synthesized in high yield, easily characterizable, and are soluble in a variety of solvents. It was proposed that if this **AuNP-OMe** were mixed with a tetraethylene glycol (TEG)-based thiol ligand possessing a terminal pyridinium-nitrone moiety, then the pyridinium-nitrone moiety could be incorporated to the AuNP surface through place exchange chemistry (**Scheme 3.2a**).

The synthetic strategy for the proposed TEG-based pyridinium-nitrone-functionalized thiol ligand is shown in **Scheme 3.2b** (see **Section 3.6.4** for experimental details). First, tetraethylene glycol was monosubstituted with nitrobenzyl bromide in the presence of sodium hydride to give **A**, which was subsequently tosylated at the alcohol moiety (to give **B**) and then substituted once more with potassium thioacetate to give **C**, which possessed a protected thiol in the form of a thioacetate moiety. Then, the nitrophenyl-moiety was transformed into the pyridinium-nitrone moiety, using the same general strategy as described in **Section 3.2**, to give **E**.

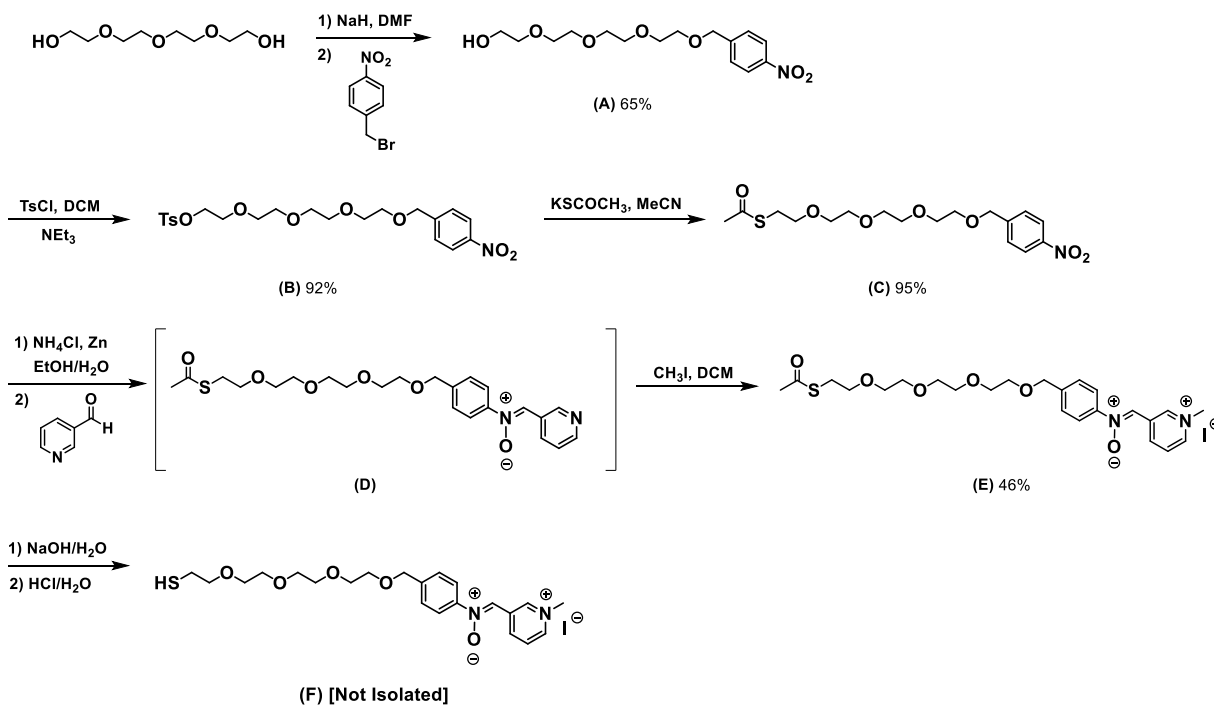
Having successfully made compound **E**, the final step was the deprotection of the thioacetate moiety by saponification with sodium hydroxide to give the corresponding thiolate moiety, and the subsequent protonation with hydrochloric acid to give the desired thiol ligand **F**.

However, this step was unsuccessful, due to the sensitivity of the pyridinium-nitronne moiety. It has been reported that nitronne moieties are prone to hydrolysis in the presence of acidic species, splitting the nitronne moiety apart into the parent aldehyde and amine moieties.^{14,17} Even at the dilute concentrations of hydrochloric acid used during the deprotection strategy, there was significant hydrolysis observed, with only a small amount of compound **F** being formed. Furthermore, once the small amount of compound **F** that formed was isolated and purified, it

(a) Proposed Synthesis for Pyridinium-Nitronne-Functionalized AuNPs



(b) Synthesis of Pyridinium-Functionalized Thiol Ligand



Scheme 3.2. (a) Proposed synthetic strategy for incorporating the pyridinium-nitronne moiety to the surface of AuNPs, using a pyridinium-functionalized thiol ligand. (b) Synthetic strategy for pyridinium-functionalized thiol ligand.

underwent further hydrolysis on its own quite rapidly, preventing characterization of **F** entirely. This indicated that, even if it could be synthesized, the pyridinium-nitrone moiety was not compatible with the thiol moiety. Although the pyridinium-nitrone moiety was demonstrated to be quite stable in the presence of water and alcohol solvents towards undesired hydrolysis, as described and shown in **Section 3.2**, **Section 3.6.11** and **Section 3.6.14**, the higher acidity of SH moieties (compared to OH moieties) makes the pyridinium-nitrone moiety more susceptible to hydrolysis in the presence of SH moieties. This susceptibility prevents the thiol moiety from being tethered to a ligand possessing a pyridinium-nitrone moiety, which unfortunately prevents the pyridinium-nitrone moiety from being incorporated to the surface of AuNPs.

3.3 Conclusion

In conclusion, the incorporation of pyridinium functionalities into nitrone moieties serves as a simple method for substantial acceleration of IED SPANC to BCN. As benzoannulated cyclooctynes are comparatively unstable and expensive to synthesize, it is highly beneficial to utilize more stable aliphatic strained-alkynes like BCN. Furthermore, the acceleration of the cycloaddition reaction serves as an important tool for the efficient conjugation of expensively-modified substrates in chemical biology and nanomaterial sciences to produce reliable and reproducible results at nano- and pico-molar concentrations. It is important to note that our approach not only creates a general method for acceleration of the SPANC reaction, but also incorporates an additional modifiable site: the pyridine functionality. In this prototype study we coupled a methyl group to the pyridine functionality to simplify the analysis. However, given the numerous methodologies for *N*-alkylation of pyridine rings, it should be possible to incorporate the pyridinium-nitrone moiety with alkyl ligands bearing additional functionality for applications using such methodologies, while retaining the rapid kinetics of the pyridinium-nitrone moiety. We are currently exploring such methodologies.

3.4 Acknowledgements

This work was funded by NSERC-DG and the University of Western Ontario. We would like to thank D. Hairsine (ESI-MS Facility) and P. Boyle (X-Ray Facility).

3.5 References

1. Laughlin, S. T.; Baskin, J. M.; Amacher, S. L.; Bertozzi, C. R., In Vivo Imaging of Membrane-Associated Glycans in Developing Zebrafish. *Science* **2008**, *320* (5876), 664.
2. MacKenzie, D. A.; Sherratt, A. R.; Chigrinova, M.; Cheung, L. L. W.; Pezacki, J. P., Strain-promoted cycloadditions involving nitrones and alkynes—rapid tunable reactions for bioorthogonal labeling. *Curr. Opin. Chem. Biol.* **2014**, *21*, 81-88.
3. Saxon, E.; Bertozzi, C. R., Cell Surface Engineering by a Modified Staudinger Reaction. *Science* **2000**, *287* (5460), 2007.
4. Sletten, E. M.; Bertozzi, C. R., From Mechanism to Mouse: A Tale of Two Bioorthogonal Reactions. *Acc. Chem. Res.* **2011**, *44* (9), 666-676.
5. Canalle, L. A.; van Berkel, S. S.; de Haan, L. T.; van Hest, J. C. M., Copper-Free Clickable Coatings. *Adv. Funct. Mater.* **2009**, *19* (21), 3464-3470.
6. Gobbo, P.; Mossman, Z.; Nazemi, A.; Niaux, A.; Biesinger, M. C.; Gillies, E. R.; Workentin, M. S., Versatile strained alkyne modified water-soluble AuNPs for interfacial strain promoted azide–alkyne cycloaddition (I-SPAAC). *J. Mater. Chem. B* **2014**, *2* (13), 1764-1769.
7. Kardelis, V.; Chadwick, R. C.; Adronov, A., Click Functionalization of a Dibenzocyclooctyne-Containing Conjugated Polyimine. *Angew. Chem. Int. Ed.* **2016**, *55* (3), 945-949.
8. Orski, S. V.; Poloukhine, A. A.; Arumugam, S.; Mao, L.; Popik, V. V.; Locklin, J., High Density Orthogonal Surface Immobilization via Photoactivated Copper-Free Click Chemistry. *J. Am. Chem. Soc.* **2010**, *132* (32), 11024-11026.
9. Prescher, J. A.; Dube, D. H.; Bertozzi, C. R., Chemical remodelling of cell surfaces in living animals. *Nature* **2004**, *430* (7002), 873-877.
10. Sletten, E. M.; Bertozzi, C. R., Bioorthogonal Chemistry: Fishing for Selectivity in a Sea of Functionality. *Angew. Chem. Inter. Ed.* **2009**, *48* (38), 6974-6998.

11. Dommerholt, J.; Rutjes, F. P. J. T.; van Delft, F. L., Strain-Promoted 1,3-Dipolar Cycloaddition of Cycloalkynes and Organic Azides. *Top. Curr. Chem.* **2016**, *374* (2), 16.
12. Agard, N. J.; Prescher, J. A.; Bertozzi, C. R., A Strain-Promoted [3 + 2] Azide–Alkyne Cycloaddition for Covalent Modification of Biomolecules in Living Systems. *J. Am. Chem. Soc.* **2004**, *126* (46), 15046-15047.
13. Ning, X.; Temming, R. P.; Dommerholt, J.; Guo, J.; Ania, D. B.; Debets, M. F.; Wolfert, M. A.; Boons, G.-J.; van Delft, F. L., Protein Modification by Strain-Promoted Alkyne–Nitrene Cycloaddition. *Angew. Chem. Int. Ed.* **2010**, *49* (17), 3065-3068.
14. McKay, C. S.; Moran, J.; Pezacki, J. P., Nitrenes as dipoles for rapid strain-promoted 1,3-dipolar cycloadditions with cyclooctynes. *Chem. Commun.* **2010**, *46* (6), 931-933.
15. Dommerholt, J.; Schmidt, S.; Temming, R.; Hendriks, L. J. A.; Rutjes, F. P. J. T.; van Hest, J. C. M.; Lefeber, D. J.; Friedl, P.; van Delft, F. L., Readily Accessible Bicyclononynes for Bioorthogonal Labeling and Three-Dimensional Imaging of Living Cells. *Angew. Chem. Int. Ed.* **2010**, *49* (49), 9422-9425.
16. Dommerholt, J.; van Rooijen, O.; Borrmann, A.; Guerra, C. F.; Bickelhaupt, F. M.; van Delft, F. L., Highly accelerated inverse electron-demand cycloaddition of electron-deficient azides with aliphatic cyclooctynes. *Nat. Commun.* **2014**, *5* (1), 5378.
17. MacKenzie, D. A.; Pezacki, J. P., Kinetics studies of rapid strain-promoted [3+2] cycloadditions of nitrenes with bicyclo[6.1.0]nonyne. *Can. J. Chem.* **2014**, *92* (4), 337-340.
18. Spinner, E., 717. The vibration spectra of some monosubstituted pyridines and pyridinium ions. *J. Chem. Soc.* **1963**, (0), 3860-3870.
19. Evans, G. J. S.; White, K.; Platts, J. A.; Tomkinson, N. C. O., Computational study of iminium ion formation: effects of amine structure. *Org. Biomol. Chem.* **2006**, *4* (13), 2616-2627.
20. Allen, F. H.; Kennard, O.; Watson, D. G.; Brammer, L.; Orpen, A. G.; Taylor, R., Tables of bond lengths determined by X-ray and neutron diffraction. Part 1. Bond lengths in organic compounds. *J. Chem. Soc., Perkin Trans. 2* **1987**, (12), S1-S19.

21. Gothelf, K.V.; Hazell, R.G.; Jorgensen K.A., On the structure of C,N-Diphenylnitrone in 1,3-Dipolar Cycloaddition Reactions. *Acta Chem. Scand.* **1997**, *51*, 1234-1235.
22. Milliken, R.S., Electronic Population Analysis on LCAO-MO Molecular Wave Functions. *I. J. Chem. Phys.*, **1955**, *23*, 1833-1840.
23. Frisch M. J.; Trucks G. W.; Schlegel H. B.; Scuseria G. E.; Robb M. A.; Cheeseman J. R.; Scalmani G.; Barone V.; Petersson G. A.; Nakatsuji H.; Li X.; Caricato M.; Marenich A.; Bloino J.; Janesko B. G.; Gomperts R.; Mennucci B.; Hratchian H. P.; Ortiz J. V.; Izmaylov A. F.; Sonnenberg J. L.; Williams-Young D.; Ding F.; Lipparini F.; Egidi F.; Goings J.; Peng B.; Petrone A.; Henderson T.; Ranasinghe D.; Zakrzewski V. G.; Gao J.; Rega N.; Zheng G.; Liang W.; Hada M.; Ehara M.; Toyota K.; Fukuda R.; Hasegawa J.; Ishida M.; Nakajima T.; Honda Y.; Kitao O.; Nakai H.; Vreven T.; Throssell K.; Montgomery, Jr. J. A.; Peralta J. E.; Ogliaro F.; Bearpark M.; Heyd J. J.; Brothers E.; Kudin K. N.; Staroverov V. N.; Keith T.; Kobayashi R.; Normand J.; Raghavachari K.; Rendell A.; Burant J. C.; Iyengar S. S.; Tomasi J.; Cossi M.; Millam J. M.; Klene M.; Adamo C.; Cammi R.; Ochterski J. W.; Martin R. L.; Morokuma K.; Farkas O.; Foresman J. B.; Fox D. J. *Gaussian 09, Revision A.02*, **2016**, Gaussian, Inc., Wallingford CT.
24. Becke, A.D.; A new mixing of Hartree-Fock and local density-functional theories. *J. Chem. Phys.* **1993**, *98*, 1372.
25. Lee, C.; Yang, W.; Parr, R.G. Development of the Colle-Salvetti correlation-energy formula into a functional of the electron density. *Phys. Rev. B.*, **1988**, *37*, 785.

3.6 Supporting Information

3.6.1 General Materials and Methods

Reagents and Solvents. The following materials were used as received. 4-nitroanisole, zinc dust (<10 μ m, \geq 98%), 3-pyridinecarboxaldehyde (98%), iodomethane (99.5%), nitrobenzene (\geq 99%), 4-nitrobenzotrile (97%), benzaldehyde (\geq 99.5%), dibenzocyclooctyne-amine, dimethyl sulfoxide-D₆ ((CD₃)₂SO, 99.96 atom %D), methanol-D₄ (CD₃OD, 99.8% atom %D)

dichloromethane-D₂ (CD₂Cl₂, 99.5 atom %D) and water-D₂ (D₂O, 99.9% atom %D) were purchased from Sigma-Aldrich (Millipore Sigma). Chloroform-D₁ (99.8 atom %D) was purchased from Cambridge Isotope Laboratories. Technical grade ammonium chloride, magnesium sulphate, hexanes, dichloromethane, dimethyl sulfoxide, di-ethyl ether, methanol, acetonitrile were purchased from Caledon. Ethanol (anhydrous) was purchased from Commercial Alcohols.

Unless otherwise state, all reactions were performed at ambient conditions.

NMR Spectroscopy. ¹H and ¹³C{¹H} spectra were recorded on a Bruker AvIII HD 400 spectrometer. ¹H NMR spectra are reported as δ in units of parts per million (ppm), and referenced against residual protio dimethylsulfoxide (2.50 ppm, quin), water (4.75 ppm, s) or methanol (3.31 ppm, quin; 4.87 ppm, s) as indicated. Multiplicities are reported as follows: s (singlet), d (doublet), t (triplet), quin (quintuplet), m (multiplet), dt (doublet of triplets) and dd (doublet of doublets). Coupling constants are reported as a *J* value in Hertz (Hz) according to the spectrometer frequency. The number of protons (*n*) for a given resonance is indicated as *n*H, and is based on spectral integration values. ¹³C{¹H} NMR spectra are reported as δ in units of parts per million (ppm) and referenced against the indicated deuterated solvent: dimethylsulfoxide-D₆ (39.5 ppm, septet), chloroform-D₁ (77.0 ppm, t).

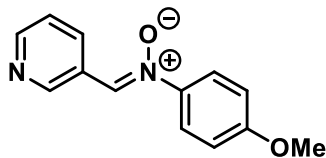
Mass Spectrometry. Electrospray ionization (ESI) mass spectra were obtained in positive-ion mode using a Bruker microTOF II spectrometer.

UV-Visible (UV-Vis) Spectroscopy. UV-Vis absorption spectra were recorded using a Cary 5000 scan instrument using standard quartz cells (1cm path length) with a scan range of 200-1000nm. The background spectrum of the indicated solvent was subtracted internally by the software.

Infrared (IR) spectroscopy. Attenuated total reflectance IR (ATR-IR) spectra were recorded using a PerkinElmer Spectrum Two FT-IR spectrometer.

3.6.2 Synthesis of Nitrones

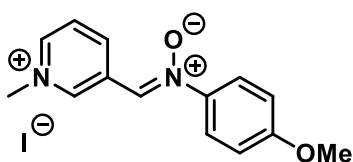
3.6.2.1 Synthesis of *N*-(4-methoxyphenyl)-*C*-(3-pyridine) Nitronone (2a)



To 1.0 g (6.5 mmol, 1eq) 4-nitroanisole and 0.37 g (7.0 mmol, 1.1 eq) ammonium chloride in 10 mL distilled water and 10 mL ethanol was added 1.3 g (20 mmol, 3eq) zinc dust portion-wise over 10 minutes at room temperature. The resulting heterogenous mixture was stirred vigorously for 20 minutes, after which the insoluble solid was removed by vacuum filtration. The supernatant was diluted with brine (50 mL) and extracted with diethyl ether (3 x 10 mL), dried over magnesium sulphate and concentrated to give the *crude hydroxylamine* as an off-white solid, which was used without further purification.

To the *crude hydroxylamine* in 15 mL dichloromethane was added 1.2 mL (13 mmol, 2 eq) 3-pyridinecarboxaldehyde and a small amount of magnesium sulphate. The resulting heterogenous mixture was stirred overnight, after which the magnesium sulphate was removed by vacuum filtration. The supernatant was concentrated via rotary evaporation and the crude residue was purified by dissolving in minimal dichloromethane and precipitating the product out with excess di-ethyl ether at -20°C overnight to give *N*-(4-methoxyphenyl)-*C*-(3-pyridine) nitronone (**2a**) as an off-white crystalline solid in 52% overall yield (0.79 g, 3.4 mmol). ¹H NMR ((CD₃)₂SO, 400 MHz): δ 9.38 (d, J=1.6 Hz, 1H), 8.97 (dt, J₁=8.0 Hz, J₂ = 1.6 Hz, 1H), 8.62 (dd, J₁ = 4.8 Hz, J₂ = 1.6 Hz, 1H), 8.56 (s, 1H), 7.90 (m, 2H), 7.52 (dd, J₁ = 8.0 Hz, J₂ = 4.8 Hz, 1H), 7.09 (m, 2H), 3.84 (s, 3H). ¹³NMR ((CD₃)₂SO, 400 MHz): δ 159.9, 149.9, 149.4, 141.0, 134.1, 129.6, 127.2, 123.1, 122.3, 113.6, 55.2. HRMS (ESI) *m/z* calc. for C₁₃H₁₂N₂O₂ (M)⁺: 228.0899, found: 228.0867. IR (ATR, cm⁻¹): 3134, 3044, 2947, 2838, 1597, 1550, 1501, 1301, 1249, 1169, 1078, 1029.

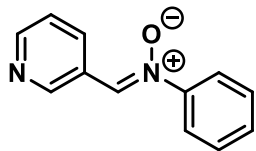
3.6.2.2 Synthesis of *N*-(4-methoxyphenyl)-*C*-(3-methylpyridinium) Nitronone (3a)



To 0.20 g (0.88 mmol, 1eq) *N*-(4-methoxyphenyl)-*C*-(3-pyridine) nitronone (**2a**) in 4 mL dry dichloromethane was added 0.54 mL (8.8 mmol, 10 eq) iodomethane. The colorless solution was stirred overnight, resulting in the precipitation of a yellow solid. The yellow

precipitate was collected by vacuum filtration and washed thoroughly with dichloromethane to give ***N*-(4-methoxyphenyl)-*C*-(3-methylpyridinium) nitron** (**3a**) as a yellow powdery solid in 90% yield (0.29 g, 0.79 mmol). ¹H NMR ((CD₃)₂SO, 400 MHz): δ 10.21 (s, 1H), 9.03 (dd, *J*₁ = 21.6 Hz, *J*₂ = 8.4 Hz, 2H), 8.91 (s, 1H), 8.24 (dd, *J*₁ = 8.4 Hz, *J*₂ = 6.4 Hz, 1H), 7.94 (m, 2H), 7.16 (m, 2H), 4.45 (s, 3H), 3.86 (s, 3H). ¹³C NMR ((CD₃)₂SO, 400 MHz): δ 161.1, 145.6, 143.2, 143.0, 140.6, 130.7, 127.6, 127.5, 122.8, 114.3, 55.8, 48.7. HRMS (ESI) *m/z* calc. for C₁₄H₁₅N₂O₂⁺ (M)⁺: 243.1128, found: 243.1138. IR (ATR, cm⁻¹): 3136, 3073, 2983, 2835, 1628, 1542, 1499, 1472, 1301, 1254, 1162, 1081, 1014.

3.6.2.3 Synthesis of *N*-phenyl-*C*-(3-pyridine) Nitron (2b)

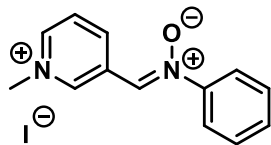


To 1.7 mL (16 mmol, 1 eq) nitrobenzene and 0.91 g (17 mmol, 1.1eq) ammonium chloride in 20 mL distilled water and 20 mL ethanol was added 3.2 g (50 mmol, 3 eq) zinc dust portion-wise over 10 minutes at room temperature. The resulting heterogenous mixture was stirred vigorously for 20 minutes, after which the insoluble white solid was removed by vacuum filtration. The supernatant was diluted with brine (100 mL) and extracted with diethyl ether (3 x 20 mL), dried over magnesium sulphate and concentrated to give the *crude hydroxylamine* as a light yellow solid, which was used without further purification.

To the *crude hydroxylamine* in 20 mL dichloromethane was added 1.9 mL (20 mmol, 1.3 eq) 3-pyridinecarboxaldehyde and a small amount of magnesium sulphate. The resulting heterogenous mixture was stirred overnight, after which the magnesium sulphate was removed by vacuum filtration. The supernatant was concentrated via rotary evaporation and the crude residue was purified by dissolving in minimal dichloromethane and precipitating the product out with excess di-ethyl ether at -20°C overnight to give ***N*-phenyl-*C*-(3-pyridine) nitron** (**2b**) as a white crystalline solid in 49% overall yield (1.56 g, 7.9 mmol). ¹H NMR ((CD₃)₂SO, 400 MHz): δ 9.40 (d, *J* = 2.0 Hz, 1H), 8.99 (dt, *J*₁ = 8.4 Hz, *J*₂ = 1.6 Hz, 1H), 8.63 (m, 1H), 8.62 (s, 1H), 7.93 (m, 2H), 7.56 (m, 4H). ¹³C NMR ((CD₃)₂SO, 400 MHz): δ 150.3, 149.8, 148.0, 134.5, 131.1, 130.0, 129.0, 127.2, 123.4, 121.3. HRMS (ESI) *m/z* calc. for C₁₂H₁₀N₂O (M)⁺: 198.0793, found: 198.0796. IR (ATR, cm⁻¹): 3130, 3065, 3062, 1582, 1555, 1484, 1466, 1403, 1335, 1272, 1203, 1175, 1164, 1072, 1022.

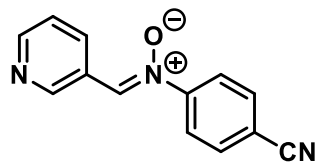
*Spectral data is similar to previously reported data in CDCl₃.¹

3.6.2.4 Synthesis of *N*-phenyl-*C*-(3-methylpyridinium) Nitron (3b)



To 0.50 g (2.5 mmol, 1 eq) *N*-phenyl-*C*-(3-pyridine) nitron (**2b**) in 10 mL dry dichloromethane was added 1.6 mL (25 mmol, 10 eq) iodomethane. The colorless solution was stirred overnight, resulting in the precipitation of a yellow solid. The yellow precipitate was collected by vacuum filtration and washed thoroughly with dichloromethane to give *N*-phenyl-*C*-(3-methylpyridinium) nitron (**3b**) as a yellow powdery solid in 96% yield (0.82 g, 2.4 mmol). ¹H NMR ((CD₃)₂SO, 400 MHz): δ 10.23 (s, 1H), 9.06 (dd, *J*₁ = 22.4 Hz, *J*₂ = 8.4 Hz, 2H), 8.98 (s, 1H), 8.26 (dd, *J*₁ = 8.4 Hz, *J*₂ = 6.4 Hz, 1H), 7.97 (m, 2H), 7.64 (m, 3H), 4.46 (s, 3H). ¹³NMR ((CD₃)₂SO, 400 MHz): δ 147.7, 146.1, 143.5, 143.4, 131.4, 130.7, 129.7, 129.2, 127.8, 121.6, 48.9. HRMS (ESI) *m/z* calc. for C₁₃H₁₃N₂O⁺ (M)⁺: 213.1022, found: 213. 1029. IR (ATR, cm⁻¹): 3099, 3049, 2922, 1616, 1549, 1490, 1464, 1404, 1190, 1154, 1082.

3.6.2.5 Synthesis of *N*-(4-cyanophenyl)-*C*-(3-pyridine) Nitron (2c)

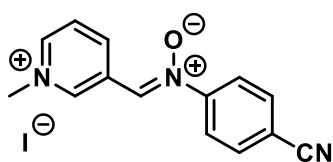


To 2.0 g (14 mmol, 1 eq) 4-nitrobenzotrile and 0.79 g (15 mmol, 1.1 eq) ammonium chloride in 20 mL distilled water and 20 mL ethanol was added 2.7 g (41 mmol, 3 eq) zinc dust portionwise over 10 minutes at room temperature. The resulting heterogenous mixture was stirred vigorously for 20 minutes, after which the insoluble white solid was removed by vacuum filtration. The supernatant was diluted with brine (100 mL) and extracted with diethyl ether (3 x 20 mL), dried over magnesium sulphate and concentrated to give the *crude hydroxylamine* as a light yellow oil, which was used without further purification.

To the *crude hydroxylamine* in 25 mL dichloromethane was added 3.0 mL (32 mmol, 2.2 eq) 3-pyridinecarboxaldehyde and a small amount of magnesium sulphate. The resulting heterogenous mixture was stirred overnight, after which the magnesium sulphate was removed by vacuum filtration. The supernatant was concentrated via rotary evaporation and the crude residue was purified by dissolving in minimal dichloromethane and precipitating the product out with excess di-ethyl ether at -20°C overnight to give *N*-(4-cyanophenyl)-*C*-(3-pyridine) nitron (**2c**)

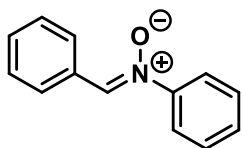
as a light yellow solid in 54% overall yield (1.7 g, 7.6 mmol). $^1\text{H NMR}$ ($(\text{CD}_3)_2\text{SO}$, 400 MHz): δ 9.42 (d, $J = 2.0$ Hz, 1H), 9.00 (dt, $J_1 = 8.0$ Hz, $J_2 = 2.0$ Hz, 1H), 8.77 (s, 1H), 8.67 (dd, $J_1 = 4.8$ Hz, $J_2 = 2.0$ Hz, 1H), 8.17 (m, 2H), 8.10 (m, 2H), 7.56 (dd, $J_1 = 8.0$ Hz, $J_2 = 4.8$ Hz, 1H). $^{13}\text{C NMR}$ ($(\text{CD}_3)_2\text{SO}$, 400 MHz): δ 151.3, 150.9, 150.5, 135.3, 133.8, 133.1, 127.3, 123.9, 122.8, 118.1, 113.0. HRMS (ESI) m/z calc. for $\text{C}_{13}\text{H}_9\text{N}_3\text{O}^+$ (M) $^+$: 223.0746, found: 223.0735. IR (ATR, cm^{-1}): 3104, 3082, 3065, 3054, 2242, 1584, 1498, 1425, 1413, 1338, 1297, 1270, 1209, 1172, 1070, 1026.

3.6.2.6 Synthesis of *N*-(4-cyanophenyl)-*C*-(3-methylpyridinium) Nitron (3c)



To 0.50 g (2.2 mmol, 1 eq) *N*-(4-cyanophenyl)-*C*-(3-pyridine) nitron (2c) in 10 mL dry dichloromethane was added 1.4 mL (22 mmol, 10 eq) iodomethane. The light yellow solution was stirred overnight, resulting in the precipitation of a yellow solid. The yellow precipitate was collected by vacuum filtration and washed thoroughly with dichloromethane to give *N*-(4-cyanophenyl)-*C*-(3-methylpyridinium) nitron (3c) as a yellow powdery solid in 86% yield (0.68 g, 1.9 mmol). $^1\text{H NMR}$ ($(\text{CD}_3)_2\text{SO}$, 400 MHz): δ 10.21 (s, 1H), 9.07 (m, 3H), 8.27 (dd, $J_1 = 8.0$ Hz, $J_2 = 6.0$ Hz, 1H), 8.17 (m, 4H), 4.46 (s, 3H). $^{13}\text{C NMR}$ ($(\text{CD}_3)_2\text{SO}$, 400MHz): δ 150.0, 146.4, 143.6, 143.6, 133.9, 130.6, 130.0, 127.7, 122.6, 117.8, 113.7, 48.8. HRMS (ESI) m/z calc. for $\text{C}_{14}\text{H}_{12}\text{N}_3\text{O}^+$ (M) $^+$: 238.0975, found: 238.0965. IR (ATR, cm^{-1}): 3114, 3049, 3024, 2933, 2230, 1629, 1596, 1555, 1499, 1309, 1160, 1097, 1064, 1024.

3.6.2.7 Synthesis of *N*-phenyl-*C*-phenyl Nitron (4)



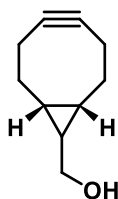
To 2.0 g (16 mmol, 1.7 mL) nitrobenzene and 0.95 g (18 mmol) ammonium chloride in 12 mL ethanol and 12 mL distilled water was added 2.1 g (32 mmol) zinc dust portion-wise over 10 minutes. The resulting heterogeneous mixture was stirred vigorously for 20 minutes, after which the insoluble solid was removed by vacuum filtration. The supernatant was diluted with brine (100 mL) and extracted with diethyl ether (3 x 20 mL), dried over magnesium sulphate and concentrated to give the *crude hydroxylamine* as a light yellow oil, which was used without further purification.

To the *crude hydroxylamine* in 20 mL dichloromethane was added 2.1 g (20 mmol, 2.0 mL) benzaldehyde and a small amount of magnesium sulphate. The resulting heterogenous mixture was stirred overnight, after which the magnesium sulphate was removed by vacuum filtration. The supernatant was concentrated via rotary evaporation and the crude residue was purified by dissolving in minimal dichloromethane and precipitating the product out with excess di-ethyl ether at -20°C overnight to give ***N*-phenyl-*C*-phenyl nitrone (4)** in 75% overall yield (2.4 g). ¹H NMR ((CD₃)₂SO, 400 MHz): 8.49 (m, 3H), 7.92 (m, 2H), 7.53 (m, 6H). ¹³C NMR ((CD₃)₂SO, 400 MHz): δ 148.5, 133.5, 131.1, 130.6, 129.9, 129.1, 128.8, 128.5, 121.5. HRMS (ESI) *m/z* calc. for C₁₃H₁₁NO (M)⁺: 197.0841, found: 197.0837. IR (ATR, cm⁻¹): 3060, 1593, 1547, 1510, 1484, 1461, 1445, 1396, 1340, 1324, 1298, 1191, 1163, 1067, 1025.

*Spectral data is similar to previously reported data in CDCl₃.¹

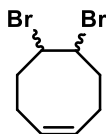
3.6.3 Synthesis of Cyclooctynes

3.6.3.1 Synthesis of BCN-OH_{exo} (5)



Synthesized according to Dommerholt *et al.*² See **Section 2.6.2.6** for characterization data.

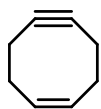
3.6.3.2 Synthesis of (*Z*)-5,6-dibromocyclooct-1-ene (6a)



To 20 mL (163 mmol) cyclooctadiene in 400 mL dichloromethane was added 3.5 mL (68 mmol) bromine in 100 mL dichloromethane dropwise over 30 minutes at room temperature. The resulting solution was stirred for 20 minutes, after which the solvent was thoroughly removed by rotary evaporation. The crude residue was purified by flash column chromatography (hexanes) to give (***Z***)-5,6-dibromocyclooct-1-ene as a colorless oil in 90% yield (16 g). ¹H NMR (CD₂Cl₂, 400 MHz): δ (ppm) 5.65 (m, 2H), 4.67 (m, 2H), 2.67 (m, 4H), 2.24 (m, 4H). ¹³C NMR (CD₂Cl₂, 400 MHz): δ (ppm) 129.2, 60.7, 36.0, 25.6. HRMS (ESI) *m/z* calc. for C₈H₁₂Br₂⁺ (M⁺): 265.9306, found: 265.9315. IR (ATR-IR, cm⁻¹): 3016, 2924, 1653, 1477, 1429, 1346, 1296, 1204, 1147.

*Analysis matches previously reported data³

3.6.3.3 Synthesis of (Z)-cyclooct-1-ene-5-yne (6b)

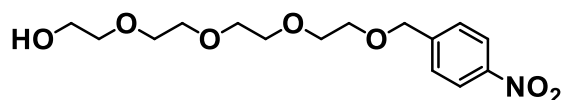


To 2.0 g (7.5 mmol) **(Z)-5,6-dibromocyclooct-1-ene** in 4 mL dry ether was added 11 mL (11 mmol) of 1 M potassium tert-butoxide in tetrahydrofuran dropwise over 10 minutes at 0°C. The solution was stirred for 30 minutes at 0°C and 30 minutes at room temperature, after which an additional 12 mL (12 mmol) of 1M potassium tert-butoxide in tetrahydrofuran was added over 10 minutes at room temperature. The solution was stirred for 2 hours at 40°C, after which the solution was cooled to room temperature and 100 mL pentane was added, resulting in cloudy dark orange solution. The resulting suspension was gravity filtered to remove insoluble solids. To the filtrate was added magnesium sulphate, and the insoluble solids were once again removed by gravity filtration, giving a yellow filtrate. The filtrate was concentrated by rotary evaporation under mild vacuum, and the resulting crude residue was purified by column chromatography (pentanes) to give **(Z)-cyclooct-1-ene-5-yne** as a yellow oil in 52% yield (0.41 g). NOTE: product is volatile (bp < 100°C), and so care must be taken when removing solvents using rotary evaporation. Also, we found that quenching the reaction with water significantly reduced the yield of product. ¹H NMR (CD₂Cl₂, 400 MHz): δ (ppm) 5.85 (m, 2H), 2.56 (m, 4H), 2.14 (m, 2H). ¹³C NMR (CDCl₃, 400 MHz): δ (ppm) 131.9, 100.8, 31.2, 19.5. HRMS (ESI) *m/z* calc. for C₈H₁₀(M⁺): 106.0783, found: 106.0782. IR (ATR-IR, cm⁻¹): 3008, 2924, 2850, 1635, 1450, 1315, 1207.

*Compound is previously reported, but no experimental or spectral data was provided⁴

3.6.4 Synthesis of TEG Ligands

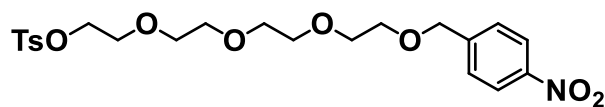
3.6.4.1 Synthesis of Nitrobenzyl-TEG-OH (A)



To 15 mL (87 mmol) tetraethylene glycol in 500 mL dimethylformamide was added 0.21 g (8.7 mmol) sodium hydride, portionwise over 10 minutes at 0°C, resulting in some bubbling. After stirring the heterogenous mixture for 60 minutes at room temperature, a solution of 2.2 g (10 mmol) nitrobenzyl bromide in 25 mL dimethylformamide was

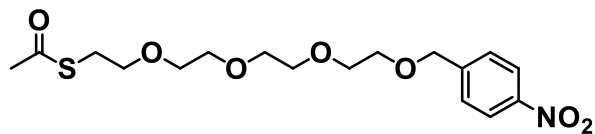
added. The reaction was stirred overnight, after which 100 mL water was added. The solution was extracted with dichloromethane (3 x 50 mL), and the solvent was removed via rotary evaporation. The crude residue was purified via flash column chromatography (1:10 ethanol:dichloromethane) to give nitrobenzyl-TEG-OH (**A**) as a pale yellow oil in 65% yield (1.9 g). ^1H NMR (CDCl_3 , 400 MHz): δ (ppm) 8.17 (d, $J = 12.0$ Hz, 2H), 7.50 (d, $J = 12.0$ Hz, 2H), 4.65 (s, 2H), 3.66 (m, 17H), 3.58 (m, 2H). ^{13}C NMR (CDCl_3 , 400 MHz): δ (ppm) 170.1, 160.92, 147.22, 145.91, 127.7, 123.5, 72.5, 71.9, 70.5, 70.5, 70.2, 70.1, 65.7, 61.6, 60.3, 20.9, 15.2, 14.1. HRMS (ESI) m/z calc. for $\text{C}_{15}\text{H}_{23}\text{NO}_7^+$ (M^+): 329.1475, found: 329.1462.

3.6.4.2 Synthesis of Nitrobenzyl-TEG-OTs (**B**)



To 1.5 g (4.6 mmol) nitrobenzyl-TEG-OH (**A**) in 100 mL dry dichloromethane was added 1.0 g (5.5 mmol) tosyl chloride in 25 mL dry dichloromethane, and then 1.9 mL (13.8 mmol) triethylamine. The reaction was stirred overnight, after which the solvent was removed via rotary evaporation. The crude residue was purified via flash column chromatography (dichloromethane to 1:10 ethanol:dichloromethane) to give nitrobenzyl-TEG-OTs (**B**) as a pale yellow oil in 92% yield (2.0 g). ^1H NMR (CDCl_3 , 400 MHz): δ (ppm) 8.20 (d, $J = 8.0$ Hz, 2H), 7.80 (d, $J = 8.0$ Hz, 2H), 7.52 (d, $J = 8.0$ Hz, 2H), 7.34 (d, $J = 8.0$ Hz, 2H), 4.68 (s, 2H), 4.16 (d, $J = 4.0$ Hz, 2H), 3.65 (m 16H), 2.45 (s, 3H). ^{13}C NMR (CDCl_3 , 400 MHz): δ (ppm) 147.6, 146.4, 145.1, 133.3, 130.1, 128.3, 128.0, 123.9, 72.3, 71.1, 71.0, 70.9, 70.5, 69.5, 69.0, 21.9. HRMS (ESI) m/z calc. for $\text{C}_{22}\text{H}_{29}\text{NO}_9\text{S}^+$ (M^+): 483.1563, found: 483.1521.

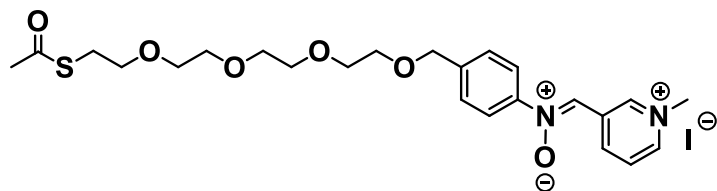
3.6.4.3 Synthesis of Nitrobenzyl-TEG-Thioacetate (**C**)



To 2.0 g (4.2 mmol) nitrobenzyl-TEG-OTs (**B**) in 150 mL acetonitrile was added 0.96 g (8.4 mmol) potassium thioacetate. The resulting heterogenous mixture was stirred overnight, after which the solvent was removed via rotary evaporation. The crude residue was purified via flash column chromatography (1:10 ethanol:dichloromethane) to give nitrobenzyl-TEG-Thioacetate (**C**) as a yellow oil in 95% yield (1.6 g). ^1H NMR (CDCl_3 , 400 MHz): δ (ppm) 8.21 (d, $J = 8.0$ Hz, 2H), 7.53 (d, $J = 8.0$ Hz, 2H),

4.68 (s, 2H), 3.67 (m, 12H), 3.60 (t, J = 8.0 Hz, 2H), 3.09 (t, J = 8.0 Hz, 2H), 2.34 (s, 3H). ^{13}C NMR (CDCl_3 , 400 MHz): δ (ppm) 195.2, 170.8, 147.0, 145.8, 127.4, 123.3, 71.7, 70.4, 70.4, 70.3, 70.2, 70.0, 69.9, 69.5, 60.1, 30.2, 28.5, 20.7, 13.9. HRMS (ESI) m/z calc. for $\text{C}_{17}\text{H}_{25}\text{NO}_7\text{S}^+$ (M^+): 387.1352, found: 387.1332.

3.6.4.4 Synthesis of Synthesis of (C-Pyridinium, N-Phenyl-TEG-Thioacetate)-Nitrone (**E**)



To 1.6 g (4.1 mmol) nitrobenzyl-TEG-Thioacetate (**C**) and 0.26 g (4.9 mmol) ammonium chloride in 10 mL ethanol and 10 mL distilled water was added 0.54 g (8.2 mmol) zinc dust portion-wise over 10 minutes. The resulting heterogenous mixture was stirred vigorously for 20 minutes, after which the insoluble solid was removed via vacuum filtration. The supernatant was diluted with brine (50 mL) and extracted with diethyl ether (3 x 25 mL), dried over magnesium sulphate and concentrated to give the *crude hydroxylamine* as a yellow oil, which was used without further purification.

To the *crude hydroxylamine* in 30 mL dichloromethane was added 0.77 mL (8.2 mmol) 3-pyridine carboxaldehyde and a small amount of magnesium sulphate. The resulting heterogenous mixture was stirred overnight, after which the magnesium sulphate was removed by vacuum filtration. The supernatant was concentrated via rotary evaporation and the crude residue was purified via flash column chromatography to give (C-Pyridinium, N-Phenyl-TEG-Thioacetate)-Nitrone (**D**) as a yellow oil.

To 0.92 g (2 mmol) (C-Pyridine, N-Phenyl-TEG-Thioacetate)-Nitrone (**D**) in 25 mL dry dichloromethane was added 1.2 mL (20 mmol) iodomethane. The resulting solution was stirred overnight, after which the solvent and unreacted iodomethane was removed via rotary evaporation, to give (C-Pyridinium, N-Phenyl-TEG-Thioacetate)-Nitrone (**E**) as a deep yellow oil in 46 % yield (1.1 g), which was used without further purification. ^1H NMR (CDCl_3 , 400 MHz): δ (ppm) 10.47 (s, 1H), 9.61 (d, J = 8.0 Hz, 1H), 9.18 (d, J = 8.0 Hz, 1H), 9.09 (s, 1H), 8.12 (t, J = 4.0 Hz, 1H), 7.98 (d, J = 8.0 Hz, 2H), 7.51 (d, J = 8.0 Hz, 2H), 4.64 (s, 2H), 4.60 (s, 3H), 3.69 (m, 16H), 3.04

(t, $J = 4.0$ Hz, 2H), 2.34 (s, 3H). ^{13}C NMR (CDCl_3 , 400 MHz): δ (ppm) 196.0, 146.3, 144.6, 143.5, 143.1, 141.5, 131.2, 128.1, 127.6, 127.4, 121.4, 71.8, 70.1, 70.0, 70.0, 69.9, 69.7, 69.6, 69.5, 53.1, 49.4, 30.4, 29.3, 28.5, 18.1. HRMS (ESI) m/z calc. for $\text{C}_{24}\text{H}_{33}\text{IN}_2\text{O}_6\text{S}^+$ (M^+): 604.1104, found: 604.1139.

3.6.5 Molecular Structures Of Nitrones

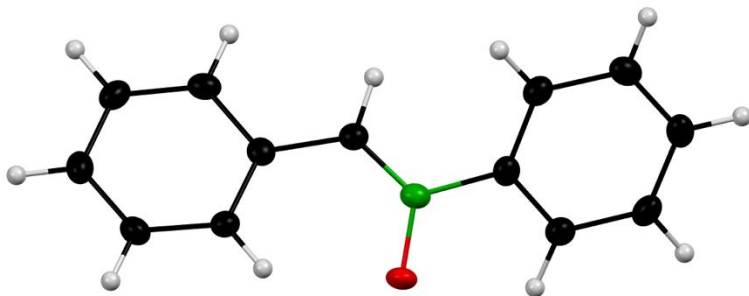


Figure S3.1. Thermal ellipsoid plot of molecular structure of **nitrone 4** at 50% probability level. Hydrogens are drawn in with arbitrary radii (black = carbon, red = oxygen, green = nitrogen, grey = hydrogen).

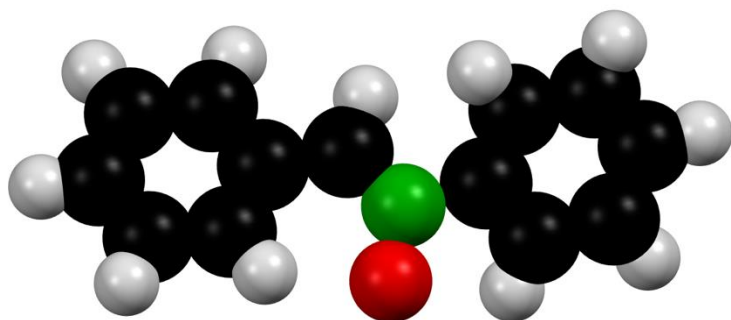


Figure S3.2. Space-filling diagrams of X-ray structure of **nitrone 4** (black = carbon, red = oxygen, green = nitrogen, grey = hydrogen, purple = iodine).

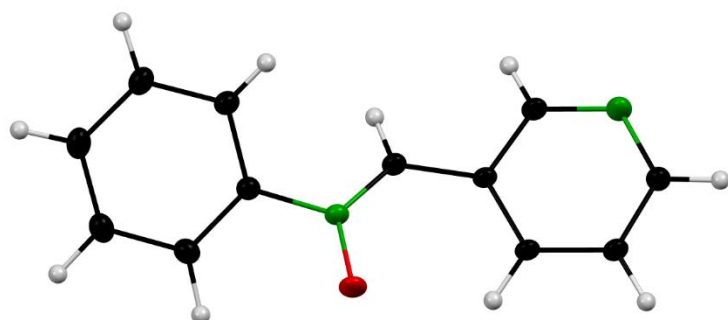


Figure S3.3. Thermal ellipsoid plot of molecular structure of **nitrone 2b** at 50% probability level. Hydrogens are drawn in with arbitrary radii (black = carbon, red = oxygen, green = nitrogen, grey = hydrogen).

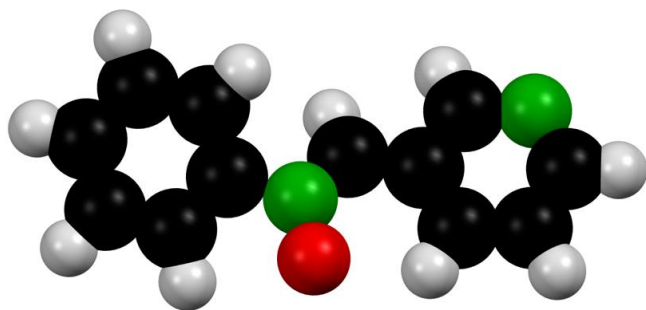


Figure S3.4. Space-filling diagrams of X-ray structure of **nitrone 2b** (black = carbon, red = oxygen, green = nitrogen, grey = hydrogen, purple = iodine).

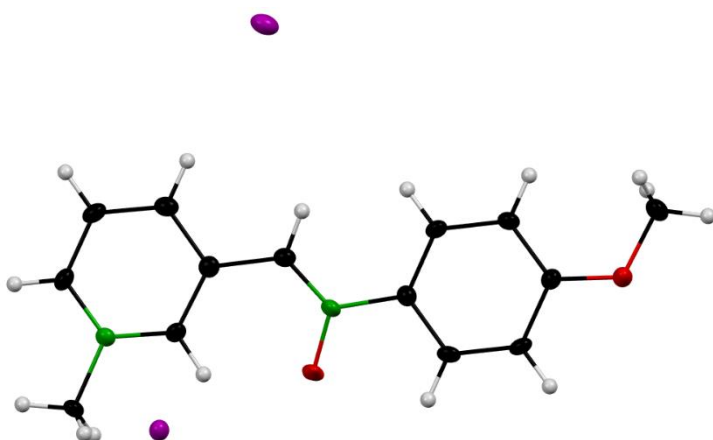


Figure S3.5. Thermal ellipsoid plot of molecular structure of **nitrone 3a** at 50% probability level. Hydrogens are drawn in with arbitrary radii (black = carbon, red = oxygen, green = nitrogen, grey = hydrogen, purple = iodine).

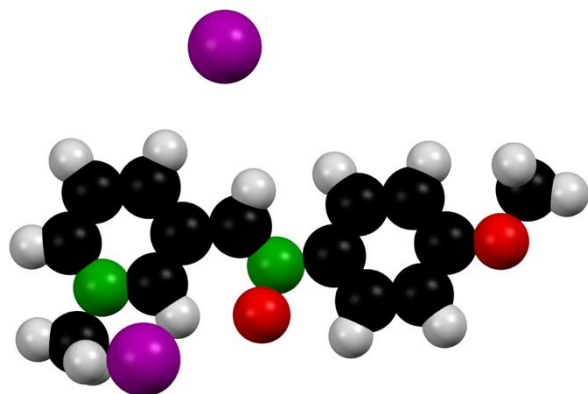


Figure S3.6. Space-filling diagrams of X-ray structure of **nitrone 3a** (black = carbon, red = oxygen, green = nitrogen, grey = hydrogen, purple = iodine).

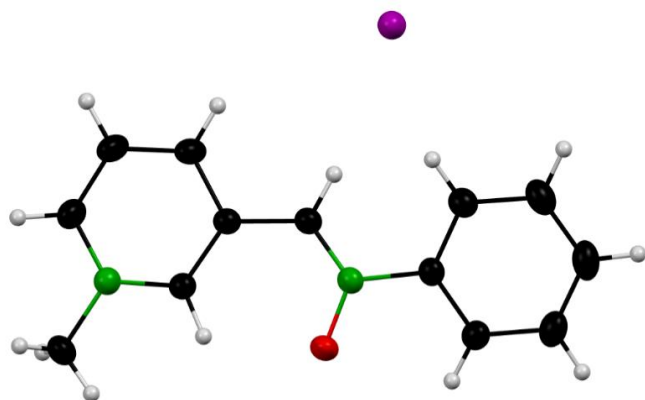


Figure S3.7. Thermal ellipsoid plot of molecular structure of **nitrone 3b** at 50% probability level. Hydrogens are drawn in with arbitrary radii (black = carbon, red = oxygen, green = nitrogen, grey = hydrogen, purple = iodine).

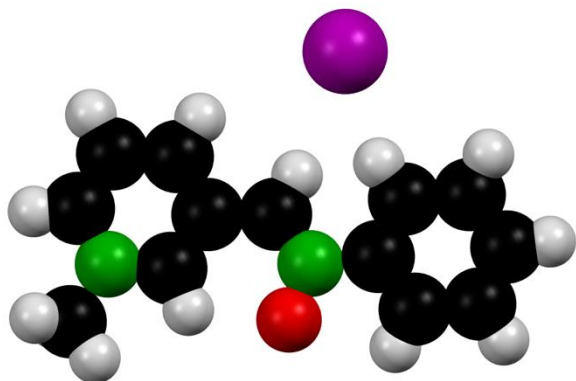


Figure S3.8. Space-filling diagrams of X-ray structure of **nitrone 3b** (black = carbon, red = oxygen, green = nitrogen, grey = hydrogen, purple = iodine).

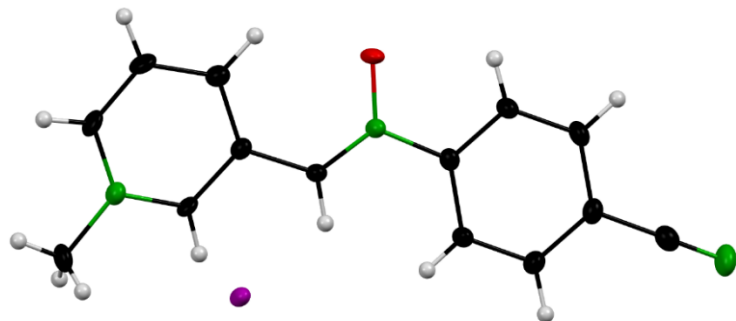


Figure S3.9. Thermal ellipsoid plot of molecular structure of **nitrone 3c** at 50% probability level. Hydrogens are drawn in with arbitrary radii (black = carbon, red = oxygen, green = nitrogen, grey = hydrogen, purple = iodine).

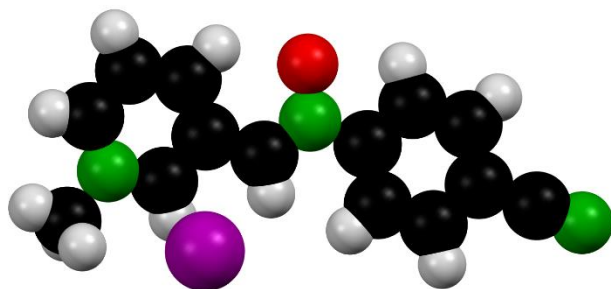


Figure S3.10. Space-filling diagrams of X-ray structure of **nitrone 3c** (black = carbon, red = oxygen, green = nitrogen, grey = hydrogen, purple = iodine).

3.6.6 General Synthesis of Cycloadducts

3.6.6.1 Synthesis of Cycloadduct between $\text{BCN}_{\text{exo-OH}}$ (5) with Nitrones 3a, 3b, 3c

To 1 equivalent of **nitrone 3a**, **3b** or **3c** in dimethylformamide (10 mg/10 mL) was added 1.1 equivalent of $\text{BCN}_{\text{exo-OH}}$ (5). The reaction mixture was stirred for 20 minutes, after which excess cold di-ethyl ether was added to precipitate out the product. The crude semi-solid was washed with numerous portions of cold di-ethyl ether to give each cycloadduct as a yellow oil. See **Section 3.6.10** for ^1H NMR spectra, ^{13}C NMR spectra and mass spectrometry data of cycloadducts.

To explore the SPANC reactivity of pyridinium-nitrones in different solvents systems (see **Section 3.6.11**), 1 equivalent of **nitrone 3c** was added to 1 equivalent of **BCN-OH_{exo} (5)** in 6:1 D₂O:(CD₃)₂SO (see **Figure S3.42** for ¹H NMR spectrum), 1:1 D₂O:(CD₃)₂SO (see **Figure S3.43** for ¹H NMR spectrum) and CD₃OD (see **Figure S3.44** for ¹H NMR spectrum).

3.6.6.2 Synthesis of Cycloadduct between BCN_{exo}-OH with Nitrone 4 and 2b

To 1 equivalent of **nitrone 4** or **2b** in dichloromethane (10 mg/mL) was added 1.1 equivalent of **BCN_{exo}-OH (5)**. The reaction mixture was stirred for 6 hours, after which excess cold di-ethyl ether was added to precipitate out the product. The crude semi-solid was washed with numerous portions of cold di-ethyl ether to give each cycloadduct as a yellow oil. See **Section 3.6.10** for ¹H NMR spectra, ¹³C NMR spectra and mass spectrometry data of cycloadducts.

3.6.6.3 Synthesis of Cycloadduct between DBCO-amine with Nitrone 3c

To 1 equivalent of **nitrone 3c** in acetonitrile (10 mg/10 mL) was added 1.1 equivalent of **DBCO-amine**. The reaction mixture was stirred for 20 minutes, after which excess cold di-ethyl ether was added to precipitate out the product. The crude semi-solid was washed with numerous portions of cold di-ethyl ether to give the cycloadduct as a yellow oil. See **Section 3.6.12** for ¹H NMR spectrum, ¹³C NMR spectrum and mass spectrometry data of cycloadduct.

3.6.6.4 Synthesis of Cycloadduct between (Z)-cyclooct-1-ene-5-yne (6b) with Nitrone 3c

To 1 equivalent of **nitrone 3c** in acetonitrile (10 mg/10 mL) was added 1.1 equivalent of **(Z)-cyclooct-1-ene-5-yne (6b)**. The reaction mixture was stirred for 20 minutes, after which excess cold pentane was added to precipitate out the product. The crude semi-solid was washed with numerous portions of cold pentane to give the cycloadduct as a yellow oil. See **Section 3.6.13** for ¹H NMR spectrum, ¹³C NMR spectrum and mass spectrometry data of cycloadduct.

3.6.7 NMR Spectra of Nitrones

3.6.7.1 Experimental Spectra for *N*-(4-methoxyphenyl)-*C*-(3-pyridine) nitronone (Nitronone 2a)

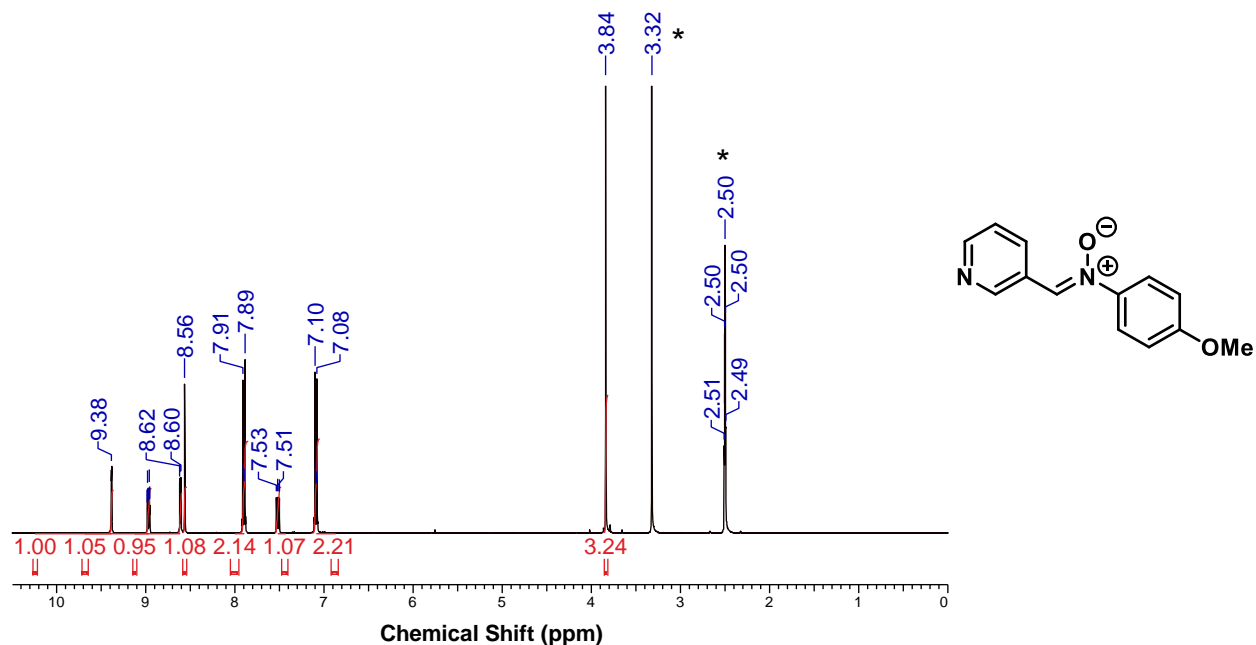


Figure S3.11. ¹H NMR spectrum of **nitronone 2a** in (CD₃)₂SO at 25°C. * denotes residual protio solvent and impurities.

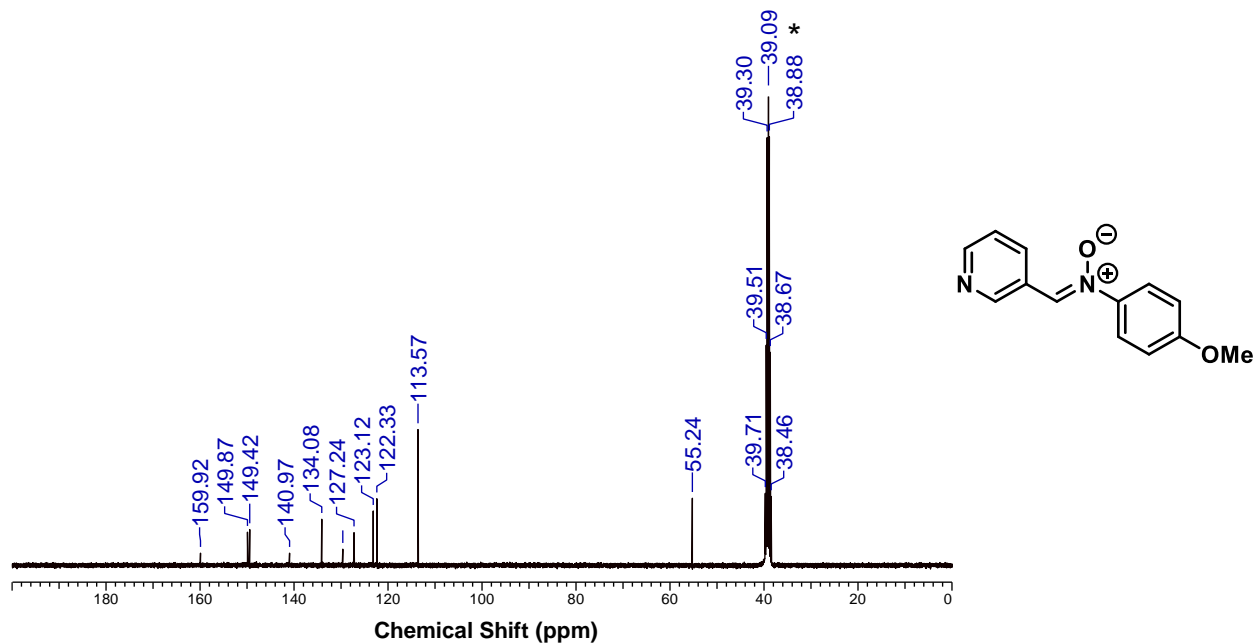


Figure S3.12. ¹³C{¹H} NMR spectrum of **nitronone 2a** in (CD₃)₂SO at 25°C. * indicates (CD₃)₂SO solvent.

3.6.7.2 Experimental Spectra for *N*-(4-methoxyphenyl)-*C*-(3-methylpyridinium) nitrone (Nitrone 3a)

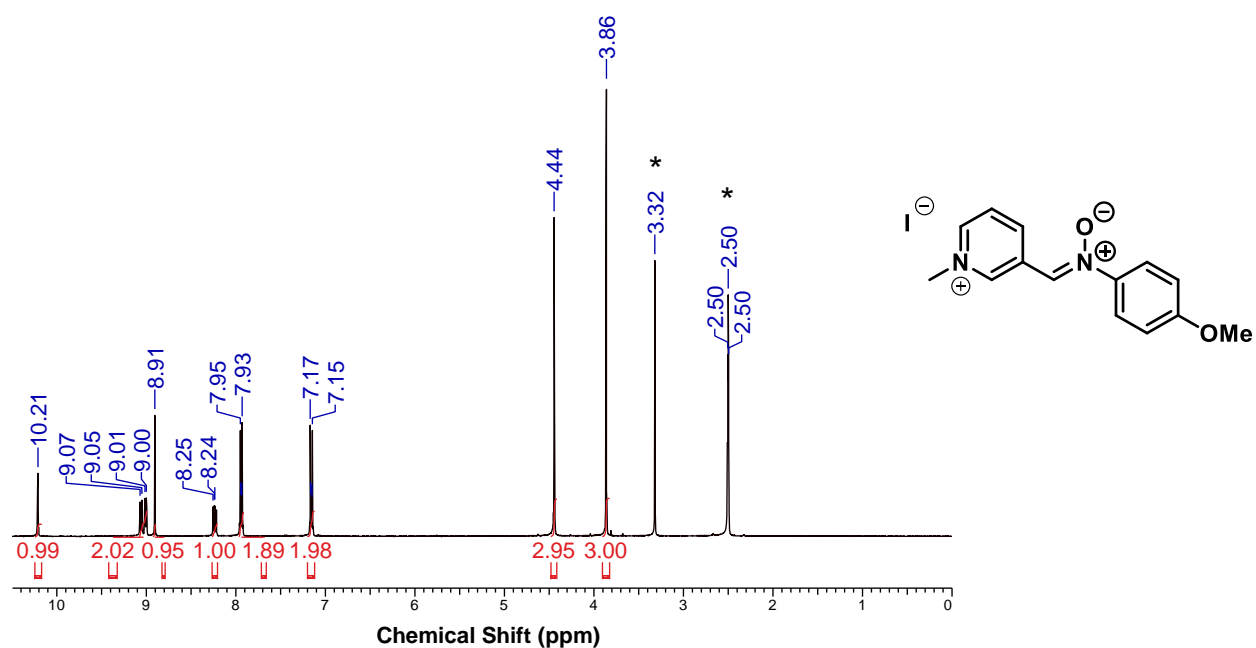


Figure S3.13. ^1H NMR spectrum of **nitrone 3a** in $(\text{CD}_3)_2\text{SO}$ at 25°C . * denotes residual protio solvent and impurities.

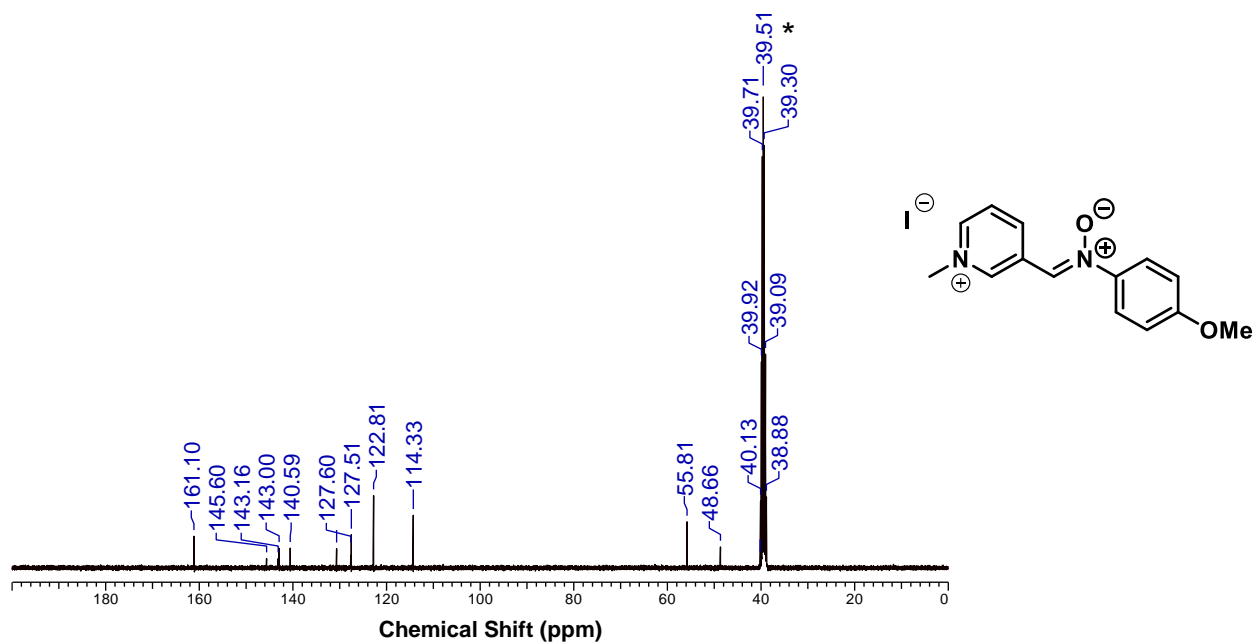


Figure S3.14. $^{13}\text{C}\{^1\text{H}\}$ NMR spectrum of **nitrone 3a** in $(\text{CD}_3)_2\text{SO}$ at 25°C . * indicates $(\text{CD}_3)_2\text{SO}$ solvent.

3.6.7.3 Experimental Spectra for *N*-phenyl-*C*-(3-pyridine) nitron (Nitron 2b)

See Section 2.6.3.16 for ^1H NMR and $^{13}\text{C}\{^1\text{H}\}$ NMR spectra of **nitron 2b**.

3.6.7.4 Experimental Spectra for *N*-phenyl-*C*-(3-methylpyridinium) nitron (Nitron 3b)

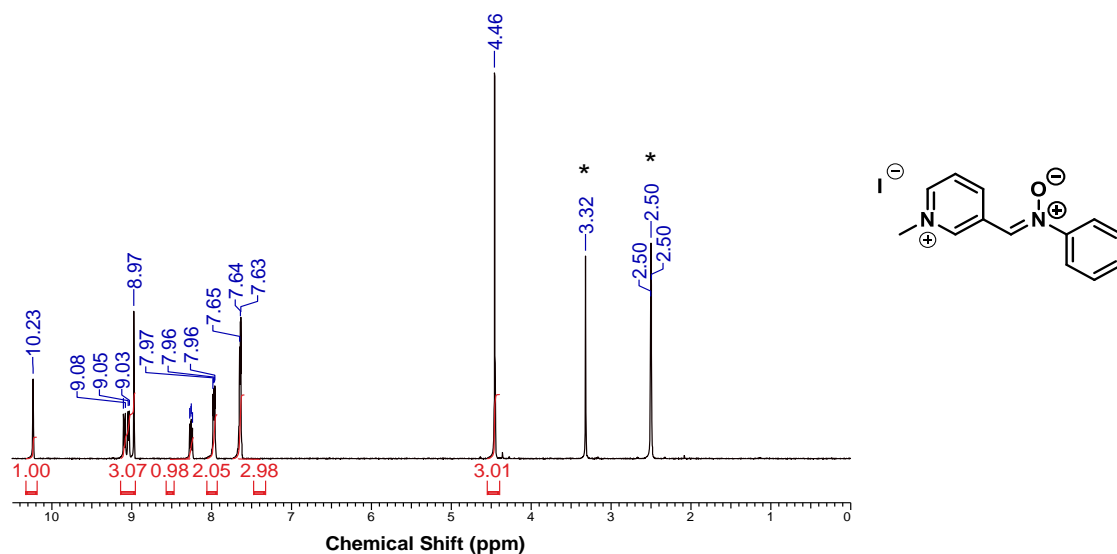


Figure S3.15. ^1H NMR spectrum of **nitron 3b** in in $(\text{CD}_3)_2\text{SO}$ at 25°C . * denotes residual protio solvent and impurities.

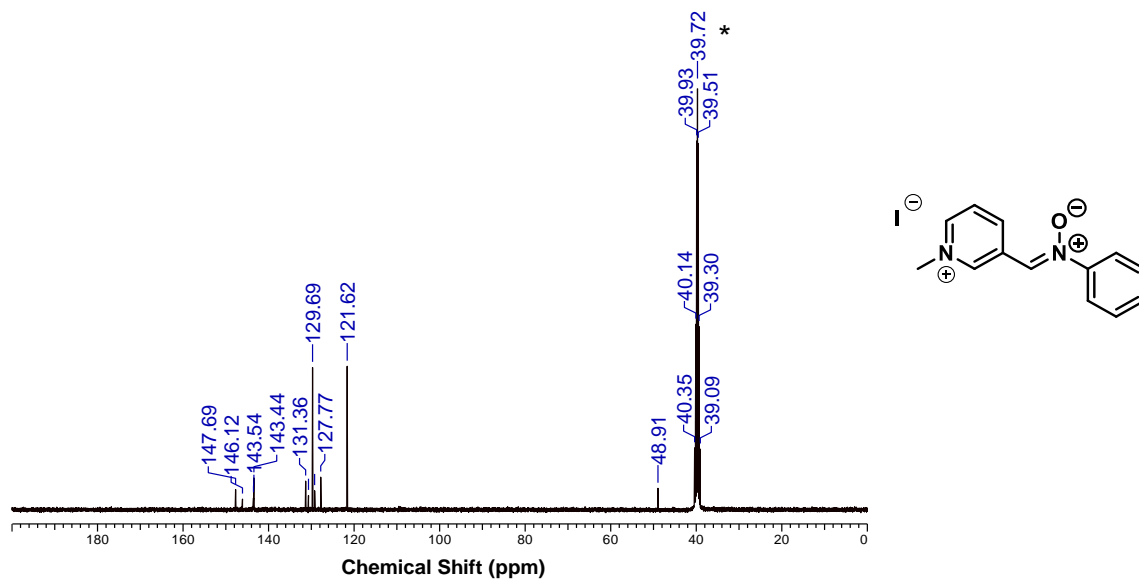


Figure S3.16. $^{13}\text{C}\{^1\text{H}\}$ NMR spectrum of **nitron 3b** in $(\text{CD}_3)_2\text{SO}$ at 25°C . * indicates $(\text{CD}_3)_2\text{SO}$ solvent.

3.6.7.5 Experimental Spectra for *N*-(4-cyanophenyl)-*C*-(3-pyridine) nitrone (Nitrone 2c)

See Section 2.6.3.17 for ^1H NMR and $^{13}\text{C}\{^1\text{H}\}$ NMR spectra of **nitrone 2c**.

3.6.7.6 Experimental Spectra for *N*-(4-cyanophenyl)-*C*-(3-methylpyridinium) nitrone (Nitrone 3c)

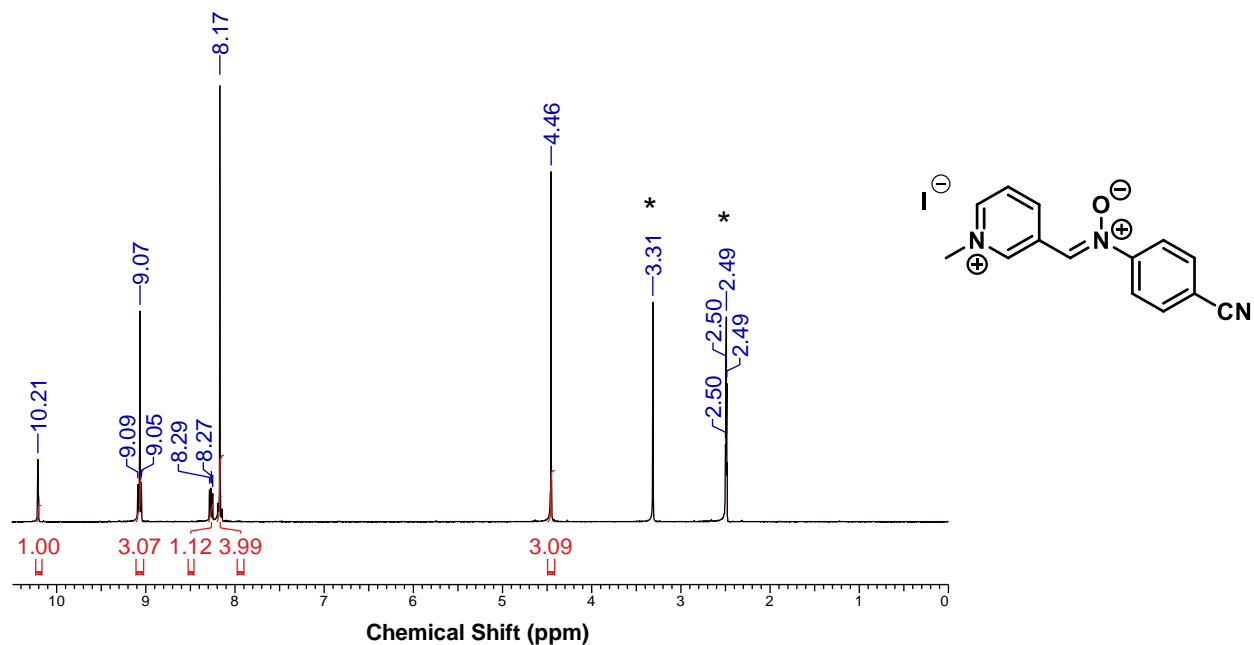


Figure S3.17. ^1H NMR spectrum of **nitrone 3c** in $(\text{CD}_3)_2\text{SO}$ at 25°C . * denotes residual protio solvent and impurities.

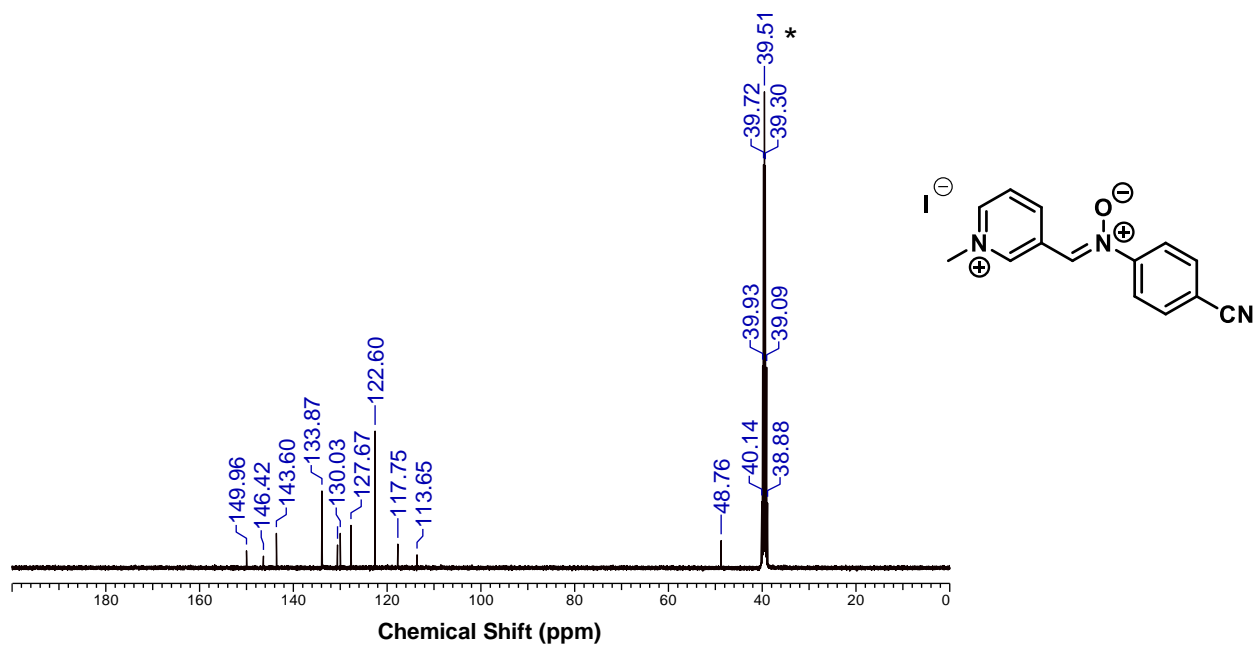


Figure S3.18. $^{13}\text{C}\{^1\text{H}\}$ NMR spectrum of **nitrone 3c** in $(\text{CD}_3)_2\text{SO}$ at 25°C . * indicates $(\text{CD}_3)_2\text{SO}$ solvent.

3.6.7.7 Experimental Spectra for *N*-phenyl-*C*-phenyl nitrone (Nitrone 4)

See **Section 2.6.3.14** for ^1H NMR and $^{13}\text{C}\{^1\text{H}\}$ NMR spectra of **nitrone 4**.

3.6.8 NMR Spectra of TEG Ligands

3.6.8.1 Experimental Spectra for Nitrobenzyl-TEG-OH (A)

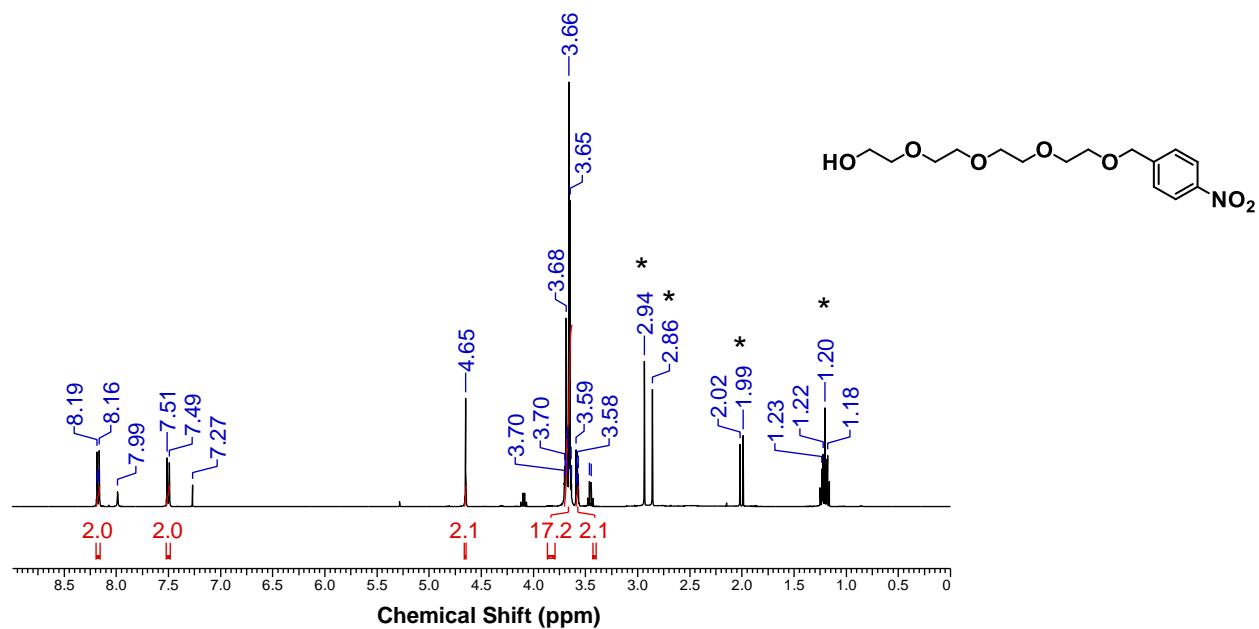


Figure S3.19. ^1H NMR spectrum of **nitrobenzyl-TEG-OH (A)** in CDCl_3 at 25°C . * denotes residual protio solvent and impurities.

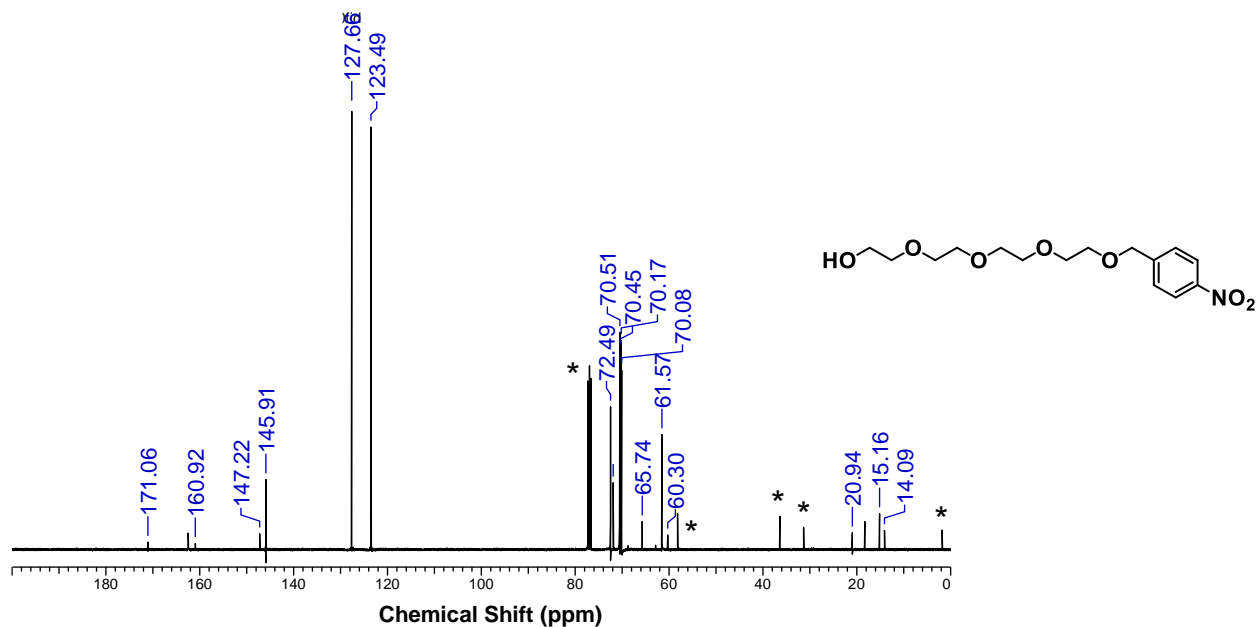


Figure S3.20. $^{13}\text{C}\{^1\text{H}\}$ NMR spectrum of **nitrobenzyl-TEG-OH (A)** in CDCl_3 at 25°C . * indicates CDCl_3 solvent.

3.6.8.2 Experimental Spectra for Nitrobenzyl-TEG-OTs (B)

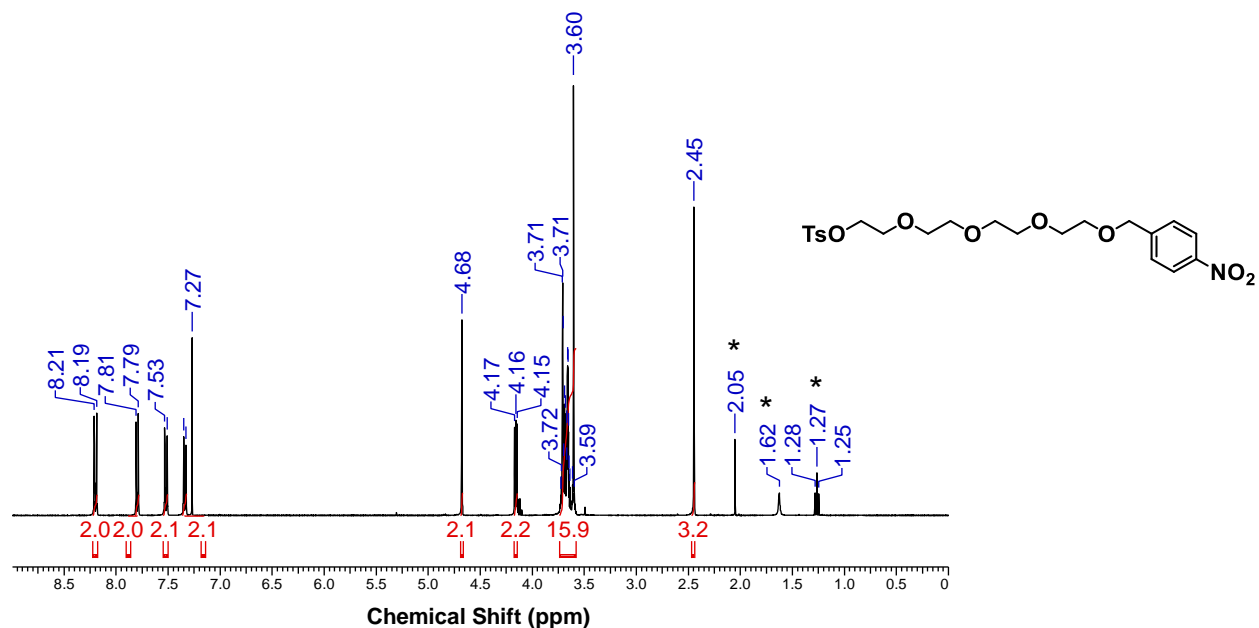


Figure S3.21. ^1H NMR spectrum of **nitrobenzyl-TEG-OTs (B)** in CDCl_3 at 25°C . * denotes residual protio solvent and impurities.

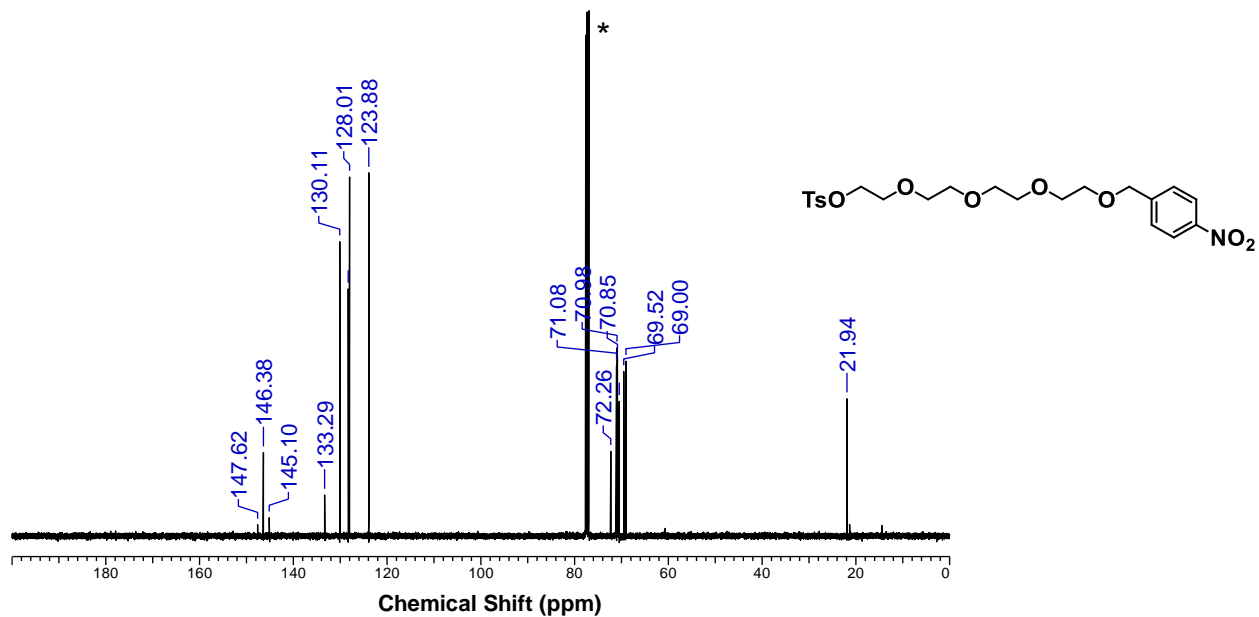


Figure S3.22. $^{13}\text{C}\{^1\text{H}\}$ NMR spectrum of **nitrobenzyl-TEG-OTs (B)** in CDCl_3 at 25°C . * indicates CDCl_3 solvent.

3.6.8.3 Experimental Spectra for Nitrobenzyl-TEG-Thioacetate (C)

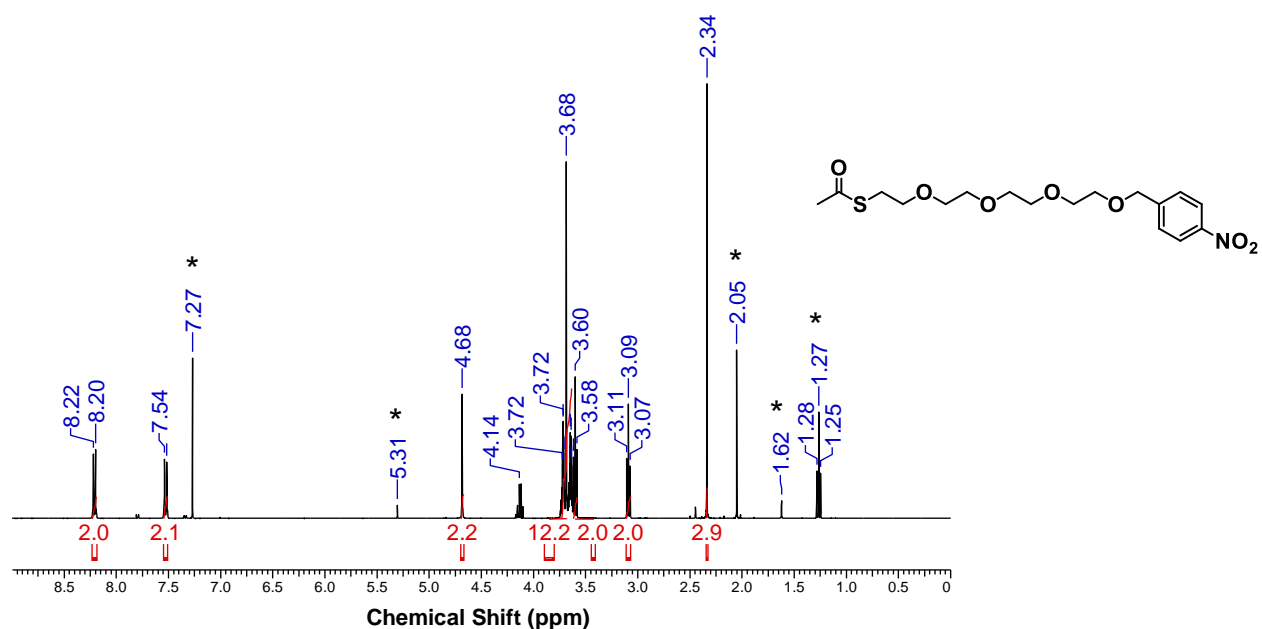


Figure S3.23. ^1H NMR spectrum of nitrobenzyl-TEG-Thioacetate (C) in CDCl_3 at 25°C . * denotes residual protio solvent and impurities.

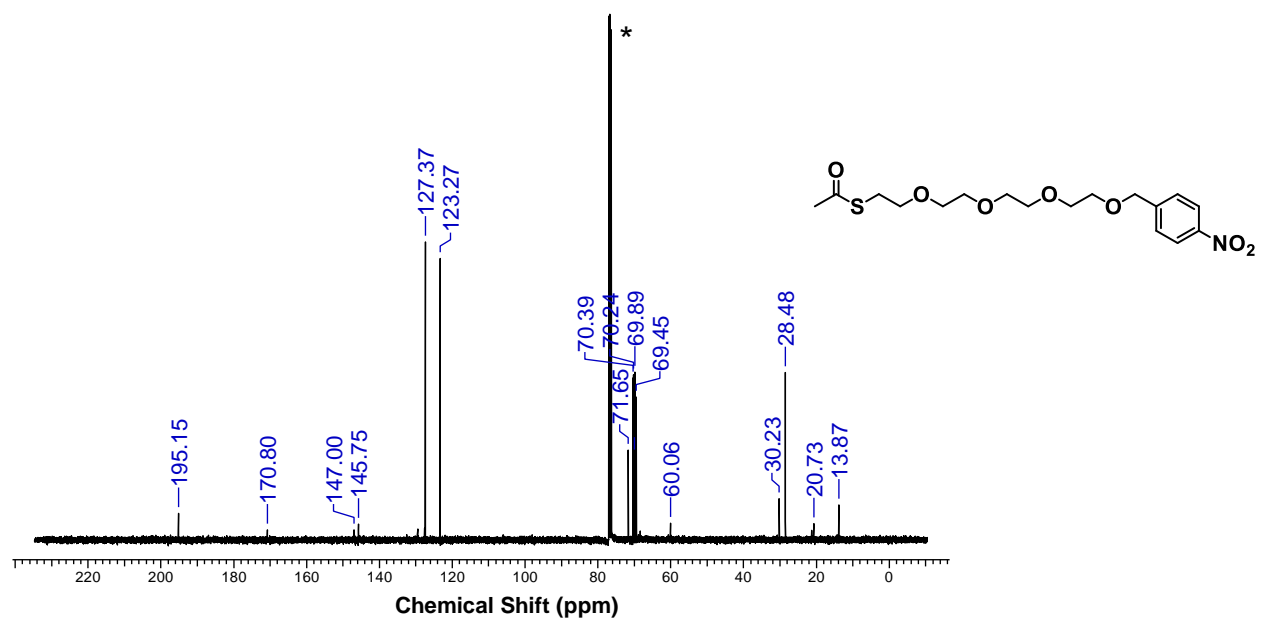


Figure S3.24. $^{13}\text{C}\{^1\text{H}\}$ NMR spectrum of nitrobenzyl-TEG-Thioacetate (C) in CDCl_3 at 25°C . * indicates CDCl_3 solvent.

3.6.8.4 Experimental Spectra for (C-Pyridinium, N-Phenyl-TEG-Thioacetate)-Nitrone (E)

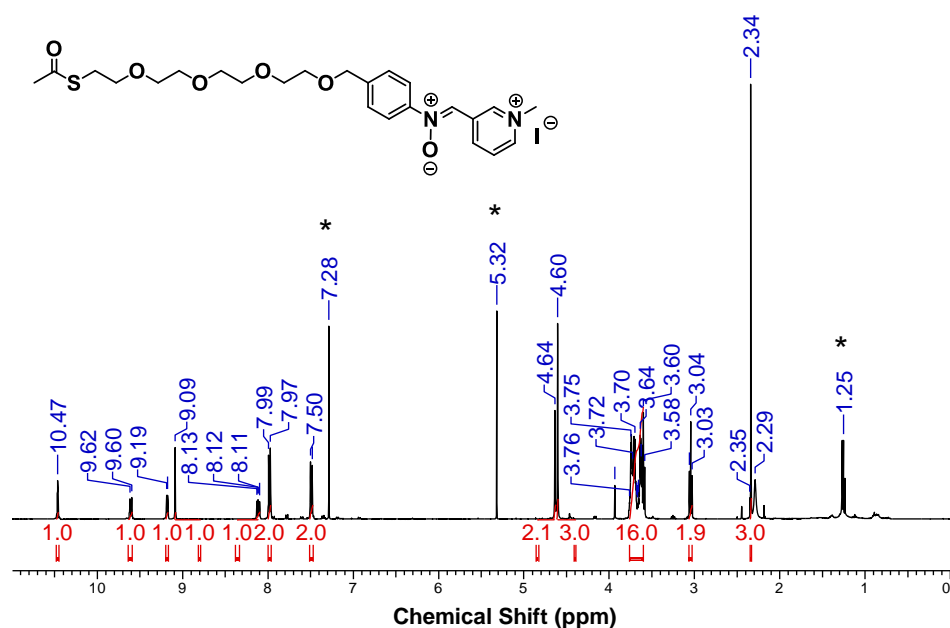


Figure S3.25. ¹H NMR spectrum of (C-pyridinium, N-phenyl-TEG-thioacetate)-nitrone (E) in CDCl₃ at 25°C. * denotes residual protio solvent and impurities.

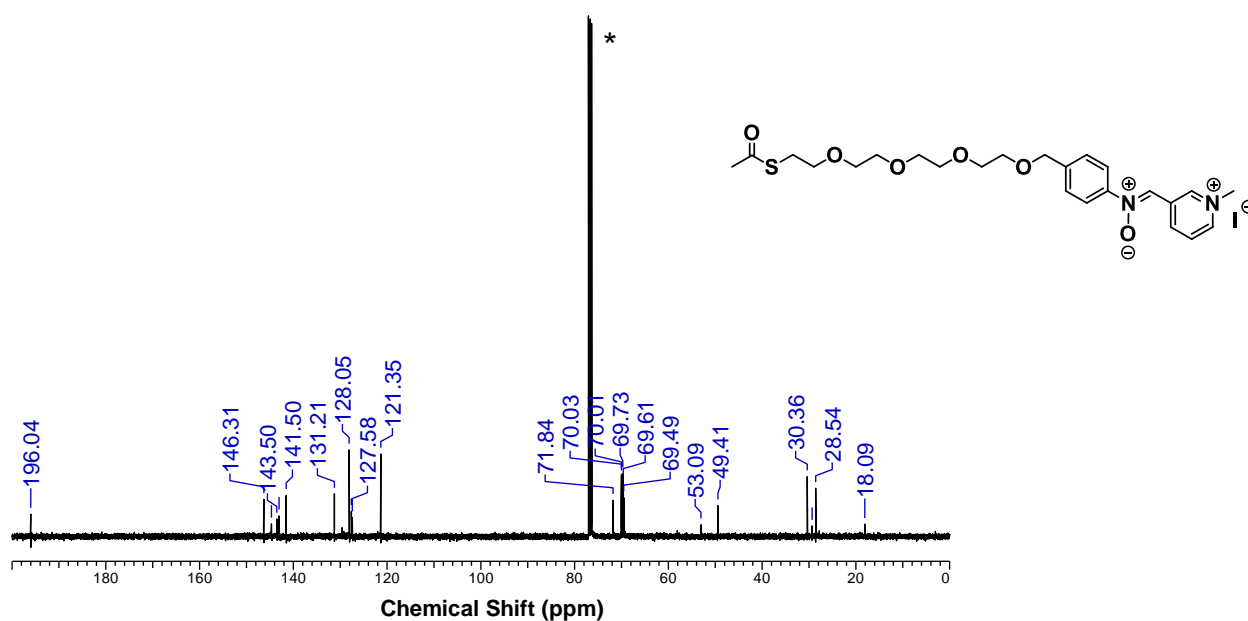


Figure S3.26. ¹³C{¹H} NMR spectrum of (C-pyridinium, N-phenyl-TEG-thioacetate)-nitrone (E) in CDCl₃ at 25°C. * indicates CDCl₃ solvent.

3.6.9 NMR Spectra of Cyclooctynes

3.6.9.1 Experimental Spectra for BCN_{exo}-OH (5)

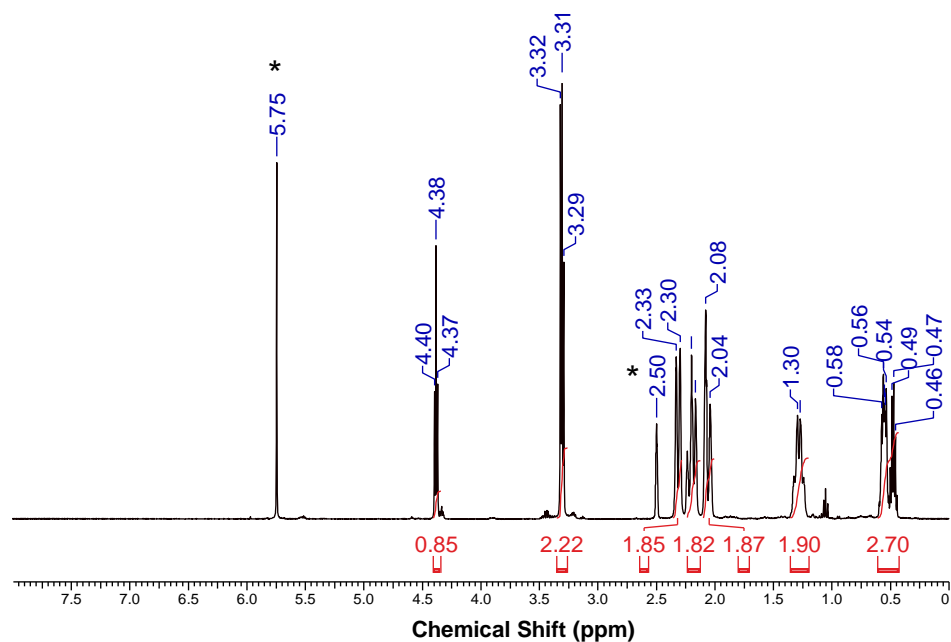


Figure S3.27. ¹H NMR spectrum of BCN_{exo}-OH (5) in in (CD₃)₂SO at 25°C. Made according to reference 2. * denotes residual protio solvent and impurities.

3.6.9.2 Experimental Spectra for (Z)-5,6-dibromocyclooct-1-ene (6a)

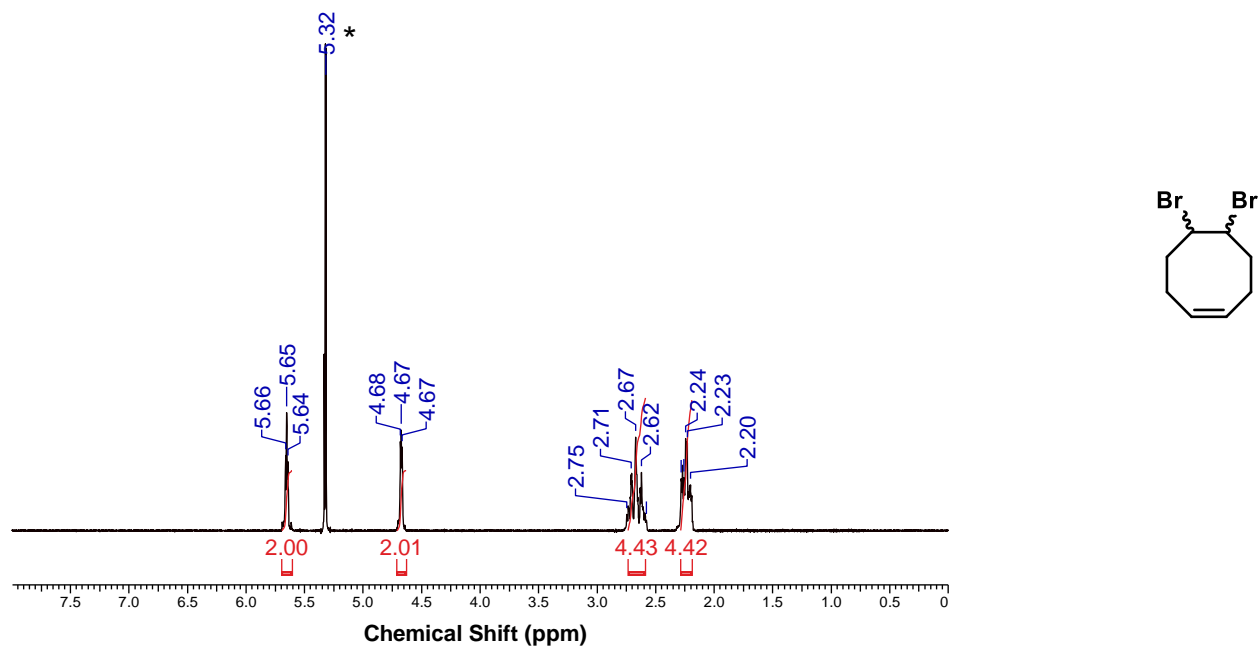


Figure S3.28. ^1H NMR spectrum of (Z)-5,6-dibromocyclooct-1-ene (6a) in CD_2Cl_2 at 25°C . * denotes residual protio solvent.

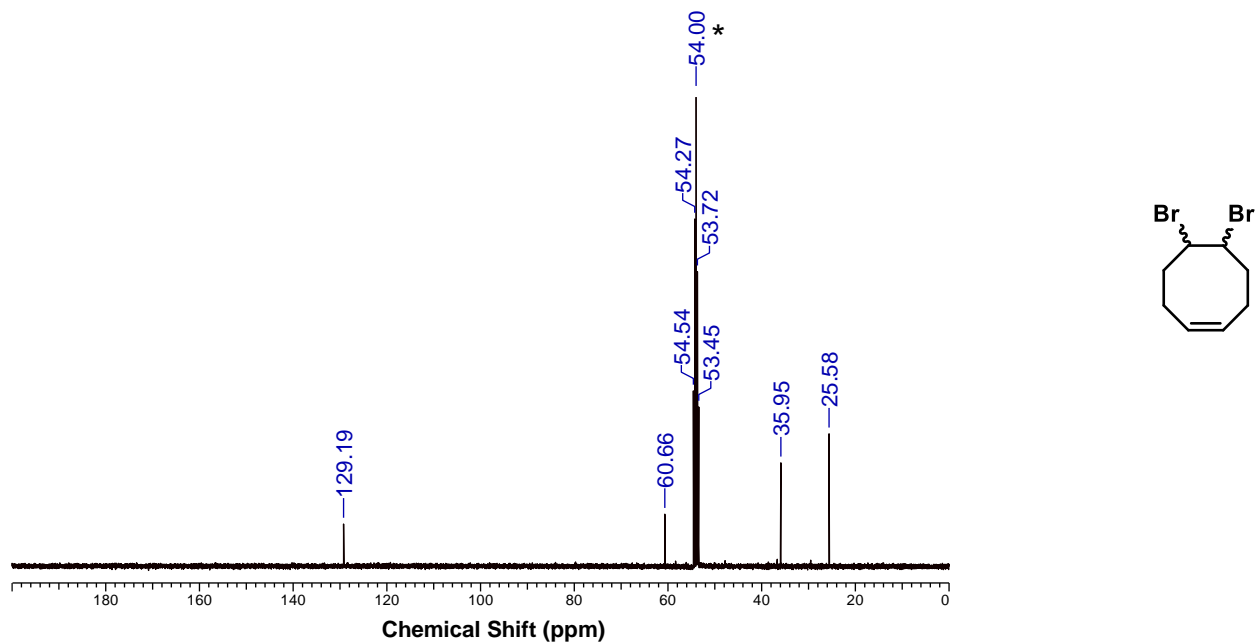


Figure S3.29. $^{13}\text{C}\{^1\text{H}\}$ NMR spectrum of (Z)-5,6-dibromocyclooct-1-ene (6a) in CD_2Cl_2 at 25°C . * indicates CD_2Cl_2 solvent.

3.6.9.3 Experimental Spectra for (*Z*)-cyclooct-1-ene-5-yne (6b)

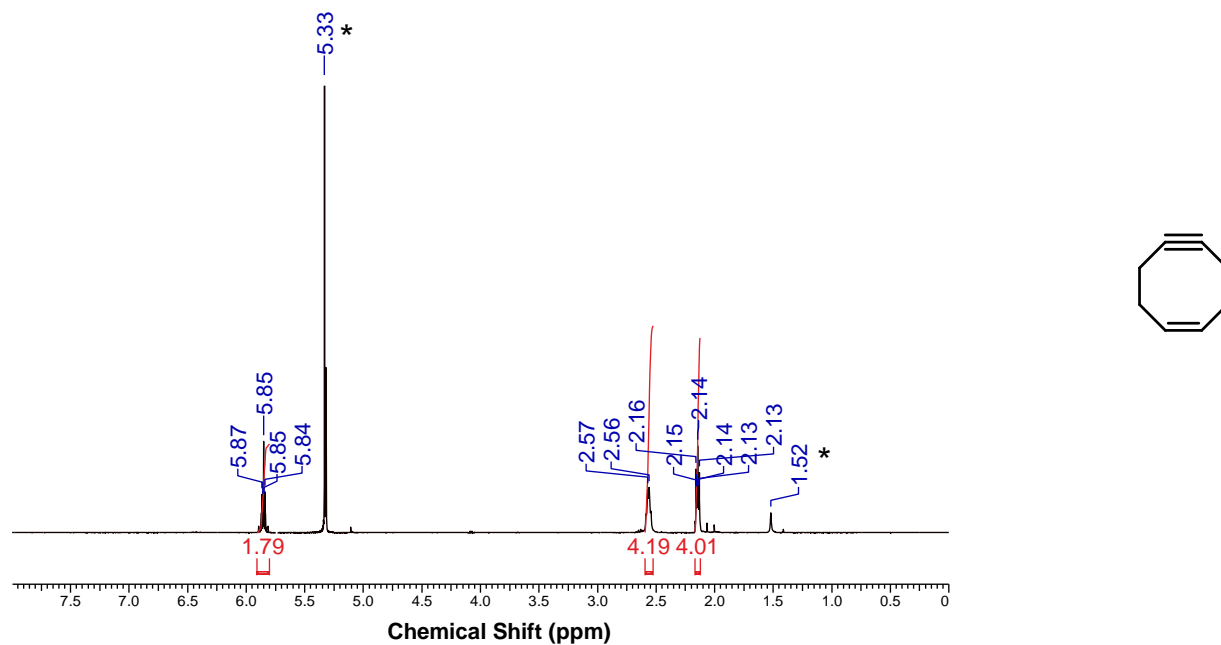


Figure S3.30. ^1H NMR spectrum of (*Z*)-cyclooct-1-ene-5-yne (**6b**) in CD_2Cl_2 at 25°C . * denotes residual protio solvent and impurities.

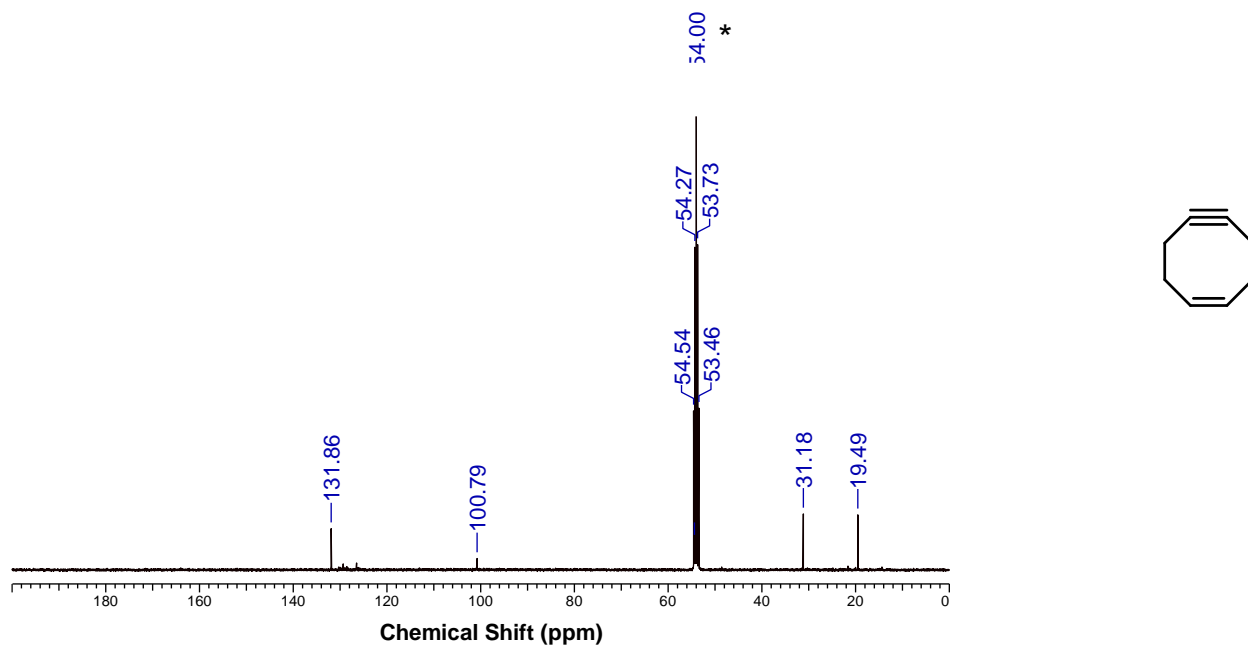


Figure S3.31. $^{13}\text{C}\{^1\text{H}\}$ NMR spectrum of (*Z*)-cyclooct-1-ene-5-yne (**6b**) in CD_2Cl_2 at 25°C . * indicates CD_2Cl_2 solvent.

3.6.10 NMR Spectra of Cycloadducts between BCN_{exo}-OH (5) and Nitrones 4, 2b, 3a, 3b and 3c

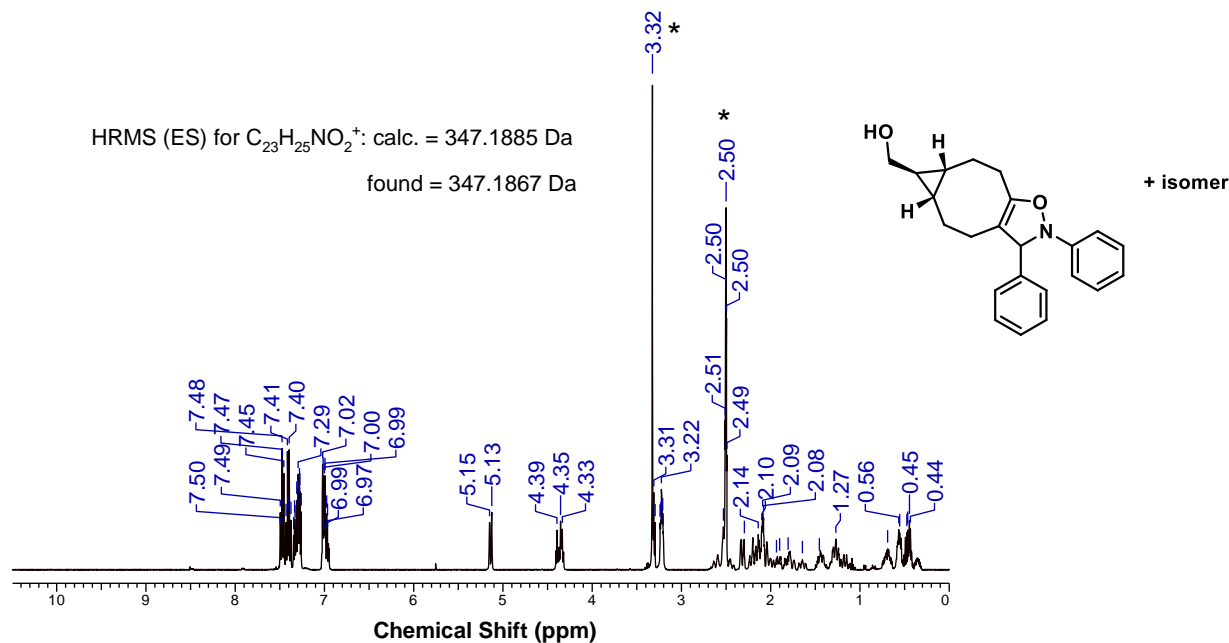


Figure S3.32. ¹H NMR spectrum of 4-BCN_{exo}-OH cycloadduct (2 isomers) in (CD₃)₂SO at 25°C. * denotes residual protio solvent and impurities.

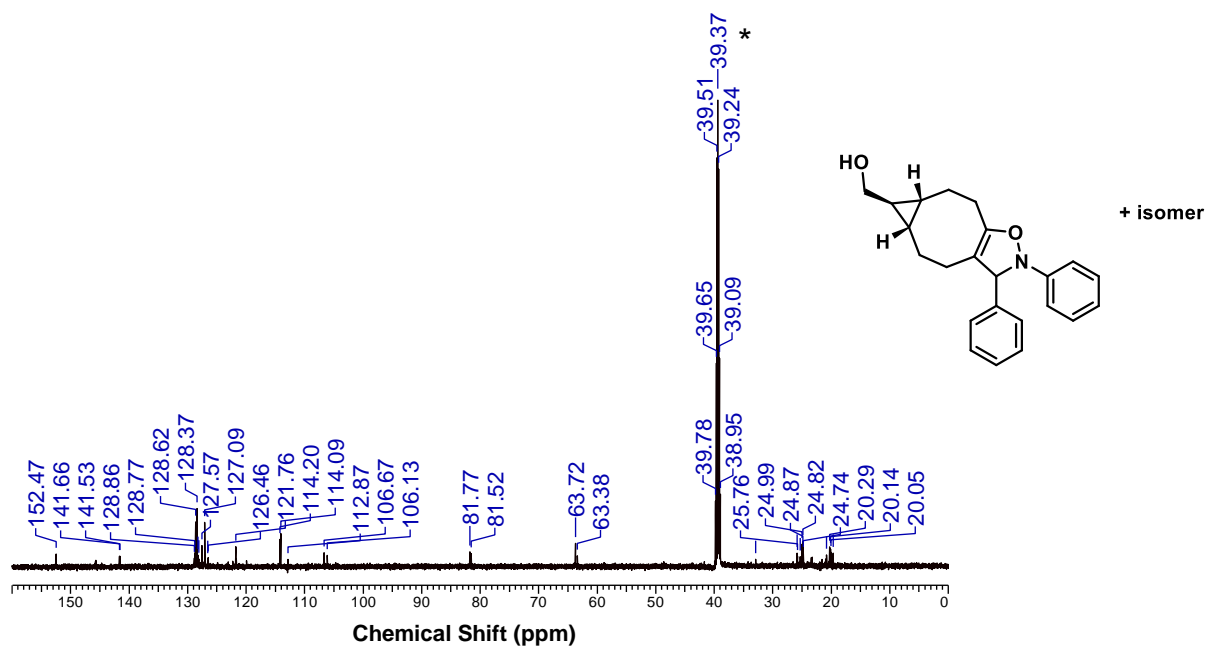


Figure S3.33. ¹³C{¹H} NMR spectrum of 4-BCN_{exo}-OH cycloadduct (2 isomers) in (CD₃)₂SO at 25°C. * indicates (CD₃)₂SO solvent.

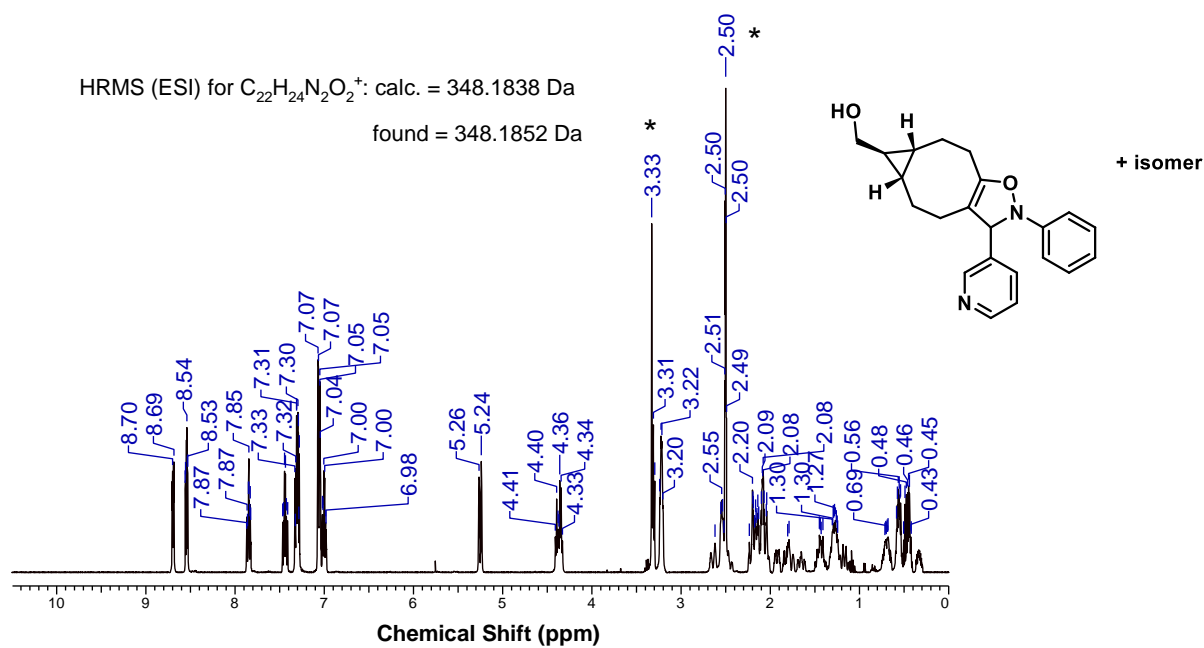


Figure S3.34. ^1H NMR spectrum of **2b-BCN_{exo}-OH cycloadduct** (2 isomers) in $(\text{CD}_3)_2\text{SO}$ at 25°C . * denotes residual protio solvent and impurities.

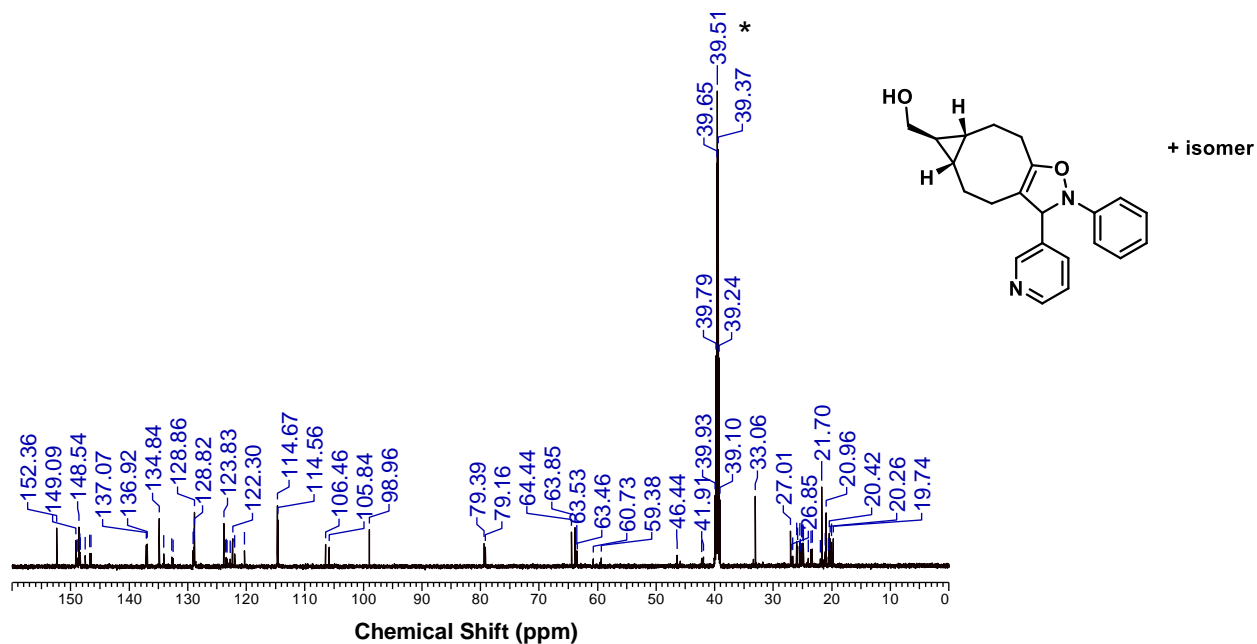


Figure S3.35. $^{13}\text{C}\{^1\text{H}\}$ NMR spectrum of **2b-BCN_{exo}-OH cycloadduct** (2 isomers) in $(\text{CD}_3)_2\text{SO}$ at 25°C . * indicates $(\text{CD}_3)_2\text{SO}$ solvent.

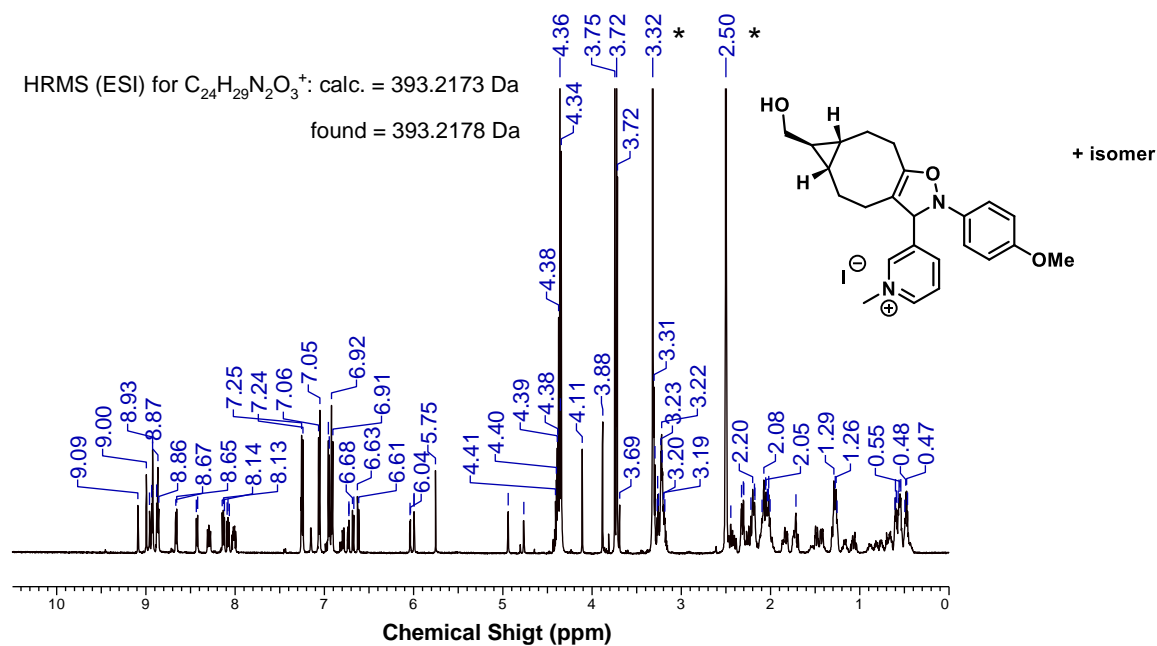


Figure S3.36. ^1H NMR spectrum of **3a-BCN_{exo}-OH cycloadduct** (2 isomers) in $(\text{CD}_3)_2\text{SO}$ at 25°C . * denotes residual protio solvent and impurities.

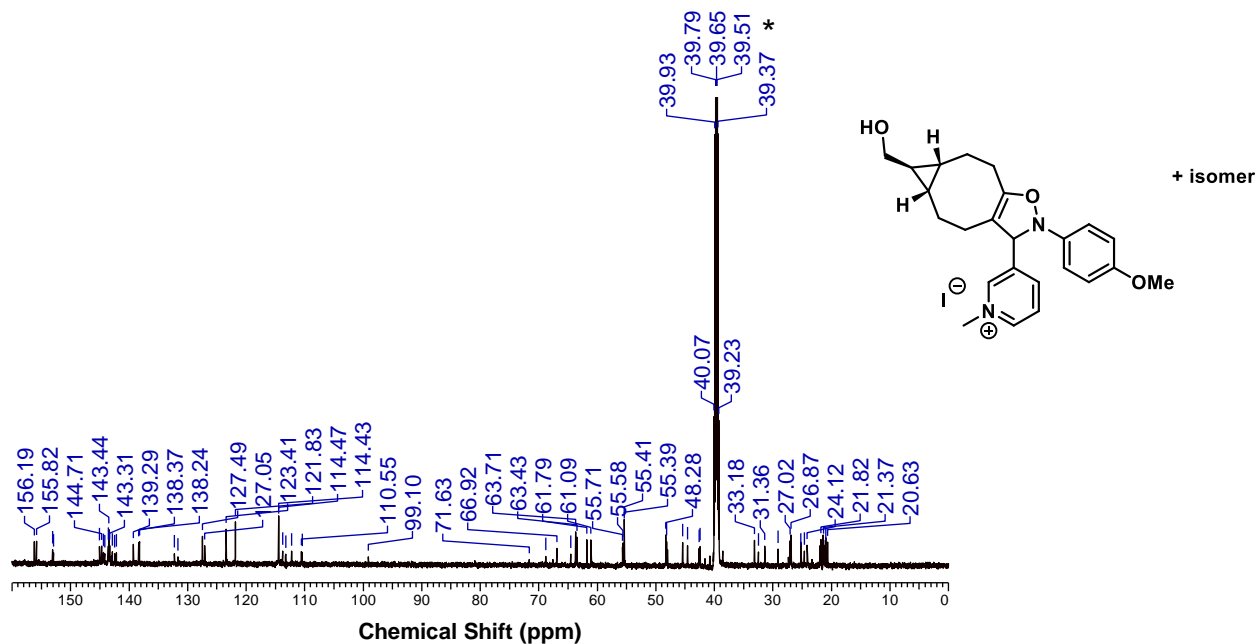


Figure S3.37. $^{13}\text{C}\{^1\text{H}\}$ NMR spectrum of **3a-BCN_{exo}-OH cycloadduct** (2 isomers) in $(\text{CD}_3)_2\text{SO}$ at 25°C . * indicates $(\text{CD}_3)_2\text{SO}$ solvent.

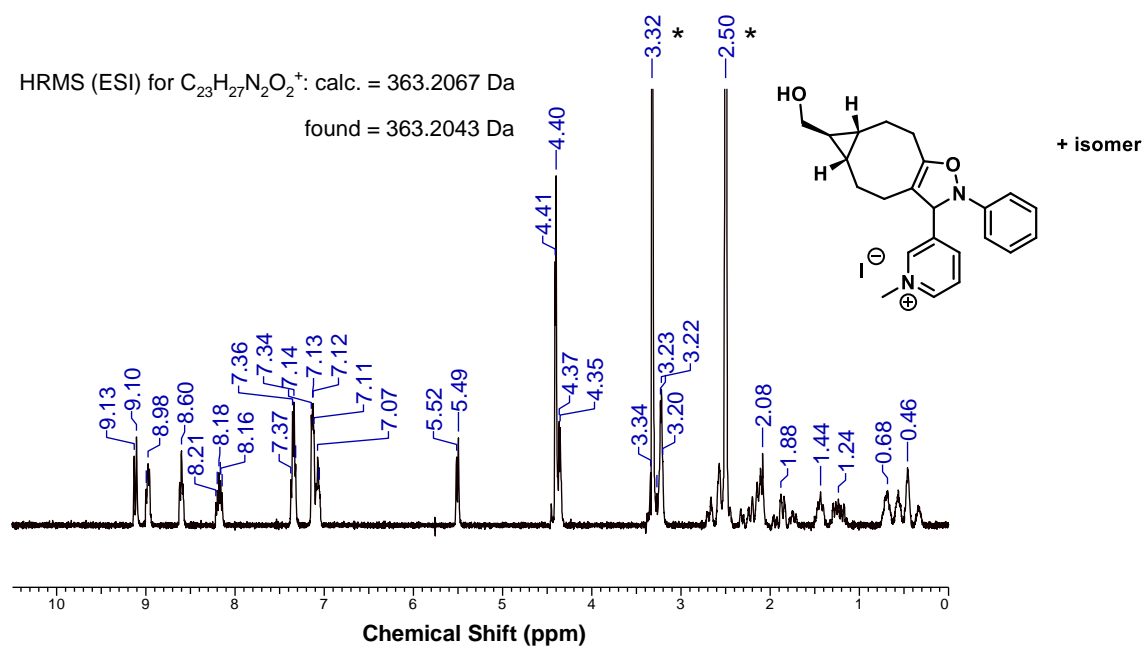


Figure S3.38. ^1H NMR spectrum of **3b-BCN_{exo}-OH cycloadduct** (2 isomers) in $(\text{CD}_3)_2\text{SO}$ at 25°C . * denotes residual protio solvent and impurities.

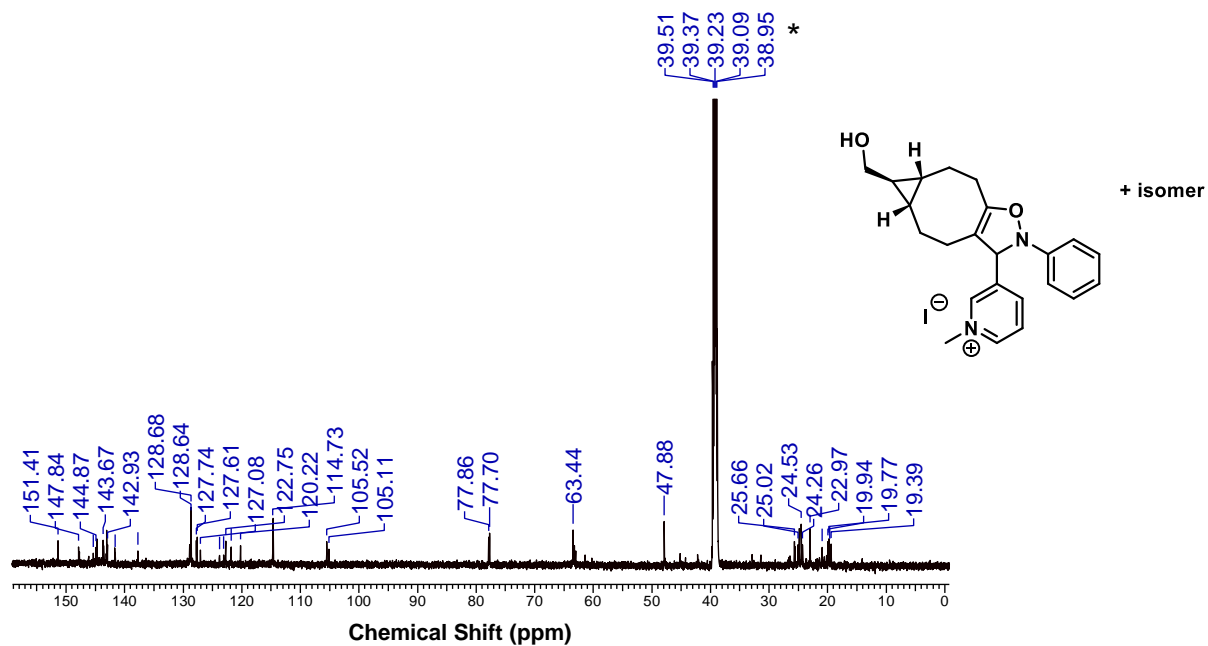


Figure S3.39. $^{13}\text{C}\{^1\text{H}\}$ NMR spectrum of **3b-BCN_{exo}-OH cycloadduct** (2 isomers) in $(\text{CD}_3)_2\text{SO}$ at 25°C . * indicates $(\text{CD}_3)_2\text{SO}$ solvent.

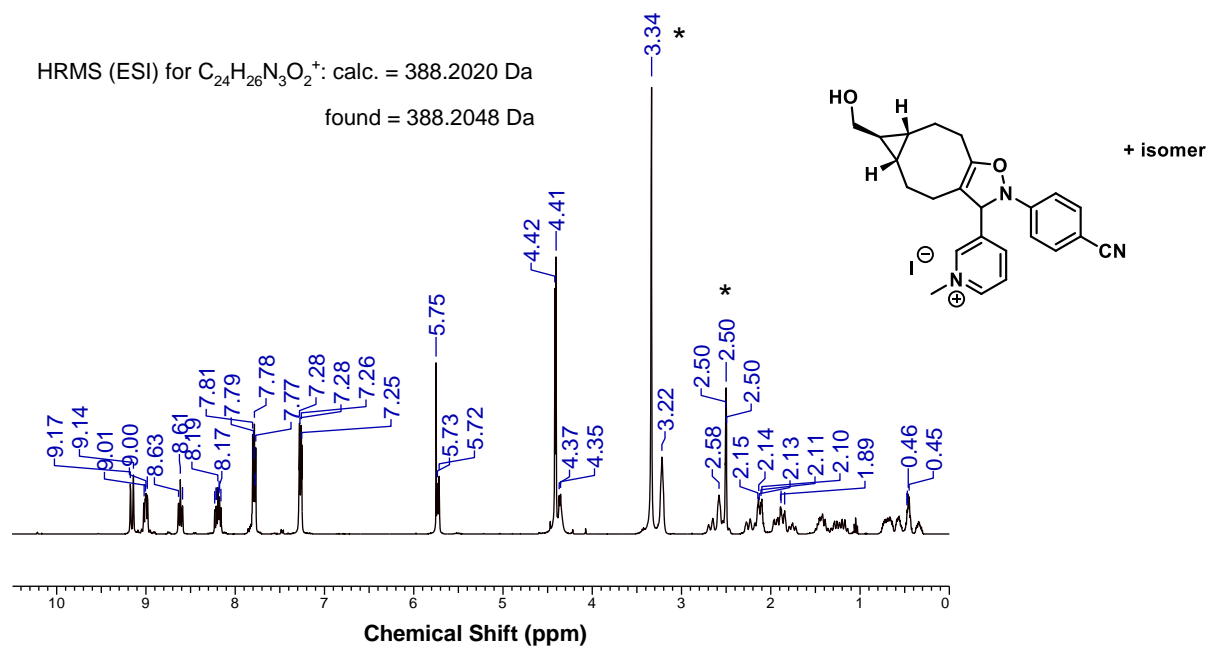


Figure S3.40. ^1H NMR spectrum of **3c-BCN_{exo}-OH cycloadduct** (2 isomers) in $(\text{CD}_3)_2\text{SO}$ at 25°C . * denotes residual protio solvent and impurities.

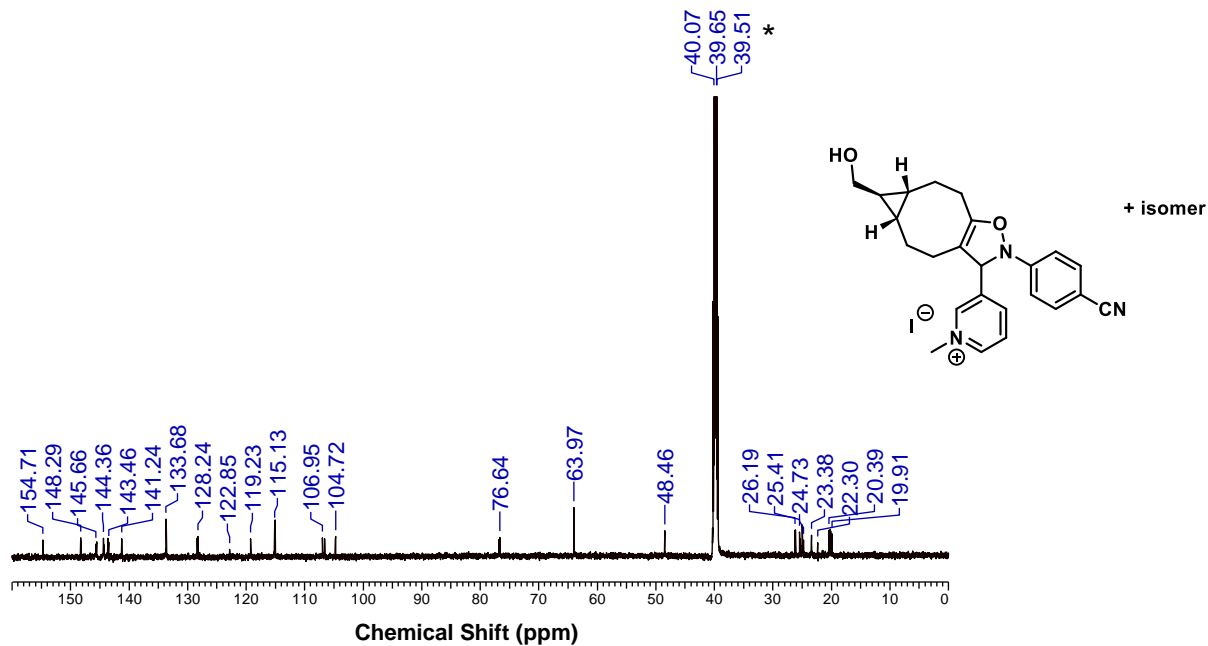


Figure S3.41. $^{13}\text{C}\{^1\text{H}\}$ NMR spectrum of **3c-BCN_{exo}-OH cycloadduct** (2 isomers) in $(\text{CD}_3)_2\text{SO}$ at 25°C . * indicates $(\text{CD}_3)_2\text{SO}$ solvent.

3.6.11 ^1H NMR Spectra of Cycloadducts between $\text{BCN}_{\text{exo-OH}}$ (5) and Nitron 3c in Other Solvents

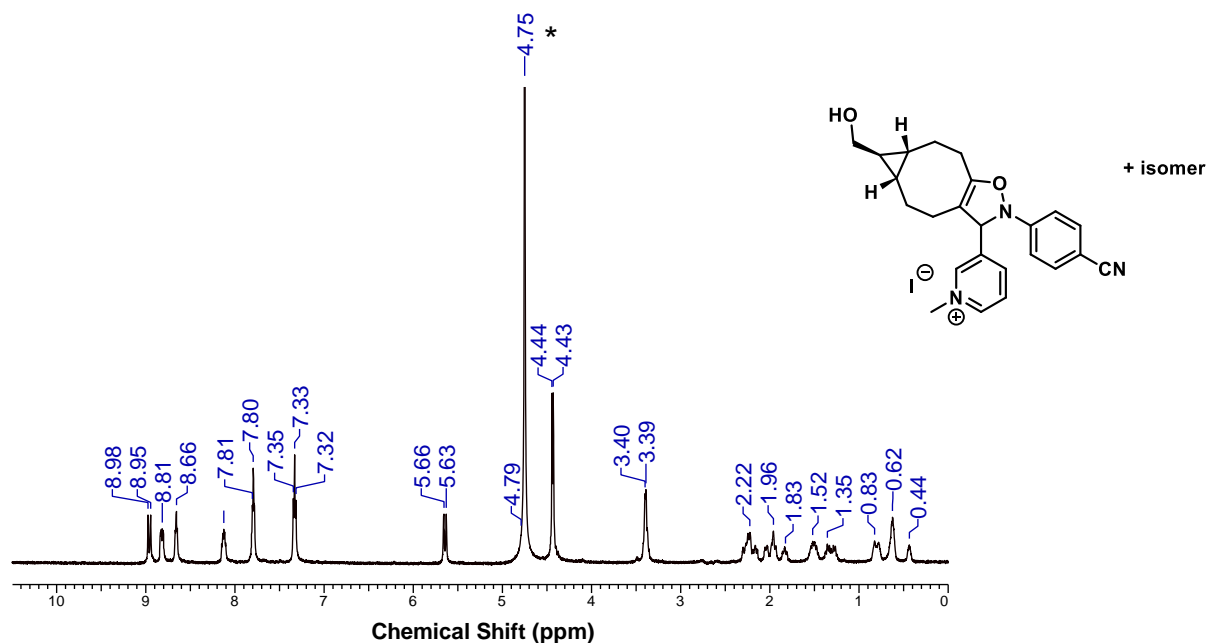


Figure S3.42. ^1H NMR spectrum of $3\text{c-BCN}_{\text{exo-OH}}$ cycloadduct (2 isomers) in 6:1 $\text{D}_2\text{O}:(\text{CD}_3)_2\text{SO}$ at 25°C . The solvents were suppressed by software. * denotes residual protio solvent.

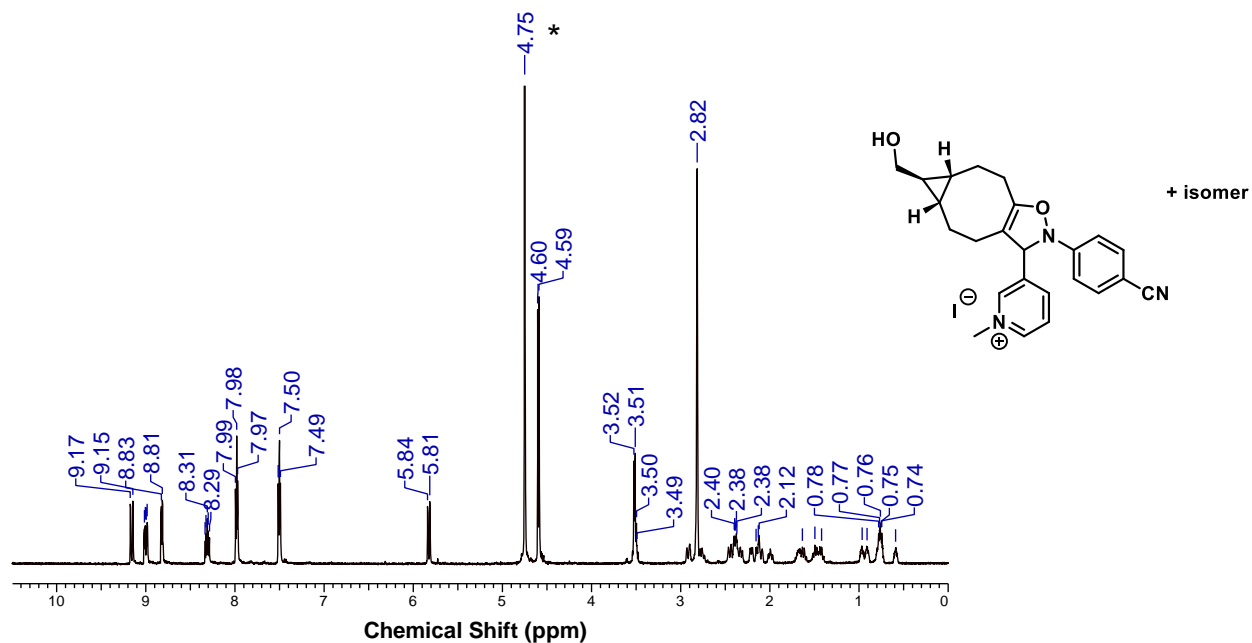


Figure S3.43. ^1H NMR spectrum of $3\text{c-BCN}_{\text{exo-OH}}$ cycloadduct (2 isomers) in 1:1 $\text{D}_2\text{O}:(\text{CD}_3)_2\text{SO}$ at 25°C . * denotes residual protio solvent.

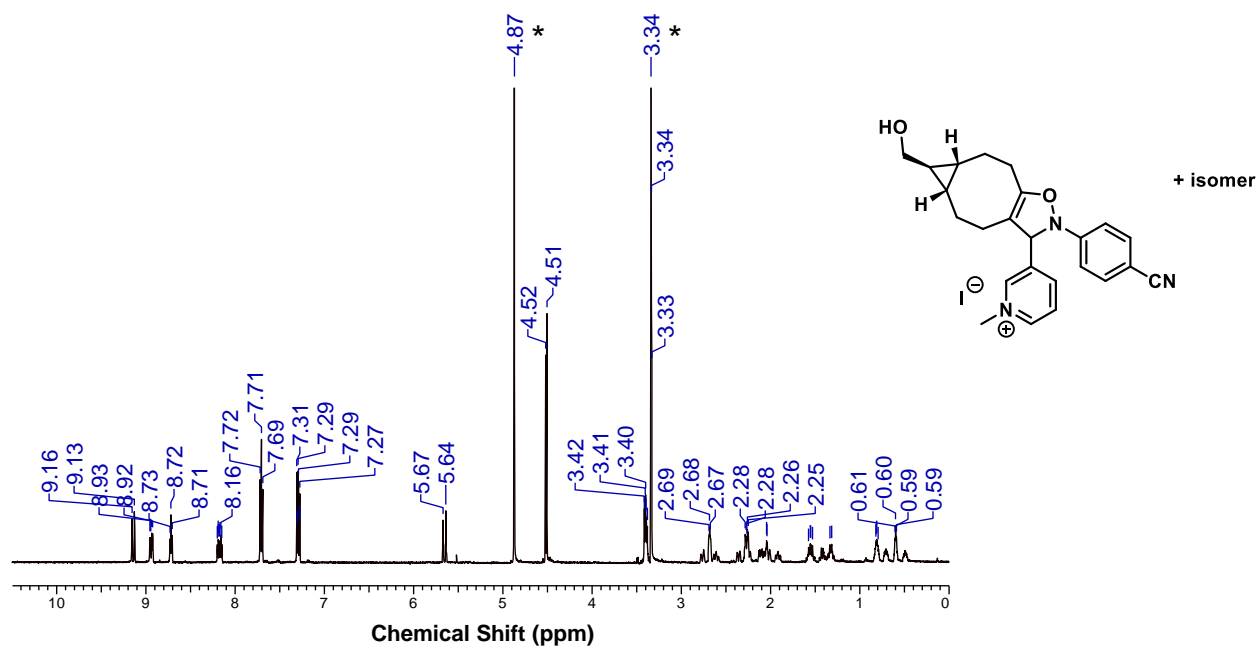


Figure S3.44. ¹H NMR spectrum of **3c-BCN_{exo}-OH cycloadduct** (2 isomers) in CD₃OD at 25°C. * denotes residual protio solvent and impurities.

3.6.12 NMR Spectra of Cycloadduct between DBCO-amine and Nitron 3c

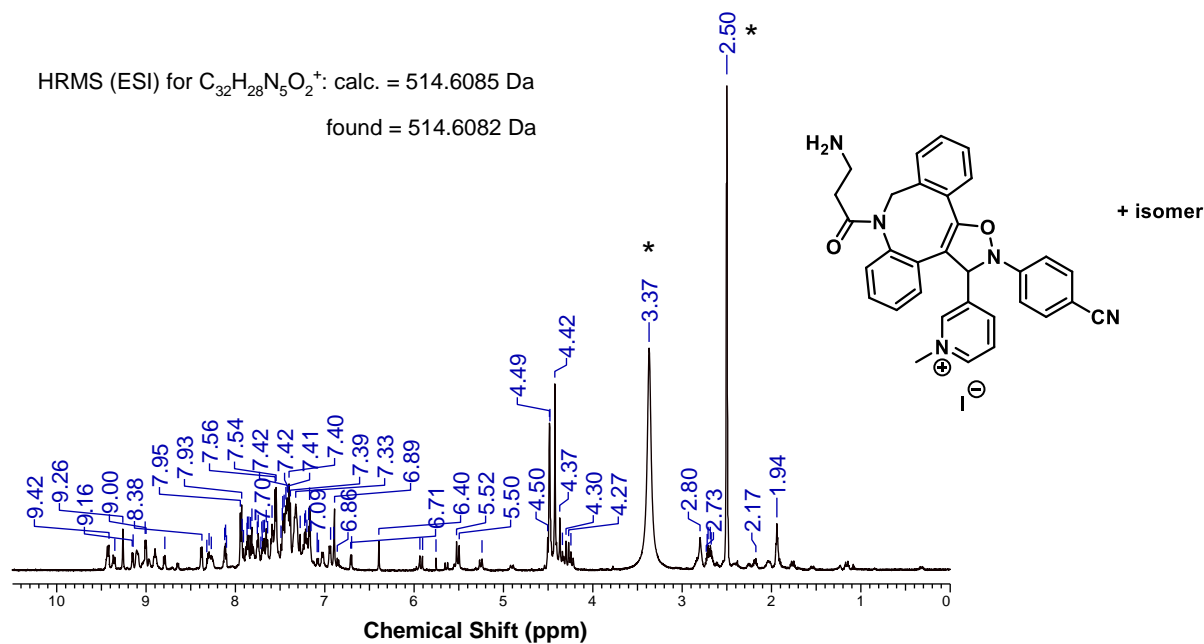


Figure S3.45. 1H NMR spectrum of **3c-DBCO-amine cycloadduct** (2 isomers) in $(CD_3)_2SO$ at $25^\circ C$. * denotes residual protio solvent and impurities.

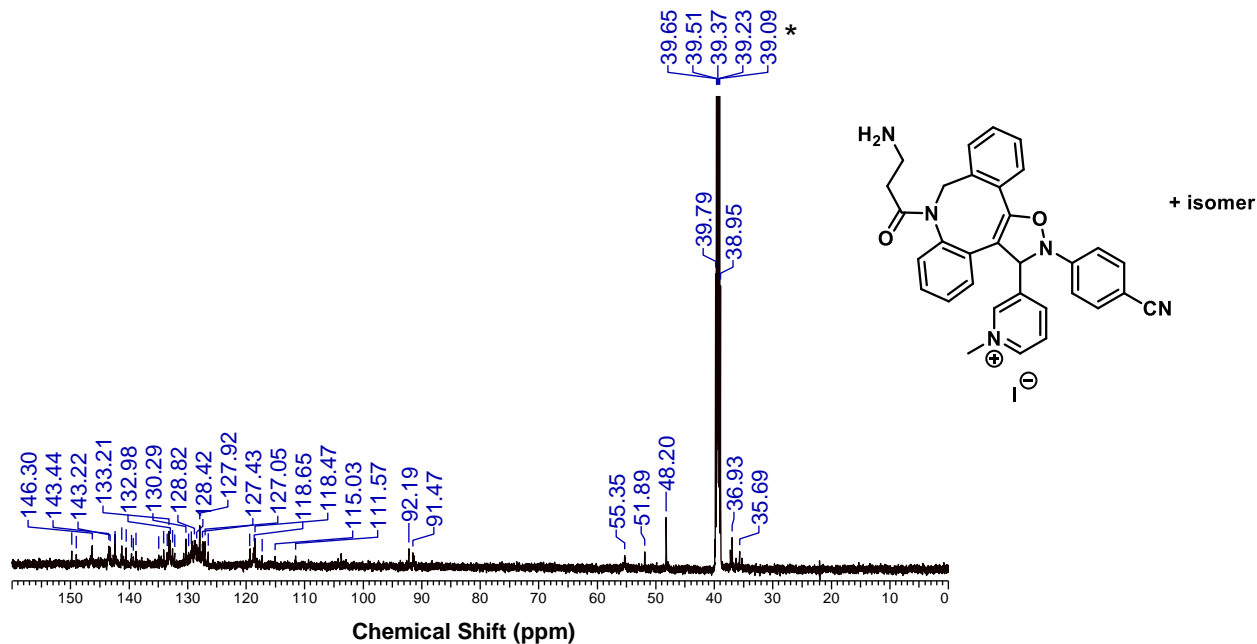


Figure S3.46. $^{13}C\{^1H\}$ NMR spectrum of **3c-DBCO-amine cycloadduct** (2 isomers) in $(CD_3)_2SO$ at $25^\circ C$. * indicates $(CD_3)_2SO$ solvent.

3.6.13 NMR Spectra of Cycloadduct between (Z)-cyclooct-1-ene-5-yne (6b) and Nitrene 3c

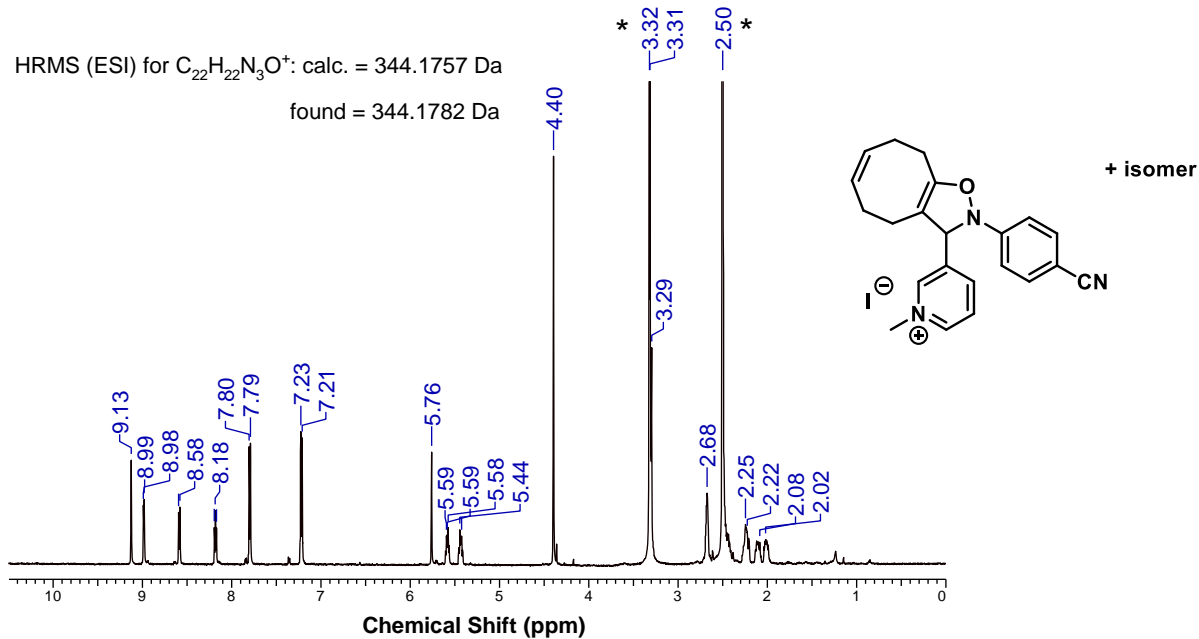


Figure S3.47. 1H NMR spectrum of **3c-6b** cycloadduct (2 isomers) in $(CD_3)_2SO$ at $25^\circ C$. * denotes residual protio solvent and impurities.

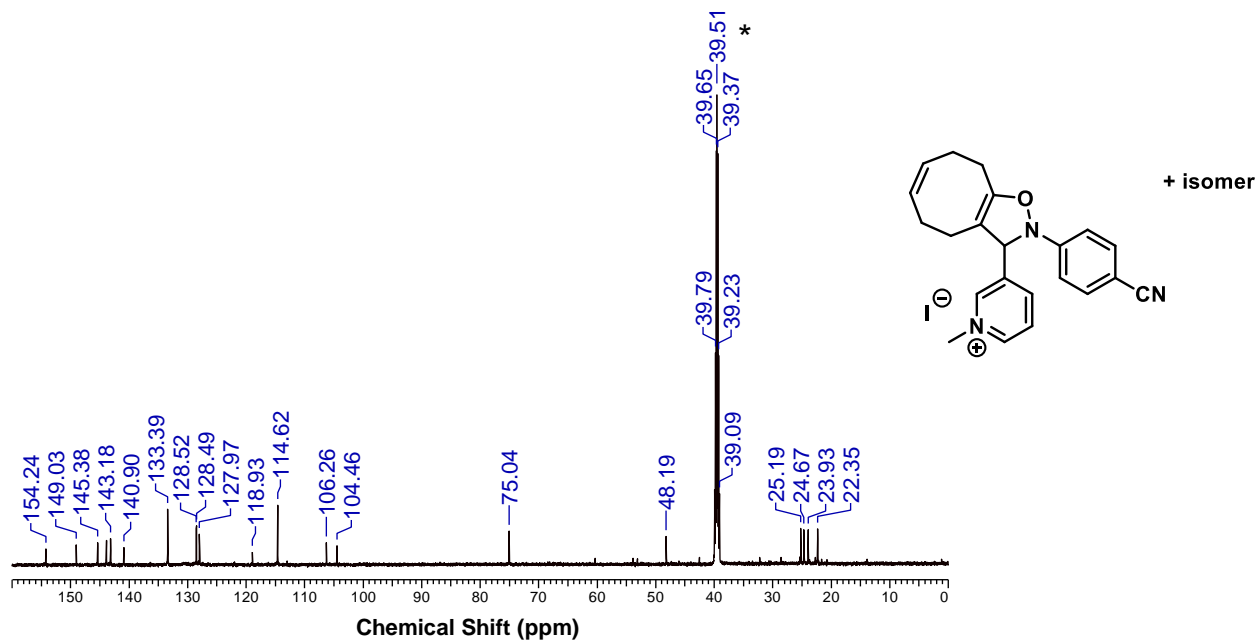


Figure S3.48. $^{13}C\{^1H\}$ NMR spectrum of **3c-6b** cycloadduct (2 isomers) in $(CD_3)_2SO$ at $25^\circ C$. * indicates $(CD_3)_2SO$ solvent.

3.6.14 Stability of Pyridinium-Nitrones 3a, 3b and 3c

To probe the stability of **nitrone 3a**, **3b** and **3c** towards solvent-induced hydrolysis, a solution of each nitrone (10 mg/mL) was prepared in 6:1 D₂O:(CD₃)₂SO. The decrease in the ¹H NMR signal from H_α (see **Table 3.1** in **Section 3.2**) was observed after 5 minutes, 1 hour, 4 hours and 12 hours relative to the residual H₂O peak. The change in the intensity of this signal was determined as a percentage of the signal after 5 minutes in the solvent system. ¹H NMR spectra after 5 minutes and 12 hours are shown below.

Table S3.1. Percentage of **nitrone 3a** remaining in 6:1 D₂O:(CD₃)₂SO over time, measured as a change in the H_α NMR signal intensity relative to the peak from residual H₂O solvent.

	Percentage of nitrone remaining
5 minutes	100
1 hour	100
4 hours	100
12 hours	100

Table S3.2. Percentage of **nitrone 3b** remaining in 6:1 D₂O:(CD₃)₂SO over time, measured as a change in the H_α NMR signal intensity relative to the peak from residual H₂O solvent.

	Percentage of nitrone remaining
5 minutes	100
1 hour	99
4 hours	98
12 hours	80

Table S3.3. Percentage of **nitron 3c** remaining in 6:1 D₂O:(CD₃)₂SO over time, measured as a change in the H_α NMR signal intensity relative to the peak from residual H₂O solvent.

	Percentage of nitron remaining
5 minutes	100
1 hour	100
4 hours	99
12 hours	94

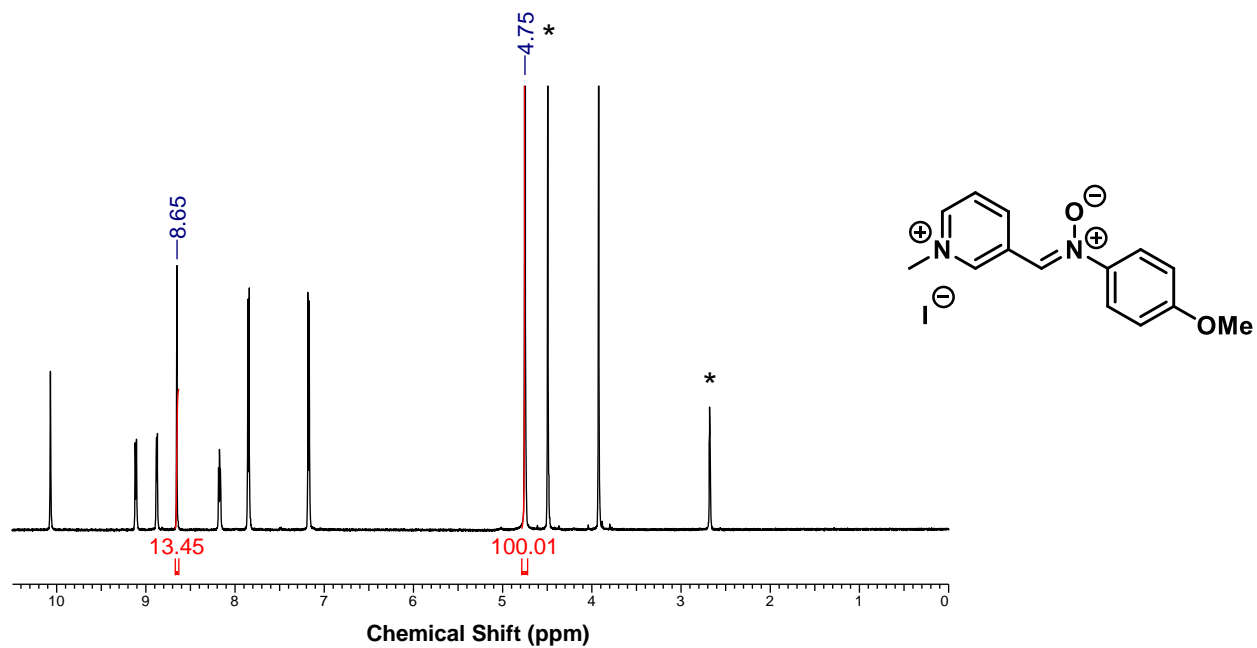


Figure S3.49. ^1H NMR spectrum of **nitron 3a** in 6:1 $\text{D}_2\text{O}:(\text{CD}_3)_2\text{SO}$ at 25°C after 5 minutes. * denotes residual protio solvent.

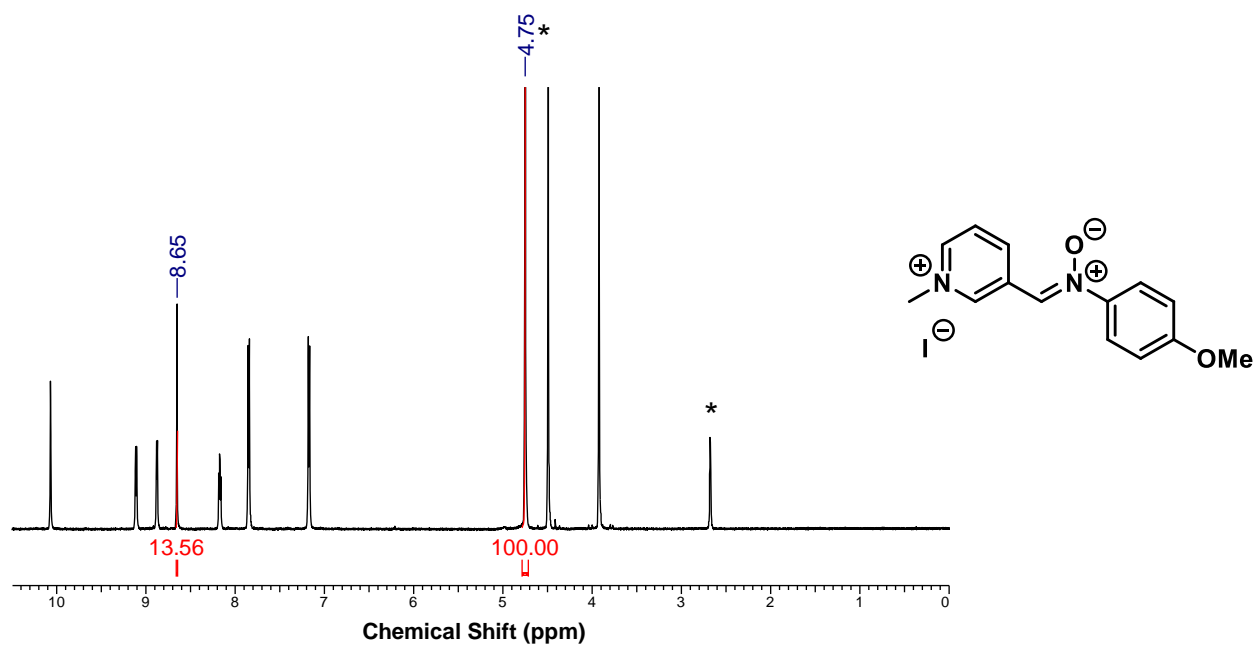
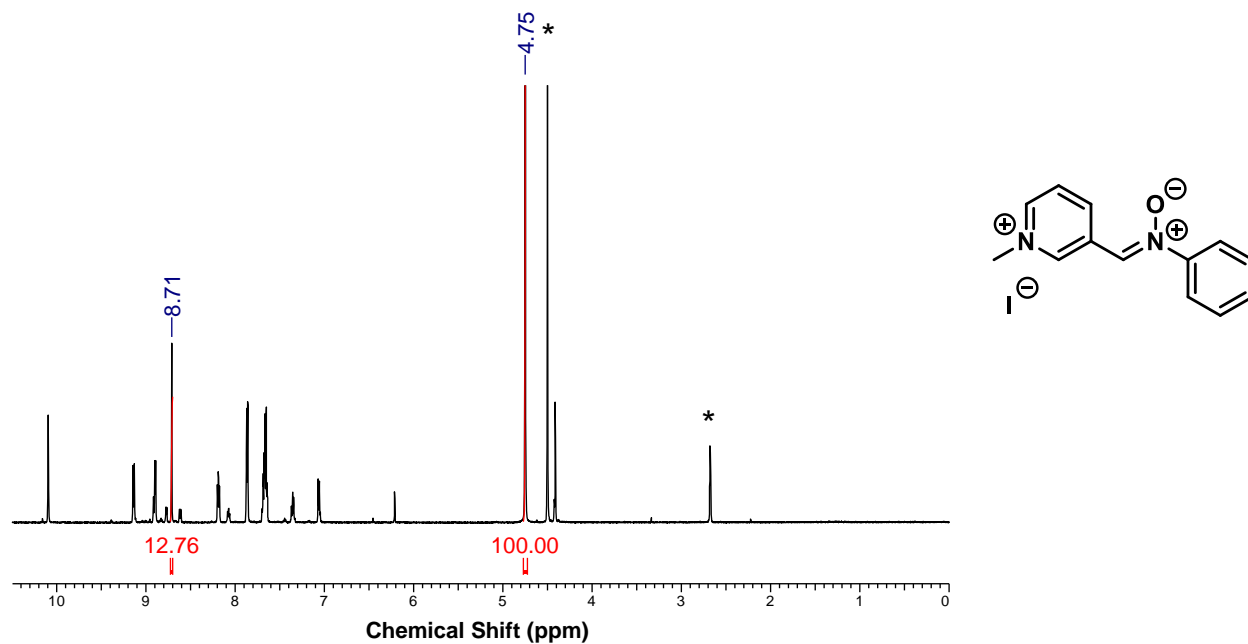
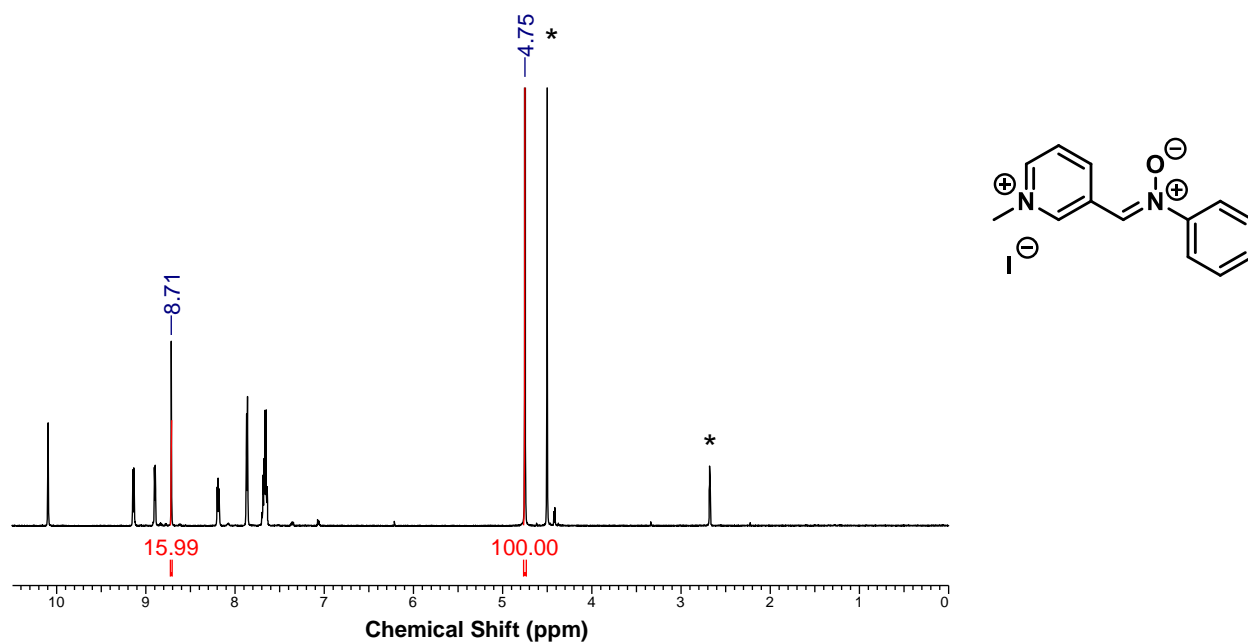


Figure S3.50. ^1H NMR spectrum of **nitron 3a** in 6:1 $\text{D}_2\text{O}:(\text{CD}_3)_2\text{SO}$ at 25°C after 12 hours. * denotes residual protio solvent.



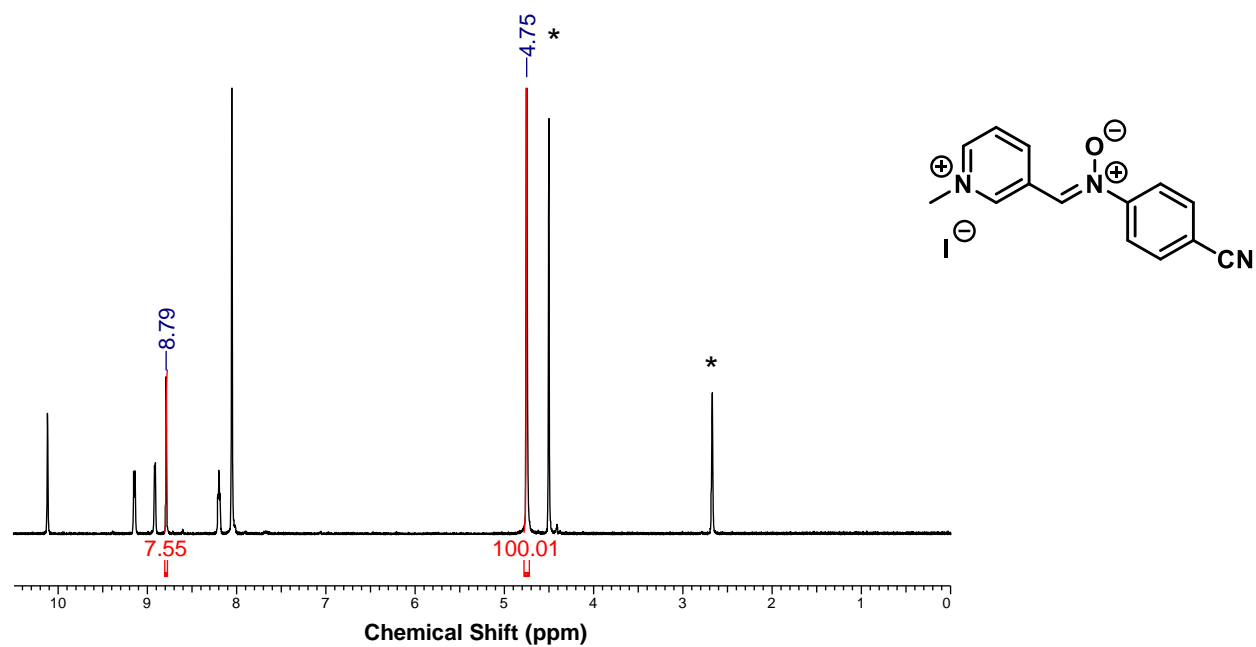


Figure S3.53. ^1H NMR spectrum of **nitrone 3c** in 6:1 $\text{D}_2\text{O}:(\text{CD}_3)_2\text{SO}$ at 25°C after 5 minutes. * denotes residual protio solvent.

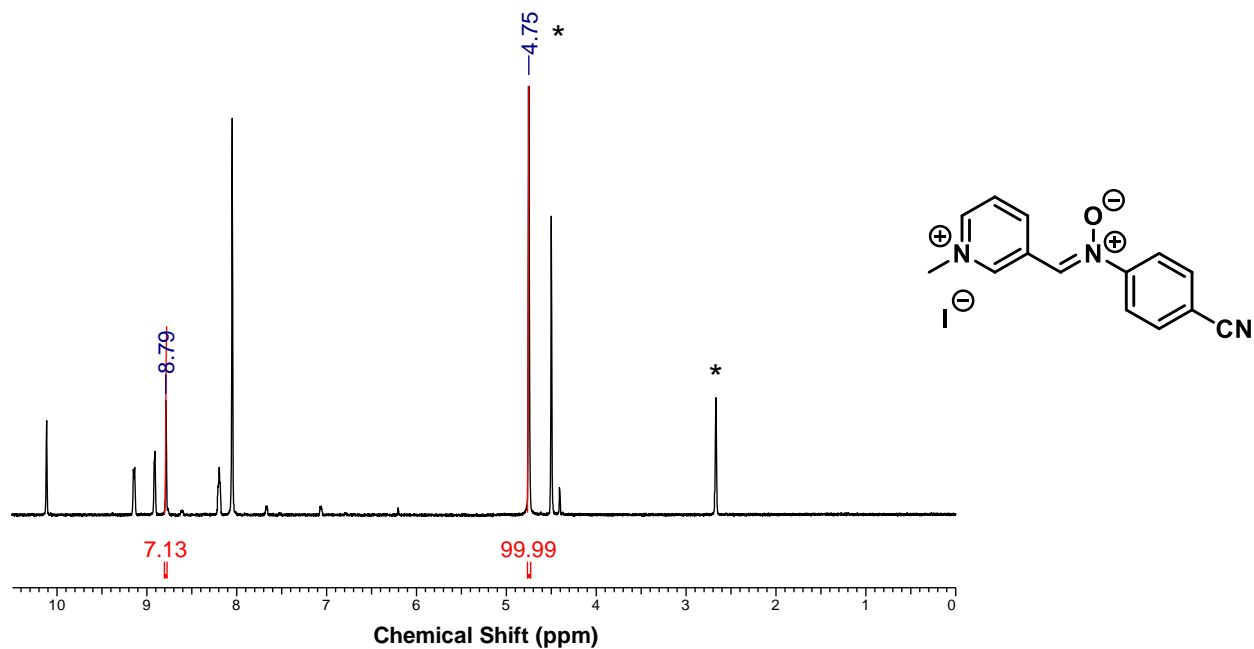


Figure S3.54. ^1H NMR spectrum of **nitrone 3c** in 6:1 $\text{D}_2\text{O}:(\text{CD}_3)_2\text{SO}$ at 25°C after 12 hours. * denotes residual protio solvent.

3.6.15 Kinetic Measurements

*Kinetic measurements were performed according to a previously reported procedure.⁵

Estimated rate constants for the pyridinium-nitrones were determined under pseudo-first order conditions in 2:1 acetonitrile:methanol at 25°C using UV-Vis absorption spectroscopy. Each nitrone was added to excess **BCN_{exo}-OH (5)** (50eq, 75eq, 100eq, 125 eq), with each trial being performed in duplicate. As the cycloaddition reaction with **BCN_{exo}-OH** proceeded, the decrease in intensity of the absorbance at 345 nm (for **nitrones 3a-c**), 316 nm (for **nitrone 4**) and 320 nm (for **nitrone 2b**) was monitored over time.

The natural logarithm of the absorbance was then plotted over time to obtain four averaged observed rate constants (k_{obs}) under pseudo-first order conditions for each nitrone at the four excess equivalencies of **BCN_{exo}-OH (5)**. The observed rate constants were then plotted against the concentration of **BCN_{exo}-OH (5)**, with the slope of the curve representing the second-order rate constant for each cycloaddition reaction of each nitrone.

3.6.15.1 Kinetic Measurements of Cycloaddition Reaction between (4) and BCN_{exo}-OH (5)

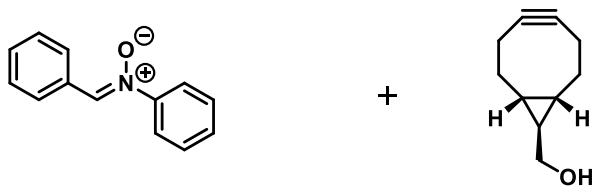


Table S3.4. Kinetic data for **nitro compound 4** and **BCN_{exo}-OH (5)**

Concentration of BCN (mM)	Observed Rate Constant, k_{obs} (s ⁻¹) – Trial 1	Observed Rate Constant, k_{obs} (s ⁻¹) – Trial 2	Average Rate Constant, k_{obs} (s ⁻¹)
0.45	1.1×10^{-5}	1.3×10^{-5}	1.2×10^{-5}
0.68	2.3×10^{-5}	2.7×10^{-5}	2.5×10^{-5}
0.91	3.5×10^{-5}	4.1×10^{-5}	3.8×10^{-5}
1.1	5.3×10^{-5}	6.0×10^{-5}	5.7×10^{-5}

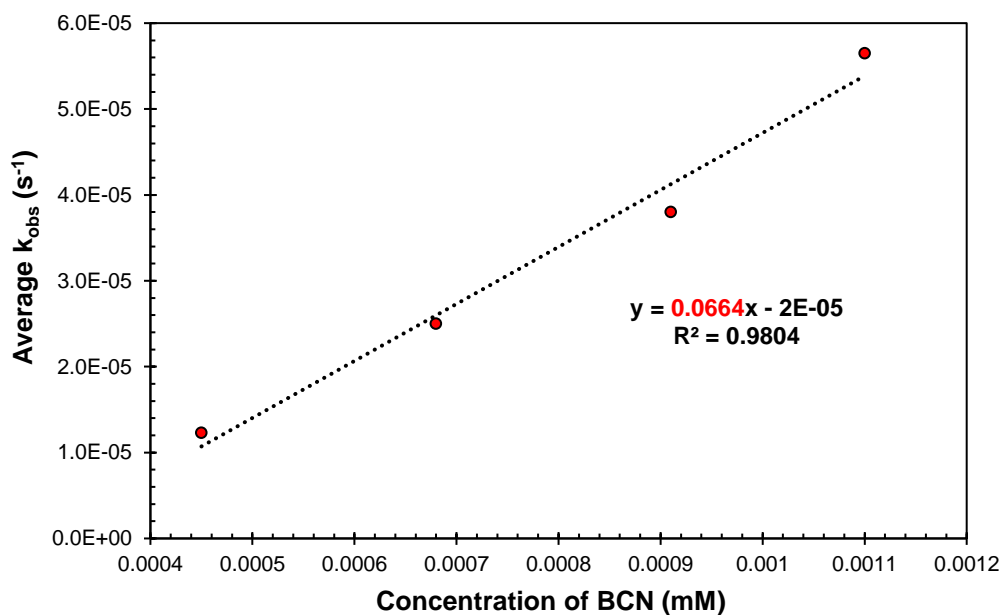


Figure S3.55. Pseudo-first order kinetics graph for **nitro compound 4** with **BCN_{exo}-OH (5)**.

3.6.15.2 Kinetic Measurements of Cycloaddition Reaction between (2b) and BCN_{exo}-OH (5)

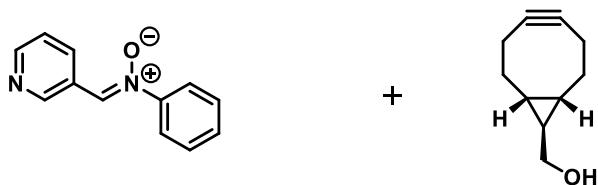


Table S3.5. Kinetic data for **nitrone 2b** and **BCN_{exo}-OH (5)**.

Concentration of BCN (mM)	Observed Rate Constant, k_{obs} (s ⁻¹) – Trial 1	Observed Rate Constant, k_{obs} (s ⁻¹) – Trial 2	Average Rate Constant, k_{obs} (s ⁻¹)
0.45	5.8×10^{-5}	6.3×10^{-5}	6.1×10^{-5}
0.68	8.5×10^{-5}	9.8×10^{-5}	9.2×10^{-5}
0.91	1.2×10^{-4}	1.3×10^{-4}	1.2×10^{-4}
1.1	1.5×10^{-4}	1.7×10^{-4}	1.6×10^{-4}

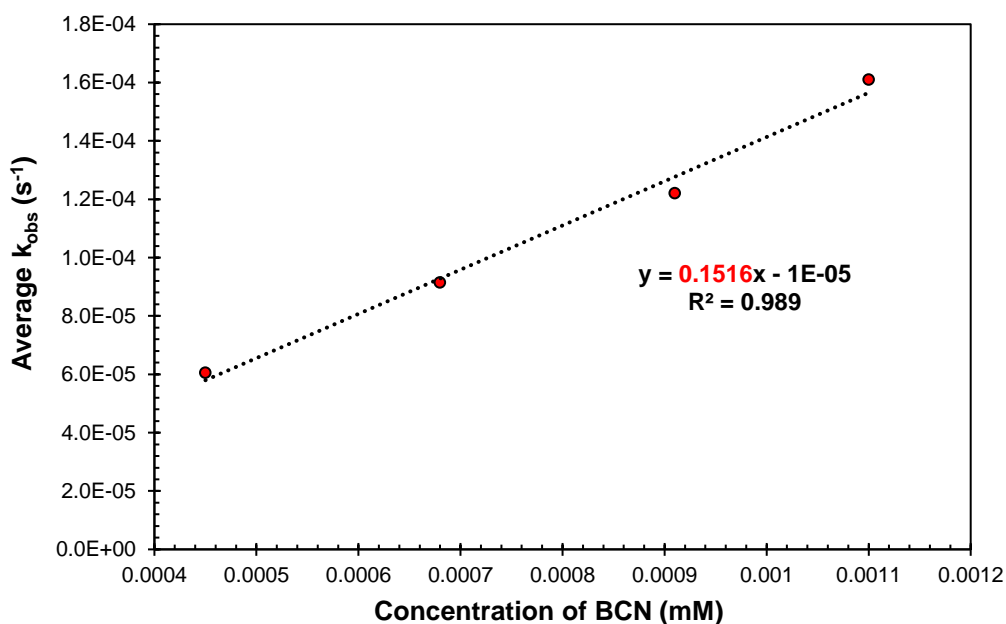


Figure S3.56. Pseudo-first order kinetics graph for **nitrone 2b** with **BCN_{exo}-OH (5)**.

3.6.15.3 Kinetic Measurements of Cycloaddition Reaction between (3a) and BCN_{exo}-OH (5)

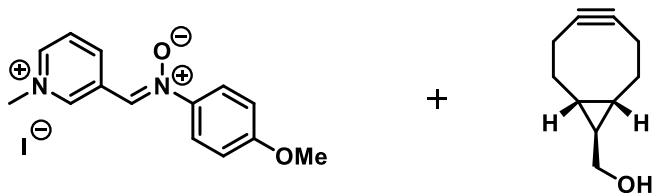


Table S3.6. Kinetic data for **nitroene 3a** and **BCN_{exo}-OH (5)**.

Concentration of BCN (mM)	Observed Rate Constant, k_{obs} (s ⁻¹) – Trial 1	Observed Rate Constant, k_{obs} (s ⁻¹) – Trial 2	Average Rate Constant, k_{obs} (s ⁻¹)
0.45	7.6×10^{-4}	8.1×10^{-4}	7.9×10^{-4}
0.68	1.2×10^{-3}	1.1×10^{-3}	1.2×10^{-3}
0.91	1.5×10^{-3}	1.4×10^{-3}	1.5×10^{-3}
1.1	1.9×10^{-3}	1.8×10^{-3}	1.9×10^{-3}

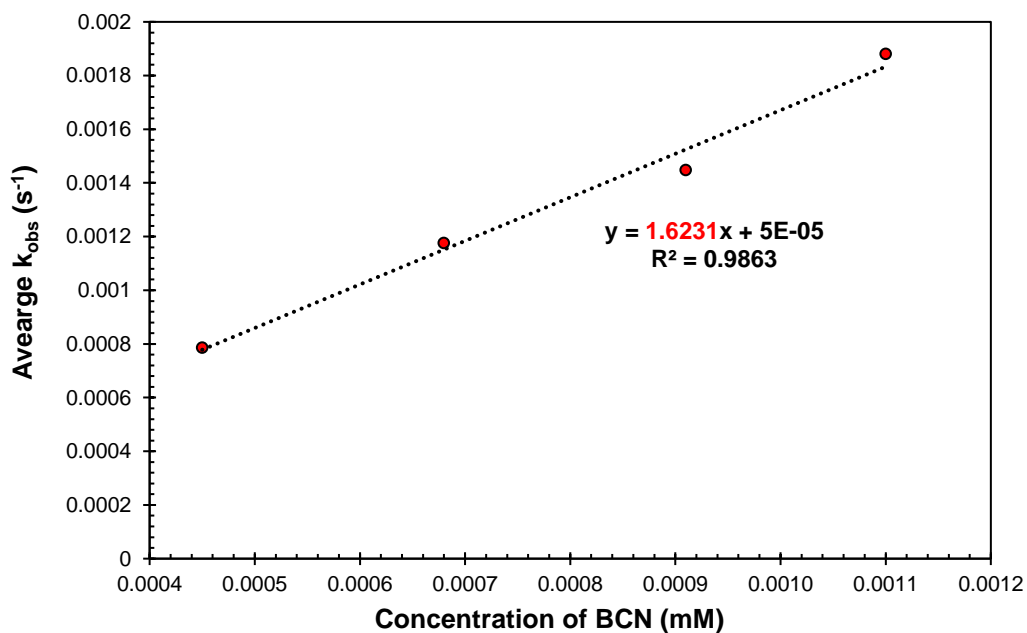


Figure S3.57. Pseudo-first order kinetics graph for **nitroene 3a** with **BCN_{exo}-OH (5)**.

3.6.15.4 Kinetic Measurements of Cycloaddition Reaction between (3b) and BCN_{exo}-OH (5)

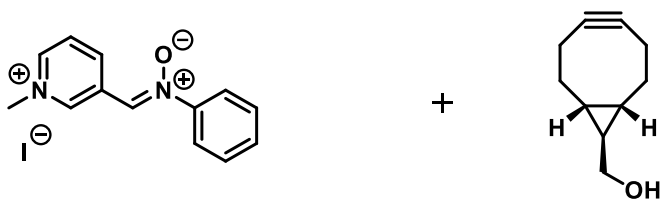


Table S3.7. Kinetic data for **nitronium 3b** and **BCN_{exo}-OH (5)**.

Concentration of BCN (mM)	Observed Rate Constant, k_{obs} (s ⁻¹) – Trial 1	Observed Rate Constant, k_{obs} (s ⁻¹) – Trial 2	Average Rate Constant, k_{obs} (s ⁻¹)
0.45	1.0×10^{-4}	1.1×10^{-4}	1.1×10^{-4}
0.68	1.4×10^{-3}	1.0×10^{-3}	1.2×10^{-3}
0.91	1.9×10^{-3}	1.5×10^{-3}	1.7×10^{-3}
1.1	2.4×10^{-3}	2.2×10^{-3}	2.3×10^{-3}

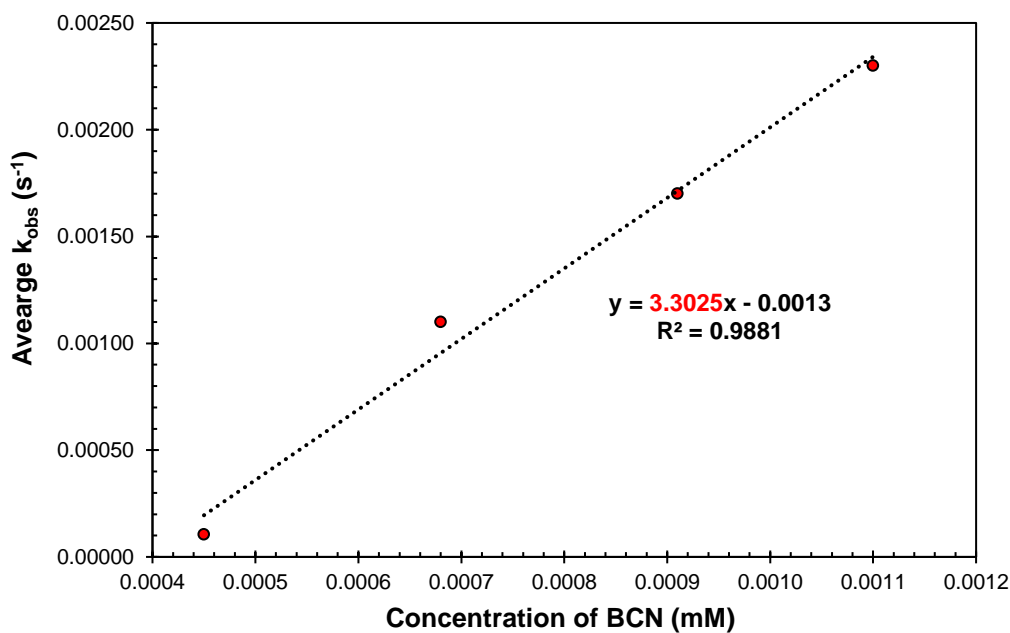


Figure S3.58. Pseudo-first order kinetics graph for **nitronium 3b** with **BCN_{exo}-OH (5)**.

3.6.15.5 Kinetic Measurements of Cycloaddition Reaction between (3c) and BCN_{exo}-OH (5)

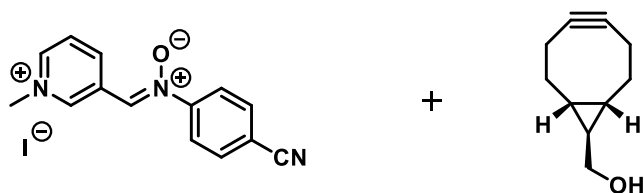


Table S3.8. Kinetic data for **nitron 3c** and **BCN_{exo}-OH (5)**.

Concentration of BCN (mM)	Observed Rate Constant, k_{obs} (s ⁻¹) – Trial 1	Observed Rate Constant, k_{obs} (s ⁻¹) – Trial 2	Average Rate Constant, k_{obs} (s ⁻¹)
0.45	5.1×10^{-3}	5.6×10^{-3}	5.4×10^{-3}
0.68	8.1×10^{-3}	7.9×10^{-3}	8.0×10^{-3}
0.91	9.6×10^{-3}	9.3×10^{-3}	9.5×10^{-3}
1.1	1.0×10^{-2}	1.1×10^{-2}	1.1×10^{-2}

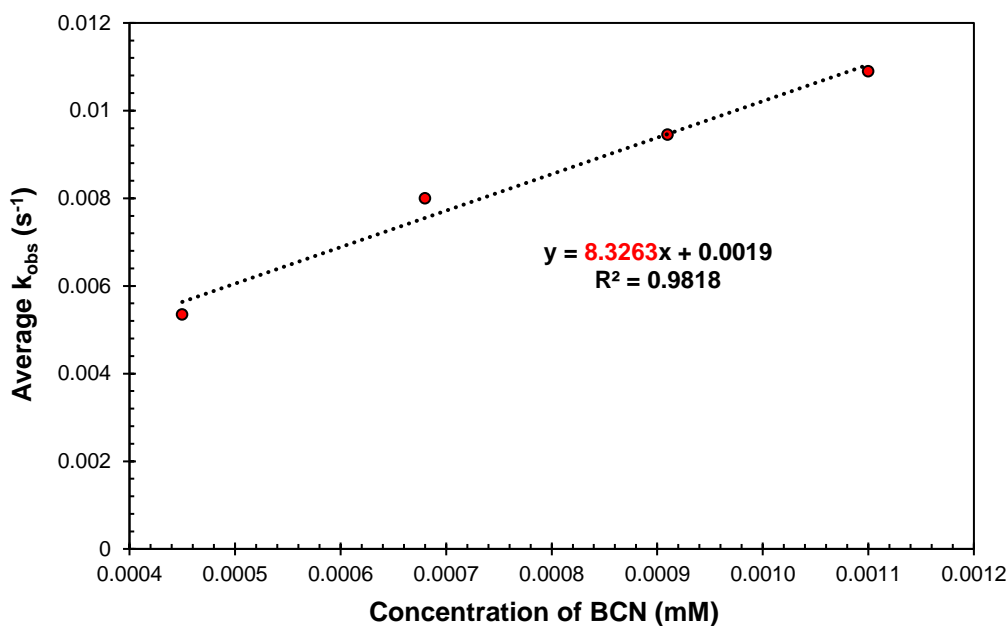


Figure S3.59. Pseudo-first order kinetics graph for **nitron 3c** with **BCN_{exo}-OH (5)**.

3.6.16 Crystallographic Information

3.6.16.1 Data Collection and Processing

The molecular structure of **4** has been previously reported⁶, where the data was collected at room temperature. However, in order to allow for direct crystallographic comparisons with **3a-3c**, we include our data for **Nitron 4**, which was collected at 110K – the same temperature used to collect structures **3a-3c** and **2b**.

Nitron 4 (N-phenyl-C-phenyl-nitron) was crystallized out of a 1:4 mixture of dichloromethane:di-ethyl ether. Crystals of **nitron 4** was mounted on a Mitegen polyimide micromount with a small amount of Paratone N oil. All X-ray measurements were made on a Bruker-Nonius KappaCCD Apex2 diffractometer at a temperature of 110 K. The unit cell dimensions were determined from a symmetry constrained fit of 7598 reflections with $6.82^\circ < 2\theta < 132.52^\circ$. The data collection strategy was a number of ω and ϕ scans which collected data up to 133.05° (2θ). The frame integration was performed using SAINT.⁷ The resulting raw data was scaled and absorption corrected using a multi-scan averaging of symmetry equivalent data using SADABS.⁸

Nitron 2b (N-phenyl-C-(3-pyridine)-nitron) was crystallized out of a 1:4 mixture of dichloromethane:di-ethyl ether. Crystals of **nitron 2b** was mounted on a Mitegen polyimide micromount with a small amount of Paratone N oil. All X-ray measurements were made on a Bruker Kappa Axis Apex2 diffractometer at a temperature of 110 K. The unit cell dimensions were determined from a symmetry constrained fit of 9938 reflections with $4.9^\circ < 2\theta < 81.22^\circ$. The data collection strategy was a number of ω and ϕ scans which collected data up to 86.246° (2θ). The frame integration was performed using SAINT.⁷ The resulting raw data was scaled and absorption corrected using a multi-scan averaging of symmetry equivalent data using SADABS.⁸

Nitron 3a (N-(4-methoxyphenyl)-C-(3-methylpyridinium) nitron) was crystallized out of a 1:2 mixture of dimethyl sulfoxide:dichloromethane. Crystals of **nitron 3a** was mounted on a Mitegen polyimide micromount with a small amount of Paratone N oil. All X-ray measurements were made on a Bruker-Nonius KappaCCD Apex2 diffractometer at a temperature of 110 K. The unit cell dimensions were determined from a symmetry constrained fit of 9872

reflections with $5.26^\circ < 2\theta < 132.74^\circ$. The data collection strategy was a number of ω and φ scans which collected data up to 132.722° (2θ). The frame integration was performed using SAINT.⁷ The resulting raw data was scaled and absorption corrected using a multi-scan averaging of symmetry equivalent data using SADABS.⁸

Nitrone 3b (*N*-phenyl-*C*-(3-methylpyridinium) nitrone) was crystallized out of a 1:2 mixture of dimethyl sulfoxide:dichloromethane. Crystals of **nitrone 3b** was mounted on a Mitegen polyimide micromount with a small amount of Paratone N oil. All X-ray measurements were made on a Bruker Kappa Axis Apex2 diffractometer at a temperature of 223 K. The unit cell dimensions were determined from a symmetry constrained fit of 9948 reflections with $5.66^\circ < 2\theta < 62.14^\circ$. The data collection strategy was a number of ω and φ scans which collected data up to 81.114° (2θ). The frame integration was performed using SAINT.⁷ The resulting raw data was scaled and absorption corrected using a multi-scan averaging of symmetry equivalent data using SADABS.⁸

Nitrone 3c (*N*-(4-cyanophenyl)-*C*-(3-methylpyridinium) nitrone) was crystallized out of a 1:2 mixture of dimethyl sulfoxide:dichloromethane. Crystals of **nitrone 3c** was mounted on a Mitegen polyimide micromount with a small amount of Paratone N oil. All X-ray measurements were made on a Bruker-Nonius KappaCCD Apex2 diffractometer at a temperature of 110 K. The unit cell dimensions were determined from a symmetry constrained fit of 9994 reflections with $8.92^\circ < 2\theta < 130.88^\circ$. The data collection strategy was a number of ω and φ scans which collected data up to 132.602° (2θ). The frame integration was performed using SAINT.⁷ The resulting raw data was scaled and absorption corrected using a multi-scan averaging of symmetry equivalent data using SADABS.⁸

3.6.16.2 Structure Solution and Refinement

The structure for **nitrone 4** was solved by using a dual space methodology using the SHELXT program.⁹ All non-hydrogen atoms were obtained from the initial solution. The hydrogen atoms were introduced at idealized positions and were allowed to refine isotropically. The structural model was fit to the data using full matrix least-squares based on F^2 . The calculated structure factors included corrections for anomalous dispersion from the usual tabulation. The structure was refined using the SHELXL program from the SHELX suite of crystallographic

software.¹⁰ Graphic plots were produced using the NRCVAX program suite.¹¹ Additional information and other relevant literature references can be found in the reference section of this website (<http://xray.chem.uwo.ca>).

The structure for **nitron 2b** was solved by using a dual space methodology using the SHELXT program.⁹ All non-hydrogen atoms were obtained from the initial solution. The hydrogen atom positions were recovered from a difference Fourier map and were allowed to refine isotropically. The structural model was fit to the data using full matrix least-squares based on F^2 . The calculated structure factors included corrections for anomalous dispersion from the usual tabulation. The structure was refined using the SHELXL program from the SHELX suite of crystallographic software.¹⁰ Graphic plots were produced using the NRCVAX program suite.¹¹

The structure for **nitron 3a** was solved by using a dual space methodology using the SHELXT program.⁹ All non-hydrogen atoms were obtained from the initial solution. The iodine atom resided on two half occupancy higher symmetry sites (an inversion centre and along a two-fold axis). The charge is balanced. The hydrogen atoms were introduced at idealized positions and were allowed to ride on the parent atom. The N bound oxygen exhibited a disorder. The normalized occupancy of the major conformer refined to a value of 0.81(9). The structural model was fit to the data using full matrix least-squares based on F^2 . The calculated structure factors included corrections for anomalous dispersion from the usual tabulation. The structure was refined using the SHELXL-2014 program from the SHELX suite of crystallographic software.¹⁰ Graphic plots were produced using the NRCVAX program suite.¹¹

The structure for **nitron 3b** was solved by using a dual space methodology using the SHELXT program.⁹ All non-hydrogen atoms were obtained from the initial solution. The hydrogen atoms were introduced at idealized positions and were allowed to refine isotropically. The structural model was fit to the data using full matrix least-squares based on F^2 . The calculated structure factors included corrections for anomalous dispersion from the usual tabulation. The structure was refined using the SHELXL-2014 program from the SHELX suite of crystallographic software.¹⁰ Graphic plots were produced using the NRCVAX program suite.¹¹

The structure for **9** was solved by using a dual space methodology using the SHELXT program.⁹ All non-hydrogen atoms were obtained from the initial solution. The hydrogen atoms

were introduced at idealized positions and were allowed to refine isotropically. During the refinement the highly obtuse β angle (130.3°) induced high correlations between the parameters in the least-squares calculation. To reduce these correlations, the basis vectors for the lattice were transformed from the C centred to I centred monoclinic ($\beta = 98.1^\circ$) setting. The structural model was fit to the data using full matrix least-squares based on F^2 . The calculated structure factors included corrections for anomalous dispersion from the usual tabulation. The structure was refined using the SHELXL program from the SHELX suite of crystallographic software.¹⁰ Graphic plots were produced using the NRCVAX program suite.¹¹

3.6.14.3 Summary of Crystallographic Data

Table S3.9. Crystallographic information of for molecular structures of nitrones.

Formula	C ₁₃ H ₁₁ NO (4)	C ₁₂ H ₁₀ N ₂ O (2b)	C ₁₄ H ₁₅ IN ₂ O ₂ (3a)	C ₁₃ H ₁₃ IN ₂ O (3b)	C ₁₄ H ₁₂ IN ₃ O (3c)
Formula Weight (g/mol)	197.23	198.22	370.18	340.15	365.17
Crystal Dimensions (mm)	0.443 × 0.174 × 0.129	0.509 × 0.381 × 0.194	0.454 × 0.365 × 0.050	0.402 × 0.094 × 0.057	0.307 × 0.221 × 0.163
Crystal Color and Habit	colourless prism	colourless prism	yellow plate	yellow plate	yellow prism
Crystal System	monoclinic	orthorhombic	monoclinic	triclinic	monoclinic
Space Group	P 2 ₁ /c	P n a 2 ₁	C 2/c	P -1	I 2/a
Temperature, K	110	110	110	223	110
<i>a</i> , Å	5.5919(11)	11.185(3)	11.3621(17)	7.505(2)	19.674(4)
<i>b</i> , Å	12.970(2)	5.3296(13)	7.4294(11)	7.8344(19)	7.0150(14)
<i>c</i> , Å	13.859(3)	16.612(5)	33.664(5)	11.648(4)	20.045(4)
<i>a</i> , °	90	90	90	100.721(7)	90
<i>b</i> , °	96.856(11)	90	91.797(6)	106.259(10)	98.09(3)
<i>g</i> , °	90	90	90	90.352(6)	90

V, Å³	997.9(3)	990.2(5)	2840.3(7)	644.8(3)	2739.1(10)
Number of reflections to determine final unit cell	7598	9938	9872	9948	9994
Min and Max 2θ for cell determination, °	6.82, 132.52	4.9, 81.22	5.26, 132.74	5.66, 62.14	8.92, 130.88
Z	4	4	8	2	8
F(000)	416	416	1456	332	1424
<i>r</i> (g/cm³)	1.313	1.330	1.731	1.752	1.771
<i>l</i>, Å	1.54178	0.71073	1.54178	0.71073	1.54178
<i>m</i>, (cm⁻¹)	0.663	0.087	17.723	2.469	18.339
Diffraction Type	Bruker-Nonius KappaCCD Apex2	Bruker Kappa Axis Apex2	Bruker-Nonius KappaCCD Apex2	Bruker Kappa Axis Apex2	Bruker-Nonius KappaCCD Apex2
Scan Type(s)	phi and omega scans	phi and omega scans	phi and omega scans	phi and omega scans	phi and omega scans
Max 2θ for data collection, °	133.05	86.246	132.722	81.114	132.602
Measured fraction of data	0.973	0.999	0.976	0.999	0.976
Number of reflections measured	13435	56730	37790	52949	23884
Unique reflections measured	1716	7112	2420	8092	2344
R_{merge}	0.0392	0.0274	0.0506	0.0271	0.0464

Number of reflections included in refinement	1716	7112	2420	8092	2344
Cut off Threshold Expression	I > 2sigma(I)	I > 2sigma(I)	I > 2sigma(I)	I > 2sigma(I)	I > 2sigma(I)
Structure refined using	full matrix least-squares using F ²	full matrix least-squares using F ²	full matrix least-squares using F ²	full matrix least-squares using F ²	full matrix least-squares using F ²
Weighting Scheme	w=1/[sigma ² (Fo ²)+(0.0452P) ² +0.3451P] where P=(Fo ² +2Fc ²)/3	w=1/[sigma ² (Fo ²)+(0.0754P) ² +0.0069P] where P=(Fo ² +2Fc ²)/3	w=1/[sigma ² (Fo ²)+(0.0469P) ² +3.8749P] where P=(Fo ² +2Fc ²)/3	w=1/[sigma ² (Fo ²)+(0.0254P) ² +0.0759P] where P=(Fo ² +2Fc ²)/3	w=1/[sigma ² (Fo ²)+(0.0374P) ² +4.9072P] where P=(Fo ² +2Fc ²)/3
Number of parameters in least-squares	180	176	186	206	220
R₁	0.0334	0.0421	0.0244	0.0264	0.0228
wR₂	0.0837	0.1043	0.0674	0.0528	0.0594
R₁ (all data)	0.0379	0.0547	0.0247	0.0437	0.0238
wR₂ (all data)	0.0883	0.1121	0.0681	0.0573	0.0602
GOF	1.059	1.043	1.070	1.030	1.062
Maximum shift/error	0.000	0.000	0.000	0.001	0.001
Min & Max peak heights on final ΔF Map (e⁻/Å)	-0.274, 0.160	-0.283, 0.512	-1.385, 0.636	-0.603, 0.856	-0.494, 0.881

Where:

$$R_1 = \sum (|F_o| - |F_c|) / \sum F_o$$

$$wR_2 = [\sum (w(F_o^2 - F_c^2)^2) / \sum (w F_o^4)]^{1/2}$$

$$\text{GOF} = [\sum (w(F_o^2 - F_c^2)^2) / (\text{No. of reflns.} - \text{No. of params.})]^{1/2}$$

3.6.17 Computational Information

3.6.17.1 Computational Methods

Calculations were carried out in Gaussian 09 revision A.02 at the B3LYP/6-31G* level of theory. Geometry optimization of the gas-phase singlet ground state was supplemented with frequency analysis to ensure the optimized structure is located at a potential energy minimum. Computed HOMO and LUMO energies and Mulliken atomic charges were from the DFT-optimized structure. Kohn–Sham orbitals were plotted using Visualization for Electronic and Structural Analysis,¹² version 3.3.2.

3.6.17.2 Optimized Structural Coordinates

Table S3.10. Structural coordinates for **BCN_{exo}-OH (5)**.

	x	y	z
O	0.046523	1.073014	0.059511
C	1.182749	1.806283	-0.388085
H	-0.649228	1.722774	0.247616
C	1.609048	2.879890	0.586518
C	0.942572	4.243847	0.592045
C	2.392796	4.092029	0.136783
H	1.872067	2.494576	1.572477
H	2.496080	4.181073	-0.946479
H	0.264807	4.417153	-0.247592
C	0.442171	4.892989	1.877033
C	3.646135	4.555575	0.869526
C	0.326146	6.445540	1.799016
C	3.989906	6.058925	0.643641
C	1.659882	6.931265	1.439444
C	2.809569	6.809396	1.077078
H	1.975824	1.060842	-0.514692
H	1.000052	2.259325	-1.377985
H	-0.543819	4.473505	2.126113
H	1.107513	4.643710	2.711644
H	3.539702	4.390215	1.947838
H	4.494907	3.939851	0.538238
H	-0.420433	6.736145	1.046974
H	-0.027255	6.841082	2.759799
H	4.894071	6.323275	1.206672
H	4.214378	6.245270	-0.415668

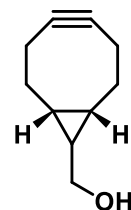
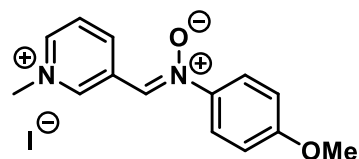
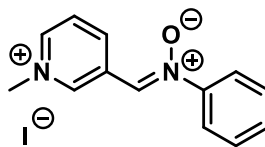


Table S3.11. Structural coordinates for **nitron 3a**.

	x	y	z
C	6.445896	5.619097	17.317141
H	7.361805	6.206486	17.250434
H	5.675535	6.052435	16.674740
H	6.648627	4.592566	17.013430
N	5.969194	5.622029	18.722288
C	6.185302	6.715499	19.489875
H	6.734876	7.530780	19.036701
C	5.702563	6.746910	20.790299
H	5.880736	7.625493	21.399786
C	5.007527	5.655793	21.290393
H	4.633374	5.677811	22.309617
C	4.781083	4.509118	20.490684
C	5.290877	4.545661	19.177175
H	5.151454	3.715381	18.501295
C	4.061636	3.400582	21.051091
H	3.679633	3.481324	22.057557
N	3.796688	2.263311	20.403947
C	3.127879	1.172980	21.075887
C	3.256147	0.961235	22.451431
H	3.901887	1.587798	23.057640
C	2.596727	-0.105230	23.053536
H	2.720122	-0.269913	24.116790
C	1.804841	-0.967945	22.274722
C	1.699368	-0.753041	20.885289
H	1.088154	-1.433624	20.302541
C	2.361664	0.301069	20.287490
H	2.293416	0.471966	19.220218
O	1.123489	-2.023372	22.753087
C	1.172961	-2.316061	24.151225
H	2.196226	-2.546445	24.469349
H	0.542226	-3.194225	24.287713
H	0.775752	-1.482881	24.742346
O	4.089432	2.085913	19.180685

**Table S3.12.** Structural coordinates for **nitron 3b**.

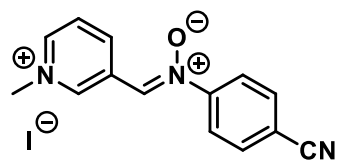
	x	y	z
C	6.796010	1.645569	2.460030
H	7.509282	2.439835	2.227048
H	7.058293	0.736803	1.918205
H	6.799403	1.445015	3.530995
N	5.435005	2.076774	2.053681
C	5.013326	1.832062	0.791374



H	5.694627	1.294519	0.143868
C	3.760915	2.270242	0.386981
H	3.430582	2.068140	-0.625503
C	2.951622	2.952839	1.284012
H	1.968940	3.293082	0.971104
C	3.389608	3.209076	2.604690
C	4.672990	2.743429	2.949047
H	5.081210	2.907051	3.935278
C	2.516128	3.914357	3.504265
H	1.557988	4.257364	3.143236
N	2.812076	4.208107	4.768439
O	3.937113	3.955246	5.296783
C	1.832020	4.877856	5.612496
C	0.462697	4.642193	5.459385
H	0.093904	3.921627	4.736993
C	-0.429634	5.308241	6.297234
H	-1.494603	5.123328	6.198566
C	0.044327	6.191269	7.270569
H	-0.656653	6.706677	7.919896
C	1.417934	6.401654	7.419702
H	1.786454	7.082805	8.180171
C	2.323531	5.738416	6.596145
H	3.392902	5.878025	6.697712

Table S3.13. Structural coordinates for **nitron 3c**.

	x	y	z
C	0.809613	-0.861925	0.225788
C	1.631883	0.252680	0.137475
C	1.080632	1.550489	0.028313
C	-0.323152	1.647348	0.017772
N	-1.096961	0.542047	0.100418
C	-0.567606	-0.698907	0.204156
H	1.223853	-1.860355	0.307234
H	2.710626	0.127934	0.150165
C	1.970562	2.679124	-0.067277
H	-0.818790	2.603982	-0.055776
C	-2.572537	0.707628	0.125872
H	-1.265693	-1.524164	0.268944
N	1.573997	3.943885	-0.174741
C	2.558220	5.010107	-0.313109
O	0.357890	4.303456	-0.139960
C	3.758032	4.806437	-1.000018
C	4.660581	5.858536	-1.108422
C	4.359553	7.105215	-0.534482
C	3.139024	7.295860	0.136648



C	2.231266	6.249549	0.240328
H	1.280467	6.377362	0.742908
H	2.909115	8.262373	0.571496
H	3.977123	3.861088	-1.484291
C	5.295197	8.185842	-0.644324
H	5.591385	5.724619	-1.648486
H	3.036555	2.510221	-0.026782
H	-3.037656	-0.178316	-0.306294
H	-2.901345	0.837150	1.159778
H	-2.841069	1.584189	-0.463093
N	6.056295	9.060133	-0.731875

Table S3.14. Structural coordinates for **nitron 2b**.

	x	y	z
N	5.430468	1.892686	2.115718
C	4.983160	1.763619	0.861409
H	5.625179	1.210740	0.177275
C	3.768179	2.294548	0.420038
H	3.449412	2.163051	-0.609788
C	2.984620	2.988697	1.329737
H	2.031388	3.414577	1.023410
C	3.425720	3.143147	2.660364
C	4.676110	2.565486	2.990484
H	5.057625	2.662544	3.998666
C	2.569441	3.870467	3.569727
H	1.640102	4.272406	3.188402
N	2.814324	4.124556	4.845409
O	3.891895	3.814440	5.459067
C	1.819927	4.841528	5.638237
C	0.449933	4.662977	5.437965
H	0.086441	3.956845	4.698754
C	-0.451438	5.371902	6.233075
H	-1.518395	5.228704	6.087992
C	0.013223	6.242176	7.220262
H	-0.692607	6.789906	7.838169
C	1.387540	6.394337	7.422498
H	1.754024	7.062955	8.196184
C	2.297153	5.687592	6.639602
H	3.367374	5.768414	6.786643

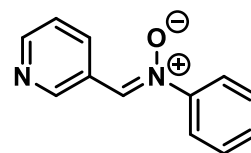
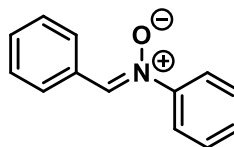


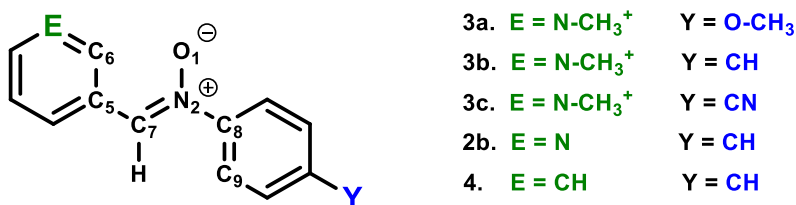
Table S3.15. Structural coordinates for **nitron 4**.

	x	y	z
H	6.456446	1.514364	2.364291
C	5.491955	1.927959	2.081500
C	5.024590	1.771630	0.775084
H	5.621192	1.238534	0.039685
C	3.783292	2.307114	0.417673
H	3.409349	2.192120	-0.596160
C	3.023629	2.988155	1.360470
H	2.057953	3.401380	1.077239
C	3.483458	3.154202	2.686775
C	4.740345	2.611517	3.034929
H	5.099718	2.738463	4.046367
C	2.614591	3.873219	3.592499
H	1.676910	4.251109	3.207542
N	2.848700	4.146547	4.866156
O	3.931196	3.869647	5.493145
C	1.835365	4.850313	5.645775
C	0.470015	4.641262	5.441982
H	0.124851	3.920125	4.708600
C	-0.450171	5.339826	6.224670
H	-1.513137	5.172661	6.075593
C	-0.009402	6.230247	7.204793
H	-0.729721	6.769672	7.813225
C	1.360464	6.412833	7.411873
H	1.709128	7.097170	8.180105
C	2.288473	5.716950	6.640903
H	3.356011	5.820882	6.792185



3.6.17.3 Comparison of DFT versus XRD

Table S3.16. Comparison of actual bond lengths and bond angles in molecular structures of nitrones to theoretical bond lengths and bond angles from DFT analysis.



		3a	3b	3c	4	5
O ₁ -N ₂	XRD	1.298(5)	1.2861(13)	1.287(3)	1.3003(13)	1.2945(11)
	DFT	1.270	1.266	1.269	1.281	1.278
N ₂ -C ₇	XRD	1.305(4)	1.3130(15)	1.314(4)	1.3126(17)	1.3126(12)
	DFT	1.335	1.331	1.330	1.324	1.324
N ₂ -C ₈	XRD	1.459(4)	1.4607(15)	1.459(4)	1.4612(16)	1.4555(12)
	DFT	1.445	1.457	1.458	1.459	1.460
C ₇ -N ₂ -O ₁	XRD	122.5(4)	123.45(10)	123.0(2)	124.60(11)	124.78(8)
	DFT	122.7	123.3	123.6	125.2	124.9
O ₁ -N ₂ -C ₈	XRD	114.8(4)	116.49(9)	116.4(2)	115.69(10)	116.02(7)
	DFT	116.7	116.6	116.3	115.4	115.6
C ₇ -N ₂ -C ₈	XRD	122.6(2)	120.05(10)	120.5(2)	119.64(11)	119.19(7)
	DFT	120.6	120.2	120.1	119.4	119.5
C ₆ -C ₅ -C ₈ -C ₉	XRD*	8.1	15.2	9.6	59.8	28.5
	DFT	28.2	31.2	31.3	32.7	44.1

* Defined as the acute angle between the two aryl rings

3.6.18 References – Supporting Information

1. Andrade M.M.; Barros M.T.; Pinto R.C. *Tetrahedron*, **2008**, *64*, 10521.
2. Dommerholt J.; Schmidt S.; Temming R.; Hendriks L.J.A.; Rutjes F.P.J.T.; van Hest J.C.M.; Lefeber D.J.; Friedl P.; van Delft F.L. *Angew. Chem. Int. Ed.* **2010**, *49*, 9422.
3. Wandler A. E. E.; Koos M. R. M.; Nieger M.; Luy B.; Braese S. *Dalton Trans.* **2018**, *47*(11), 3689-3692.
4. Petersen H.; Kolshorn H.; Meier H. *Angew. Chem. Inter. Ed.* **1978**, *6*, 461-462.
5. MacKenzie D.A.; Pezacki J.P. *Can. J. Chem.* **2014**, *92*, 337.
 - (i) Gothelf K.V.; Hazell R.G.; Jorgensen K.A. *Acta Chem. Scand.*, **1997**, *51*, 1234. (ii) Heinenberg M.; Ritter H.; Schollmeyer. CCDC 813074: Experimental Crystal Structure Determination, **2001**, DOI: 10.5517/ccw926f.
6. Bruker-AXS, SAINT version 2013.8, **2013**, Bruker-AXS, Madison, WI 53711, USA.
7. Bruker-AXS, SADABS version 2012.1, **2013**, Bruker-AXS, Madison, WI 53711, USA.
8. Sheldrick G.M. *Acta Crystallographica Section A*, **2015**, *A71*, 3.
9. Sheldrick G.M. *Acta Crystallographica Section C*, **2015**, *C71*, 3.
10. Gabe E.J.; Le Page Y.; Charland J.P.; Lee F.L.; White P.S. *J. Appl. Cryst.* **1989**, *22*, 384.
11. Momma, K.; Izumi, F. VESTA 3 for Three-dimensional Visualization of Crystal, Volumetric and Morphology Data. *J. Appl. Cryst.* **2011**, *44*, 1272–1276

Chapter 4

4 A Clickable Azide-Functionalized $[\text{Au}_{25}(\text{SR})_{18}]^-$ Nanocluster platform for Interfacial Surface Modifications

This chapter has been published as a full paper. The corresponding reference is: P.N. Gunwardene, J.F. Corrigan, M.S. Workentin, *J. Am. Chem. Soc.* **2019**, *141*, 30, 11781-11785. Copyright 2019 American Chemical Society.

All synthesis and characterization were completed by the author. The manuscript was written by the author, and edited by Prof. John F. Corrigan and Prof. Mark S. Workentin.

4.1 Introduction

The molecular-type properties and high stability of atomically precise monolayer-protected gold nanoclusters in the ultrasmall size regime (<2nm) render them prominent nanomaterials for structure-property studies^{1,2} with applications in chemical sensing,^{3,4} catalysis,^{5,6} nanomedicine,⁷⁻⁹ and optical imaging.^{10, 11} Such physical and chemical properties of gold nanoclusters are manifested in a manner that is primarily determined by the core configuration and ligand structure.¹ However, the notoriously sensitive relationship between ligand structure and nanocluster integrity leads to only specific ligand types and structures being compatible with direct syntheses of gold nanocluster frameworks. There recently have been reports of robust carbene-stabilized gold nanoclusters.¹² However, the ease-of-synthesis and ability to introduce structural diversity onto thiol (R-SH) ligands make them the most common type of stabilizing ligands and there have been a wide range of exceptionally stable thiolate-protected gold nanocluster frameworks reported.^{1, 2, 13-16}

To date, direct syntheses of thiolate-protected gold nanoclusters utilize relatively simple, non-functional thiols as protecting ligands (phenylethanethiol being the most popular). To introduce functional diversity onto the gold nanocluster, ligand exchange has been demonstrated¹⁷ but this methodology is limited by an inability to establish complete surface exchange of native thiols¹⁸ and by synthetic incompatibilities when ligating thiols to functional substrates. This

highlights a deficiency in the gold nanocluster literature - a variant that can undergo interfacial surface chemistry. Given our history of developing methodologies for post-assembly interfacial modifications of nanomaterials,^{19,20} we believed that the strain-promoted alkyne-azide cycloaddition (SPAAC) would be an excellent reaction candidate for this purpose. The SPAAC reaction is a subset of bioorthogonal “click” chemistry that occurs between a largely inert azide (N_3^-) dipole, and a strained cyclooctyne dipolarophile to generate a triazole moiety.²¹ This reaction occurs with high chemoselectivity, reaction kinetics and atom efficiency without the need of a catalyst. The ability to incorporate a compatible reactive azide group to the nanocluster surface as a template provides a route to deliver property-enhancing substrates to the nanocluster framework through interfacial reaction with functional substrates possessing the complementary strained cyclooctyne reactive partner. Such efficient post-assembly interfacial modifications will transform gold nanoclusters from a simple nanomaterial *framework* into a surface-reactive nanomaterial *platform*.

Within the rich library of atomically precise thiolate-protected gold nanoclusters, the $[Au_{25}(SR)_{18}]$ framework is the most prominent because, unlike many other popular thiolated frameworks, it can be synthesized at room temperature in high yield under mild conditions.² Furthermore, there are three charge states ($z = -1, 0, +1$) that are accessible, manifesting charge-dependent properties in addition to the pre-existent structure-dependent properties, providing an additional level of control over structure-property relationships. Here, we report the first direct synthesis of a surface reactive gold nanocluster platform, which utilizes an azide-functionalized thiol ligand ($HSCH_2CH_2-p-C_6H_4-N_3$) to give a surface reactive $[Au_{25}(SR)_{18}]$ platform. Although two other charge states are theoretically accessible, we focused our attention on the directly accessible anionic (-1) form, $[(CH_3-(CH_2)_7)_4N][Au_{25}(SCH_2CH_2-p-C_6H_4-N_3)_{18}]$ (hereafter referred to as **4.1-azido** in current chapter (and referred to as **p-azido**¹⁻ in **Chapter 5** and **6.1-azido** in **Chapter 6**). To establish simple proof-of-concept *cluster-surface* SPAAC (*CS-SPAAC*) reactivity of the platform, we reacted it with a symmetrical strained-cyclooctyne, which greatly aided the characterization of the modified platform. Remarkably, the data show that *all* surface azide moieties are available for *CS-SPAAC*, while retaining the internal nanocluster core configuration. Such post-assembly *CS-SPAAC* on our azide-functionalized $[Au_{25}(SR)_{18}]$ platform provides an exciting new avenue towards the development of structurally and multifunctionally complex

[Au₂₅(SR)₁₈] nanoclusters whose molecular-type physical and chemical properties can more easily be tuned for potential applications.

4.2 Results and Discussion

In order to selectively synthesize a fully clickable [Au₂₅(SR)₁₈]⁻¹ platform in high yield, we developed an azide-modified thiol ligand that structurally mimicked the standard phenylethanethiol that is most commonly used. The simple four-step synthetic strategy ligates an azide moiety directly to the 4-position of the aryl-ring, giving rise to HSCH₂CH₂-*p*-C₆H₄-N₃, or *p*-azido-phenylethanethiol (see **Section 4.6.2.1** to **Section 4.6.2.4** for detailed synthesis). The synthesis of the **4.1-azido** platform (**Figure 4.1**) was carried out with modifications to our previously reported procedure²² for synthesizing the [(CH₃-(CH₂)₇)₄N][Au₂₅(SCH₂CH₂-C₆H₅)₁₈] framework²³ (hereafter referred to as **4.1-phenyl**) (see **Section 4.6.2.8** for detailed synthesis). The negative mode ESI-MS spectrum of the purified sample is shown in **Figure S4.3**, which shows a large peak centered at 8132.9 Da that corresponds to the parent [Au₂₅(SCH₂CH₂-*p*-C₆H₄-N₃)₁₈]⁻¹ anion of the **4.1-azido** cluster (expected *m/z* = 8132.4 Da).

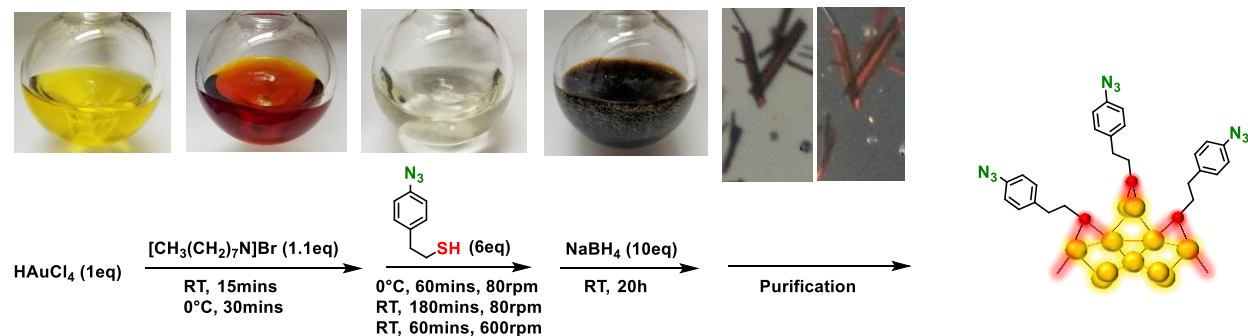


Figure 4.1. Synthesis of [(CH₃-(CH₂)₇)₄N][Au₂₅(SCH₂CH₂-*p*-C₆H₄-N₃)₁₈] (**1-azido**).

The core configuration and monolayer composition of **4.1-azido** was confirmed by single-crystal X-ray diffraction (**Figure 4.2(a)**). Crystals were obtained in a saturated solution of 3:1 ethanol:toluene at 0 °C over 2 days. As with **4.1-phenyl**,²³ the internal body-centered icosahedron is comprised of one central Au atom ligated to Au atoms at 12 vertices (**Figure 4.2(b)**). The centered icosahedral kernel has an external scaffold of six “staple motifs” (-SR-Au-SR-Au-SR-) (**Figure 4.2(c)**). Each of the six staple motifs possess three μ₂-thiolate ligands in which the central μ₂-thiolate ligands occupy a distinguishable surface site (“outer” ligands, site 2 in **Figure 4.2(c)**), while the remaining twelve μ₂-thiolates on the staple edges occupy a second distinguishable

surface site (“inner” ligands, site 1 in **Figure 4.2(c)**). In the cluster-surface thiolates (**Figure 4.2(d)**), the N_α of the azide moieties are ligated on each aryl ring at an average C-C- N_α angle of $122.7 \pm 1.3^\circ$, indicating the primarily sp^2 character of N_α , while the N_α - N_β - N_γ bond angle is $173.3 \pm 1.5^\circ$, indicating the near-linear nature of the azide moiety. The bond distance ranges for the azide moiety are 1.23(3) to 1.28(4) Å (N_α - N_β) and 1.18(4) to 1.21(5) Å (N_β - N_γ), which is similar to a previously reported phenyl azide structure,²⁴ although the uncertainties associated with these values preclude any further distinctions. The space-filling diagram (**Figure S4.4**) shows that the azide moieties are extended outward in a highly symmetrical and stellated pattern that suggests that the azide groups are all available to undergo the CS-SPAAC reaction.

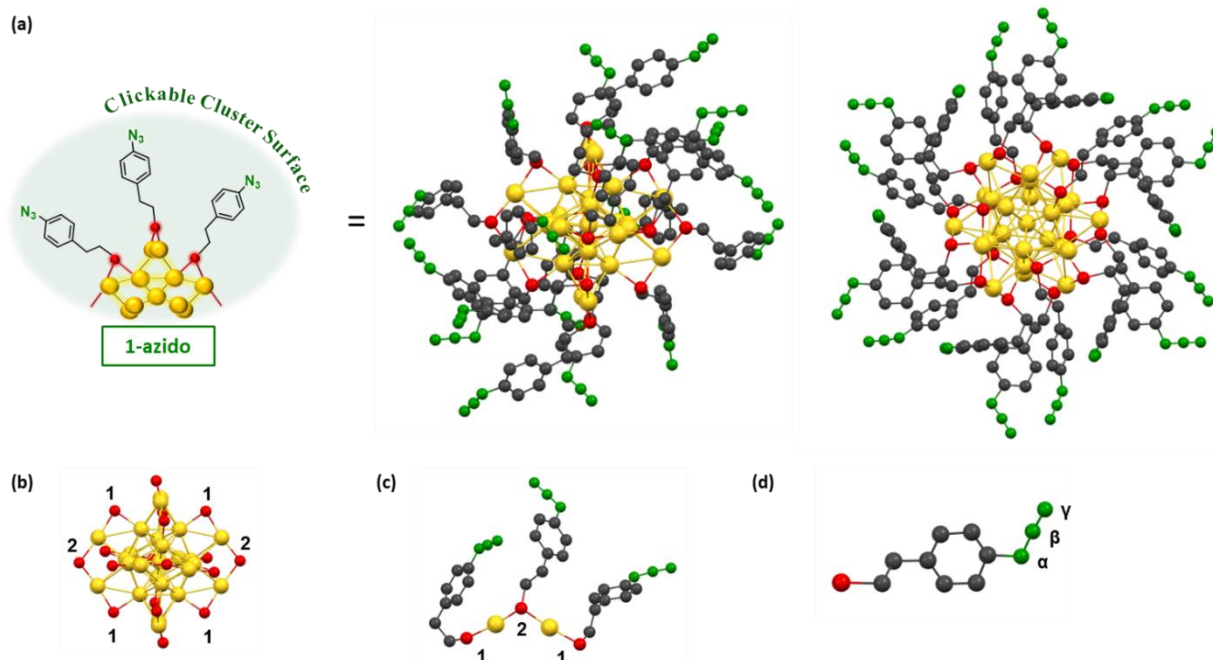
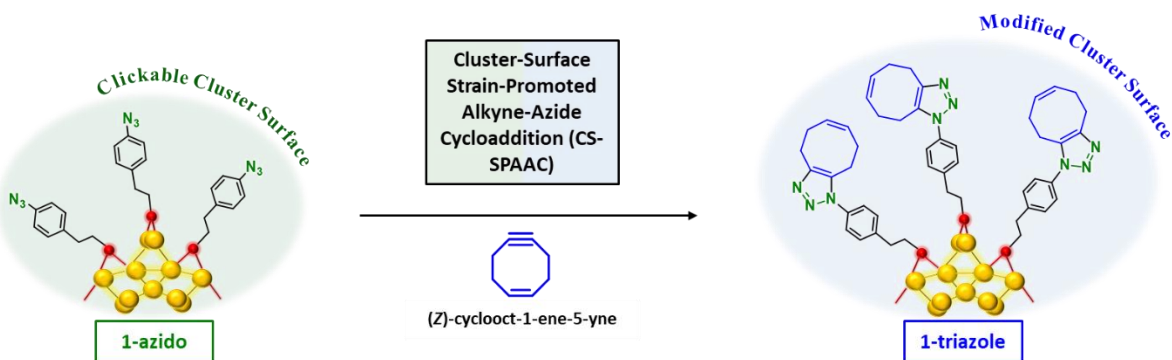


Figure 4.2 (a) Molecular structure of the anion $[\text{Au}_{25}(\text{SCH}_2\text{CH}_2\text{-}p\text{-C}_6\text{H}_4\text{-N}_3)_{18}]^-$ of **4.1-azido** (crystallized in R-3 space group). Tetraoctylammonium counterion is not shown. Au = yellow, S = red, C = grey, N = green (b) Au_{25} core configuration (c) Staple motif with three μ_2 -thiolate ligands (d) *p*-azido-phenylethanethiolate.

To investigate a proof-of-concept CS-SPAAC, we reacted one equivalent of **4.1-azido** with excess (*Z*)-cyclooct-1-ene-5-yne, transforming the **4.1-azido** platform to the surface-modified, $[(\text{CH}_3\text{-(CH}_2)_7)_4\text{N}][\text{Au}_{25}(\text{SCH}_2\text{CH}_2\text{-}p\text{-C}_6\text{H}_4\text{-C}_8\text{H}_{10}\text{N}_3)_{18}]$ framework (hereafter referred to as **4.1-triazole** in current chapter (and referred to as **p-triazole**¹⁻ in Chapter 5) (Scheme 4.1). Given the

non-regioselective nature of the SPAAC reaction, a symmetric, achiral cyclooctyne creates a single regioisomer after the CS-SPAAC reaction,²⁵ facilitating characterization (especially NMR spectroscopy) after the cluster-surface reaction. The synthesis is a simple mix and stir reaction and can be done at room temperature in a variety of solvents such as tetrahydrofuran, dichloromethane and toluene. Due to the high strain of the alkyne moiety, the CS-SPAAC reaction is complete in under 5 minutes at millimolar concentrations regardless of solvent choice. Removal of excess (*Z*)-cyclooct-1-ene-5-yne was accomplished through simple trituration with acetonitrile, in which **4.1-triazole** is insoluble. The linear negative mode MALDI-TOF spectrum (**Figure S4.9**) of the purified product has a well-resolved peak at 10048.4 Da that can be assigned to the parent $[\text{Au}_{25}(\text{SCH}_2\text{CH}_2\text{-}p\text{-C}_6\text{H}_4\text{-C}_8\text{H}_{10}\text{N}_3)_{18}]^{1-}$ anion of the **4.1-triazole** cluster (expected $m/z = 10043.4$ Da). To demonstrate the generality of the CS-SPAAC reaction, **4.1-azido** was also reacted with *exo*-bicyclo[6.1.0]non-4-yn-9-ol (**BCN_{exo}-OH**), a bicyclo[6.1.0]nonyne (BCN) derivative that contains a functionalizable -OH handle. The linear negative mode MALDI-TOF spectrum (**Figure S4.12**) of the purified product has a well-resolved peak at 10837.5 Da that matches the parent surface-modified $[\text{Au}_{25}(\text{SCH}_2\text{CH}_2\text{-}p\text{-C}_6\text{H}_4\text{-C}_{10}\text{H}_{14}\text{N}_3\text{O})_{18}]^{1-}$ anionic product (expected $m/z = 10836.3$ Da).



Scheme 4.1. CS-SPAAC reaction between $[(\text{CH}_3\text{-(CH}_2)_7)_4\text{N}][\text{Au}_{25}(\text{SCH}_2\text{CH}_2\text{-}p\text{-C}_6\text{H}_4\text{-N}_3)_{18}]$ (**4.1-azido**) and (*Z*)-cyclooct-1-ene-5-yne, giving surface modified $[(\text{CH}_3\text{-(CH}_2)_7)_4\text{N}][\text{Au}_{25}(\text{SCH}_2\text{CH}_2\text{-}p\text{-C}_6\text{H}_4\text{-C}_8\text{H}_{10}\text{N}_3)_{18}]$ (**4.1-triazole**).

Figure 4.3(a) (black) shows the UV-Vis absorption spectrum of **4.1-azido**, which features prominent optical absorption bands at 682 nm, 443 nm and 404 nm, which correlates well with the established optical fingerprint of conventional **4.1-phenyl** nanoclusters²⁶. The UV-Vis absorption spectrum of the CS-SPAAC product, **4.1-triazole** is also shown in **Figure 4.3(a)** (red), and as can be seen, the optical fingerprint of the anionic $[\text{Au}_{25}(\text{SR})_{18}]^{1-}$ framework has been retained after the

CS-SPAAC reaction, showing distinct absorption maxima at 682 nm, 446 nm and 394 nm. As the absorption maximum at 682 nm occurs from an intra-band metallic transition whose energy is characteristic of the Au₂₅ core,²⁶ the retention of this absorption maximum after the CS-SPAAC reaction further demonstrates that the anionic [Au₂₅(SR)₁₈]¹⁻ core configuration has been preserved.

Because of the diagnostic N₃ stretch, IR spectroscopy is a useful tool in both the characterization of **4.1-azido** and subsequent surface chemistry. As shown in **Figure 4.3(b)** (black), the IR spectrum of **4.1-azido** contains a well-resolved peak at 2098 cm⁻¹ that is also found in the IR spectrum of free *p*-azido-phenylethanethiol, which can be attributed to the N₃ stretch of the ligated azide groups. In the IR spectrum of **4.1-triazole** (**Figure 4.3(b)** (red)), the peak at 2098 cm⁻¹ has completely disappeared, indicating that all surface azide moieties have been consumed during the CS-SPAAC reaction.

The synthesis of **4.1-azido** was also confirmed using ¹H NMR spectroscopy (**Figure 4.3(c)** (black)). As with **4.1-phenyl**, the tetraoctylammonium signals appear at 0.90 (-CH₃), 1.31 (-CH₂), 1.37 (-CH₂-) and 3.09 ppm (N⁺-CH₂-). As with other [Au₂₅(SR)₁₈]¹⁻ frameworks,²⁷⁻²⁹ appending SCH₂CH₂-*p*-C₆H₄-N₃ to the Au₂₅ core results in a 12:6 inner:outer ligand distinction (*inner*: those attached at position 2 in **Figure 4.2(b)** and *outer*: those attached at position 1 in **Figure 4.2(b)**) that is distinguishable in the ¹H NMR spectrum and was confirmed by COSY spectroscopy. The methylene protons alpha to the thiol (H_α protons) in the 12 inner ligands produce a well-resolved triplet at 3.54 ppm, which is downfield to the methylene protons beta to the thiol (H_β protons) that produce a peak at 3.09 ppm. In the remaining 6 outer ligands, the downfield H_α protons produce a peak at 3.09 ppm while the H_β protons produce a well-resolved triplet at 2.93 ppm. In spite of their remoteness to the sulfur atom, appending SCH₂CH₂-*p*-C₆H₄-N₃ to the Au₂₅ core results in a change in the chemical environment of both binary sets of aromatic protons, which produce doublets at 7.20 and 6.98 ppm in *p*-azido-phenylethanethiol (**Figure S4.27**). As with H_α and H_β, the aromatic protons appear in two resolvable sets, with the 12 inner ligands producing well-resolved doublets at 7.17 and 6.80 ppm and the 6 outer ligands producing well-resolved doublets at 6.86 and 7.12 ppm. Hence, the total removal of residual thiol and disulfide can be assessed through the total disappearance of the signals at 7.20 and 6.98 ppm from *p*-azido-phenylethanethiol.

The CS-SPAAC reaction between **4.1-azido** and (*Z*)-cyclooct-1-ene-5-yne generates a triazole ring, which gives a characteristic change in the chemical environment of the binary sets of aromatic protons. As can be seen in the NMR spectrum of **4.1-triazole** (Figure 4.3(c) (red)), there are new sets of doublets at 7.37 and 7.20 ppm from the 12 outer ligands, while the 6 outer ligands produce new doublets at 7.28 and 7.18 ppm. The appearance of these new downfield signals is a

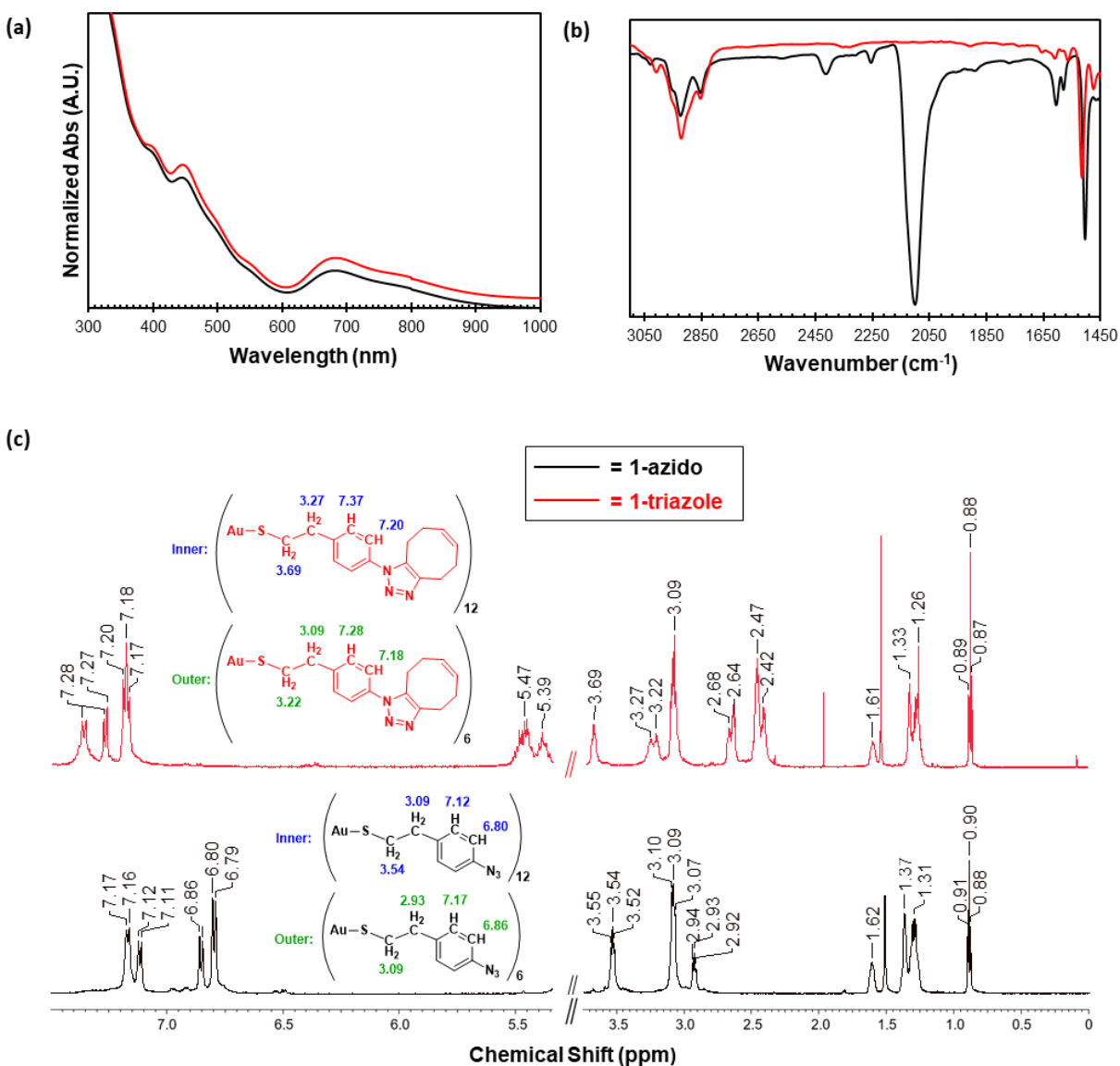


Figure 4.3 (a) UV-Vis spectrum of 0.2 mM solution of [(CH₃-(CH₂)₇)₄N][Au₂₅(SCH₂CH₂-p-C₆H₄-N₃)₁₈] (**4.1-azido**) (black) and surface modified [(CH₃-(CH₂)₇)₄N][Au₂₅(SCH₂CH₂-p-C₆H₄-C₈H₁₀N₃)₁₈] (**4.1-triazole**) (red) in dichloromethane at 23°C (b) ATR-IR spectrum of **4.1-azido** (black) and **4.1-triazole** (red) (c) ¹H NMR spectrum of **4.1-azido** (black) and **4.1-triazole** (red), taken in CD₂Cl₂ at 25°C. Chemical shifts of relevant protons are shown for inner ligands (blue) and outer ligands (green). * denotes residual H₂O.

diagnostic NMR fingerprint for successful CS-SPAAC chemistry on the surface of **4.1-azido**, regardless of the cyclooctyne structure (this can also be seen in the ^1H NMR spectrum of $[(\text{CH}_3(\text{CH}_2)_7)_4\text{N}][\text{Au}_{25}(\text{SCH}_2\text{CH}_2\text{-}p\text{-C}_6\text{H}_4\text{-C}_{10}\text{H}_{14}\text{N}_3\text{O})_{18}]$ that forms from the reaction between **4.1-azido** and **BCN_{exo}-OH** (Figure S4.11)). The protons associated with the eight-membered ring also occur in a 2:1 ratio and appear at a higher chemical shift compared to **(Z)-cyclooct-1-ene-5-yne**, which can be attributed to the loss of the alkyne moiety. Expectedly, given the more electron-deficient aryl ring, the signals from the H $_{\beta}$ protons also appear at higher chemical shifts. However, the signals from the H $_{\alpha}$ protons also appear at higher chemical shifts, with the 12 inner ligands producing a well-resolved triplet at 3.69 ppm, and the 6 outer ligands producing a signal at 3.22 ppm. Given their proximity to the metallic core, which has remained chemically unaltered, we believe that the change in the H $_{\alpha}$ signals can be attributed to a change in the packing of the surface monolayer after the CS-SPAAC reaction, altering the electronic environment of the H $_{\alpha}$ protons relative to the gold core.

4.3 Conclusions

Here we have described the direct synthesis and characterization of a stable azide-modified $[(\text{CH}_3\text{-(CH}_2)_7)_4\text{N}][\text{Au}_{25}(\text{SCH}_2\text{CH}_2\text{-}p\text{-C}_6\text{H}_4\text{-N}_3)_{18}]$ that is structurally similar to the well-studied benchmark $[(\text{CH}_3\text{-(CH}_2)_7)_4\text{N}][\text{Au}_{25}(\text{SCH}_2\text{CH}_2\text{-C}_6\text{H}_5)_{18}]$. The incorporation of a reactive azide group amenable to cluster-surface strain-promoted alkyne-azide cycloaddition transforms the $[\text{Au}_{25}(\text{SR})_{18}]^{1-}$ framework into a surface-modifiable $[\text{Au}_{25}(\text{SR})_{18}]^{1-}$ platform, capable of being structurally modified through a simple-to-perform interfacial post-assembly click reaction, which will address many of the challenges for developing functional Au₂₅ nanoclusters. As there are many established protocols for incorporating strained-alkynes into a variety of substrates (such as fluorophores, biomolecules and redox species), this new Au₂₅ platform allows an easy approach to append additional functionality via the CS-SPAAC reaction to tune the properties of Au₂₅ nanoclusters. Furthermore, because each azide is chemically accessible from this single platform, it can allow the preparation of *multifunctional* Au₂₅ nanoclusters by challenging the platform to a mixture of functional strained alkynes. Studies directed at highlighting these new advantages are currently ongoing.

4.4 Acknowledgements

This work was funded by NSERC-DG and Western. We thank Dr. P. Boyle (X-ray Facility), D. Hairsine (MS Facility), K. Jurcic (MALDI MS Facility -Biochemistry) and J. Wong and Dr. Z. Ding (PL facility).

4.5 References

1. Jin, R.; Zeng, C.; Zhou, M.; Chen, Y., Atomically Precise Colloidal Metal Nanoclusters and Nanoparticles: Fundamentals and Opportunities. *Chem. Rev.* **2016**, *116* (18), 10346-10413.
2. Kang, X.; Chong, H.; Zhu, M., Au₂₅(SR)₁₈: the captain of the great nanocluster ship. *Nanoscale* **2018**, *10* (23), 10758-10834.
3. Pu, K.-Y.; Luo, Z.; Li, K.; Xie, J.; Liu, B., Energy Transfer between Conjugated-Oligoelectrolyte-Substituted POSS and Gold Nanocluster for Multicolor Intracellular Detection of Mercury Ion. *J. Phys. Chem. C* **2011**, *115* (26), 13069-13075.
4. Xie, J.; Zheng, Y.; Ying, J. Y., Highly selective and ultrasensitive detection of Hg²⁺ based on fluorescence quenching of Au nanoclusters by Hg²⁺-Au⁺ interactions. *Chem. Commun.* **2010**, *46* (6), 961-963.
5. Li, G.; Abroshan, H.; Liu, C.; Zhuo, S.; Li, Z.; Xie, Y.; Kim, H. J.; Rosi, N. L.; Jin, R., Tailoring the Electronic and Catalytic Properties of Au₂₅ Nanoclusters via Ligand Engineering. *ACS Nano* **2016**, *10* (8), 7998-8005.
6. Nasaruddin, R. R.; Yao, Q.; Chen, T.; Hulse, M. J.; Yan, N.; Xie, J., Hydride-induced ligand dynamic and structural transformation of gold nanoclusters during a catalytic reaction. *Nanoscale* **2018**, *10* (48), 23113-23121.
7. Fernandez, T. D.; Pearson, J. R.; Leal, M. P.; Torres, M. J.; Blanca, M.; Mayorga, C.; Le Guevel, X., Intracellular accumulation and immunological properties of fluorescent gold nanoclusters in human dendritic cells. *Biomaterials* **2015**, *43*, 1-12.

8. Wang, Y.; Wang, Y.; Zhou, F.; Kim, P.; Xia, Y., Protein-Protected Au Clusters as a New Class of Nanoscale Biosensor for Label-Free Fluorescence Detection of Proteases. *Small* **2012**, *8* (24), 3769-3773.
9. Zheng, K.; Setyawati, M. I.; Leong, D. T.; Xie, J., Antimicrobial Gold Nanoclusters. *ACS Nano* **2017**, *11* (7), 6904-6910.
10. Polavarapu, L.; Manna, M.; Xu, Q.-H., Biocompatible glutathione capped gold clusters as one- and two-photon excitation fluorescence contrast agents for live cells imaging. *Nanoscale* **2011**, *3* (2), 429-434.
11. Raut, S. L.; Shumilov, D.; Chib, R.; Rich, R.; Gryczynski, Z.; Gryczynski, I., Two photon induced luminescence of BSA protected gold clusters. *Chem. Phys. Lett.* **2013**, *561-562*, 74-76.
12. Narouz, M. R.; Unsworth, P. J.; Padmos, J. D.; Ayoo, K.; Garrett, P. J.; Horton, J. H.; Crudden, C. M.; Osten, K. M.; Man, R. W. Y.; Salorinne, K.; Nambo, M.; Crudden, C. M.; Takano, S.; Tomihara, R.; Tsukuda, T.; Kaappa, S.; Malola, S.; Hakkinen, H.; Dinh, C.-T.; Sargent, E. H.; Tsukuda, T., N-heterocyclic carbene-functionalized magic-number gold nanoclusters. *Nat. Chem.* **2019**.
13. Chen, Y.; Zeng, C.; Kauffman, D. R.; Jin, R., Tuning the Magic Size of Atomically Precise Gold Nanoclusters via Isomeric Methylbenzenethiols. *Nano Lett.* **2015**, *15* (5), 3603-3609.
14. Das, A.; Li, T.; Li, G.; Nobusada, K.; Zeng, C.; Rosi, N. L.; Jin, R., Crystal structure and electronic properties of a thiolate-protected Au₂₄ nanocluster. *Nanoscale* **2014**, *6* (12), 6458-6462.
15. Qian, H.; Zhu, Y.; Jin, R., Size-Focusing Synthesis, Optical and Electrochemical Properties of Monodisperse Au₃₈(SC₂H₄Ph)₂₄ Nanoclusters. *ACS Nano* **2009**, *3* (11), 3795-3803.
16. Zeng, C.; Liu, C.; Chen, Y.; Rosi, N. L.; Jin, R., Gold-Thiolate Ring as a Protecting Motif in the Au₂₀(SR)₁₆ Nanocluster and Implications. *J. Am. Chem. Soc.* **2014**, *136* (34), 11922-11925.
17. Tracy, J. B.; Crowe, M. C.; Parker, J. F.; Hampe, O.; Fields-Zinna, C. A.; Dass, A.; Murray, R. W., Electrospray Ionization Mass Spectrometry of Uniform and Mixed Monolayer

Nanoparticles: Au₂₅[S(CH₂)₂Ph]₁₈ and Au₂₅[S(CH₂)₂Ph]_{18-x}(SR)_x. *J. Am. Chem. Soc.* **2007**, *129* (51), 16209-16215.

18. Dass, A.; Stevenson, A.; Dubay, G. R.; Tracy, J. B.; Murray, R. W., Nanoparticle MALDI-TOF Mass Spectrometry without Fragmentation: Au₂₅(SCH₂CH₂Ph)₁₈ and Mixed Monolayer Au₂₅(SCH₂CH₂Ph)_{18-x}(L)_x. *J. Am. Chem. Soc.* **2008**, *130* (18), 5940-5946.

19. Gobbo, P.; Novoa, S.; Biesinger, M. C.; Workentin, M. S., Interfacial strain-promoted alkyne-azide cycloaddition (I-SPAAC) for the synthesis of nanomaterial hybrids. *Chem. Commun.* **2013**, *49* (38), 3982-3984.

20. Wang, X.; Gobbo, P.; Suchy, M.; Workentin, M. S.; Hudson, R. H. E., Peptide-decorated gold nanoparticles via strain-promoted azide-alkyne cycloaddition and post assembly deprotection. *RSC Adv.* **2014**, *4* (81), 43087-43091.

21. Agard, N. J.; Prescher, J. A.; Bertozzi, C. R., A strain-promoted [3+2] azide-alkyne cycloaddition for covalent modification of biomolecules in living systems. *J. Am. Chem. Soc.* **2004**, *126* (46), 15046-15047.

22. Swanick, K. N.; Hesari, M.; Workentin, M. S.; Ding, Z., Interrogating Near-Infrared Electrogenenerated Chemiluminescence of Au₂₅(SC₂H₄Ph)₁₈⁺ Clusters. *J. Am. Chem. Soc.* **2012**, *134* (37), 15205-15208.

23. Heaven, M. W.; Dass, A.; White, P. S.; Holt, K. M.; Murray, R. W., Crystal Structure of the Gold Nanoparticle [N(C₈H₁₇)₄][Au₂₅(SCH₂CH₂Ph)₁₈]. *J. Am. Chem. Soc.* **2008**, *130* (12), 3754-3755.

24. Takayama, T.; Mitsumori, T.; Kawano, M.; Sekine, A.; Uekusa, H.; Ohashi, Y.; Sugawara, T., Direct observation of arylnitrene formation in the photoreaction of arylazide crystals. *Acta Cryst., Section B: Struct. Sci.* **2010**, *66* (6), 639-646.

25. Dommerholt, J.; Rutjes, F. P. J. T.; van Delft, F. L., Strain-Promoted 1,3-Dipolar Cycloaddition of Cycloalkynes and Organic Azides. *Top. Curr. Chem.* **2016**, *374* (2), 1-20.

26. Zhu, M.; Eckenhoff, W. T.; Pintauer, T.; Jin, R., Conversion of Anionic $[\text{Au}_{25}(\text{SCH}_2\text{CH}_2\text{Ph})_{18}]^-$ Cluster to Charge Neutral Cluster via Air Oxidation. *J. Phys. Chem. C* **2008**, *112* (37), 14221-14224.
27. Agrachev, M.; Antonello, S.; Dainese, T.; Gascon, J. A.; Pan, F.; Rissanen, K.; Ruzzi, M.; Venzo, A.; Zoleo, A.; Maran, F., A magnetic look into the protecting layer of Au_{25} clusters. *Chem. Sci.* **2016**, *7* (12), 6910-6918.
28. Dainese, T.; Antonello, S.; Gascón, J. A.; Pan, F.; Perera, N. V.; Ruzzi, M.; Venzo, A.; Zoleo, A.; Rissanen, K.; Maran, F., $\text{Au}_{25}(\text{SEt})_{18}$, a Nearly Naked Thiolate-Protected Au_{25} Cluster: Structural Analysis by Single Crystal X-ray Crystallography and Electron Nuclear Double Resonance. *ACS Nano* **2014**, *8* (4), 3904-3912.
29. Qian, H.; Zhu, M.; Gayathri, C.; Gil, R. R.; Jin, R., Chirality in Gold Nanoclusters Probed by NMR Spectroscopy. *ACS Nano* **2011**, *5* (11), 8935-8942.

4.6 Supporting Information

4.6.1 General Materials and Methods

Reagents and Solvents. The following materials were used as received. Potassium thioacetate (98%), zinc dust ($<10\mu\text{m}$, $\geq 98\%$), sodium azide ($\geq 99.5\%$), gold (III) chloride trihydrate ($\geq 99.9\%$ trace metal basis), tetraoctylammonium bromide (98%), sodium borohydride ($\geq 98\%$), 1,5-cyclooctadiene ($\geq 99\%$), bromine (reagent grade), potassium *tert*-butoxide solution (1.0M in THF), dichloromethane- D_2 (CD_2Cl_2 , 99.5 atom %D) and dimethyl sulfoxide- D_6 ($(\text{CD}_3)_2\text{SO}$, 99.96 atom %D) were purchased from Sigma-Aldrich (Millipore Sigma). 4-nitrophenylethyl bromide was purchased from Oakwood Chemicals. Sodium chloride, sodium hydroxide pellets and tetrahydrofuran were purchased from Fischer Scientific. Technical grade ammonium chloride, magnesium sulphate, hexanes, dichloromethane, ethyl acetate, 12M hydrochloric acid, di-ethyl ether, dimethyl sulfoxide, sodium nitrite, methanol, toluene, isopropanol, acetonitrile and pentane

were purchased from Caledon. Chloroform-D₁ (CDCl₃, 99.8 atom %D) was purchased from Cambridge Isotope Laboratories. Ethanol (anhydrous) was purchased from Commercial Alcohols.

Unless otherwise state, all reactions were performed at ambient conditions.

NMR Spectroscopy. ¹H and ¹³C{¹H} spectra were recorded on either a Bruker AvIII HD 400 spectrometer or Varian INOVA 600 spectrometer, as indicated. ¹H NMR spectra are reported as δ in units of parts per million (ppm), and referenced against residual protio chloroform (7.27 ppm, s), dimethylsulfoxide (2.50 ppm, quin) or dichloromethane (5.32 ppm, t), as indicated. Multiplicities are reported as follows: s (singlet), d (doublet), t (triplet), q (quartet), quin (quintuplet), m (multiplet) and br (broad signal). Coupling constants are reported as a *J* value in Hertz (Hz) according to the spectrometer frequency. The number of protons (*n*) for a given resonance is indicated as *n*H, and is based on spectral integration values. ¹³C{¹H} NMR spectra are reported as δ in units of parts per million (ppm) and referenced against the indicated deuterated solvent: chloroform-D₁ (77.0 ppm, t), dimethylsulfoxide-D₆ (39.5 ppm, septet) or dichloromethane-D₂ (54.0 ppm, quin).

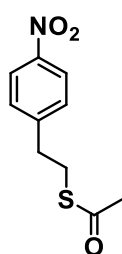
Mass Spectrometry. Electrospray ionization (ESI) mass spectra were obtained in either positive-ion or negative-ion mode using a Bruker microTOF II spectrometer. Set capillary was 4000 V, set end plate offset was -400 V, set nebulizer was 1.0 Bar and set dry heater was 100°C. To obtain the ESI spectrum of [Au₂₅(SCH₂CH₂-*p*-C₆H₄-N₃)₁₈]⁻ nanoclusters (obtained in negative-ion mode), a sample was dissolved in 1:5 toluene:methanol (10mg/mL). We generally found that in order to obtain mass spectra of [Au₂₅SR₁₈] clusters, the sample solution must contain some methanol in order to minimize excessive fragmentation. Matrix-assisted laser desorption/ionization-time of flight (MALDI-TOF) mass spectra were obtained using an AB Sciex 5800 TOF/TOF system. To obtain the MALDI-TOF spectrum of [Au₂₅(SCH₂CH₂-*p*-C₆H₄-C₈H₁₀N₃)₁₈]⁻ nanoclusters (obtained in linear negative mode), a 1 g/L sample solution was mixed with a 10 g/L solution of trans-2-[3-(4-tert-butylphenyl)-2-methyl-2-propenyldene]malononitrile (DCTB) in a ratio of 1:400 by mass. Data acquisition and data processing were respectively done using a TOF TOF Series Explore and Data Explorer (both from AB Sciex). The laser pulse rate was set to 400Hz. The mass spectrum was collected as a sum of 1000 shots.

UV-Visible (UV-Vis) Spectroscopy. UV-Vis absorption spectra were recorded using a Cary 5000 scan instrument using standard quartz cells (1 cm path length) with a scan range of 200-1000nm. Samples were dissolved in the indicated solvents at the indicated concentrations. The background spectrum of the indicated solvent was subtracted internally by the software.

Infrared (IR) spectroscopy. Attenuated total reflectance IR (ATR-IR) spectra were recorded using a PerkinElmer Spectrum Two FT-IR spectrometer.

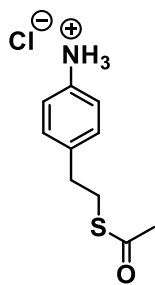
4.6.2 Experimental Procedures

4.6.2.1 Synthesis of *p*-nitro-phenylethanethioacetate



To 8.6 g (38 mmol, 1 eq.) 4-nitrophenylethyl bromide in 250 mL acetone was added 6.5 g (57 mmol, 1.5 eq.) potassium thioacetate. The resulting mixture was stirred at room temperature for 6 hours, after which the solid was removed by gravity filtration and the solution was concentrated by rotary evaporation. The resultant crude residue was purified by flash column chromatography (2:1 hexanes:dichloromethane) to give *p*-nitro-phenylethanethioacetate as a yellow solid in 98% yield (8.4 g). ¹H NMR (CDCl₃, 400 MHz): δ (ppm) 8.17 (d, 2H, J=8 Hz), 7.39 (d, 2H, J=8 Hz), 3.15 (t, 2H, J=8 Hz), 2.99 (t, 2H, J=8 Hz), 2.35 (s, 3H). ¹³C NMR (CDCl₃, 400 MHz): δ (ppm) 195.2, 147.4, 146.8, 129.5, 123.7, 35.6, 30.6, 29.7. HRMS (ESI) *m/z* calc. for C₁₀H₁₁NO₃S (M⁺): 225.0460, found: 225.0467. IR (ATR-IR, cm⁻¹): 3025, 1680, 1597, 1513, 1448, 1411, 1340, 1280, 1129, 1096. UV-Vis (Dichloromethane, 1x10⁻⁴ mol.L⁻¹): λ_{max} = 276 nm, ε = 1100 M⁻¹cm⁻¹.

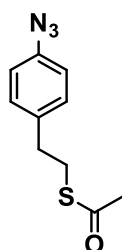
4.6.2.2 Synthesis of *p*-ammonium-phenylethanethioacetate chloride



To 8.4 g (37 mmol, 1eq.) *p*-nitro-phenylethanethioacetate in 70 mL ethanol and 70 mL distilled water was added 15.5 g (296 mmol, 8 eq) technical grade ammonium chloride, and then 12.0 g (185 mmol, 4 eq) zinc dust portion-wise under vigorous stirring over 5 minutes. The resulting suspension was stirred for 2 hours at room temperature, after which the solids were filtered off. The solids were washed with 50 mL of ethanol, after which 100 mL brine was added to the supernatant, which was then extracted with ethyl acetate (3 x 50 mL). The collected organic phases were diluted to

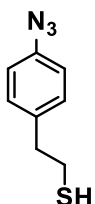
approximately 500 mL of ethyl acetate, after which 10 mL of 12 M hydrochloric acid was added slowly to the colorless solution under vigorous stirring, resulting in a pale yellow solution. After stirring the solution for 15 minutes, and then removing the solvent by rotary evaporation, the resulting crude residue was suspended in di-ethyl ether and the precipitate was collected by vacuum filtration to give ***p*-ammonium-phenylethanethioacetate chloride** as a bright white solid in 82% yield (7.0 g). $^1\text{H NMR}$ ($(\text{CD}_3)_2\text{SO}$, 400 MHz): δ (ppm) 7.34 (m, 4H), 4.01 (br, 3H), 3.10 (t, 2H, $J=8$ Hz), 2.84 (t, 2H, $J=8$ Hz), 2.31 (s, 3H). $^{13}\text{C NMR}$ ($(\text{CD}_3)_2\text{SO}$, 400 MHz): δ (ppm) 195.1, 139.9, 130.0, 129.8, 123.2, 34.3, 30.6, 29.6. HRMS (ESI) m/z calc. for $\text{C}_{10}\text{H}_{14}\text{NOS}^+$ (M^+): 196.0791, found: 196.0719. IR (ATR-IR, cm^{-1}): 2828, 2595, 1950, 1680, 1620, 1556, 1507, 1356, 1315, 1206, 1140, 1105. UV-Vis (Dimethyl sulfoxide, 1×10^{-4} mol.L $^{-1}$): $\lambda_{\text{max}} = 300$ nm, $\epsilon = 1400$ M $^{-1}\text{cm}^{-1}$.

4.6.2.3 Synthesis of *p*-azido-phenylethanethioacetate



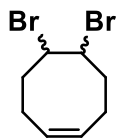
To 7.0 g (30 mmol, 1 eq.) ***p*-ammonium-phenylethanethioacetate chloride** in 350 mL 1 M hydrochloric acid was added 3.1 g (45 mmol, 1.5 eq) sodium nitrite in 75 mL distilled water dropwise over 20 minutes at 0°C. After stirring the solution for an additional 20 minutes at 0°C, 3.9 g (60 mmol, 2 eq) sodium azide in 75 mL distilled water was added dropwise over 10 minutes at 0°C. The solution was stirred for 20 minutes at 0°C, and then an additional 30 minutes at room temperature, after which the crude solution was extracted with dichloromethane (3 x 50 mL), dried over magnesium sulphate and concentrated using rotary evaporation. The crude residue was purified by flash column chromatography (2:1 hexanes:dichloromethane) to give ***p*-nitro-phenylethanethioacetate** as a pale yellow oil in 57% yield (3.8 g). $^1\text{H NMR}$ (CDCl_3 , 400 MHz): δ (ppm) 7.21 (d, 2H, $J=8$ Hz), 6.97 (d, 2H, $J=8$ Hz), 3.10 (t, 2H, $J=8$ Hz), 2.85 (t, 2H, $J=8$ Hz), 2.34 (s, 3H). $^{13}\text{C NMR}$ (CDCl_3 , 400 MHz): δ (ppm) 195.6, 138.3, 136.7, 130.0, 119.1, 35.1, 30.7, 30.4. HRMS (ESI) m/z calc. for $\text{C}_{10}\text{H}_{14}\text{NOS}^+$ (M^+): 221.0623, found: 221.0630. IR (ATR-IR, cm^{-1}): 3026, 2106, 1690, 1602, 1506, 1418, 1356, 1285, 1128, 1102. UV-Vis (Dichloromethane, 1×10^{-4} mol.L $^{-1}$): $\lambda_{\text{max}} = 255$ nm, $\epsilon = 2340$ M $^{-1}\text{cm}^{-1}$; $\lambda_{\text{max}} = 283$ nm, $\epsilon = 870$ M $^{-1}\text{cm}^{-1}$.

4.6.2.4 Synthesis of *p*-azido-phenylethanethiol



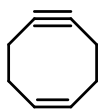
To 3.8 g (17 mmol, 1 eq.) ***p*-nitro-phenylethanethioacetate** in 100 mL deoxygenated methanol was added 25 mL (25 mmol, 1.5 eq.) of deoxygenated 1 M sodium hydroxide in water and the solution was stirred for 20 minutes at room temperature under argon, resulting in a yellow solution. Next, 50 mL (50 mmol, 3 eq.) of deoxygenated 1 M hydrochloric acid in water was added. The solution was stirred for 15 minutes at room temperature under argon, resulting in a pale yellow solution, after which distilled water (100 mL) was added and the product was extracted with dichloromethane (3 x 25 mL), dried over magnesium sulphate and concentrated using rotary evaporation. The crude residue was purified by flash column chromatography (2:1 hexanes:dichloromethane) to give ***p*-azido-phenylethanethiol** as a pale yellow oil in 94% yield (2.9 g). ¹H NMR (CD₂Cl₂, 400 MHz): δ (ppm) 7.20 (d, 2H, J=8 Hz), 6.98 (d, 2H, J=8 Hz), 2.89 (t, 2H, J=8 Hz), 2.75 (q, 2H, J=8 Hz), 1.40 (t, 2H, J=8 Hz). ¹³C NMR (CD₂Cl₂, 400 MHz): δ (ppm) 138.8, 137.4, 130.6, 119.5, 40.0, 26.5. HRMS (ESI) *m/z* calc. for C₁₀H₁₄NOS⁺ (M⁺): 179.0517, found: 179.0514. IR (ATR-IR, cm⁻¹): 3035, 2936, 2559, 2106, 1601, 1504, 1430, 1283, 1131. UV-Vis (Dichloromethane, 1x10⁻⁴ mol.L⁻¹): λ_{max} = 256 nm, ε = 2350 M⁻¹cm⁻¹; λ_{max} = 283 nm, ε = 890 M⁻¹cm⁻¹.

4.6.2.5 Synthesis of (*Z*)-5,6-dibromocyclooct-1-ene



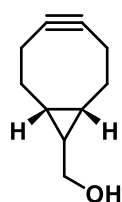
See **Section 3.6.3.2** for detailed synthesis of (*Z*)-5,6-dibromocyclooct-1-ene.

4.6.2.6 Synthesis of (*Z*)-cyclooct-1-ene-5-yne



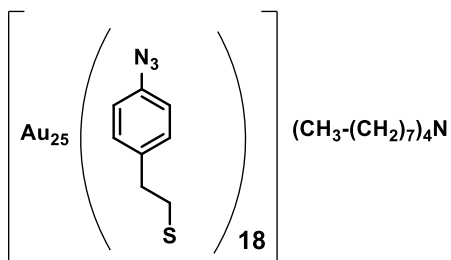
See **Section 3.6.3.3** for detailed synthesis of (*Z*)-cyclooct-1-ene-5-yne.

4.6.2.7 Synthesis of bicyclo[6.1.0]nonyne (BCN_{exo}-OH)



Synthesized according to Dommerholt *et al.*³ See **Section 2.6.2.6** for characterization data.

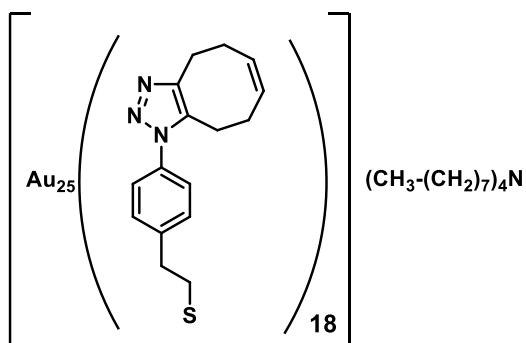
4.6.2.8 Synthesis of [(CH₃-(CH₂)₇)₄N][Au₂₅(SCH₂CH₂-*p*-C₆H₄-N₃)₁₈] (4.1-azido)



To a yellow solution of 393 mg (1.0 mmol) tetrachloroauric(III) acid trihydrate in 41 mL tetrahydrofuran was added 600 mg (1.1 eq, 1.1 mmol) tetraoctylammonium bromide at a stirring speed of 600 rpm. The solution was stirred for 15 minutes at room temperature and 30 minutes at 0°C, resulting in a dark red solution. The stirring was reducing to 80 rpm, and to the red solution was added an ice-cold solution of 1.07 g (6 eq, 6.0 mmol) of *p*-azido-phenylethanethiol in 1 mL tetrahydrofuran over 6 minutes at 0°C at 80 rpm. The resulting solution was stirred at 0°C for 1 hour at 80 rpm, then at room temperature for 3 hours at 80 rpm, then at room temperature for 1 hour at 600 rpm. Over the stirring period, the solution turned from dark red to yellow within the first hour, and once the temperature was increased to room temperature and stirred for four hours, it turned a very pale yellow color. After the stirring period, the pale yellow solution was cooled to 0°C for 15 minutes at 600 rpm, after which an ice-cold, freshly-prepared solution of 378 mg (10 mmol) sodium borohydride in 7.7 mL milli-Q water was added over approximately 15-20 seconds at 600 rpm, resulting in bubbling and an immediate color change from pale yellow to black. The neck of the flask was covered with a cap, and a light stream of argon was passed over the top of the flask, and the solution was stirred for 18 hours at room temperature at 600 rpm. After the overnight reaction, there was white precipitate on the side of the flask, and the solution turned from black to a reddish-brown color. The crude solution was filtered through glass wool, and the tetrahydrofuran was removed by rotary evaporation. The crude residue was dissolved in 50mL toluene and extracted

with 200 mL milli-Q water. The organic phase was removed, and the toluene was removed by rotary evaporation. To the crude brownish-red oil was added approximately 20 mL isopropanol, resulting in the formation of small insoluble black solids. The solids were collected by filtering the suspension through glass wool in a funnel. NOTE: the solution may have to be filtered more than once to collect all black solids. The glass wool was washed thoroughly with isopropanol to fully remove residual thiols and disulfides. After the isopropanol washes, 10 mL acetonitrile was added, resulting in dissolution of most of the black solids to give reddish brown filtrate. The acetonitrile was removed by rotary evaporation, resulting in a film on the flask wall. The film was washed again with isopropanol, and then re-dissolved in acetonitrile and filtered once more through glass wool. Removal of the acetonitrile by rotary evaporation gave a reddish-black oily film of purified $[(\text{CH}_3-(\text{CH}_2)_7)_4\text{N}][\text{Au}_{25}(\text{SCH}_2\text{CH}_2-p\text{-C}_6\text{H}_4\text{-N}_3)]$ that was stored as a film at 0°C . The typical yield of $[(\text{CH}_3-(\text{CH}_2)_7)_4\text{N}][\text{Au}_{25}(\text{SCH}_2\text{CH}_2-p\text{-C}_6\text{H}_4\text{-N}_3)]$ is 80-90 mg. ^1H NMR (CD_2Cl_2 , 600 MHz): δ (ppm) 7.17 (d, 24H, $J=6$ Hz), 7.12 (d, 12H, $J=6$ Hz), 6.86 (d, 12H, $J=6$ Hz), 6.80 (d, 24H, $J=6$ Hz), 3.54 (t, 24H, $J=6$ Hz), 3.09 (m, 44H), 2.93 (t, 12H, $J=6$ Hz), 1.62 (m, 8H), 1.37-1.31 (m, 48H), 0.90 (t, 12H, $J=6$ Hz). HRMS (ESI[negative]) m/z calc. for $\text{C}_{144}\text{H}_{144}\text{Au}_{25}\text{N}_5\text{S}$ (M^-): 8132.4 Da, found: 8132.9 Da. IR (ATR-IR, cm^{-1}): 2904, 2845, 2411, 2254, 2098, 1604, 1581, 1504. UV-Vis (Dichloromethane, 2×10^{-4} mol L^{-1}): $\lambda_{\text{max}} = 682$ nm, $\epsilon = 1908$ $\text{M}^{-1}\text{cm}^{-1}$, $\lambda_{\text{max}} = 443$ nm, $\epsilon = 6600$ $\text{M}^{-1}\text{cm}^{-1}$, $\lambda_{\text{max}} = 404$ nm, $\epsilon = 7650$ $\text{M}^{-1}\text{cm}^{-1}$.

4.6.2.9 Synthesis of $[(\text{CH}_3-(\text{CH}_2)_7)_4\text{N}][\text{Au}_{25}(\text{SCH}_2\text{CH}_2-p\text{-C}_6\text{H}_4\text{-C}_8\text{H}_{10}\text{N}_3)_{18}]$ (4.1-triazole)



To 10 mg (0.0012 mmol, 1 eq) $[(\text{CH}_3-(\text{CH}_2)_7)_4\text{N}][\text{Au}_{25}(\text{SCH}_2\text{CH}_2-p\text{-C}_6\text{H}_4\text{-N}_3)]$ in 5 mL tetrahydrofuran was added 2.5 mg (0.024 mmol, 20 eq) **(Z)-cyclooct-1-ene-5-yne** in 1 mL tetrahydrofuran. The solution was stirred for 10 minutes, after which the solvent and residual cyclooctyne starting material was removed by rotary

evaporation. Upon removal of the solvent, a reddish brown film formed on the flask interior, which was then triturated with acetonitrile to remove residual azide-clusters, giving $[(\text{CH}_3-(\text{CH}_2)_7)_4\text{N}][\text{Au}_{25}(\text{SCH}_2\text{CH}_2-p\text{-C}_6\text{H}_4\text{-C}_8\text{H}_{10}\text{N}_3)_{18}]$ as a reddish black film in 96% yield (12 mg).

^1H NMR (CD_2Cl_2 , 600 MHz): δ (ppm) 7.37 (d, 24H, $J=12$ Hz), 7.28 (d, 12H, $J=6$ Hz), 7.18 (m, 36H), 5.47 (m, 24H), 5.39 (m, 12H), 3.69 (t, 24H, $J=6$ Hz), 3.27-3.22 (m, 36H), 3.09 (m, 56H), 2.68-2.64 (m, 36H), 2.47-2.42 (m, 72H), 1.61 (m, 8H), 1.33-1.26 (m, 48H), 0.88 (t, 12H, $J=6$ Hz). MS (MALDI-TOF[negative]) m/z calc. for $\text{C}_{288}\text{H}_{324}\text{Au}_{25}\text{N}_{54}\text{S}$ (M^-): 10043.4 Da, found: 10048.4 Da. IR (ATR-IR, cm^{-1}): 2920, 2852, 1608, 1563, 1517. UV-Vis (Dichloromethane, 2×10^{-4} mol L^{-1}): $\lambda_{\text{max}} = 682$ nm, $\epsilon = 2040$ $\text{M}^{-1}\text{cm}^{-1}$, $\lambda_{\text{max}} = 446$ nm, $\epsilon = 7250$ $\text{M}^{-1}\text{cm}^{-1}$, $\lambda_{\text{max}} = 394$ nm, $\epsilon = 7780$ $\text{M}^{-1}\text{cm}^{-1}$.

4.6.3 Experimental Spectra and Diagrams

4.6.3.1 Experimental Spectra and Diagrams for $[\text{Au}_{25}(\text{SCH}_2\text{CH}_2\text{-}p\text{-C}_6\text{H}_4\text{-N}_3)_{18}][(\text{CH}_3\text{-(CH}_2)_7)_4\text{N}]$ (4.1-azido)

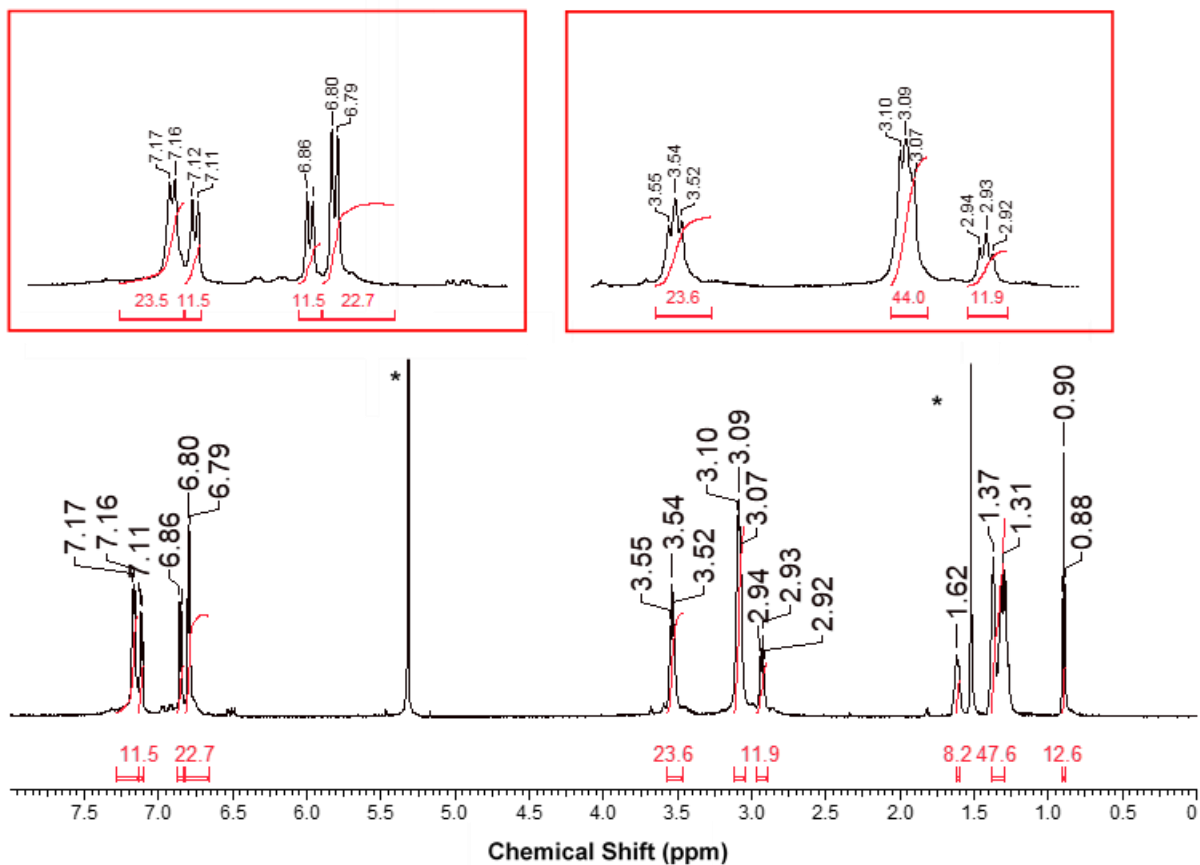


Figure S4.1. 600 MHz ^1H NMR spectrum of $[(\text{CH}_3\text{-(CH}_2)_7)_4\text{N}][\text{Au}_{25}(\text{SCH}_2\text{CH}_2\text{-}p\text{-C}_6\text{H}_4\text{-N}_3)_{18}]$ (4.1-azido) in CD_2Cl_2 at 25°C . Red insets are zoom-in regions of relevant sections of spectrum. * indicates residual protio solvent and impurities.

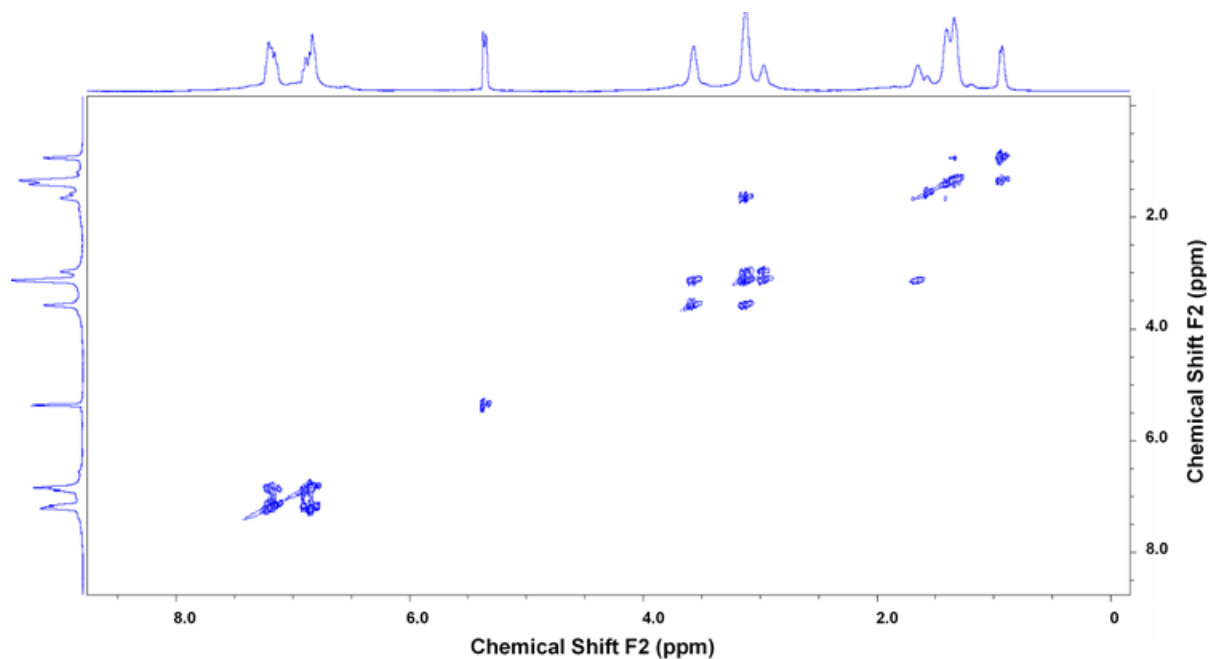


Figure S4.2. COSY NMR spectrum of $[(\text{CH}_3-(\text{CH}_2)_7)_4\text{N}][\text{Au}_{25}(\text{SCH}_2\text{CH}_2\text{-}p\text{-C}_6\text{H}_4\text{-N}_3)_{18}]$ (4.1-azido) in CD_2Cl_2 at 25°C .

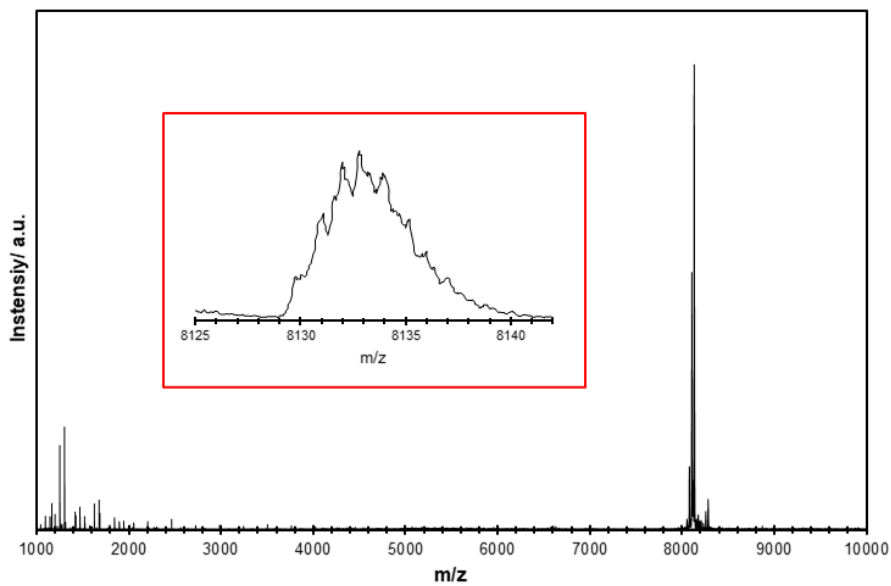


Figure S4.3. Negative ion mode ESI mass spectrum of anionic $[\text{Au}_{25}(\text{SCH}_2\text{CH}_2\text{-}p\text{-C}_6\text{H}_4\text{-N}_3)_{18}]^{1-}$.

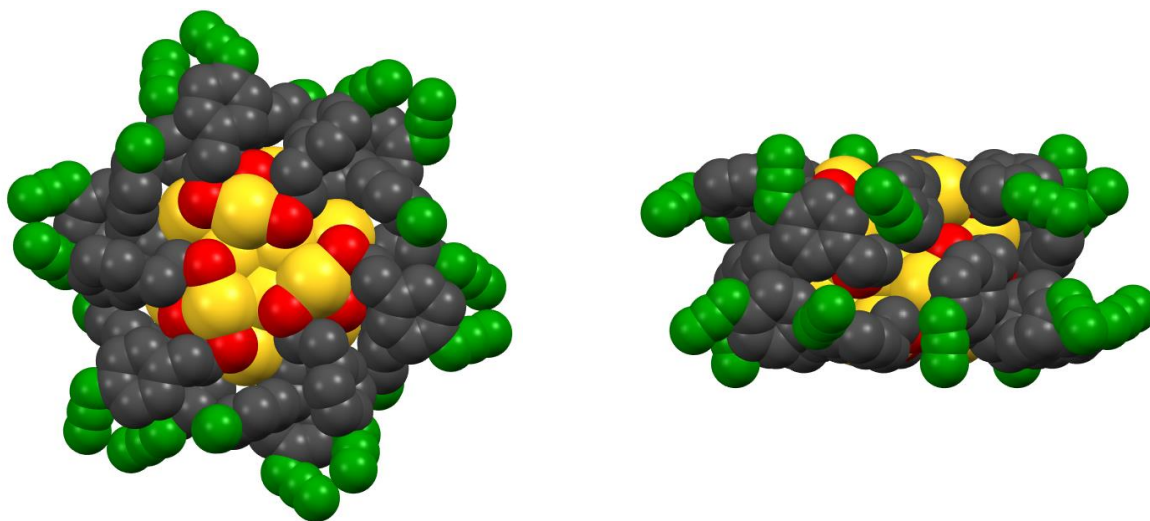


Figure S4.4. Space-filling X-ray structure diagram of $[(\text{CH}_3-(\text{CH}_2)_7)_4\text{N}][\text{Au}_{25}(\text{SCH}_2\text{CH}_2-p\text{-C}_6\text{H}_4\text{-N}_3)_{18}]$ (**4.1-azido**). Yellow = gold, red = sulfur, black = carbon, green = nitrogen. Tetraoctylammonium counterion is not shown.

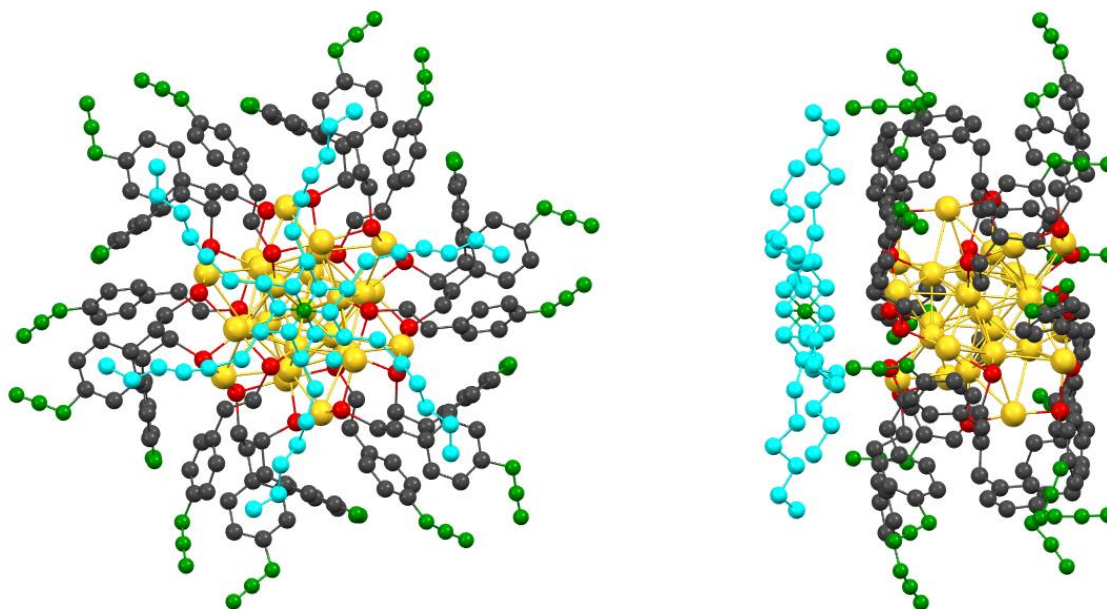


Figure S4.5. Molecular structure of $[(\text{CH}_3-(\text{CH}_2)_7)_4\text{N}][\text{Au}_{25}(\text{SCH}_2\text{CH}_2-p\text{-C}_6\text{H}_4\text{-N}_3)_{18}]$ (**4.1-azido**) showing disordered tetraoctylammonium counterion. Yellow = gold, red = sulfur, black = carbon_{cluster}, light blue = carbon_{counterion}, green = nitrogen.

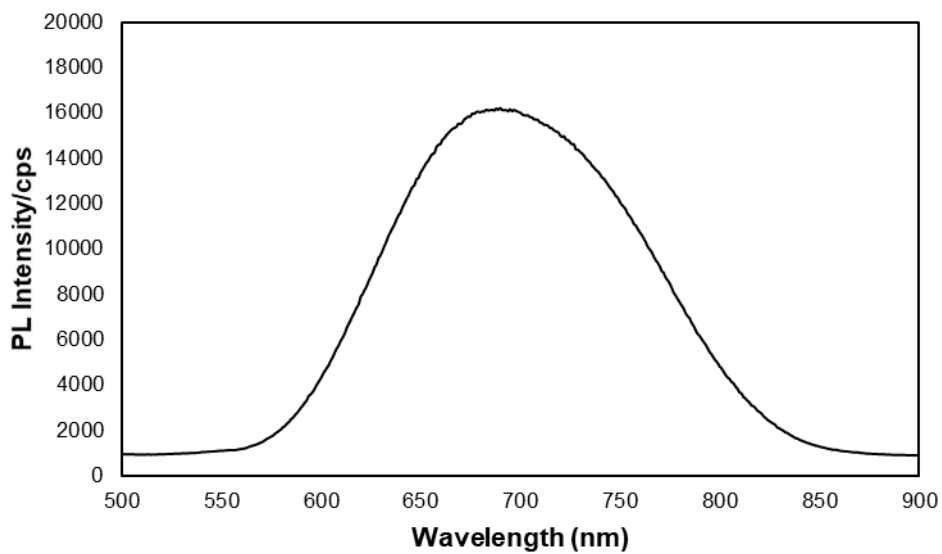


Figure S4.6. Photoluminescence spectrum of a 3 $\mu\text{mol/L}$ solution of $[(\text{CH}_3-(\text{CH}_2)_7)_4\text{N}][\text{Au}_{25}(\text{SCH}_2\text{CH}_2\text{-}i>p\text{-C}_6\text{H}_4\text{-N}_3)_{18}]$ (**4.1-azido**) in dichloromethane at 22°C, recorded with a 532 nm laser and 0.1 second exposure time.

4.6.3.2 Experimental Spectra for $[(\text{CH}_3-(\text{CH}_2)_7)_4\text{N}][\text{Au}_{25}(\text{SCH}_2\text{CH}_2-p\text{-C}_6\text{H}_4\text{-C}_8\text{H}_{10}\text{N}_3)_{18}]$ (4.1-triazole)

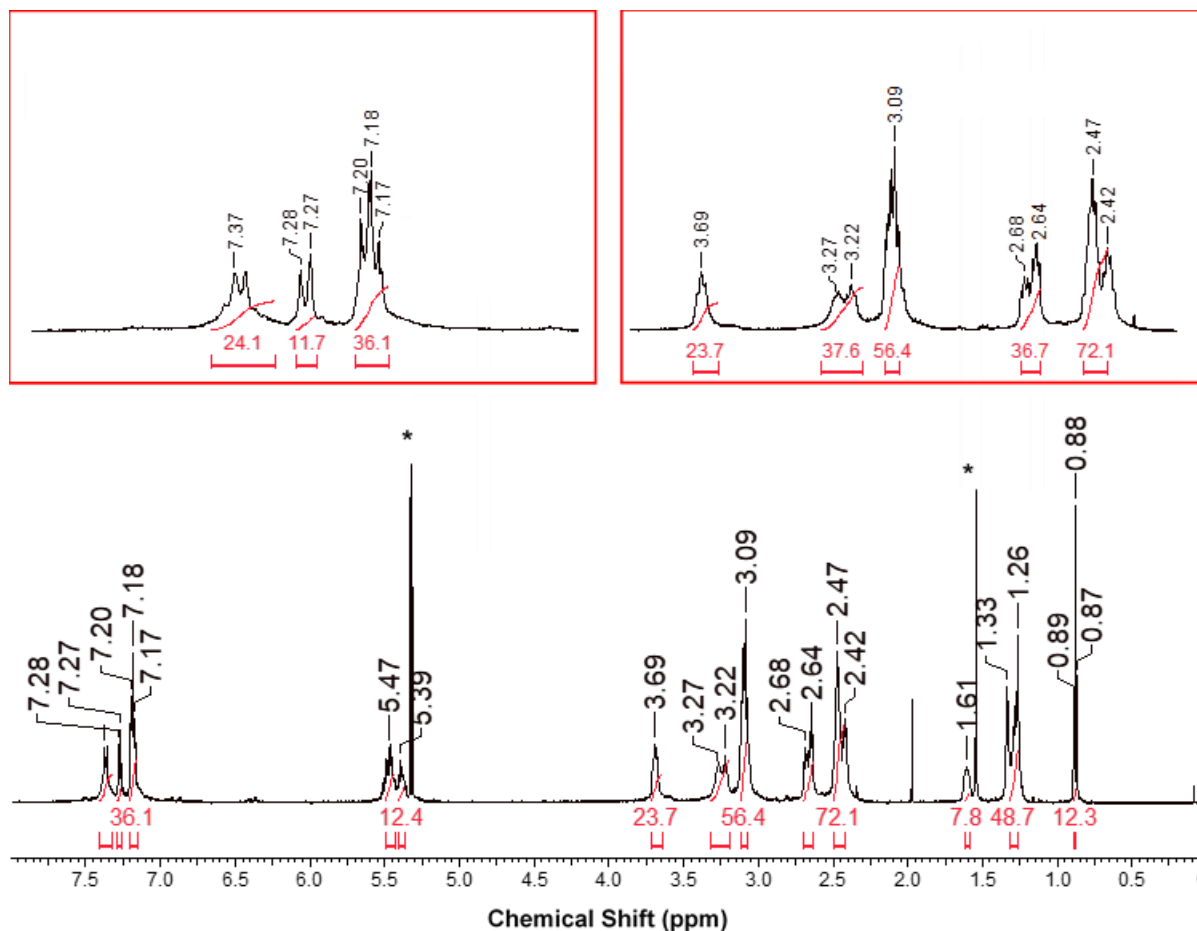


Figure S4.7. 600 MHz ^1H NMR spectrum of $[(\text{CH}_3-(\text{CH}_2)_7)_4\text{N}][\text{Au}_{25}(\text{SCH}_2\text{CH}_2-p\text{-C}_6\text{H}_4\text{-C}_8\text{H}_{10}\text{N}_3)_{18}]$ (4.1-triazole) in CD_2Cl_2 at 25°C . Red insets are zoom-in regions of relevant sections of spectrum. * indicates residual protio solvent and impurities.

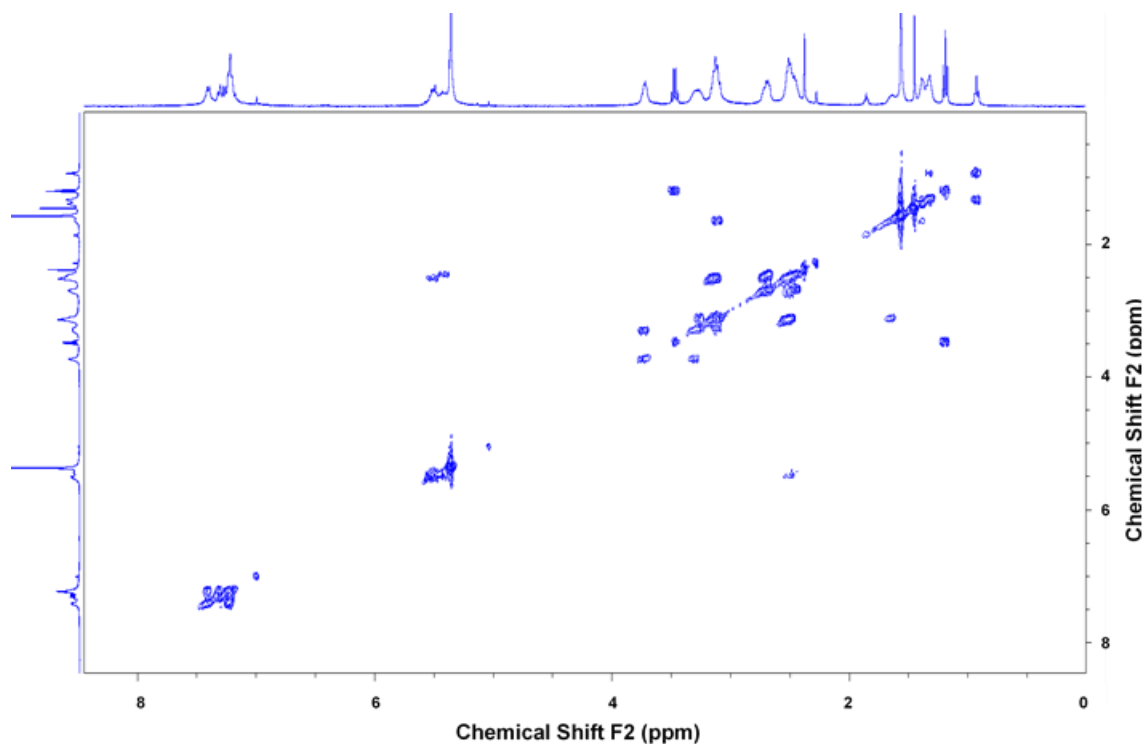


Figure S4.8. COSY spectrum of $[(\text{CH}_3-(\text{CH}_2)_7)_4\text{N}][\text{Au}_{25}(\text{SCH}_2\text{CH}_2\text{-}i>p\text{-C}_6\text{H}_4\text{-C}_8\text{H}_{10}\text{N}_3)_{18}]$ (4.1-triazole) in CD_2Cl_2 at 25°C .

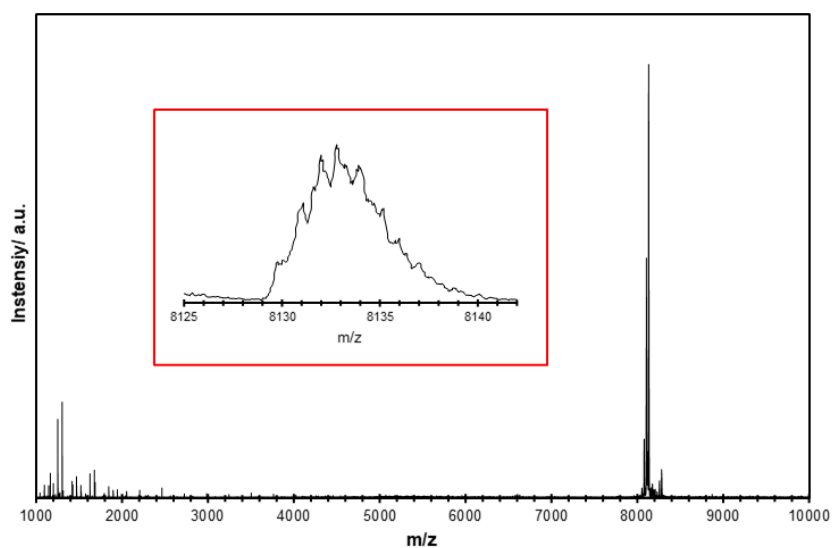


Figure S4.9. Linear negative mode MALDI-TOF mass spectrum of anionic $[\text{Au}_{25}(\text{SCH}_2\text{CH}_2\text{-}i>p\text{-C}_6\text{H}_4\text{-C}_8\text{H}_{10}\text{N}_3)_{18}]^{1-}$.

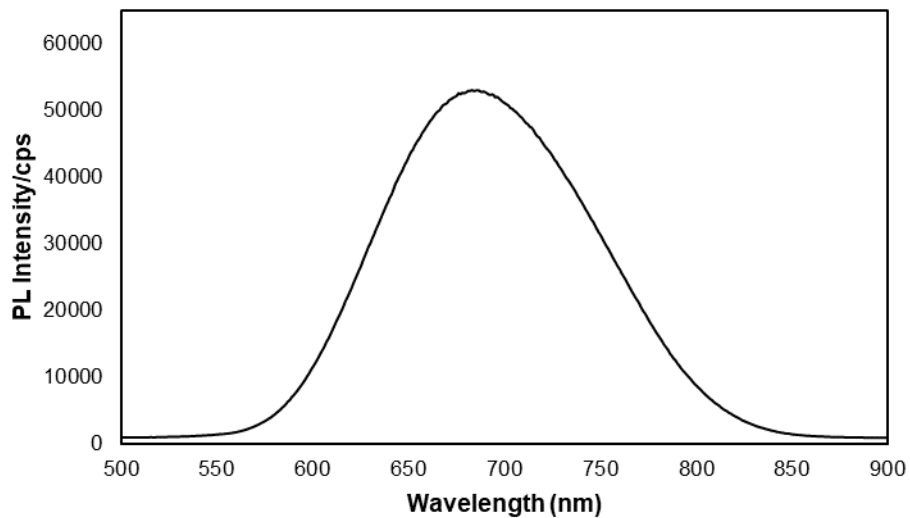


Figure S4.10. Photoluminescence spectrum of a 3 $\mu\text{mol/L}$ solution of $[(\text{CH}_3-(\text{CH}_2)_7)_4\text{N}][\text{Au}_{25}(\text{SCH}_2\text{CH}_2-p\text{-C}_6\text{H}_4\text{-C}_8\text{H}_{10}\text{N}_3)_{18}]$ (**4.1-triazole**) in dichloromethane at 22°C, recorded with a 532 nm laser and 0.1 second exposure time.

4.6.3.3 Experimental Spectra for $[(\text{CH}_3-(\text{CH}_2)_7)_4\text{N}][\text{Au}_{25}(\text{SCH}_2\text{CH}_2-p\text{-C}_6\text{H}_4\text{-C}_{10}\text{H}_{14}\text{N}_3\text{O})_{18}]^-$. Reaction of 4.1-azido with $\text{BCN}_{\text{exo-OH}}$

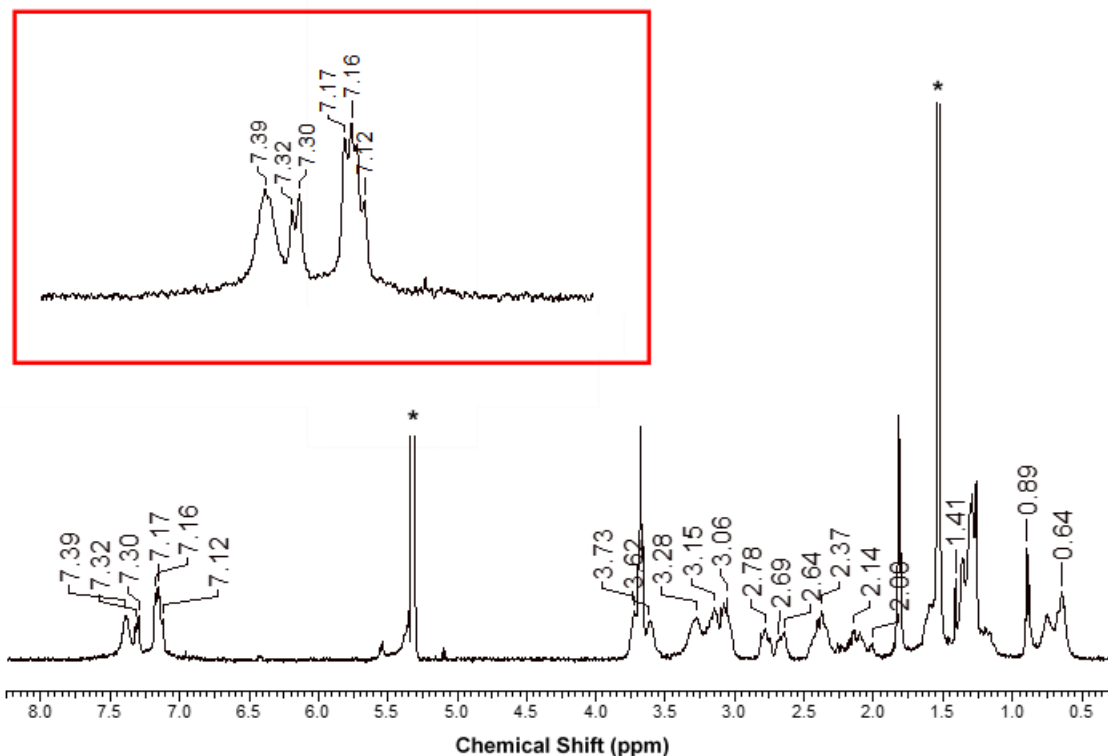


Figure S4.11. 600 MHz ^1H NMR spectrum of $[(\text{CH}_3-(\text{CH}_2)_7)_4\text{N}][\text{Au}_{25}(\text{SCH}_2\text{CH}_2-p\text{-C}_6\text{H}_4\text{-C}_{10}\text{H}_{14}\text{N}_3\text{O})_{18}]^-$ in CD_2Cl_2 at 25°C . Red insets are zoom-in region of relevant section of spectrum. * indicates residual protio solvents and impurities.

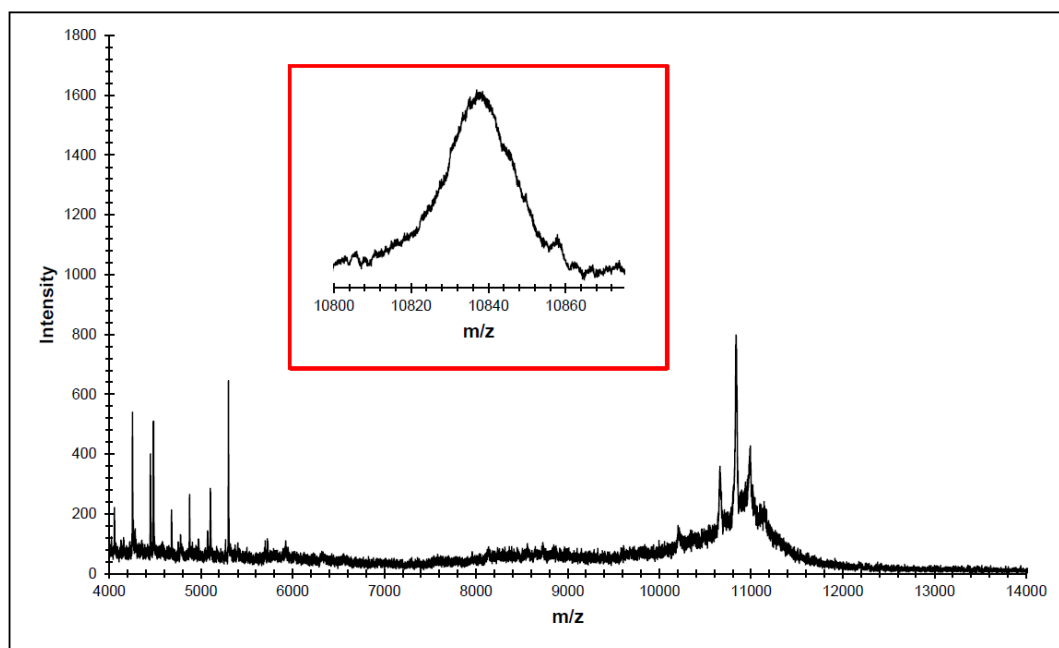


Figure S4.12. Linear negative mode MALDI-TOF mass spectrum of anionic $[(\text{CH}_3-(\text{CH}_2)_7)_4\text{N}][\text{Au}_{25}(\text{SCH}_2\text{CH}_2\text{-}i>p\text{-C}_6\text{H}_4\text{-C}_{10}\text{H}_{14}\text{N}_3\text{O})_{18}]^{1-}$.

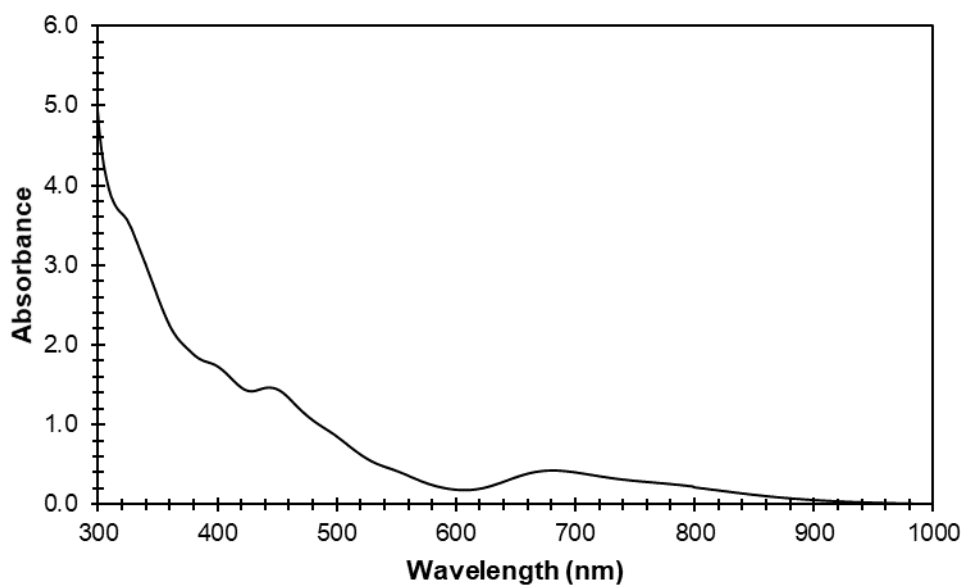


Figure S4.13. UV-Vis absorption spectrum of 1×10^{-4} M solution of $[(\text{CH}_3-(\text{CH}_2)_7)_4\text{N}][\text{Au}_{25}(\text{SCH}_2\text{CH}_2\text{-}i>p\text{-C}_6\text{H}_4\text{-C}_{10}\text{H}_{14}\text{N}_3\text{O})_{18}]$ in dichloromethane at 23°C .

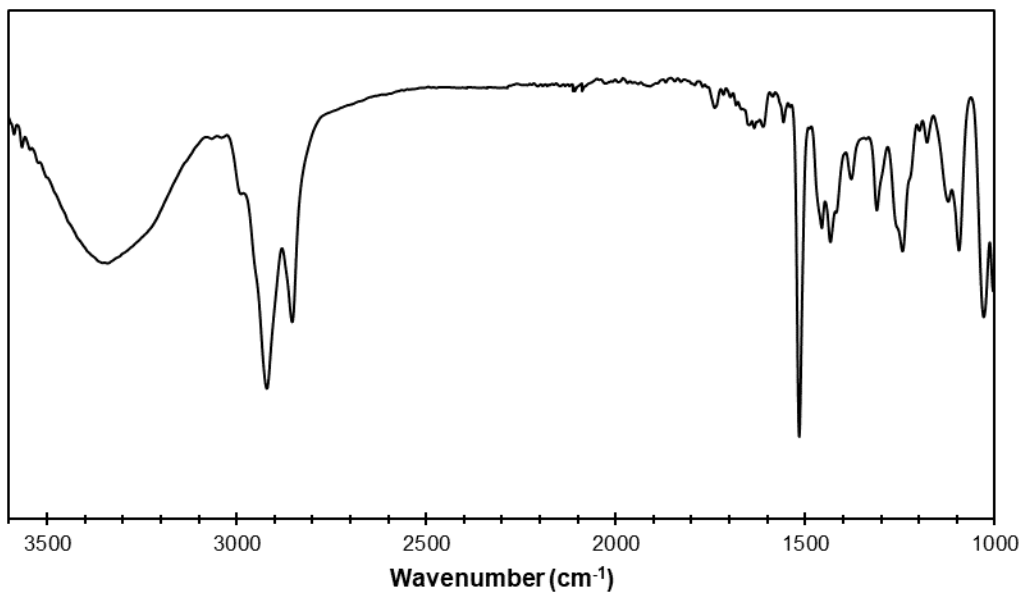


Figure S4.14. Infrared spectrum of $[(\text{CH}_3-(\text{CH}_2)_7)_4\text{N}][\text{Au}_{25}(\text{SCH}_2\text{CH}_2\text{-}p\text{-C}_6\text{H}_4\text{-C}_{10}\text{H}_{14}\text{N}_3\text{O})_{18}]$.

4.6.3.4 Experimental Spectra for *p*-nitro-phenylethanethioacetate

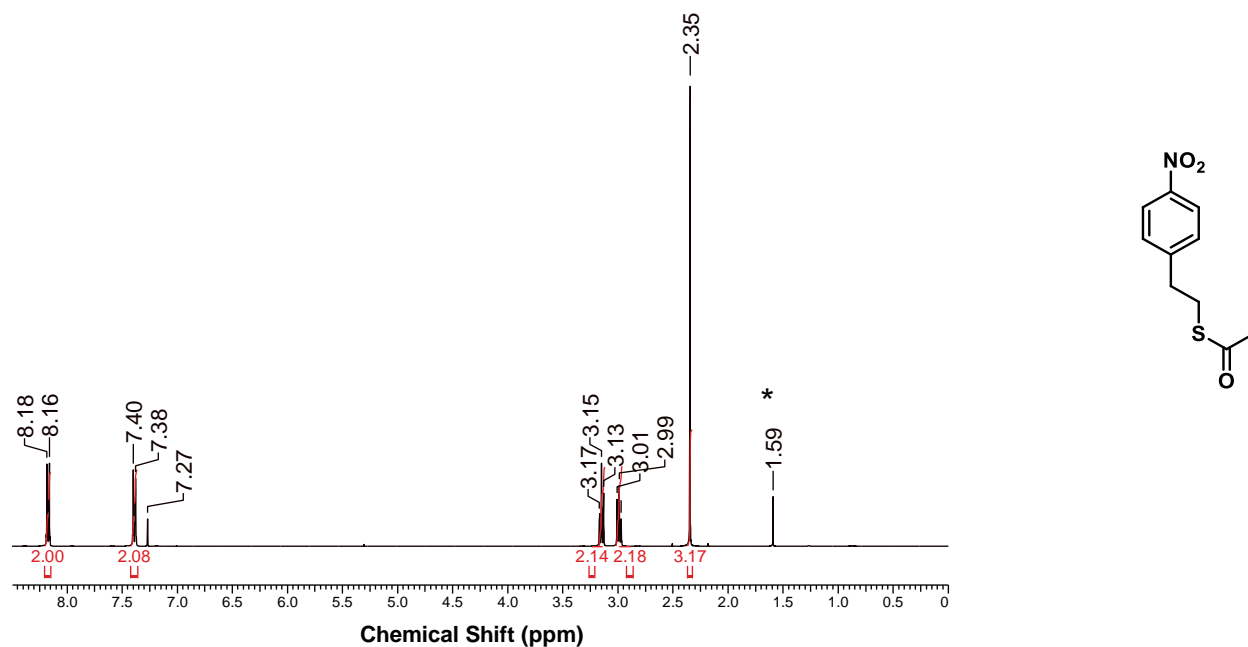


Figure S4.15. ^1H NMR spectrum of *p*-nitro-phenylethanethioacetate in CDCl_3 at 25°C . * indicates residual protio solvent and impurities.

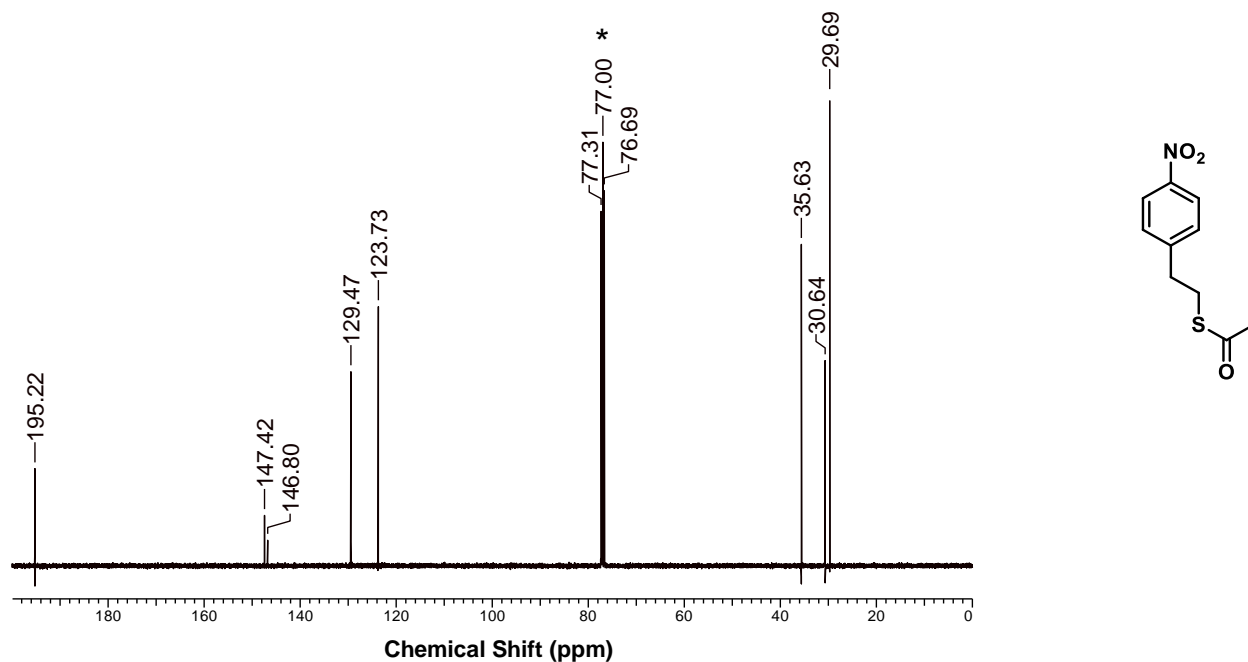


Figure S4.16. $^{13}\text{C}\{^1\text{H}\}$ NMR spectrum of *p*-nitro-phenylethanethioacetate in CDCl_3 at 25°C . * indicates CDCl_3 solvent.

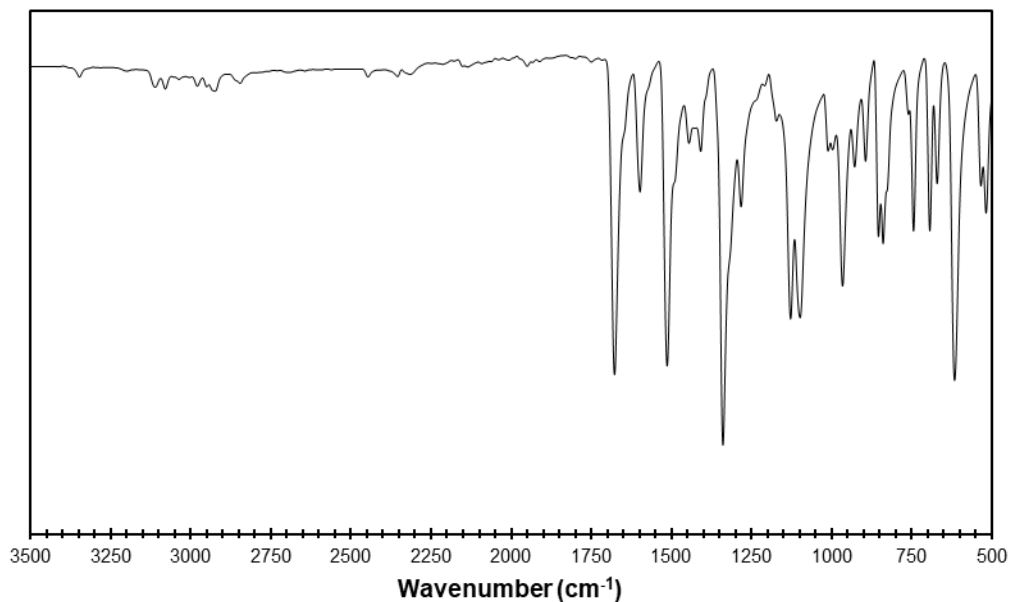


Figure S4.17. Infrared spectrum of *p*-nitro-phenylethanethioacetate.

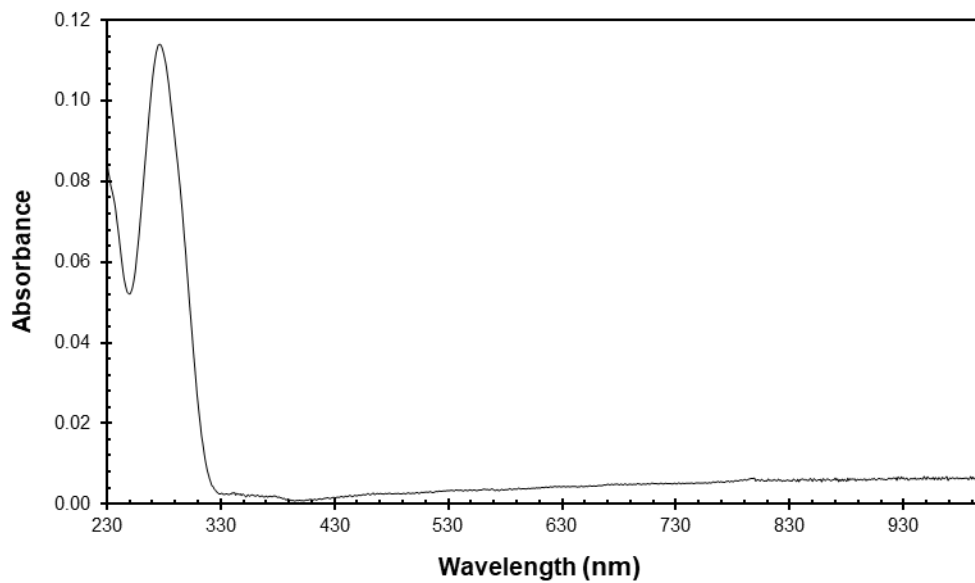


Figure S4.18. UV-Vis absorption spectrum of 1×10^{-4} M solution of *p*-nitro-phenylethanethioacetate in dichloromethane at 23°C.

4.6.3.5 Experimental Spectra for *p*-ammonium-phenylethanethioacetate chloride

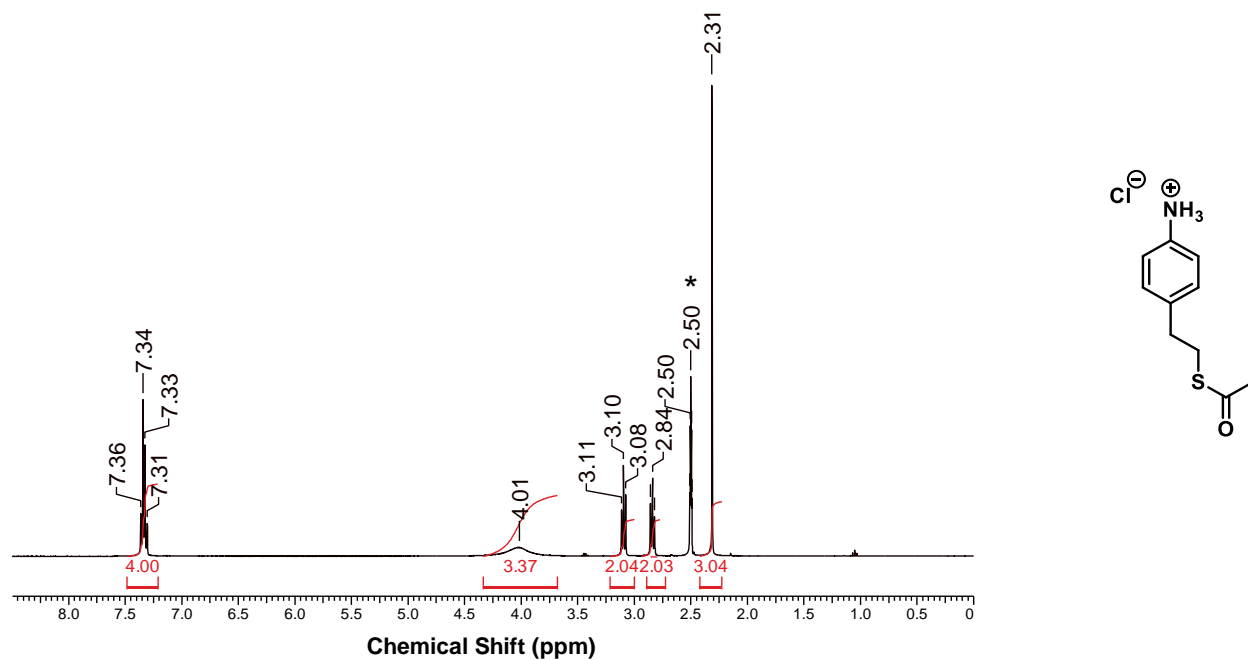


Figure S4.19. ^1H NMR spectrum of *p*-ammonium-phenylethanethioacetate chloride in $(\text{CD}_3)_2\text{SO}$ at 25°C . * indicates residual protio solvent.

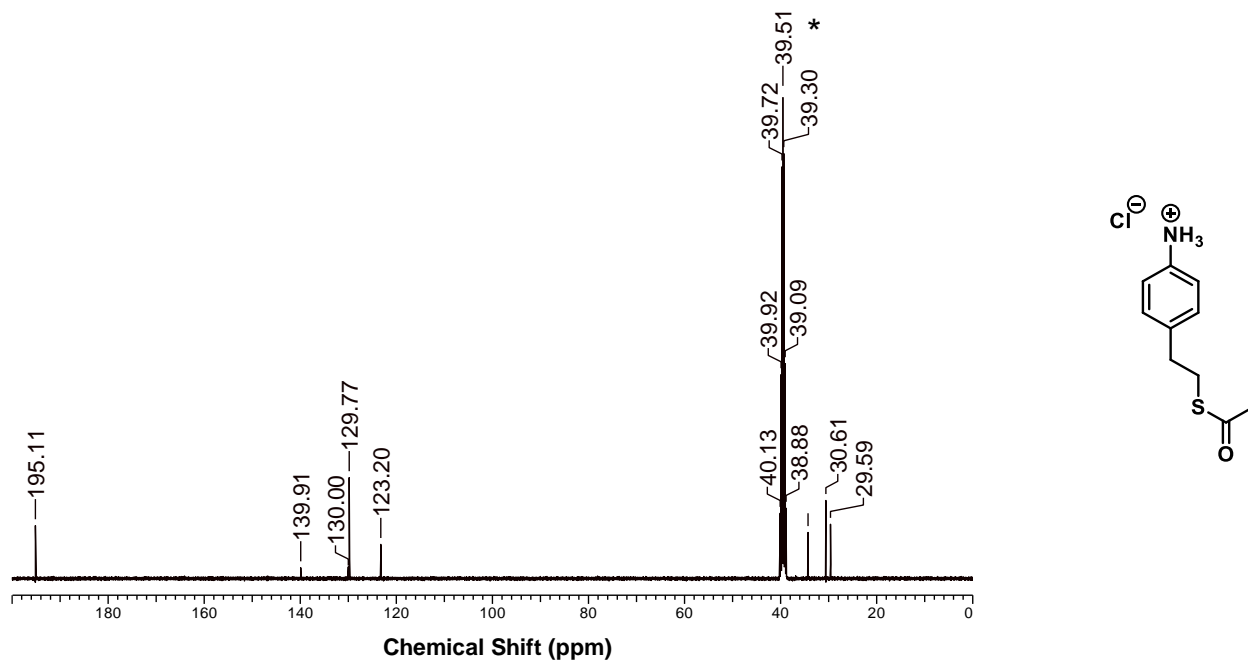


Figure S4.20. $^{13}\text{C}\{^1\text{H}\}$ NMR spectrum of *p*-ammonium-phenylethanethioacetate chloride in $(\text{CD}_3)_2\text{SO}$ at 25°C . * indicates $(\text{CD}_3)_2\text{SO}$ solvent.

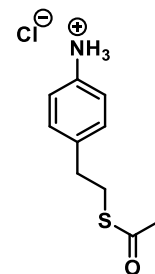
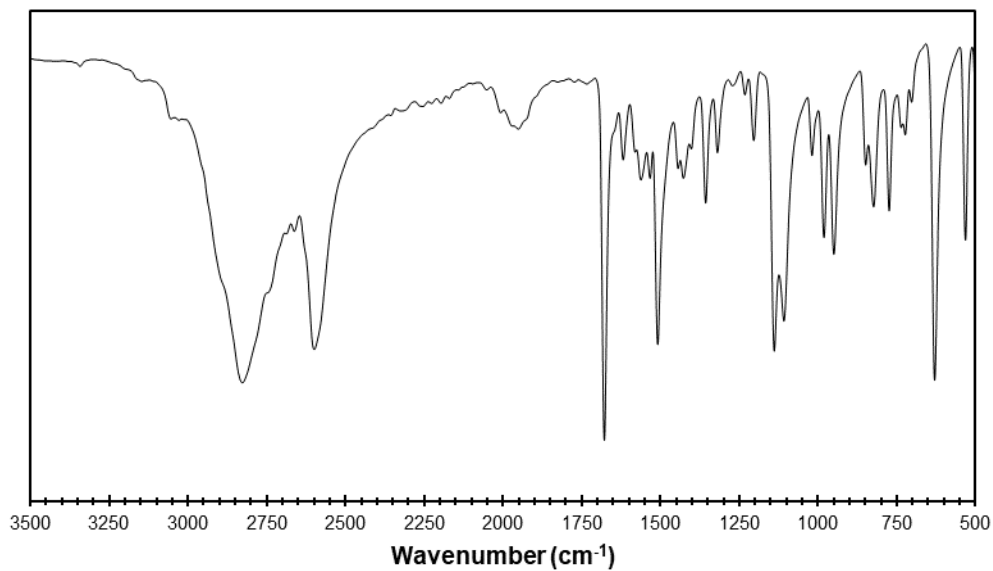


Figure S4.21. Infrared spectrum of *p*-ammonium-phenylethanethioacetate chloride.

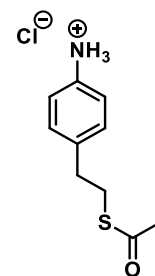
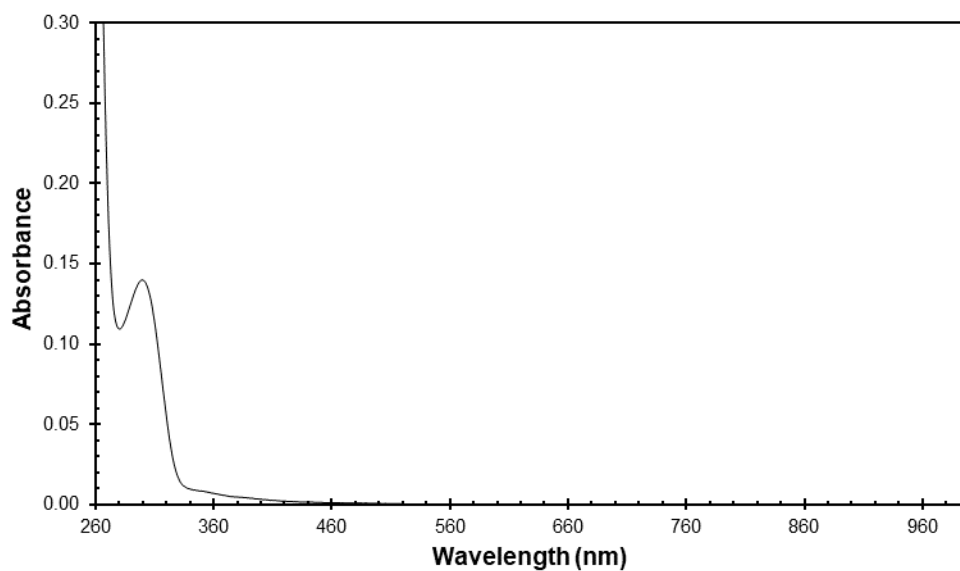


Figure S4.22. UV-Vis absorption spectrum of 1×10^{-4} M solution of *p*-ammonium-phenylethanethioacetate chloride in dichloromethane at 23°C.

4.6.3.6 Experimental Spectra for *p*-azido-phenylethanethioacetate

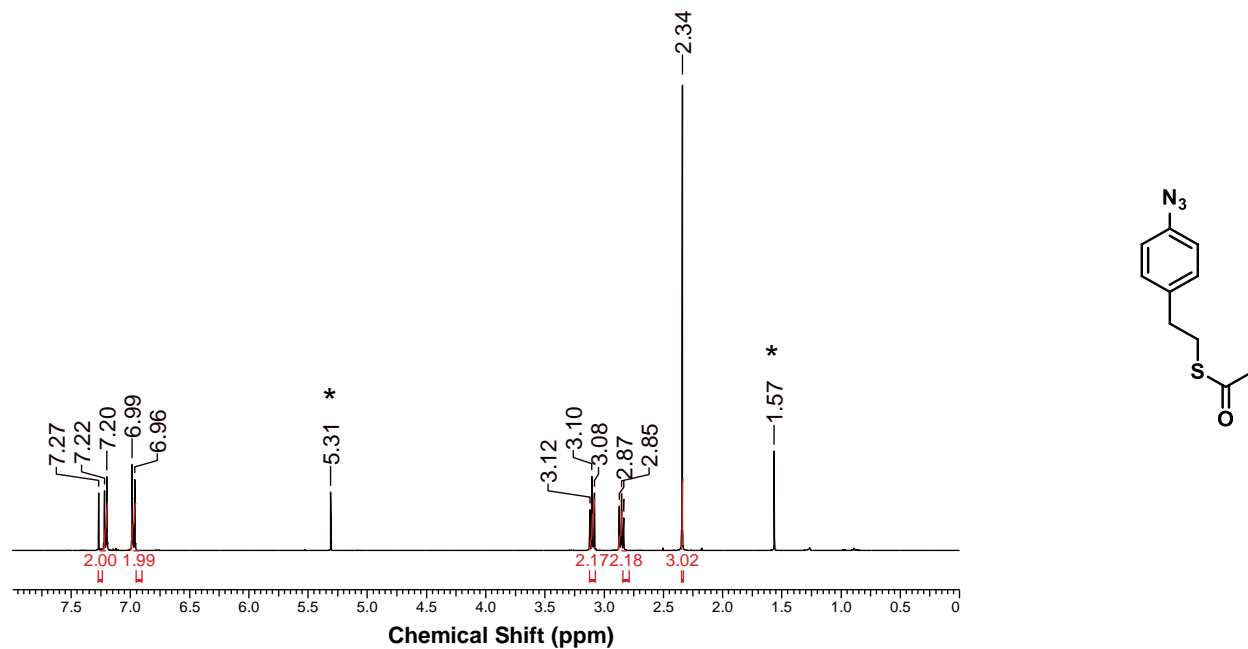


Figure S4.23. ^1H NMR spectrum of *p*-azido-phenylethanethioacetate in CDCl_3 at 25°C . * indicates residual protio solvent and impurities.

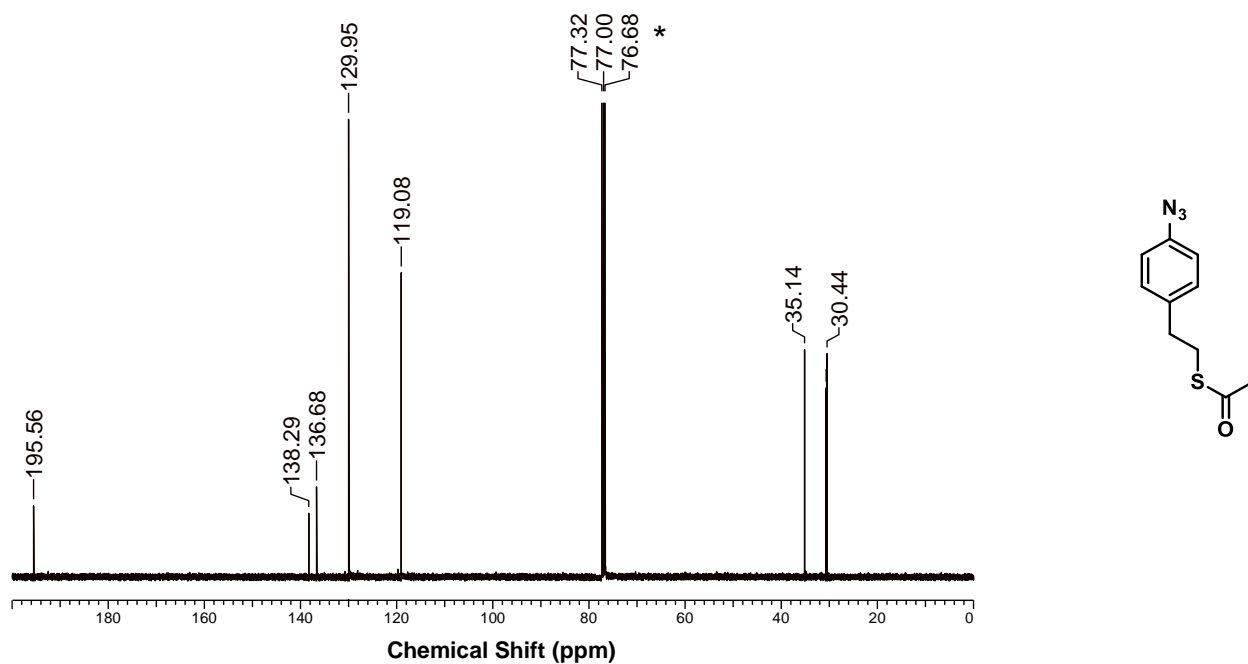


Figure S4.24. $^{13}\text{C}\{^1\text{H}\}$ NMR spectrum of *p*-azido-phenylethanethioacetate in CDCl_3 at 25°C . * indicates CDCl_3 solvent.

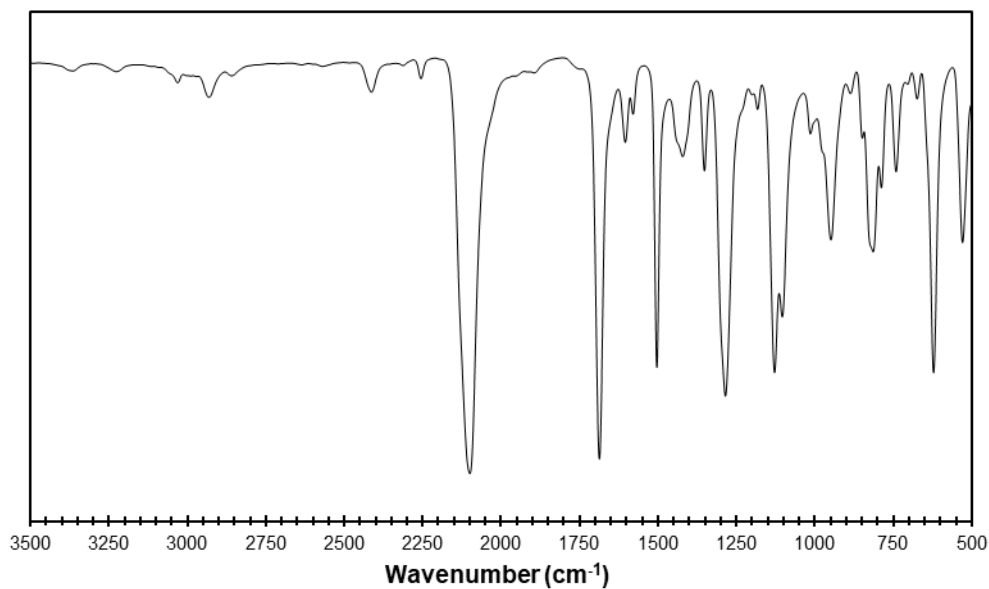


Figure S4.25. Infrared spectrum of *p*-azido-phenylethanethioacetate.

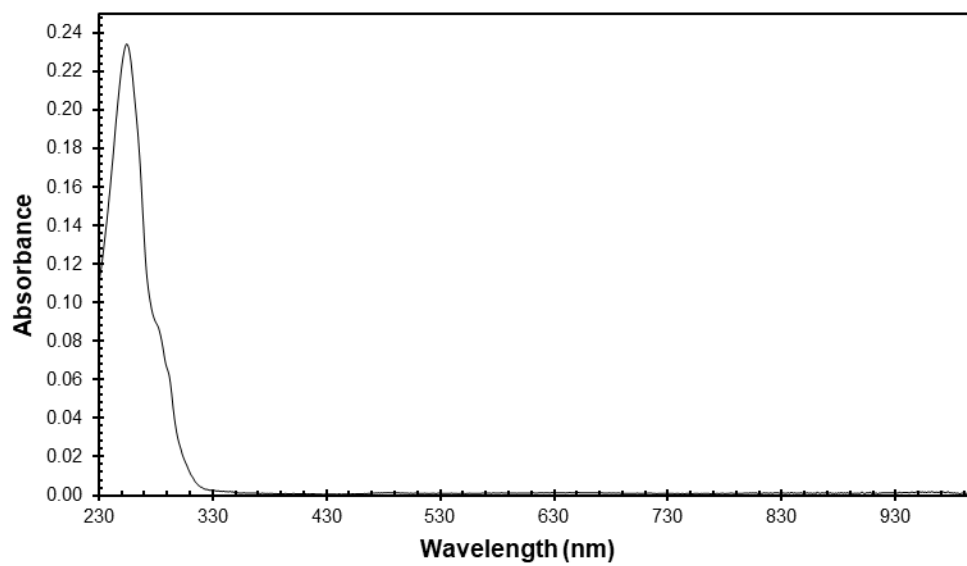


Figure S4.26. UV-Vis absorption spectrum of 1×10^{-4} M solution of *p*-azido-phenylethanethioacetate in dichloromethane at 23°C.

4.6.3.7 Experimental Spectra for *p*-azido-phenylethanethiol

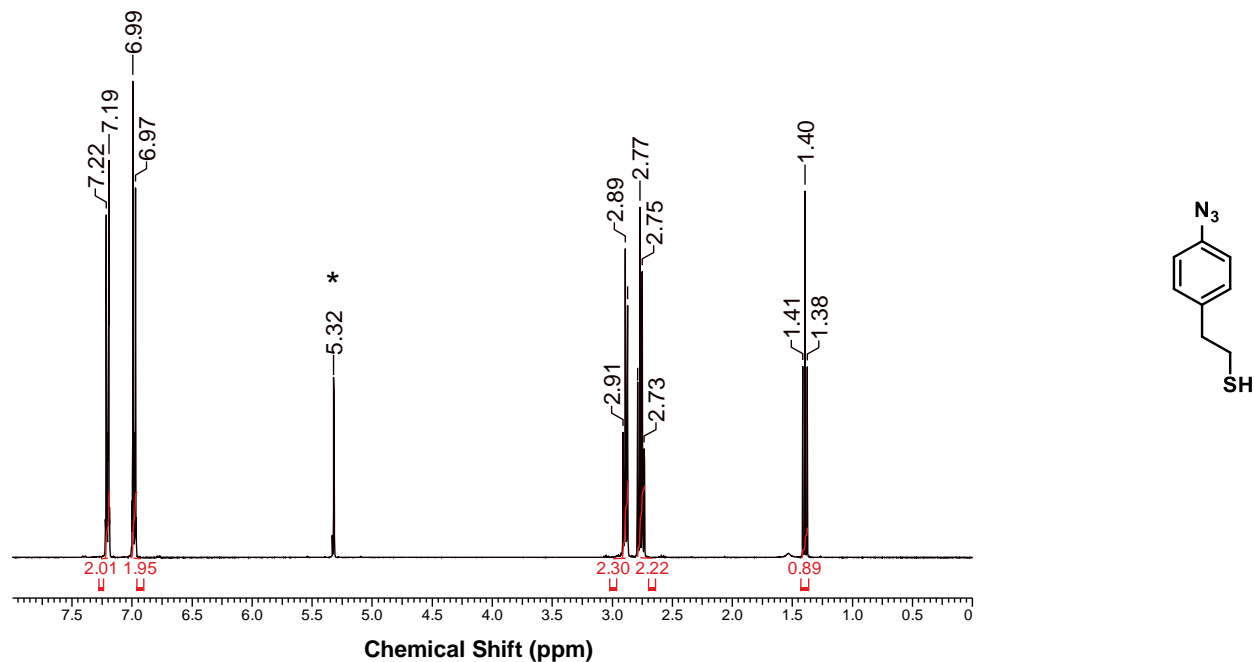


Figure S4.27. ^1H NMR spectrum of *p*-azido-phenylethanethiol in CD_2Cl_2 at 25°C . * indicates residual protio solvent.

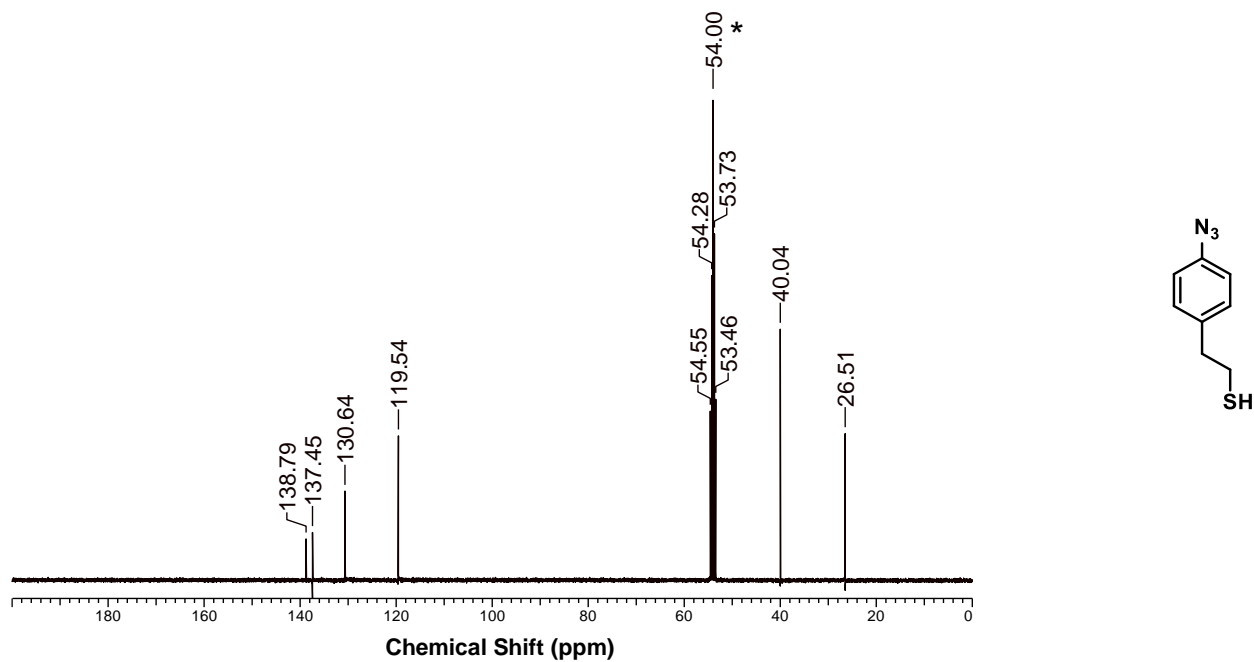


Figure S4.28. $^{13}\text{C}\{^1\text{H}\}$ NMR spectrum of *p*-azido-phenylethanethiol in CD_2Cl_2 at 25°C . * indicates CD_2Cl_2 solvent.

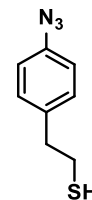
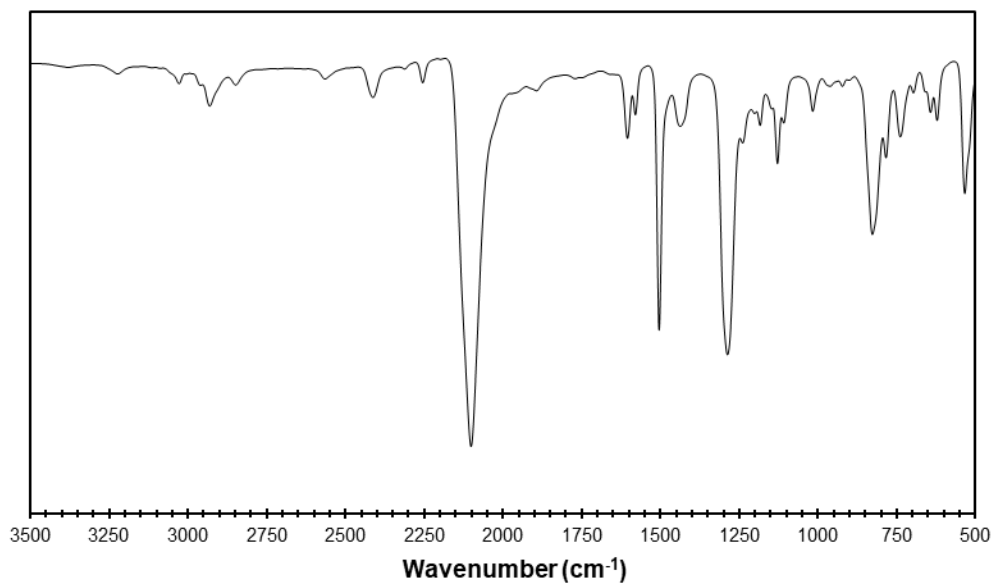


Figure S4.29. Infrared spectrum of *p*-azido-phenylethanethiol.

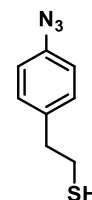
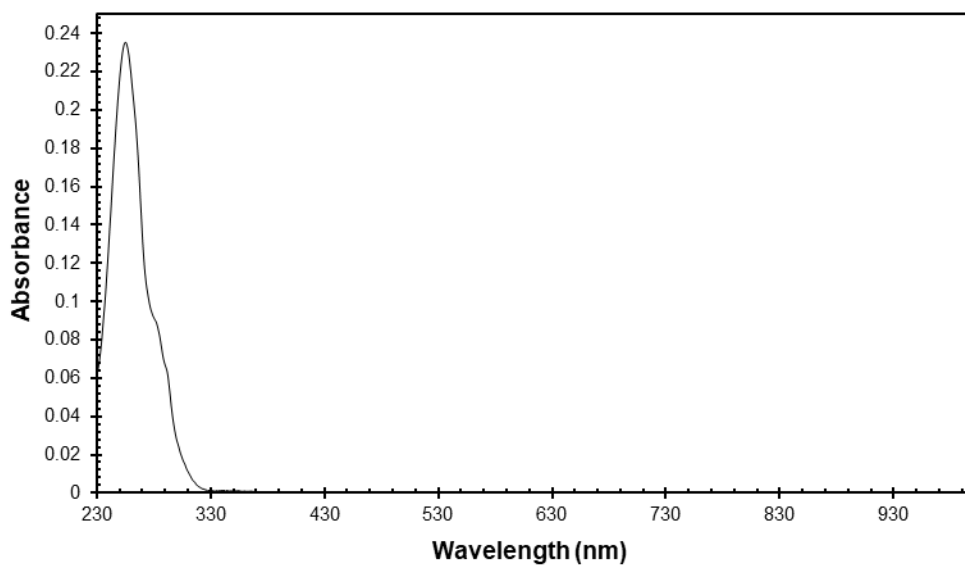


Figure S4.30. UV-Vis absorption spectrum of 1×10^{-4} M solution of *p*-azido-phenylethanethiol in dichloromethane at 23°C.

4.6.3.8 Experimental Spectra for (Z)-5,6-dibromocyclooct-1-ene

See Section 3.6.9.2 for ^1H NMR and $^{13}\text{C}\{^1\text{H}\}$ NMR spectra for (Z)-5,6-dibromocyclooct-1-ene.

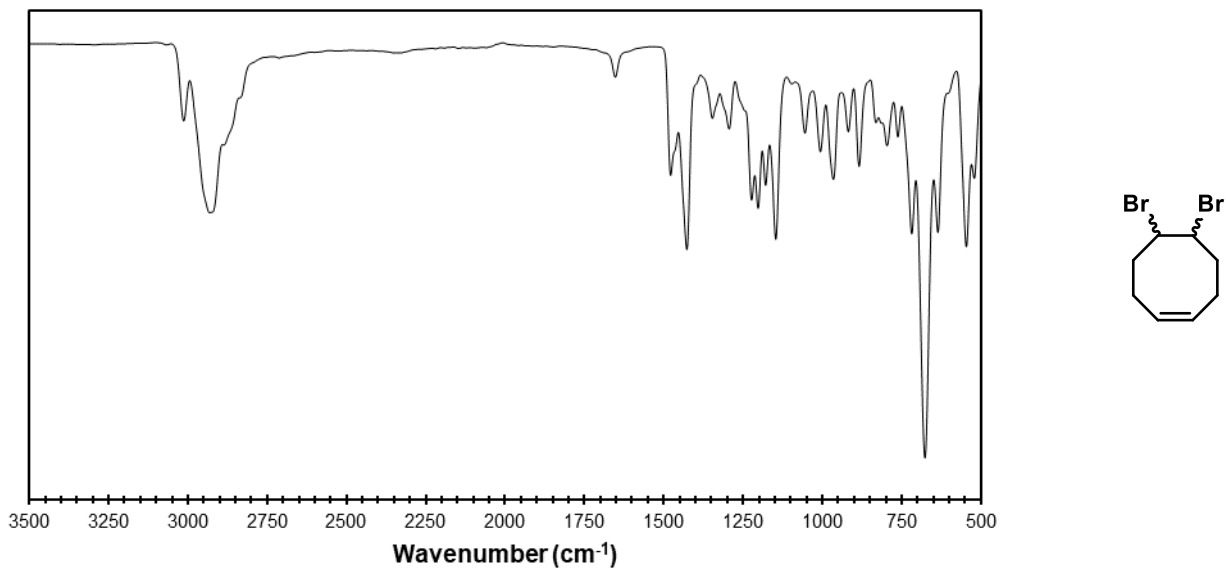


Figure S4.31. Infrared spectrum of (Z)-5,6-dibromocyclooct-1-ene.

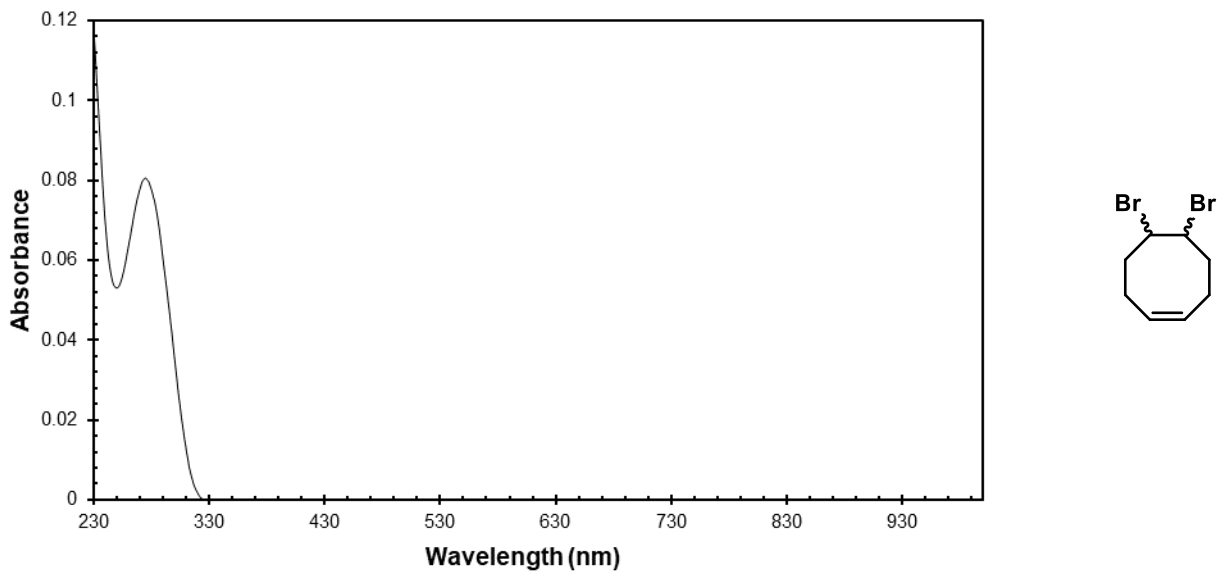


Figure S4.32. UV-Vis absorption spectrum of 1×10^{-4} M solution of (Z)-5,6-dibromocyclooct-1-ene in dichloromethane at 23°C.

4.6.3.9 Experimental Spectra for (Z)-cyclooct-1-ene-5-yne

See Section 3.6.9.3 for ^1H NMR and $^{13}\text{C}\{^1\text{H}\}$ NMR spectra for (Z)-cyclooct-1-ene-5-yne.

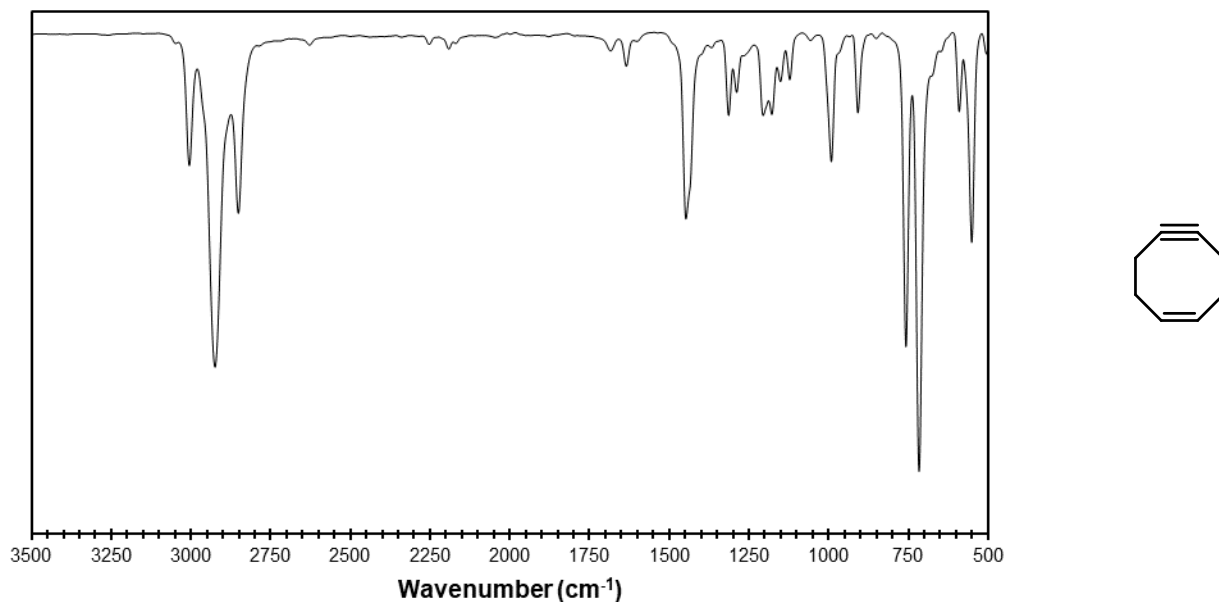


Figure S4.33. Infrared spectrum of (Z)-cyclooct-1-ene-5-yne.

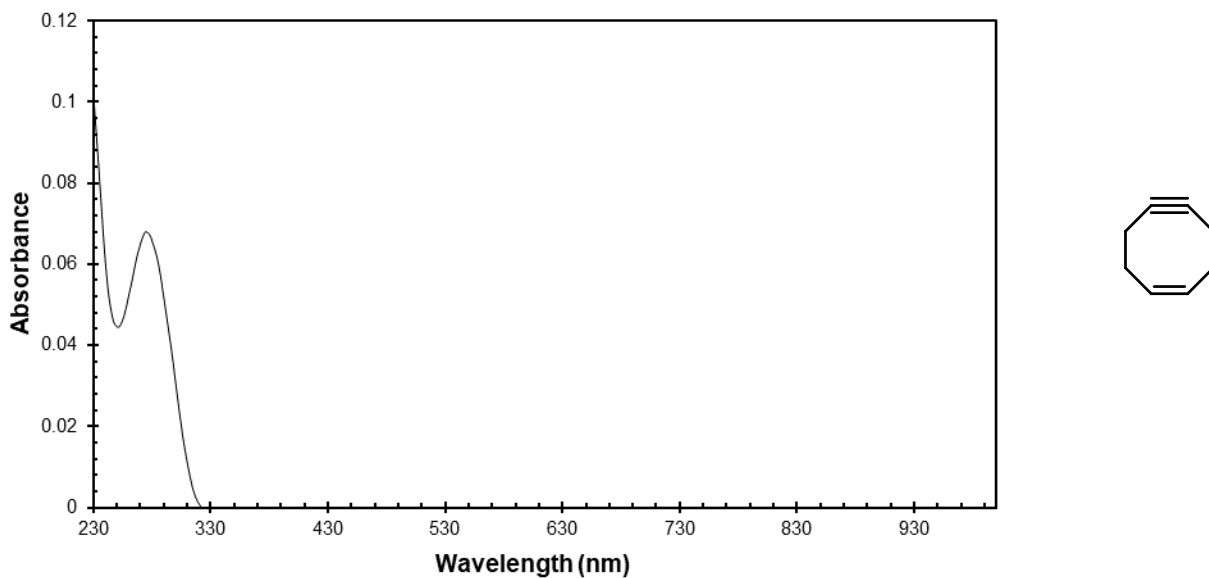


Figure S4.34. UV-Vis absorption spectrum of 1×10^{-4} M solution of (Z)-cyclooct-1-ene-5-yne in dichloromethane at 23°C .

4.6.4 Crystallographic Information

4.6.4.1 Data Collection and Processing

The sample was mounted on a Mitegen polyimide micromount with a small amount of Paratone N oil. All X-ray measurements were made on a Bruker Kappa Axis Apex2 diffractometer at a temperature of 110 K. The unit cell dimensions were determined from a symmetry constrained fit of 9034 reflections with $4.7^\circ < 2\theta < 47.48^\circ$. The data collection strategy was a number of ω and φ scans which collected data up to 47.692° (2θ). The frame integration was performed using SAINT⁴. The resulting raw data was scaled and absorption corrected using a multi-scan averaging of symmetry equivalent data using SADABS⁵.

4.6.4.2 Structure Solution and Refinement

The structure was solved by using a dual space methodology using the SHELXT program⁶. All Au and S atoms were obtained from the initial solution. C and N atoms were located in the subsequent difference Fourier maps. The Oct_4N^+ cation was found to exhibit disorder, residing about a crystallographic $\bar{3}$ site. Disordered C atoms were thus refined with partial occupancies; N-C and C-C distances were restrained (DFIX command). One of the crystallographically independent $-\text{CH}_2\text{CH}_2\text{C}_6\text{H}_4\text{N}_3$ thiolate moieties (C19-N9) also appeared to have site disorder but this could not be resolved/modelled. It was thus refined using the restraint SAME and SIMU in the software. The hydrogen atoms for the thiolate ligands were introduced at idealized positions and were allowed to ride on the parent atom. The structural model was fit to the data using full matrix least-squares based on F^2 . The calculated structure factors included corrections for anomalous dispersion from the usual tabulation. The structure was refined using the SHELXL program from the SHELXTL suite of crystallographic software⁷. Graphic plots were produced using the NRCVAX program suite⁸. Additional information and other relevant literature references can be found in the reference section of this website (<http://xray.chem.uwo.ca>). CCDC 1936245 contains the supplementary crystallographic data for this paper. These data can be obtained free of charge from The Cambridge Crystallographic Data Center via www.ccdc.cam.ac.uk/data_request/cif.

4.6.4.3 Summary of Crystal Data

Formula	$C_{176}H_{212}Au_{25}N_{55}S_{18}$
Formula Weight (<i>g/mol</i>)	8599.24
Crystal Dimensions (<i>mm</i>)	$0.242 \times 0.040 \times 0.032$
Crystal Color and Habit	black needle
Crystal System	trigonal
Space Group	R-3
Temperature, K	110
a , Å	34.623(14)
b , Å	34.623(14)
c , Å	15.731(4)
α , °	90
β , °	90
γ , °	120
V , Å ³	16331(14)
Number of reflections to determine final unit cell	9034
Min and Max 2θ for cell determination, °	4.7, 47.48
Z	3
F(000)	11748
ρ (<i>g/cm</i> ³)	2.623

λ , Å, (MoK α)	0.71073
μ , (cm ⁻¹)	16.998
Diffractometer Type	Bruker Kappa Axis Apex2
Scan Type(s)	phi and omega scans
Max 2 θ for data collection, °	47.692
Measured fraction of data	0.997
Number of reflections measured	208329
Unique reflections measured	5593
R _{merge}	0.1027
Number of reflections included in refinement	5593
Cut off Threshold Expression	I > 2sigma(I)
Structure refined using	full matrix least-squares using F ²
Weighting Scheme	w=1/[sigma ² (Fo ²)+(0.0545P) ² +179 0.3613P] where P=(Fo ² +2Fc ²)/3
Number of parameters in least-squares	400
R ₁	0.0515
wR ₂	0.1266
R ₁ (all data)	0.0859
wR ₂ (all data)	0.1592
GOF	1.145

Maximum shift/error	0.000
Min & Max peak heights on final ΔF Map ($e^-/\text{\AA}$)	-1.755, 2.848

Where:

$$R_1 = \sum (|F_o| - |F_c|) / \sum F_o$$

$$wR_2 = [\sum (w(F_o^2 - F_c^2)^2) / \sum (w F_o^4)]^{1/2}$$

$$GOF = [\sum (w(F_o^2 - F_c^2)^2) / (\text{No. of reflns.} - \text{No. of params.})]^{1/2}$$

4.6.5 References – Supporting Information

1. Wandler A. E. E.; Koos M. R. M.; Nieger M.; Luy B.; Braese S., 1,5-cyclooctadienyl alcohols and ketones generate a new class of COD Pt complexes. *Dalton Trans.* **2018**, 47(11), 3689-3692.
2. Petersen H.; Kolshorn H.; Meier H., Cyclooctenyne. *Angew. Chem. Inter. Ed.* **1978**, 6, 461-462.
3. Dommerholt J.; Schmidt S.; Temming R.; Hendriks L.J.A.; Rutjes F.P.J.T.; van Hest J.C.M.; Lefeber D.J.; Friedl P.; van Delft F.L. *Angew. Chem. Inter. Ed.* **2010**, 49, 9422.
4. Bruker-AXS, SAINT version 2013.8, **2013**, Bruker-AXS, Madison, WI 53711, USA.
5. Bruker-AXS, SADABS version 2012.1, **2012**, Bruker-AXS, Madison, WI 53711, USA
6. Sheldrick G.M., *Acta Crystallographica Section A.* **2015**, A71, 3-8
7. Sheldrick G.M., *Acta Crystallographica Section C.* **2015**, C71, 3-8
8. Gabe E.J.; Le Page Y.; Charland J.P.; Lee F.L.; White P.S. *J. Appl. Cryst.* **1989**, 22, 384-387

Chapter 5

5 Expanding the Library of Clickable Azide-Functionalized Au₂₅SR₁₈ Nanocluster Platforms: A study of Ligand Modifications on Structure, Properties and Surface Reactivity

This chapter is being submitted as a short paper and is in manuscript format. Julia Martin and Jonathan M. Wong are co-authors, along with professors Zhifeng Ding, John F. Corrigan and Mark S. Workentin.

Martin was an undergraduate thesis student under my direct co-supervision, along with my supervisor, Prof. Mark S. Workentin, who assisted in the synthesis and characterization of the three isomeric clusters and obtaining the molecular structures presented. Wong was a graduate student, who under the co-supervision of his supervisor, Prof. Zhifeng Ding, obtained the electrochemical measurements of the three isomeric clusters. Prof. John F. Corrigan was involved in obtaining and refining the molecular structures presented. The draft of the manuscript was written by the author and edited by Prof. Mark S. Workentin and Prof. John F. Corrigan.

5.1 Introduction

In contemporary nanomaterials science, ligand-protected gold nanoclusters (AuNCs) are among the most currently researched due to their superior stability and ease of synthesis compared to other noble metal nanocluster systems that tend to be more chemically sensitive. Given their synthetic accessibility, there has been extensive efforts towards understanding the fundamental conditions to produce atomically precise AuNCs, with well-defined physical and optical properties that are fingerprinted to each individual combination of surface ligand and metal configuration.¹ It is this ability to influence the core configuration and related properties through careful alterations to reaction conditions, stoichiometries and surface ligand structure that has led to the prominent library of AuNCs currently existing, with many of the AuNCs having become promising candidates for a wide variety of applications, including in catalysis,²⁻⁴ chemical sensing⁵⁻⁷ and biomedicine.⁸⁻¹⁰

Of the fundamental factors that can be manipulated to construct AuNCs of various sizes in an experimentally pre-defined manner, the correlation between the type and structure of the protecting surface ligand and acquired nanocluster configuration has received significant attention.¹¹⁻¹³ Recently, there have been many examples of chemically robust N-heterocyclic carbene (NHC)-stabilized AuNCs reported.¹⁴⁻¹⁶ However, due to their ease of synthesis and chemical versatility, thiol-based ligands are the most common types of protecting surface ligands that are currently employed towards the construction of very stable AuNCs frameworks.¹⁷ Through protection-deprotection strategies, the thiol moiety can easily be appended to a wide variety of alkyl and aromatic ligands, and it is the ability to generate such a wide variety of thiolated ligand structures that has led to a rich and diverse library of thiolate-protected AuNC frameworks.¹ Changes to the size, sterics and electronic composition of the thiol-based ligand have profound impacts on which AuNC system can be acquired.^{18, 19} It should also be noted that changes to experimental conditions such as reaction temperature and the ratio of Au(III) precursor to ligand play a vital role in what cluster framework is constructed, but under such similar reaction conditions, markedly different thiol-based ligands lead to distinctly different thiolated AuNC frameworks.²⁰ It has also been demonstrated that through ligand exchange-induced size/structure transformation (LEIST), exchange of secondary thiol-based ligands onto parent AuNCs can alter the parent AuNC in a predictable manner to generate a distinct, different-sized AuNC system.²¹⁻²³ There are also several thiol-based ligands, such as phenylethanethiol, that can be used to generate different-sized AuNC systems when the experimental conditions are changed.²⁴⁻²⁶

Although such investigations have resulted in a deep understanding of the relationship between the ligand structure and acquired core configuration, there has been little research on how regio-isomerization of the thiol-based ligand impacts the acquired AuNC configuration. Jin and co-workers reported that adding (*o/m/p*)-methylbenzenethiols (MBT) to a gold precursor, followed by size-focusing at elevated temperatures in the presence of an excess of the corresponding thiol-based ligand, led to the development of Au₄₀(*o*-MBT)₂₄, Au₁₀₄(*m*-MBT)₄₁ and Au₁₃₀(*p*-MBT)₅₀.²⁷ They confirmed these structures by absorption spectroscopy, mass spectrometry and thermogravimetric analysis. In the absence of such high-temperature size-focusing, Antoine and co-workers reported that, using (*o/m/p*)-mercaptobenzoic acid (MBA), they were able to synthesize Au₂₅(*o*-MBA)₁₈, Au₂₅(*m*-MBA)₁₈ and Au₂₅(*p*-MBA)₁₈ under kinetic control. They

confirmed these structures by absorption spectroscopy and mass spectrometry, and found that these three regioisomeric Au₂₅(SR)₁₈ systems had identical absorption profiles.²⁸

In addition to conferring the ability to predictably adjust the size and nuclearity of the AuNC core structure, a significant advantage for using thiol-based surface ligands is the ability to conduct ligand exchange chemistry to develop functional varieties of thiolated-AuNC frameworks having properties and applications that are dependent on the appended functionalities.²⁹ Conventional syntheses of thiolated AuNC nanoclusters involve addition of an excess of thiol-based ligand to an Au(III) precursor to generate an Au(I)-thiolate intermediate, which is subsequently reduced to generate the desired Au(0)-containing AuNC frameworks. Functional thiol-based ligands tend not to be compatible with the reducing conditions of the synthesis, and so functional AuNC systems cannot be directly accessed. However, the mild lability of the gold-sulfur bond allows for ligand exchange chemistry to be executed, in which native inert thiolated ligands in the parent system can be replaced with secondary thiol-based ligands possessing various functional substrates.³⁰

Although this strategy has found some utility, it is often limited by synthetic incompatibilities between the appended functional substrate on the ligand and the protection-deprotection strategies necessary to successfully incorporate the thiol moiety. Furthermore, ligand exchange with secondary thiol-based ligands are often not ‘orthogonal’ to the parent AuNC systems and can lead to unpredictable core variations and formation of larger undesired by-products.^{31, 32} The shortcomings of ligand exchange methodologies onto AuNCs necessitate investigations towards developing more ‘*nanoorthogonal*’ strategies for developing functional AuNC systems for application-based research, in which functionality can be appended to the AuNC surface in a predictable manner without altering the internal AuNC framework.

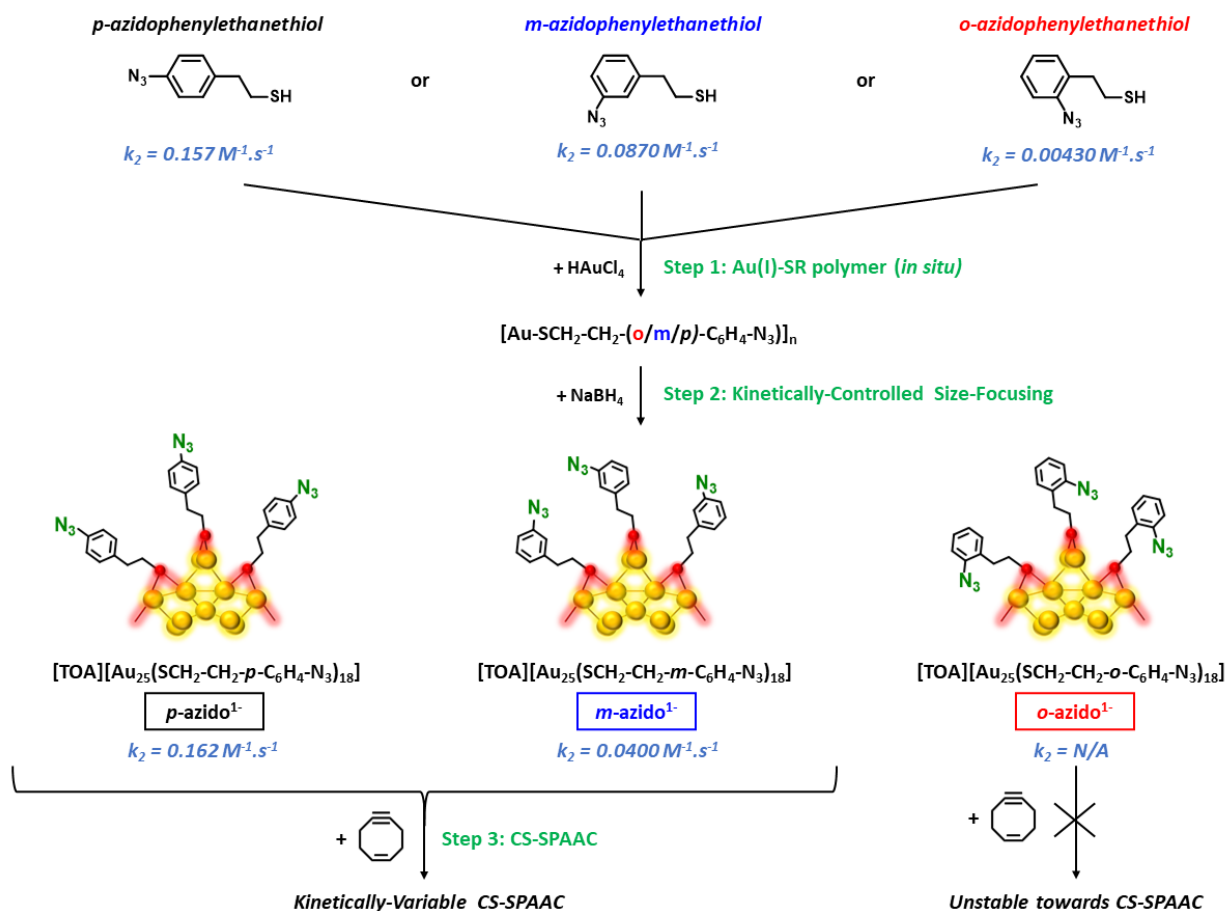
To this end, we previously communicated the first synthesis of a ‘clickable’, surface-reactive [(CH₃-(CH₂)₇)₄N][Au₂₅(SCH₂CH₂-*p*-C₆H₄-N₃)₁₈] nanocluster platform (hereafter referred to as *p*-azido¹⁻ in current chapter (and referred to as **4.1-azido** in **Chapter 4** and **6.1-azido** in **Chapter 6**)), using *p*-azidophenylethanethiol (HSCH₂CH₂-*p*-C₆H₄-N₃) as the surface thiol-based ligand.³³ This platform is capable of undergoing post-assembly modifications at all the surface azido-benzene moieties, through the cluster-surface strain-promoted alkyne-azide cycloaddition

(CS-SPAAC) reaction, in which the surface azido moieties undergo a 1,3-dipolar cycloaddition reaction with non-linear cyclooctynes to generate a surface triazole cycloadduct. Commonly utilized as a ‘*bioorthogonal click reaction*’ to append substrates to biologically sensitive molecular systems, the reaction between azides and cyclooctynes is highly chemoselective and occurs under mild conditions. Not only were all surface azido moieties on ***p*-azido¹⁻** amendable to CS-SPAAC chemistry, but analysis indicated there was no change to the core framework, establishing the CS-SPAAC reaction as a “*nanoorthogonal click reaction*” that can be used to efficiently conduct surface modifications on chemically sensitive AuNC systems.³⁴ To highlight the generality of this nanoorthogonal surface modification strategy, after reporting the development of ***p*-azido¹⁻**, Kang *et al.* developed additional azide-modified platforms, including azide-modified Au₂₈(SR)₂₀ and Au₃₆(SR)₂₄, through nanocluster transformation in which they performed ligand exchange of azido-thiophenol onto pre-synthesized nanocluster precursors.³⁴ Similar to our observations, they reported that their systems could also do SPAAC (which we coined CS-SPAAC), but also copper-catalyzed alkyne-azide cycloaddition chemistry,³⁴ for nanoorthogonal surface modifications of these AuNC systems.

Two regioisomeric variants of the ***p*-azido¹⁻** platform are herein reported: the [(CH₃-(CH₂)₇)₄N][Au₂₅(SCH₂CH₂-*m*-C₆H₄-N₃)₁₈] platform (hereafter referred to as ***m*-azido¹⁻**), which can be made using *m*-azidophenylethanethiol (HSCH₂CH₂-*m*-C₆H₄-N₃), and the [(CH₃-(CH₂)₇)₄N][Au₂₅(SCH₂CH₂-*o*-C₆H₄-N₃)₁₈] platform (hereafter referred to as ***o*-azido¹⁻**), which can be made using *o*-azidophenylethanethiol (HSCH₂CH₂-*o*-C₆H₄-N₃) (**Scheme 1**). As was reported by Antoine and co-workers for their three regioisomeric forms of Au₂₅(*o/m/p*-MBA)₁₈ nanoclusters,²⁸ the optical properties of these regioisomeric nanoclusters were identical. However, the electrochemical behaviour and structure showed some correlated differences as the position of the azido group was changed, while the feasibility and kinetics of the CS-SPAAC reactivity was substantially different for each isomeric variant. This provides great insight into how ligand isomerization affects structure-property relationships of Au₂₅(SR)₁₈ nanoclusters, as well as how it affects the ability to conduct post-assembly surface modifications on Au₂₅(SR)₁₈ systems nanoorthogonally.

5.2 Results and Discussion

In order to synthesize the three regioisomeric variants of azide-functionalized $[\text{Au}_{25}(\text{SR})_{18}]^{1-}$ nanoclusters, the corresponding azide-modified thiol-based ligands were prepared according to a modified version of our previously reported procedure for the synthesis of *p*-azidophenylethanethiol.³³ Whereas a four-step synthesis was previously implemented, a general three-step synthesis is herein reported that can be used to synthesize *p*-azidophenylethanethiol, *m*-azidophenylethanethiol and *o*-azidophenylethanethiol in an overall higher yield than the previous four-step synthesis (see **Section 5.6.2** for detailed syntheses). The azide-modified $[\text{Au}_{25}(\text{SR})_{18}]^{1-}$ nanocluster platforms, *p*-azido¹⁻, *m*-azido¹⁻ and *o*-azido¹⁻, were synthesized according to our



Scheme 5.1. Synthesis of $[(\text{CH}_3-(\text{CH}_2)_7)_4\text{N}][\text{Au}_{25}(\text{SCH}_2\text{CH}_2-p-\text{C}_6\text{H}_4-\text{N}_3)_{18}]$ (*p*-azido¹⁻, black), $[(\text{CH}_3-(\text{CH}_2)_7)_4\text{N}][\text{Au}_{25}(\text{SCH}_2\text{CH}_2-m-\text{C}_6\text{H}_4-\text{N}_3)_{18}]$ (*m*-azido¹⁻, blue) and $[(\text{CH}_3-(\text{CH}_2)_7)_4\text{N}][\text{Au}_{25}(\text{SCH}_2\text{CH}_2-o-\text{C}_6\text{H}_4-\text{N}_3)_{18}]$ (*o*-azido¹⁻, red). Rate of reaction (k_2) between AuNCs and $\text{BCN}_{\text{exo}}\text{-OH}$ were determined under second order conditions using ¹H NMR spectroscopy, and are indicated for *p*-azidophenylethanethiol, *m*-azidophenylethanethiol, *o*-azidophenylethanethiol, *p*-azido¹⁻ and *m*-azido¹⁻.

previously reported procedure,³³ using *p*-azidophenylethanethiol, *m*-azidophenylethanethiol and *o*-azidophenylethanethiol, respectively (see **Section 5.6.2.12** to **Section 5.6.2.14** for detailed syntheses). The general procedure involves slow reduction of HAuCl₄·3H₂O as the Au(III) precursor to an [-Au(I)-SR-]_n coordination intermediate at low temperature in the presence of one of the three azide-modified thiol-based ligands, followed by rapid reduction of the [-Au(I)-SR-]_n intermediate using aqueous sodium borohydride (**Scheme 5.1**). The negative mode electrospray ionization mass spectrometry (ESI-MS) spectrum of purified *m*-azido¹⁻ shows a large peak at 8131.9 Da (**Figure S5.2**), and the ESI-MS spectrum of *o*-azido¹⁻ shows a large peak at 8132.1 Da (**Figure S5.4**). These observed peaks are consistent with the ESI-MS spectrum for *p*-azido¹⁻ that was previously reported which contained a large peak centered at 8132.9 Da, and corresponds to the [Au₂₅(SCH₂CH₂-(*o/m/p*)-C₆H₄-N₃)₁₈]¹⁻ anions of the parent nanocluster platforms (expected m/z = 8132.4 Da).

As determined by ¹H NMR spectroscopy, the clusters directly prepared were anionic, with the presence of ¹H NMR signals from the tetraoctylammonium counterion (see **Figure S4.1**, **Figure S5.1** and **Figure S5.3** for ¹H NMR spectra). However, unlike *p*-azido¹⁻, the anionic forms of *o*-azido¹⁻ and *m*-azido¹⁻ could not be successfully crystallized under all conditions tried. Fortunately, slow oxidation of *o*-azido¹⁻, *m*-azido¹⁻ and *p*-azido¹⁻ in 3:1 ethanol:toluene under ambient conditions over approximately two weeks led to black needle-like crystals of the neutral cluster forming, [Au₂₅(SCH₂CH₂-*o/m/p*-C₆H₄-N₃)₁₈]⁰ (hereafter referred to as *o*-azido⁰, *m*-azido⁰ and *p*-azido⁰, respectively). The core configuration and monolayer composition of these neutral forms were confirmed by single-crystal X-ray diffraction (**Figure 5.1a**). It should be noted that although all other characterization and surface chemistry was conducted on the anionic forms, the structural similarities between *p*-azido¹⁻ and *p*-azido⁰ (particularly of the monolayer composition) indicate that the molecular structures of the neutral forms provide sufficient indications as to the general molecular features of the anionic forms. Furthermore, transitioning from the anionic to the neutral form is a core transformation, and will not affect the composition of the surface monolayer that has been confirmed in the molecular structures of the neutral forms.

The *o*-azido⁰ and *p*-azido⁰ clusters crystallize in the triclinic space group *P* $\bar{1}$ and the *m*-azido⁰ cluster crystallizes in the monoclinic space group *P*2₁/*c*. All three molecular structures of the neutral forms comprise an internal body-centered icosahedron where the central Au atom

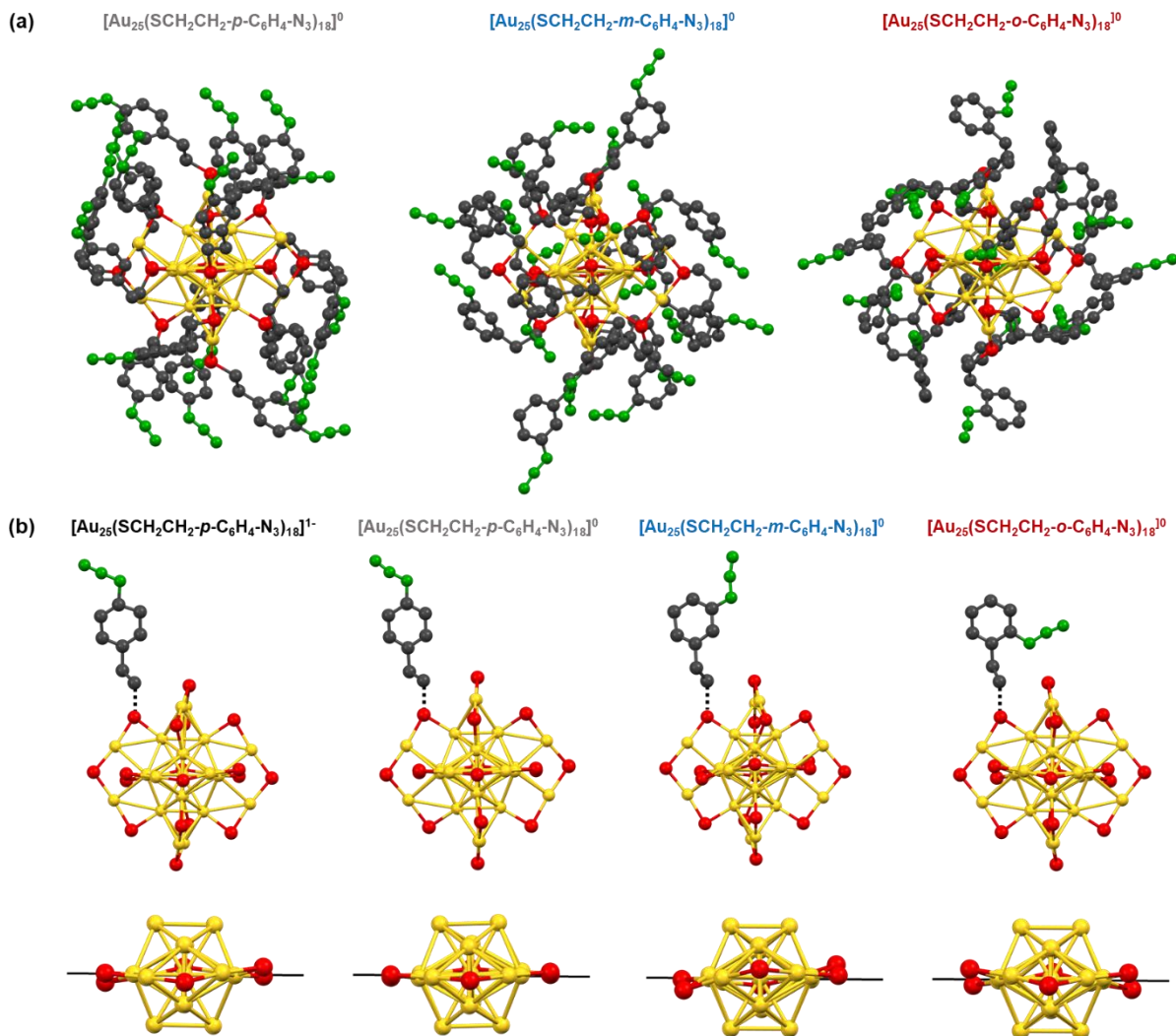


Figure 5.1. (a) *Left to right.* Molecular structure of $[\text{Au}_{25}(\text{SCH}_2\text{CH}_2\text{-}p\text{-C}_6\text{H}_4\text{-N}_3)_{18}]^0$ (*p-azido*⁰), $[\text{Au}_{25}(\text{SCH}_2\text{CH}_2\text{-}m\text{-C}_6\text{H}_4\text{-N}_3)_{18}]^0$ (*m-azido*⁰) and $[\text{Au}_{25}(\text{SCH}_2\text{CH}_2\text{-}o\text{-C}_6\text{H}_4\text{-N}_3)_{18}]^0$ (*o-azido*⁰). Au = yellow, S = red, C = black, N = green. (b) *Left to right.* Comparison of core structures of *p-azido*¹⁻, *p-azido*⁰, *m-azido*⁰ and *o-azido*⁰.

(Au_{cent}) at the inversion center is ligated to twelve Au atoms at the icosahedral vertices (Au_{vert}), with the $\text{Au}_{\text{cent}}\text{-Au}_{\text{vert}}$ bond lengths being between 2.769 (1) to 2.799 (2) Å for all three structures, typical for core Au-Au bonds in Au_{25} clusters.³⁵⁻³⁷ As observed in the molecular structure of *p-azido*¹⁻, the internal Au_{13} cores are circumscribed by an external scaffold of six “staple motifs” ($\text{-SR-Au}_{\text{scaf}}\text{-SR-Au}_{\text{scaf}}\text{-SR-}$), with the $\text{Au}_{\text{vert}}\text{-Au}_{\text{scaf}}$ bond lengths being between 3.107 (2) to 3.334 (2) Å and $\text{Au}_{\text{scaf}}\text{-S}$ bond lengths being between 2.294 (7) to 2.324 (7) Å, which is consistent with previously reported structures.³⁶⁻³⁸ The six staple motifs comprise two μ_2 -thiolate ligands in which the six central μ_2 -thiolate ligands occupy a distinguishable surface site (the “outer ligands”)

while the remaining twelve μ_2 -thiolate ligands on the edges occupy a separate site (the “inner ligands”) (**Figure 5.1b**).

Despite these many structural similarities inherent to the molecular structures of *o*-azido⁰, *m*-azido⁰, *p*-azido⁰ and *p*-azido¹⁻, there are some noteworthy differences. Jin and co workers reported the molecular structures of anionic [Au₂₅(SCH₂CH₂-C₆H₅)₁₈]¹⁻ and its neutral form [Au₂₅(SCH₂CH₂-C₆H₅)₁₈]⁰.³⁹ When the σ_h symmetry element of the cluster cores are viewed in the *x*-*y* plane, they observed a distortion in the molecular structure of the anionic form, where one of the external sulfur atoms of the staple motifs was bent upwards and another was bent downwards out of the *x*-*y* plane.³⁹ However, in the molecular structure of the neutral form this distortion was essentially not present, and the sulfur atoms were essentially coplanar. As can be seen in **Figure 5.1b**, a similar correlation exists when comparing the molecular structures of *p*-azido¹⁻ and *p*-azido⁰, in which the sulphur atoms are twisted out of the *x*-*y* plane in the molecular structure of the former. This structural distortion is essentially absent in the molecular structure of *p*-azido⁰. As was hypothesized by Jin and co workers for their structures, this can likely be attributed to the negative charge of the *p*-azido¹⁻ core and/or could be a steric distortion imposed by the presence of the large tetraoctylammonium counterion. Although essentially absent in the molecular structure of *p*-azido⁰, this structural distortion does appear in the molecular structures of *o*-azido⁰ and *m*-azido⁰ and is most pronounced in the core structure of *o*-azido⁰ (**Figure 5.1b**). This increasing molecular distortion is likely due to the steric distortion created as the azido moiety is moved closer to the internal metal core.

The electrochemistry of *o*-azido¹⁻, *m*-azido¹⁻ and *p*-azido¹⁻ was also investigated by means of cyclic voltammetry (CV) and differential pulse voltammetry (DPV). The cyclic voltammograms of *o*-azido¹⁻, *m*-azido¹⁻ and *p*-azido¹⁻ can be found in the Supporting Information, Section 4.0. In the DPV (**Figure 5.2**), under the same experimental conditions, the qualitative electrochemical oxidation pattern of the three isomeric clusters looks similar to that which we have previously reported for conventional phenylethanethiol-capped [Au₂₅(SR)₁₈]¹⁻ (hereafter referred to as **Au₂₅¹⁻**):⁴⁰ two adjacent quasi-reversible oxidation waves corresponding to the azido¹⁻/azido⁰ and azido⁰/azido¹⁺ oxidation state transformations. There is also an irreversible oxidation peak in the further anodic scan at around 1.000 V vs SCE that corresponds to the azido¹⁺/azido²⁺ oxidation state change (the irreversibility can be attributed to the chemical instability of the +2 form). The

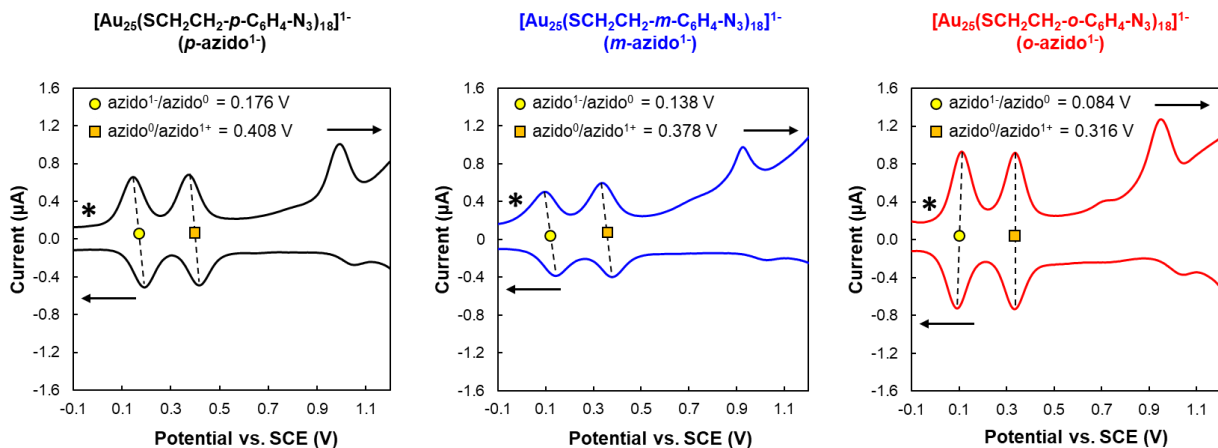


Figure 5.2. *Left to right.* Differential pulse voltammogram (DPV) of 0.1 mM solution of ***p*-azido¹⁻**, ***m*-azido¹⁻** and ***o*-azido¹⁻**, in 1:1 acetonitrile:benzene. Supporting electrolyte for DPV measurements was 0.1 M tetra-*n*-butylammonium perchlorate (TBAP). Arrows indicate potential scanning direction, and asterisk indicates starting position of measurements. Formal potentials of first two oxidation reactions are indicated.

reduction of **azido¹⁻** to **azido²⁻** was not seen in the potential window. Interestingly, there is a correlation between the formal potentials of the **azido¹⁻/azido⁰** and **azido⁰/azido¹⁺** waves and the regioisomers. As shown in **Figure 5.2**, the formal potentials of the **azido¹⁻/azido⁰** oxidation state change are at 0.176 V for ***p*-azido¹⁻**, 0.138 V for ***m*-azido¹⁻** and 0.084 V for ***o*-azido¹⁻**, while that for **Au₂₅¹⁻/Au₂₅⁰** was reported by us to be 0.038 V. Similarly, the formal potentials of the second oxidation reaction of the **azido⁰/azido¹⁺** were determined to be at 0.408 V for ***p*-azido¹⁻**, 0.378 V for ***m*-azido¹⁻** and 0.316 V for ***o*-azido¹⁻**, whereas that for **Au₂₅⁰/Au₂₅¹⁺** is 0.280 V. These suggest that the energy required to remove electrons from the regioisomers and access to different oxidation states are dependent on the existence of the azido moieties and its positions.

It is plausible that the easiness of the two oxidation reactions depends on the dielectric constants (and polarity) caused by the regioisomeric nature. The dielectric constants for *para*-disubstituted benzene derivatives are typically highest and those for *ortho* derivatives are typically the lowest, with *meta* derivatives having intermediate polarity.⁴¹ The observed tendency agrees with that of the investigation on correlation between the surface ligand structure and electrochemical behaviour of [Au₂₅(SR)₁₈]¹⁻ systems by Liao *et al.*⁴² They reported higher formal potentials for the 1-/0 and 0/1+ oxidation state changes when more polar non-isomeric surface thiolate ligands were tethered to the AuNC surface,⁴² correlating well with previous theoretical results on the same systems.⁴³ Specifically, they observed the lowest formal potentials when

hexanethiolate (S-C₆H₁₃) was the ligand, intermediate formal potentials for **Au₂₅¹⁻**, and the highest formal potentials when thiophenolate (S-C₆H₅) was the ligand.⁴² Thus, the current study reinforces this correlation between the electrochemical profile of [Au₂₅(SR)₁₈]¹⁻ systems and the polarity of the surface ligands, with ***p*-azido¹⁻** having the highest formal potentials and ***o*-azido¹⁻** having the lowest. Moreover, the formal potentials of ***o*-azido¹⁻** is higher than those of **Au₂₅¹⁻** due to the absence of the polar azido groups in the latter. On the other hand, the three regioisomers and conventional **Au₂₅¹⁻** all have a similar potential difference value of 0.230 to 0.240 V between the first and second oxidation reactions. This difference represents charging energy or electron addition energy,^{40,44} which should not depend on the surface ligand properties.

As with the initial study using ***p*-azido¹⁻**,³³ the CS-SPAAC chemistry of the three regioisomeric clusters was explored by reacting them with excess (***Z***)-cyclooct-1-ene-5-yne, which was expected to transform the ***p*-azido¹⁻** platform to the surface-modified [(CH₃-(CH₂)₇)₄N][Au₂₅(SCH₂CH₂-*p*-C₆H₄-C₈H₁₀N₃)₁₈] framework (hereafter referred to as ***p*-triazole¹⁻** in current chapter (and referred to as **4.1-triazole** in **Chapter 4**)), the ***m*-azido¹⁻** platform to the surface-modified [(CH₃-(CH₂)₇)₄N][Au₂₅(SCH₂CH₂-*m*-C₆H₄-C₈H₁₀N₃)₁₈] framework (hereafter referred to as ***m*-triazole¹⁻**), and the ***o*-azido¹⁻** platform to the surface-modified [(CH₃-(CH₂)₇)₄N][Au₂₅(SCH₂CH₂-*o*-C₆H₄-C₈H₁₀N₃)₁₈] framework (hereafter referred to as ***o*-triazole¹⁻**). Each reaction was carried out as a simple mix and stir with approximately 20 equivalents of strained alkyne; subsequent purification to remove the excess strained-alkyne was accomplished through simple trituration with isopropanol, in which the triazole-modified frameworks were insoluble (see **Section 5.6.2.15 to Section 5.6.2.17** for experimental details).

In the linear negative mode matrix-assisted laser desorption/ionization time-of-flight (MALDI-TOF) spectrum of the purified ***m*-triazole¹⁻** product, there is a large peak centered at 10047.0 Da (**Figure S5.9**), which is similar to the peak at 10048.4 Da found in the MALDI-TOF spectrum of ***p*-triazole¹⁻** that was previously reported (**Figure S4.9**). These peaks can be assigned to the parent [Au₂₅(SCH₂CH₂-(*m/p*)-C₆H₄-C₈H₁₀N₃)₁₈]¹⁻ anion of both surface-modified frameworks in which all surface azido moieties have undergone the CS-SPAAC reaction (expected *m/z* = 10043.4 Da). However, there was no peak observed in this same *m/z* range in the linear negative mode MALDI-TOF spectrum of ***o*-triazole¹⁻** (**Figure S5.11**). Under the same experimental conditions, the MALDI-TOF spectrum of ***o*-triazole¹⁻** showed the formation of a

wide range of products of different sizes, none of which corresponded to the expected surface-modified framework. This suggests that although ***o*-azido¹⁻** can be successfully synthesized and characterized, once the small azido moiety is modified through the CS-SPAAC reaction, the proximity of the larger triazole-moiety to the Au₂₅ core results in a dismantling of the nanocluster structure.

The instability of ***o*-azido¹⁻** towards CS-SPAAC was also confirmed by ¹H NMR spectroscopy, where the ¹H NMR spectrum of ***o*-triazole¹⁻** (**Figure S5.10**) displays a general broadening of the signals compared to the ¹H NMR spectrum of ***o*-azido¹⁻** (**Figure S5.3**). In the ¹H NMR spectra of ***p*-triazole¹⁻** (**Figure S4.7**) and ***m*-triazole¹⁻** (**Figure S5.8**) there were sharp and resolvable peaks, as is generally expected in the ¹H NMR spectra of Au₂₅(SR)₁₈ nanoclusters. Unlike in the ¹H NMR spectra of the ***p*-triazole¹⁻** and ***m*-triazole¹⁻** frameworks, there were many broad peaks in the ¹H NMR spectrum of ***o*-triazole¹⁻** that could not be easily assigned to expected proton environments, further confirming that the ligand protons were no longer in expected surface environments.

The CS-SPAAC reaction of the three regioisomeric forms of the azide-modified platforms was also investigated by UV-Vis and IR spectroscopy. In the IR spectrum of ***p*-azido¹⁻**, ***m*-azido¹⁻** and ***o*-azido¹⁻** (**Figure 5.3a**), there is a large peak observed between 2100-2117 cm⁻¹ that can be assigned to the N-N stretches of the surface azido moieties. After the CS-SPAAC reaction with excess (***Z***)-**cyclooct-1-ene-5-yne**, the IR spectrum of the three triazole-modified products (**Figure 5.3b**) showed a total disappearance of this large peak, demonstrating that in all three cases, all the azido moieties were being consumed upon addition of the strained-alkyne, albeit that the ***o*-azido¹⁻** platform appears to undergo dismantling after the cluster-surface reaction.

The UV-Vis absorption spectra of ***o*-azido¹⁻** and ***m*-azido¹⁻** show the same absorption fingerprint as ***p*-azido¹⁻** (**Figure 5.3c**), with absorption peaks at ~680 nm, ~440 nm and ~400 nm, and correlates with the well-established absorption pattern of [Au₂₅(SR)₁₈]¹⁻ nanoclusters, including Au₂₅¹⁻.⁴⁵ In particular, the absorption at ~680 nm results from an intraband metallic transition that is explicitly associated with the anionic Au₂₅ core configuration, and occurs at different absorption energies when the internal core configuration or surface ligand is significantly

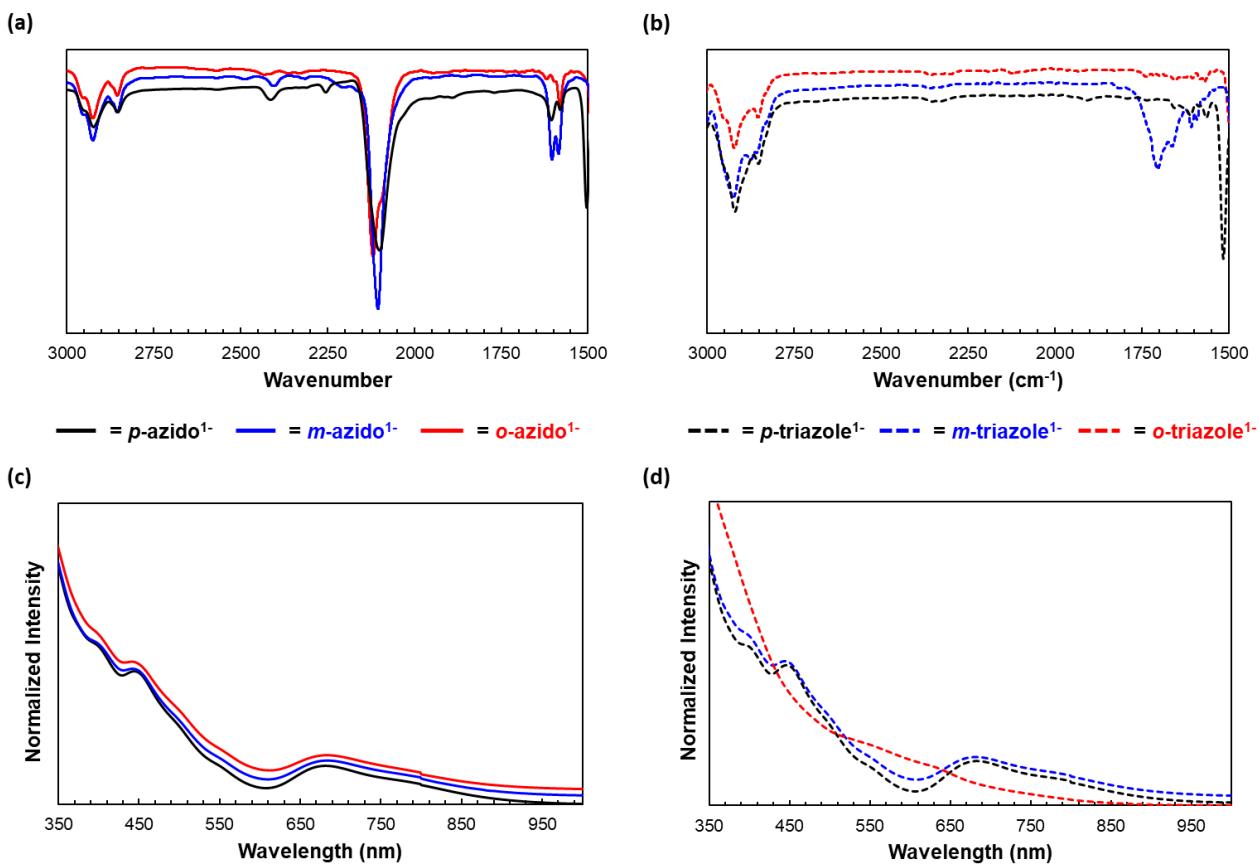


Figure 5.3. (a) ATR-IR spectra of *p*-azido¹⁻ (black), *m*-azido¹⁻ (blue) and *o*-azido¹⁻ (red). (b) ATR-IR spectra of *p*-triazole¹⁻ (dotted black), *m*-triazole¹⁻ (dotted blue) and *o*-triazole¹⁻ (dotted red). (c) UV-Vis absorption spectra of 0.2 mM solutions of *p*-azido¹⁻ (black), *m*-azido¹⁻ (blue) and *o*-azido¹⁻ (red) in dichloromethane at 23°C. (d) UV-Vis absorption spectra of 0.2 mM solutions of *p*-triazole¹⁻ (dotted black), *m*-triazole¹⁻ (dotted blue) and *o*-triazole¹⁻ (dotted red) in dichloromethane at 23°C.

altered.⁴⁶ In this way, this absorption peak is the main indicator in the electronic absorption pattern that the anionic azide-modified [Au₂₅(SR)₁₈]¹⁻ core configuration has been attained.

An absorption pattern similar to the parent azide-modified clusters can be seen for the *p*-triazole¹⁻ and *m*-triazole¹⁻ frameworks. Specifically, there is a retention of the peak at ~680 nm, indicating that the anionic Au₂₅ core configuration has been retained after the CS-SPAAC reaction (Figure 5.3d). However, in the absorption spectrum of the expected *o*-triazole¹⁻ framework (Figure 5.3d, dotted red), there is a deterioration of the pattern of electronic transitions that diverges from the expected pattern for [Au₂₅(SR)₁₈]¹⁻ nanoclusters, with a specific disappearance of the peak at ~680 nm. In fact, the lack of distinct electronic transitions, which is a key absorption feature for ultrasmall gold nanoclusters, is consistent with the absorption behavior of larger

nanoparticles. In this way, although IR spectroscopy indicates that the surface azido moieties in *o*-**azido**¹⁻ are expectedly available for the CS-SPAAC reaction, UV spectroscopy provides evidence that upon total consumption the azido groups through CS-SPAAC, there is a deterioration of the [Au₂₅(SR)₁₈]¹⁻ structure, and leads to aggregation to form larger, polydisperse particles. The ability to synthesize [Au₂₅(SR)₁₈]¹⁻ nanoclusters with *o*-azidophenylethanethiol as a surface ligand, but modification of the azido moieties to triazole moieties leading to nanocluster deterioration, highlights the importance not only on the correlation between core nuclearity and surface ligand employed, but also the large dependence on surface ligand and nanocluster stability.

The second order rate constants (k_2) with the aliphatic strained alkyne, *exo*-bicyclo-[6.1.0]non-4-yn-9-ol (**BCN_{exo}-OH**) were estimated for the SPAAC reactivity of three thiol-based ligands, as well as the CS-SPAAC reactivity of *p*-**azido**¹⁻ and *m*-**azido**¹⁻, using ¹H NMR spectroscopy (see **Section 5.6.5** for experimental details and graphs). **BCN_{exo}-OH** was chosen for the kinetic study instead of (**Z**)-**cyclooct-1-ene-5-yne** because the presence of the alkene in (**Z**)-**cyclooct-1-ene-5-yne** makes the alkyne moiety more strained, and consequently more reactive, and so both the SPAAC and CS-SPAAC reactions were too fast to measure for some analytes using ¹H NMR spectroscopy. It should be noted that although the *exo*-isomer was used for this study because it is synthesized in higher yield, the *endo*-isomer could have also been used and should have similar reaction kinetics.

Dommerholt and co-workers previously reported that the SPAAC reaction kinetics of azido-benzene derivatives with **BCN_{exo}-OH** is dependent on the presence of either electron withdrawing or electron donating groups on the phenyl ring.⁴⁷ Delocalization into electron withdrawing substituents accelerate the rate of reaction and electron donating substituents decelerate the rate of reaction. We herein report an additional structural feature that affects the SPAAC reaction kinetics. Specifically, the isomeric position of the substituent (for example, the mildly electron-donating ethanethiol substituent) also has a profound impact on the observed reaction kinetics. Specifically, *p*-azidophenylethanethiol had the fastest reaction kinetics ($k_2 = 0.157 \text{ M}^{-1} \cdot \text{s}^{-1}$), *m*-azidophenylethanethiol had an intermediate reaction rate ($k_2 = 0.087 \text{ M}^{-1} \cdot \text{s}^{-1}$) and *o*-azidophenylethanethiol had an extremely slow reaction rate ($k_2 = 0.00430 \text{ M}^{-1} \cdot \text{s}^{-1}$) (**Scheme 5.1**). As the electronic composition of these three structures are identical, this observed correlation in SPAAC reaction kinetics is likely due to a steric effect, rather than the electronic effect that has

been previously reported. That is, the azido moiety is most sterically (and kinetically) accessible in the *para*-substituted structure, and far less accessible for SPAAC chemistry in the *ortho*-substituted structure, which may have contributed to the incompatibility of the ***o*-azido¹⁻** platform towards CS-SPAAC chemistry.

As shown in **Scheme 5.1**, the CS-SPAAC reaction kinetics of ***p*-azido¹⁻** ($k_2 = 0.162 \text{ M}^{-1}.\text{s}^{-1}$) was similar to the SPAAC reaction kinetics of *p*-azidophenylethanethiol ($k_2 = 0.157 \text{ M}^{-1}.\text{s}^{-1}$), indicating that the azido groups in ***p*-azido¹⁻** are equally accessible as in the free thiol-based ligand. However, the CS-SPAAC reaction kinetics of ***m*-azido¹⁻** ($k_2 = 0.0400 \text{ M}^{-1}.\text{s}^{-1}$) was approximately 2 times slower than the SPAAC reaction kinetics of *m*-azidophenylethanethiol ($k_2 = 0.0870 \text{ M}^{-1}.\text{s}^{-1}$). This provides evidence that the azido groups are kinetically less reactive in ***m*-azido¹⁻**, compared to the free thiol-based ligand, which is likely due to a more pronounced steric inaccessibility of the azido moieties when the meta-substituted thiolate ligand is tethered to the AuNC core.

5.3 Conclusions

The ability to develop functional variants of AuNC systems is of paramount importance for application-based research using these promising nanomaterial frameworks. We have developed three regioisomeric forms of azide-modified $[\text{Au}_{25}(\text{SR})_{18}]^{1-}$ nanocluster platforms, in which the azide moiety was appended to the *para*, *meta* and *ortho* phenylic positions in the phenylethanethiolate ligands, respectively, that surrounds the internal Au_{25} core configuration, to give ***p*-azido¹⁻**, ***m*-azido¹⁻** and ***o*-azido¹⁻**. The three regioisomeric clusters demonstrated near identical optical properties, exhibited subtle but correlated differences in their electrochemical behaviour, and drastic differences in their ability to undergo the CS-SPAAC reaction with excess strained alkyne. In fact, although the surface azides in the ***o*-azido¹⁻** platform were reactive towards the surface cycloaddition reaction, analysis of the resulting product indicates that the nanocluster structure underwent deterioration during the post-assembly surface modification. The results of this study provides valuable information into the sensitive structure-ligand relationship that exists for gold nanocluster systems and extends our current knowledge on the effect of ligand

isomerization on the properties of $[\text{Au}_{25}(\text{SR})_{18}]^{1-}$ nanocluster systems and their resulting properties and reactivity.

5.4 Acknowledgements

This work was funded by NSERC-DG and the University of Western Ontario. We would like to thank P. Boyle (X-Ray Facility), D. Hairsine (ESI-MS Facility) and K. Jurcic (MALDI-MS Facility-Biochemistry).

5.5 References

1. Jin, R.; Zeng, C.; Zhou, M.; Chen, Y., Atomically Precise Colloidal Metal Nanoclusters and Nanoparticles: Fundamentals and Opportunities. *Chem. Rev.* **2016**, *116* (18), 10346-10413.
2. Higaki, T.; Li, Y.; Zhao, S.; Li, Q.; Li, S.; Du, X.-S.; Yang, S.; Chai, J.; Jin, R., Atomically Tailored Gold Nanoclusters for Catalytic Application. *Angew. Chem. Int. Ed.* **2019**, *58* (25), 8291-8302.
3. Chen, H.; Liu, C.; Wang, M.; Zhang, C.; Luo, N.; Wang, Y.; Abroshan, H.; Li, G.; Wang, F., Visible Light Gold Nanocluster Photocatalyst: Selective Aerobic Oxidation of Amines to Imines. *ACS Catalysis* **2017**, *7* (5), 3632-3638.
4. Li, G.; Zeng, C.; Jin, R., Thermally Robust $\text{Au}_{99}(\text{SPh})_{42}$ Nanoclusters for Chemoselective Hydrogenation of Nitrobenzaldehyde Derivatives in Water. *J. Am. Chem. Soc.* **2014**, *136* (9), 3673-3679.
5. Bonanno, A.; Pérez-Herráez, I.; Zaballos-García, E.; Pérez-Prieto, J., Gold nanoclusters for ratiometric sensing of pH in extremely acidic media. *Chem. Commun.* **2020**, *56* (4), 587-590.
6. Shu, T.; Wang, J.; Su, L.; Zhang, X., Chemical Etching of Bovine Serum Albumin-Protected Au_{25} Nanoclusters for Label-Free and Separation-Free Ratiometric Fluorescent Detection of Tris(2-carboxyethyl)phosphine. *Anal. Chem.* **2016**, *88* (22), 11193-11198.
7. Guan, G.; Zhang, S.-Y.; Cai, Y.; Liu, S.; Bharathi, M. S.; Low, M.; Yu, Y.; Xie, J.; Zheng, Y.; Zhang, Y.-W.; Han, M.-Y., Convenient purification of gold clusters by co-precipitation

for improved sensing of hydrogen peroxide, mercury ions and pesticides. *Chem. Commun.* **2014**, 50 (43), 5703-5705.

8. Xie, Y.; Liu, Y.; Yang, J.; Liu, Y.; Hu, F.; Zhu, K.; Jiang, X., Gold Nanoclusters for Targeting Methicillin-Resistant *Staphylococcus aureus* In Vivo. *Angew. Chem. Int. Ed.* **2018**, 57 (15), 3958-3962.

9. Katla, S. K.; Zhang, J.; Castro, E.; Bernal, R. A.; Li, X., Atomically Precise Au₂₅(SG)₁₈ Nanoclusters: Rapid Single-Step Synthesis and Application in Photothermal Therapy. *ACS Appl. Mater. Interfaces* **2018**, 10 (1), 75-82.

10. Luo, Z.; Zheng, K.; Xie, J., Engineering ultrasmall water-soluble gold and silver nanoclusters for biomedical applications. *Chem. Commun.* **2014**, 50 (40), 5143-5155.

11. Halawa, M. I.; Lai, J.; Xu, G., Gold nanoclusters: synthetic strategies and recent advances in fluorescent sensing. *Mater. Today Nano* **2018**, 3, 9-27.

12. Nishigaki, J.-i.; Yamazoe, S.; Kohara, S.; Fujiwara, A.; Kurashige, W.; Negishi, Y.; Tsukuda, T., A twisted bi-icosahedral Au₂₅ cluster enclosed by bulky arenethiolates. *Chem. Commun.* **2014**, 50 (7), 839-841.

13. Krommenhoek, P. J.; Wang, J.; Hentz, N.; Johnston-Peck, A. C.; Kozek, K. A.; Kalyuzhny, G.; Tracy, J. B., Bulky Adamantanethiolate and Cyclohexanethiolate Ligands Favor Smaller Gold Nanoparticles with Altered Discrete Sizes. *ACS Nano* **2012**, 6 (6), 4903-4911.

14. Yi, H.; Osten, K. M.; Levchenko, T. I.; Veinot, A. J.; Aramaki, Y.; Ooi, T.; Nambo, M.; Crudden, C. M., Synthesis and enantioseparation of chiral Au₁₃ nanoclusters protected by bis-N-heterocyclic carbene ligands. *Chem. Sci.* **2021**.

15. Narouz, M. R.; Osten, K. M.; Unsworth, P. J.; Man, R. W. Y.; Salorinne, K.; Takano, S.; Tomihara, R.; Kaappa, S.; Malola, S.; Dinh, C.-T.; Padmos, J. D.; Ayoo, K.; Garrett, P. J.; Nambo, M.; Horton, J. H.; Sargent, E. H.; Häkkinen, H.; Tsukuda, T.; Crudden, C. M., N-heterocyclic carbene-functionalized magic-number gold nanoclusters. *Nat. Chem.* **2019**, 11 (5), 419-425.

16. Shen, H.; Deng, G.; Kaappa, S.; Tan, T.; Han, Y.-Z.; Malola, S.; Lin, S.-C.; Teo, B. K.; Häkkinen, H.; Zheng, N., Highly Robust but Surface-Active: An N-Heterocyclic Carbene-Stabilized Au₂₅ Nanocluster. *Angew. Chem. Int. Ed.* **2019**, *58* (49), 17731-17735.
17. Jin, R.; Li, G.; Sharma, S.; Li, Y.; Du, X., Toward Active-Site Tailoring in Heterogeneous Catalysis by Atomically Precise Metal Nanoclusters with Crystallographic Structures. *Chem. Rev.* **2021**, *121* (2), 567-648.
18. Du, Y.; Sheng, H.; Astruc, D.; Zhu, M., Atomically Precise Noble Metal Nanoclusters as Efficient Catalysts: A Bridge between Structure and Properties. *Chem. Rev.* **2020**, *120* (2), 526-622.
19. Nishigaki, J.-i.; Tsunoyama, R.; Tsunoyama, H.; Ichikuni, N.; Yamazoe, S.; Negishi, Y.; Ito, M.; Matsuo, T.; Tamao, K.; Tsukuda, T., A New Binding Motif of Sterically Demanding Thiolates on a Gold Cluster. *J. Am. Chem. Soc.* **2012**, *134* (35), 14295-14297.
20. Li, Y.; Jin, R., Seeing Ligands on Nanoclusters and in Their Assemblies by X-ray Crystallography: Atomically Precise Nanochemistry and Beyond. *J. Am. Chem. Soc.* **2020**, *142* (32), 13627-13644.
21. Hirai, H.; Ito, S.; Takano, S.; Koyasu, K.; Tsukuda, T., Ligand-protected gold/silver superatoms: current status and emerging trends. *Chem. Sci.* **2020**, *11* (45), 12233-12248.
22. Zeng, C.; Chen, Y.; Das, A.; Jin, R., Transformation Chemistry of Gold Nanoclusters: From One Stable Size to Another. *J. Phys. Chem. Lett.* **2015**, *6* (15), 2976-2986.
23. Zeng, C.; Liu, C.; Chen, Y.; Rosi, N. L.; Jin, R., Gold–Thiolate Ring as a Protecting Motif in the Au₂₀(SR)₁₆ Nanocluster and Implications. *J. Am. Chem. Soc.* **2014**, *136* (34), 11922-11925.
24. Jensen, K. M. Ø.; Juhas, P.; Tofanelli, M. A.; Heinecke, C. L.; Vaughan, G.; Ackerson, C. J.; Billinge, S. J. L., Polymorphism in magic-sized Au₁₄₄(SR)₆₀ clusters. *Nat. Commun.* **2016**, *7* (1), 11859.

25. Zeng, C.; Chen, Y.; Iida, K.; Nobusada, K.; Kirschbaum, K.; Lambright, K. J.; Jin, R., Gold Quantum Boxes: On the Periodicities and the Quantum Confinement in the Au₂₈, Au₃₆, Au₄₄, and Au₅₂ Magic Series. *J. Am. Chem. Soc.* **2016**, *138* (12), 3950-3953.
26. Qian, H.; Eckenhoff, W. T.; Zhu, Y.; Pintauer, T.; Jin, R., Total Structure Determination of Thiolate-Protected Au₃₈ Nanoparticles. *J. Am. Chem. Soc.* **2010**, *132* (24), 8280-8281.
27. Chen, Y.; Zeng, C.; Kauffman, D. R.; Jin, R., Tuning the Magic Size of Atomically Precise Gold Nanoclusters via Isomeric Methylbenzenethiols. *Nano Lett.* **2015**, *15* (5), 3603-3609.
28. Bertorelle, F.; Russier-Antoine, I.; Comby-Zerbino, C.; Chirot, F.; Dugourd, P.; Brevet, P.-F.; Antoine, R., Isomeric Effect of Mercaptobenzoic Acids on the Synthesis, Stability, and Optical Properties of Au₂₅(MBA)₁₈ Nanoclusters. *ACS Omega* **2018**, *3* (11), 15635-15642.
29. Shibu, E. S.; Muhammed, M. A. H.; Tsukuda, T.; Pradeep, T., Ligand Exchange of Au₂₅SG₁₈ Leading to Functionalized Gold Clusters: Spectroscopy, Kinetics, and Luminescence. *J. Phys. Chem. C* **2008**, *112* (32), 12168-12176.
30. Wang, Y.; Bürgi, T., Ligand exchange reactions on thiolate-protected gold nanoclusters. *Nanoscale Adv.* **2021**, *3* (10), 2710-2727.
31. Yan, N.; Xia, N.; Wu, Z., Metal Nanoparticles Confronted with Foreign Ligands: Mere Ligand Exchange or Further Structural Transformation? *Small* **2021**, *17* (27), 2000609.
32. Kang, X.; Zhu, M., Structural Isomerism in Atomically Precise Nanoclusters. *Chem. Mater.* **2021**, *33* (1), 39-62.
33. Gunawardene, P. N.; Corrigan, J. F.; Workentin, M. S., Golden Opportunity: A Clickable Azide-Functionalized [Au₂₅(SR)₁₈]⁻ Nanocluster Platform for Interfacial Surface Modifications. *J. Am. Chem. Soc.* **2019**, *141* (30), 11781-11785.
34. Kang, X.; Ren, M.; Zhu, M.; Zhang, K., Azide-Functionalized Nanoclusters via a Ligand-Induced Rearrangement. *Chem. Mater.* **2020**, *32* (15), 6736-6743.

35. Tofanelli, M. A.; Salorinne, K.; Ni, T. W.; Malola, S.; Newell, B.; Phillips, B.; Häkkinen, H.; Ackerson, C. J., Jahn–Teller effects in Au₂₅(SR)₁₈. *Chem. Sci.* **2016**, *7* (3), 1882-1890.
36. Dainese, T.; Antonello, S.; Gascón, J. A.; Pan, F.; Perera, N. V.; Ruzzi, M.; Venzo, A.; Zoleo, A.; Rissanen, K.; Maran, F., Au₂₅(SET)₁₈, a Nearly Naked Thiolate-Protected Au₂₅ Cluster: Structural Analysis by Single Crystal X-ray Crystallography and Electron Nuclear Double Resonance. *ACS Nano* **2014**, *8* (4), 3904-3912.
37. Akola, J.; Walter, M.; Whetten, R. L.; Häkkinen, H.; Grönbeck, H., On the Structure of Thiolate-Protected Au₂₅. *J. Am. Chem. Soc.* **2008**, *130* (12), 3756-3757.
38. Venzo, A.; Antonello, S.; Gascón, J. A.; Guryanov, I.; Leapman, R. D.; Perera, N. V.; Sousa, A.; Zamuner, M.; Zanella, A.; Maran, F., Effect of the Charge State ($z = -1, 0, +1$) on the Nuclear Magnetic Resonance of Monodisperse Au₂₅[S(CH₂)₂Ph]₁₈^z Clusters. *Anal. Chem.* **2011**, *83* (16), 6355-6362.
39. Zhu, M.; Eckenhoff, W. T.; Pintauer, T.; Jin, R., Conversion of Anionic [Au₂₅(SCH₂CH₂Ph)₁₈]⁻ Cluster to Charge Neutral Cluster via Air Oxidation. *J. Phys. Chem. C* **2008**, *112* (37), 14221-14224.
40. Hesari, M.; Workentin, M. S.; Ding, Z., NIR electrochemiluminescence from Au₂₅⁻ nanoclusters facilitated by highly oxidizing and reducing co-reactant radicals. *Chem. Sci.* **2014**, *5* (10), 3814-3822.
41. Maryott, A. A., *Table of Dielectric Constants of Pure Liquids*. U.S. Government Printing Office: 1951.
42. Liao, L.; Zhou, S.; Dai, Y.; Liu, L.; Yao, C.; Fu, C.; Yang, J.; Wu, Z., Mono-Mercury Doping of Au₂₅ and the HOMO/LUMO Energies Evaluation Employing Differential Pulse Voltammetry. *J. Am. Chem. Soc.* **2015**, *137* (30), 9511-9514.
43. Tlahuice-Flores, A.; Whetten, R. L.; Jose-Yacaman, M., Ligand Effects on the Structure and the Electronic Optical Properties of Anionic Au₂₅(SR)₁₈ Clusters. *J. Phys. Chem. C* **2013**, *117* (40), 20867-20875.

44. Lee, D.; Donkers, R. L.; Wang, G.; Harper, A. S.; Murray, R. W., Electrochemistry and Optical Absorbance and Luminescence of Molecule-like Au₃₈ Nanoparticles. *J. Am. Chem. Soc.* **2004**, *126* (19), 6193-6199.
45. Jin, R., Atomically precise metal nanoclusters: stable sizes and optical properties. *Nanoscale* **2015**, *7* (5), 1549-1565.
46. Zhou, M.; Higaki, T.; Li, Y.; Zeng, C.; Li, Q.; Sfeir, M. Y.; Jin, R., Three-Stage Evolution from Non-scalable to Scalable Optical Properties of Thiolate-Protected Gold Nanoclusters. *J. Am. Chem. Soc.* **2019**, *141* (50), 19754-19764.
47. Dommerholt, J.; van Rooijen, O.; Borrmann, A.; Guerra, C. F.; Bickelhaupt, F. M.; van Delft, F. L., Highly accelerated inverse electron-demand cycloaddition of electron-deficient azides with aliphatic cyclooctynes. *Nat. Commun.* **2014**, *5* (1), 5378.

5.6 Supporting Information

5.6.1 General Materials and Methods

Reagents and Solvents. The following materials were used as received. 2-nitrophenethyl bromide (97%), 3-nitrophenethyl bromide (97%), potassium thioacetate (98%), zinc dust (<10 μ m, \geq 98%), sodium azide (\geq 99.5%), gold (III) chloride trihydrate (\geq 99.9% trace metal basis), tetraoctylammonium bromide (98%), sodium borohydride (\geq 98%), 1,5-cyclooctadiene (\geq 99%), bromine (reagent grade), potassium *tert*-butoxide solution (1.0M in THF), dichloromethane-d₂ (CD₂Cl₂, 99.5 atom %D) and dimethyl sulfoxide-d₆ ((CD₃)₂SO, 99.96 atom %D) were purchased from Sigma-Aldrich (Millipore Sigma). 4-nitrophenylethyl bromide was purchased from Oakwood Chemicals. Sodium chloride, sodium hydroxide pellets, methanol, tetrahydrofuran, toluene, and acetonitrile were purchased from Fischer Scientific. Technical grade ammonium chloride, magnesium sulphate, hexanes, dichloromethane, ethyl acetate, 12M hydrochloric acid, sodium nitrite, isopropanol, and pentane were purchased from Caledon. Chloroform-D₁ (CDCl₃,

99.8 atom %D) was purchased from Cambridge Isotope Laboratories. Ethanol (anhydrous) was purchased from Commercial Alcohols.

Unless otherwise state, all reactions were performed at ambient conditions.

NMR Spectroscopy. ^1H and $^{13}\text{C}\{^1\text{H}\}$ spectra were recorded on either a Bruker AvIII HD 400 spectrometer or Varian INOVA 600 spectrometer, as indicated. ^1H NMR spectra are reported as δ in units of parts per million (ppm), and referenced against residual protio chloroform (7.27 ppm, s) or dichloromethane (5.32 ppm, t), as indicated. Multiplicities are reported as follows: s (singlet), d (doublet), t (triplet), q (quartet), quin (quintuplet), m (multiplet) and br (broad signal). Coupling constants are reported as a J value in Hertz (Hz) according to the spectrometer frequency. The number of protons (n) for a given resonance is indicated as $n\text{H}$, and is based on spectral integration values. $^{13}\text{C}\{^1\text{H}\}$ NMR spectra are reported as δ in units of parts per million (ppm) and referenced against the indicated deuterated solvent: chloroform- D_1 (77.0 ppm, t), dimethylsulfoxide- D_6 (39.5 ppm, septet) or dichloromethane- D_2 (54.0 ppm, quin), as indicated.

Mass Spectrometry. Electrospray ionization (ESI) mass spectra were obtained in either positive-ion or negative-ion mode using a Bruker microTOF II spectrometer. Set capillary was 4000 V, set end plate offset was -400 V, set nebulizer was 1.0 Bar and set dry heater was 100°C. To obtain the ESI spectrum of nanoclusters (obtained in negative-ion mode), a sample was dissolved in 1:5 toluene:methanol (10mg/mL). We generally found that in order to obtain mass spectra of $[\text{Au}_{25}\text{SR}_{18}]$ clusters, the sample solution must contain some methanol in order to minimize excessive fragmentation. Matrix-assisted laser desorption/ionization-time of flight (MALDI-TOF) mass spectra were obtained using an AB Sciex 5800 TOF/TOF system. To obtain the MALDI-TOF spectrum of nanoclusters (obtained in linear negative mode), a 1 g/L sample solution was mixed with a 10 g/L solution of trans-2-[3-(4-tert-butylphenyl)-2-methyl-2-propenylidene]malononitrile (DCTB) in a ratio of 1:400 by mass. Data acquisition and data processing were respectively done using a TOF TOF Series Explore and Data Explorer (both from AB Sciex). The laser pulse rate was set to 400Hz. The mass spectrum was collected as a sum of 1000 shots.

UV-Visible (UV-Vis) Spectroscopy. UV-Vis absorption spectra were recorded using a Cary 5000 scan instrument using standard quartz cells (1 cm path length) with a scan range of 200-1000nm.

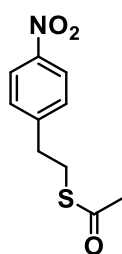
Samples were dissolved in the indicated solvents at the indicated concentrations. The background spectrum of the indicated solvent was subtracted internally by the software.

Infrared (IR) spectroscopy. Attenuated total reflectance IR (ATR-IR) spectra were recorded using a PerkinElmer Spectrum Two FT-IR spectrometer.

Electrochemistry. All cyclic voltammograms and differential pulse voltammograms were performed on a CHI 610A electrochemical analyzer (CH Instruments, Austin, Texas). A three-electrode system was used: the working electrode was a 2 mm diameter platinum disc inlaid in a glass (Pt) electrode; two Pt coils served as the counter and reference electrodes, respectively. Prior to each experiment, the glass electrochemical cell was cleaned in an acid bath overnight, then placed in a base bath to prevent any contamination. The platinum disc electrode was polished using 0.3 micron then 0.05 micron alumina polishing slurry (CH Instruments) until a mirror like finish was obtained. The electrode was then subjected to electrochemical cleaning by performing cyclic voltammetry in 0.1 M dilute sulfuric acid solution for 200 cycles between the cathodic and anodic potential limits. The electrode was then rinsed with ultra-pure Type-1 water and left to fully dry before use. Each electrochemical cell consisted of a 0.67mg/mL solution of gold clusters dispersed in a 1:1 anhydrous acetonitrile:benzene mixture (Sure/Seal™ acetonitrile and benzene, Sigma Aldrich), with 0.1M tetrabutylammonium perchlorate (TBAP, Sigma Aldrich) being added as the supporting electrolyte. All electrochemical cells were assembled in an inert Ar atmosphere.

5.6.2 Experimental Procedures

5.6.2.1 Synthesis of *p*-nitro-phenylethanethioacetate

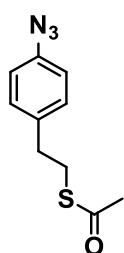


See Section 4.6.2.1 for detailed synthesis of **p-azido-phenylethanethioacetate**.

^1H NMR (CDCl_3 , 400 MHz): δ (ppm) 8.17 (d, 2H, $J = 8$ Hz), 7.39 (d, 2H, $J = 8$ Hz), 3.15 (t, 2H, $J = 8$ Hz), 2.99 (t, 2H, $J = 8$ Hz), 2.35 (s, 3H). ^{13}C NMR (CDCl_3 , 400 MHz): δ (ppm) 195.2, 147.4, 146.8, 129.5, 123.7, 35.6, 30.6, 29.7. HRMS (ESI) m/z calc. for $\text{C}_{10}\text{H}_{11}\text{NO}_3\text{S}$ (M^+): 225.0460, found: 225.0467. IR (ATR-IR, cm^{-1}): 3025,

1680, 1597, 1513, 1448, 1411, 1340, 1280, 1129, 1096.

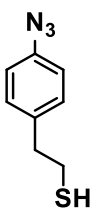
5.6.2.2 Synthesis of *p*-azido-phenylethanethioacetate



To 13.7 g (60 mmol, 1 eq.) ***p*-nitro-phenylethanethioacetate** in 120 mL ethanol and 120 mL distilled water was added 25.7 g (480 mmol, 8 eq) technical grade ammonium chloride, and then 24 g (360 mmol, 6 eq) zinc dust portion-wise under vigorous stirring over 5 minutes. The resulting suspension was stirred for 2 hours at room temperature, after which the solids were filtered off and washed with 50 mL of ethanol. To the supernatant was added 55 mL 12 M hydrochloric acid in 220 mL distilled water at 0°C, giving a colorless solution. To this solution was added 6.2 g (89 mmol, 1.5 eq) sodium nitrite in 130 mL distilled water dropwise over 20 minutes at 0°C under rapid stirring, resulting in a reddish solution. After stirring the solution for an additional 20 minutes at 0°C, 7.8 g (120 mmol, 2 eq) sodium azide in 130 mL distilled water was added dropwise over 15 minutes at 0°C. The solution was stirred for 20 minutes at 0°C, and then an additional 30 minutes at room temperature, after which the crude solution was extracted with dichloromethane (3 x 50 mL), dried over magnesium sulphate and concentrated using rotary evaporation. The crude residue was purified by flash column chromatography (2:1 hexanes:dichloromethane) to give ***p*-azido-phenylethanethioacetate** as a pale yellow oil in 70% yield (9.2 g). ¹H NMR (CDCl₃, 400 MHz): δ (ppm) 7.21 (d, 2H, *J* = 8 Hz), 6.97 (d, 2H, *J* = 8 Hz), 3.10 (t, 2H, *J* = 8 Hz), 2.85 (t, 2H, *J* = 8 Hz), 2.34 (s, 3H). ¹³C NMR (CDCl₃, 400 MHz): δ (ppm) 195.6, 138.3, 136.7, 130.0, 119.1, 35.1, 30.7, 30.4. HRMS (ESI) *m/z* calc. for C₁₀H₁₄NOS⁺ (M⁺): 221.0623, found: 221.0630. IR (ATR-IR, cm⁻¹): 3026, 2106, 1690, 1602, 1506, 1418, 1356, 1285, 1128, 1102.

*Spectral data matches our previously reported data¹.

5.6.2.3 Synthesis of *p*-azido-phenylethanethiol

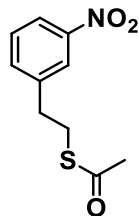


See **Section 4.6.2.4** for detailed synthesis of ***p*-azido-phenylethanethiol**.

¹H NMR (CD₂Cl₂, 400 MHz): δ (ppm) 7.20 (d, 2H, *J* = 8 Hz), 6.98 (d, 2H, *J* = 8 Hz), 2.89 (t, 2H, *J* = 8 Hz), 2.75 (q, 2H, *J* = 8 Hz), 1.40 (t, 2H, *J* = 8 Hz). ¹³C NMR (CD₂Cl₂, 400 MHz): δ (ppm) 138.8, 137.4, 130.6, 119.5, 40.0, 26.5. HRMS (ESI) *m/z* calc. for C₁₀H₁₄NOS⁺ (M⁺): 179.0517, found: 179.0514. IR (ATR-IR, cm⁻¹): 3035, 2936, 2559, 2106, 1601, 1504, 1430, 1283, 1131.

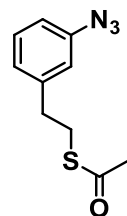
*Spectral data matches our previously reported data¹.

5.6.2.4 Synthesis of *m*-nitro-phenylethanethioacetate



To 10.0 g (44 mmol, 1 eq.) 3-nitrophenylethyl bromide in 300 mL acetone was added 6.0 g (53 mmol, 1.2 eq.) potassium thioacetate. The resulting mixture was stirred at room temperature for 6 hours, after which the solid was removed by gravity filtration and the solution was concentrated by rotary evaporation. The resultant crude residue was purified by flash column chromatography (2:1 hexanes:dichloromethane) to give ***m*-nitro-phenylethanethioacetate** as a yellow solid in 96% yield (9.6 g). ¹H NMR (CDCl₃, 400 MHz): δ (ppm) 8.11 (m, 2H), 7.58 (m, 1H), 7.50 (m, 1H), 3.17 (t, 2H, *J* = 8 Hz), 3.00 (t, 2H, *J* = 8 Hz), 2.35 (s, 3H). ¹³C NMR (CDCl₃, 400 MHz): δ (ppm) 195.2, 143.8, 141.8, 134.9, 129.4, 123.5, 121.8, 35.4, 30.7, 29.9. HRMS (ESI) *m/z* calc. for C₁₀H₁₁NO₃S (M⁺): 225.0460, found: 225.0489. IR (ATR-IR, cm⁻¹): 2930, 2861, 1681, 1522, 1349, 1312, 1130, 1099, 1078.

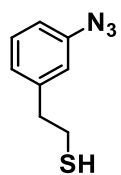
5.6.2.5 Synthesis of *m*-azido-phenylethanethioacetate



To 7.9 g (35 mmol, 1eq.) ***m*-nitro-phenylethanethioacetate** in 70 mL ethanol and 70 mL distilled water was added 15.0 g (280 mmol, 8 eq) technical grade ammonium chloride, and then 13.8 g (210 mmol, 6 eq) zinc dust portion-wise under vigorous stirring over 5 minutes. The resulting suspension was stirred for 2 hours at room temperature, after which the solids were filtered off and washed with 30 mL of ethanol. To the supernatant was added 32 mL 12 M hydrochloric acid in 140 mL distilled water at 0°C, giving a colorless solution. To this solution was added 3.7 g (53 mmol, 1.5 eq) sodium nitrite in 75 mL distilled water dropwise over 20 minutes at 0°C under rapid stirring, resulting in a reddish solution. After stirring the solution for an additional 20 minutes at 0°C, 4.6 g (70 mmol, 2 eq) sodium azide in 75 mL distilled water was added dropwise over 15 minutes at 0°C. The solution was stirred for 20 minutes at 0°C, and then an additional 30 minutes at room temperature, after which the crude solution was extracted with dichloromethane (3 x 50 mL), dried over magnesium sulphate and concentrated using rotary evaporation. The crude residue was purified by flash column chromatography (2:1 hexanes:dichloromethane) to give ***m*-azido-phenylethanethioacetate** as a pale yellow oil in 75% yield (5.8 g). ¹H NMR (CDCl₃, 400 MHz):

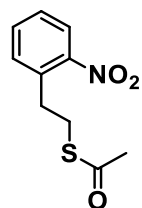
δ (ppm) 7.29 (t, 1H, $J = 8$ Hz), 7.01 (d, 1H, $J = 8$ Hz), 6.90 (m, 2H), 3.12 (t, 2H, $J = 8$ Hz), 2.87 (t, 2H, $J = 8$ Hz), 2.35 (s, 3H). ^{13}C NMR (CDCl_3 , 400 MHz): δ (ppm) 195.2, 141.6, 139.8, 129.5, 124.9, 118.9, 116.9, 35.3, 30.3, 29.9. HRMS (ESI) m/z calc. for $\text{C}_{10}\text{H}_{14}\text{NOS}^+$ (M^+): 221.0623, found: 221.0652. IR (ATR-IR, cm^{-1}): 2927, 2858, 2405, 2102, 1686, 1586, 1487, 1445, 1288, 1132.

5.6.2.6 Synthesis of *m*-azido-phenylethanethiol



To 5.8 g (26 mmol, 1 eq.) ***m*-azido-phenylethanethioacetate** in 250 mL deoxygenated methanol was added 40 mL (40 mmol, 1.5 eq.) of deoxygenated 1 M sodium hydroxide in water and the solution was stirred for 20 minutes at room temperature under argon, resulting in a yellow solution. Next, 80 mL (80 mmol, 3 eq.) of deoxygenated 1 M hydrochloric acid in water was added. The solution was stirred for 15 minutes at room temperature under argon, resulting in a pale yellow solution, after which distilled water (150 mL) was added and the product was extracted with dichloromethane (3 x 50 mL), dried over magnesium sulphate and concentrated using rotary evaporation. The crude residue was purified by flash column chromatography (2:1 hexanes:dichloromethane) to give ***m*-azido-phenylethanethiol** as a pale yellow oil in 92% yield (4.7 g). ^1H NMR (CD_2Cl_2 , 400 MHz): δ (ppm) 7.30 (t, 1H, $J = 8$ Hz), 6.98 (d, 1H, $J = 8$ Hz), 6.90 (m, 2H), 2.91 (t, 2H, $J = 8$ Hz), 2.78 (q, 2H, $J = 8$ Hz), 1.40 (t, 2H, $J = 8$ Hz). ^{13}C NMR (CD_2Cl_2 , 400 MHz): δ (ppm) 142.7, 140.7, 130.3, 125.9, 119.8, 117.6, 40.5, 26.3. HRMS (ESI) m/z calc. for $\text{C}_{10}\text{H}_{14}\text{NOS}^+$ (M^+): 179.0517, found: 179.0532. IR (ATR-IR, cm^{-1}): 2931, 2849, 2105, 1585, 1486, 1446, 1288.

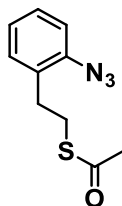
5.6.2.7 Synthesis of *o*-nitro-phenylethanethioacetate



To 9.6 g (44 mmol, 1 eq.) 2-nitrophenylethyl bromide in 280 mL acetone was added 5.7 g (50 mmol, 1.2 eq.) potassium thioacetate. The resulting mixture was stirred at room temperature for 6 hours, after which the solid was removed by gravity filtration and the solution was concentrated by rotary evaporation. The resultant crude residue was purified by flash column chromatography (2:1 hexanes:dichloromethane) to give ***o*-nitro-phenylethanethioacetate** as a yellow solid in 99% yield (9.5 g). ^1H NMR (CDCl_3 , 400 MHz): δ (ppm) 7.96 (dd, 1H, $J_1 = 8$ Hz, $J_2 = 1$ Hz), 7.57 (dt, 1H, dd, 1H, $J_1 = 8$ Hz, $J_2 = 1$ Hz),

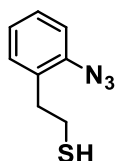
7.43 (m, 2H), 3.19 (m, 4H), 2.34 (s, 3H). ^{13}C NMR (CDCl_3 , 400 MHz): δ (ppm) 195.5, 149.2, 134.8, 133.1, 132.6, 127.8, 124.9, 33.3, 30.6, 29.4. HRMS (ESI) m/z calc. for $\text{C}_{10}\text{H}_{11}\text{NO}_3\text{S}$ (M^+): 225.0460, found: 225.0463. IR (ATR-IR, cm^{-1}): 3062, 2930, 2862, 1686, 1522, 1345, 1129.

5.6.2.8 Synthesis of *o*-azido-phenylethanethioacetate



To 5.1 g (23 mmol, 1 eq.) ***o*-nitro-phenylethanethioacetate** in 45 mL ethanol and 45 mL distilled water was added 9.8 g (184 mmol, 8 eq) technical grade ammonium chloride, and then 9.1 g (138 mmol, 6 eq) zinc dust portion-wise under vigorous stirring over 5 minutes. The resulting suspension was stirred for 2 hours at room temperature, after which the solids were filtered off and washed with 50 mL of ethanol. To the supernatant was added 20 mL 12 M hydrochloric acid in 80 mL distilled water at 0°C , giving a colorless solution. To this solution was added 2.4 g (35 mmol, 1.5 eq) sodium nitrite in 50 mL distilled water dropwise over 20 minutes at 0°C under rapid stirring, resulting in a reddish solution. After stirring the solution for an additional 20 minutes at 0°C , 3.0 g (46 mmol, 2 eq) sodium azide in 50 mL distilled water was added dropwise over 15 minutes at 0°C . The solution was stirred for 20 minutes at 0°C , and then an additional 30 minutes at room temperature, after which the crude solution was extracted with dichloromethane (3 x 50 mL), dried over magnesium sulphate and concentrated using rotary evaporation. The crude residue was purified by flash column chromatography (2:1 hexanes:dichloromethane) to give ***o*-azido-phenylethanethioacetate** as a pale yellow oil in 43% yield (2.2 g). ^1H NMR (CDCl_3 , 400 MHz): δ (ppm) 7.29 (dt, 1H, $J_1 = 8$ Hz, $J_2 = 1$ Hz), 7.21 (dd, 1H, $J_1 = 8$ Hz, $J_2 = 1$ Hz), 7.15 (dd, 1H, $J_1 = 8$ Hz, $J_2 = 1$ Hz), 7.09 (dt, 1H, $J_1 = 8$ Hz, $J_2 = 1$ Hz), 3.12 (t, 2H, $J = 8$ Hz), 2.85 (t, 2H, $J = 8$ Hz), 2.34 (s, 3H). ^{13}C NMR (CDCl_3 , 400 MHz): δ (ppm) 195.7, 138.2, 131.1, 130.9, 128.1, 124.7, 118.1, 31.2, 30.6, 29.2. HRMS (ESI) m/z calc. for $\text{C}_{10}\text{H}_{14}\text{NOS}^+$ (M^+): 221.0623, found: 221.0648. IR (ATR-IR, cm^{-1}): 3025, 2928, 2118, 1688, 1581, 1488, 1283, 1132.

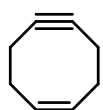
5.6.2.9 Synthesis of *o*-azido-phenylethanethiol



To 2.2 g (10 mmol, 1 eq.) ***o*-nitro-phenylethanethioacetate** in 160 mL deoxygenated methanol was added 15 mL (15 mmol, 1.5 eq.) of deoxygenated 1 M sodium hydroxide in water and the solution was stirred for 20 minutes at room temperature under argon,

resulting in a yellow solution. Next, 30 mL (30 mmol, 3 eq.) of deoxygenated 1 M hydrochloric acid in water was added. The solution was stirred for 15 minutes at room temperature under argon, resulting in a pale yellow solution, after which distilled water (100 mL) was added and the product was extracted with dichloromethane (3 x 25 mL), dried over magnesium sulphate and concentrated using rotary evaporation. The crude residue was purified by flash column chromatography (2:1 hexanes:dichloromethane) to give ***o*-azido-phenylethanethiol** as a pale yellow oil in 90% yield (1.6 g). ¹H NMR (CD₂Cl₂, 400 MHz): δ (ppm) 7.28 (dt, 1H, *J*₁ = 8 Hz, *J*₂ = 1 Hz), 6.98 (m, 2H), 7.08 (dt, 1H, *J*₁ = 8 Hz, *J*₂ = 1 Hz), 2.86 (t, 2H, *J* = 8 Hz), 2.73 (q, 2H, *J* = 8 Hz), 1.40 (t, 2H, *J* = 8 Hz). ¹³C NMR (CD₂Cl₂, 400 MHz): δ (ppm) 138.8, 131.9, 131.5, 128.6, 125.2, 118.8, 36.5, 25.2. HRMS (ESI) *m/z* calc. for C₁₀H₁₄NOS⁺ (M⁺): 179.0517, found: 179.0539. IR (ATR-IR, cm⁻¹): 2980, 2930, 2116, 1580, 1487, 1450, 1282, 1155.

5.6.2.10 Synthesis of (*Z*)-cyclooct-1-ene-5-yne

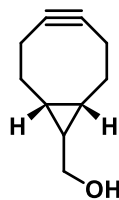


See **Section 3.6.3.3** for detailed synthesis of (*Z*)-cyclooct-1-ene-5-yne.

¹H NMR (CD₂Cl₂, 400 MHz): δ (ppm) 5.85 (m, 2H), 2.56 (m, 4H), 2.14 (m, 2H). ¹³C NMR (CDCl₃, 400 MHz): δ (ppm) 131.9, 100.8, 31.2, 19.5. HRMS (ESI) *m/z* calc. for C₈H₁₀ (M⁺): 106.0783, found: 106.0782. IR (ATR-IR, cm⁻¹): 3008, 2924, 2850, 1635, 1450, 1315, 1207.

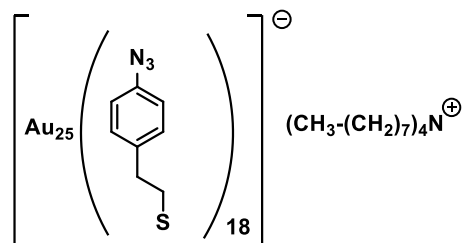
*Spectral data matches our previously reported data¹.

5.6.2.11 Synthesis of BCN_{exo}-OH



*Synthesized according to Dommerholt *et al.*² See **Section 2.6.2.6** for characterization data.

5.6.2.12 Synthesis of $[(\text{CH}_3-(\text{CH}_2)_7)_4\text{N}][\text{Au}_{25}(\text{SCH}_2\text{CH}_2-p\text{-C}_6\text{H}_4\text{-N}_3)_{18}]$ (*p*-azido¹⁻)

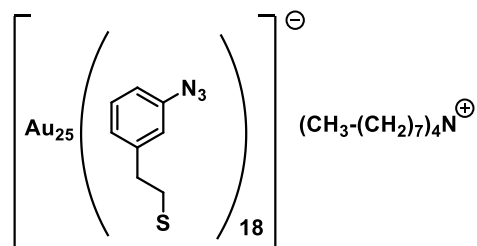


See **Section 4.6.2.8** for detailed synthesis of $[(\text{CH}_3-(\text{CH}_2)_7)_4\text{N}][\text{Au}_{25}(\text{SCH}_2\text{CH}_2-p\text{-C}_6\text{H}_4\text{-N}_3)_{18}]$ (**p-azido¹⁻**). The yield of was 26% atomic Au basis.

¹H NMR (CD₂Cl₂, 600 MHz): δ (ppm) 7.17 (d, 24H, J = 6 Hz), 7.12 (d, 12H, J = 6 Hz), 6.86 (d, 12H, J = 6 Hz), 6.80 (d, 24H, J = 6 Hz), 3.54 (t, 24H, J = 6 Hz), 3.09 (m, 44H), 2.93 (t, 12H, J = 6 Hz), 1.62 (m, 8H), 1.37-1.31 (m, 48H), 0.90 (t, 12H, J = 6 Hz). HRMS (ESI [negative]) *m/z* calc. for C₁₄₄H₁₄₄Au₂₅N₅₄S (M⁻): 8132.4 Da, found: 8132.9 Da. IR (ATR-IR, cm⁻¹): 2904, 2845, 2411, 2254, 2098, 1604, 1581, 1504. UV-Vis (Dichloromethane, 2x10⁻⁴ mol L⁻¹): λ_{max} = 682 nm, ε = 1908 M⁻¹cm⁻¹, λ_{max} = 443 nm, ε = 6600 M⁻¹cm⁻¹, λ_{max} = 404 nm, ε = 7650 M⁻¹cm⁻¹.

*Spectral data matches our previously reported data¹.

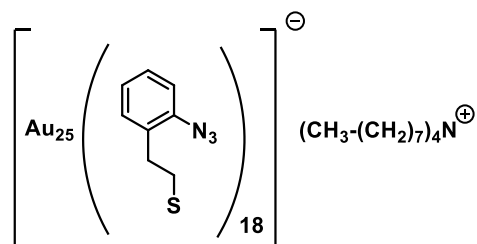
5.6.2.13 Synthesis of $[(\text{CH}_3-(\text{CH}_2)_7)_4\text{N}][\text{Au}_{25}(\text{SCH}_2\text{CH}_2-m\text{-C}_6\text{H}_4\text{-N}_3)_{18}]$ (*m*-azido¹⁻)



To a yellow solution of 230 mg (0.58 mmol) tetrachloroauric(III) acid trihydrate in 24 mL tetrahydrofuran was added 350 mg (1.1 eq, 0.64 mmol) tetraoctylammonium bromide at a stirring speed of 600 rpm. The solution was stirred for 15 minutes at room temperature and 30 minutes at 0°C, resulting in a dark red solution. The stirring was reducing to 80 rpm, and to the red solution was added an ice-cold solution of 630 mg (6 eq, 3.5 mmol) of ***m*-azido-phenylethylthiol** in 1.2 mL tetrahydrofuran over 4 minutes at 0°C at 80 rpm. The resulting solution was stirred at 0°C for 1 hour at 80 rpm, then at room temperature for 3 hours at 80 rpm, then at room temperature for 1 hour at 600 rpm. Over the stirring period, the solution turned from dark red to yellow within the first hour, and once the temperature was increased to room temperature and stirred for four hours, it turned a very pale-yellow color. After the stirring period, the pale-yellow solution was cooled to 0°C for 15 minutes

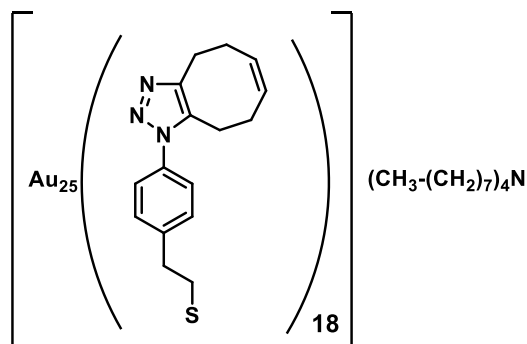
at 600 rpm, after which an ice-cold, freshly prepared solution of 220 mg (10 eq, 5.8 mmol) sodium borohydride in 4.5 mL milli-Q water was added over approximately 15-20 seconds at 600 rpm, resulting in bubbling and an immediate color change from pale yellow to black. The neck of the flask was covered with a cap, and a light stream of argon was passed over the top of the flask, and the solution was stirred for 18 hours at room temperature at 600 rpm. After the overnight reaction, there was white precipitate on the side of the flask, and the solution turned from black to a reddish-brown color. The crude solution was filtered through glass wool, and the tetrahydrofuran was removed by rotary evaporation. The crude residue was dissolved in 50 mL toluene and extracted with 200 mL milli-Q water. The organic phase was removed, and the toluene was removed by rotary evaporation. To the crude brownish-red oil was added approximately 20 mL isopropanol, resulting in the formation of small insoluble black solids. The solids were collected by filtering the suspension through glass wool in a funnel. NOTE: the solution may have to be filtered more than once to collect all black solids. The glass wool was washed thoroughly with isopropanol to fully remove residual thiols and disulfides. After the isopropanol washes, 10 mL acetonitrile was added, resulting in dissolution of most of the black solids to give reddish brown filtrate. The acetonitrile was removed by rotary evaporation, resulting in a film on the flask wall. The film was washed again with isopropanol, and then re-dissolved in acetonitrile and filtered once more through glass wool. Removal of the acetonitrile by rotary evaporation gave a reddish-black oily film of purified $[(\text{CH}_3-(\text{CH}_2)_7)_4\text{N}][\text{Au}_{25}(\text{SCH}_2\text{CH}_2\text{-}m\text{-C}_6\text{H}_4\text{-N}_3)](m\text{-azido}^{1-})$ that was stored as a film at 0°C. The yield of $m\text{-azido}^{1-}$ was 38% atomic Au basis. $^1\text{H NMR}$ (CD_2Cl_2 , 600 MHz): δ (ppm) 7.17 (t, 6H, $J = 12$ Hz), 7.10 (t, 12H, $J = 12$ Hz), 6.96 (m, 30H), 6.83 (m, 12H), 6.74 (m, 12H), 3.56 (m, 24H), 3.12 (m, 44H), 2.95 (t, 12H, $J = 12$ Hz), 1.62 (m, 8H), 1.33 (m, 48H), 0.89 (t, 12H, $J = 6$ Hz). HRMS (ESI [negative]) m/z calc. for $\text{C}_{144}\text{H}_{144}\text{Au}_{25}\text{N}_{54}\text{S}$ (M^-): 8132.4 Da, found: 8131.9 Da. IR (ATR-IR, cm^{-1}): 2938, 2920, 2848, 2390, 2107, 1601, 1583. UV-Vis (Dichloromethane, 2×10^{-4} mol L^{-1}): $\lambda_{\text{max}} = 682$ nm, $\epsilon = 1940$ $\text{M}^{-1}\text{cm}^{-1}$, $\lambda_{\text{max}} = 444$ nm, $\epsilon = 6620$ $\text{M}^{-1}\text{cm}^{-1}$, $\lambda_{\text{max}} = 406$ nm, $\epsilon = 7660$ $\text{M}^{-1}\text{cm}^{-1}$.

5.6.2.14 Synthesis of $[(\text{CH}_3-(\text{CH}_2)_7)_4\text{N}][\text{Au}_{25}(\text{SCH}_2\text{CH}_2-o\text{-C}_6\text{H}_4\text{-N}_3)_{18}]$ (*o*-azido¹⁻)



To a yellow solution of 244 mg (0.62 mmol) tetrachloroauric(III) acid trihydrate in 27 mL tetrahydrofuran was added 373 mg (1.1 eq, 0.68 mmol) tetraoctylammonium bromide at a stirring speed of 600 rpm. The solution was stirred for 15 minutes at room temperature and 30 minutes at 0°C, resulting in a dark red solution. The stirring was reducing to 80 rpm, and to the red solution was added an ice-cold solution of 660 mg (6 eq, 3.7 mmol) of ***o*-azido-phenylethanethiol** in 1.2 mL tetrahydrofuran over 4 minutes at 0°C at 80 rpm. The resulting solution was stirred at 0°C for 1 hour at 80 rpm, then at room temperature for 3 hours at 80 rpm, then at room temperature for 1 hour at 600 rpm. Over the stirring period, the solution turned from dark red to yellow within the first hour, and once the temperature was increased to room temperature and stirred for four hours, it turned a very pale-yellow color. After the stirring period, the pale-yellow solution was cooled to 0°C for 15 minutes at 600 rpm, after which an ice-cold, freshly prepared solution of 234 mg (10 eq, 6.2 mmol) sodium borohydride in 4.8 mL milli-Q water was added over approximately 15-20 seconds at 600 rpm, resulting in bubbling and an immediate color change from pale yellow to black. *The remainder of the protocol was identical to that used to synthesize *m*-azido¹⁻* (see **Section 5.6.2.13**). The yield of $[(\text{CH}_3-(\text{CH}_2)_7)_4\text{N}][\text{Au}_{25}(\text{SCH}_2\text{CH}_2-o\text{-C}_6\text{H}_4\text{-N}_3)_{18}]$ was 47% atomic Au basis. ¹H NMR (CD₂Cl₂, 600 MHz): δ (ppm) 7.35 (d, 12H, *J* = 12 Hz), 7.21 (m, 12H), 7.13 (m, 12H), 7.08 (d, 6H, *J* = 12 Hz), 6.96 (m, 12H), 6.91 (m, 18H), 3.57 (t, 24H, *J* = 12 Hz), 3.07 (m, 44H), 2.95 (t, 12H, *J* = 12Hz), 1.62 (m, 8H), 1.32 (m, 48H), 0.89 (t, 12H, *J* = 12 Hz). HRMS (ESI [negative]) *m/z* calc. for C₁₄₄H₁₄₄Au₂₅N₅₄S (M⁻): 8132.4 Da, found: 8132.1 Da. IR (ATR-IR, cm⁻¹): 2964, 2933, 2875, 2117, 1578. UV-Vis (Dichloromethane, 2x10⁻⁴ mol L⁻¹): λ_{max} = 681 nm, ε = 1982 M⁻¹cm⁻¹, λ_{max} = 442 nm, ε = 6690 M⁻¹cm⁻¹, λ_{max} = 405 nm, ε = 7600 M⁻¹cm⁻¹.

5.6.2.15 Synthesis of $[(\text{CH}_3-(\text{CH}_2)_7)_4\text{N}][\text{Au}_{25}(\text{SCH}_2\text{CH}_2-p\text{-C}_6\text{H}_4\text{-C}_8\text{H}_{10}\text{N}_3)_{18}]$ (*p*-triazole¹⁻)

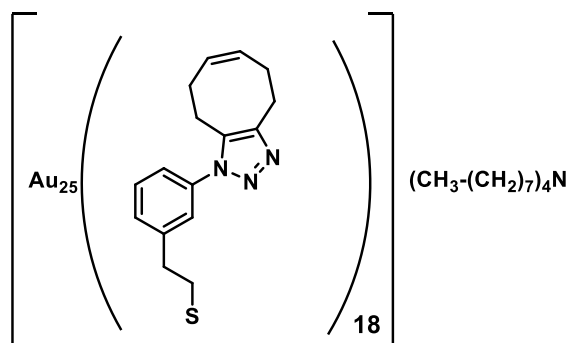


See **Section 4.6.2.9** for detailed synthesis of $[(\text{CH}_3-(\text{CH}_2)_7)_4\text{N}][\text{Au}_{25}(\text{SCH}_2\text{CH}_2-p\text{-C}_6\text{H}_4\text{-C}_8\text{H}_{10}\text{N}_3)_{18}]$ (*p*-triazole¹⁻).

¹H NMR (CD₂Cl₂, 600 MHz): δ (ppm) 7.37 (d, 24H, J=12 Hz), 7.28 (d, 12H, J=6 Hz), 7.18 (m, 36H), 5.47 (m, 24H), 5.39 (m, 12H), 3.69 (t, 24H, J=6 Hz), 3.27-3.22 (m, 36H), 3.09 (m, 56H), 2.68-2.64 (m, 36H), 2.47-2.42 (m, 72H), 1.61 (m, 8H), 1.33-1.26 (m, 48H), 0.88 (t, 12H, J=6 Hz). MS (MALDI-TOF [negative]) *m/z* calc. for C₂₈₈H₃₂₄Au₂₅N₅₄S (M⁻): 10043.4 Da, found: 10048.4 Da. IR (ATR-IR, cm⁻¹): 2920, 2852, 1608, 1563, 1517. UV-Vis (Dichloromethane, 2 x 10⁻⁴ mol L⁻¹): λ_{max} = 682 nm, ε = 2040 M⁻¹ cm⁻¹, λ_{max} = 446 nm, ε = 7250 M⁻¹ cm⁻¹, λ_{max} = 394 nm, ε = 7780 M⁻¹ cm⁻¹.

*Spectral data matches our previously reported data¹.

5.6.2.16 Synthesis of $[(\text{CH}_3-(\text{CH}_2)_7)_4\text{N}][\text{Au}_{25}(\text{SCH}_2\text{CH}_2-m\text{-C}_6\text{H}_4\text{-C}_8\text{H}_{10}\text{N}_3)_{18}]$ (*m*-triazole¹⁻)

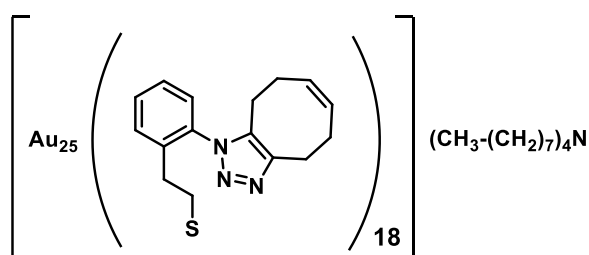


To 10 mg (0.0012 mmol, 1 eq) $[(\text{CH}_3-(\text{CH}_2)_7)_4\text{N}][\text{Au}_{25}(\text{SCH}_2\text{CH}_2-m\text{-C}_6\text{H}_4\text{-N}_3)]$ (*m*-azido¹⁻) in 5 mL tetrahydrofuran was added 2.5 mg (0.024 mmol, 20 eq) (*Z*)-cyclooct-1-ene-5-yne in 1 mL tetrahydrofuran. The solution was stirred for 10 minutes, after which the solvent and residual

cyclooctyne starting material was removed by rotary evaporation. Upon removal of the solvent, a reddish brown film formed on the flask interior, which was then triturated with acetonitrile to remove residual azide-clusters, giving $[(\text{CH}_3-(\text{CH}_2)_7)_4\text{N}][\text{Au}_{25}(\text{SCH}_2\text{CH}_2-m\text{-C}_6\text{H}_4\text{-C}_8\text{H}_{10}\text{N}_3)_{18}]$ as a reddish black film. ¹H NMR (CD₂Cl₂, 600 MHz): δ (ppm) 7.26-7.06 (m, 72H), 5.44 (m, 12H),

5.40 (m, 24H), 3.59 (t, 18H, J = 12 Hz), 3.15-2.95 (m, 90H), 2.70 (t, 36H, J = 12 Hz), 2.42 (m, 72H), 1.59 (m, 8H), 1.33-1.26 (m, 48H), 0.87 (t, 12H, J = 6Hz). MS (MALDI-TOF [negative]) m/z calc. for $C_{288}H_{324}Au_{25}N_{54}S$ (M^-): 10043.4 Da, found: 10047.0 Da. IR (ATR-IR, cm^{-1}): 2912, 1704, 1662, 1607. UV-Vis (Dichloromethane, $2 \times 10^{-4} \text{ mol L}^{-1}$): $\lambda_{max} = 680 \text{ nm}$, $\epsilon = 2100 \text{ M}^{-1} \text{ cm}^{-1}$, $\lambda_{max} = 442 \text{ nm}$, $\epsilon = 7350 \text{ M}^{-1} \text{ cm}^{-1}$, $\lambda_{max} = 399 \text{ nm}$, $\epsilon = 7890 \text{ M}^{-1} \text{ cm}^{-1}$.

5.6.2.17 Synthesis of $[(CH_3-(CH_2)_7)_4N][Au_{25}(SCH_2CH_2-o-C_6H_4-C_8H_{10}N_3)_{18}]$ (o-triazole $^{1-}$)



To 10 mg (0.0012 mmol, 1 eq) $[(CH_3-(CH_2)_7)_4N][Au_{25}(SCH_2CH_2-o-C_6H_4-N_3)_{18}]$ (o-azido $^{1-}$) in 5 mL tetrahydrofuran was added 2.5 mg (0.024 mmol, 20 eq) (Z)-cyclooct-1-ene-5-yne in 1 mL tetrahydrofuran. The solution was stirred for 10 minutes, after which the solvent and

residual cyclooctyne starting material was removed by rotary evaporation. Upon removal of the solvent, a reddish brown film formed on the flask interior, which was then triturated with acetonitrile to remove residual azide-clusters. *The film was not very soluble in dichloromethane, particulates could be seen in solution, indicating the sample had undergone some aggregation.*

5.6.3 Experimental Spectra and Diagrams

5.6.3.1 Experimental Spectra and Diagrams for $[(\text{CH}_3-(\text{CH}_2)_7)_4\text{N}][\text{Au}_{25}(\text{SCH}_2\text{CH}_2-p\text{-C}_6\text{H}_4\text{-N}_3)_{18}] (p\text{-azido}^{1-})$

See Section 4.6.3.1 for ^1H NMR spectrum and ESI-MS spectrum of $[(\text{CH}_3-(\text{CH}_2)_7)_4\text{N}][\text{Au}_{25}(\text{SCH}_2\text{CH}_2-p\text{-C}_6\text{H}_4\text{-N}_3)_{18}] (p\text{-azido}^{1-})$.

5.6.3.2 Experimental Spectra and Diagrams for $[(\text{CH}_3-(\text{CH}_2)_7)_4\text{N}][\text{Au}_{25}(\text{SCH}_2\text{CH}_2-m\text{-C}_6\text{H}_4\text{-N}_3)_{18}] (m\text{-azido}^{1-})$

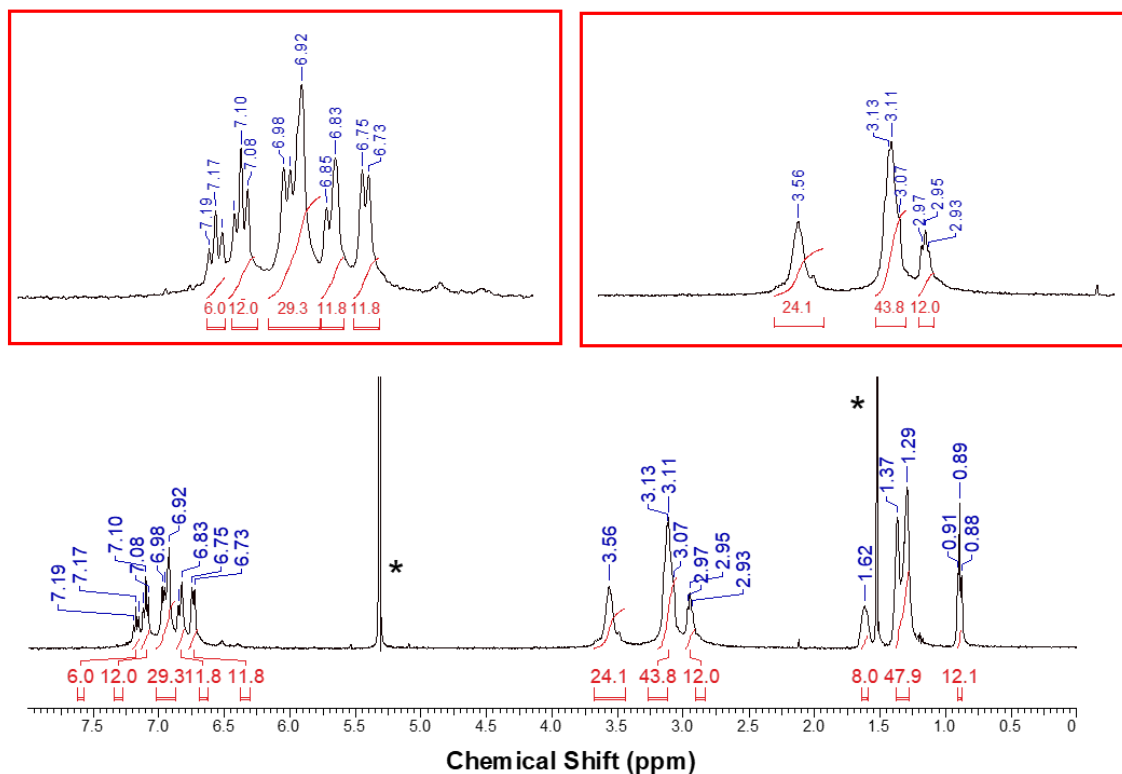


Figure S5.1. 600 MHz ^1H NMR spectrum of $[(\text{CH}_3-(\text{CH}_2)_7)_4\text{N}][\text{Au}_{25}(\text{SCH}_2\text{CH}_2-m\text{-C}_6\text{H}_4\text{-N}_3)_{18}] (m\text{-azido}^{1-})$ in CD_2Cl_2 at 25°C . Red insets are zoom-in regions of relevant sections of spectrum. * indicates residual protio solvent and impurities.

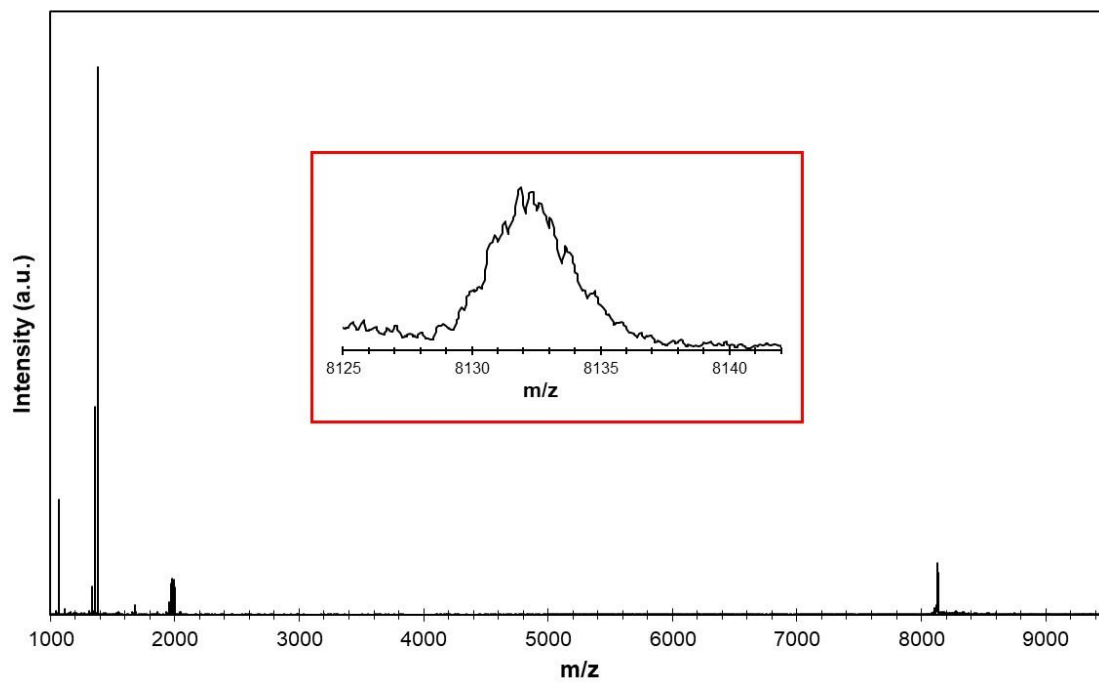


Figure S5.2. Negative ion mode ESI mass spectrum of anionic $[\text{Au}_{25}(\text{SCH}_2\text{CH}_2\text{-}m\text{-C}_6\text{H}_4\text{-N}_3)]^{1-}$.

5.6.3.3 Experimental Spectra and Diagrams for $[(\text{CH}_3\text{-(CH}_2)_7)_4\text{N}][\text{Au}_{25}(\text{SCH}_2\text{CH}_2\text{-}o\text{-C}_6\text{H}_4\text{-N}_3)_{18}] (o\text{-azido}^{1-})$

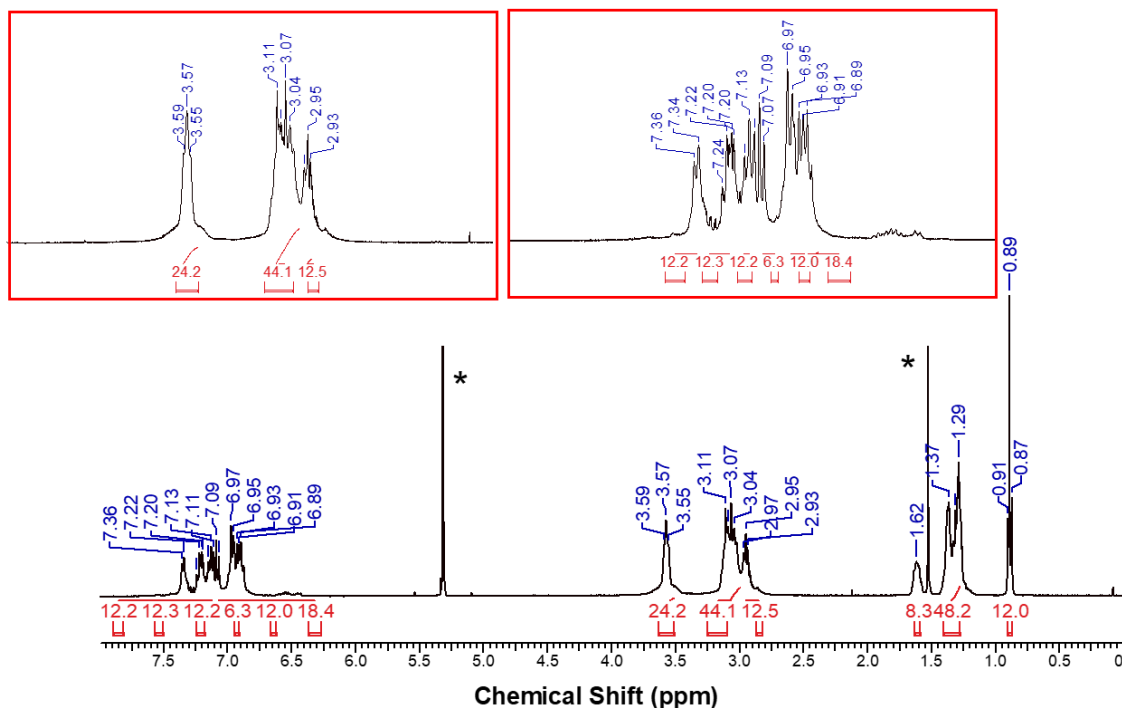


Figure S5.3. 600 MHz ^1H NMR spectrum of $[(\text{CH}_3\text{-(CH}_2)_7)_4\text{N}][\text{Au}_{25}(\text{SCH}_2\text{CH}_2\text{-}o\text{-C}_6\text{H}_4\text{-N}_3)_{18}] (o\text{-azido}^{1-})$ in CD_2Cl_2 at 25°C . Red insets are zoom-in regions of relevant sections of spectrum. * indicates residual protio solvent and impurities.

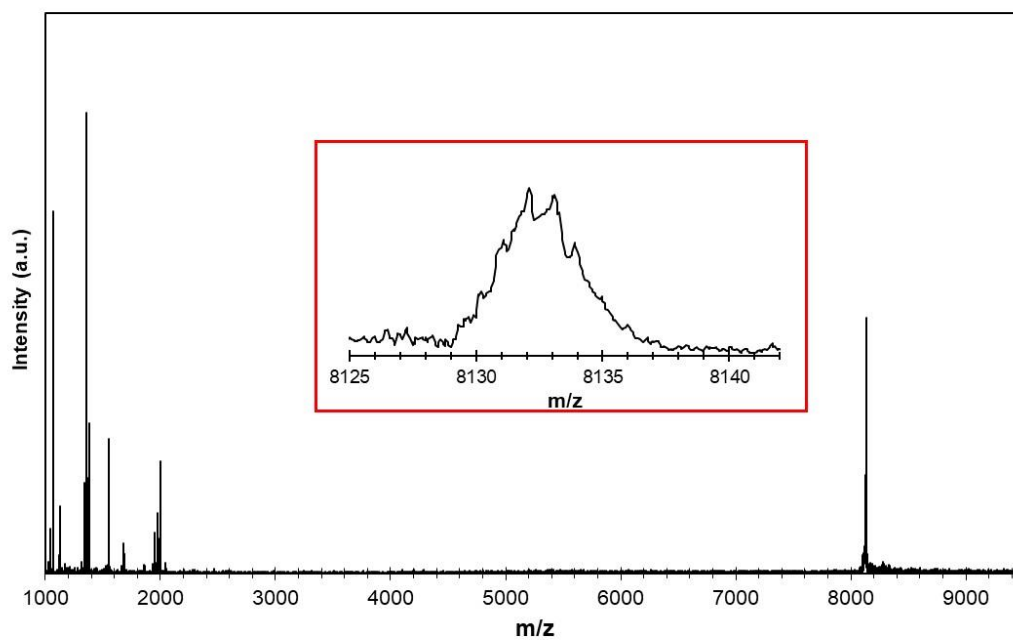


Figure S5.4. Negative ion mode ESI mass spectrum of anionic $[\text{Au}_{25}(\text{SCH}_2\text{CH}_2\text{-}o\text{-C}_6\text{H}_4\text{-N}_3)]^{1-}$.

5.6.3.4 Experimental Diagrams for $[\text{Au}_{25}(\text{SCH}_2\text{CH}_2\text{-}p\text{-C}_6\text{H}_4\text{-N}_3)_{18}]$ ($p\text{-azido}^0$)

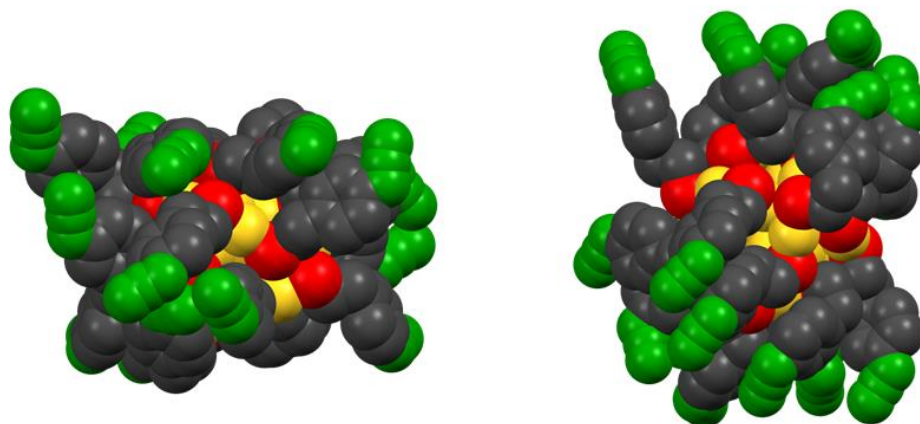


Figure S5.5. Space-filling X-ray structure diagram of $[\text{Au}_{25}(\text{SCH}_2\text{CH}_2\text{-}p\text{-C}_6\text{H}_4\text{-N}_3)_{18}]$ ($p\text{-azido}^0$). Au = yellow, S = red, C = black, N = green.

5.6.3.5 Experimental Diagrams for $[\text{Au}_{25}(\text{SCH}_2\text{CH}_2\text{-}m\text{-C}_6\text{H}_4\text{-N}_3)_{18}]$ ($m\text{-azido}^0$)

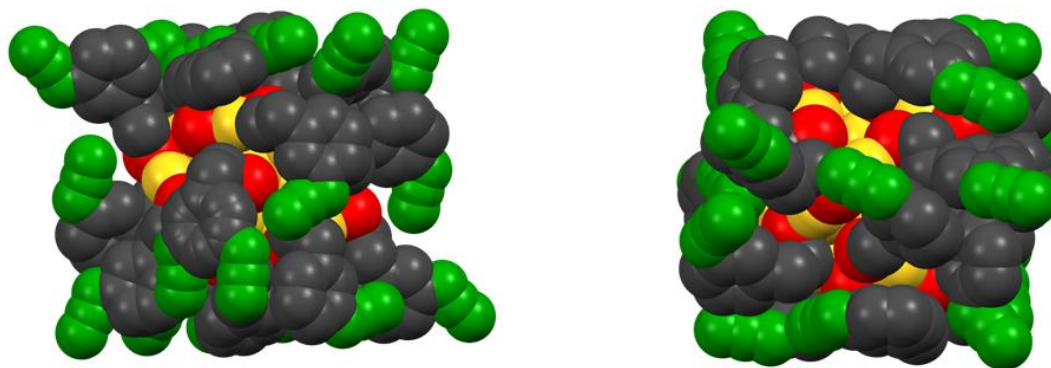


Figure S5.6. Space-filling X-ray structure diagram of $[\text{Au}_{25}(\text{SCH}_2\text{CH}_2\text{-}m\text{-C}_6\text{H}_4\text{-N}_3)_{18}]$ ($m\text{-azido}^0$). Au = yellow, S = red, C = black, N = green.

5.6.3.6 Experimental Diagrams for $[\text{Au}_{25}(\text{SCH}_2\text{CH}_2\text{-}o\text{-C}_6\text{H}_4\text{-N}_3)_{18}]$ (*o*-azido⁰)

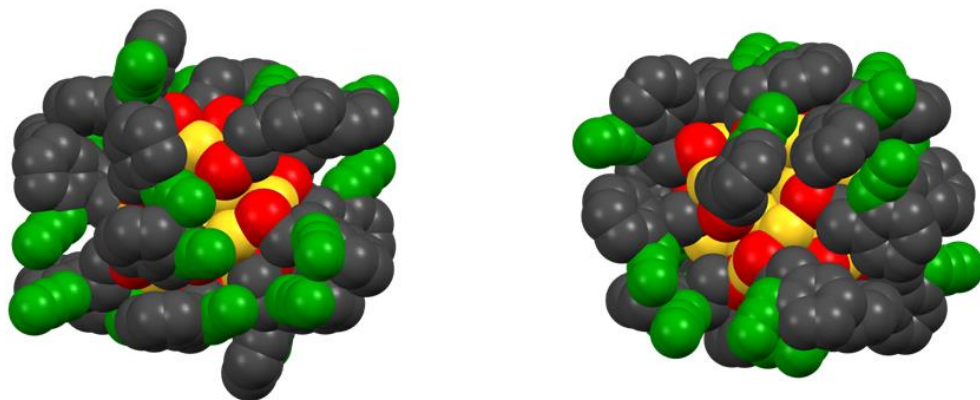


Figure S5.7. Space-filling X-ray structure diagram of $[\text{Au}_{25}(\text{SCH}_2\text{CH}_2\text{-}o\text{-C}_6\text{H}_4\text{-N}_3)_{18}]$ (*o*-azido⁰). Au = yellow, S = red, C = black, N = green.

5.6.3.7 Experimental Spectra and Diagrams for $[(\text{CH}_3-(\text{CH}_2)_7)_4\text{N}][\text{Au}_{25}(\text{SCH}_2\text{CH}_2-p\text{-C}_6\text{H}_4\text{-C}_8\text{H}_{10}\text{N}_3)_{18}]$ (*p*-triazole¹⁻)

See Section 5.6.3.2 for ¹H NMR spectrum and linear negative mode MALDI-TOF mass spectrum of $[(\text{CH}_3-(\text{CH}_2)_7)_4\text{N}][\text{Au}_{25}(\text{SCH}_2\text{CH}_2-p\text{-C}_6\text{H}_4\text{-C}_8\text{H}_{10}\text{N}_3)_{18}]$ (*p*-triazole¹⁻).

5.6.3.8 Experimental Spectra and Diagrams for $[(\text{CH}_3-(\text{CH}_2)_7)_4\text{N}][\text{Au}_{25}(\text{SCH}_2\text{CH}_2-m\text{-C}_6\text{H}_4\text{-C}_8\text{H}_{10}\text{N}_3)_{18}]$ (*m*-triazole¹⁻)

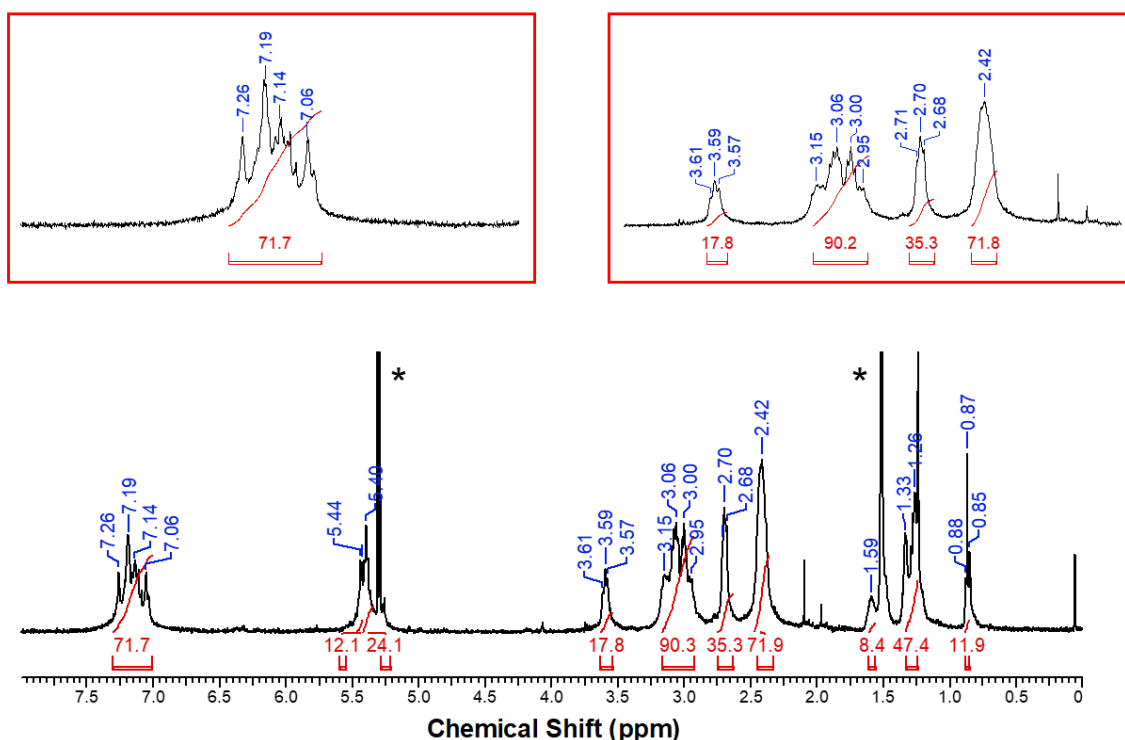


Figure S5.8. 600 MHz ¹H NMR spectrum of $[(\text{CH}_3-(\text{CH}_2)_7)_4\text{N}][\text{Au}_{25}(\text{SCH}_2\text{CH}_2-m\text{-C}_6\text{H}_4\text{-C}_8\text{H}_{10}\text{N}_3)_{18}]$ (*m*-triazole¹⁻) in CD_2Cl_2 at 25°C. Red insets are zoom-in regions of relevant sections of spectrum. * indicates residual protio solvent and impurities.

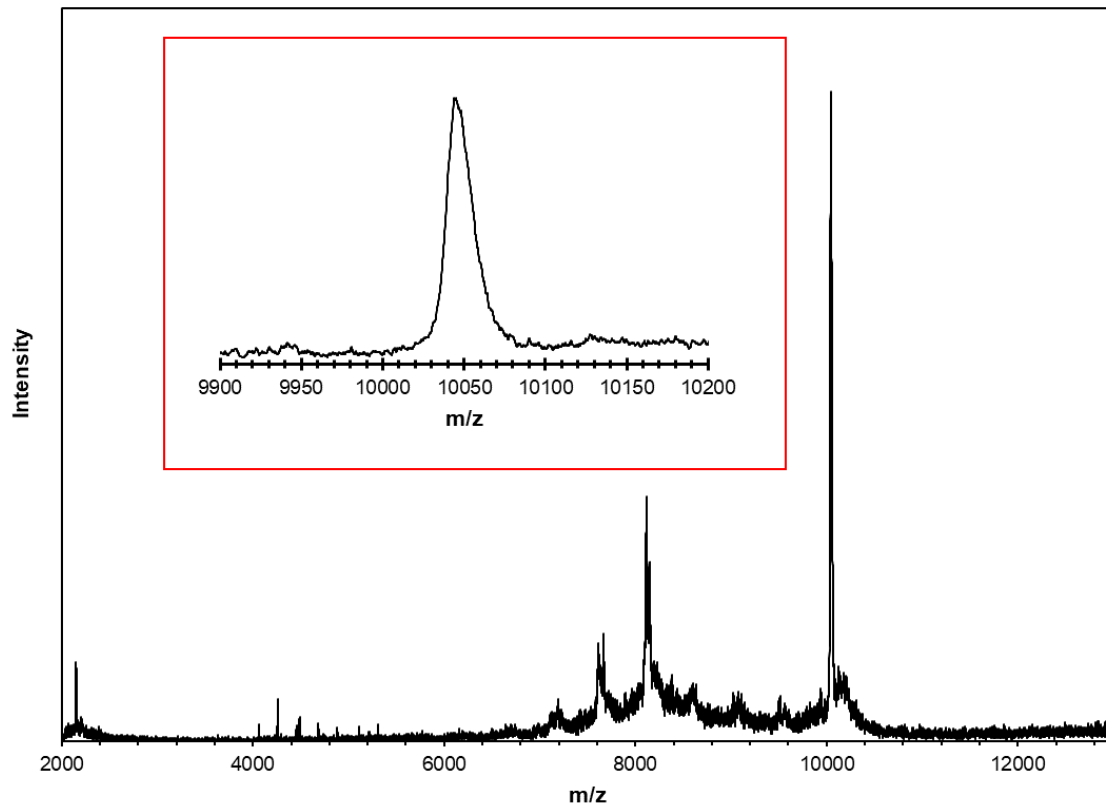


Figure S5.9. Linear negative mode MALDI-TOF mass spectrum of anionic $[\text{Au}_{25}(\text{SCH}_2\text{CH}_2\text{-}m\text{-C}_6\text{H}_4\text{-C}_8\text{H}_{10}\text{N}_3)_{18}]^{1-}$.

5.6.3.9 Experimental Spectra and Diagrams for $[(\text{CH}_3-(\text{CH}_2)_7)_4\text{N}][\text{Au}_{25}(\text{SCH}_2\text{CH}_2-o\text{-C}_6\text{H}_4\text{-C}_8\text{H}_{10}\text{N}_3)_{18}]$ (*o*-triazole¹⁻)

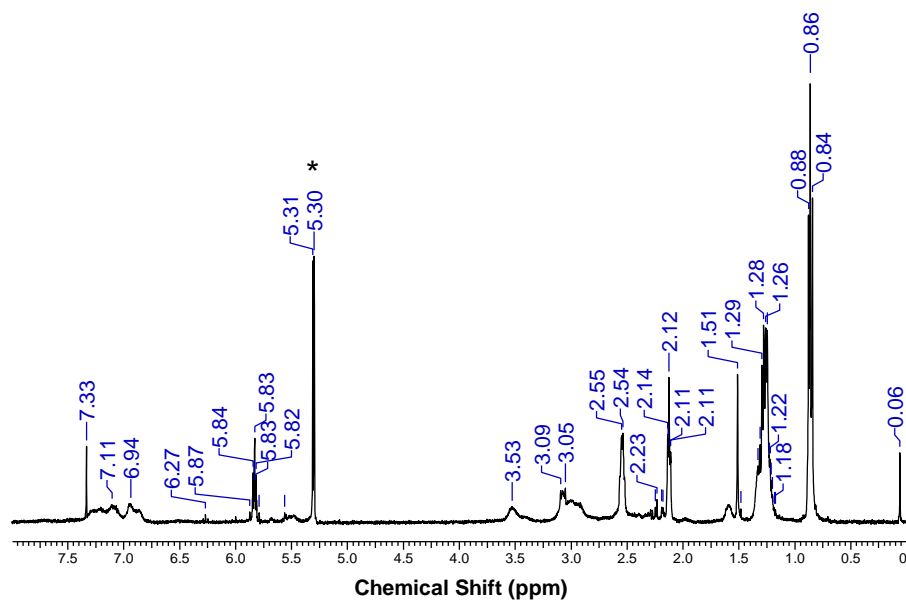


Figure S5.10. 600 MHz ^1H NMR spectrum of $[(\text{CH}_3-(\text{CH}_2)_7)_4\text{N}][\text{Au}_{25}(\text{SCH}_2\text{CH}_2-o\text{-C}_6\text{H}_4\text{-C}_8\text{H}_{10}\text{N}_3)_{18}]$ (*o*-triazole¹⁻) in CD_2Cl_2 at 25°C . * indicates residual protio solvents.

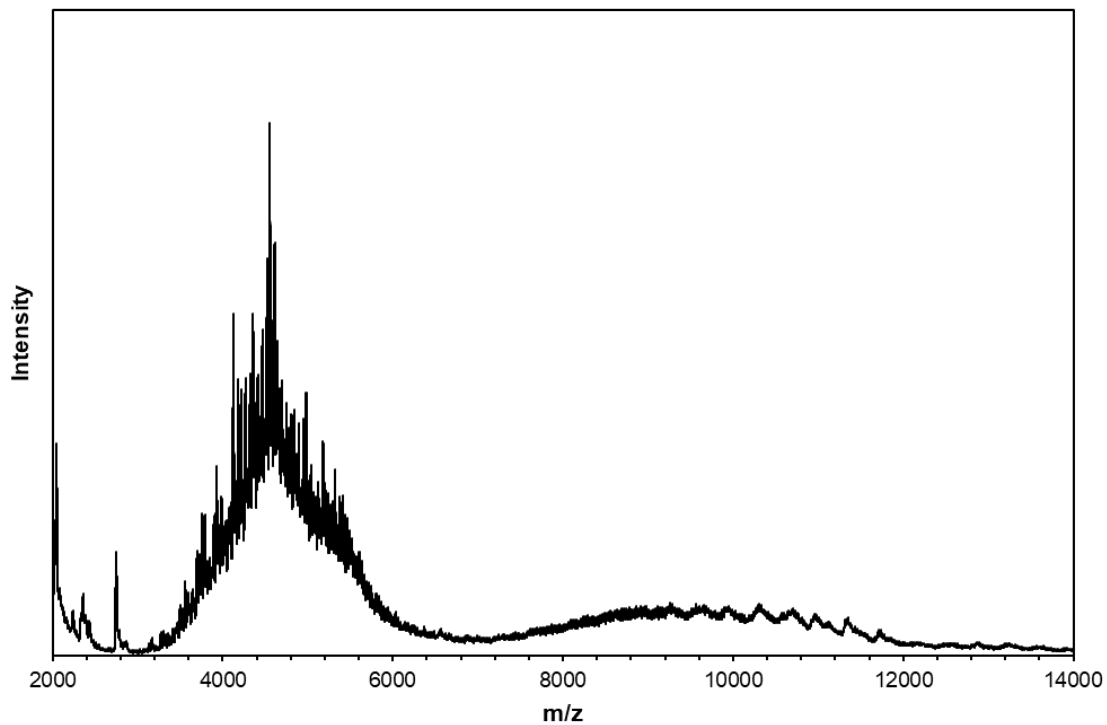


Figure S5.11. Linear negative mode MALDI-TOF mass spectrum of anionic $[\text{Au}_{25}(\text{SCH}_2\text{CH}_2\text{-}o\text{-C}_6\text{H}_4\text{-C}_8\text{H}_{10}\text{N}_3)_{18}]^{1-}$.

5.6.3.10 Experimental Spectra for *p*-nitro-phenylethanethioacetate

See **Section 4.6.3.4** for ^1H NMR, ^{13}C $\{^1\text{H}\}$ NMR and IR spectra of ***p*-nitro-phenylethanethioacetate**.

5.6.3.11 Experimental Spectra for *p*-azido-phenylethanethioacetate

See **Section 4.6.3.6** for ^1H NMR, ^{13}C $\{^1\text{H}\}$ NMR and IR spectra of ***p*-azido-phenylethanethioacetate**.

5.6.3.12 Experimental Spectra for *p*-azido-phenylethanethiol

See **Section 4.6.3.7** for ^1H NMR, ^{13}C $\{^1\text{H}\}$ NMR and IR spectra of ***p*-azido-phenylethanethiol**.

5.6.3.13 Experimental Spectra for *m*-nitro-phenylethanethioacetate

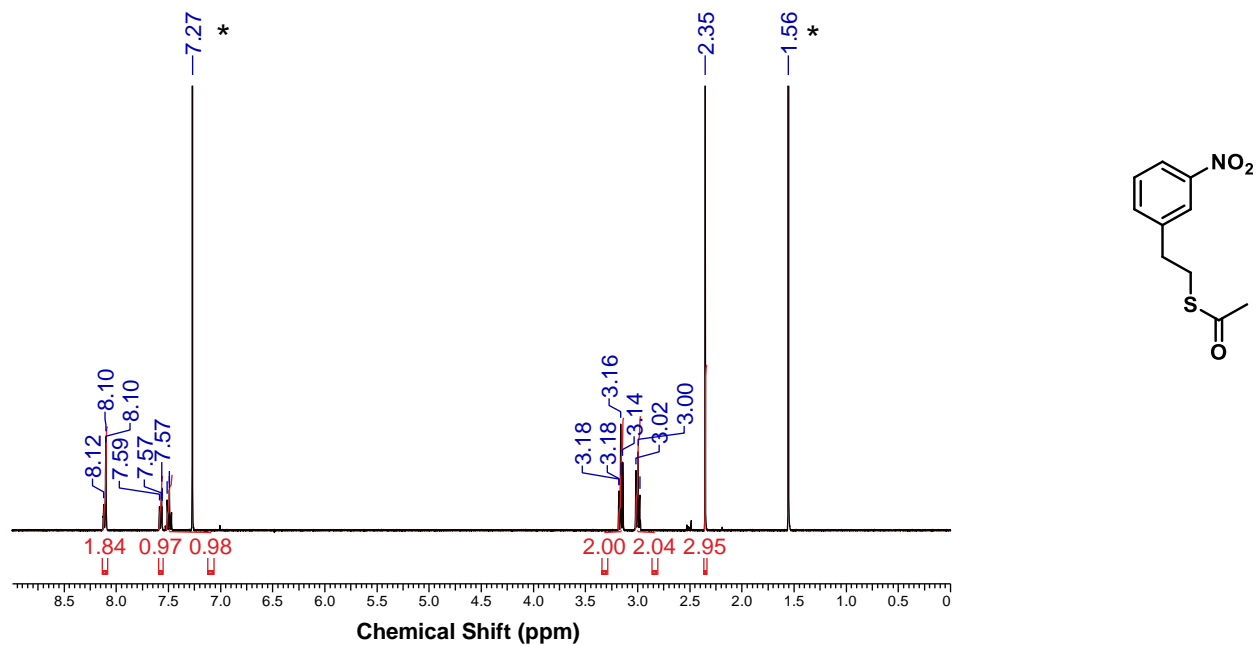


Figure S5.12. ¹H NMR spectrum of *m*-nitro-phenylethanethioacetate in CDCl₃ at 25°C. * indicates residual protio solvent and impurities.

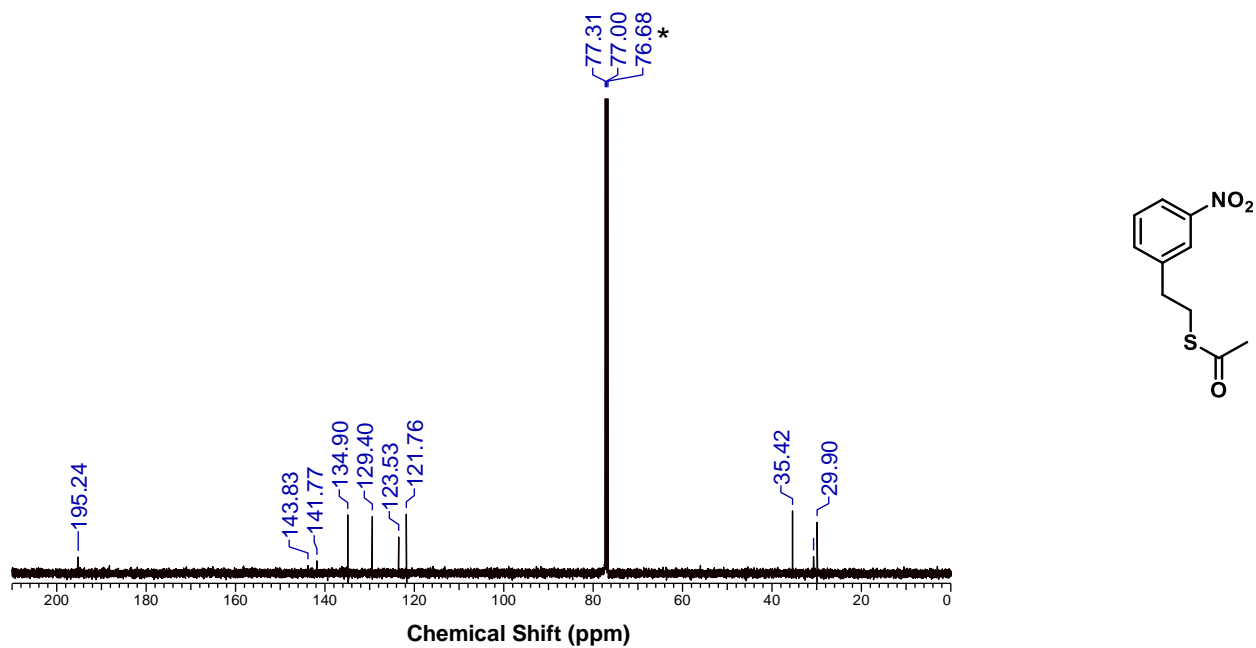


Figure S5.13. ¹³C{¹H} NMR spectrum of *m*-nitro-phenylethanethioacetate in CDCl₃ at 25°C. * indicates CDCl₃ solvent.

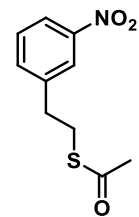
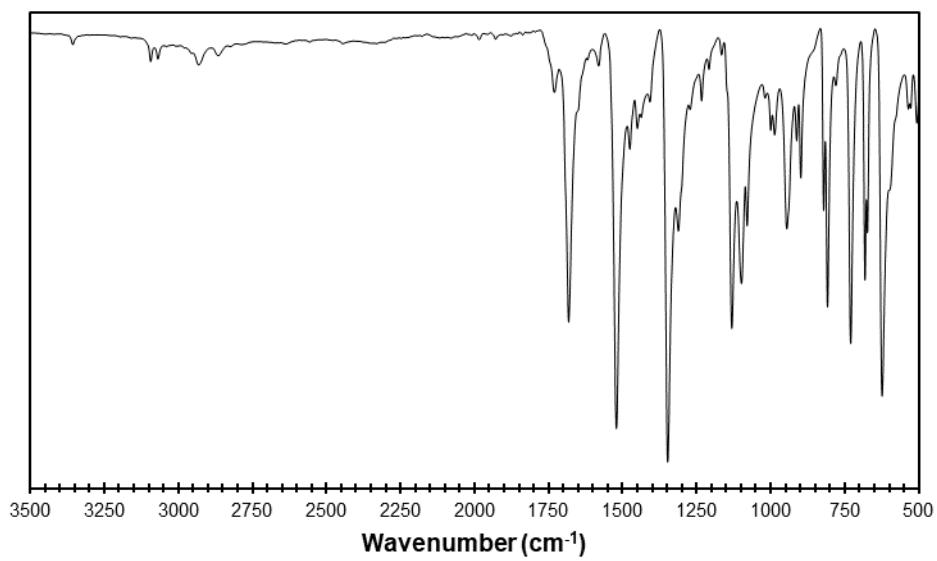
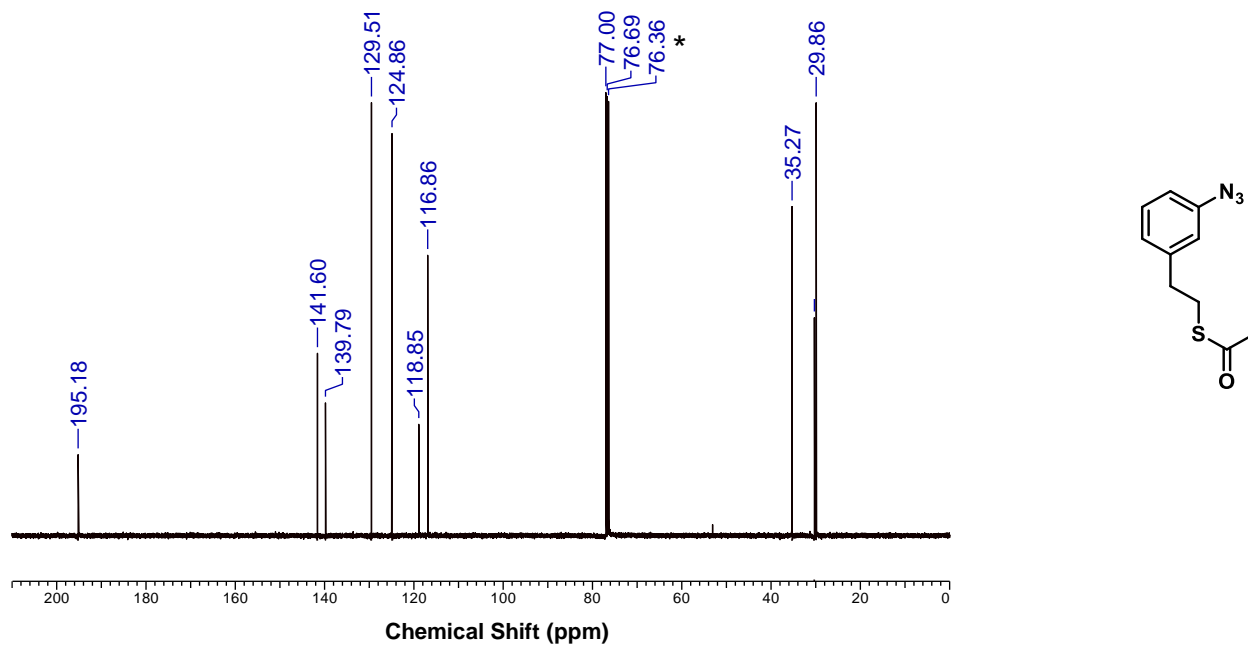
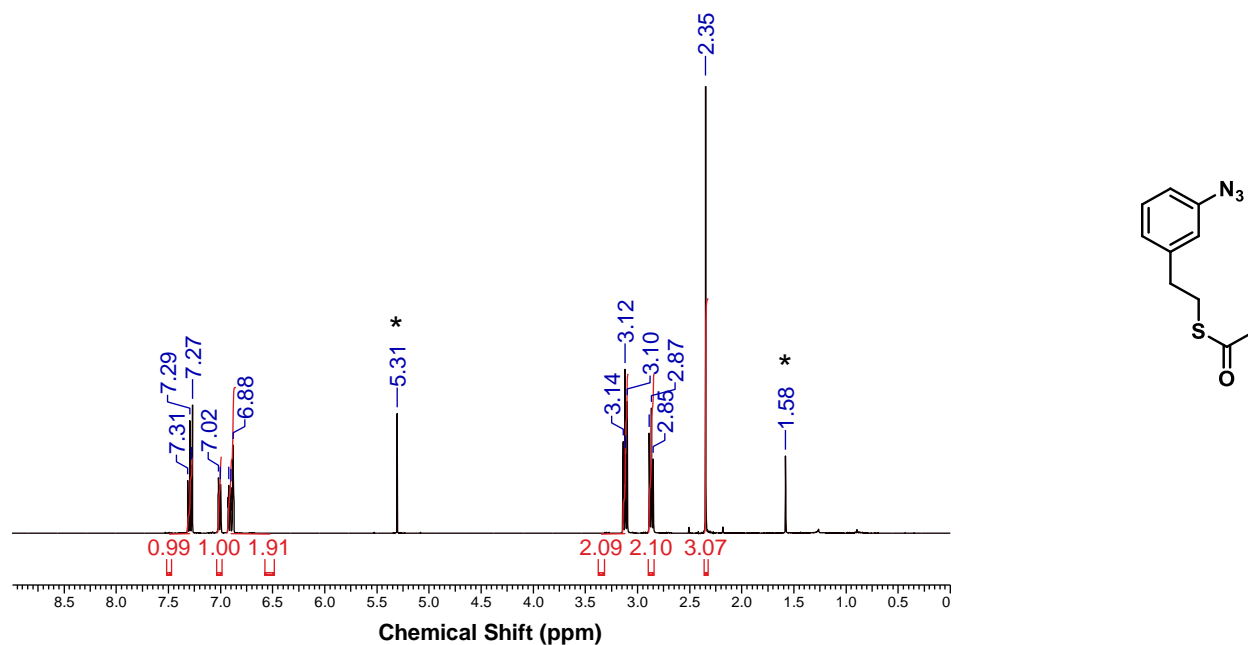


Figure S5.14. Infrared spectrum of *m*-nitro-phenylethanethioacetate.

5.6.3.14 Experimental Spectra for *m*-azido-phenylethanethioacetate



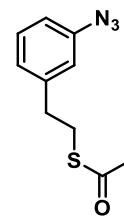
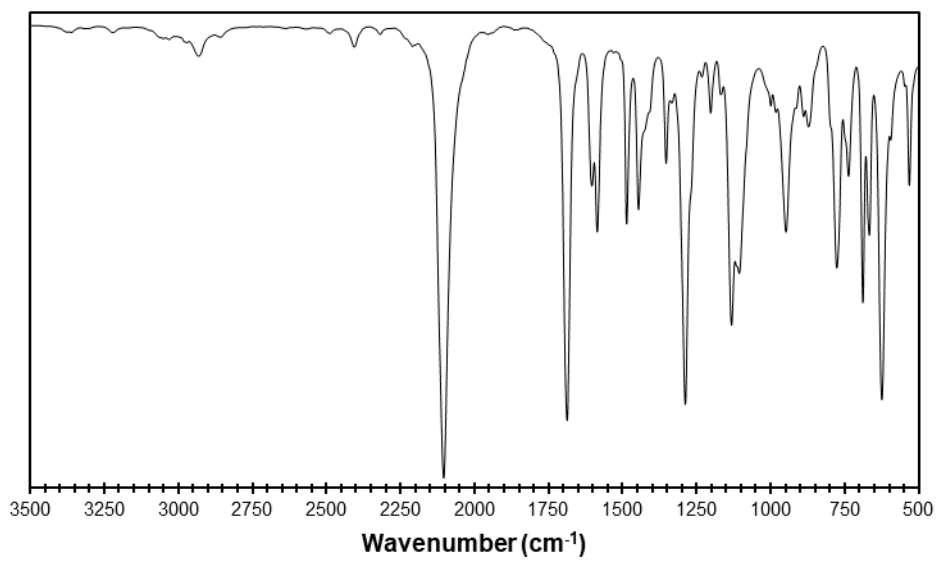


Figure S5.17. Infrared spectrum of *m*-azido-phenylethanethioacetate.

5.6.3.15 Experimental Spectra for *m*-azido-phenylethanethiol

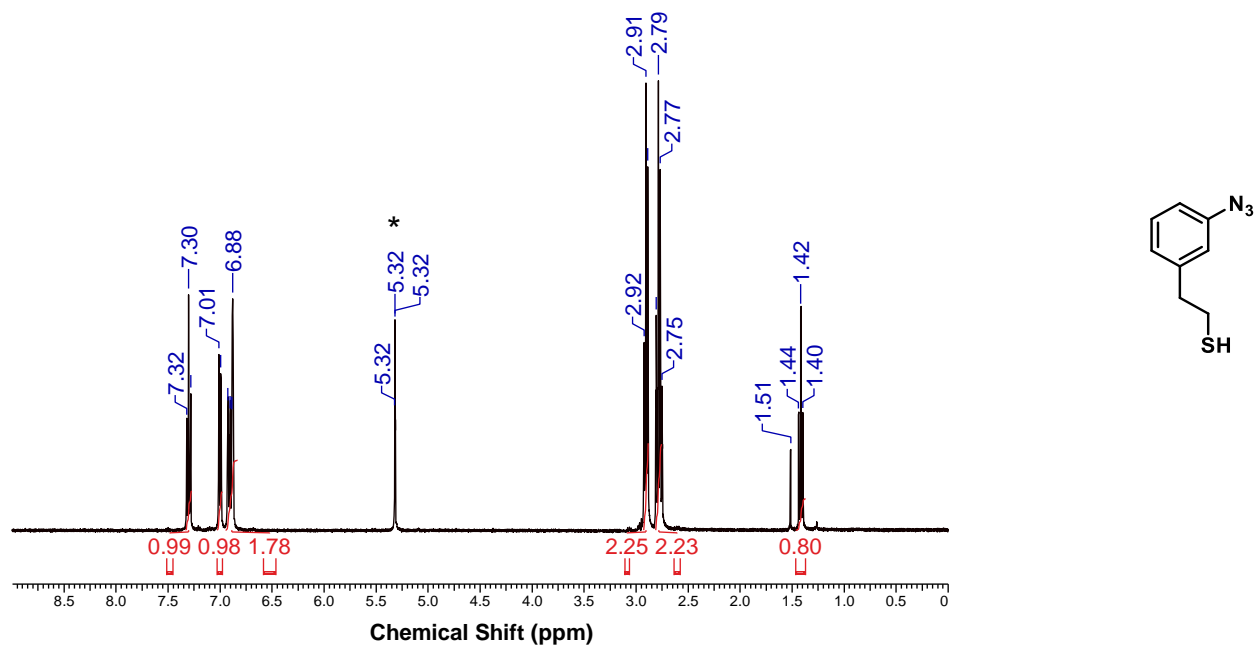


Figure S5.18. ^1H NMR spectrum of *m*-azido-phenylethanethiol in CD_2Cl_2 at 25°C . * indicates residual protio solvent.

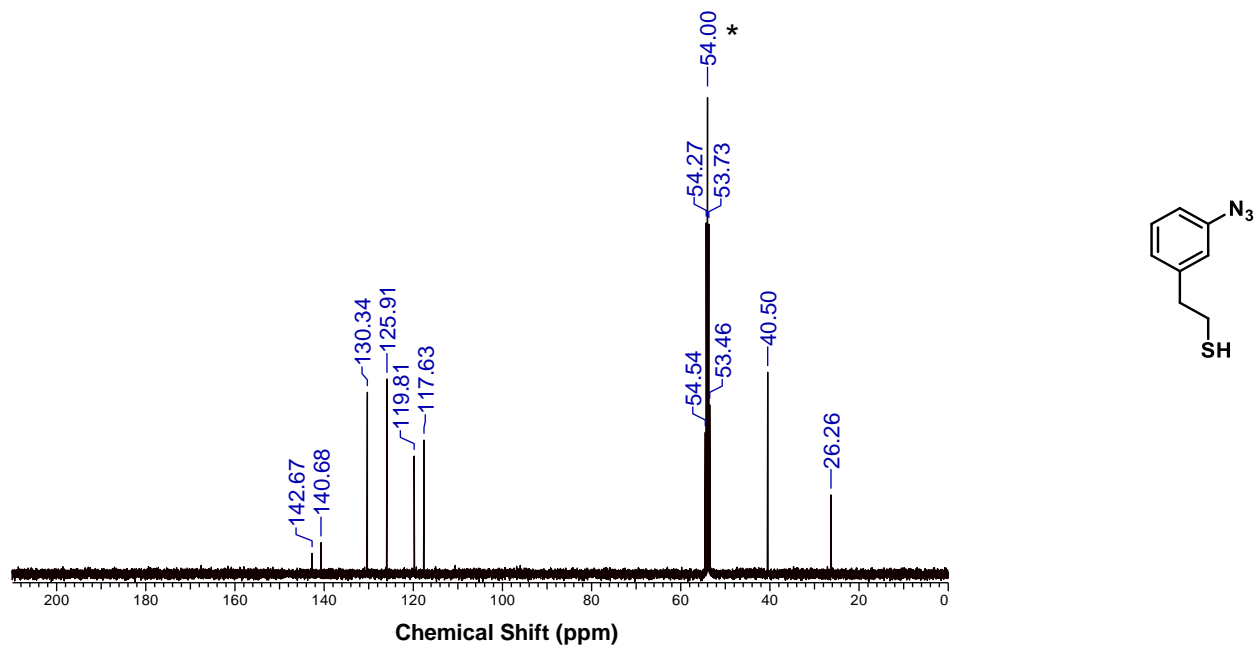


Figure S5.19. $^{13}\text{C}\{^1\text{H}\}$ NMR spectrum of *m*-azido-phenylethanethiol in CD_2Cl_2 at 25°C . * indicates CD_2Cl_2 solvent.

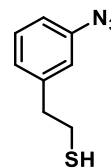
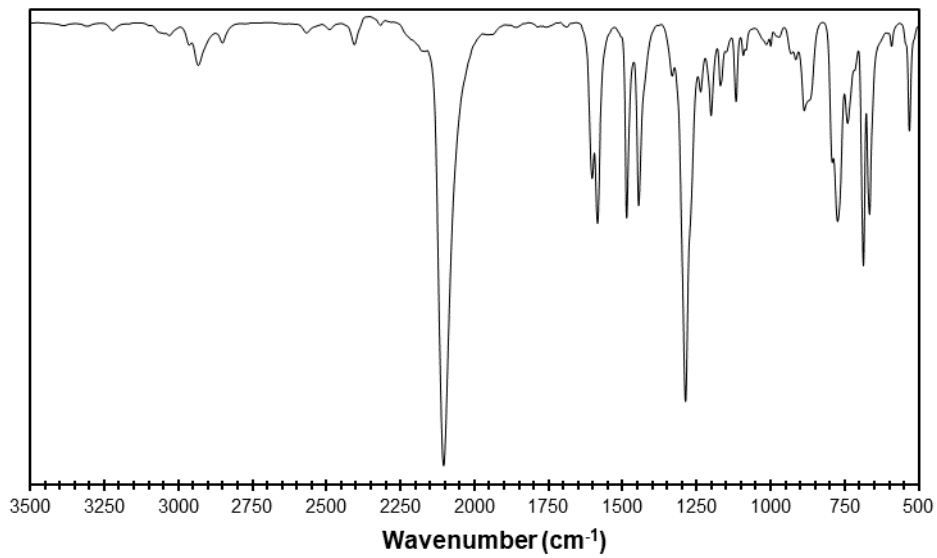


Figure S5.20. Infrared spectrum of *m*-azido-phenylethanethiol.

5.6.3.16 Experimental Spectra for *o*-nitro-phenylethanethioacetate

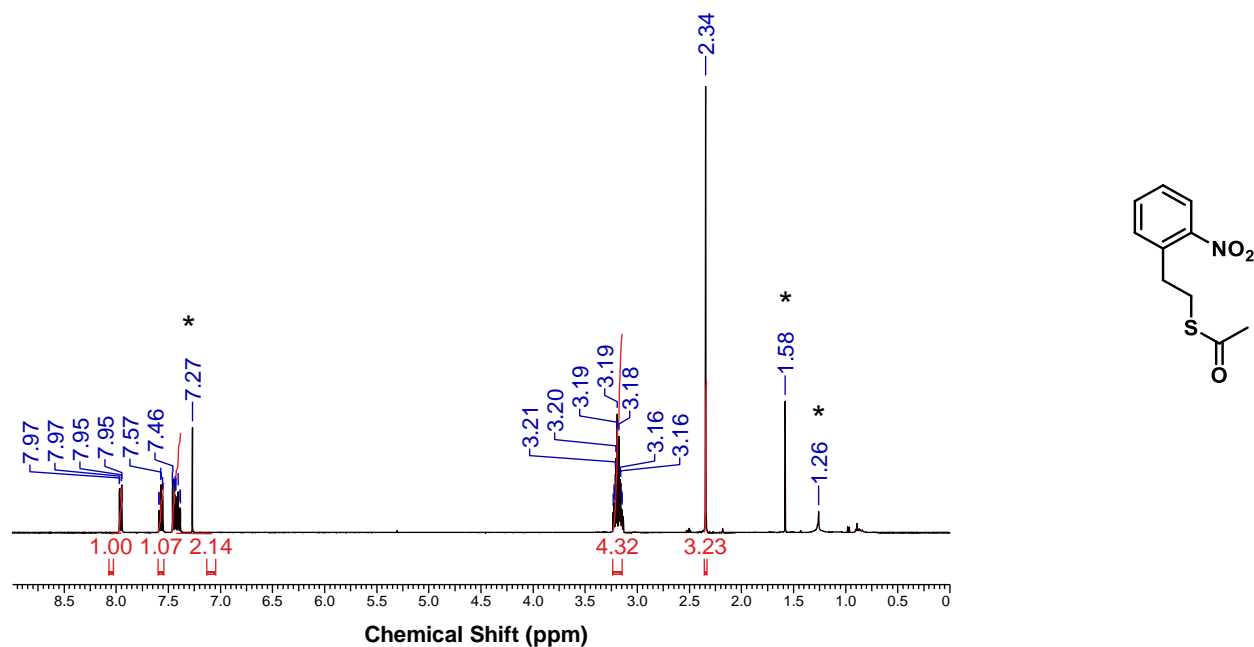


Figure S5.21. ^1H NMR spectrum of *o*-nitro-phenylethanethioacetate in CDCl_3 at 25°C . * indicates residual protio solvent and impurities.

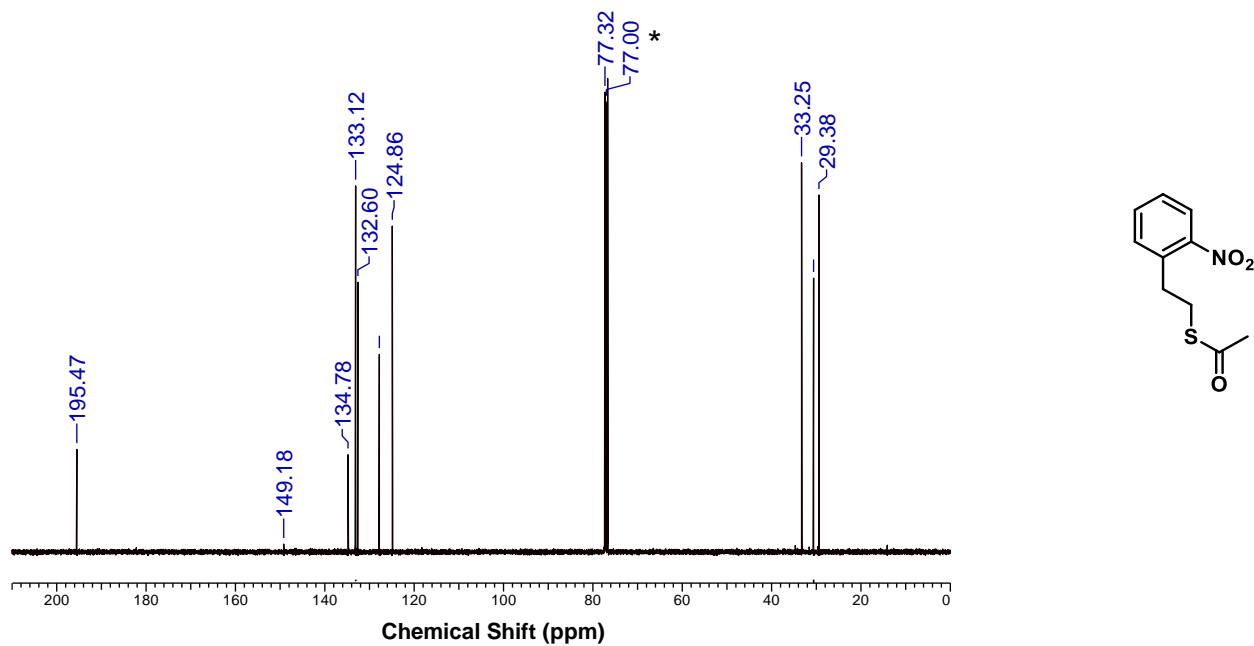


Figure S5.22. $^{13}\text{C}\{^1\text{H}\}$ NMR spectrum of *o*-nitro-phenylethanethioacetate in CDCl_3 at 25°C . * indicates CDCl_3 solvent.

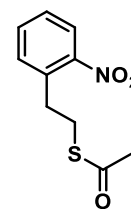
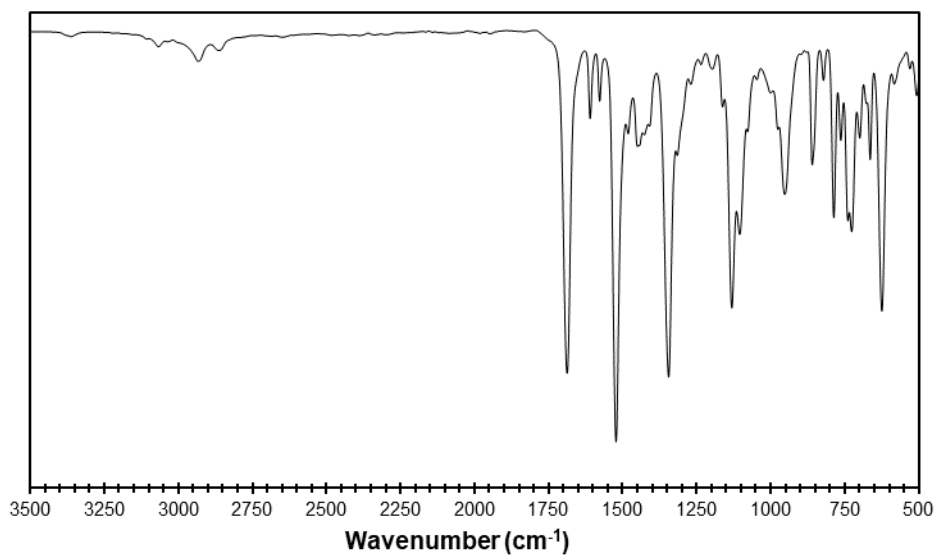


Figure S5.23. Infrared spectrum of *o*-nitro-phenylethanethioacetate.

5.6.3.17 Experimental Spectra for *o*-azido-phenylethanethioacetate

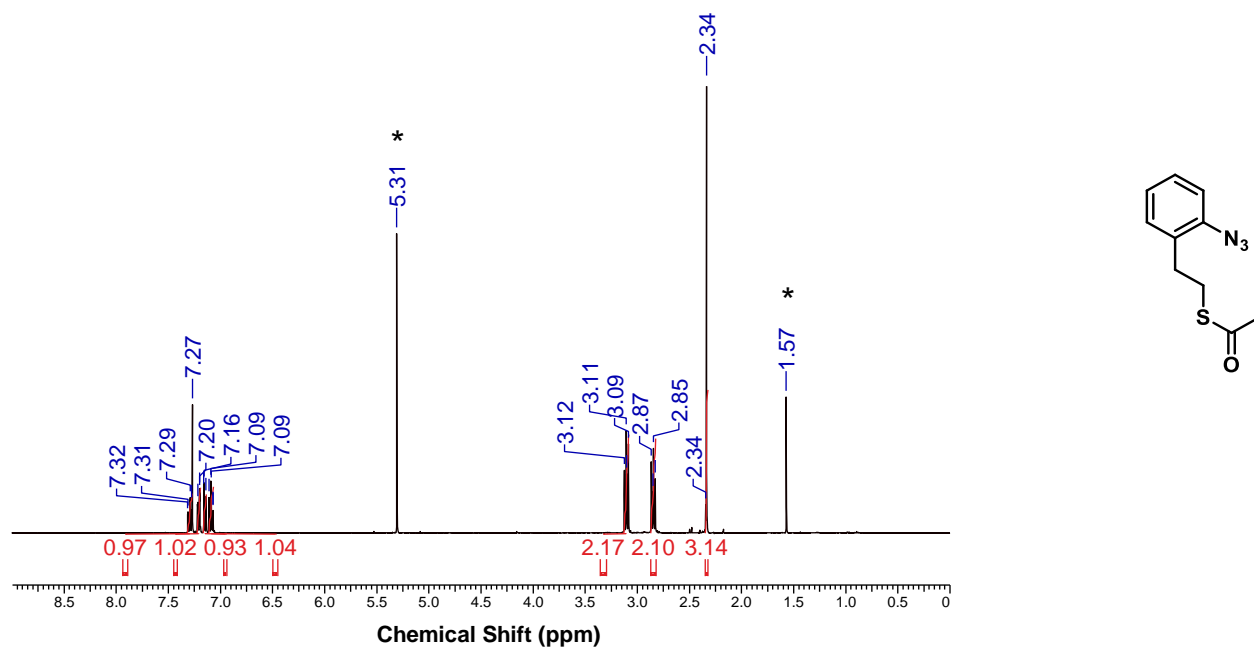


Figure S5.24. ¹H NMR spectrum of *o*-azido-phenylethanethioacetate in CDCl₃ at 25°C. * indicates residual protio solvent and impurities.

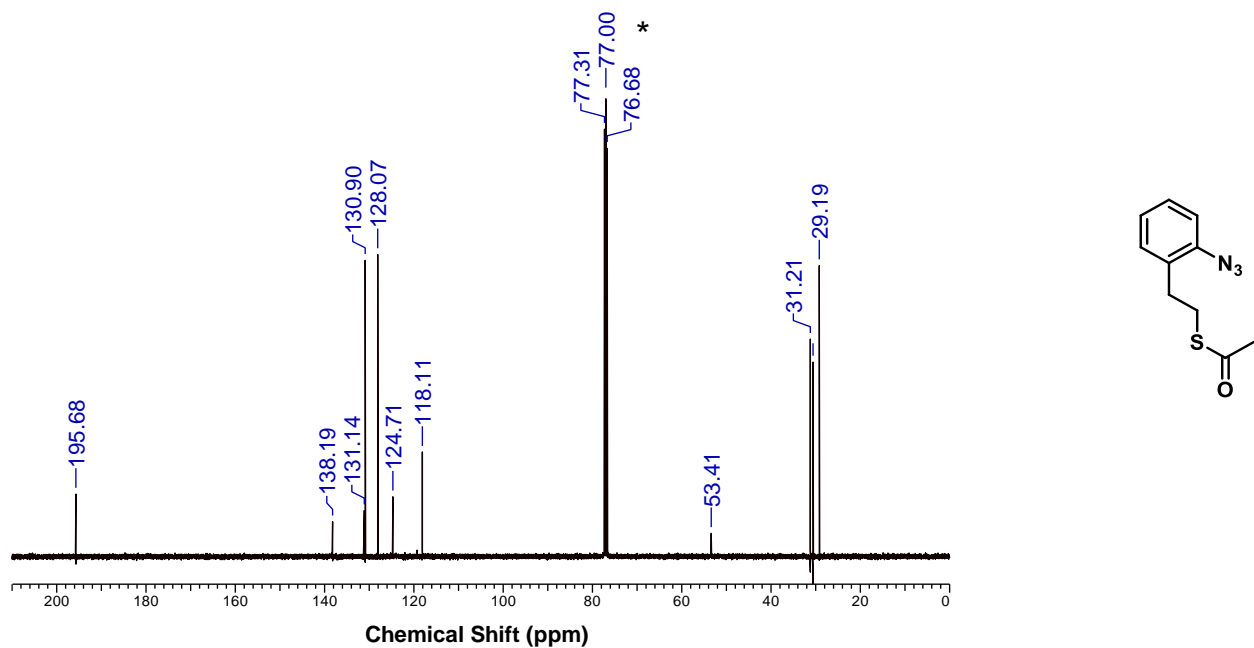


Figure S5.25. ¹³C{¹H} NMR spectrum of *o*-azido-phenylethanethioacetate in CDCl₃ at 25°C. * indicates CDCl₃ solvent.

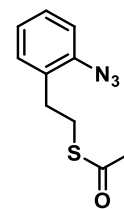
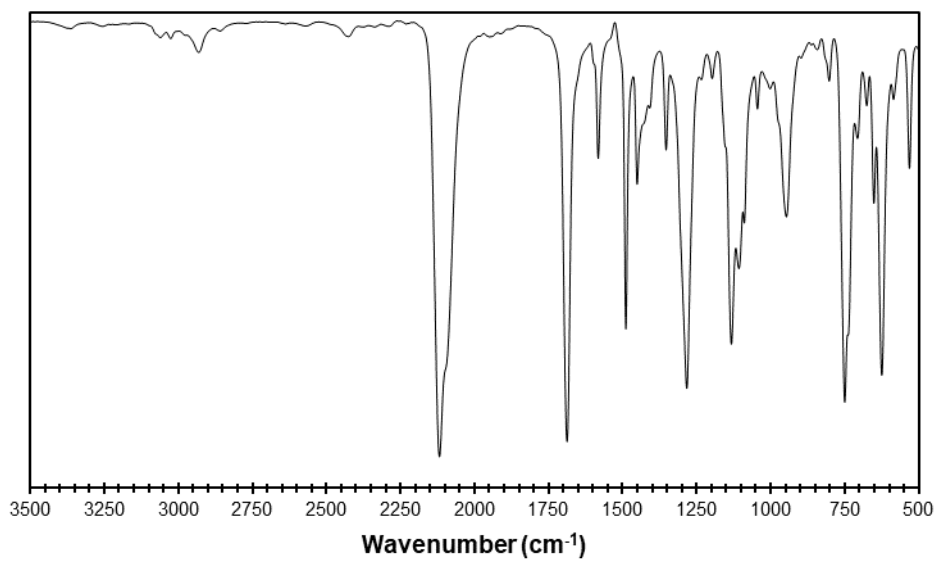


Figure S5.26. Infrared spectrum of *o*-azido-phenylethanethioacetate.

5.6.3.18 Experimental Spectra for *o*-azido-phenylethanethiol

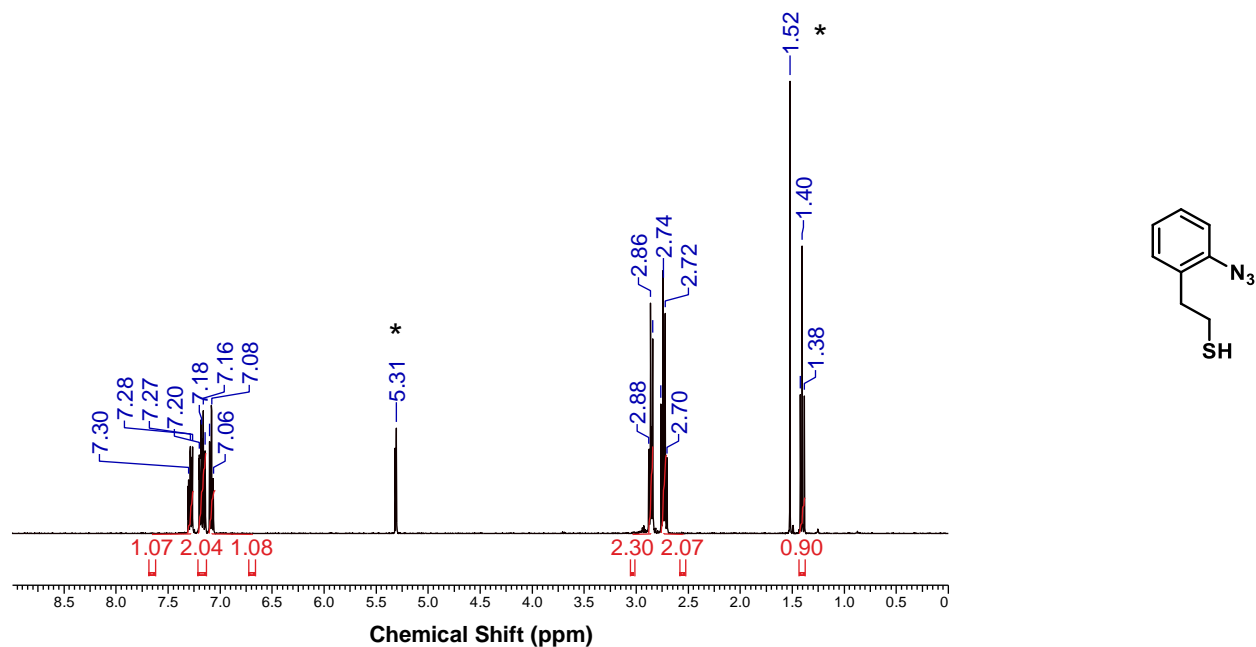


Figure S5.27. ^1H NMR spectrum of *o*-azido-phenylethanethiol in CD_2Cl_2 at 25°C . * indicates residual protio solvent and impurities.

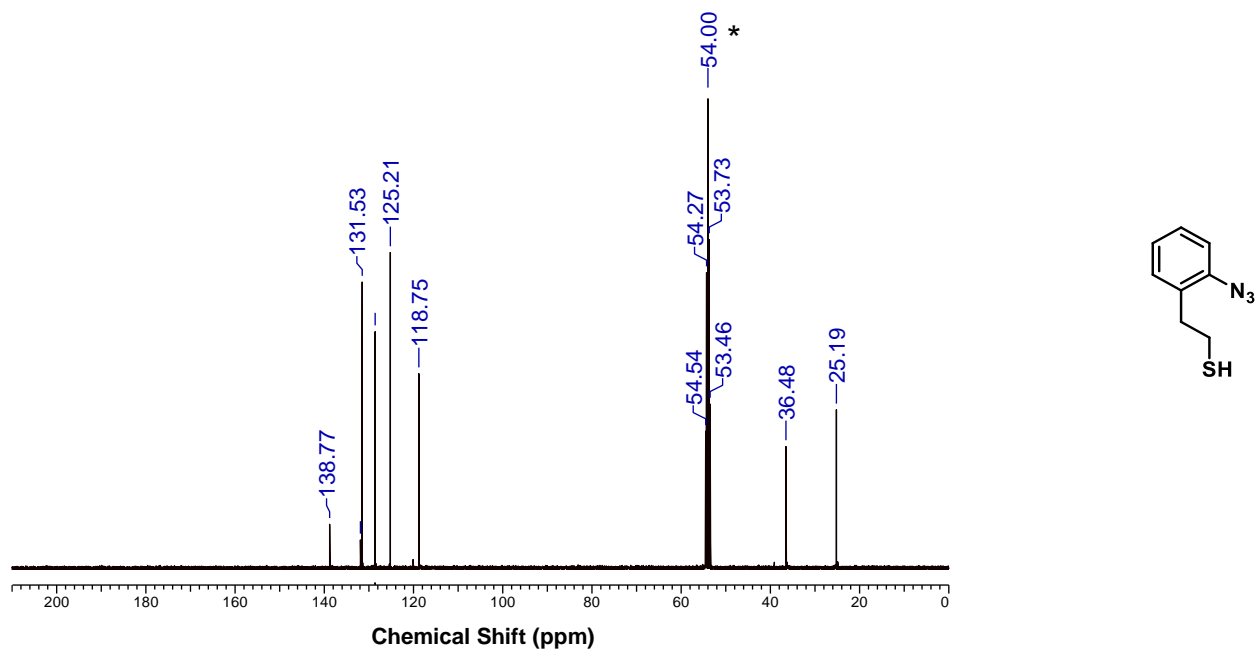


Figure S5.28. $^{13}\text{C}\{^1\text{H}\}$ NMR spectrum of *o*-azido-phenylethanethiol in CD_2Cl_2 at 25°C . * indicates CD_2Cl_2 solvent.

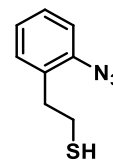
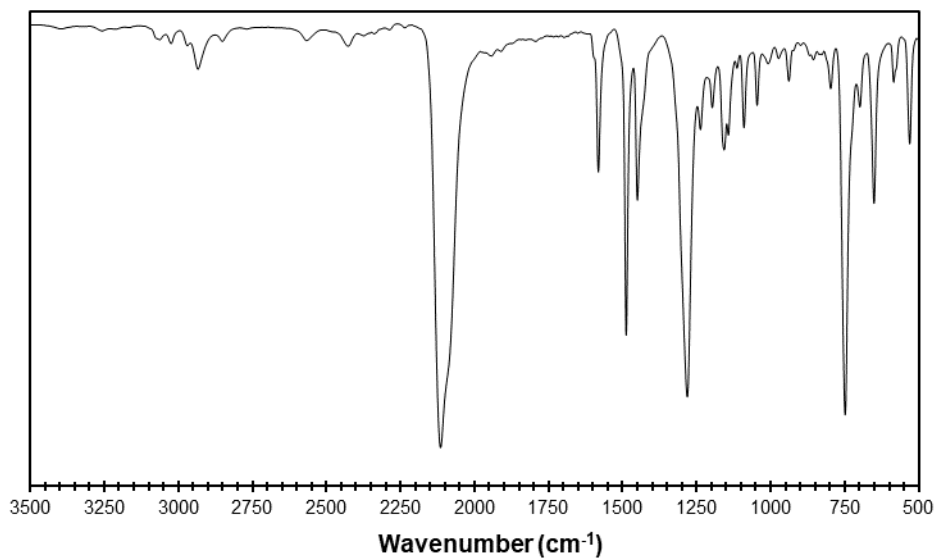


Figure S5.29. Infrared spectrum of *o*-azido-phenylethanethiol.

5.6.4 Electrochemical Graphs

5.6.4.1 Cyclic Voltammetry (CV) Graph of $[(\text{CH}_3-(\text{CH}_2)_7)_4\text{N}][\text{Au}_{25}(\text{SCH}_2\text{CH}_2-p\text{-C}_6\text{H}_4\text{-N}_3)_{18}]$ (*p*-azido¹⁻)

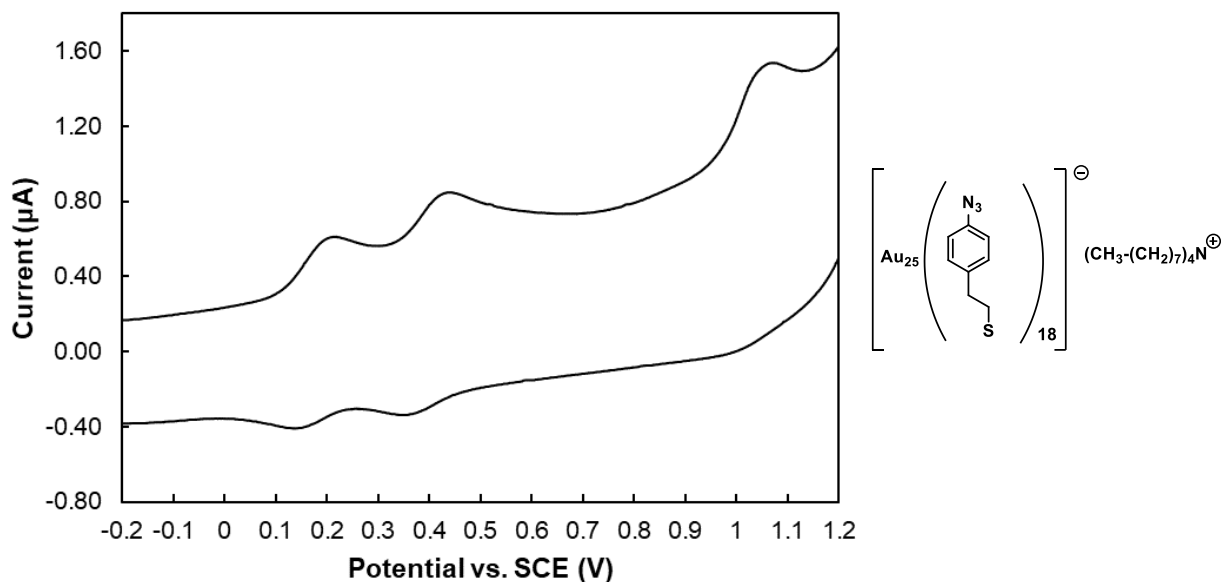


Figure S5.30. Cyclic voltammetry (CV) graph of 0.1 mM solution of $[(\text{CH}_3-(\text{CH}_2)_7)_4\text{N}][\text{Au}_{25}(\text{SCH}_2\text{CH}_2-p\text{-C}_6\text{H}_4\text{-N}_3)_{18}]$ (*p*-azido¹⁻) in 1:1 acetonitrile:benzene. Supporting electrolyte for CV measurements was 0.1 M tetra-*n*-butylammonium perchlorate (TBAP).

5.6.4.2 Cyclic Voltammetry (CV) Graph of $[(\text{CH}_3-(\text{CH}_2)_7)_4\text{N}][\text{Au}_{25}(\text{SCH}_2\text{CH}_2-m\text{-C}_6\text{H}_4\text{-N}_3)_{18}]$ (*m*-azido¹⁻)

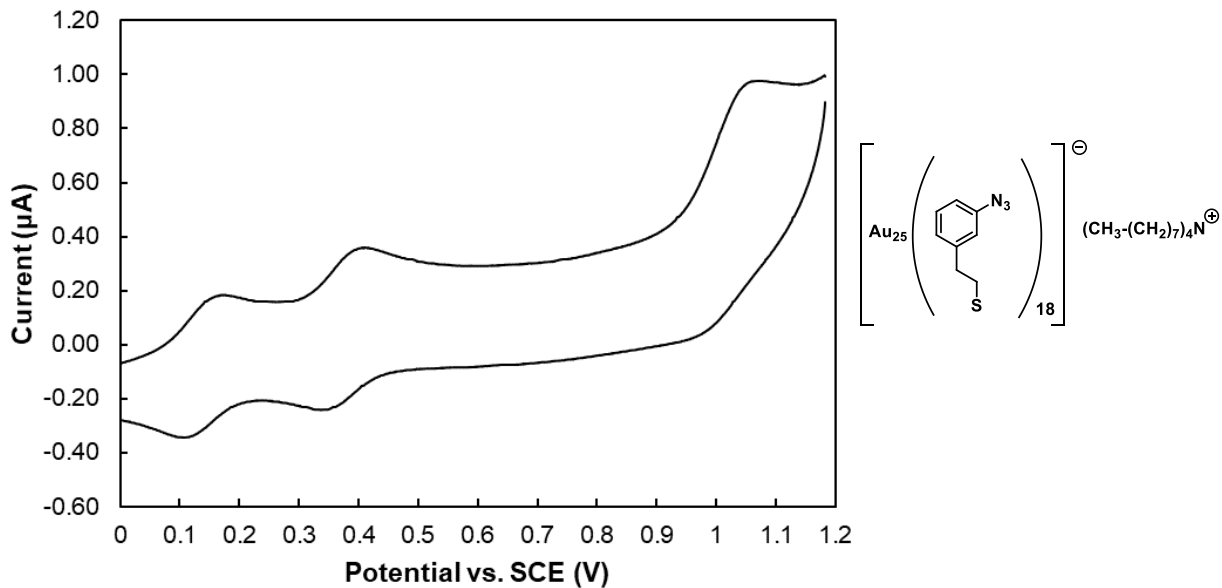


Figure S5.31. Cyclic voltammetry (CV) graph of 0.1 mM solution of $[(\text{CH}_3-(\text{CH}_2)_7)_4\text{N}][\text{Au}_{25}(\text{SCH}_2\text{CH}_2-m\text{-C}_6\text{H}_4\text{-N}_3)_{18}]$ (*m*-azido¹⁻) in 1:1 acetonitrile:benzene. Supporting electrolyte for CV measurements was 0.1 M tetra-*n*-butylammonium perchlorate (TBAP).

5.6.4.3 Cyclic Voltammetry (CV) Graph of $[(\text{CH}_3-(\text{CH}_2)_7)_4\text{N}][\text{Au}_{25}(\text{SCH}_2\text{CH}_2-o\text{-C}_6\text{H}_4\text{-N}_3)_{18}]$ (*o*-azido¹⁻)

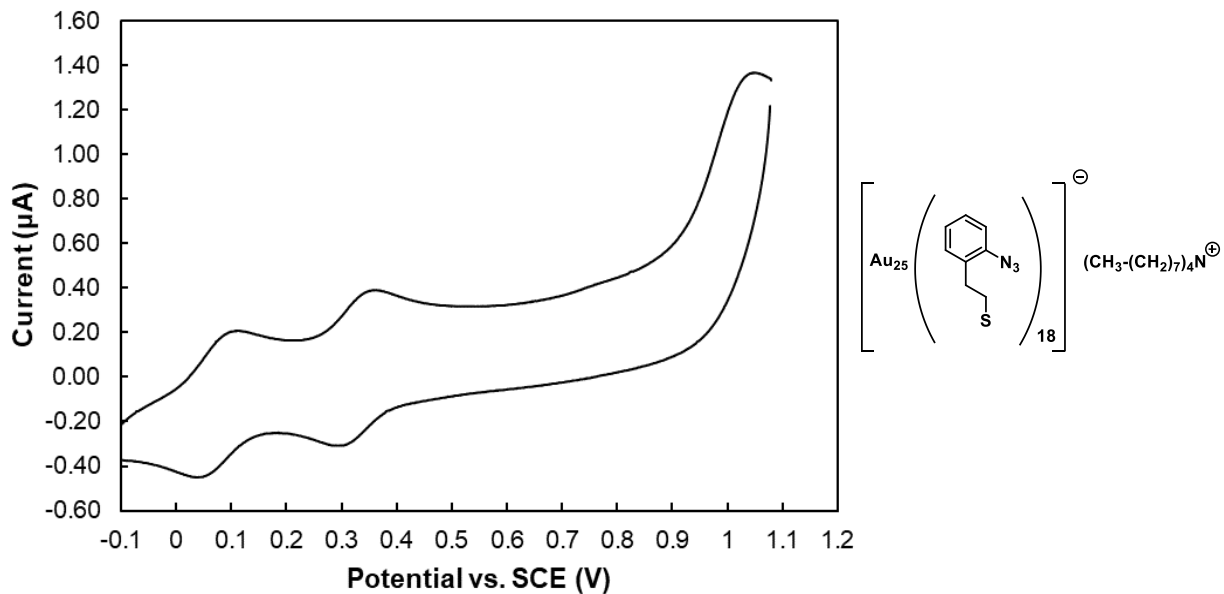


Figure S5.32. Cyclic voltammetry (CV) graph of 0.1 mM solution of $[(\text{CH}_3-(\text{CH}_2)_7)_4\text{N}][\text{Au}_{25}(\text{SCH}_2\text{CH}_2-o\text{-C}_6\text{H}_4\text{-N}_3)_{18}]$ (*o*-azido¹⁻) in 1:1 acetonitrile:benzene. Supporting electrolyte for CV measurements was 0.1 M tetra-*n*-butylammonium perchlorate (TBAP).

5.6.5 Kinetic Measurements

5.6.5.1 General Experimental Details

Estimated rate constants for *p*-azidophenylethanethiol, *m*-azidophenylethanethiol and *o*-azidophenylethanethiol, *p*-azido¹⁻ and *m*-azido¹⁻ were determined under second order conditions (k_2) in deuterated dichloromethane at 25°C using ¹H NMR spectroscopy.

In order to estimate k_2 values for *p*-azidophenylethanethiol, *m*-azidophenylethanethiol and *o*-azidophenylethanethiol, stock solutions of the thiols and **BCN_{exo}-OH** were first prepared and then equimolar quantities of each were added to an NMR tube. To prepare the stock solution of each thiol, 10 mg of each thiol was dissolved in 3 mL of deuterated dichloromethane, from which 0.3 mL (containing 0.1 mg (0.58 μmol, 1 equivalent) thiol) was transferred to an NMR tube. A t_0 (time zero) ¹H NMR spectrum was taken of this sample containing only the azide-modified thiol. To prepare the stock solution of **BCN_{exo}-OH**, 8.7 mg of **BCN_{exo}-OH** was dissolved in 1000 μL deuterated dichloromethane, from which 10 μL (containing 0.087 mg (0.58 μmol, 1 equivalent) **BCN_{exo}-OH**) was added to the NMR tube containing the thiol sample, and ¹H NMR spectra were acquired over pre-determined time intervals according to the speed of the reaction.

In order to estimate k_2 values for *p*-azido¹⁻ and *m*-azido¹⁻, a solution was prepared by dissolving 5 mg (0.58 μmol, 1 equivalent) of each Au₂₅ sample in 0.3 mL deuterated dichloromethane in an NMR tube. A t_0 (time zero) ¹H NMR spectrum was taken of this sample containing only the azide-modified Au₂₅ sample. A stock solution of **BCN_{exo}-OH** was prepared by dissolving 16 mg of **BCN_{exo}-OH** in 100 μL deuterated dichloromethane, from which 10 μL (containing 1.6 mg (10.6 μmol, 18 equivalents) **BCN_{exo}-OH**) was added to the NMR tube containing the Au₂₅ sample, and ¹H NMR spectra were acquired over pre-determined time intervals according to the speed of the reaction.

Second order rate constants were determined by plotting the 1/[azide] versus time, where the slope gives the rate constant (k_2). In order to determine [azide] at each time interval, in each time zero NMR spectrum, the ratio of a signal integral in the parent azide (either in the free thiol or Au₂₅ sample) to the signal integral of residual protio CH₂Cl₂ in the sample was determined, to give the 'time zero azide signal'. After addition of **BCN_{exo}-OH** to each sample, the ratio of the

integral of this decreasing signal in each acquired ^1H NMR spectra versus the integral of the initial ‘time zero azide signal’ was calculated and multiplied by the initial concentration of azide at time zero (0.0019 M) to give [azide] at each time interval. Experiments were performed in duplicate.

5.6.5.2 Kinetic Measurements for *p*-azidophenylethanethiol

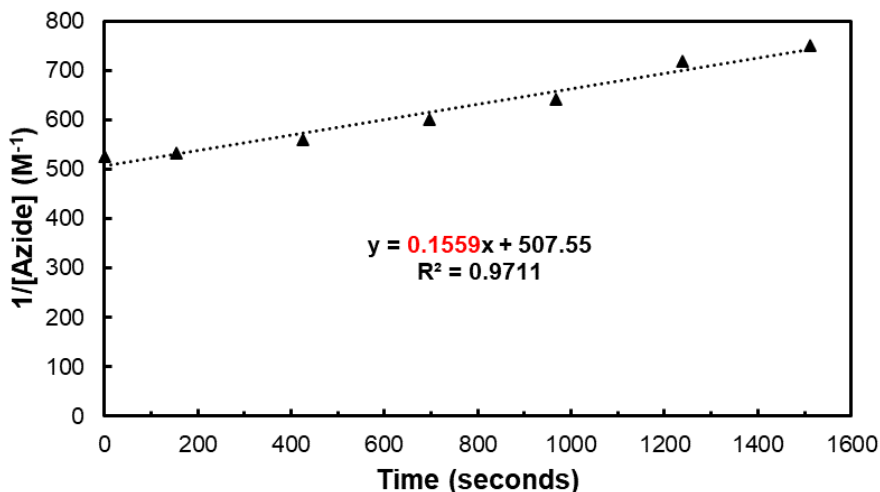


Figure S5.33. Second order kinetics graph for *p*-azidophenylethanethiol with $\text{BCN}_{\text{exo}}\text{-OH}$ (Trial 1).

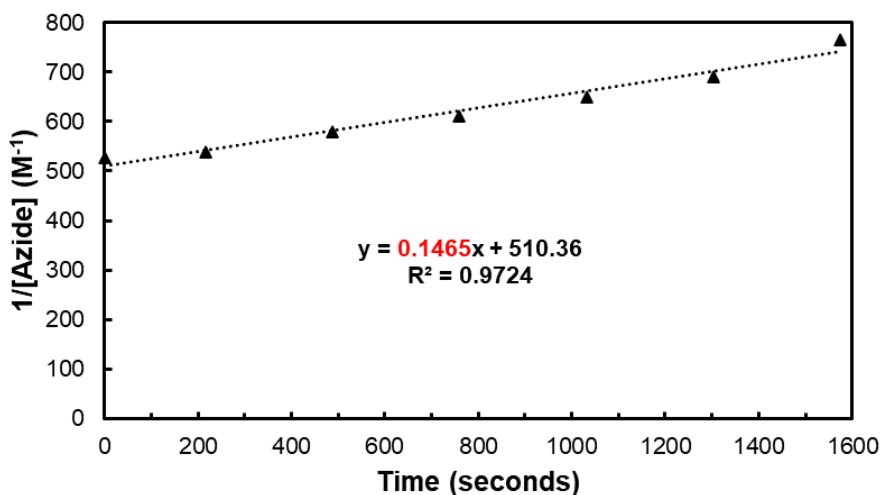


Figure S5.34. Second order kinetics graph for *p*-azidophenylethanethiol with $\text{BCN}_{\text{exo}}\text{-OH}$ (Trial 2).

5.6.5.3 Kinetic Measurements for *m*-azidophenylethanethiol

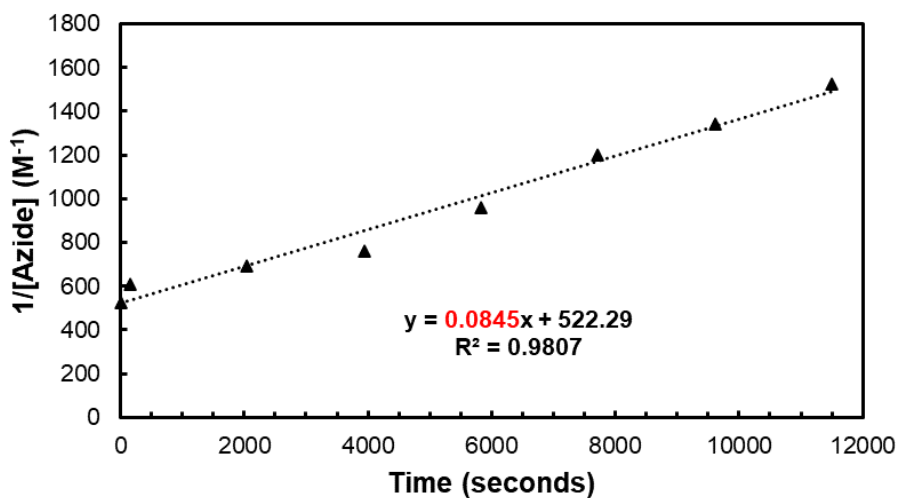


Figure S5.35. Second order kinetics graph for *m*-azidophenylethanethiol with $\text{BCN}_{\text{exo}}\text{-OH}$ (Trial 1).

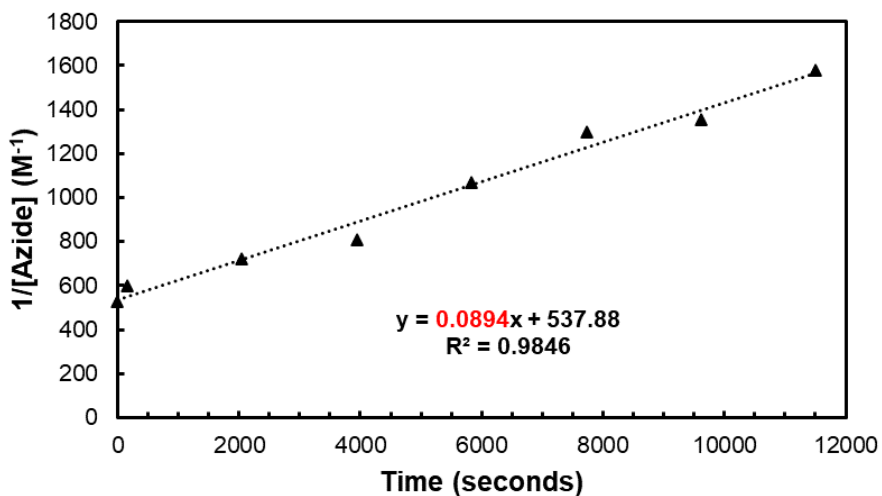


Figure S5.36. Second order kinetics graph for *m*-azidophenylethanethiol with $\text{BCN}_{\text{exo}}\text{-OH}$ (Trial 2).

5.6.5.4 Kinetic Measurements for *o*-azidophenylethanethiol

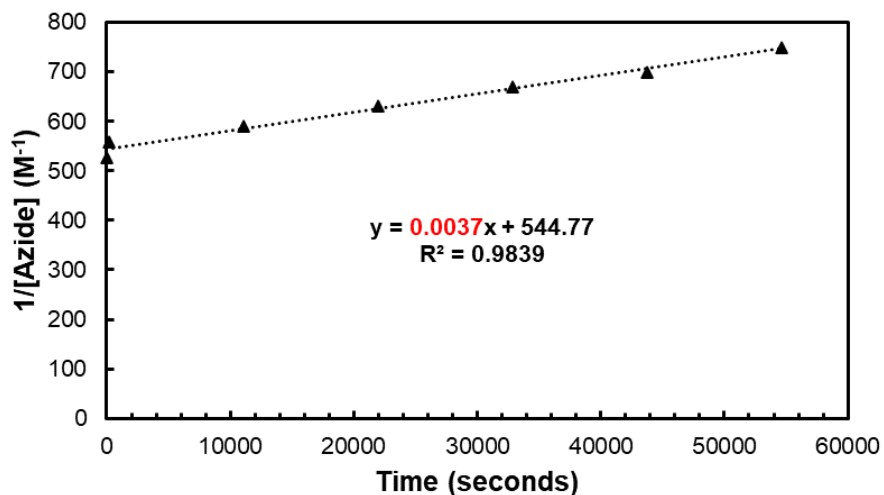


Figure S5.37. Second order kinetics graph for *o*-azidophenylethanethiol with $\text{BCN}_{\text{exo-OH}}$ (Trial 1).

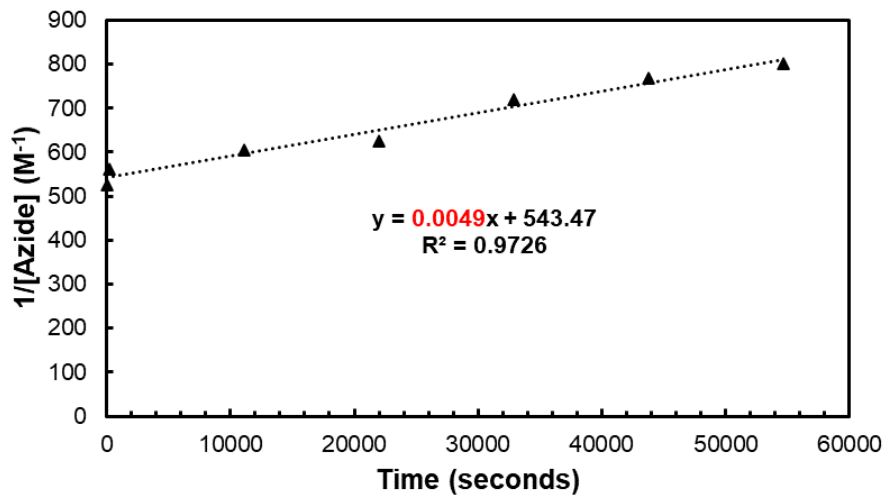


Figure S5.38. Second order kinetics graph for *o*-azidophenylethanethiol with $\text{BCN}_{\text{exo-OH}}$ (Trial 2).

5.6.5.5 Kinetic Measurements for $[(\text{CH}_3-(\text{CH}_2)_7)_4\text{N}][\text{Au}_{25}(\text{SCH}_2\text{CH}_2-p\text{-C}_6\text{H}_4\text{-N}_3)_{18}]$ ($p\text{-azido}^{1-}$)

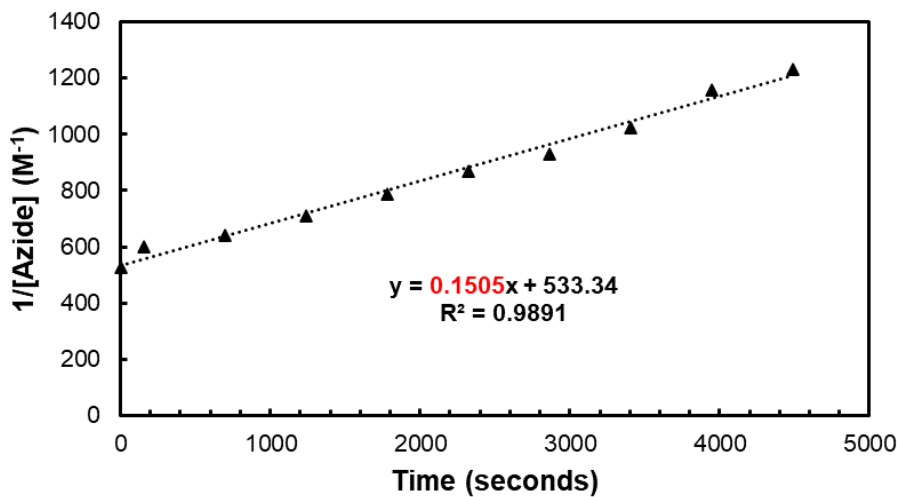


Figure S5.39. Second order kinetics graph for $p\text{-azido}^{1-}$ with $\text{BCN}_{\text{exo}}\text{-OH}$ (Trial 1).

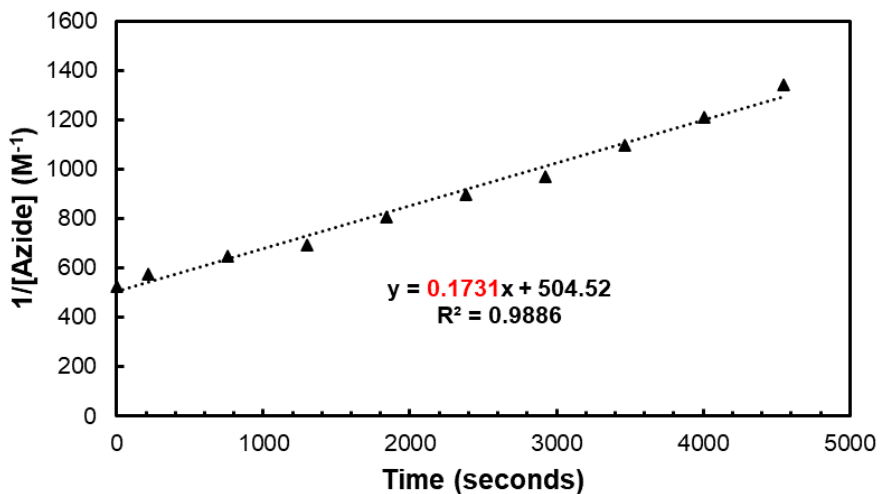


Figure S5.40. Second order kinetics graph for $p\text{-azido}^{1-}$ with $\text{BCN}_{\text{exo}}\text{-OH}$ (Trial 2).

5.6.5.6 Kinetic Measurements for $[(\text{CH}_3-(\text{CH}_2)_7)_4\text{N}][\text{Au}_{25}(\text{SCH}_2\text{CH}_2-m\text{-C}_6\text{H}_4\text{-N}_3)_{18}]$ ($m\text{-azido}^{1-}$)

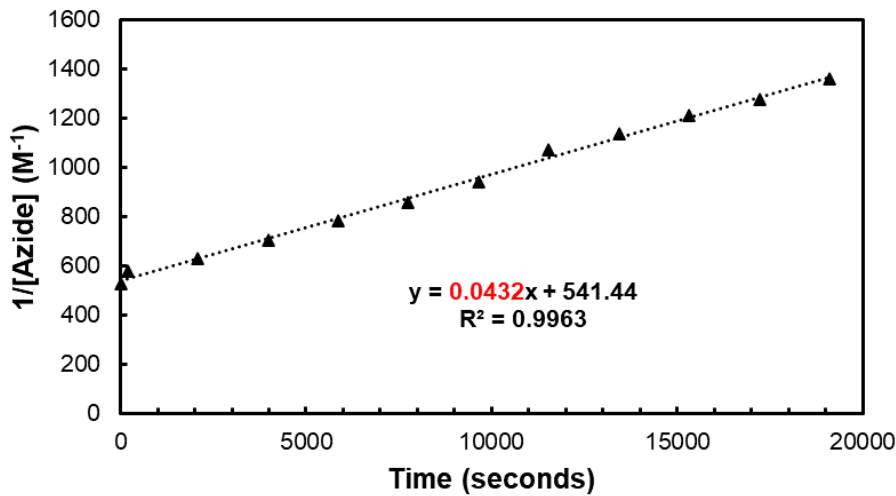


Figure S5.41. Second order kinetics graph for $m\text{-azido}^{1-}$ with $\text{BCN}_{\text{exo}}\text{-OH}$ (Trial 1).

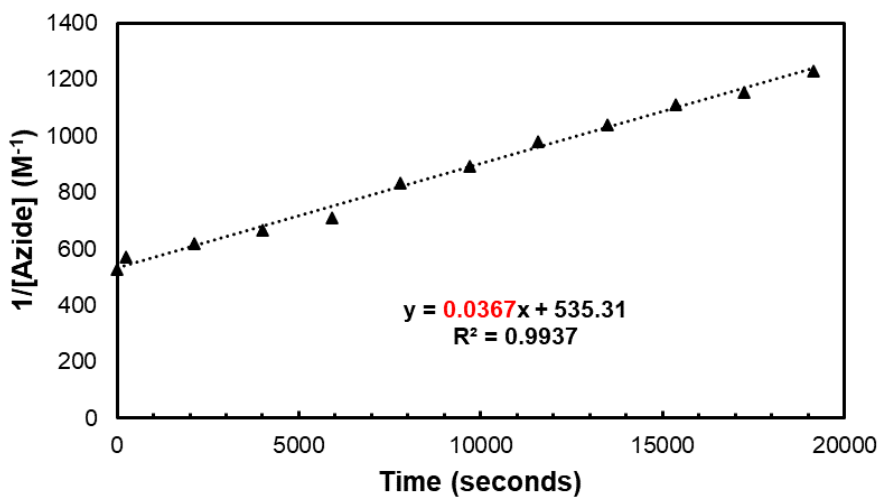


Figure S5.42. Second order kinetics graph for $m\text{-azido}^{1-}$ with $\text{BCN}_{\text{exo}}\text{-OH}$ (Trial 2).

5.6.6 Crystallographic Information

5.6.6.1 Data Collection and Processing

The sample *p*-azido⁰, *m*-azido⁰ and *o*-azido⁰ were crystallized out of a 1:4 mixture of toluene:ethanol over two weeks at ambient conditions. A crystal of each sample was mounted on a Mitegen polyimide micromount with a small amount of Paratone N oil. All X-ray measurements were made on a Bruker Kappa Axis Apex2 diffractometer at a temperature of 110 K.

The unit cell dimensions for *p*-azido⁰ were determined from a symmetry constrained fit of 9989 reflections with $4.42^\circ < 2\theta < 39.64^\circ$. The data collection strategy was a number of ω and ϕ scans which collected data up to 39.778° (2θ). The unit cell dimensions for *o*-azido⁰ were determined from a symmetry constrained fit of 9919 reflections with $5.92^\circ < 2\theta < 49.22^\circ$. The data collection strategy was a number of w and j scans which collected data up to 49.458° (2θ). The unit cell dimensions for *o*-azido⁰ were determined from a symmetry constrained fit of 9821 reflections with $4.86^\circ < 2\theta < 58.52^\circ$.

The frame integration was performed using SAINT.³ The resulting raw data were scaled and absorption corrected using a multi-scan averaging of symmetry equivalent data using SADABS.⁴

5.6.5.2 Structure Solution and Refinement

The structures for *p*-azido⁰, *m*-azido⁰ and *o*-azido⁰ was solved by using a dual space methodology using the SHELXT program.⁵ All non-hydrogen atoms were obtained from the initial solution. The hydrogen atoms were introduced at idealized positions and were allowed to ride on the parent atom. The structural model was fit to the data using full matrix least-squares based on F^2 . The calculated structure factors included corrections for anomalous dispersion from the usual tabulation. The structure was refined using the SHELXL program from the SHELXTL suite of crystallographic software.⁶ For all structures, the aryl-azide groups exhibited significant disorder and were refined using available restraints in the SHELXTL software. Graphic plots were produced using the Mercury program suite. Additional information and other relevant literature references can be found in the reference section of this website (<http://xray.chem.uwo.ca>).

5.6.6.3 Summary of Crystal Data for $[(\text{CH}_3-(\text{CH}_2)_7)_4\text{N}][\text{Au}_{25}(\text{SCH}_2\text{CH}_2-p\text{-C}_6\text{H}_4\text{-N}_3)_{18}] (p\text{-azido}^{1-})$

See **Section 4.6.4.3** for crystallographic summary of $[(\text{CH}_3-(\text{CH}_2)_7)_4\text{N}][\text{Au}_{25}(\text{SCH}_2\text{CH}_2-p\text{-C}_6\text{H}_4\text{-N}_3)_{18}] (p\text{-azido}^{1-})$.

5.6.6.4 Summary of Crystal Data for $[\text{Au}_{25}(\text{SCH}_2\text{CH}_2-p\text{-C}_6\text{H}_4\text{-N}_3)_{18}] (p\text{-azido}^0)$

Formula	$\text{C}_{158}\text{H}_{160}\text{Au}_{25}\text{N}_{54}\text{S}_{18}$
Formula Weight (<i>g/mol</i>)	8316.63
Crystal Dimensions (<i>mm</i>)	$0.226 \times 0.023 \times 0.015$
Crystal Color and Habit	black needle
Crystal System	triclinic
Space Group	P -1
Temperature, K	110
a , Å	20.518(7)
b , Å	24.356(10)
c , Å	30.469(14)
α , °	92.58(3)
β , °	93.561(19)
γ , °	97.12(2)
V , Å ³	15059(11)

Number of reflections to determine final unit cell	9989
Min and Max 2θ for cell determination, °	4.42, 39.64
Z	3
F(000)	11247
ρ (g/cm^3)	2.751
λ , Å, (MoK α)	0.71073
μ , (cm^{-1})	18.429
Diffractometer Type	Bruker Kappa Axis Apex2
Scan Type(s)	phi and omega scans
Max 2θ for data collection, °	39.778
Measured fraction of data	0.990
Number of reflections measured	270892
Unique reflections measured	27398
R_{merge}	0.1593
Number of reflections included in refinement	27398
Cut off Threshold Expression	$I > 2\sigma(I)$
Structure refined using	full matrix least-squares using F^2
Weighting Scheme	$w=1/[\sigma^2(F_o^2)+(0.0288P)^2+531.4702P]$ where $P=(F_o^2+2F_c^2)/3$

Number of parameters in least-squares	3412
R ₁	0.0467
wR ₂	0.0911
R ₁ (all data)	0.0965
wR ₂ (all data)	0.1102
GOF	1.021
Maximum shift/error	0.001
Min & Max peak heights on final ΔF Map (e ⁻ /Å)	-1.550, 1.852

Where:

$$R_1 = \frac{\sum (|F_o| - |F_c|)}{\sum F_o}$$

$$wR_2 = \left[\frac{\sum w(F_o^2 - F_c^2)^2}{\sum w F_o^4} \right]^{1/2}$$

$$GOF = \left[\frac{\sum w(F_o^2 - F_c^2)^2}{(\text{No. of reflns.} - \text{No. of params.})} \right]^{1/2}$$

5.6.6.5 Summary of Crystal Data for [Au₂₅(SCH₂CH₂-*m*-C₆H₄-N₃)₁₈ (*m*-azido⁰)

Formula	C ₁₄₄ H ₁₄₄ Au ₂₅ N ₅₄ S ₁₈
Formula Weight (g/mol)	8132.37
Crystal Dimensions (mm)	0.052 × 0.032 × 0.019
Crystal Color and Habit	black prism

Crystal System	monoclinic
Space Group	P 2 ₁ /c
Temperature, K	110
<i>a</i> , Å	18.808(6)
<i>b</i> , Å	21.725(7)
<i>c</i> , Å	22.897(8)
α, °	90
β, °	106.885(18)
γ, °	90
<i>V</i> , Å ³	8952(5)
Number of reflections to determine final unit cell	9919
Min and Max 2θ for cell determination, °	5.92, 49.22
<i>Z</i>	2
F(000)	7298
ρ (g/cm ³)	3.017
λ, Å, (MoKα)	0.71073
μ, (cm ⁻¹)	20.663
Diffractometer Type	Bruker Kappa Axis Apex2
Scan Type(s)	phi and omega scans

Max 2θ for data collection, °	49.458
Measured fraction of data	0.994
Number of reflections measured	133112
Unique reflections measured	15188
R _{merge}	0.1770
Number of reflections included in refinement	15188
Cut off Threshold Expression	I > 2sigma(I)
Structure refined using	full matrix least-squares using F ²
Weighting Scheme	w=1/[sigma ² (Fo ²)+(0.0273P) ²] where P=(Fo ² +2Fc ²)/3
Number of parameters in least-squares	1010
R ₁	0.0399
wR ₂	0.0762
R ₁ (all data)	0.0766
wR ₂ (all data)	0.0838
GOF	0.857
Maximum shift/error	0.001
Min & Max peak heights on final ΔF Map (e ⁻ /Å)	-2.019, 2.641

Where:

$$R_1 = \Sigma (|F_o| - |F_c|) / \Sigma F_o$$

$$wR_2 = [\sum (w(F_o^2 - F_c^2)^2) / \sum (w F_o^4)]^{1/2}$$

$$GOF = [\sum (w(F_o^2 - F_c^2)^2) / (\text{No. of reflns.} - \text{No. of params.})]^{1/2}$$

5.6.6.6 Summary of Crystal Data for [Au₂₅(SCH₂CH₂-o-C₆H₄-N₃)₁₈] (o-azido⁰)

Formula	C ₁₄₄ H ₁₄₄ Au ₂₅ N ₅₄ S ₁₈
Formula Weight (g/mol)	8132.37
Crystal Dimensions (mm)	0.137 × 0.123 × 0.033
Crystal Color and Habit	black prism
Crystal System	triclinic
Space Group	P -1
Temperature, K	110
<i>a</i> , Å	17.243(7)
<i>b</i> , Å	17.985(6)
<i>c</i> , Å	18.242(8)
α, °	97.476(11)
β, °	109.976(14)
γ, °	113.353(10)
<i>V</i> , Å ³	4644(3)
Number of reflections to determine final unit cell	9821

Min and Max 2θ for cell determination, $^{\circ}$	4.86, 58.52
Z	1
F(000)	3649
ρ (g/cm^3)	2.908
λ , \AA , (MoK α)	0.71073
μ , (cm^{-1})	19.914
Diffractionmeter Type	Bruker Kappa Axis Apex2
Scan Type(s)	phi and omega scans
Max 2θ for data collection, $^{\circ}$	58.736
Measured fraction of data	0.998
Number of reflections measured	118552
Unique reflections measured	25346
R_{merge}	0.0531
Number of reflections included in refinement	25346
Cut off Threshold Expression	$I > 2\sigma(I)$
Structure refined using	full matrix least-squares using F^2
Weighting Scheme	$w=1/[\sigma^2(F_o^2)+(0.0350P)^2+10.8644P]$ where $P=(F_o^2+2F_c^2)/3$
Number of parameters in least-squares	1505

R ₁	0.0341
wR ₂	0.0769
R ₁ (all data)	0.0658
wR ₂ (all data)	0.0859
GOF	1.069
Maximum shift/error	0.008
Min & Max peak heights on final ΔF Map (e ⁻ /Å)	-1.999, 2.244

Where:

$$R_1 = \sum (|F_o| - |F_c|) / \sum F_o$$

$$wR_2 = [\sum (w(F_o^2 - F_c^2)^2) / \sum (w F_o^4)]^{1/2}$$

$$GOF = [\sum (w(F_o^2 - F_c^2)^2) / (\text{No. of reflns.} - \text{No. of params.})]^{1/2}$$

5.6.7 References – Supporting Information

1. Gunawardene, P.N.; Corrigan, J.F.; Workentin M.S., Golden Opportunity: A Clickable Azide-Functionalized [Au₂₅(SR)₁₈]⁻ Nanocluster Platform for Interfacial Surface Modifications. *J. Am. Chem. Soc.* **2019**, *141*, 11781-11785.
2. Dommerholt, J.; Schmidt, S.; Temming, R.; Hendriks, L. J. A.; Rutjes, F. P. J. T.; van Hest, J. C. M.; Lefeber, D. J.; Friedl, P.; van Delft, F. L., Readily Accessible Bicyclononynes for Bioorthogonal Labeling and Three-Dimensional Imaging of Living Cells. *Angew. Chem. Int. Ed.* **2010**, *49* (49), 9422-9425.
3. Bruker-AXS, SAINT *version 2013.8*, **2013**, Bruker-AXS, Madison, WI 53711, USA

4. Bruker-AXS, SADABS *version 2012.1*, **2012**, Bruker-AXS, Madison, WI 53711, USA
5. Sheldrick, G.M., *Acta Crystallographica Section A*. **2015**, *A71*, 3-8
6. Sheldrick, G. M., *Acta Crystallographica Section C*. **2015**, *C71*, 3-8
7. Gabe, E. J.; Le Page, Y.; Charland, J. P.; Lee, F. L. and White, P. S. *J. Appl. Cryst.* **1989**, *22*, 384-387

Chapter 6

6 Expanding the Frontiers of Ultrasmall Gold Nanocluster Surface Composition through Cluster-Surface Click Chemistry: A Ferrocenyl-Modified Au₂₅(SR)₁₈ Nanocluster

This chapter is being submitted as a short paper and is in manuscript format. Jonathan M. Wong is a co-author, along with professors Zhifeng Ding, John F. Corrigan and Mark S. Workentin.

Wong was a graduate student, who under the co-supervision of his supervisor, Prof. Zhifeng Ding, obtained the electrochemical measurements. The draft of the manuscript was written by the author and edited by Prof. Mark S. Workentin and Prof. John F. Corrigan.

6.1 Introduction

In recent years, monolayer-protected metallic nanomaterials have emerged as prominent frameworks within the fast-paced realm of nanomaterial research, whose functional complexity can be tuned through changes to the surface composition while retaining the properties of the internal core framework. Thiolate-protected gold nanomaterials are amongst the most widely-studied, largely due to the stability of core gold-gold interactions and ease-of-synthesis of structurally diverse thiol ligands, both of which facilitates not only their synthesis, but applications in settings which tend to be incompatible with other metallic or intermetallic frameworks. Distinguished by their larger size, functionally complex thiolate-protected gold nanoparticles (AuNPs) have found extensive use in a wide variety of biomedical applications¹⁻³. However, when the smaller atomically precise gold nanocluster (AuNC) size regime (<2nm) is accessed, discrete core electronic characteristics manifest molecular-type features that distinguishes these thiolate-protected AuNCs. Not only are they in smaller size, but their unique molecule-like properties (which are not observed with larger AuNPs) are contingent on the core framework and surface thiolate composition^{4, 5}. Furthermore, unlike their larger counterparts, gold nanoclusters can be synthesized in an atomically predictable and definable manner, permitting analysis by techniques that are largely reserved for small molecules such as X-ray crystallography and ¹H NMR spectroscopy. This has yielded an enormous understanding of the bonding features within the

framework and surface monolayer^{6, 7} and how their structure correlates with their properties^{8, 9}. Overall, these characteristics have rendered thiolate-protected gold nanoclusters very prominent nanomaterials in a variety of applications such as chemical sensing¹⁰⁻¹², catalysis¹³⁻¹⁷, nanomedicine¹⁸⁻²¹ and optical imaging²²⁻²⁴.

To date there exists an extensive library of atomically precise thiolate-protected gold nanoclusters, whose core framework and surface composition can be tuned through very sensitive changes to ratio of gold (III) precursor to thiol, the structure of the thiol ligand and reaction conditions⁶. The notoriously sensitive relationship between thiol structure and acquired core configuration has imparted their popular nickname: the so-called “magic clusters”.⁶ For this reason, the vast majority of magic clusters are synthesized using small inert thiol ligands, as more complex and functional thiol ligands are incompatible with direct synthetic strategies and does not lead to the desired core configuration. Application-based research on magic clusters is primarily reliant on place exchange chemistry, in which native inert ligands are replaced with functional thiol ligands. However, such strategies are limited by inability to establish total exchange of native thiol ligands and synthetic difficulties in developing functionally complex thiolated substrates, which often requires difficult protection/deprotection strategies. Cluster rearrangements are also observed.^{6, 25, 26} Given the significant application potential for thiolate-protected gold nanoclusters, these limitations of place exchange strategies warrant investigations to explore new methods for introducing functional complexity onto the nanocluster surface.

In contrast to direct syntheses and place exchange strategies towards introducing functional complexity on the nanocluster surface, we recently presented the first atomically precise $[\text{Au}_{25}(\text{SR})_{18}]^{-1}$ thiolate-protected gold nanocluster platform with a reactive azide moiety appended to each of the 18 surface ligands, $[(\text{CH}_3-(\text{CH}_2)_7)_4\text{N}][\text{Au}_{25}(\text{SCH}_2\text{CH}_2-p\text{-C}_6\text{H}_4\text{-N}_3)_{18}]$ (hereafter referred to as **6.1-azido** in current chapter (and referred to as **4.1-azido** in **Chapter 4** and **p-azido**⁰ in **Chapter 5**)²⁷. The novelty of this strategy is that this platform is capable of undergoing post-assembly surface modifications in which the surface azide groups orthogonally and chemoselectively reacts with strained-alkynes through the cluster-surface strain-promoted alkyne-azide cycloaddition (CS-SPAAC), without perturbing the internal core configuration. Unlike with place exchange chemistry, since all surface azide moieties are amenable to this cluster-surface reaction, it is possible to incorporate functional substrates with an appended strained-alkyne

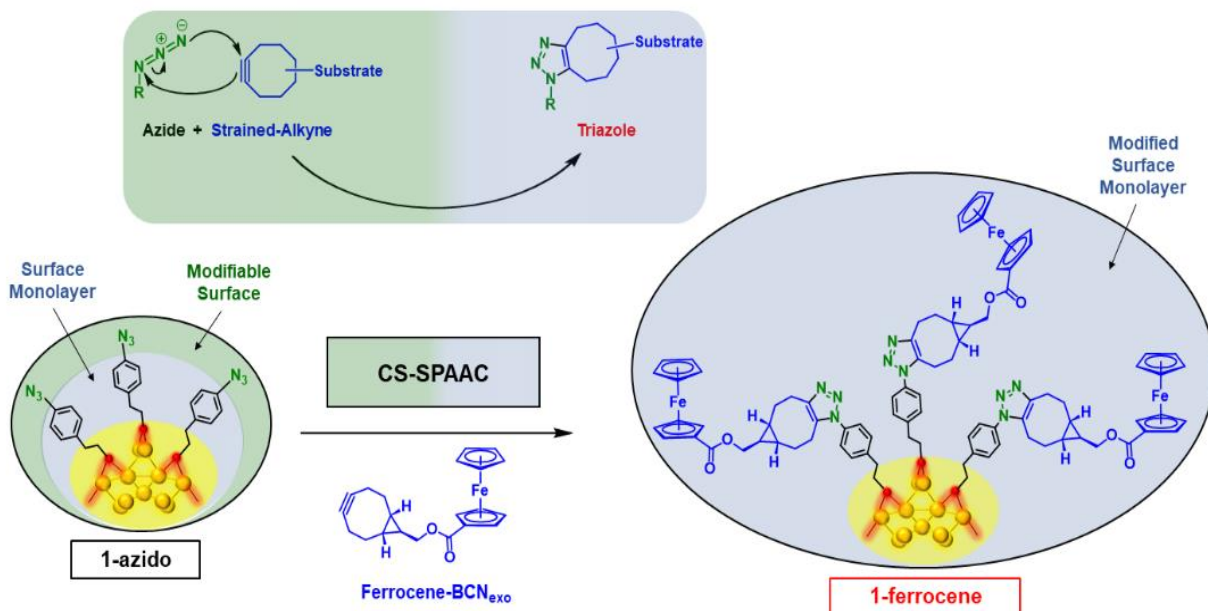
moiety to all surface ligand simply by using a slight excess of the strained-alkyne coupled substrate. This presents an exciting new avenue towards developing functional varieties of AuNC systems by transforming the surface monolayer through a high-yielding method that is dependent only on the creation of functional substrates possessing the complementary strained-alkyne moiety. For our seminal study, we demonstrated CS-SPAAC chemistry by reacting **6.1-azido** with an inert symmetrical strained-alkyne, (*Z*)-cyclooct-1-ene-5-yne. To demonstrate the true power of utilizing post-assembly CS-SPAAC chemistry, we herein report the first example of a $[\text{Au}_{25}\text{SR}_{18}]^{1-}$ nanocluster with ferrocenyl moieties on all the surface ligands, by reacting **6.1-azido** with a ferrocene-coupled strained-alkyne. We show that all surface ligands are amendable to the incorporation of the electroactive ferrocenyl moieties through CS-SPAAC, which is amongst the largest functional $\text{Au}_{25}\text{SR}_{18}$ nanocluster systems reported to date.

6.2 Results and Discussion

The first step in synthesizing azide-modified $[\text{Au}_{25}(\text{SR})_{18}]^{1-}$ clusters is the synthesis of the corresponding thiol ligand, *p*-azido-phenylethanethiol ($\text{HSCH}_2\text{CH}_2\text{-}p\text{-C}_6\text{H}_4\text{-N}_3$), which was carried out according to our previous established procedure²⁷ with one major modification. Specifically, the 4-step procedure was reduced to a 3-step procedure, which at the same time gives a higher overall yield of *p*-azido-phenylethanethiol (see **Section 5.6.2** for detailed synthesis). The synthesis of **6.1-azido** was carried out according to our previously reported procedure without modifications²⁷ (see **Section 4.6.2.8** for detailed synthesis). The ¹H NMR, IR and UV spectroscopic data and electrospray-ionization mass spectral data for **6.1-azido** was consistent with the data from our first report (see **Section 4.6.3.1** for spectra of **6.1-azido**)

In order to synthesize a ferrocene-coupled strained-alkyne, ferrocene-carboxylic acid was coupled to *exo*-bicyclo[6.1.0]non-4-yn-9-ol ($\text{BCN}_{\text{exo}}\text{-OH}$) in the presence of *N,N'*-dicyclohexylcarbodiimide (DCC) and 4-dimethylaminopyridine (DMAP) to give “**ferrocene-BCN_{exo}**”. Although kinetically less reactive, the aliphatic BCN was the strained-alkyne chosen for this study because it is more stable than other benzoannulated strained-alkynes (such as dibenzocyclooctyne, DBCO), can be synthesized on gram scale, and has minimal reactivity with thiols²⁸⁻³⁰. As with (*Z*)-cyclooct-1-ene-5-yne, the reaction between **6.1-azido** and a slight excess of **ferrocene-BCN_{exo}** is a simple mix and stir at room temperature, transforming **6.1-azido** into the

ferrocenated $[(\text{CH}_3-(\text{CH}_2)_7)_4\text{N}][\text{Au}_{25}(\text{SCH}_2\text{CH}_2-p\text{-C}_6\text{H}_4\text{-C}_{21}\text{H}_{22}\text{FeN}_3\text{O}_2)_{18}]$ (hereafter referred to as **6.1-ferrocenyl**) (**Scheme 6.1**) Removal of excess **ferrocene-BCN_{exo}** was accomplished through simple trituration with 2-propanol. The linear negative mode matrix-assisted laser desorption/ionization time-of-flight (MALDI-TOF) mass spectrum of the purified product contained a well-resolved peak at 14,662.1 Da that can be assigned to the parent $[\text{Au}_{25}(\text{SCH}_2\text{CH}_2-p\text{-C}_6\text{H}_4\text{-C}_{21}\text{H}_{22}\text{FeN}_3\text{O}_2)_{18}]^{1-}$ anion of the **6.1-ferrocenyl** cluster (expected $m/z = 14,562$ Da).



Scheme 6.1. Synthetic approach to the preparation of fully-ferrocenated $[(\text{CH}_3-(\text{CH}_2)_7)_4\text{N}][\text{Au}_{25}(\text{SCH}_2\text{CH}_2-p\text{-C}_6\text{H}_4\text{-C}_{21}\text{H}_{22}\text{FeN}_3\text{O}_2)_{18}]$ (**6.1-ferrocenyl**) through CS-SPAAC between $[(\text{CH}_3-(\text{CH}_2)_7)_4\text{N}][\text{Au}_{25}(\text{SCH}_2\text{CH}_2-p\text{-C}_6\text{H}_4\text{-N}_3)_{18}]$ (**6.1-azido**) and **ferrocene-BCN_{exo}**.

The completion of the CS-SPAAC reaction can easily be evaluated using IR spectroscopy. The IR spectrum of **6.1-azido** (**Figure 6.1a**, black) contains a large stretch at 2098 cm^{-1} that can be attributed to N-N stretches of the azide moiety, which disappears entirely upon quantitative consumption of all surface azide groups, as can be seen in the IR spectrum of **6.1-ferrocenyl** (**Figure 6.1a**, red). Furthermore, there is a signal at 1703 cm^{-1} in the IR spectrum of **6.1-ferrocenyl** that results from C=O stretches at the carbamate linkage, which is also present in the IR spectrum of **ferrocene-BCN_{exo}**.

The UV-Vis absorption spectrum of **6.1-azido** (**Figure 6.1b**, black) is nearly identical to the observed pattern of absorption maxima as other thiolate-protected Au₂₅(SR)₁₈ clusters,⁷ there are absorption maxima at 682, 443 and 404 nm. The absorption maxima at 682 nm has been previously assigned to an intraband metallic transition specifically within an Au₂₅ core framework, and any difference in the observed energy of this transition suggests the presence of a different core framework other than Au₂₅.⁶ As can be seen in the UV-Vis absorption spectrum of **6.1-ferrocenyl** (**Figure 6.1b**, red), both the energy and intensity of the transition at 682 nm remains after the CS-SPAAC reaction, indicating the retention of the Au₂₅ core framework. Similar to the UV-Vis absorption spectrum of **6.1-azido**, there are also transitions at 405 and 445 nm in the UV-Vis absorption spectrum of **6.1-ferrocenyl**. However, the absorption intensity of the transition at 445 nm is larger in **6.1-ferrocenyl**, which can be attributed to the newly incorporated surface ferrocene moieties that have their own low intensity d-d transition at 445 nm, which can also be seen in the UV-Vis absorption spectrum of **ferrocene-BCN_{exo}**.

Figure 6.1c (black) shows the ¹H NMR spectrum of **6.1-ferrocenyl** in deuterated dichloromethane at 23°C. As with the ¹H NMR spectrum of **6.1-azido**²⁷, there are signals arising from the tetraoctylammonium counterion at 0.87 (-CH₃), 1.25 (-CH₂-), 1.31 (-CH₂-) and 3.09 ppm (N⁺-CH₂-), verifying that the anionic core configuration of **6.1-ferrocenyl** predominates and minimal oxidation has occurred after the CS-SPAAC reaction (see **Figure S6.1** for full ¹H NMR spectrum). As in our first study in which (Z)-cyclooct-1-ene-5-yne and bicyclo[6.1.0]non-4-yn-9-ol were used, the CS-SPAAC reaction between **6.1-azido** and **ferrocene-BCN_{exo}** leads to a distinct change in the chemical environment of the aromatic ligand protons. In **6.1-azido**, each of the two binary sets of aromatic protons produce two signals in a 2:1 ratio that correlates with the 2:1 ratio of chemically inequivalent inner ligand to outer ligand ratio on the cluster surface, with the twelve inner ligands producing doublet signals at 6.80 and 7.12 ppm and the six outer ligands producing doublet signals at 6.86 and 7.17 ppm. As seen in **Figure 6.1c**, after the CS-SPAAC reaction, these two sets of doublets disappear entirely, and there are new sets of doublets at 7.36 and 7.15 ppm from the twelve inner ligands and another set of doublets at 7.29 and 7.14 ppm from the six outer ligands. The appearance of these new sets of doublets and their associated chemical shifts are the same regardless of the cyclooctyne structure, and hence can be used as an NMR fingerprint to evaluate the success and completion of the CS-SPAAC reaction.

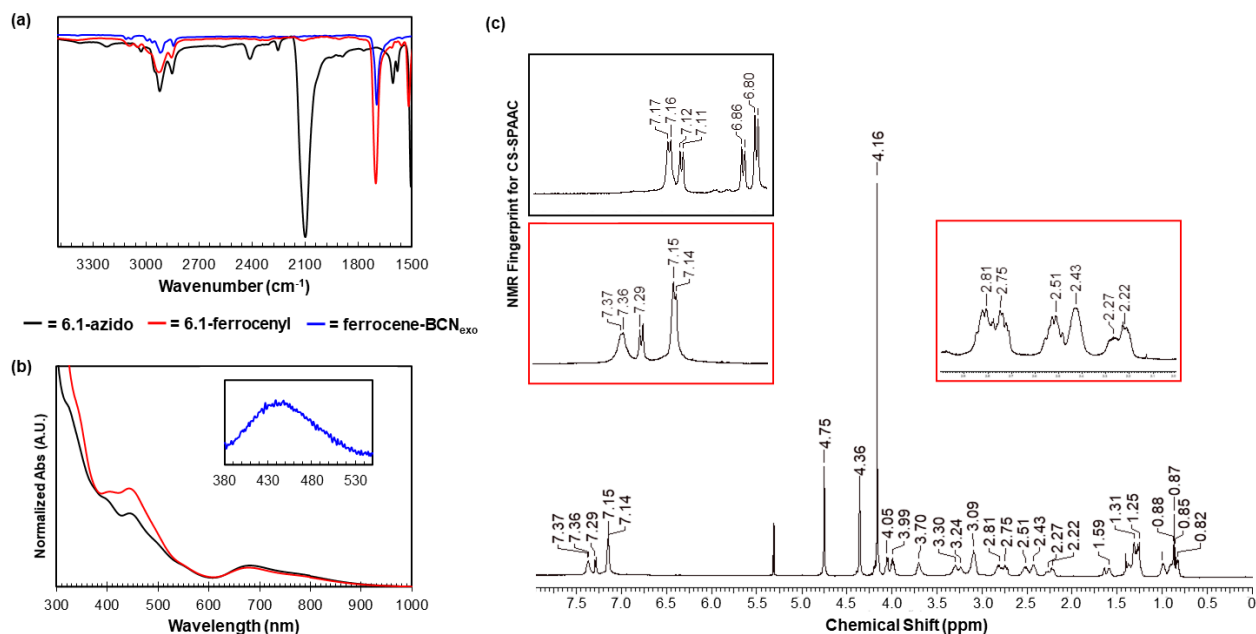


Figure 6.1. (a) ATR-IR spectrum of $[(\text{CH}_3-(\text{CH}_2)_7)_4\text{N}][\text{Au}_{25}(\text{SCH}_2\text{CH}_2-p\text{-C}_6\text{H}_4\text{-N}_3)_{18}]$ (**6.1-azido**) (black), $[(\text{CH}_3-(\text{CH}_2)_7)_4\text{N}][\text{Au}_{25}(\text{SCH}_2\text{CH}_2-p\text{-C}_6\text{H}_4\text{-C}_{21}\text{H}_{22}\text{FeN}_3\text{O}_2)_{18}]$ (**6.1-ferrocenyl**) (red) and **ferrocene-BCN_{exo}** (blue). (b) UV-Vis absorption spectrum of (**6.1-azido**) (black, 0.2 mM), **6.1-ferrocenyl** (red, 0.2 mM) and **ferrocene-BCN_{exo}** (blue, 5 μM) in dichloromethane at 23°C. (c) ^1H NMR spectrum of **6.1-ferrocenyl** taken in CD_2Cl_2 at 25°C. Red insets show expanded sections of spectrum of **6.1-ferrocenyl**, and black inset shows relevant expanded section of ^1H spectrum of **6.1-azido**, which was also taken in CD_2Cl_2 at 25°C.

After the CS-SPAAC reaction between **6.1-azido** and **ferrocene-BCN_{exo}**, there are also new sets of signals between 0.82 and 3.70 ppm that correspond to the eight membered ring. In our first study in which (*Z*)-cyclooct-1-ene-5-yne was reacted with **6.1-azido**, the symmetrical and achiral nature of the strained-alkyne eliminated the common problem of creating two isomers after the SPAAC reaction, and so these signals could be resolved in a 2:1 ratio that corresponded with the expected inner:outer ligand ratio. However, when chiral strained-alkynes are used, such as **BCN_{exo}**, two isomers form in what is typically an inequivalent ratio. Consequently, the signals that correspond to the protons in the eight membered ring and the methylene protons do not appear in a distinguishable 2:1 ratio. The incorporation of the **ferrocene-BCN_{exo}** to the cluster surface is accompanied by two new signals at 4.05 ppm and 3.99 ppm in a 2:1 ratio, which can be attributed to the α -methylene protons in **ferrocene-BCN_{exo}**. There are also new triplets at 4.36 and 4.75 ppm and a new singlet at 4.16 ppm that corresponds to the cyclopentadienyl protons of the newly incorporated ferrocenyl rings. However, unlike with all the other surface protons that are closer to

the central core, and produce signals in a 2:1 ratio due to the presence of the two distinguishable ligand environments, the cyclopentadienyl signals from the surface ferrocenyl groups appear as one signal instead of two. This indicates an interplay between the observed chemical inequivalence of the surface protons and the proximity to the central metallic core. Chemical inequivalence in the surface ligands is generated for the more proximal ligand components, but the ferrocenyl moieties are far enough away from the central core that the inner to outer ligand distinction becomes inconsequential, and the surface ferrocenyl become effectively magnetically equivalent.

The electrochemistry of **6.1-azido** and **6.1-ferrocenyl** was investigated by cyclic voltammetry (CV) and differential pulse voltammetry (DPV) using our previously reported conditions³¹. The CV spectra of **6.1-azido** and **6.1-ferrocenyl** can be found in the Supporting Information (**Figure S5.30** and **Figure S6.7**, respectively). In the DPV for **6.1-azido** (**Figure 6.2a**), two redox waves can be observed with formal potentials of 0.178 V and 0.405 V (vs. saturated calomel electrode (SCE)) in the potential range between 0.2 and 1.2 V. These two redox waves can be attributed to the conversion between $\text{Au}_{25}^{1-}/\text{Au}_{25}^0$ (0.178 V) and $\text{Au}_{25}^0/\text{Au}_{25}^{1+}$ (0.405 V), and the quasi-reversible nature of these waves in the anodic (black) and cathodic (red) scans is indicative of the stability of the -1, 0 and +1 forms of the Au_{25} nanoclusters. These are the benchmark peaks for the $\text{Au}_{25}\text{SR}_{18}$ core configuration. It should be noted that the formal potential of these waves for our azido-phenylethanethiolate protected Au_{25} nanocluster system differ from our previously reported values for the conventional phenylethanethiolate-protected Au_{25} nanocluster system, where the $\text{Au}_{25}^{1-}/\text{Au}_{25}^0$ redox event has a formal potential of 0.038 V and the $\text{Au}_{25}^0/\text{Au}_{25}^{1+}$ redox event has a formal potential of 0.280 V.³¹ This signifies the effect of the surface ligand structure on the electrochemical behaviour of the central gold core. There is another half-wave in the anodic scan with a potential of 1.062 V which is caused by the $\text{Au}_{25}^{1+}/\text{Au}_{25}^{2+}$ redox event. Due to the chemical instability of the +2 form, this half-wave has limited reversibility in the cathodic scan. We were unable to observe a $\text{Au}_{25}^{1-}/\text{Au}_{25}^{2-}$ redox event in either the cathodic or anodic scans, indicating that the surface azide-modified ligands make the -2 form of the cluster chemically inaccessible.

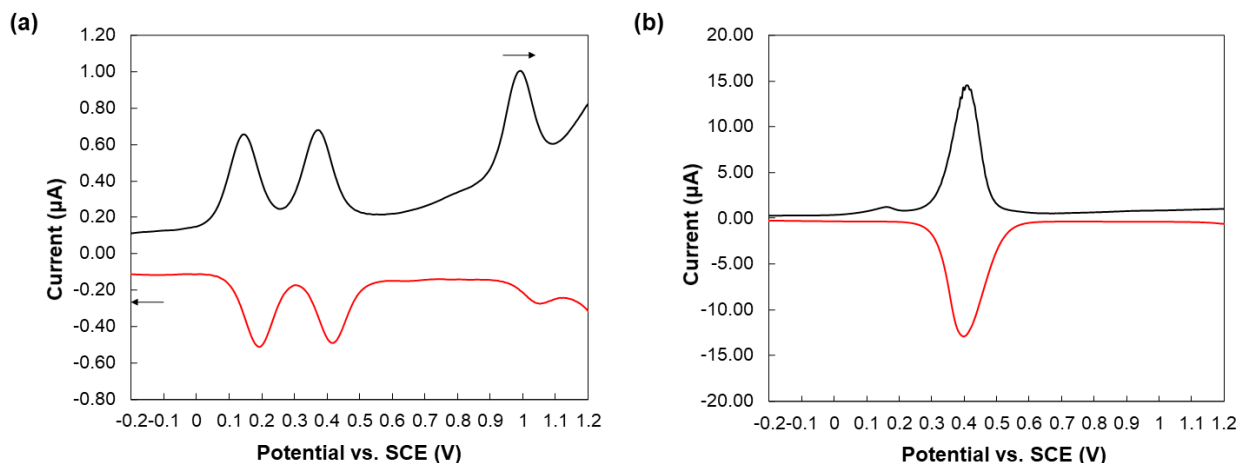


Figure 6.2. (a) Differential pulse voltammogram (DPV) of 0.1 mM solution of **6.1-azido** in 1:1 acetonitrile with 0.1M tetra-n-butylammonium perchlorate (TBAP) as a supporting electrolyte. (b) Differential pulse voltammogram (DPV) of 0.1 mM solution of **6.1-ferrocenyl** in 1:1 acetonitrile with 0.1M tetra-n-butylammonium perchlorate (TBAP) as a supporting electrolyte. Arrows indicate scanning potential direction. Note the different vertical scales for the two nanoclusters.

In the DPV of **6.1-ferrocenyl** (**Figure 6.2b**) there is a large quasi-reversible wave with a formal potential of 0.409 V (vs. SCE) which can be attributed to all surface ferrocenyl moieties undergoing a redox event. There is also a half-wave in the anodic scan with a formal potential of 0.172 V which is likely caused by the $\text{Au}_{25}^{1-}/\text{Au}_{25}^0$ redox event in the central core. Given that the regeneration of the parent -1 form of the nanocluster during the cathodic scan requires an approximate 20 electron transfer process into both the 18 surface ferrocenyl and internal gold core, the irreversibility of $\text{Au}_{25}^{1-}/\text{Au}_{25}^0$ wave is not surprising. Looking at the area under the half-waves at 0.172 V and 0.413 V in the anodic scan, the area of the half-wave from the expected 18 electron transfer process within the surface ferrocenyl moieties is approximately 20 times larger than the $\text{Au}_{25}^{1-}/\text{Au}_{25}^0$ single electron process within the cluster core, further indicating that all surface ferrocenyl moieties are electrochemically accessible.

6.3 Conclusions

In order to highlight the power of utilizing post-assembly surface modifications towards the development of functionally complex nanocluster systems, the development of the first example of a fully ferrocenated $[\text{Au}_{25}(\text{SR})_{18}]^{1-}$ (**6.1-ferrocenyl**) nanocluster framework is herein reported, which is the largest $[\text{Au}_{25}(\text{SR})_{18}]^{1-}$ nanocluster currently reported. This study not only demonstrates

that all surface azido groups in **6.1-azido** are accessible for CS-SPAAC, but that *all* surface ferrocene moieties are electrochemically accessible for pseudo-reversible redox chemistry. This demonstrates that CS-SPAAC chemistry not only bestows the ability to modify the surfaces of $[\text{Au}_{25}(\text{SR})_{18}]^{1-}$ in a nanoorthogonal manner (i.e. without altering the parent nanocluster structure), but can be done with substrates that retain their properties after incorporation. We are currently exploring other functional substrates to incorporate onto the surface $[\text{Au}_{25}(\text{SR})_{18}]^{1-}$ for more directed applications.

6.4 Acknowledgements

This work was funded by NSERC-DG and the University of Western Ontario. We thank D. Hairsine (MS Facility), K Jurcic (MALDI-MS Facility – Biochemistry).

6.5 References

1. Goddard, Z. R.; Marin, M. J.; Russell, D. A.; Searcey, M., Active targeting of gold nanoparticles as cancer therapeutics. *Chem. Soc. Rev.* **2020**, *49* (23), 8774-8789.
2. Popovtzer, A.; Mizrahi, A.; Motiei, M.; Bragilovski, D.; Lubimov, L.; Levi, M.; Hilly, O.; Ben-Aharon, I.; Popovtzer, R., Actively targeted gold nanoparticles as novel radiosensitizer agents: an in vivo head and neck cancer model. *Nanoscale* **2016**, *8* (5), 2678-2685.
3. Yeom, J.-H.; Lee, B.; Kim, D.; Lee, J.-k.; Kim, S.; Bae, J.; Park, Y.; Lee, K., Gold nanoparticle-DNA aptamer conjugate-assisted delivery of antimicrobial peptide effectively eliminates intracellular *Salmonella enterica* serovar Typhimurium. *Biomaterials* **2016**, *104*, 43-51.
4. Jin, R.; Li, G.; Sharma, S.; Li, Y.; Du, X., Toward Active-Site Tailoring in Heterogeneous Catalysis by Atomically Precise Metal Nanoclusters with Crystallographic Structures. *Chem. Rev.* **2021**, *121* (2), 567-648.
5. Takano, S.; Tsukuda, T., Chemically Modified Gold/Silver Superatoms as Artificial Elements at Nanoscale: Design Principles and Synthesis Challenges. *J. Am. Chem. Soc.* **2021**, *143* (4), 1683-1698.

6. Jin, R.; Zeng, C.; Zhou, M.; Chen, Y., Atomically Precise Colloidal Metal Nanoclusters and Nanoparticles: Fundamentals and Opportunities. *Chem. Rev.* **2016**, *116* (18), 10346-10413.
7. Kang, X.; Chong, H.; Zhu, M., Au₂₅(SR)₁₈: the captain of the great nanocluster ship. *Nanoscale* **2018**, *10* (23), 10758-10834.
8. Li, G.; Jin, R., Atomically Precise Gold Nanoclusters as New Model Catalysts. *Acc. Chem. Res.* **2013**, *46* (8), 1749-1758.
9. Li, G.; Jin, R., Gold Nanocluster-Catalyzed Semihydrogenation: A Unique Activation Pathway for Terminal Alkynes. *J. Am. Chem. Soc.* **2014**, *136* (32), 11347-11354.
10. Guan, G.; Zhang, S.-Y.; Cai, Y.; Liu, S.; Bharathi, M. S.; Low, M.; Yu, Y.; Xie, J.; Zheng, Y.; Zhang, Y.-W.; Han, M.-Y., Convenient purification of gold clusters by co-precipitation for improved sensing of hydrogen peroxide, mercury ions and pesticides. *Chem. Commun.* **2014**, *50* (43), 5703-5705.
11. Shu, T.; Wang, J.; Su, L.; Zhang, X., Chemical Etching of Bovine Serum Albumin-Protected Au₂₅ Nanoclusters for Label-Free and Separation-Free Ratiometric Fluorescent Detection of Tris(2-carboxyethyl)phosphine. *Anal. Chem.* **2016**, *88* (22), 11193-11198.
12. Wang, M.; Wu, Z.; Yang, J.; Wang, G.; Wang, H.; Cai, W., Au₂₅(SG)₁₈ as a fluorescent iodide sensor. *Nanoscale* **2012**, *4* (14), 4087-4090.
13. Kauffman, D. R.; Alfonso, D.; Matranga, C.; Ohodnicki, P.; Deng, X.; Siva, R. C.; Zeng, C.; Jin, R., Probing active site chemistry with differently charged Au₂₅^q nanoclusters (q = -1, 0, +1). *Chem. Sci.* **2014**, *5* (8), 3151-3157.
14. Li, G.; Abroshan, H.; Liu, C.; Zhuo, S.; Li, Z.; Xie, Y.; Kim, H. J.; Rosi, N. L.; Jin, R., Tailoring the Electronic and Catalytic Properties of Au₂₅ Nanoclusters via Ligand Engineering. *ACS Nano* **2016**, *10* (8), 7998-8005.
15. Wu, Z.; Jiang, D.-e.; Mann, A. K. P.; Mullins, D. R.; Qiao, Z.-A.; Allard, L. F.; Zeng, C.; Jin, R.; Overbury, S. H., Thiolate Ligands as a Double-Edged Sword for CO Oxidation on

CeO₂ Supported Au₂₅(SCH₂CH₂Ph)₁₈ Nanoclusters. *J. Am. Chem. Soc.* **2014**, *136* (16), 6111-6122.

16. Yoskamtorn, T.; Yamazoe, S.; Takahata, R.; Nishigaki, J.-i.; Thivasasith, A.; Limtrakul, J.; Tsukuda, T., Thiolate-Mediated Selectivity Control in Aerobic Alcohol Oxidation by Porous Carbon-Supported Au₂₅ Clusters. *ACS Catalysis* **2014**, *4* (10), 3696-3700.

17. Chong, H.; Zhu, M., Catalytic Reduction by Quasi-Homogeneous Gold Nanoclusters in the Liquid Phase. *ChemCatChem* **2015**, *7* (15), 2296-2304.

18. Goswami, N.; Zheng, K.; Xie, J., Bio-NCs – the marriage of ultrasmall metal nanoclusters with biomolecules. *Nanoscale* **2014**, *6* (22), 13328-13347.

19. Katla, S. K.; Zhang, J.; Castro, E.; Bernal, R. A.; Li, X., Atomically Precise Au₂₅(SG)₁₈ Nanoclusters: Rapid Single-Step Synthesis and Application in Photothermal Therapy. *ACS Appl. Mater. Interfaces* **2018**, *10* (1), 75-82.

20. Luo, Z.; Zheng, K.; Xie, J., Engineering ultrasmall water-soluble gold and silver nanoclusters for biomedical applications. *Chem. Commun.* **2014**, *50* (40), 5143-5155.

21. Wong, O. A.; Hansen, R. J.; Ni, T. W.; Heinecke, C. L.; Compel, W. S.; Gustafson, D. L.; Ackerson, C. J., Structure–activity relationships for biodistribution, pharmacokinetics, and excretion of atomically precise nanoclusters in a murine model. *Nanoscale* **2013**, *5* (21), 10525-10533.

22. Lin, C.-A. J.; Yang, T.-Y.; Lee, C.-H.; Huang, S. H.; Sperling, R. A.; Zanella, M.; Li, J. K.; Shen, J.-L.; Wang, H.-H.; Yeh, H.-I.; Parak, W. J.; Chang, W. H., Synthesis, Characterization, and Bioconjugation of Fluorescent Gold Nanoclusters toward Biological Labeling Applications. *ACS Nano* **2009**, *3* (2), 395-401.

23. Raut, S.; Chib, R.; Rich, R.; Shumilov, D.; Gryczynski, Z.; Gryczynski, I., Polarization properties of fluorescent BSA protected Au₂₅ nanoclusters. *Nanoscale* **2013**, *5* (8), 3441-3446.

24. Wu, X.; He, X.; Wang, K.; Xie, C.; Zhou, B.; Qing, Z., Ultrasmall near-infrared gold nanoclusters for tumor fluorescence imaging in vivo. *Nanoscale* **2010**, *2* (10), 2244-2249.

25. Das, A.; Li, T.; Nobusada, K.; Zeng, C.; Rosi, N. L.; Jin, R., Nonsuperatomic $[\text{Au}_{23}(\text{SC}_6\text{H}_{11})_{16}]^-$ Nanocluster Featuring Bipyramidal Au_{15} Kernel and Trimeric $\text{Au}_3(\text{SR})_4$ Motif. *J. Am. Chem. Soc.* **2013**, *135* (49), 18264-18267.
26. Das, A.; Li, T.; Li, G.; Nobusada, K.; Zeng, C.; Rosi, N. L.; Jin, R., Crystal structure and electronic properties of a thiolate-protected Au_{24} nanocluster. *Nanoscale* **2014**, *6* (12), 6458-6462.
27. Gunawardene, P. N.; Corrigan, J. F.; Workentin, M. S., Golden Opportunity: A Clickable Azide-Functionalized $[\text{Au}_{25}(\text{SR})_{18}]^-$ Nanocluster Platform for Interfacial Surface Modifications. *J. Am. Chem. Soc.* **2019**, *141* (30), 11781-11785.
28. Nguyen, S. S.; Prescher, J. A., Developing bioorthogonal probes to span a spectrum of reactivities. *Nat. Rev. Chem.* **2020**, *4* (9), 476-489.
29. Gunawardene, P. N.; Luo, W.; Polgar, A. M.; Corrigan, J. F.; Workentin, M. S., Highly Electron-Deficient Pyridinium-Nitrones for Rapid and Tunable Inverse-Electron-Demand Strain-Promoted Alkyne-Nitrone Cycloaddition. *Org. Lett.* **2019**, *21* (14), 5547-5551.
30. Bilodeau, D. A.; Margison, K. D.; Serhan, M.; Pezacki, J. P., Bioorthogonal Reactions Utilizing Nitrones as Versatile Dipoles in Cycloaddition Reactions. *Chem. Rev.* **2021**.
31. Hesari, M.; Workentin, M. S.; Ding, Z., NIR electrochemiluminescence from Au_{25}^- nanoclusters facilitated by highly oxidizing and reducing co-reactant radicals. *Chem. Sci.* **2014**, *5* (10), 3814-3822.

6.6 Supporting Information

6.6.1 General Methods and Reagents

Reagents and Solvents. The following materials were used as received. Potassium thioacetate (98%), zinc dust ($<10\mu\text{m}$, $\geq 98\%$), sodium azide ($\geq 99.5\%$), gold (III) chloride trihydrate ($\geq 99.9\%$ trace metal basis), tetraoctylammonium bromide (98%), sodium borohydride ($\geq 98\%$), 1,5-

cyclooctadiene ($\geq 99\%$), bromine (reagent grade), potassium *tert*-butoxide solution (1.0M in THF) and dichloromethane-D₂ (CD₂Cl₂, 99.5 atom %D) were purchased from Sigma-Aldrich (Millipore Sigma). 4-nitrophenylethyl bromide was purchased from Oakwood Chemicals. Sodium chloride, sodium hydroxide pellets and tetrahydrofuran were purchased from Fischer Scientific. Technical grade ammonium chloride, magnesium sulphate, hexanes, dichloromethane, ethyl acetate, 12M hydrochloric acid, di-ethyl ether, dimethyl sulfoxide, sodium nitrite, methanol, toluene, isopropanol, acetonitrile and pentane were purchased from Caledon. Chloroform-D₁ (CDCl₃, 99.8 atom %D) was purchased from Cambridge Isotope Laboratories. Ethanol (anhydrous) was purchased from Commercial Alcohols.

Unless otherwise state, all reactions were performed at ambient conditions.

NMR Spectroscopy. ¹H and ¹³C{¹H} spectra were recorded on either a Bruker AvIII HD 400 spectrometer or Varian INOVA 600 spectrometer, as indicated. ¹H NMR spectra are reported as δ in units of parts per million (ppm), and referenced against residual protio chloroform (7.27 ppm, s), dimethylsulfoxide (2.50 ppm, quin) or dichloromethane (5.32 ppm, t), as indicated. Multiplicities are reported as follows: s (singlet), d (doublet), t (triplet), q (quartet), quin (quintuplet), m (multiplet) and br (broad signal). Coupling constants are reported as a *J* value in Hertz (Hz) according to the spectrometer frequency. The number of protons (*n*) for a given resonance is indicated as *n*H, and is based on spectral integration values. ¹³C{¹H} NMR spectra are reported as δ in units of parts per million (ppm) and referenced against the indicated deuterated solvent: chloroform-D₁ (77.0 ppm, t) or dichloromethane-D₂ (54.0 ppm, quin).

Mass Spectrometry. Electrospray ionization (ESI) mass spectra were obtained in either positive-ion or negative-ion mode using a Bruker microTOF II spectrometer. To obtain the ESI spectrum of [Au₂₅(SCH₂CH₂-*p*-C₆H₄-N₃)₁₈]⁻ nanoclusters (obtained in negative-ion mode), a sample was dissolved in 1:5 toluene:methanol (10mg/mL). We generally found that in order to obtain mass spectra of [Au₂₅SR₁₈] clusters, the sample solution must contain some methanol in order to minimize excessive fragmentation. Matrix-assisted laser desorption/ionization-time of flight (MALDI-TOF) mass spectra were obtained using an AB Sciex 5800 TOF/TOF system. To obtain the MALDI-TOF spectrum of [Au₂₅(SCH₂CH₂-*p*-C₆H₄-C₈H₁₀N₃)₁₈]⁻ nanoclusters (obtained in linear negative mode), a 1g/L sample solution was mixed with a 10g/L solution of trans-2-[3-(4-

tert-butylphenyl)-2-methyl-2-propenylidene]malononitrile (DCTB) in a ratio of 1:400 by mass. Data acquisition and data processing were respectively done using a TOF TOF Series Explore and Data Explorer (both from AB Sciex). The laser pulse rate was set to 400Hz. The mass spectrum was collected as a sum of 1000 shots.

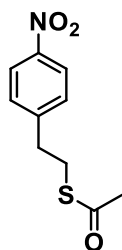
UV-Visible (UV-Vis) Spectroscopy. UV-Vis absorption spectra were recorded using a Cary 5000 scan instrument using standard quartz cells (1cm path length) with a scan range of 200-1000nm. Samples were dissolved in the indicated solvents at the indicated concentrations. The background spectrum of the indicated solvent was subtracted internally by the software.

Infrared (IR) spectroscopy. Attenuated total reflectance IR (ATR-IR) spectra were recorded using a PerkinElmer Spectrum Two FT-IR spectrometer.

Electrochemistry. All cyclic voltammograms and differential pulse voltammograms were performed on a CHI 610A electrochemical analyzer (CH Instruments, Austin, Texas). A three-electrode system was used: the working electrode was a 2 mm diameter platinum disc inlaid in a glass (Pt) electrode; two Pt coils served as the counter and reference electrodes, respectively. Prior to each experiment, the glass electrochemical cell was cleaned in an acid bath overnight, then placed in a base bath to prevent any contamination. The platinum disc electrode was polished using 0.3 micron then 0.05 micron alumina polishing slurry (CH Instruments) until a mirror like finish was obtained. The electrode was then subjected to electrochemical cleaning by performing cyclic voltammetry in 0.1 M dilute sulfuric acid solution for 200 cycles between the cathodic and anodic potential limits. The electrode was then rinsed with ultra-pure Type-1 water and left to fully dry before use. Each electrochemical cell consisted of a 0.67mg/mL solution of gold clusters dispersed in a 1:1 anhydrous acetonitrile:benzene mixture (Sure/Seal™ acetonitrile and benzene, Sigma Aldrich), with 0.1M tetrabutylammonium perchlorate (TBAP, Sigma Aldrich) being added as the supporting electrolyte. All electrochemical cells were assembled in an inert Ar atmosphere.

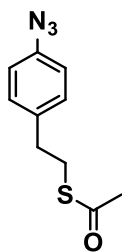
6.6.2 Experimental Procedures

6.6.2.1 Synthesis of *p*-nitro-phenylethanethioacetate



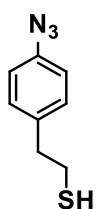
See **Section 4.6.2.1** for detailed synthesis and characterization data of ***p*-nitro-phenylethanethioacetate**.

6.6.2.2 Synthesis of *p*-azido-phenylethanethioacetate



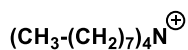
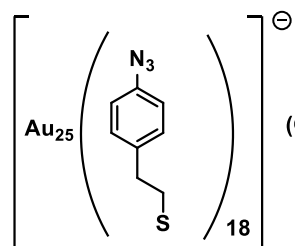
See **Section 5.6.2.2** for detailed synthesis and characterization data of ***p*-azido-phenylethanethioacetate**.

6.6.2.3 Synthesis of *p*-azido-phenylethanethiol



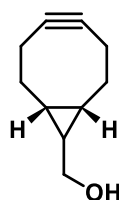
See **Section 4.6.2.4** for detailed synthesis and characterization data of ***p*-azido-phenylethanethiol**.

6.6.2.4 Synthesis of $[(\text{CH}_3-(\text{CH}_2)_7)_4\text{N}][\text{Au}_{25}(\text{SCH}_2\text{CH}_2-p\text{-C}_6\text{H}_4\text{-C}_8\text{H}_{10}\text{N}_3)_{18}]$ (6.1-azido)



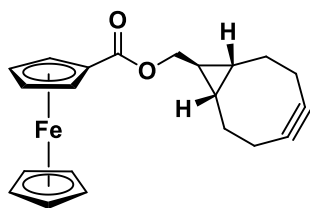
See **Section 4.6.2.8** for detailed synthesis and characterization data of $[(\text{CH}_3-(\text{CH}_2)_7)_4\text{N}][\text{Au}_{25}(\text{SCH}_2\text{CH}_2-p\text{-C}_6\text{H}_4\text{-C}_8\text{H}_{10}\text{N}_3)_{18}]$ (**6.1-azido**).

6.6.2.5 Synthesis of $\text{BCN}_{exo}\text{-OH}$



Synthesized according to Dommerholt *et al.*¹ See **Section 2.6.2.6** for characterization data.

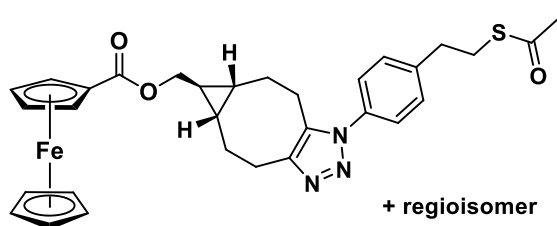
6.6.2.6 Synthesis of Ferrocene- BCN_{exo}



To a solution of 0.52 g (2.3 mmol, 1 eq) ferrocenecarboxylic acid and 0.14 g (1.2 mmol, 0.5 eq) 4-dimethylaminopyridine in 25 mL dichloromethane was added 0.58 g (2.8 mmol, 1.2 eq) *N,N'*-dicyclohexylcarbodiimide in 5 mL dichloromethane. The resulting solution was stirred for 10 minutes, after which 0.42 g (2.8 mmol, 1.2 eq) **BCN_{exo}-OH** in 5 mL dichloromethane was added. The solution was stirred for 5 hours, after which the solvent was removed by rotary evaporation and the resulting crude residue was purified by flash column chromatography (100% dichloromethane) to give **ferrocene-BCN_{exo}** as a light orange solid in 72% yield (0.6 g). ¹H NMR (CD₂Cl₂, 400 MHz): δ (ppm) 4.77 (t, 2H, *J* = 4 Hz), 4.39 (t, 2H, *J* = 4 Hz), 4.19 (s, 5H), 4.11 (d, 2H, *J* = 8 Hz), 2.43 (m, 2H), 2.27 (m, 2H), 2.14 (m, 2H), 1.42 (m, 2H), 0.80 (m, 3H). ¹³C NMR (CD₂Cl₂, 400 MHz): δ (ppm) 171.9, 99.2, 72.3, 71.8, 70.6, 70.3, 68.7, 33.9, 24.3, 23.6, 21.8. HRMS (ESI) *m/z* calc. for C₂₁H₂₂FeO₂ (M⁺): 362.0969, found: 362.0982. IR

(ATR-IR, cm^{-1}): 3112, 3084, 2971, 2921, 2846, 1697, 1460, 1373, 1274, 1131, 1008. UV-Vis (Dichloromethane, $5 \times 10^{-4} \text{ mol.L}^{-1}$): $\delta_{\text{max}} = 448 \text{ nm}$, $\epsilon = 522 \text{ M}^{-1}\text{cm}^{-1}$.

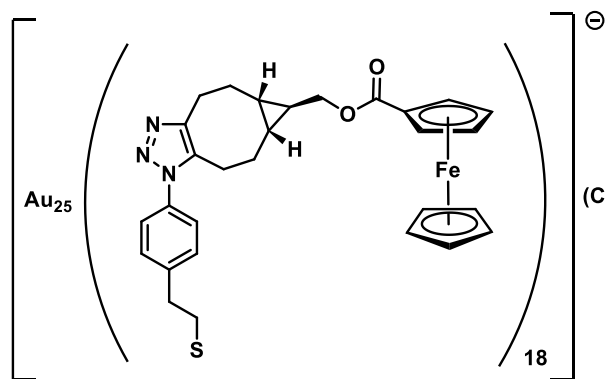
6.6.2.7 Synthesis of Ferrocene-Triazole-Thioacetate



To a solution of 0.11 g (0.30 mmol, 1.0 eq) **ferrocene-BCN_{exo}** in 5 mL dichloromethane was added 0.080 g (0.36 mmol, 1.2 eq) **p-azido-phenylethanethioacetate** in 1 mL dichloromethane. The resulting solution was stirred

for 4 hours, after which the solvent was evaporated and the resulting crude residue was purified by gradient column chromatography (100% dichloromethane to tetrahydrofuran) to give **ferrocene-triazole-thioacetate** as a light orange oil in 93% yield (0.15 g). $^1\text{H NMR}$ (CD_2Cl_2 , 400 MHz): δ (ppm) 7.34 (d, 2H, $J = 8 \text{ Hz}$), 7.27 (d, 2H, $J = 8 \text{ Hz}$), 4.77 (t, 2H, $J = 4 \text{ Hz}$), 4.36 (t, 2H, $J = 4 \text{ Hz}$), 4.16 (s, 5H), 4.06 (d, 2H, $J = 8 \text{ Hz}$), 3.19 (m, 1H), 3.11 (m, 2H), 2.91 (m, 3H), 2.83 (m, 1H), 2.61 (m, 1H), 2.48 (m, 1H), 2.37 (m, 1H), 2.31 (s, 3H), 1.42 (m, 1H), 1.36 (m, 1H), 0.96 (m, 3H). HRMS (ESI) m/z calc. for $\text{C}_{21}\text{H}_{22}\text{FeO}_2$ (M^+): 540.1408, found: 540.1421.

6.6.2.8 Synthesis of $[(\text{CH}_3-(\text{CH}_2)_7)_4\text{N}][\text{Au}_{25}(\text{SCH}_2\text{CH}_2-p\text{-C}_6\text{H}_4\text{-C}_{21}\text{H}_{22}\text{FeN}_3\text{O}_2)_{18}]$ (6.1-ferrocenyl)



To 50 mg (0.0060 mmol, 1 eq) $[(\text{CH}_3-(\text{CH}_2)_7)_4\text{N}][\text{Au}_{25}(\text{SCH}_2\text{CH}_2-p\text{-C}_6\text{H}_4\text{-N}_3)]$ (**6.1-azido**) in 10 mL tetrahydrofuran was added 2.6 mg (0.0072 mmol, 1.2 eq) **ferrocene-BCN_{exo}** in 1 mL tetrahydrofuran. The solution was stirred for 2 hours, after which the solvent was removed by

rotary evaporation. Upon removal of the solvent, a reddish brown film formed on the flask interior, which was then triturated with isopropanol to remove residual starting materials, giving [(CH₃(CH₂)₇)₄N][Au₂₅(SCH₂CH₂-*p*-C₆H₄-C₂₁H₂₂FeN₃O₂)₁₈] (**6.1-ferrocenyl**) as a reddish black film in 96% yield (12 mg). ¹H NMR (CD₂Cl₂, 600 MHz): δ (ppm) 7.37 (d, 24H, J = 6 Hz), 7.28 (d, 12H, J = 6 Hz), 7.14 (d, 36H, J = 6 Hz), 4.75 (t, 36H, J = 3 Hz), 4.36 (t, 36H, J = 3 Hz), 4.16 (s, 90H), 4.05 (m, 18H), 3.98 (m, 18H), 3.70 (m, 18H), 3.30 (m, 18H), 3.24 (m, 18H), 3.09 (m, 54H), 2.78 (m, 36H), 2.48 (m, 36H), 2.23 (m, 18H), 1.59 (m, 8H), 1.38 (m, 18H), 1.28 (m, 48H), 0.99 (m, 18H), 0.90 (m, 18H), 0.87 (t, 12H, J = 6 Hz), 0.83 (m, 18H). MS (MALDI-TOF[negative]) *m/z* calc. for C₅₂₂H₅₄₀Au₂₅Fe₁₈N₅₄S₁₈ (M⁻): 14653.2 Da, found: 14662.1 Da. IR (ATR-IR, cm⁻¹): 3107, 3066, 2959, 2859, 1702, 1515, 1456, 1376, 1273, 1134. UV-Vis (Dichloromethane, 2x10⁻⁴ mol L⁻¹): λ_{max} = 679 nm, ε = 1715 M⁻¹cm⁻¹, λ_{max} = 443 nm, ε = 8888 M⁻¹cm⁻¹, λ_{max} = 405 nm, ε = 8597 M⁻¹cm⁻¹.

6.6.3 Experimental Spectra and Diagrams

6.6.3.1 Experimental Spectra for $[(\text{CH}_3-(\text{CH}_2)_7)_4\text{N}][\text{Au}_{25}(\text{SCH}_2\text{CH}_2-p\text{-C}_6\text{H}_4\text{-C}_8\text{H}_{10}\text{N}_3)_{18}]$ (6.1-azido)

See Section 4.6.3.1 for ^1H NMR spectrum and ESI-MS spectrum of $[(\text{CH}_3-(\text{CH}_2)_7)_4\text{N}][\text{Au}_{25}(\text{SCH}_2\text{CH}_2-p\text{-C}_6\text{H}_4\text{-N}_3)_{18}]$ (6.1-azido 1).

6.6.3.2 Experimental Spectra for $[(\text{CH}_3-(\text{CH}_2)_7)_4\text{N}][\text{Au}_{25}(\text{SCH}_2\text{CH}_2-p\text{-C}_6\text{H}_4\text{-C}_{21}\text{H}_{22}\text{FeN}_3\text{O}_2)_{18}]$ (6.1-ferrocenyl)

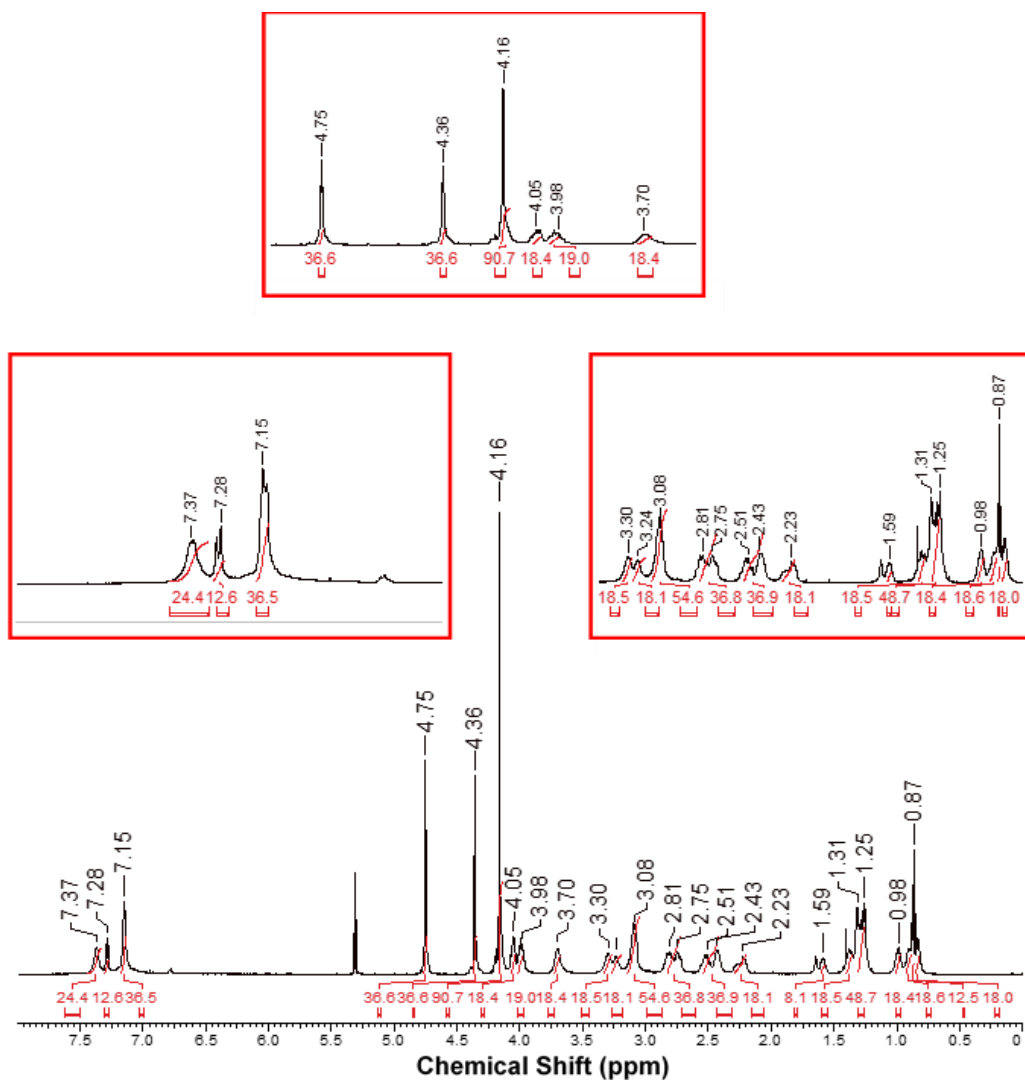


Figure S6.1. 600 MHz ^1H NMR spectrum of $[(\text{CH}_3-(\text{CH}_2)_7)_4\text{N}][\text{Au}_{25}(\text{SCH}_2\text{CH}_2-p\text{-C}_6\text{H}_4\text{-C}_{21}\text{H}_{22}\text{FeN}_3\text{O}_2)_{18}]$ (6.1-ferrocenyl) in CD_2Cl_2 at 25°C . Red insets are zoom-in regions of relevant sections of spectrum. * indicates residual protio solvent and impurities.

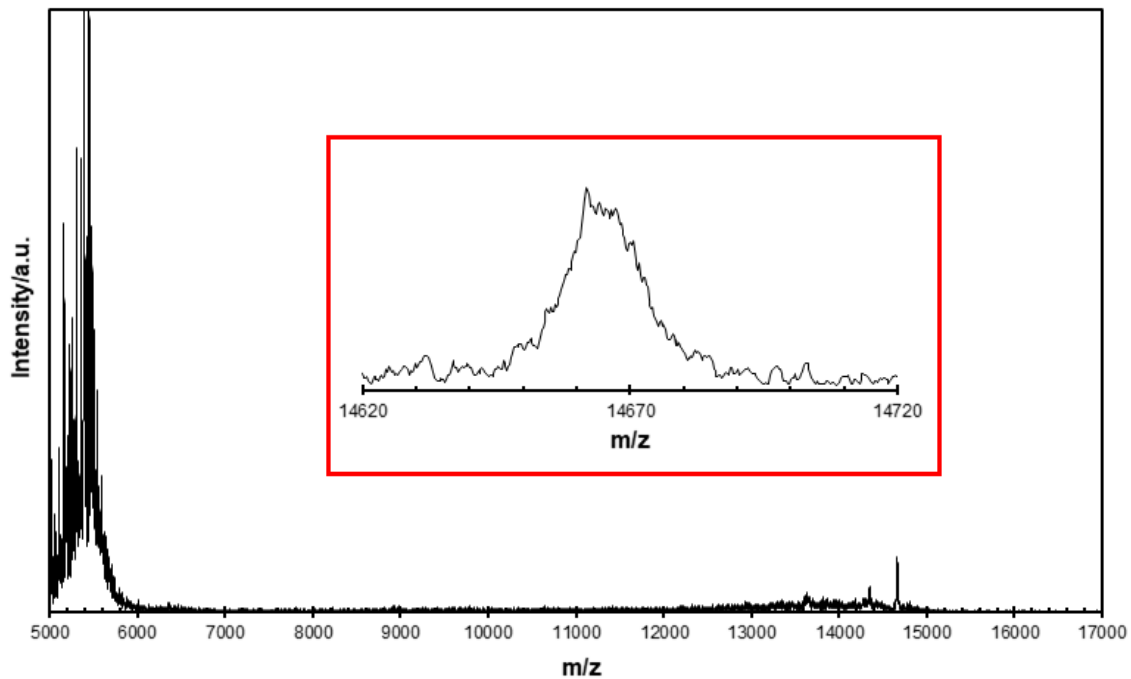


Figure S6.2. Linear negative mode MALDI-TOF mass spectrum of anionic $[\text{Au}_{25}(\text{SCH}_2\text{-CH}_2\text{-}p\text{-C}_6\text{H}_4\text{-C}_{21}\text{H}_{22}\text{FeN}_3\text{O}_2)_{18}]^{1-}$.

6.6.3.3 Experimental Spectra for Ferrocene-BCN_{exo}

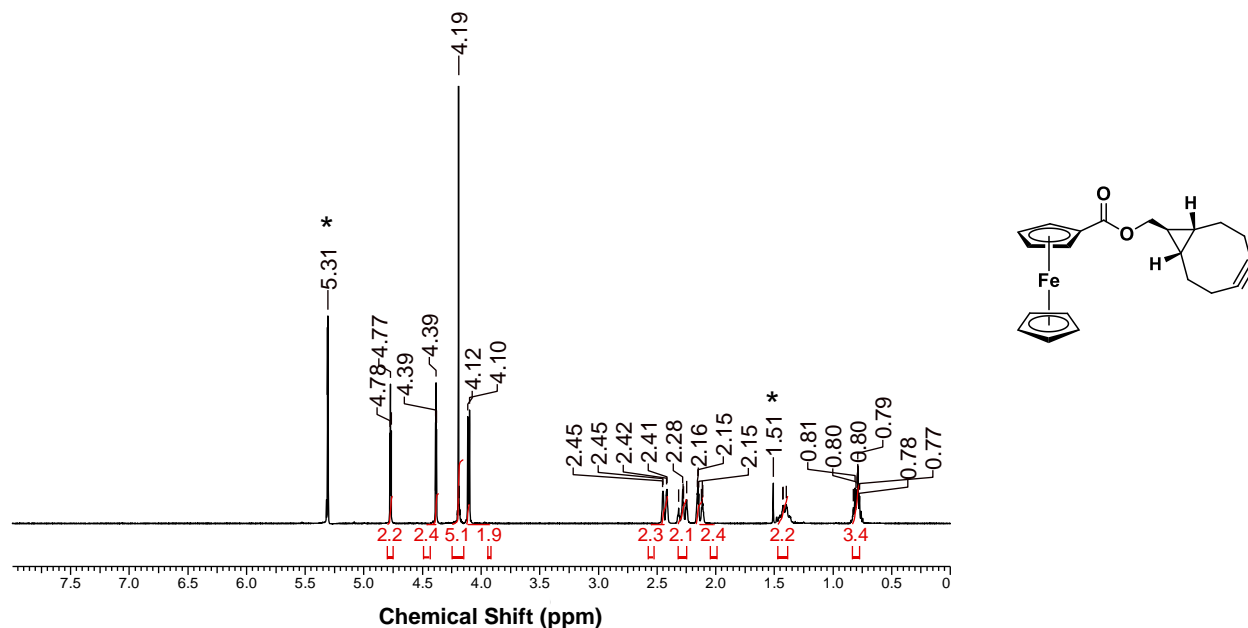


Figure S6.3. ¹H NMR spectrum of ferrocene-BCN_{exo} in CD₂Cl₂ at 25°C. * indicates residual protio solvent and impurities.

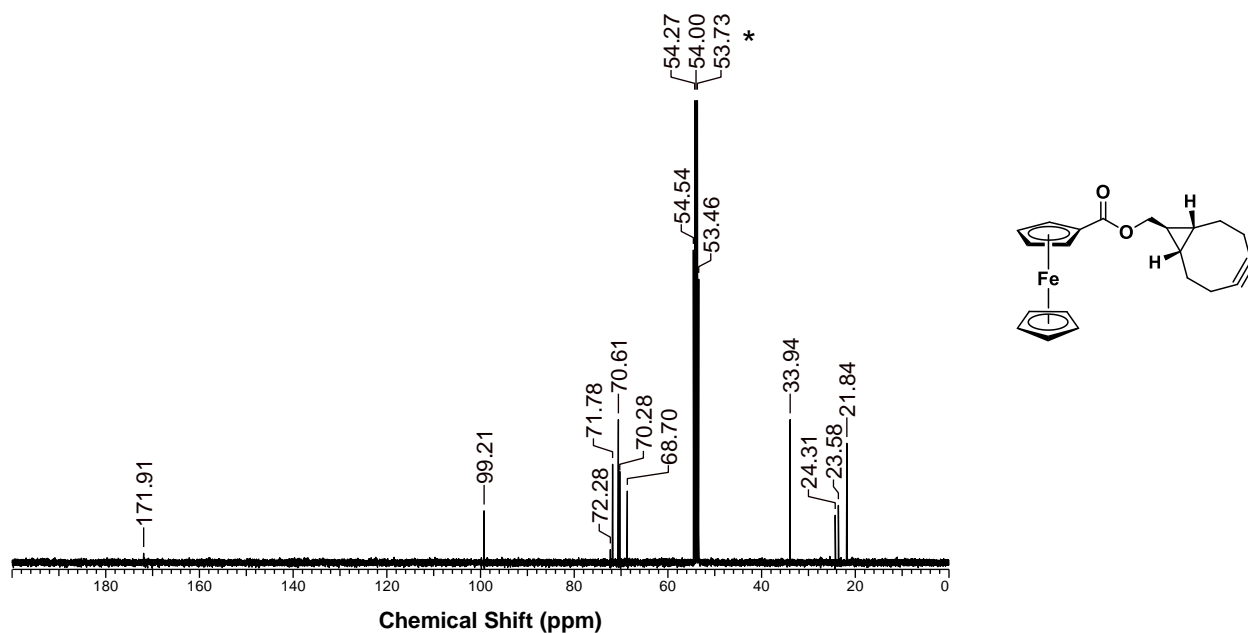


Figure S6.4. ¹³C{¹H} NMR spectrum of ferrocene-BCN_{exo} in CD₂Cl₂ at 25°C. * indicates residual protio solvent.

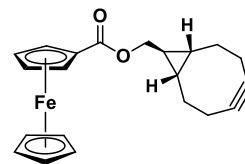
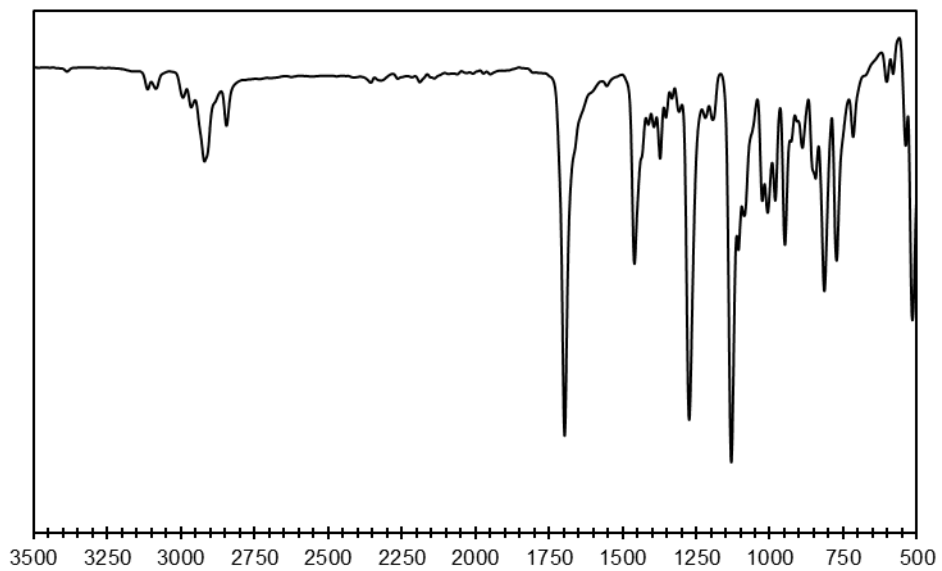


Figure S6.5. Infrared spectrum of **ferrocene-BCN_{exo}**.

6.6.3.4 Experimental Spectra of Ferrocene-Triazole-Thioacetate

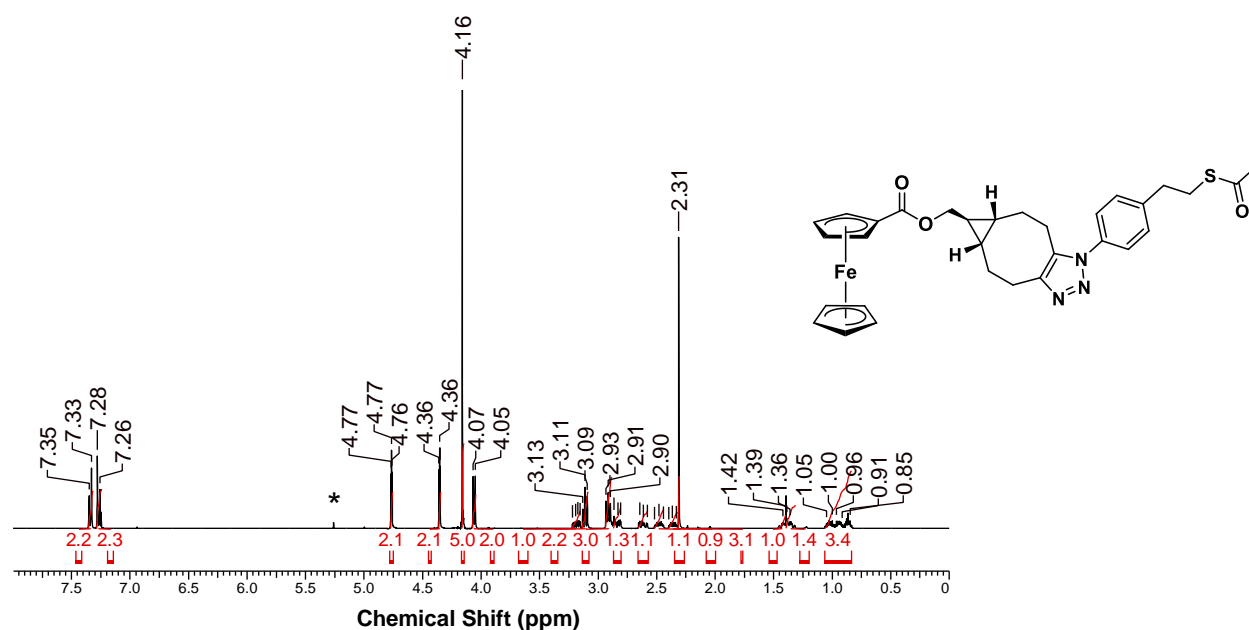


Figure S6.6. ¹H NMR spectrum of ferrocene-triazole-thioacetate in CD₂Cl₂ at 25°C. * indicates residual protio solvent.

6.6.4 Electrochemical Graphs

6.6.4.1 Cyclic Voltammogram (CV) of $[(\text{CH}_3-(\text{CH}_2)_7)_4\text{N}][\text{Au}_{25}(\text{SCH}_2\text{CH}_2-p\text{-C}_6\text{H}_4\text{-C}_8\text{H}_{10}\text{N}_3)_{18}]$ (1-azido)

See Section 5.6.4.1 for CV spectrum of $[(\text{CH}_3-(\text{CH}_2)_7)_4\text{N}][\text{Au}_{25}(\text{SCH}_2\text{CH}_2-p\text{-C}_6\text{H}_4\text{-C}_8\text{H}_{10}\text{N}_3)_{18}]$ (6.1-azido).

6.6.4.2 Cyclic Voltammogram (CV) of $[(\text{CH}_3-(\text{CH}_2)_7)_4\text{N}][\text{Au}_{25}(\text{SCH}_2\text{CH}_2-p\text{-C}_6\text{H}_4\text{-C}_{21}\text{H}_{22}\text{FeN}_3\text{O}_2)_{18}]$ (6.1-ferrocenyl)

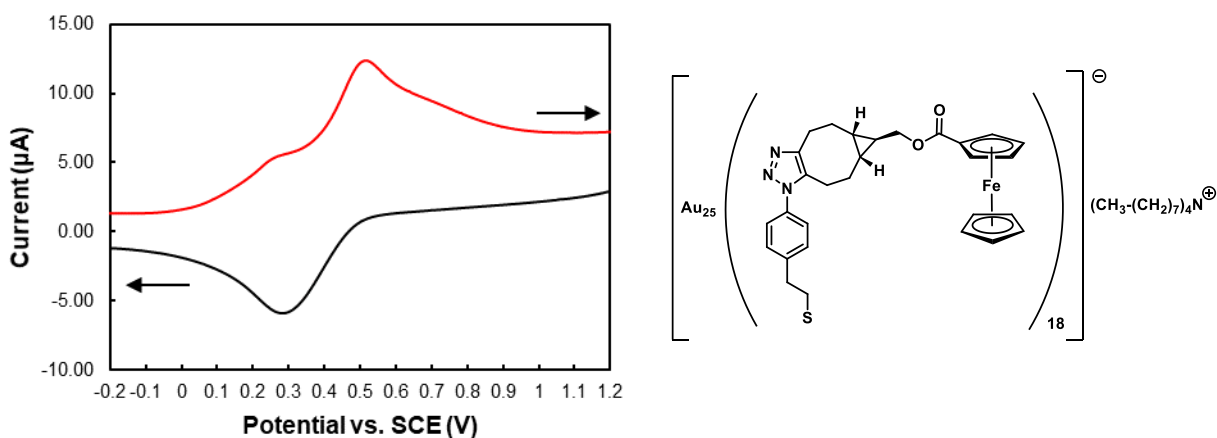


Figure S6.7. Cyclic voltammogram of a 0.1 mM solution of $[(\text{CH}_3-(\text{CH}_2)_7)_4\text{N}][\text{Au}_{25}(\text{SCH}_2\text{CH}_2-p\text{-C}_6\text{H}_4\text{-C}_{21}\text{H}_{22}\text{FeN}_3\text{O}_2)_{18}]$ (6.1-ferrocenyl) in 1:1 acetonitrile:benzene, containing 0.1 M TBAP as the supporting electrolyte, with a scan rate of 100 mV/s. The arrows show the potential scanning direction.

6.6.4.3 Cyclic Voltammogram (CV) of *p*-azido-phenylethanethioacetate

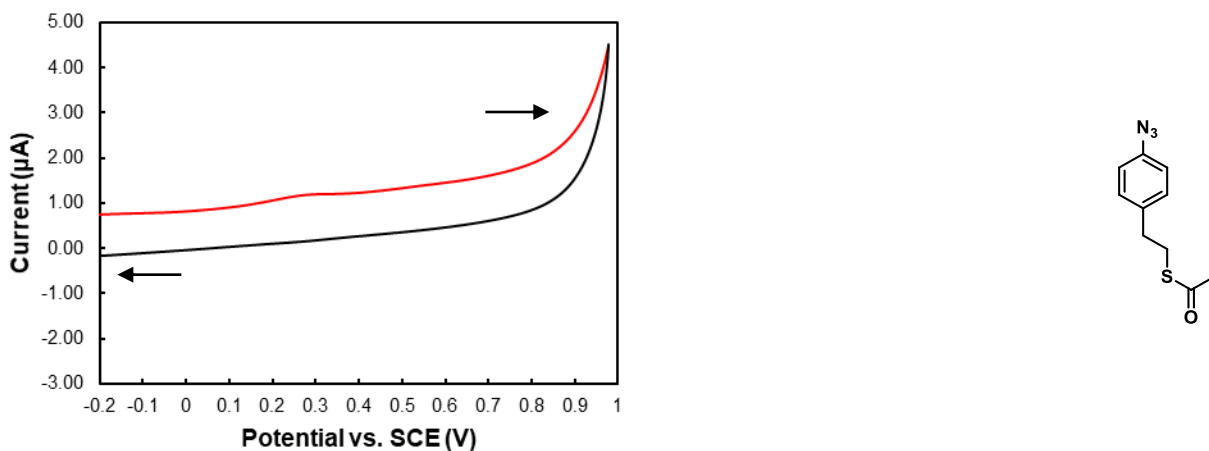


Figure S6.8. Cyclic voltammogram of a 1 mM solution of *p*-azido-phenylethanethioacetate in 1:1 acetonitrile:benzene, containing 0.1 M TBAP as the supporting electrolyte, with a scan rate of 100 mV/s. The arrows show the potential scanning direction.

6.6.4.4 Differential Pulse Voltammogram (DPV) of *p*-azido-phenylethanethioacetate

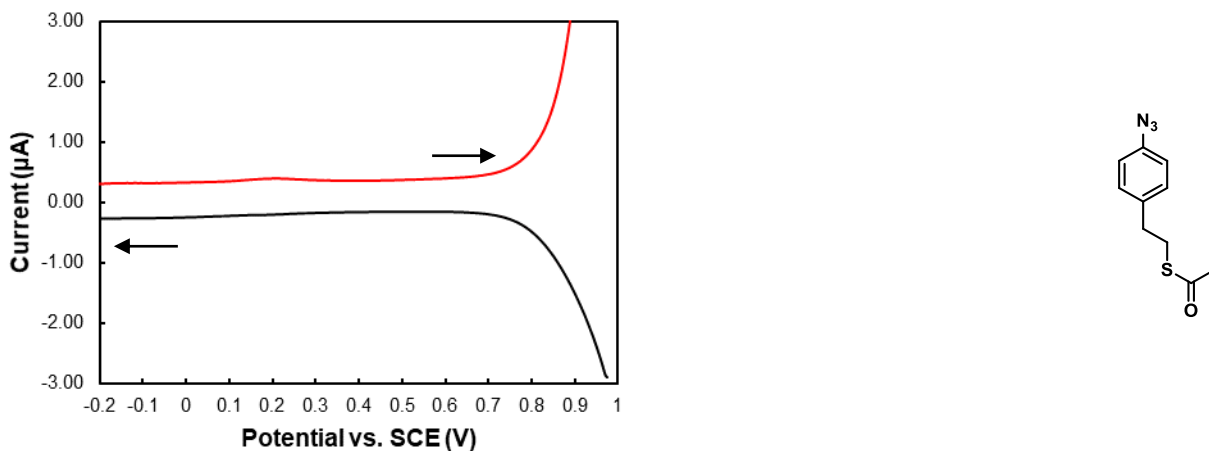


Figure S6.9. Differential pulse voltammogram of a 1 mM solution of *p*-azido-phenylethanethioacetate in 1:1 acetonitrile:benzene, containing 0.1 M TBAP as the supporting electrolyte, with a scan rate of 100 mV/s. The arrows show the potential scanning direction.

6.6.4.5 Cyclic Voltammogram (CV) of Ferrocene-Triazole-Thioacetate

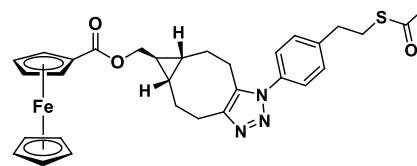
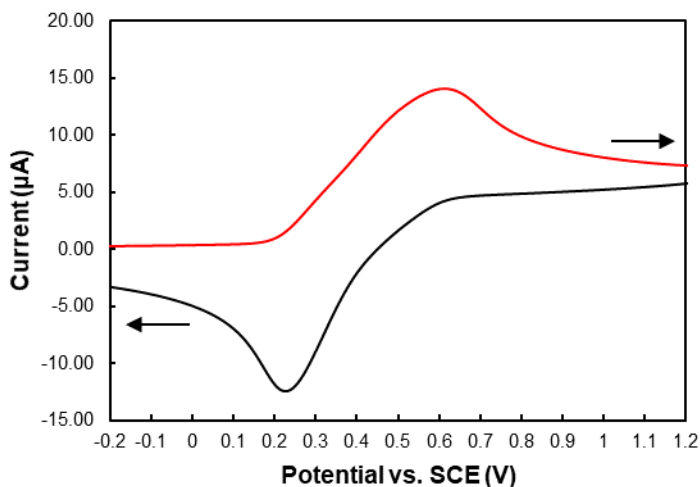


Figure S6.10. Cyclic voltammogram of a 3 mM solution of **ferrocene-triazole-thioacetate** in 1:1 acetonitrile:benzene, containing 0.1 M TBAP as the supporting electrolyte, with a scan rate of 100 mV/s. The arrows show the potential scanning direction.

6.6.4.6 Differential Pulse Voltammogram (DPV) of Ferrocene-Triazole-Thioacetate

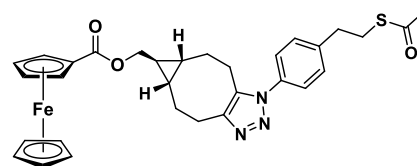
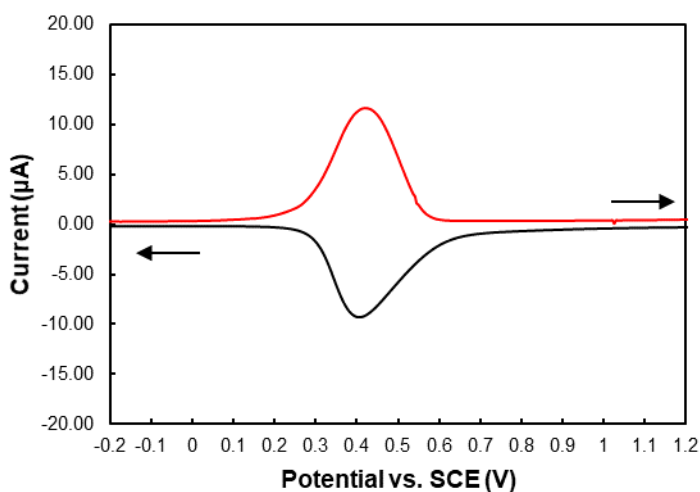


Figure S6.11. Differential pulse voltammogram of a 3 mM solution of **ferrocene-triazole-thioacetate** in 1:1 acetonitrile:benzene, containing 0.1 M TBAP as the supporting electrolyte, with a scan rate of 100 mV/s. The arrows show the potential scanning direction.

6.6.5 References – Supporting Information

1. Dommerholt, J.; Schmidt, S.; Temming, R.; Hendriks, L. J. A.; Rutjes, F. P. J. T.; van Hest, J. C. M.; Lefeber, D. J.; Friedl, P.; van Delft, F. L., Readily Accessible Bicyclononynes for Bioorthogonal Labeling and Three-Dimensional Imaging of Living Cells. *Angew. Chem. Int. Ed.* **2010**, *49* (49), 9422-9425.

Chapter 7

7 Contributions and Future Perspectives

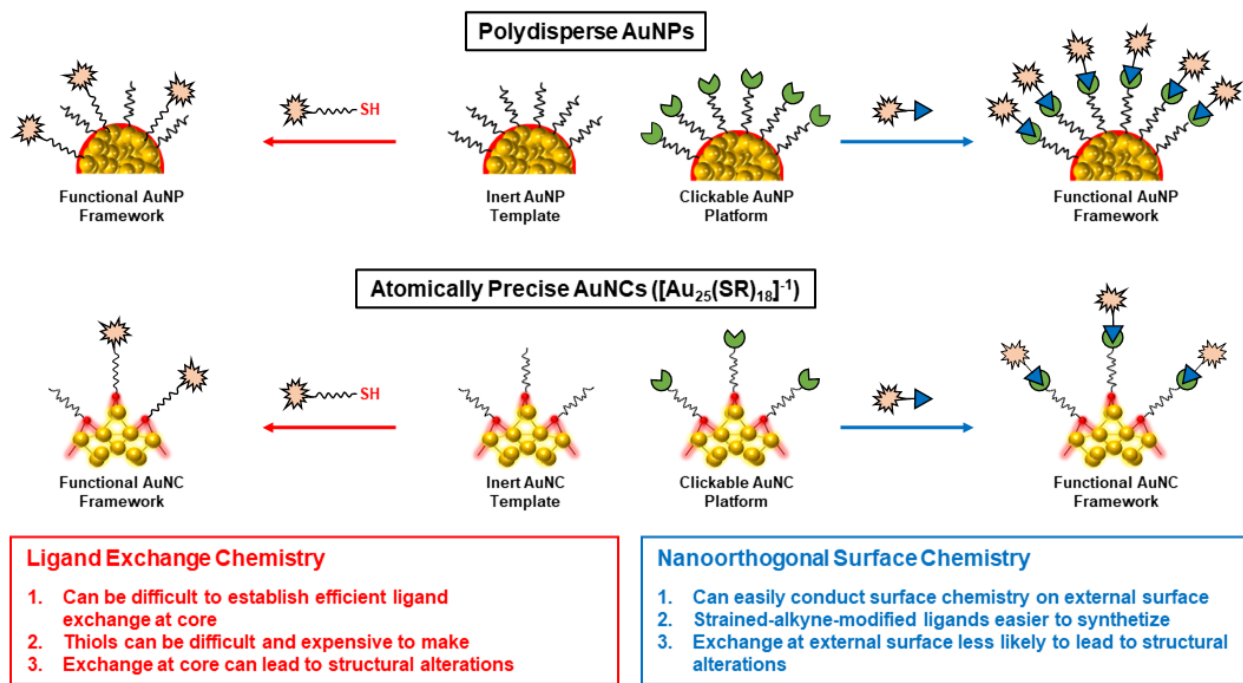
7.1 Contributions

Application-based research using polydisperse gold nanoparticles (AuNPs) and atomically precise gold nanoclusters (AuNCs) is contingent on synthetic strategies in which the composition of their surface structure can be modified in a reliable and efficient manner. As outlined in **Section 1.2.4** and **Section 1.3.5**, there exists a delicate and modifiable relationship between the exhibited properties of these popular nanomaterials and the overall structure of the framework (including the surface structure), with small changes to the surface structure leading to well-defined changes to these structure-property relationships.^{1,2} In addition, the ability to tether functional substrates onto the surfaces of AuNPs and AuNCs renders these nanomaterial frameworks very promising platforms in a variety of applications such as biotechnology, nanomedicine and catalysis.^{3,4}

The traditional synthetic method for derivatizing the surfaces of AuNPs and AuNCs is ligand exchange, in which template frameworks (possessing inert thiolated ligands) are mixed with functional thiolated ligands (possessing the desired structure or functionality). Although ligand exchange strategies have found great utility, there are several problems associated with them: (1) It is often difficult to establish effective ligand exchange (2) it is difficult to tether reactive thiol groups to sensitive substrates and (3) changes to the ligand structure can alter the internal core framework (which is especially problematic with exchange strategies on the more chemically sensitive AuNC systems) (**Section 1.4**).

This thesis describes the use of two popular “bioorthogonal click reactions” (the strain-promoted alkyne-azide cycloaddition (SPAAC) reaction and strain-promoted alkyne-nitrone cycloaddition (SPANC) reaction) as an alternative and more reliable approach for derivatizing the surface structures of polydisperse AuNPs and atomically precise AuNCs, without the limitations inherent to ligand exchange strategies (Scheme 7.1). Of the bioorthogonal reactions developed to date, the SPAAC and SPANC reactions are among the most popular, because: (1) the two reactive partners are chemically stable (2) the two reactive partners chemoselectively react

with each other in the presence of other reactive moieties (3) can be performed at ambient, physiological conditions and (4) have fast and adjustable reaction kinetics.



Scheme 7.1. Scheme illustrating ligand exchange chemistry and nanoorthogonal surface chemistry for surface modifications of polydisperse AuNPs and atomically precise AuNCs. Green = first reactive partner. Blue = second, complementary reactive partner. Brown = functional substrate.

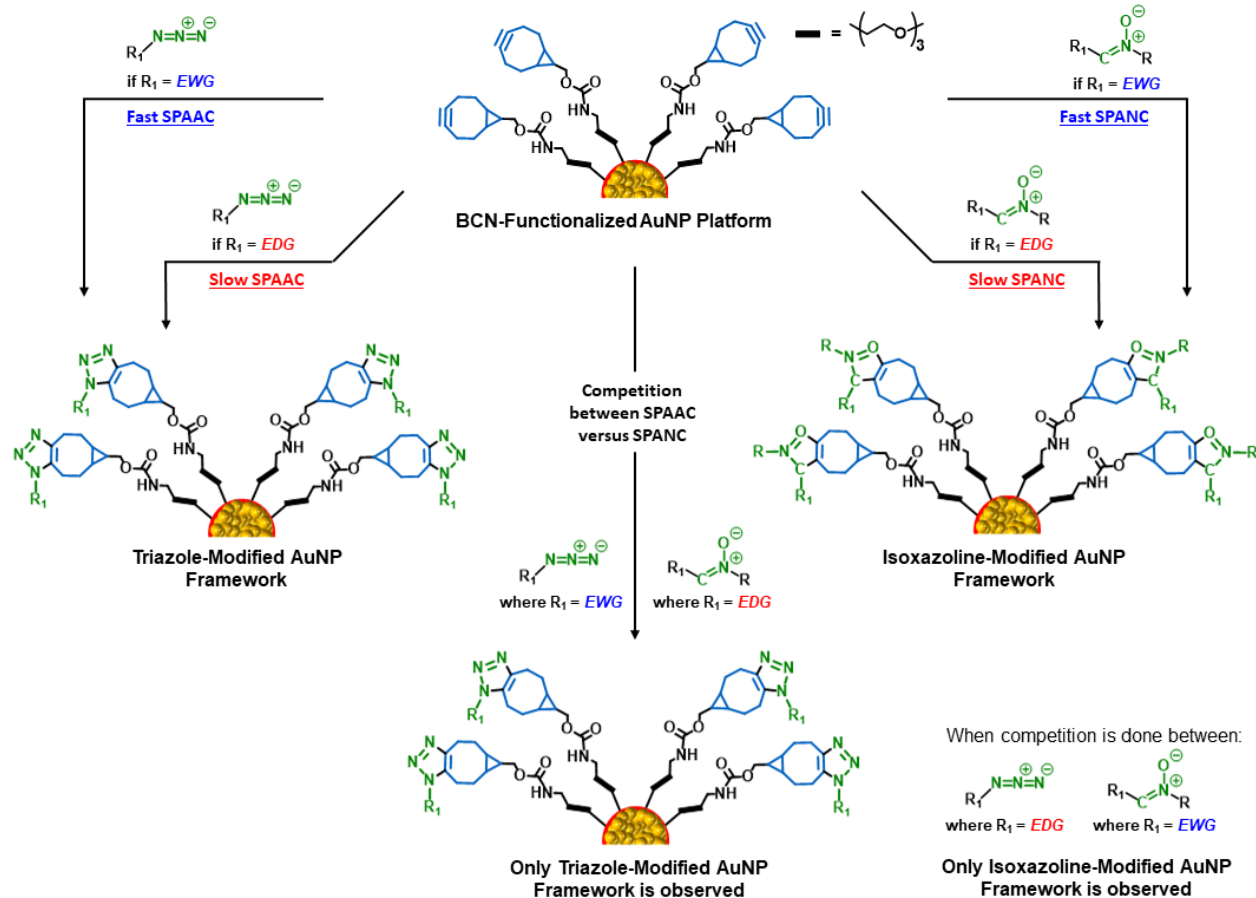
The goal of this thesis is to transpose these advantageous characteristics of SPAAC and SPANC from the biologically sensitive settings in which they are primarily conducted to the chemically sensitive AuNP and AuNC surface settings. This approach not only allows for clean, quantitative and well-defined modifications to the surface corona, but by eliminating the necessity of risky ligand exchanges at the core, it also provides a means to orthogonally link functional substrate reporters to the AuNP/AuNC surfaces without altering the chemically sensitive core structures. In this way, this thesis demonstrates that the SPAAC and SPANC reactions are not only “*bioorthogonal click reactions*” but can also be classified as “*nanoorthogonal click reactions*”, allowing for nanoorthogonal and efficient surface modifications of AuNPs and AuNCs while retaining the internal parent frameworks.

Our group has previously explored the use of SPAAC and SPANC on the surfaces of AuNPs, in which azide-terminated,^{5,6} strained-alkyne-terminated,⁷ and nitrene-terminated⁸ AuNP

platforms have been reported, each of which could undergo interfacial SPAAC chemistry with the complementary reactive partner for nanoorthogonal surface modifications. We have also demonstrated that other bioorthogonal click reactions, such as the Staudinger-Bertozzi ligation⁹ and maleimide-thiol reaction,^{10, 11} can be performed nanoorthogonally on AuNP surfaces. In our previous strained-alkyne-terminated AuNP platform, the benzoannulated strained-alkyne, dibenzocyclooctyne (DBCO), was incorporated onto the AuNP surface.⁷ Although this represented an exciting new approach for nanoorthogonal surface modifications of AuNPs, the main limitation was the instability of the benzoannulated DBCO moiety (see **Section 1.5.5**).

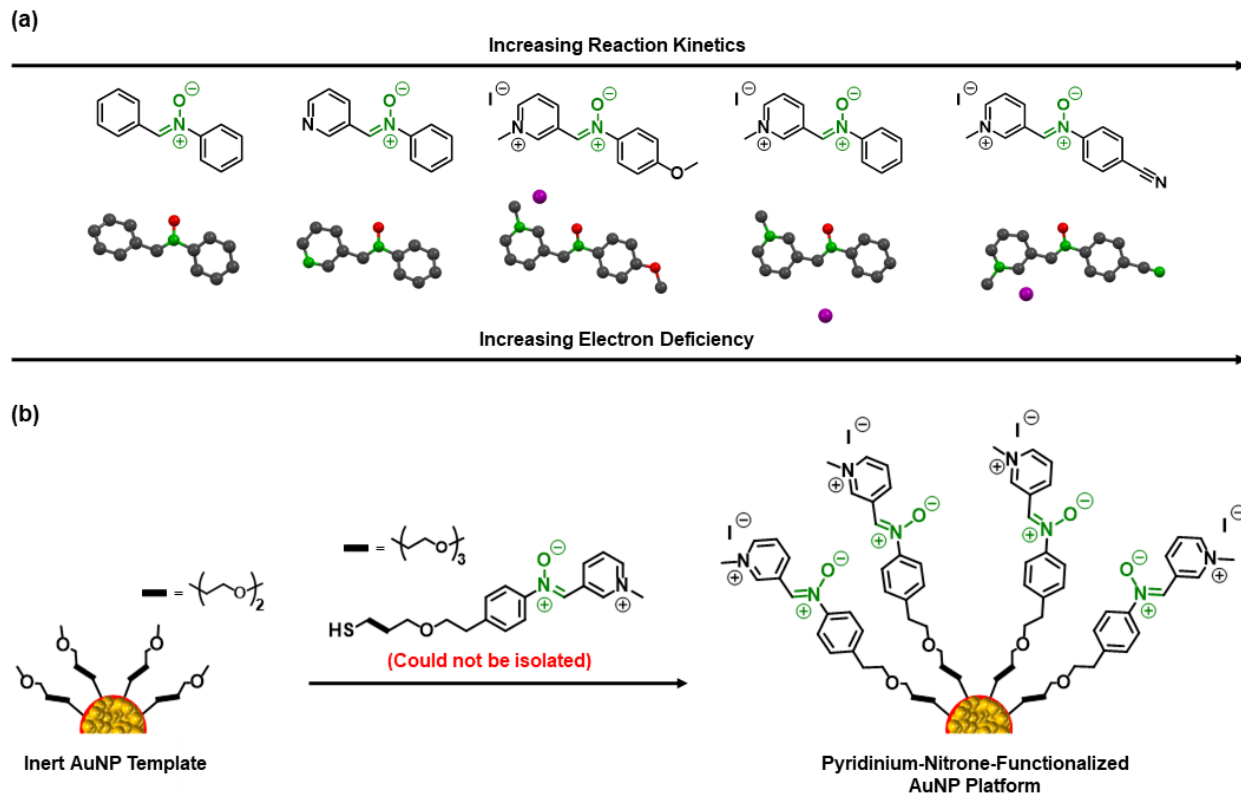
To address this limitation, **Chapter 2** describes the development of an AuNP platform in which the less stable benzoannulated DBCO moieties were replaced with the more stable aliphatic strained-alkyne, *exo*-bicyclo[6.1.0]nonyne (BCN_{*exo*}) (hereafter referred to as “AuNP-BCN”). The incorporation of the interfacial BCN_{*exo*} moieties was confirmed by ¹H NMR and X-ray photoelectron spectroscopies. Interfacial SPAAC (*I*-SPAAC) and interfacial SPANC (*I*-SPANC) were demonstrated using a library of azides and nitrones, respectively. For the first time, it was shown that alterations to the kinetic profiles of SPAAC and SPANC (see **Section 1.5.5**) could be transposed to the AuNP-BCN platform, with more electron-deficient dipoles undergoing more rapid interfacial cycloaddition chemistry than their electron-rich counterparts (**Scheme 7.2**). In competition experiments between equimolar amounts of an azide, a nitrone and AuNP-BCN, exclusive reactivity with one dipolar species over the other was also demonstrated, which was dependent on the electronic composition of the dipolar species (**Scheme 7.2**).

Having established that *I*-SPAAC could be conducted to modify the surfaces of AuNPs, our group subsequently reported the development of a nitrone-functionalized AuNP platform which was capable of undergoing nanoorthogonal *I*-SPANC with complementary strained-alkynes. For this prototype study, the nitrone chosen possessed an electron-rich methyl group on the N α of the nitrone moiety and another electron-rich alkyl group on the C α of the nitrone moiety, which had slow reaction kinetics due to the two electron donating groups (see **Section 1.5.5**). **Chapter 3** sought to explore the development of a more reactive nitrone-functionalized AuNP platform for more efficient and rapid surface modifications. This chapter describes the first synthesis of nitrones possessing highly electron-deficient pyridinium groups on the C α of the nitrone moiety, which resulted in substantial improvements to the kinetic profile of the SPANC



Scheme 7.2. Chapter 2. Development of BCN-functionalized AuNP platform (AuNP) for kinetically variable SPAAC and SPANC, and kinetically directed competitive reactions.

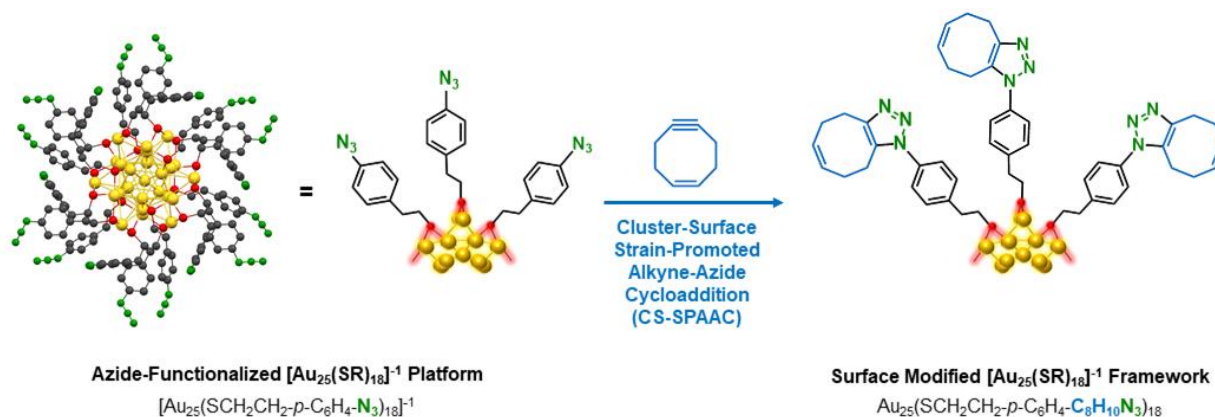
reaction.¹² The kinetics of these “pyridinium-nitrones” could be modulated by changing the $N\alpha$ substituents, where an electron-rich anisole substituent resulted in kinetic deceleration, and an electron-deficient benzonitrile substituent resulting in a substantial kinetic acceleration (**Scheme 7.3**). In fact, density functional theory indicates that LUMO energy of this latter nitrone (“ $C\alpha$ -pyridinium- $N\alpha$ -cyanophenyl nitrone”) has a similar energy to the HOMO energy of BCN, giving rise to the fastest cycloaddition reaction between a nitrone and BCN currently reported.¹² To translate this rapid cycloaddition chemistry onto the surface of AuNPs, a thiolated ligand possessing the pyridinium-nitron moiety was pursued, which could be incorporated to the AuNP surface using either a direct synthetic approach or ligand exchange strategy. However, unlike in our previously reported prototype study, the high reactivity of the pyridinium-nitron moiety made it incompatible with the thiol moiety and the necessary deprotection of the thiol, preventing the development of such a thiolated ligand.



Scheme 7.3. Chapter 3. (a) Development of highly reactive pyridinium-nitrones for rapid and tunable SPANC chemistry. (b) Proposed synthesis for the development of pyridinium-nitronium-functionalized AuNP platform. However, the necessary thiolated-ligand possessing the terminal pyridinium-nitronium moiety could not be isolated.

To date, our group has reported many examples of nanoorthogonal modifications of AuNPs using a variety of bioorthogonal click reactions. Although AuNPs have shown to be promising candidates for a variety of applications, atomically precise AuNCs have also shown great promise for application-based research. However, whereas the AuNP core frameworks are more rigid due to their larger size, and their internal structure is less sensitive to surface alterations, the relationship between the surface structure and metallic framework of monodisperse AuNCs is much more sensitive. Small structural changes to the protecting ligand can lead to larger changes to the nuclearity and configuration of the internal metallic framework of AuNCs. In this way, ligand exchange strategies at the metallic core are particularly problematic with AuNC systems, and so nanoorthogonal click chemistry at the surface corona (instead of at the metallic core) serves as a promising alternative to contemporary strategies to reliably derivatize the surface structures of AuNCs.

To demonstrate nanoorthogonal click chemistry on AuNCs, the $[\text{Au}_{25}(\text{SR})_{18}]^{1-}$ framework was chosen, because it features superior chemical stability and ease of synthesis compared to other popular atomically precise AuNC systems. **Chapter 4** describes the first example of an azide-functionalized $[\text{Au}_{25}(\text{SCH}_2\text{CH}_2\text{-}p\text{-C}_6\text{H}_5\text{-N}_3)_{18}]^{1-}$ platform that was capable of undergoing nanoorthogonal cluster-surface SPAAC (CS-SPAAC) chemistry (**Scheme 7.4**).¹³ This was not only the first example of an $[\text{Au}_{25}(\text{SR})_{18}]^{1-}$ platform whose surface could be modified through nanoorthogonal click chemistry, but the first example of an AuNC system that could be modified using such a strategy. This platform was characterized by UV, IR, ^1H NMR spectroscopies, mass spectrometry, and its molecular structure was confirmed by single crystal X-Ray diffraction. Quantitative consumption of all surface azides after the CS-SPAAC reaction with a small strained-alkyne, (Z)-cyclooct-1-ene-5-yne, was also confirmed using the same spectroscopic techniques as before, although the molecular structure of this modified framework could not be acquired. This previously unreported nanoorthogonal approach represents an exciting new paradigm for efficient and reliable surface modifications of $[\text{Au}_{25}(\text{SR})_{18}]^{1-}$ frameworks with functional substrate reporter without changing the internal metallic nuclearity, for application-based research using $[\text{Au}_{25}(\text{SR})_{18}]^{1-}$ frameworks.



Scheme 7.4. Chapter 4. Development of azide-functionalized $[\text{Au}_{25}(\text{SR})_{18}]^{1-}$ platform for nanoorthogonal CS-SPAAC chemistry for efficient and reliable surface modifications.

Having developed the azide-modified platform reported in **Chapter 4**, the relationship between the isomeric position of the azide moiety on the surface phenyl ligands and the related properties and reactivity were explored. **Chapter 5** describes the synthesis of two isomeric forms of the $[\text{Au}_{25}(\text{SCH}_2\text{CH}_2\text{-}p\text{-C}_6\text{H}_5\text{-N}_3)_{18}]^{1-}$ platform: the $[\text{Au}_{25}(\text{SCH}_2\text{CH}_2\text{-}m\text{-C}_6\text{H}_5\text{-N}_3)_{18}]^{1-}$ platform

and the $[\text{Au}_{25}(\text{SCH}_2\text{CH}_2\text{-}o\text{-C}_6\text{H}_5\text{-N}_3)_{18}]^{1-}$ platform (**Figure 7.1**). These previously unreported $[\text{Au}_{25}(\text{SR})_{18}]^{1-}$ isomers were confirmed by UV and IR spectroscopy and mass spectrometry. Slow oxidation of the three anionic forms led to the neutral forms of the AuNCs forming, whose molecular structures were confirmed using single crystal X-ray diffraction. The CS-SPAAC chemistry was explored using the small strained-alkyne, (*Z*)-cyclooct-1-ene-5-yne. As with the $[\text{Au}_{25}(\text{SCH}_2\text{CH}_2\text{-}p\text{-C}_6\text{H}_5\text{-N}_3)_{18}]^{1-}$ platform, all the surface azides in the $[\text{Au}_{25}(\text{SCH}_2\text{CH}_2\text{-}p\text{-C}_6\text{H}_5\text{-N}_3)_{18}]^{1-}$ platform were consumed while retaining the internal framework. Kinetic analysis indicates that the $[\text{Au}_{25}(\text{SCH}_2\text{CH}_2\text{-}p\text{-C}_6\text{H}_5\text{-N}_3)_{18}]^{1-}$ platform had a higher reaction rate with $\text{BCN}_{exo}\text{-OH}$ compared to $[\text{Au}_{25}(\text{SCH}_2\text{CH}_2\text{-}m\text{-C}_6\text{H}_5\text{-N}_3)_{18}]^{1-}$, which is likely due to a steric effect. For the $[\text{Au}_{25}(\text{SCH}_2\text{CH}_2\text{-}o\text{-C}_6\text{H}_5\text{-N}_3)_{18}]^{1-}$ platform, spectroscopic analysis and mass spectrometry indicate that the CS-SPAAC reaction is not nanoorthogonal to this azide-modified AuNC system, and the $[\text{Au}_{25}(\text{SR})_{18}]^{1-}$ configuration appears to deteriorate after the surface reaction. This emphasizes the sensitive relationship between the structure of the protecting ligand and the configuration (and integrity) of the internal metallic framework.

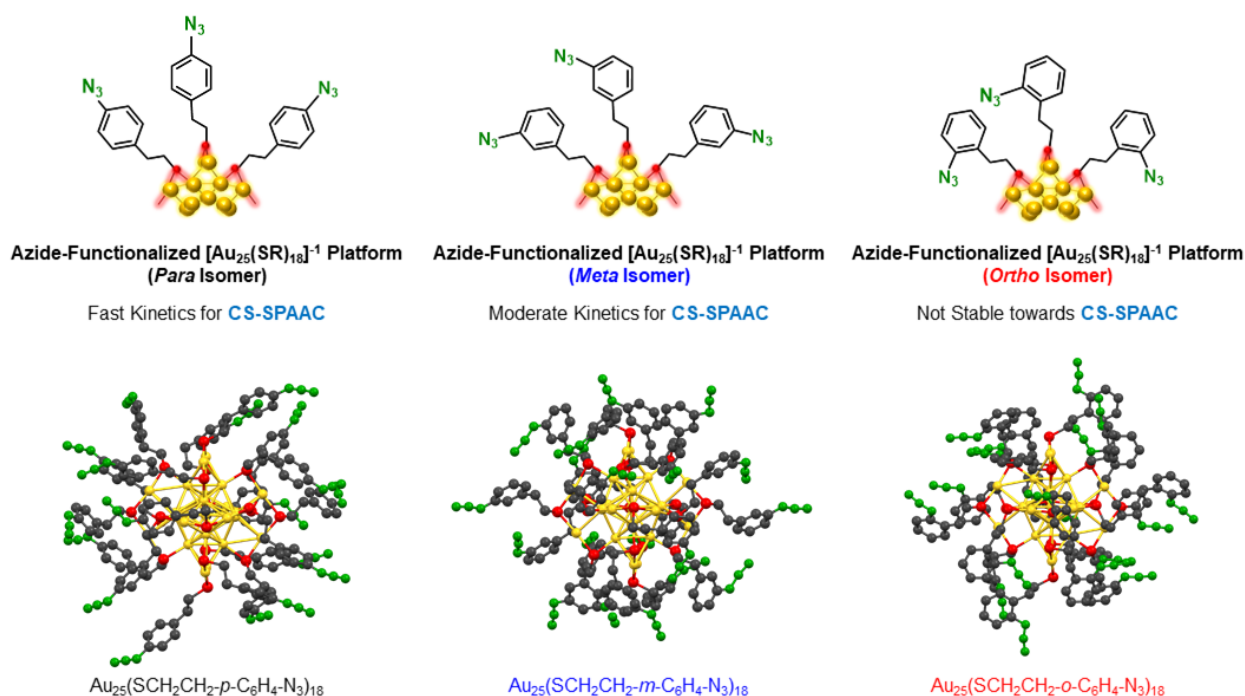
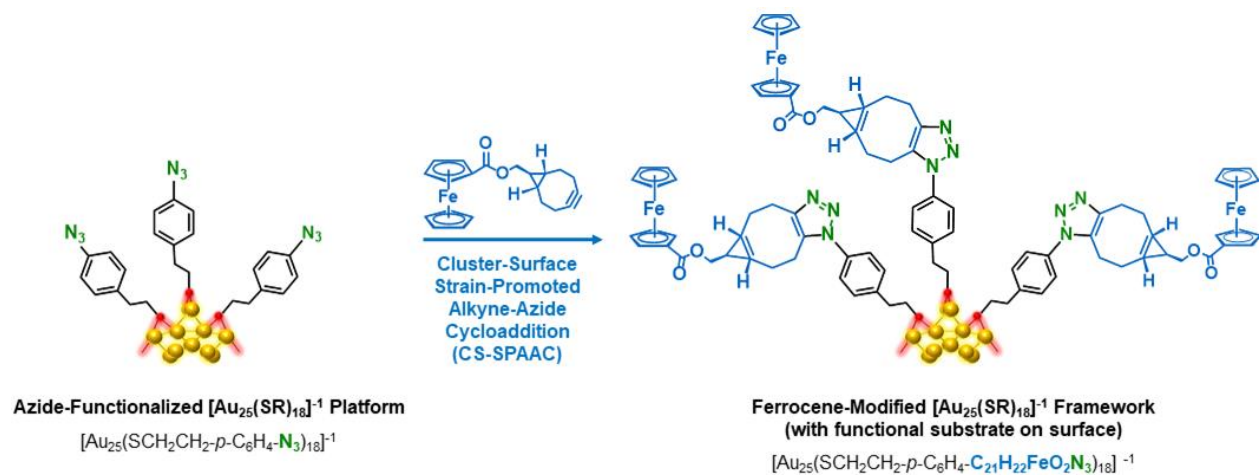


Figure 7.1. Chapter 5. Investigation of isomeric effects of the azide position on the surface ligands in azide-functionalized $[\text{Au}_{25}(\text{SR})_{18}]^{1-}$ platforms, and related properties, structure and surface reactivity.

Having developed the three clickable platforms and establishing that the $[\text{Au}_{25}(\text{SCH}_2\text{CH}_2-p\text{-C}_6\text{H}_5\text{-N}_3)_{18}]^{1-}$ platform is the most reactive, **Chapter 6** focuses on incorporating a model functional substrate reporter to the surface of this azide-modified $[\text{Au}_{25}(\text{SR})_{18}]^{1-}$ platform. For this prototype study, a strained-alkyne-modified ferrocenyl moiety was nanoorthogonally tethered to the external interface of $[\text{Au}_{25}(\text{SCH}_2\text{CH}_2-p\text{-C}_6\text{H}_5\text{-N}_3)_{18}]^{1-}$ through CS-SPAAC to give the $[\text{Au}_{25}(\text{SCH}_2\text{CH}_2-p\text{-C}_6\text{H}_4\text{-C}_{21}\text{H}_{22}\text{FeN}_3\text{O}_2)_{18}]^{1-}$ framework (**Scheme 7.5**), which was confirmed by IR and ^1H NMR spectroscopy and mass spectrometry. UV-Vis spectroscopy demonstrates that the absorption fingerprint of ferrocenated AuNC changes due to the presence of the newly incorporated surface ferrocenyl groups. Most importantly, due to the two different stable charge states of each of the 18 surface ferrocene moieties, the electrochemical pattern of the ferrocenated AuNC possesses a large peak that is attributed to the surface ferrocenyl moieties. This not only confirms the incorporation of the ferrocenyl moieties, but the analysis signifies that all surface ferrocenyl groups are electrochemically active.



Scheme 7.5. Chapter 6. Development of ferrocene-modified $[\text{Au}_{25}(\text{SR})_{18}]^{1-}$ framework through nanoorthogonal CS-SPAAC chemistry.

7.2 Future Perspectives

7.2.1 General Comments

The research presented in this thesis examines conducting “nanoorthogonal” surface modifications of polydisperse AuNPs and atomically precise $[\text{Au}_{25}(\text{SR})_{18}]^{1-}$ AuNCs using two of the most

popular bioorthogonal click reactions. Whereas ligand exchange chemistry has found utility for surface derivatization, the practicality of this approach is primarily limited by (1) inefficient and/or ineffective exchanges at core that leads to poorly defined mixed surface systems and (2) ligand exchanges at the core can lead to alterations to the size, shape and nuclearity of the internal core structure, again leading to a poorly defined system. Furthermore, if multi-functional systems are required (e.g. one possessing a targeting agent and therapeutic agent for more targeted drug delivery than that described in **Section 1.2.4** and **Section 1.3.5**), ligand exchange strategies prevents well-defined systems from being developed, which prevents conclusive and systematic analyses of how the application-based responses are related to the system being used.

The work presented in this thesis seeks to mitigate all the limitations of ligand exchange chemistry and presents nanoorthogonal strategies for clean, efficient, and high-yielding surface modifications of AuNPs and the $[\text{Au}_{25}(\text{SR})_{18}]^{1-}$ system using the chemoselective and atom-efficient SPAAC and SPANC reactions. *One particular advantage is that the methodologies presented herein navigates around the necessity of synthesizing thiolated ligands possessing functional substrates.* This is dually restrictive by the incompatibility that often exists between the thiol moiety and desired substrate, as well as synthetic incompatibilities between protection/deprotection protocols of the thiol moiety and the desired substrate. Due to the comparative chemical stability of the reactive partners in SPAAC and SPANC, incorporation of the azide/nitrone moiety or the strained-alkyne moiety onto ligands possessing the desired substrate can be accomplished via substitution chemistry, in the absence of protection/deprotection strategies. This not only permits greater synthetic accessibility of functional varieties of AuNP and $[\text{Au}_{25}(\text{SR})_{18}]^{1-}$ systems but also expands the range of the types and sizes of functional substrates that can be incorporated to their surfaces that cannot achieved via ligand exchange chemistry with thiolated ligands.

The research presented primarily explores prototype investigations in which quantitative consumption of the reactive groups are accomplished using model reactive partners. For example, in **Chapter 6**, the surface of the azide-functionalized $[\text{Au}_{25}(\text{SCH}_2\text{CH}_2\text{-}p\text{-C}_6\text{H}_5\text{-N}_3)_{18}]^{1-}$ platform was quantitatively modified with the ferrocenyl substrate via nanoorthogonal CS-SPAAC to enhance the electrochemical response of the $[\text{Au}_{25}(\text{SR})_{18}]^{1-}$ system. *However, another general advantage of the methodologies presented is that they can be used to more reliably develop*

multifunctional systems using multiplexes of functional reactive partners, since surface modifications is reliant on well-defined chemical transformations rather than poorly defined and inefficient exchange equilibria. In this way, future work can be directed towards semi-incorporation of property-altering substrates such as ferrocene, while also concurrently being able to incorporate other substrates to the surfaces of AuNPs and the $[\text{Au}_{25}(\text{SR})_{18}]^{1-}$ framework that can either further tune and alter the structure-property relationships (e.g. further enhance electrochemical responses) or target them for specific applications (e.g. incorporation of biomolecules or targeting agents for intracellular responses).

As outlined in **Chapter 3**, although a thiolated ligand possessing a pyridinium-nitrone moiety could not be achieved to incorporate this reactive moiety to the AuNP surface, our group is interested in translating the rapid reaction kinetics of pyridinium-nitrones to the surfaces of other materials systems that do not require the development of thiolated ligands. In particular, we have explored surface derivatization of carbonaceous materials (such as carbon nanotubes and glassy carbon electrodes), using the SPAAC reaction⁵ and diazine-alkene reactions¹⁴. Although these strategies represented a clean and reliable way to incorporate property-altering substrates to their surfaces to create hybrid carbonaceous nanomaterial systems, their efficiency was limited by slow reaction kinetics (using the SPAAC reaction) and necessity for photolytic conditions (using the diazine-alkene reactions). *To this end, execution of the rapid SPANC chemistry reported in Chapter 3 using pyridinium-nitrones serves as a more efficient derivatization method for carbonaceous materials.*

7.2.2 Future Perspectives for AuNPs

Our group has previously explored the use of many bioorthogonal click reactions for surface modifications of AuNPs, including the Staudinger-Bertozzi ligation and thiol-maleimide reactions. The research presented in **Chapter 2** expands upon our group's toolbox for more efficient surface modifications of AuNPs that can be achieved via ligand exchange chemistry. *In particular, the kinetically modifiable SPAAC and SPANC chemistry onto AuNP-BCN presented in Chapter 2 represents a very practical strategy towards developing multi-functional AuNP systems using a kinetically-directed approach, in which nitrone- and azide-functionalized substrates can be incorporated to the surface in a kinetically predictable manner.* Our group is now interested in

translating such surface modifications through this kinetically-directed approach to ‘self-sorting’ applications, which encompasses the hierarchical construction of complex nanomaterial systems from simpler nanomaterial building blocks. Conventional self-sorting methodologies are reliant on chemically orthogonal ‘*host/guest information*’ between building blocks, in which building blocks possess reactive groups (host) on their surfaces that are known to react exclusively with complementary reactive groups (guest) on the surfaces of other building blocks.¹⁵ However, as presented in **Chapter 2**, the ability to kinetically isolate surface reactivity exclusively to one reactive partner in the presence of another, presents a new potential self-sorting paradigm, which is now reliant on well-defined ‘*kinetic information*’ that is inherent to the electronic composition of the azide or nitrene species on other building blocks.

7.2.3 Future Perspectives for AuNCs

Whereas application-based research using AuNPs is quite mature, the more recent discovery of AuNCs renders their application-based research field quite underdeveloped, and there is an ongoing pursuit in contemporary literature to explore how these promising nanomaterial systems can be exploited in different scientific disciplines (see **Section 1.3.5**). Having developed an extensive toolbox of surface derivatization strategies for AuNP surfaces using nanoorthogonal click chemistry, our group has now become interested in exploring such strategies on the surfaces of AuNCs to similarly derivatize their surfaces with functional reporter substrates. As their configurations are more reminiscent of molecular species compared to larger plasmonic AuNP structures, the structure of AuNCs is very sensitive to the structure of the protecting surface ligand. This poses a particular challenge to derivatize their surfaces, as ligand exchange at the core with non-native ligands very often leads to either deterioration of the internal core or a change in its nuclearity and size. For this reason, nanoorthogonal click chemistry serves as a promising new paradigm to conduct derivatization on the external interface of AuNCs (instead of relying on risky exchanges at the core) to create functional varieties of these nanomaterial systems.

In **Chapter 4**, the first example of an AuNC system (specifically the $[\text{Au}_{25}(\text{SR})_{18}]^{1-}$ system) capable of undergoing post-assembly surface chemistry was reported, in which the surface of this azide-functionalized AuNC platform can be modified nanoorthogonally via CS-SPAAC chemistry. Having developed three isomeric forms of this platform in **Chapter 5**, and

authenticating that the *para*-isomer is the most reactive, a functional ferrocene reporter was incorporated to the surface of this platform in **Chapter 6** to create a prototypical functional variety of the $[\text{Au}_{25}(\text{SR})_{18}]^{-1}$ system that had an enhanced electrochemical response. *The establishment of this foundation for nanoorthogonal surface modifications of the $[\text{Au}_{25}(\text{SR})_{18}]^{-1}$ system set in this thesis inaugurates a new and previously unrealized scope for surface derivatization of this nanomaterial system with functional substrates that up to this point could not be incorporated using other strategies.* As outlined in **Section 1.3.5**, the $[\text{Au}_{25}(\text{SR})_{18}]^{-1}$ system is a promising candidate for applications such as drug delivery, bioimaging and catalysis, requiring surface derivatization with therapeutic agents, fluorophores, and structurally complex organic functionalities, respectively. Such applications have so far relied on risky ligand exchanges to incorporate such functionality to the $[\text{Au}_{25}(\text{SR})_{18}]^{-1}$ surface to tailor their structure-property relationships and surface compositions to the desired application. The nanoorthogonal approaches for surface derivatization presented herein presents an alternative and more reliable method to

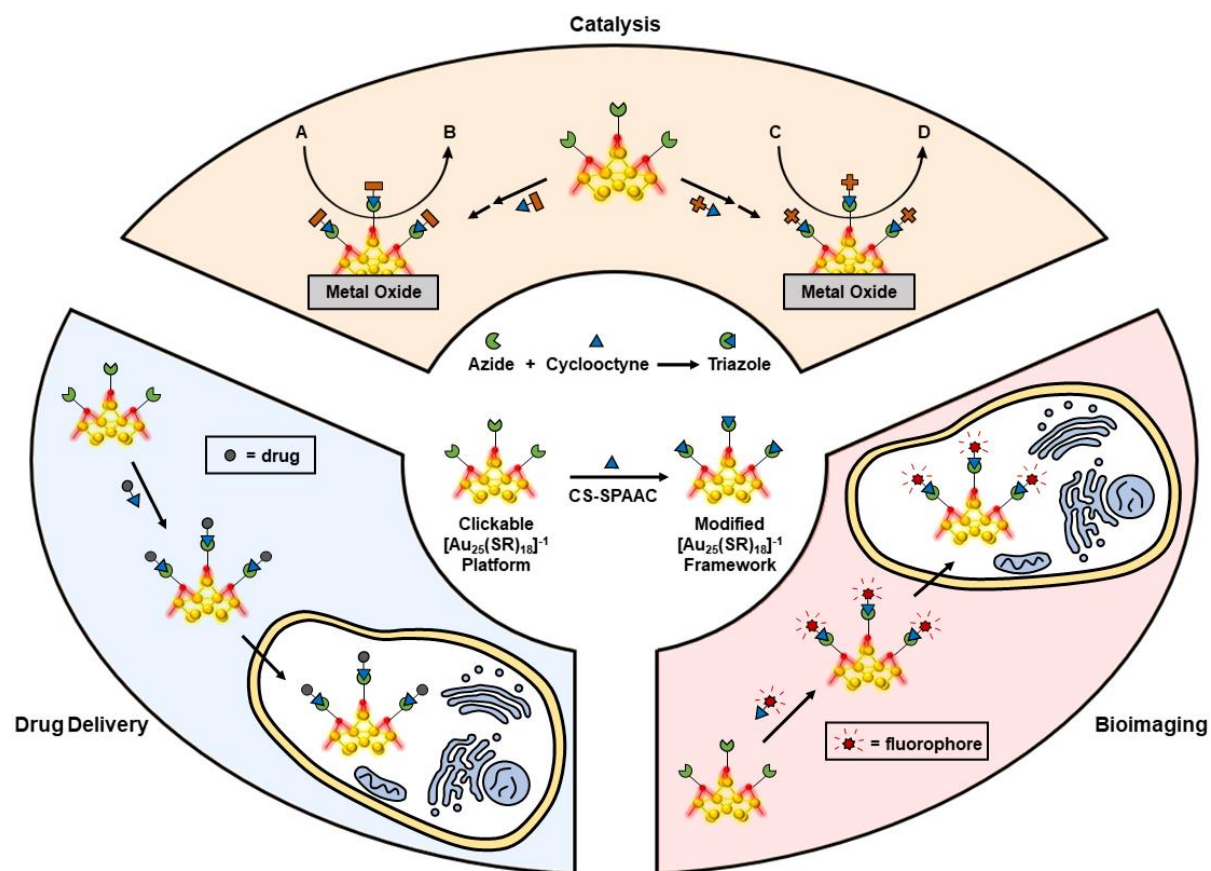


Figure 7.2. Development of functional $[\text{Au}_{25}(\text{SR})_{18}]^{-1}$ systems using nanoorthogonal CS-SPAAC chemistry for applications in drug delivery, bioimaging and catalysis.

incorporate such functional substrates (**Figure 7.2**), without risking the integrity and configuration of the internal structure, which broadens the range of applications that the $[\text{Au}_{25}(\text{SR})_{18}]^{1-}$ system can be used for. *Furthermore, having established a prolific nanoorthogonal toolbox for surface modifications of AuNPs using the assortment of bioorthogonal click reactions available to date, future work will be directed towards transposing this toolbox to the $[\text{Au}_{25}(\text{SR})_{18}]^{1-}$ system.* Described in **Section 1.5.2**, bioorthogonal click reactions such as the Staudinger-Bertozzi ligation, the *trans*-cyclooctene-tetrazine ligation and azide-oxanorbornadiene cycloaddition reactions also serve as promising candidates for the modification of $[\text{Au}_{25}(\text{SR})_{18}]^{1-}$ without the necessity of risky ligand exchange strategies.

7.3 References


1. Li, G.; Jin, R., Atomically Precise Gold Nanoclusters as New Model Catalysts. *Acc. Chem. Res.* **2013**, *46* (8), 1749-1758.
2. Link, S.; El-Sayed, M. A., Shape and size dependence of radiative, non-radiative and photothermal properties of gold nanocrystals. *Int. Rev. Phys. Chem.* **2000**, *19* (3), 409-453.
3. Kang, X.; Chong, H.; Zhu, M., $\text{Au}_{25}(\text{SR})_{18}$: the captain of the great nanocluster ship. *Nanoscale* **2018**, *10* (23), 10758-10834.
4. Dreaden, E. C.; Alkilany, A. M.; Huang, X.; Murphy, C. J.; El-Sayed, M. A., The golden age: gold nanoparticles for biomedicine. *Chem. Soc. Rev.* **2012**, *41* (7), 2740-2779.
5. Gobbo, P.; Novoa, S.; Biesinger, M. C.; Workentin, M. S., Interfacial strain-promoted alkyne–azide cycloaddition (*I*-SPAAC) for the synthesis of nanomaterial hybrids. *Chem. Commun.* **2013**, *49* (38), 3982-3984.
6. Wang, X.; Gobbo, P.; Suchy, M.; Workentin, M. S.; Hudson, R. H. E., Peptide-decorated gold nanoparticles via strain-promoted azide–alkyne cycloaddition and post assembly deprotection. *RSC Adv.* **2014**, *4* (81), 43087-43091.

7. Gobbo, P.; Mossman, Z.; Nazemi, A.; Niaux, A.; Biesinger, M. C.; Gillies, E. R.; Workentin, M. S., Versatile strained alkyne modified water-soluble AuNPs for interfacial strain promoted azide–alkyne cycloaddition (I-SPAAC). *J. Mater. Chem. B* **2014**, *2* (13), 1764-1769.
8. Ghiassian, S.; Yu, L.; Gobbo, P.; Nazemi, A.; Romagnoli, T.; Luo, W.; Luyt, L. G.; Workentin, M. S., Nitrene-Modified Gold Nanoparticles: Synthesis, Characterization, and Their Potential as ¹⁸F-Labeled Positron Emission Tomography Probes via I-SPANC. *ACS Omega* **2019**, *4* (21), 19106-19115.
9. Gobbo, P.; Luo, W.; Cho, S. J.; Wang, X.; Biesinger, M. C.; Hudson, R. H. E.; Workentin, M. S., Small gold nanoparticles for interfacial Staudinger–Bertozzi ligation. *Org. Biomol. Chem.* **2015**, *13* (15), 4605-4612.
10. Gobbo, P.; Workentin, M. S., Improved Methodology for the Preparation of Water-Soluble Maleimide-Functionalized Small Gold Nanoparticles. *Langmuir* **2012**, *28* (33), 12357-12363.
11. Ghiassian, S.; Gobbo, P.; Workentin, M. S., Water-Soluble Maleimide-Modified Gold Nanoparticles (AuNPs) as a Platform for Cycloaddition Reactions. *Eur. J. Org. Chem.* **2015**, *2015* (24), 5438-5447.
12. Gunawardene, P. N.; Luo, W.; Polgar, A. M.; Corrigan, J. F.; Workentin, M. S., Highly Electron-Deficient Pyridinium-Nitrones for Rapid and Tunable Inverse-Electron-Demand Strain-Promoted Alkyne-Nitrene Cycloaddition. *Org. Lett.* **2019**, *21* (14), 5547-5551.
13. Gunawardene, P. N.; Corrigan, J. F.; Workentin, M. S., Golden Opportunity: A Clickable Azide-Functionalized [Au₂₅(SR)₁₈][−] Nanocluster Platform for Interfacial Surface Modifications. *J. Am. Chem. Soc.* **2019**, *141* (30), 11781-11785.
14. Gobbo, P.; Ghiassian, S.; Hesari, M.; Stampelcoskie, K. G.; Kazemi-Zanjani, N.; Laguné-Labarthe, F.; Workentin, M. S., Electrochemistry of robust gold nanoparticle–glassy carbon hybrids generated using a patternable photochemical approach. *J. Mater. Chem.* **2012**, *22* (45), 23971-23980.
15. Safont-Sempere, M. M.; Fernández, G.; Würthner, F., Self-Sorting Phenomena in Complex Supramolecular Systems. *Chem. Rev.* **2011**, *111* (9), 5784-5814.

Appendices

A.1 Permission to Reproduce Copyrighted Material

Permission to reproduce **Figure 1.1a (Top, Left)** – [Section 1.2.1, Reference 12]

 **ACS Publications**
Most Trusted. Most Cited. Most Read.

Size Evolution of Alkanethiol-Protected Gold Nanoparticles by Heat Treatment in the Solid State
Author: Takami Shimizu, Toshiharu Teranishi, Satoshi Hasegawa, et al
Publication: The Journal of Physical Chemistry B
Publisher: American Chemical Society
Date: Mar 1, 2003
Copyright © 2003, American Chemical Society

PERMISSION/LICENSE IS GRANTED FOR YOUR ORDER AT NO CHARGE

This type of permission/license, instead of the standard Terms and Conditions, is sent to you because no fee is being charged for your order. Please note the following:

- Permission is granted for your request in both print and electronic formats, and translations.
- If figures and/or tables were requested, they may be adapted or used in part.
- Please print this page for your records and send a copy of it to your publisher/graduate school.
- Appropriate credit for the requested material should be given as follows: "Reprinted (adapted) with permission from {COMPLETE REFERENCE CITATION}. Copyright {YEAR} American Chemical Society." Insert appropriate information in place of the capitalized words.
- One-time permission is granted only for the use specified in your RightsLink request. No additional uses are granted (such as derivative works or other editions). For any uses, please submit a new request.

If credit is given to another source for the material you requested from RightsLink, permission must be obtained from that source.

Permission to reproduce **Figure 1.1a (Top, Right)** – [Section 1.2.1, Reference 13]

 **ACS Publications**
Most Trusted. Most Cited. Most Read.

Seeded High Yield Synthesis of Short Au Nanorods in Aqueous Solution
Author: Tapan K. Sau, Catherine J. Murphy
Publication: Langmuir
Publisher: American Chemical Society
Date: Jul 1, 2004
Copyright © 2004, American Chemical Society


PERMISSION/LICENSE IS GRANTED FOR YOUR ORDER AT NO CHARGE

This type of permission/license, instead of the standard Terms and Conditions, is sent to you because no fee is being charged for your order. Please note the following:

- Permission is granted for your request in both print and electronic formats, and translations.
- If figures and/or tables were requested, they may be adapted or used in part.
- Please print this page for your records and send a copy of it to your publisher/graduate school.
- Appropriate credit for the requested material should be given as follows: "Reprinted (adapted) with permission from {COMPLETE REFERENCE CITATION}. Copyright {YEAR} American Chemical Society." Insert appropriate information in place of the capitalized words.
- One-time permission is granted only for the use specified in your RightsLink request. No additional uses are granted (such as derivative works or other editions). For any uses, please submit a new request.

If credit is given to another source for the material you requested from RightsLink, permission must be obtained from that source.

Permission to reproduce **Figure 1.1a (Bottom, Left)** – [Section 1.2.1, Reference 14]



Observation of a Quadrupole Plasmon Mode for a Colloidal Solution of Gold Nanoprisms
Author: Jill E. Millstone, Sungho Park, Kevin L. Shuford, et al
Publication: Journal of the American Chemical Society
Publisher: American Chemical Society
Date: Apr 1, 2005
Copyright © 2005, American Chemical Society


PERMISSION/LICENSE IS GRANTED FOR YOUR ORDER AT NO CHARGE

This type of permission/license, instead of the standard Terms and Conditions, is sent to you because no fee is being charged for your order. Please note the following:

- Permission is granted for your request in both print and electronic formats, and translations.
- If figures and/or tables were requested, they may be adapted or used in part.
- Please print this page for your records and send a copy of it to your publisher/graduate school.
- Appropriate credit for the requested material should be given as follows: "Reprinted (adapted) with permission from {COMPLETE REFERENCE CITATION}. Copyright {YEAR} American Chemical Society." Insert appropriate information in place of the capitalized words.
- One-time permission is granted only for the use specified in your RightsLink request. No additional uses are granted (such as derivative works or other editions). For any uses, please submit a new request.

If credit is given to another source for the material you requested from RightsLink, permission must be obtained from that source.

Permission to reproduce **Figure 1.1a (Bottom, Right)** – [Section 1.2.1, Reference 15]



Selective Synthesis of Single-Crystalline Rhombic Dodecahedral, Octahedral, and Cubic Gold Nanocrystals
Author: Wenxin Niu, Shanliang Zheng, Dawei Wang, et al
Publication: Journal of the American Chemical Society
Publisher: American Chemical Society
Date: Jan 1, 2009
Copyright © 2009, American Chemical Society

PERMISSION/LICENSE IS GRANTED FOR YOUR ORDER AT NO CHARGE

This type of permission/license, instead of the standard Terms and Conditions, is sent to you because no fee is being charged for your order. Please note the following:

- Permission is granted for your request in both print and electronic formats, and translations.
- If figures and/or tables were requested, they may be adapted or used in part.
- Please print this page for your records and send a copy of it to your publisher/graduate school.
- Appropriate credit for the requested material should be given as follows: "Reprinted (adapted) with permission from {COMPLETE REFERENCE CITATION}. Copyright {YEAR} American Chemical Society." Insert appropriate information in place of the capitalized words.
- One-time permission is granted only for the use specified in your RightsLink request. No additional uses are granted (such as derivative works or other editions). For any uses, please submit a new request.

If credit is given to another source for the material you requested from RightsLink, permission must be obtained from that source.

Permission to reproduce **Figure 1.1b** – [Section 1.2.1, Reference 16]



This is a License Agreement between Praveen Gunawardene ("User") and Copyright Clearance Center, Inc. ("CCC") on behalf of the Rightsholder identified in the order details below. The license consists of the order details, the CCC Terms and Conditions below, and any Rightsholder Terms and Conditions which are included below. All payments must be made in full to CCC in accordance with the CCC Terms and Conditions below.

Order Date	18-Aug-2021	Type of Use	Republish in a thesis/dissertation
Order License ID	1141519-1	Publisher	ROYAL SOCIETY OF CHEMISTRY, ETC.]
ISSN	0306-0012	Portion	Image/photo/illustration

LICENSED CONTENT

Publication Title	Chemical Society reviews	Rightsholder	Royal Society of Chemistry
Article Title	The golden age: gold nanoparticles for biomedicine.	Publication Type	Journal
Author/Editor	CHEMICAL SOCIETY (GREAT BRITAIN)	Start Page	2740
Date	01/01/1972	End Page	2779
Language	English	Issue	7
Country	United Kingdom of Great Britain and Northern Ireland	Volume	41

REQUEST DETAILS

Portion Type	Image/photo/illustration	Distribution	Worldwide
Number of images / photos / illustrations	1	Translation	Original language of publication
Format (select all that apply)	Electronic	Copies for the disabled?	No
Who will republish the content?	Academic institution	Minor editing privileges?	No
Duration of Use	Life of current edition	Incidental promotional use?	No
Lifetime Unit Quantity	Up to 14,999	Currency	CAD
Rights Requested	Main product		

NEW WORK DETAILS

Title	Nanoorthogonal Surface Modifications of Gold Nanoparticles and Nanoclusters Through Strain-Promoted Cycloaddition Chemistry	Institution name	Western University
Instructor name	Mark S. Workentin	Expected presentation date	2021-08-18

ADDITIONAL DETAILS

Order reference number	N/A	The requesting person / organization to appear on the license	Praveen Gunawardene
------------------------	-----	---	---------------------

REUSE CONTENT DETAILS

Title, description or numeric reference of the portion(s)	Image	Title of the article/chapter the portion is from	The golden age: gold nanoparticles for biomedicine.
Editor of portion(s)	Dreaden, Erik C.; Alkilany, Alaaldin M.; Huang, Xiaohua; Murphy, Catherine J.; El-Sayed, Mostafa A.	Author of portion(s)	Dreaden, Erik C.; Alkilany, Alaaldin M.; Huang, Xiaohua; Murphy, Catherine J.; El-Sayed, Mostafa A.
Volume of serial or monograph	41	Issue, if republishing an article from a serial	7
Page or page range of portion	2740-2779	Publication date of portion	2012-03-12

Permission to reproduce **Figure 1.2a** – [Section 1.2.3, Reference 33]



This is a License Agreement between Praveen Gunawardene ("User") and Copyright Clearance Center, Inc. ("CCC") on behalf of the Rightsholder identified in the order details below. The license consists of the order details, the CCC Terms and Conditions below, and any Rightsholder Terms and Conditions which are included below. All payments must be made in full to CCC in accordance with the CCC Terms and Conditions below.

Order Date	18-Aug-2021	Type of Use	Republish in a thesis/dissertation
Order License ID	1141522-1	Publisher	ROYAL SOCIETY OF CHEMISTRY, ETC.]
ISSN	0306-0012	Portion	Image/photo/illustration

LICENSED CONTENT

Publication Title	Chemical Society reviews	Rightsholder	Royal Society of Chemistry
Article Title	Why gold nanoparticles are more precious than pretty gold: noble metal surface plasmon resonance and its enhancement of the radiative and nonradiative properties of nanocrystals of different shapes.	Publication Type	Journal
Author/Editor	CHEMICAL SOCIETY (GREAT BRITAIN)	Start Page	209
Date	01/01/1972	End Page	217
Language	English	Issue	3
Country	United Kingdom of Great Britain and Northern Ireland	Volume	35

REQUEST DETAILS

Portion Type	Image/photo/illustration	Distribution	Worldwide
Number of images / photos / illustrations	1	Translation	Original language of publication
Format (select all that apply)	Electronic	Copies for the disabled?	No
Who will republish the content?	Academic institution	Minor editing privileges?	No
Duration of Use	Life of current edition	Incidental promotional use?	No
Lifetime Unit Quantity	Up to 14,999	Currency	CAD
Rights Requested	Main product		

NEW WORK DETAILS

Title	Nanoorthogonal Surface Modifications of Gold Nanoparticles and Nanoclusters Through Strain-Promoted Cycloaddition Chemistry	Institution name	Western University
Instructor name	Mark S. Workentin	Expected presentation date	2021-08-18

ADDITIONAL DETAILS

Order reference number	N/A	The requesting person / organization to appear on the license	Praveen Gunawardene
------------------------	-----	---	---------------------

REUSE CONTENT DETAILS

Title, description or numeric reference of the portion(s)	Image	Title of the article/chapter the portion is from	Why gold nanoparticles are more precious than pretty gold: noble metal surface plasmon resonance and its enhancement of the radiative and nonradiative properties of nanocrystals of different shapes.
Editor of portion(s)	Eustis, Susie; El-Sayed, Mostafa A.	Author of portion(s)	Eustis, Susie; El-Sayed, Mostafa A.
Volume of serial or monograph	35	Issue, if republishing an article from a serial	3
Page or page range of portion	209-217	Publication date of portion	2006-02-27

Permission to reproduce **Figure 1.2b** – [Section 1.2.3, Reference 37]

Interparticle Coupling Effects on Plasmon Resonances of Nanogold Particles



Author: K.-H. Su, Q.-H. Wei, X. Zhang, et al
Publication: Nano Letters
Publisher: American Chemical Society
Date: Aug 1, 2003

Copyright © 2003, American Chemical Society

PERMISSION/LICENSE IS GRANTED FOR YOUR ORDER AT NO CHARGE

This type of permission/license, instead of the standard Terms and Conditions, is sent to you because no fee is being charged for your order. Please note the following:

- Permission is granted for your request in both print and electronic formats, and translations.
- If figures and/or tables were requested, they may be adapted or used in part.
- Please print this page for your records and send a copy of it to your publisher/graduate school.
- Appropriate credit for the requested material should be given as follows: "Reprinted (adapted) with permission from {COMPLETE REFERENCE CITATION}. Copyright {YEAR} American Chemical Society." Insert appropriate information in place of the capitalized words.
- One-time permission is granted only for the use specified in your RightsLink request. No additional uses are granted (such as derivative works or other editions). For any uses, please submit a new request.

If credit is given to another source for the material you requested from RightsLink, permission must be obtained from that source.

Permission to reproduce **Figure 1.3a** – [Section 1.2.3, Reference 43]

Determining the Size and Shape Dependence of Gold Nanoparticle Uptake into Mammalian Cells



Author: B. Devika Chithrani, Arezou A. Ghazani, Warren C. W. Chan
Publication: Nano Letters
Publisher: American Chemical Society
Date: Apr 1, 2006

Copyright © 2006, American Chemical Society

PERMISSION/LICENSE IS GRANTED FOR YOUR ORDER AT NO CHARGE

This type of permission/license, instead of the standard Terms and Conditions, is sent to you because no fee is being charged for your order. Please note the following:

- Permission is granted for your request in both print and electronic formats, and translations.
- If figures and/or tables were requested, they may be adapted or used in part.
- Please print this page for your records and send a copy of it to your publisher/graduate school.
- Appropriate credit for the requested material should be given as follows: "Reprinted (adapted) with permission from {COMPLETE REFERENCE CITATION}. Copyright {YEAR} American Chemical Society." Insert appropriate information in place of the capitalized words.
- One-time permission is granted only for the use specified in your RightsLink request. No additional uses are granted (such as derivative works or other editions). For any uses, please submit a new request.

If credit is given to another source for the material you requested from RightsLink, permission must be obtained from that source.

Permission to reproduce **Figure 1.3b** – [Section 1.2.3, Reference 45]

CCC | RightsLink® Home ? Help Live Chat Praveen Gunawardene

Transferrin-Mediated Gold Nanoparticle Cellular Uptake
 Author: Pei-Hui Yang, Xuesong Sun, Jen-Fu Chiu, et al
 Publication: Bioconjugate Chemistry
 Publisher: American Chemical Society
 Date: May 1, 2005
 Copyright © 2005, American Chemical Society

PERMISSION/LICENSE IS GRANTED FOR YOUR ORDER AT NO CHARGE

This type of permission/license, instead of the standard Terms and Conditions, is sent to you because no fee is being charged for your order. Please note the following:

- Permission is granted for your request in both print and electronic formats, and translations.
- If figures and/or tables were requested, they may be adapted or used in part.
- Please print this page for your records and send a copy of it to your publisher/graduate school.
- Appropriate credit for the requested material should be given as follows: "Reprinted (adapted) with permission from {COMPLETE REFERENCE CITATION}. Copyright {YEAR} American Chemical Society." Insert appropriate information in place of the capitalized words.
- One-time permission is granted only for the use specified in your RightsLink request. No additional uses are granted (such as derivative works or other editions). For any uses, please submit a new request.

If credit is given to another source for the material you requested from RightsLink, permission must be obtained from that source.

Permission to reproduce spectra in **Figure 1.4a (right)** – [Section 1.2.4, Reference 48]

CCC | RightsLink® Home ? Help Live Chat Praveen Gunawardene

License Number	5132031404920	Order Details	
License date	Aug 18, 2021	Type of use	Dissertation/Thesis
Licensed Content		Requestor type	University/Academic
Licensed Content Publisher	John Wiley and Sons	Format	Electronic
Licensed Content Publication	Angewandte Chemie International Edition	Portion	Figure/table
Licensed Content Title	A Simple Strategy for Prompt Visual Sensing by Gold Nanoparticles: General Applications of Interparticle Hydrogen Bonds	Number of figures/tables	1
Licensed Content Author	Shu-Yi Lin, Sung-Hsun Wu, Chun-hsien Chen	Will you be translating?	No
Licensed Content Date	Jul 20, 2006		
Licensed Content Volume	45		
Licensed Content Issue	30		
Licensed Content Pages	4		
About Your Work		Additional Data	
Title	Nanoorthogonal Surface Modifications of Gold Nanoparticles and Nanoclusters Through Strain-Promoted Cycloaddition Chemistry	Portions	Figure 2
Institution name	Western University		
Expected presentation date	Aug 2021		
Requestor Location		Tax Details	
	Western University	Publisher Tax ID	EU826007151
Requestor Location	London, ON N6H 5W7 Canada Attn: Western University		

Permission to reproduce spectra in **Figure 1.4b (right)** – [Section 1.2.4, Reference 49]



This is a License Agreement between Praveen Gunawardene ("User") and Copyright Clearance Center, Inc. ("CCC") on behalf of the Rightsholder identified in the order details below. The license consists of the order details, the CCC Terms and Conditions below, and any Rightsholder Terms and Conditions which are included below. All payments must be made in full to CCC in accordance with the CCC Terms and Conditions below.

Order Date	18-Aug-2021	Type of Use	Republish in a thesis/dissertation
Order License ID	1141532-1	Publisher	ROYAL SOCIETY OF CHEMISTRY
ISSN	1364-548X	Portion	Image/photo/illustration

LICENSED CONTENT

Publication Title	Chemical communications	Rightsholder	Royal Society of Chemistry
Article Title	Parameters for selective colorimetric sensing of mercury(II) in aqueous solutions using mercaptopropionic acid-modified gold nanoparticles.	Publication Type	e-Journal
Author/Editor	Royal Society of Chemistry (Great Britain)	Start Page	1215
Date	01/01/1996	End Page	1217
Language	English	Issue	12
Country	United Kingdom of Great Britain and Northern Ireland	Volume	0

REQUEST DETAILS

Portion Type	Image/photo/illustration	Distribution	Worldwide
Number of images / photos / illustrations	1	Translation	Original language of publication
Format (select all that apply)	Electronic	Copies for the disabled?	No
Who will republish the content?	Academic institution	Minor editing privileges?	No
Duration of Use	Life of current edition	Incidental promotional use?	No
Lifetime Unit Quantity	Up to 14,999	Currency	CAD
Rights Requested	Main product		

NEW WORK DETAILS

Title	Nanoorthogonal Surface Modifications of Gold Nanoparticles and Nanoclusters Through Strain-Promoted Cycloaddition Chemistry	Institution name	Western University
Instructor name	Mark S. Workentin	Expected presentation date	2021-08-18

ADDITIONAL DETAILS

Order reference number	N/A	The requesting person / organization to appear on the license	Praveen Gunawardene
------------------------	-----	---	---------------------

REUSE CONTENT DETAILS

Title, description or numeric reference of the portion(s)	Image	Title of the article/chapter the portion is from	Parameters for selective colorimetric sensing of mercury(II) in aqueous solutions using mercaptopropionic acid-modified gold nanoparticles.
Editor of portion(s)	Huang, Chih-Ching; Chang, Huan-Tsung	Author of portion(s)	Huang, Chih-Ching; Chang, Huan-Tsung
Volume of serial or monograph	0	Issue, if republishing an article from a serial	12
Page or page range of portion	1215-1217	Publication date of portion	2007-03-28

Permission to reproduce **Figure 1.5b,c,d** – [Section 1.2.4, Reference 53]

CCC | RightsLink®

Home ? Live Chat Praveen Gunawardene

License Number	5132041195522		
License date	Aug 18, 2021		
Licensed Content		Order Details	
Licensed Content Publisher	John Wiley and Sons	Type of use	Dissertation/Thesis
Licensed Content Publication	Angewandte Chemie International Edition	Requestor type	University/Academic
Licensed Content Title	Tuning the In Vivo Transport of Anticancer Drugs Using Renal-Clearable Gold Nanoparticles	Format	Electronic
Licensed Content Author	Jie Zheng, Jer-Tsong Hsieh, Payal Kapur, et al	Portion	Figure/table
Licensed Content Date	May 14, 2019	Number of figures/tables	2
Licensed Content Volume	58	Will you be translating?	No
Licensed Content Issue	25		
Licensed Content Pages	5		
About Your Work		Additional Data	
Title	Nanoorthogonal Surface Modifications of Gold Nanoparticles and Nanoclusters Through Strain-Promoted Cycloaddition Chemistry	Portions	Figure 1d, Figure 3b
Institution name	Western University		
Expected presentation date	Aug 2021		
Requestor Location		Tax Details	
	Western University	Publisher Tax ID	EU826007151
Requestor Location	London, ON N6H 5W7 Canada Attn: Western University		

Permission to reproduce **Figure 1.6b,c** – [Section 1.2.4, Reference 56]

CCC | RightsLink®

Home ? Live Chat Praveen Gunawardene

Nano-Flares: Probes for Transfection and mRNA Detection in Living Cells

Author: Dwight S. Seferos, David A. Gijjohann, Haley D. Hill, et al

Publication: Journal of the American Chemical Society

Publisher: American Chemical Society

Date: Dec 1, 2007

Copyright © 2007, American Chemical Society

PERMISSION/LICENSE IS GRANTED FOR YOUR ORDER AT NO CHARGE

This type of permission/license, instead of the standard Terms and Conditions, is sent to you because no fee is being charged for your order. Please note the following:

- Permission is granted for your request in both print and electronic formats, and translations.
- If figures and/or tables were requested, they may be adapted or used in part.
- Please print this page for your records and send a copy of it to your publisher/graduate school.
- Appropriate credit for the requested material should be given as follows: "Reprinted (adapted) with permission from {COMPLETE REFERENCE CITATION}. Copyright (YEAR) American Chemical Society." Insert appropriate information in place of the capitalized words.
- One-time permission is granted only for the use specified in your RightsLink request. No additional uses are granted (such as derivative works or other editions). For any uses, please submit a new request.

If credit is given to another source for the material you requested from RightsLink, permission must be obtained from that source.

Permission to produce **Figure 1.7 (Top, Left)** from supplementary data – [Section 1.3.1, Reference 59]

CCC | RightsLink® Home Help ▾ Live Chat Praveen Gunawardene ▾

Gold–Thiolate Ring as a Protecting Motif in the Au₂₀(SR)₁₆ Nanocluster and Implications
Author: Chenjie Zeng, Chong Liu, Yuxiang Chen, et al
Publication: Journal of the American Chemical Society
Publisher: American Chemical Society
Date: Aug 1, 2014
Copyright © 2014, American Chemical Society

PERMISSION/LICENSE IS GRANTED FOR YOUR ORDER AT NO CHARGE

This type of permission/license, instead of the standard Terms and Conditions, is sent to you because no fee is being charged for your order. Please note the following:

- Permission is granted for your request in both print and electronic formats, and translations.
- If figures and/or tables were requested, they may be adapted or used in part.
- Please print this page for your records and send a copy of it to your publisher/graduate school.
- Appropriate credit for the requested material should be given as follows: "Reprinted (adapted) with permission from {COMPLETE REFERENCE CITATION}. Copyright {YEAR} American Chemical Society." Insert appropriate information in place of the capitalized words.
- One-time permission is granted only for the use specified in your RightsLink request. No additional uses are granted (such as derivative works or other editions). For any uses, please submit a new request.

If credit is given to another source for the material you requested from RightsLink, permission must be obtained from that source.

Permission to produce **Figure 1.7 (Top, Middle)** from supplementary data – [Section 1.3.1, Reference 60]

CCC | RightsLink® Home Help ▾ Live Chat Praveen Gunawardene ▾

Nonsuperatomic [Au₂₃(SC₆H₁₁)₁₆]– Nanocluster Featuring Bipyramidal Au₁₅ Kernel and Trimeric Au₃(SR)₄ Motif
Author: Anindita Das, Tao Li, Katsuyuki Nobusada, et al
Publication: Journal of the American Chemical Society
Publisher: American Chemical Society
Date: Dec 1, 2013
Copyright © 2013, American Chemical Society

PERMISSION/LICENSE IS GRANTED FOR YOUR ORDER AT NO CHARGE

This type of permission/license, instead of the standard Terms and Conditions, is sent to you because no fee is being charged for your order. Please note the following:

- Permission is granted for your request in both print and electronic formats, and translations.
- If figures and/or tables were requested, they may be adapted or used in part.
- Please print this page for your records and send a copy of it to your publisher/graduate school.
- Appropriate credit for the requested material should be given as follows: "Reprinted (adapted) with permission from {COMPLETE REFERENCE CITATION}. Copyright {YEAR} American Chemical Society." Insert appropriate information in place of the capitalized words.
- One-time permission is granted only for the use specified in your RightsLink request. No additional uses are granted (such as derivative works or other editions). For any uses, please submit a new request.

If credit is given to another source for the material you requested from RightsLink, permission must be obtained from that source.

Permission to produce **Figure 1.7 (Top, Right)** from supplementary data – [Section 1.3.1, Reference 61]



This is a License Agreement between Praveen Gunawardene ("User") and Copyright Clearance Center, Inc. ("CCC") on behalf of the Rightsholder identified in the order details below. The license consists of the order details, the CCC Terms and Conditions below, and any Rightsholder Terms and Conditions which are included below. All payments must be made in full to CCC in accordance with the CCC Terms and Conditions below.

Order Date	18-Aug-2021	Type of Use	Republish in a thesis/dissertation
Order License ID	1141536-1	Publisher	RSC Pub
ISSN	2040-3364	Portion	Chart/graph/table/figure

LICENSED CONTENT

Publication Title	Nanoscale	Rightsholder	Royal Society of Chemistry
Article Title	Crystal structure and electronic properties of a thiolate-protected Au ₂₄ nanocluster.	Publication Type	Journal
Author/Editor	Guo jia na mi ke xue zhong xin (China), Royal Society of Chemistry (Great Britain)	Start Page	6458
Date	01/01/2009	Issue	12
Language	English	Volume	6
Country	United Kingdom of Great Britain and Northern Ireland		

REQUEST DETAILS

Portion Type	Chart/graph/table/figure	Distribution	Worldwide
Number of charts / graphs / tables / figures requested	1	Translation	Original language of publication
Format (select all that apply)	Electronic	Copies for the disabled?	No
Who will republish the content?	Academic institution	Minor editing privileges?	No
Duration of Use	Life of current edition	Incidental promotional use?	No
Lifetime Unit Quantity	Up to 14,999	Currency	CAD
Rights Requested	Main product		

NEW WORK DETAILS

Title	Nanoorthogonal Surface Modifications of Gold Nanoparticles and Nanoclusters Through Strain-Promoted Cycloaddition Chemistry	Institution name	Western University
Instructor name	Mark S. Workentin	Expected presentation date	2021-08-18

ADDITIONAL DETAILS

Order reference number	N/A	The requesting person / organization to appear on the license	Praveen Gunawardene
------------------------	-----	---	---------------------

REUSE CONTENT DETAILS

Title, description or numeric reference of the portion(s)	Image	Title of the article/chapter the portion is from	Crystal structure and electronic properties of a thiolate-protected Au ₂₄ nanocluster.
Editor of portion(s)	Das, Anindita; Li, Tao; Li, Gao; Nobusada, Katsuyuki; Zeng, Chenjie; Rosi, Nathaniel L.; Jin, Rongchao	Author of portion(s)	Das, Anindita; Li, Tao; Li, Gao; Nobusada, Katsuyuki; Zeng, Chenjie; Rosi, Nathaniel L.; Jin, Rongchao
Volume of serial or monograph	6	Issue, if republishing an article from a serial	12
Page or page range of portion	6458	Publication date of portion	2014-05-29

Permission to produce **Figure 1.7 (Middle, Left)** from supplementary data – [Section 1.3.1, Reference 62]

CCC | RightsLink®

Home ? Live Chat Praveen Gunawardene

Correlating the Crystal Structure of A Thiol-Protected Au₂₅ Cluster and Optical Properties

Author: Manzhou Zhu, Christine M. Aikens, Frederick J. Hollander, et al
Publication: Journal of the American Chemical Society
Publisher: American Chemical Society
Date: May 1, 2008
Copyright © 2008, American Chemical Society

ACSPublications
Most Trusted. Most Cited. Most Read.

PERMISSION/LICENSE IS GRANTED FOR YOUR ORDER AT NO CHARGE

This type of permission/license, instead of the standard Terms and Conditions, is sent to you because no fee is being charged for your order. Please note the following:

- Permission is granted for your request in both print and electronic formats, and translations.
- If figures and/or tables were requested, they may be adapted or used in part.
- Please print this page for your records and send a copy of it to your publisher/graduate school.
- Appropriate credit for the requested material should be given as follows: "Reprinted (adapted) with permission from (COMPLETE REFERENCE CITATION). Copyright (YEAR) American Chemical Society." Insert appropriate information in place of the capitalized words.
- One-time permission is granted only for the use specified in your RightsLink request. No additional uses are granted (such as derivative works or other editions). For any uses, please submit a new request.

If credit is given to another source for the material you requested from RightsLink, permission must be obtained from that source.

Permission to produce **Figure 1.7 (Middle, Right)** from supplementary data – [Section 1.3.1, Reference 63]

CCC | RightsLink®

Home ? Live Chat Praveen Gunawardene

Chiral Structure of Thiolate-Protected 28-Gold-Atom Nanocluster Determined by X-ray Crystallography

Author: Chenjie Zeng, Tao Li, Anindita Das, et al
Publication: Journal of the American Chemical Society
Publisher: American Chemical Society
Date: Jul 1, 2013
Copyright © 2013, American Chemical Society

ACSPublications
Most Trusted. Most Cited. Most Read.


PERMISSION/LICENSE IS GRANTED FOR YOUR ORDER AT NO CHARGE

This type of permission/license, instead of the standard Terms and Conditions, is sent to you because no fee is being charged for your order. Please note the following:


- Permission is granted for your request in both print and electronic formats, and translations.
- If figures and/or tables were requested, they may be adapted or used in part.
- Please print this page for your records and send a copy of it to your publisher/graduate school.
- Appropriate credit for the requested material should be given as follows: "Reprinted (adapted) with permission from (COMPLETE REFERENCE CITATION). Copyright (YEAR) American Chemical Society." Insert appropriate information in place of the capitalized words.
- One-time permission is granted only for the use specified in your RightsLink request. No additional uses are granted (such as derivative works or other editions). For any uses, please submit a new request.

If credit is given to another source for the material you requested from RightsLink, permission must be obtained from that source.

Permission to produce **Figure 1.7 (Bottom, Left)** from supplementary data – [Section 1.3.1, Reference 64]

 Home Help Live Chat Praveen Gunawardene

Total Structure Determination of Thiolate-Protected Au38 Nanoparticles

 **Author:** Huifeng Qian, William T. Eckenhoff, Yan Zhu, et al
Publication: Journal of the American Chemical Society
Publisher: American Chemical Society
Date: Jun 1, 2010
Copyright © 2010, American Chemical Society


PERMISSION/LICENSE IS GRANTED FOR YOUR ORDER AT NO CHARGE

This type of permission/license, instead of the standard Terms and Conditions, is sent to you because no fee is being charged for your order. Please note the following:


- Permission is granted for your request in both print and electronic formats, and translations.
- If figures and/or tables were requested, they may be adapted or used in part.
- Please print this page for your records and send a copy of it to your publisher/graduate school.
- Appropriate credit for the requested material should be given as follows: "Reprinted (adapted) with permission from (COMPLETE REFERENCE CITATION). Copyright (YEAR) American Chemical Society." Insert appropriate information in place of the capitalized words.
- One-time permission is granted only for the use specified in your RightsLink request. No additional uses are granted (such as derivative works or other editions). For any uses, please submit a new request.

If credit is given to another source for the material you requested from RightsLink, permission must be obtained from that source.

Permission to produce **Figure 1.7 (Bottom, Right)** from supplementary data – [Section 1.3.1, Reference 65]

 Home Help Live Chat Praveen Gunawardene

Gold Quantum Boxes: On the Periodicities and the Quantum Confinement in the Au28, Au36, Au44, and Au52 Magic Series

 **Author:** Chenjie Zeng, Yuxiang Chen, Kenji Iida, et al
Publication: Journal of the American Chemical Society
Publisher: American Chemical Society
Date: Mar 1, 2016
Copyright © 2016, American Chemical Society

PERMISSION/LICENSE IS GRANTED FOR YOUR ORDER AT NO CHARGE

This type of permission/license, instead of the standard Terms and Conditions, is sent to you because no fee is being charged for your order. Please note the following:

- Permission is granted for your request in both print and electronic formats, and translations.
- If figures and/or tables were requested, they may be adapted or used in part.
- Please print this page for your records and send a copy of it to your publisher/graduate school.
- Appropriate credit for the requested material should be given as follows: "Reprinted (adapted) with permission from (COMPLETE REFERENCE CITATION). Copyright (YEAR) American Chemical Society." Insert appropriate information in place of the capitalized words.
- One-time permission is granted only for the use specified in your RightsLink request. No additional uses are granted (such as derivative works or other editions). For any uses, please submit a new request.

If credit is given to another source for the material you requested from RightsLink, permission must be obtained from that source.

Permission to produce **Figure 1.8** from supplementary data – [Section 1.3.3, Reference 62]

Correlating the Crystal Structure of A Thiol-Protected Au₂₅ Cluster and Optical Properties



Author: Manzhou Zhu, Christine M. Aikens, Frederick J. Hollander, et al

Publication: Journal of the American Chemical Society

Publisher: American Chemical Society

Date: May 1, 2008

Copyright © 2008, American Chemical Society

PERMISSION/LICENSE IS GRANTED FOR YOUR ORDER AT NO CHARGE

This type of permission/license, instead of the standard Terms and Conditions, is sent to you because no fee is being charged for your order. Please note the following:

- Permission is granted for your request in both print and electronic formats, and translations.
- If figures and/or tables were requested, they may be adapted or used in part.
- Please print this page for your records and send a copy of it to your publisher/graduate school.
- Appropriate credit for the requested material should be given as follows: "Reprinted (adapted) with permission from {COMPLETE REFERENCE CITATION}. Copyright {YEAR} American Chemical Society." Insert appropriate information in place of the capitalized words.
- One-time permission is granted only for the use specified in your RightsLink request. No additional uses are granted (such as derivative works or other editions). For any uses, please submit a new request.

If credit is given to another source for the material you requested from RightsLink, permission must be obtained from that source.

Permission to reproduce **Figure 1.9a** – [Section 1.3.4, Reference 88]

Quantum Sized Gold Nanoclusters with Atomic Precision



Author: Huifeng Qian, Manzhou Zhu, Zhikun Wu, et al

Publication: Accounts of Chemical Research

Publisher: American Chemical Society

Date: Sep 1, 2012

Copyright © 2012, American Chemical Society

PERMISSION/LICENSE IS GRANTED FOR YOUR ORDER AT NO CHARGE

This type of permission/license, instead of the standard Terms and Conditions, is sent to you because no fee is being charged for your order. Please note the following:

- Permission is granted for your request in both print and electronic formats, and translations.
- If figures and/or tables were requested, they may be adapted or used in part.
- Please print this page for your records and send a copy of it to your publisher/graduate school.
- Appropriate credit for the requested material should be given as follows: "Reprinted (adapted) with permission from {COMPLETE REFERENCE CITATION}. Copyright {YEAR} American Chemical Society." Insert appropriate information in place of the capitalized words.
- One-time permission is granted only for the use specified in your RightsLink request. No additional uses are granted (such as derivative works or other editions). For any uses, please submit a new request.

If credit is given to another source for the material you requested from RightsLink, permission must be obtained from that source.

Permission to reproduce **Figure 1.9b** – [Section 1.3.4, Reference 62]

Correlating the Crystal Structure of A Thiol-Protected Au₂₅ Cluster and Optical Properties



Author: Manzhou Zhu, Christine M. Aikens, Frederick J. Hollander, et al

Publication: Journal of the American Chemical Society

Publisher: American Chemical Society

Date: May 1, 2008

Copyright © 2008, American Chemical Society

PERMISSION/LICENSE IS GRANTED FOR YOUR ORDER AT NO CHARGE

This type of permission/license, instead of the standard Terms and Conditions, is sent to you because no fee is being charged for your order. Please note the following:

- Permission is granted for your request in both print and electronic formats, and translations.
- If figures and/or tables were requested, they may be adapted or used in part.
- Please print this page for your records and send a copy of it to your publisher/graduate school.
- Appropriate credit for the requested material should be given as follows: "Reprinted (adapted) with permission from {COMPLETE REFERENCE CITATION}. Copyright {YEAR} American Chemical Society." Insert appropriate information in place of the capitalized words.
- One-time permission is granted only for the use specified in your RightsLink request. No additional uses are granted (such as derivative works or other editions). For any uses, please submit a new request.

If credit is given to another source for the material you requested from RightsLink, permission must be obtained from that source.

Permission to reproduce **Figure 1.10a,b** – [Section 1.3.4, Reference 81]

On the Ligand's Role in the Fluorescence of Gold Nanoclusters



Author: Zhikun Wu, Rongchao Jin

Publication: Nano Letters

Publisher: American Chemical Society

Date: Jul 1, 2010

Copyright © 2010, American Chemical Society

PERMISSION/LICENSE IS GRANTED FOR YOUR ORDER AT NO CHARGE

This type of permission/license, instead of the standard Terms and Conditions, is sent to you because no fee is being charged for your order. Please note the following:

- Permission is granted for your request in both print and electronic formats, and translations.
- If figures and/or tables were requested, they may be adapted or used in part.
- Please print this page for your records and send a copy of it to your publisher/graduate school.
- Appropriate credit for the requested material should be given as follows: "Reprinted (adapted) with permission from {COMPLETE REFERENCE CITATION}. Copyright {YEAR} American Chemical Society." Insert appropriate information in place of the capitalized words.
- One-time permission is granted only for the use specified in your RightsLink request. No additional uses are granted (such as derivative works or other editions). For any uses, please submit a new request.

If credit is given to another source for the material you requested from RightsLink, permission must be obtained from that source.

Permission to reproduce **Figure 1.11** – [Section 1.3.4, Reference 94]

Electrochemistry and Optical Absorbance and Luminescence of Molecule-like Au38 Nanoparticles



Author: Dongil Lee, Robert L. Donkers, Gangli Wang, et al

Publication: Journal of the American Chemical Society

Publisher: American Chemical Society

Date: May 1, 2004

Copyright © 2004, American Chemical Society

PERMISSION/LICENSE IS GRANTED FOR YOUR ORDER AT NO CHARGE

This type of permission/license, instead of the standard Terms and Conditions, is sent to you because no fee is being charged for your order. Please note the following:

- Permission is granted for your request in both print and electronic formats, and translations.
- If figures and/or tables were requested, they may be adapted or used in part.
- Please print this page for your records and send a copy of it to your publisher/graduate school.
- Appropriate credit for the requested material should be given as follows: "Reprinted (adapted) with permission from {COMPLETE REFERENCE CITATION}. Copyright {YEAR} American Chemical Society." Insert appropriate information in place of the capitalized words.
- One-time permission is granted only for the use specified in your RightsLink request. No additional uses are granted (such as derivative works or other editions). For any uses, please submit a new request.

If credit is given to another source for the material you requested from RightsLink, permission must be obtained from that source.

Permission to reproduce spectra in **Figure 1.12 (right)** – [Section 1.3.5, Reference 97]



This is a License Agreement between Praveen Gunawardene ("User") and Copyright Clearance Center, Inc. ("CCC") on behalf of the Rightsholder identified in the order details below. The license consists of the order details, the CCC Terms and Conditions below, and any Rightsholder Terms and Conditions which are included below. All payments must be made in full to CCC in accordance with the CCC Terms and Conditions below.

Order Date	18-Aug-2021	Type of Use	Republish in a thesis/dissertation
Order License ID	1141537-1	Publisher	ROYAL SOCIETY OF CHEMISTRY
ISSN	1364-548X	Portion	Image/photo/illustration

LICENSED CONTENT

Publication Title	Chemical communications	Rightsholder	Royal Society of Chemistry
Article Title	Highly selective and ultrasensitive detection of Hg(2+) based on fluorescence quenching of Au nanoclusters by Hg(2+)-Au(+) interactions.	Publication Type	e-Journal
Author/Editor	Royal Society of Chemistry (Great Britain)	Start Page	961
Date	01/01/1996	End Page	963
Language	English	Issue	6
Country	United Kingdom of Great Britain and Northern Ireland	Volume	46

REQUEST DETAILS

Portion Type	Image/photo/illustration	Distribution	Worldwide
Number of images / photos / illustrations	1	Translation	Original language of publication
Format (select all that apply)	Electronic	Copies for the disabled?	No
Who will republish the content?	Academic institution	Minor editing privileges?	No
Duration of Use	Life of current edition	Incidental promotional use?	No
Lifetime Unit Quantity	Up to 14,999	Currency	CAD
Rights Requested	Main product		

NEW WORK DETAILS

Title	Nanoorthogonal Surface Modifications of Gold Nanoparticles and Nanoclusters Through Strain-Promoted Cycloaddition Chemistry	Institution name	Western University
Instructor name	Mark S. Workentin	Expected presentation date	2021-08-18

ADDITIONAL DETAILS

Order reference number	N/A	The requesting person / organization to appear on the license	Praveen Gunawardene
------------------------	-----	---	---------------------

REUSE CONTENT DETAILS

Title, description or numeric reference of the portion(s)	Image	Title of the article/chapter the portion is from	Highly selective and ultrasensitive detection of Hg(2+) based on fluorescence quenching of Au nanoclusters by Hg(2+)-Au(+) interactions.
Editor of portion(s)	Xie, Jianping; Zheng, Yuangang; Ying, Jackie Y.	Author of portion(s)	Xie, Jianping; Zheng, Yuangang; Ying, Jackie Y.
Volume of serial or monograph	46	Issue, if republishing an article from a serial	6
Page or page range of portion	961-963	Publication date of portion	2010-02-14

Permission to reproduce synthetic data in **Figure 1.13a** – [Section 1.3.5, Reference 101]

Tailoring the Electronic and Catalytic Properties of Au₂₅ Nanoclusters via Ligand Engineering



Author: Gao Li, Hadi Abroshan, Chong Liu, et al

Publication: ACS Nano

Publisher: American Chemical Society

Date: Aug 1, 2016

Copyright © 2016, American Chemical Society

PERMISSION/LICENSE IS GRANTED FOR YOUR ORDER AT NO CHARGE

This type of permission/license, instead of the standard Terms and Conditions, is sent to you because no fee is being charged for your order. Please note the following:

- Permission is granted for your request in both print and electronic formats, and translations.
- If figures and/or tables were requested, they may be adapted or used in part.
- Please print this page for your records and send a copy of it to your publisher/graduate school.
- Appropriate credit for the requested material should be given as follows: "Reprinted (adapted) with permission from (COMPLETE REFERENCE CITATION). Copyright (YEAR) American Chemical Society." Insert appropriate information in place of the capitalized words.
- One-time permission is granted only for the use specified in your RightsLink request. No additional uses are granted (such as derivative works or other editions). For any uses, please submit a new request.

If credit is given to another source for the material you requested from RightsLink, permission must be obtained from that source.

Permission to reproduce synthetic data in **Figure 1.13b** – [Section 1.3.5, Reference 103]

Gold Nanocluster-Catalyzed Semihydrogenation: A Unique Activation Pathway for Terminal Alkynes



Author: Gao Li, Rongchao Jin

Publication: Journal of the American Chemical Society

Publisher: American Chemical Society

Date: Aug 1, 2014

Copyright © 2014, American Chemical Society

PERMISSION/LICENSE IS GRANTED FOR YOUR ORDER AT NO CHARGE

This type of permission/license, instead of the standard Terms and Conditions, is sent to you because no fee is being charged for your order. Please note the following:

- Permission is granted for your request in both print and electronic formats, and translations.
- If figures and/or tables were requested, they may be adapted or used in part.
- Please print this page for your records and send a copy of it to your publisher/graduate school.
- Appropriate credit for the requested material should be given as follows: "Reprinted (adapted) with permission from (COMPLETE REFERENCE CITATION). Copyright (YEAR) American Chemical Society." Insert appropriate information in place of the capitalized words.
- One-time permission is granted only for the use specified in your RightsLink request. No additional uses are granted (such as derivative works or other editions). For any uses, please submit a new request.

If credit is given to another source for the material you requested from RightsLink, permission must be obtained from that source.

Permission to reproduce confocal images in **Figure 1.14 (right)** – [Section 1.3.5, Reference 104]

License date	Aug 18, 2021		
Licensed Content		Order Details	
Licensed Content Publisher	Elsevier	Type of Use	reuse in a thesis/dissertation
Licensed Content Publication	Journal of Colloid and Interface Science	Portion	figures/tables/illustrations
Licensed Content Title	Synthesis of ultrastable and multifunctional gold nanoclusters with enhanced fluorescence and potential anticancer drug delivery application	Number of figures/tables/illustrations	1
Licensed Content Author	Xiaodong Zhang,Fu-Gen Wu,Peidang Liu,Hong-Yin Wang,Ning Gu,Zhan Chen	Format	electronic
Licensed Content Date	Oct 1, 2015	Are you the author of this Elsevier article?	No
Licensed Content Volume	455	Will you be translating?	No
Licensed Content Issue	n/a		
Licensed Content Pages	10		
About Your Work		Additional Data	
Title	Nanoorthogonal Surface Modifications of Gold Nanoparticles and Nanoclusters Through Strain-Promoted Cycloaddition Chemistry	Portions	Figure 8
Institution name	Western University		
Expected presentation date	Aug 2021		
Requestor Location		Tax Details	
	Western University	Publisher Tax ID	GB 494 6272 12
Requestor Location	London, ON N6H 5W7 Canada Attn: Western University		

A.2 Curriculum Vitae

EDUCATION

Doctor of Philosophy (*Organic Chemistry*)

University of Western Ontario, London, Ontario **2021**

Bachelor of Science (*Honors Specialization in Chemistry and Biochemistry*) **2015**

The University of Western Ontario, London, Ontario

- Deans Honor List – 2013, 2014, 2015
- Relevant Courses – Organic Chemistry, Inorganic Chemistry, Physical Chemistry, Analytical Chemistry, Quantum Chemistry, Biochemistry, Genetics, Molecular Biology, Biological Macromolecules, Cell Biology

Ontario College Diploma (*Chemical Laboratory Technology*) **2012**

Seneca College, York, Ontario

- President's Honor List
- Relevant Courses: General Chemistry, Organic Chemistry, Applied Inorganic Chemistry, Chemical Instrumentation, Biology, Biochemistry, Physics, Pharmaceutical Analysis, Techniques in Analytical Chemistry, Introductory Microbiology, Industrial Microbiology

Ontario Secondary School Diploma

Crescent High School, Toronto, Ontario

GCE Ordinary Level Diploma

Saltus Grammar School, Hamilton, Bermuda

RESEARCH EXPERIENCE

Organic Chemistry Summer Research Scholar

Apr 2015 – Aug 2015

University of Western Ontario – Mark Workentin Research Group

Organic Chemistry Pre-Thesis Summer Research Scholar

Apr 2014 – Aug 2014

University of Western Ontario – Mark Workentin Research Group

- Responsible for assisting PhD candidate and member of Workentin research group, Pierangelo Gobbo.
- Projects involved in: Rhodamine (fluorescent dye) synthesis and potential nanomaterial applications.

Organic Chemistry Volunteer Research Assistant

May 2013 – Apr 2014

University of Western Ontario – Mark Workentin Research Group

- Responsible for assisting PhD candidate and member of Workentin research group, Mahdi Hesari.
- Projects involved in: BODIPY (fluorescent dye) synthesis and potential nanomaterial applications, diazarine synthesis and potential applications.
- Independently responsible for synthetic procedures assigned and applications in gold nanoparticle and graphene research.

Organic Chemistry Laboratory Technician

Jan 2011 – Oct 2011

AGAT Laboratories

- Responsible for gathering samples from incoming clients and distributing samples to appropriate laboratory sections.
- Responsible for government-mandated CCME determinations of hydrocarbon levels in both water and soil samples sent in from clients.
- Responsible for proper disposal of waste materials and glassware.
- Responsible for dispersal of incoming materials and solvents to appropriate laboratory sections.

SCHOLARSHIPS AND ACADEMIC HONOURS

Ontario Graduate Scholarship

2018

Dean's Honor List

2015

Pre-Thesis Award	2014
Dean's Honor List	2014
Dean's Honor List	2013
President's Honor List	2012

PRESENTATIONS

Canadian Society for Chemistry (CSC) Conference **June 2019**

- Oral Presentation: “*Synthesis of Bicyclononyne-Functionalized Gold Nanoparticles for Variable and Competitive Interfacial Strain-Promoted Alkyne-Azide Cycloaddition*”

Physical Organic Mini-Symposium (POMS) Conference **Nov 2017**

- Oral Presentation: “*Kinetically Modifiable Interfacial Strain-Promoted Alkyne/Nitrone Cycloaddition for Tunable Modifications of Gold Nanoparticles*”
- Awarded 1st Prize for Oral Presentation

Canadian Society for Chemistry (CSC) Conference **May 2017**

- Oral Presentation: “*The Clickable Gold Nanoclusters: An Exciting New Chapter in Au₂₅SR₁₈ Chemistry*”

PUBLICATIONS

1. Gunawardene P.N.; Corrigan J.F.; Workentin M.S. (2019), Golden Opportunity: A Clickable Azide-Functionalized [Au₂₅(SR)₁₈]⁻ Nanocluster Platform for Interfacial Surface Modifications. *J. Am. Chem. Soc.* 141, 30, 11781-11785.
2. Gunawardene P.N.; Luo W.; Polgar A.M.; Corrigan J.F.; Workentin M.S. (2019), Highly Electron-Deficient Pyridinium-Nitrones for Rapid and Tunable Inverse-Electron-Demand Strain-Promoted Alkyne-Nitrone Cycloaddition. *Org. Lett.* 21(14), 5547-5551.
3. Somasundaram V.; Gunawardene P.N.; Polgar A.M.; Workentin M.S.; Corrigan J.F. (2018), NHC-Ligated Group 11 Metal-Arylthiolates Containing An Azide Functionality Amenable to “Click” Reaction Chemistry. *Inorg. Chem.* 57(17): 11184-11192.

4. Luo W.; Gobbo P.; Gunawardene P.N.; Workentin M.S. (2017) Fluorogenic Gold Nanoparticle (AuNP) Substrate: A Model for the Controlled Release of Molecules from AuNP Nanocarriers via Interfacial Staudinger-Bertozzi Ligation. *Langmuir*. 33(8): 1908-1913.
5. Gobbo P.; Gunawardene P.; Luo W.; Workentin M.S. (2015) Synthesis of a Toolbox of Clickable Rhodamine B derivatives. *Syn. Lett.* 26(9): 1169-1174.

CERTIFICATION AND TRAINING

General Laboratory Safety and Hazardous Waste Management

2014

Comprehensive WHIMIS Certification